Zhiping Zheng   *Editor*

Recent Development in Clusters of Rare Earths and Actinides: Chemistry and Materials

Springer

173
Structure and Bonding

Aims and Scope

Structure and Bonding is a publication which uniquely bridges the journal and book format. Organized into topical volumes, the series publishes in depth and critical reviews on all topics concerning structure and bonding. With over 50 years of history, the series has developed from covering theoretical methods for simple molecules to more complex systems.

Topics addressed in the series now include the design and engineering of molecular solids such as molecular machines, surfaces, two dimensional materials, metal clusters and supramolecular species based either on complementary hydrogen bonding networks or metal coordination centers in metal-organic framework materials (MOFs). Also of interest is the study of reaction coordinates of organometallic transformations and catalytic processes, and the electronic properties of metal ions involved in important biochemical enzymatic reactions.

Volumes on physical and spectroscopic techniques used to provide insights into structural and bonding problems, as well as experimental studies associated with the development of bonding models, reactivity pathways and rates of chemical processes are also relevant for the series.

Structure and Bonding is able to contribute to the challenges of communicating the enormous amount of data now produced in contemporary research by producing volumes which summarize important developments in selected areas of current interest and provide the conceptual framework necessary to use and interpret mega-databases.

We welcome proposals for volumes in the series within the scope mentioned above. Structure and Bonding offers our authors and readers:

- OnlineFirst publication. Each chapter is published online as it is finished, ahead of the print volume
- Wide dissemination. The chapters and the volume will be available on our platform SpringerLink, one of the largest collections of scholarly content in the world. SpringerLink attracts more than 50 million users at 15.000 institutions worldwide.
- Easy manuscript preparation. Authors do not have to spend their valuable time on the layout of their contribution. Springer will take care of all the layout related issues and will provide support throughout the complete process.

More information about this series at http://www.springer.com/series/430

Zhiping Zheng
Editor

Recent Development in Clusters of Rare Earths and Actinides: Chemistry and Materials

With contributions by

P.C. Burns · Y-C. Chen · J-W. Cheng · Y-S. Ding · T. Han ·
S. Hickam · Z. Hou · S. Huang · R.A. Jones · X-J. Kong ·
J-L. Liu · L-S. Long · T. Shima · M-L. Tong · C. Wang ·
S. Wang · G-Y. Yang · X. Yang · Y. Zhang · Z. Zhang ·
Z. Zheng · X-Y. Zheng · Y-Z. Zheng

Editor
Zhiping Zheng
Department of Chemistry and Biochemistry
University of Arizona
Tucson, Arizona
USA

Preface

Lanthanides and actinides have traditionally been treated as the "footnote" elements in the periodic table. However, the recent past has witnessed increasing interest and efforts in the fundamental and applied research of these unique metal elements, due primarily to the interesting and potentially useful properties that are primarily governed by their unique f-electronic configurations. Among the numerous complexes containing these elements, polynuclear lanthanide and actinide complexes or clusters are arguably most intriguing, due not only to their complex and frequently aesthetically pleasing molecular structures but also the synthetic challenge, interesting physical properties, and useful applications, realized or envisioned.

It should be noted that the term "cluster" is used throughout this book. According to Cotton's original definition, a metal cluster is "a finite group of metal atoms that are held together mainly or at least to a significant extent, by bonds directly between metal atoms, even though some non-metal atoms may also be intimately associated with the cluster" (Cotton FA, Quarterly Rev Chem Soc 20:389–401, 1966). Should this original definition of "cluster" be strictly followed, few of the polynuclear complexes of the f-elements are qualified as such, as for most such compounds, there is no apparent metal–metal bonding, nor are there any significant interactions mediated by the commonly observed bridging ligands. The reference of such species as "clusters" is thus primarily from a structural perspective to convey the distinct polyhedral cluster-type core motifs. Also of note is the inclusion of cluster species of scandium and yttrium where available for the sake of completeness as these two elements are traditionally grouped with the lanthanides under the collective term of "rare earths."

The materials presented in this book are organized according to the research focus of individual chapters with the first four chapters concentrating on the synthetic and structural chemistry of these unique complex species and the remaining four chapters focusing on the interesting luminescence, magnetic, and catalytic properties, as well as chemical and materials applications of such substances.

The chapter by Professor Zhiping Zheng, Zhonghao Zhang, and Yanan Zhang surveyed the recent progress in the development of lanthanide hydroxide cluster complexes prepared by the approach of ligand-controlled hydrolysis of the lanthanide ions. With the large number of cluster complexes discussed, it has become clear that structurally and functionally diverse ligands including carboxylate, diketonate, phosphate, sulfonate, and polyoxometalate are capable of supporting the assembly of lanthanide hydroxide cluster species that exhibit a great variety of core motifs. It has also been shown that a number of cluster motifs are prevalent and can be used as secondary building units for the formal assembly of higher-nuclearity clusters. Collectively, the results presented in this chapter and those reviewed before provide validation that the chemistry of lanthanide hydroxide complexes, once a synthetic serendipity, is now a legitimate new paradigm of lanthanide coordination chemistry that is of fundamental interest and potential useful applications.

The ligand-controlled hydrolysis approach can be extended to heterometallic systems. Professors Xiangjian Kong and Lasheng Long, and Xiu-Ying Zheng discussed in their contribution the synthetic and structural chemistry of heterometallic cluster complexes containing both transition metal and lanthanide elements. It has been shown that the choice of the ligands is critical in dictating the construction of the cluster products which include cage-like, ringlike, ball-like, and disklike structures. The unique topological arrangement of the different metal ions within these clusters often leads to interesting optic, electric, magnetic, and catalytic properties.

The chapter by Professors Jian-Wen Cheng and Guo-Yu Yang focused its discussions on the construction of framework structures using lanthanide–copper heterometallic clusters and linear rigid bridging ligands containing both pyridine and carboxylate groups as building blocks. The readers are introduced to hydro-/solvothermal synthesis as a mild and soft technique for the preparation of a large number of crystalline lanthanide-containing materials, some of which exhibit exquisite structural beauty. The synergistic coordination between different ligands, with or without the working of templating species, was emphasized in the formation of the novel lanthanide cluster-organic frameworks.

Although not nearly as extensive as the chemistry of the rare earth elements, the wealth of the cluster chemistry of the 5f-elements was revealed by the contribution by Professor Peter C. Burns and Sarah Hickam. As exotic as it may sound, the authors admirably presented a clear and cogent discussion of recent developments in the field of actinide oxo clusters. The authors did an excellent job in laying out the development of peroxide-bridged uranyl clusters. The description of clusters based on organic capping ligands or on other inorganic bridging units sets the stage and provides tools for further fundamental inquiry and synthesis in the field.

Following the summary of the tour de force syntheses of lanthanide and actinide clusters, the remaining chapters bring the research out of the fundamental confinement into potentially practically useful realms by focusing on their unique luminescence and magnetic properties, as well as catalytic potentials. The authors

entertained futuristic applications of these unique substances for time-resolved immunoassays, highly efficient light-emitting devices, molecule-based magnetism, magnetic cooling technology, and stereospecific catalysis in polymerization reactions.

Professor Richard A. Jones and coauthors offered an in-depth discussion of the synthesis, structural characterization, and, most importantly, photophysical properties of a large number of 4f and d-4f cluster complexes with salen-type Schiff base ligands. The antenna-like function of the multidentate in efficiently sensitizing lanthanide emissions was firmly established. Moreover, the molecular design of "enclosed" structures for impressive luminescence properties was elegantly illustrated with the lanthanide ions encapsulated by the chromophoric ligands and thus shielded from luminescence-quenching solvent molecules.

The following two chapters detailed the unique magnetic properties associated with lanthanide ions in the form of polynuclear cluster species, lanthanide-exclusive or heterometallic with coexisting transition metal ion(s). Professor Ming-Liang Tong, Yan-Cong Chen, and Jun-Liang Liu focused their discussion on the magnetocaloric effect displayed by various lanthanide-containing cluster complexes. The authors provided ample examples of 4f clusters and 4f cluster-based coordination polymers with the hopes of establishing structure-magnetocaloric correlations among such giant magnetic cluster species.

Focusing on a different aspect of the magnetic properties of lanthanide-containing cluster compounds, Professor Yanzhen Zheng, Tian Han, and You-Song Ding surveyed thoroughly the recent development of lanthanide-based single-molecule magnets (SMMs). The authors painstakingly organized the magnetic compounds into groups from dinuclear 4f complexes to high-nuclearity 4f clusters. Detailed structural descriptions were provided, and corresponding magnetic properties were analyzed. The magneto-structural correlations revealed in the lanthanide-based SMMs will help gain further insights into the molecular design of cluster complexes with enhanced SMM properties.

The last chapter in this second group provides a much-desired overview of the chemical reactivity of rare earth compounds. Professor Zhaomin Hou and Takanori Shima described the synthesis, structure, and reactivity of molecular rare earth hydride clusters. Focusing on clusters consisting of the dihydride unit "(L)LnH$_2$" (L = ligand), the authors demonstrated that the molecular structure and reactivity of the clusters are significantly influenced by both the bulkiness of the ancillary ligands and the size of the metal ions. Unique reactivity toward CO, CO_2, H_2, and unsaturated C–C and C–N bonds was discussed, based on which the synergistic effects of the multiple metal hydride sites were established.

To the best of our knowledge, this is the first monograph dedicated to a very unique chemistry of the rare earth and actinide elements. As written and presented, I expect this book, in conjunction with the previous reviews and primary literature, to be an excellent resource for researchers entering the field and/or those wishing to know the current status of challenges and opportunities pertinent to the research of rare earth and actinide elements.

I would like to thank all authors who have put much effort in their valuable contributions that provide interested readers with the most exciting new development in this topical research field. I suspect it was their very desire to stimulate further development of this research that made them commit to this tremendous task.

Tucson, AZ, USA   Zhiping Zheng

Contents

Lanthanide Hydroxide Cluster Complexes via Ligand-Controlled Hydrolysis of the Lanthanide Ions

Zhonghao Zhang, Yanan Zhang, and Zhiping Zheng

Abstract We survey in this chapter the lanthanide hydroxide cluster complexes since the publication of the comprehensive review on the same subject (Handbook of physics and chemistry of rare earths 40:109–240, 2010). Specifically, polynuclear complexes with carboxylate, diketonate, phosphate, sulfonate, and polyoxometalate (POM) ligands featuring polyhedral cluster-type lanthanide-hydroxo (Ln-OH) core motifs are summarized. The synthetic procedures leading to the production of the cluster species and the unique cluster core motifs are the focus of the discussion. Within each ligand family, we organize the cluster complexes according to their nuclearity with the intention to demonstrate the formal assembly of higher-nuclearity complexes using smaller and recognizable motifs as secondary building units. It is clear that a number of such motifs are prevalent and are shared by cluster complexes with ligands that are structurally and functionally distinct. With the work reviewed previously and the rapidly increasing number of polynuclear lanthanide hydroxide complexes, we hope to validate that once a synthetic serendipity, the chemistry of lanthanide hydroxide complexes is now a legitimate new paradigm of lanthanide coordination chemistry that is of fundamental interest and potential useful applications.

Keywords Cluster • Hydrolysis • Hydroxide • Ligand • Nuclearity

Z. Zhang and Z. Zheng (✉)
Department of Chemistry and Biochemistry, The University of Arizona, Tucson, AZ 85721, USA
e-mail: zhiping@email.arizona.edu

Y. Zhang
College of Chemistry and Chemical Engineering, Shaanxi University of Science and Technology, Xi'an, Shaanxi 710021, China

Contents

1   Introduction

Polynuclear lanthanide hydroxide clusters are a class of fundamentally interesting and practically significant substances. They are attracting widespread current interest because of their appealing structures, synthetic challenges, and, most importantly, their potential applications. Continuous development of this burgeoning class of lanthanide complexes will help define a new paradigm of coordination chemistry of these unique metal elements. These fundamental efforts will also lead to the development of advanced materials of practical applications. For example, some lanthanide hydroxide clusters have been used as precursors for oxide-based electrical and optical materials [1], while others have been incorporated into polymers to prepare hybrid materials with enhanced mechanical properties [2]. In addition, intriguing molecule-based magnetic phenomena have been observed in lanthanide hydroxide clusters, potentially useful for quantum computing, magnetic information storage [3], and environmentally friendly magnetic refrigeration [4]. Some lanthanide hydroxide cluster complexes have been found to catalyze chemical transformations including hydrolytic cleavage of nucleic acids [5]. Some cluster complexes have also been proposed as potentially more efficient contrast-enhancing agents in biomedical imaging [6]. Indeed, molar relaxivities greatly surpassing those of current working force of contrast agents in magnetic resonance imaging (MRI) have been demonstrated in the laboratories. Moreover, fixation of atmospheric CO_2 by lanthanide hydroxide complexes has recently been reported, which bears significant environmental ramifications [7]. These exciting and useful applications of lanthanide hydroxide cluster complexes are probably the main driving force for the presently widespread interest in this special class of lanthanide-containing substance, and the extensive research activities, some of which being reviewed below, are consistent with this assessment.

In order to put the materials reviewed here in the developmental context and to help the readers who are interested in this research topic but not necessarily working in the field, the following explanatory notes are warranted:

1. Should Cotton's original definition [8] of a metal cluster be strictly followed, few of these polynuclear lanthanide hydroxide complexes may be qualified as

"clusters" simply because metal–metal bonding or electronic/magnetic interactions between individual metal centers are insignificant in these species. The use of the term is thus for the description of an assembly of metal atoms bridged by ligands from a mere structural perspective.

2. Lanthanide cluster compounds have been obtained by two major routes, one involving organometallic syntheses that typically generate moisture and/or air-sensitive species and the other under hydrolytic conditions but not necessarily in aqueous solutions. We limit our discussion to the cluster-type polynuclear lanthanide hydroxide complexes prepared by the latter means with a note that similar products have also been isolated but generally unexpectedly from some organometallic procedures.

3. As the chemistry of lanthanide hydroxide clusters has been enjoying a rapid development, there are now a large number of such compounds in the literature, with the number still growing at a fast pace. If species containing both lanthanides and other metal elements are included, this number is even bigger. We therefore limit our discussion to only new lanthanide-exclusive species since the publication of the 2010 review on a similar topic in the *Handbook of Physical and Chemistry of the Rare Earth Elements* [9].

2 Ligand-Controlled Lnathanide Hydrolysis

The lanthanide ions, prevalently trivalent, are hard Lewis acids that prefer O-based ligands with aqua coordination being most revealing. Lewis acid-activation of the coordinated water molecule renders the complex susceptible to hydrolysis, and if the pH condition is not carefully controlled, intractable product mixture consisting of lanthanide hydroxides and/or oxides are typically obtained. In fact, except for certain multiply charged chelating ligands such as ethylenediaminetetraacetate (EDTA), lanthanide complexes are generally prepared under highly acidic conditions. However, adventitious hydrolysis does occur with the production of lanthanide complexes characterized by the unexpected presence of hydroxo and/or, much less frequently, oxo groups in the cluster-type core structures. Though interesting, reports of such species were sporadic and reproducibility was problematic prior to the systematic work by Zheng and coworkers [10].

Attracted by the structural aesthetics and tempted by the potential of developing rational synthesis of such otherwise synthetically elusive species, we set out almost two decades ago to explore a systematic approach in which deliberate hydrolysis of the lanthanide ions is carried out in the presence of ligands capable of limiting the degree of hydrolysis of the lanthanide ions [11, 12]. Three considerations went into our hypothesis. First, adventitious hydrolysis was commonly accepted as being responsible for the unexpected production and isolation of the hydroxo/oxo complexes. But can such unintended hydrolysis be exploited in a deliberate and, more importantly, reproducible manner? Second, the presence of the primary ligand, with respect to the "secondary" hydroxo/oxo ligand, is probably critical in arresting or
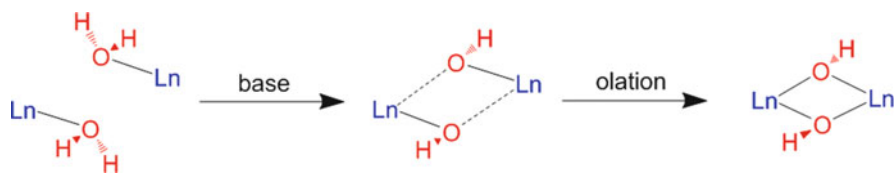
Fig. 1 Ligand-controlled hydrolytic approach to the assembly of lanthanide hydroxide clusters

limiting the otherwise extensive hydrolysis of the lanthanide ion to prevent the formation of the eventual precipitate products. If so, are there any specific structural and functional features required for such ligands? Third, despite the different lanthanide ions and/or ligands used, a number of these unexpected hydroxo cluster complexes share some prevalent Ln-OH core motifs. This suggests that a common reaction pathway may exist for the assembly of the cluster core. In other words, a systematic synthetic approach to these new lanthanide hydroxide complexes may be developed. Then, what is the scope of such a new paradigm of lanthanide coordination chemistry in terms of the nature of the lanthanide ions and any applicable supporting ligands?

These thoughts are reflected in the approach of "ligand-controlled hydrolysis" schematically shown in Fig. 1. Key to the success of this approach is the pre-occupation of part of the lanthanide coordination sphere by the supporting ligands, leaving only a limited number of sites available for aqua coordination. Deprotonation of the lanthanide-activated aqua ligands upon base addition is thus limited, and so is olation – the aggregation of the resulting lanthanide-hydroxo (Ln-OH) species via sharing of the hydroxo groups – leading eventually to cluster species rather than intractable precipitates of lanthanide oxides/hydroxides.
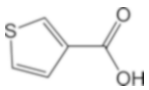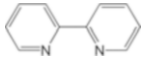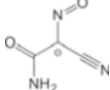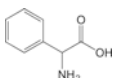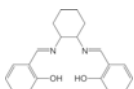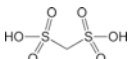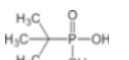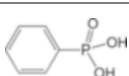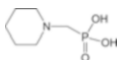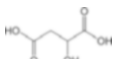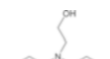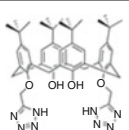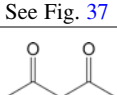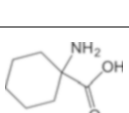
Significant progress in this new chemistry of lanthanide coordination has been made through our own efforts and those of others [9] since our first report of a pentadecanuclear europium cluster complex assembled by using tyrosine as the hydrolysis-limiting ligand [11]. With almost two decades of development, ligand-controlled hydrolysis has become a time-honored approach to the synthesis of lanthanide hydroxide/oxide clusters [9, 10].

The survey of the new cluster species and related discussion in this chapter are organized according to the type of ligands used for hydrolysis control (Table 1). Within each type of ligands, clusters are presented and discussed in ascending order of the cluster's nuclearity. A brief summary will be provided at the conclusion of the chapter in which the authors' personal perspective of what future directions this research may head toward is offered.

2.1 Carboxylates
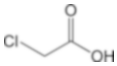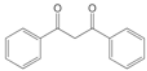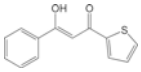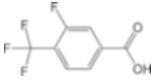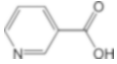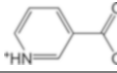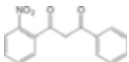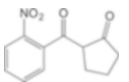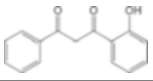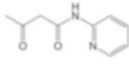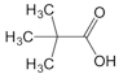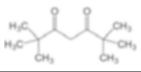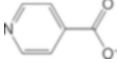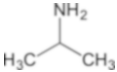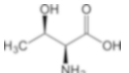
Carboxylates are time-honored ligands for lanthanide coordination. These include simple carboxylates such as formate and acetate [13–16], (poly)amino(poly)

Table 1 Abbreviations of ligands

3-TCAH	Thiophene-3-carboxylic acid	Fig. 10	
bipy	2,2′-Bipyridine	Fig. 5 Fig. 9	
ccnm	Carbamoylcyanonitrosomethanide	Fig. 48	
D-PhGly	D-Phenyl glycine	Fig. 28	
H_2L_6	*N,N′*-bis(salicylidene)-1,2-Cyclohexanediamine	Fig. 25	
H_2mds	Methylenedisulfonic acid	Fig. 38	
$H_2O_3P^tBu$	*Tert*-butyl phosphonic acid	Fig. 11 Fig. 34 Fig. 35	
H_2PhPO_3	Phenylphosphonic acid	Fig. 37	
H_2pmp	*N*-Pipe-ridinomethane-1-phosphonic acid	Fig. 36	
H_3mal	Malic acid	Fig. 43	
H_3tea	Triethanolamine	Fig. 21	
H_41	Tetrazole-functionalized calixarene	Fig. 13	
H_8TBC8A	*p-Tert*-butylcalix[8]arene	Fig. 37	See Fig. 37
Hacac	Acetylacetone	Fig. 22 Fig. 25 Fig. 31 Fig. 32	
HAcc	1-Amino-cyclohexanel-carboxylic acid	Fig. 2 Fig. 7	
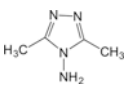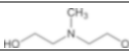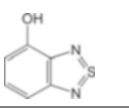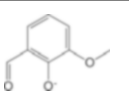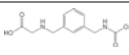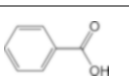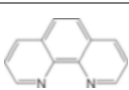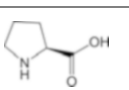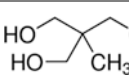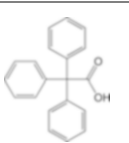
(continued)

Table 1 (continued)

HCAA	Chloroacetic acid	Fig. 16	
Hdbm	Dibenzoylmethane	Fig. 24 Fig. 28 Fig. 33	
Hhtp	(Z)-3-Hydroxy-3-phenyl-1-(thiophen-2-yl)prop-2-en-1-one	Fig. 26 Fig. 27	
HL	3-Fluoro-4-(trifluoromethyl)benzoic acid	Fig. 5 Fig. 9	
Hnic	Niconitic acid	Fig. 15 Fig. 17	
Hnic	Pyridinium nicotinate	Fig. 3	
Hnmc	*Ortho* ring-functionalized 1-phenylbutane-1,3-dione ligand 1	Fig. 23	
HO-Hdbm	*Ortho*-hydroxydibenzoylmethane	Fig. 29	
Hnpd	*Ortho* ring-functionalised 1-phenylbutane-1,3-dione ligand 2	Fig. 23	
HO^{i}Bu	Isobutyl alcohol	Fig. 35	
Hpaa	*N*-(2-pyridyl)-acetoacetamide	Fig. 21	
HO$_2$C^{t}Bu	Pivalic acid	Fig. 6 Fig. 11 Fig. 34 Fig. 35	
Hthd	2,2,6,6-Tetramethylheptane-3,5-dione	Fig. 30	
ina	Isonicotinate	Fig. 4 Fig. 12 Fig. 14	
^{i}PrNH$_2$	Isopropylamine	Fig. 35	
L-thre	L-Threonine	Fig. 18	

(continued)

Table 1 (continued)

L$_8$	4-Amino-3,5-dimethyl-1,2,4-triazole	Fig. 47	
mdeaH$_2$	*N*-Methyldiethanolamine	Fig. 6	
O-btd	4-Hydroxo-2,1,3-benzothiadiazolate	Fig. 24	
o-van	3-Methoxysalicylaldehydato anion	Fig. 6 Fig. 12	
PepCO$_2$H	2-[{3-(((*tert*-butoxycarbonyl)amino)methyl)ben-zyl}-amino]acetic acid	Fig. 33	
PhCO$_2$H	Phenylcarboxylic acid	Fig. 13	
phen	1,10-Phenanthroline	Fig. 48	
proline	L-Proline	Fig. 42	
py	Pyridine	Fig. 4	
thmeH$_3$	Tris(hydroxymethyl)ethane	Fig. 8	
tpaH	Triphenylacetic acid	Fig. 8	

carboxylates [10], and those that are structurally and functionally more sophisticated [17]. It should be noted that lanthanide carboxylate complexes have traditionally been prepared under highly acidic conditions (pH 3–4) due exactly to the hydrolysis concern alluded to above. It was Zheng et al. who explored the otherwise well-established lanthanide coordination chemistry with α-amino acids under pH conditions that are 2–3 orders of magnitude higher than the commonly accepted acidic conditions that uncovered the wealth of the "high-pH" coordination chemistry of the lanthanides [10–12]. Polynuclear lanthanide complexes characterized

by the presence of polyhedral lanthanide-oxo/hydroxo core motifs have been obtained with the amino acid ligands serving as hydrolysis-limiting and structure-supporting ligands. It is believed that the presence of amino group and other hydrophilic functional group(s) helps enhance the water solubility of the complexes formed at a lower pH, allowing subsequent deprotonation of any available aqua ligand(s) or hydrolysis to occur upon addition of a base. It is understandable that not all carboxylate ligands can be used to support the hydroxide complexes due to the fact that many lanthanide complexes with such ligands are insoluble and precipitate out before the pH of the reaction mixture may be enhanced. Equally possible is that researchers, wary of the formation of intractable lanthanide oxide/hydroxide precipitates, were simply trying to avoid any high-pH conditions.

This ligand-controlled hydrolytic approach has since become a standard method for the preparation of lanthanide hydroxide cluster complexes. Understandably, drastically different cluster species have been obtained depending sensitively on the supporting ligands used. The structure of the resulting cluster is also dependent on other reaction conditions such as the presence of any additional ligands or reactants, although these species may not eventually be incorporated into the final cluster products.

2.1.1 Tetra-, Penta-, and Heptanuclear Clusters

Long et al. reported two tetranuclear lanthanide hydroxide cluster complexes $[Ln_4(\mu_3\text{-OH})_4(Acc)_6(H_2O)_7(ClO_4)]\cdot(ClO_4)_7\cdot11H_2O\cdot(Ln = Dy, Yb)\cdot(HAcc = 1\text{-amino-cyclohexanel-carboxylic acid})$ by using amino acid-like ligand HAcc to control the lanthanide hydrolysis [18]. The cluster core, now a well-established motif in the literature, consists of four Ln^{3+} ions and four triply bridging hydroxo groups occupying the alternating vertices of a distorted cubane. Each edge of the Ln_4 tetrahedron is bridged by a carboxylate group of the organic ligand. The coordination spheres are completed by aqua ligands and for one of them, a monodentate perchlorate (Fig. 2a). It is of note that the reactions using two lighter lanthanide ions La^{3+} and Nd^{3+} under otherwise identical conditions produced trinulcear complexes of the common formula $[Ln_3(Acc)_{10}(H_2O)_6]\cdot(ClO_4)_9\cdot4H_2O\cdot(Ln = La, Nd)$ in which three lanthanide ions are in a linear arrangement with neighboring Ln^{3+} ions being bridged by four carboxylate groups from different Acc^- ligands. Each of the terminal Ln^{3+} ions is further coordinated by three aqua ligands and a carboxylate group, one being monodentate and the other, chelating (Fig. 2b). Formation of different products probably reflects the influences of the size and/or Lewis acidity of the lanthanide ions: The lighter and larger lanthanide ions (La^{3+} and Nd^{3+}) may not be as adequately Lewis acidic to be hydrolyzed as the heavier and smaller, and therefore more acidic Dy^{3+} and Yb^{3+}.

Using nicotinic acid in a similar capacity, Zheng et al. obtained and structurally characterized isostructural tetranuclear complexes of the formula $[Ln_4(\mu_3\text{-OH})_4(Hnic)_5(H_2O)_{12}](ClO_4)_8\cdot(Ln = Eu, Gd; Hnic = pyridinium nicotinate)$ [19]. The cluster core is the same as the aforementioned distorted cubane. However,
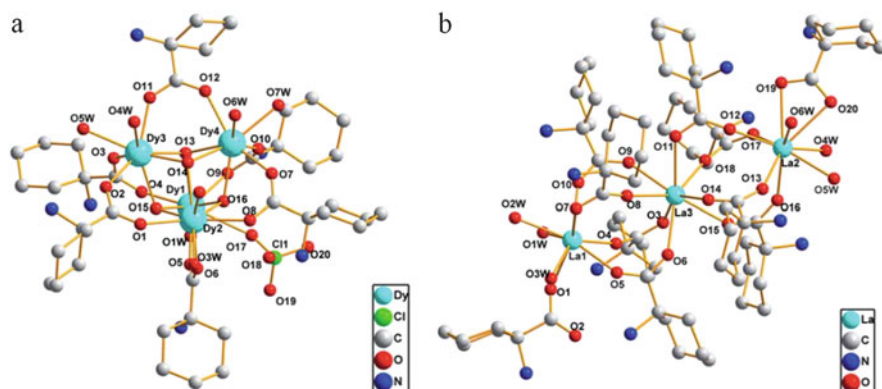
Fig. 2 Structure of: (**a**) $[Dy_4(\mu_3\text{-OH})_4(Acc)_6(H_2O)_7(ClO_4)]^{7+}$ and (**b**) $[La_3(Acc)_{10}(H_2O)_6]^{9+}$. Reprinted with the permission from [18] Copyright 2011 Royal Society of Chemistry
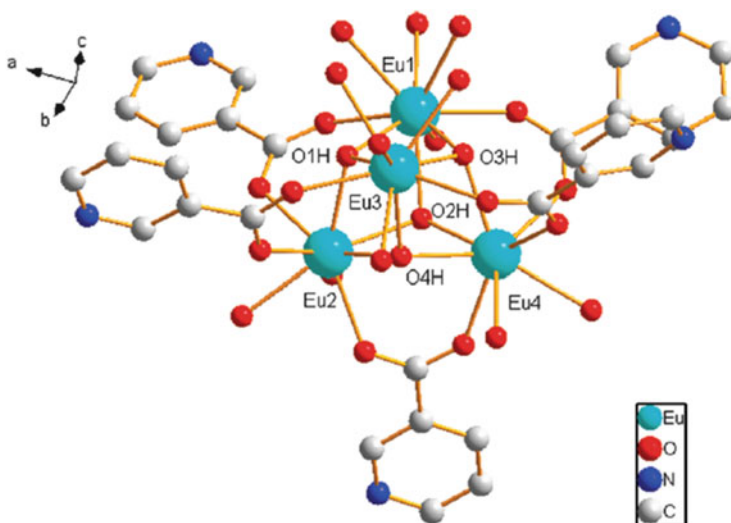
Fig. 3 Structure of the $[Eu_4(\mu_3\text{-OH})_4(Hnic)_5(H_2O)_{12}]^{8+}$. Reprinted with the permission from [19] Copyright 2009 American Chemical Society

only five of the six edges of the Ln_4 tetrahedron are bridged by the carboxylate group of the zwitterionic ligand; the coordination of the two unique lanthanide ions is made up for by using additional aqua ligands (Fig. 3).

When hydrolysis was carried out with the use of isonicotinate (ina) as supporting ligand, a tetranuclear complex formulated as $[Dy_4(\mu_3\text{-OH})_4(ina)_6(py)(CH_3OH)_7]$ $(ClO_4)_2 \cdot py \cdot 4CH_3OH$ (py = pyridine) was obtained [20]. Its core structure is the same as the one when nicotinic acid was used [19]. In addition to the bridging by in a carboxylate group, seven methanol molecules and one pyridine molecule help
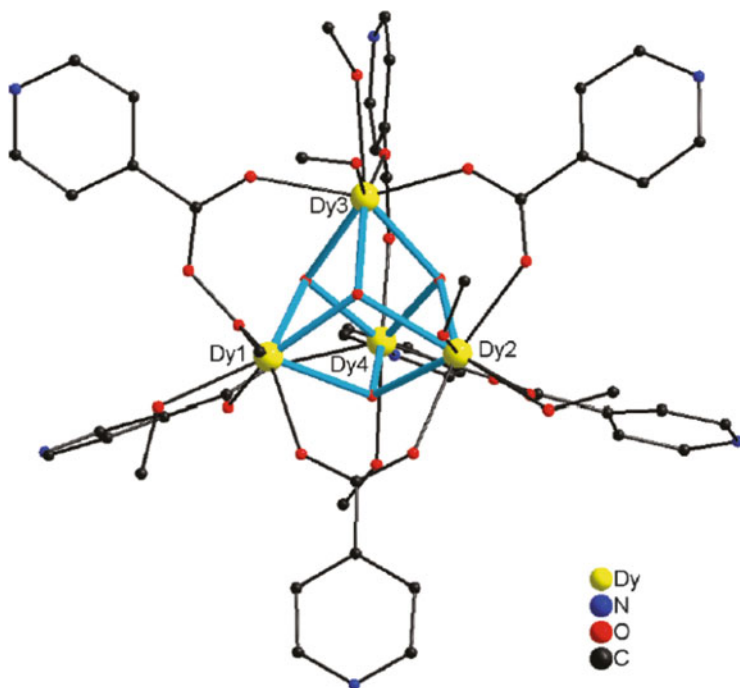
Fig. 4 Structure of $[Dy_4(\mu_3\text{-}OH)_4(ina)_6(py)(CH_3OH)_7]^{2+}$. Reprinted with the permission from [20] Copyright 2009 American Chemical Society

complete the metal coordination (Fig. 4). This cluster complex was shown to display properties characteristic of a single-molecule magnet.

In ligand-supported assembly of hydroxide clusters, the use of organic co-ligand (s) other than coordinating solvent(s) is a common practice. For example, Zhao et al. reported a tetranuclear complex $[Dy_4(\mu_3\text{-}OH)_2(L)_{10}(bipy)_2(H_2O)_2]$ (HL = 3-fluoro-4-(trifluoromethyl)benzoic acid; bipy = 2,2'-bipyridine) in which the metal coordination is achieved by both L and the chelating bipy, in addition to the hydroxo and aqua ligands [21]. The parallelogram-shaped cluster core consists of four coplanar lanthanide atoms connected by two μ_3-OH groups, one on each opposite sides of the plane. This motif is also frequently encountered in lanthanide hydroxide complexes. Two of the four edges of the parallelogram are each bridged by two carboxylate groups from different L ligands, while the other two are each bridged by one carboxylate group and one μ_2-H_2O molecule. The coordination sphere is completed by either a bipy or a monodentate L ligand (Fig. 5).

Two additional series of tetranuclear hydroxide clusters featuring the same core motif were reported. Murray et al. reported the isostructural complexes $[Ln_4(\mu_3\text{-}OH)_2(o\text{-}van)_4(O_2C^tBu)_4(NO_3)_2]\cdot CH_2Cl_2\cdot1.5H_2O\cdot(Ln = Gd,$ Dy; o-van = 3-methoxysalicylaldehydato anion; O_2C^tBu = pivalate or $(CH_3)_3CCO_2^-$) [22], while Powell et al. reported five isostructural complexes of the common formula $[Ln_4(\mu_3\text{-}OH)_2(mdeaH)_2(O_2C^tBu)_8]$ (mdeaH$_2$ = N-methyldiethanolamine; Ln = Tb,
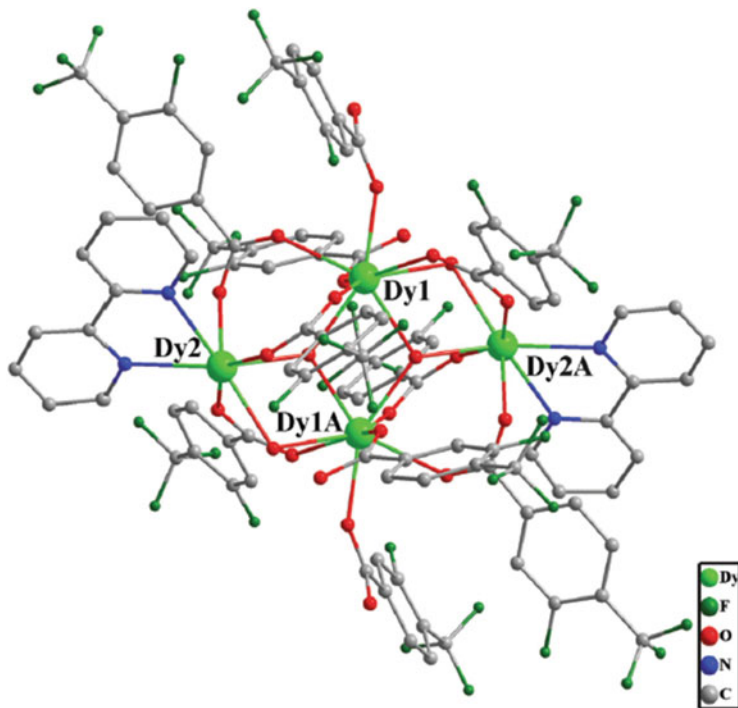
Fig. 5 Structure of $[Dy_4(\mu_3\text{-}OH)_2(L)_{10}(bipy)_2(H_2O)_2]$. Reprinted with the permission from [21] Copyright 2014 Royal Society of Chemistry

Dy, Ho, Er, Tm) [23]. Together with *o*-van in the former and mdeaH in the latter, pivalate serves in both series to stabilize the cluster core. Crystal structures of the complexes representing the two series are shown in Fig. 6.

With the use of 1-amino-cyclohexanel-carboxylic acid (Acc), Long et al. isolated $[Dy_5(\mu_3\text{-}OH)_6(Acc)_6(H_2O)_{10}]\cdot Cl_9\cdot 24H_2O$ [24] when $DyCl_3$ was used, which differs sharply from the tetranuclear species when $Dy(ClO_4)_3$ was used as the starting lanthanide salt [18]. The profound anion-template effects on the cluster nuclearity have previously been established [25], but we note that the anions do not participate in the metal coordination in either of these two complexes. Thus, the exact roles played by the anions in dictating the outcome of the reactions carried out under otherwise identical conditions remain to be understood.

In the cluster core, the five Dy^{3+} ions are organized into a trigonal bipyramidal geometry. Alternatively, it may be viewed as two distorted cubanes joined together by sharing a trimetallic face. Each triangular metal face is capped by a μ_3-OH group, while each non-equatorial metal edge is bridged by an Acc carboxylate group. The coordination sphere of each Dy^{3+} ion is completed by two aqua ligands (Fig. 7).

Collison et al. reported two isostructural heptanuclear complexes $[Ln_7(OH)_6(thmeH_2)_5(thmeH)(tpa)_6(MeCN)_2](NO_3)_2\cdot(Ln = Gd, Dy; thmeH_3 = tris$
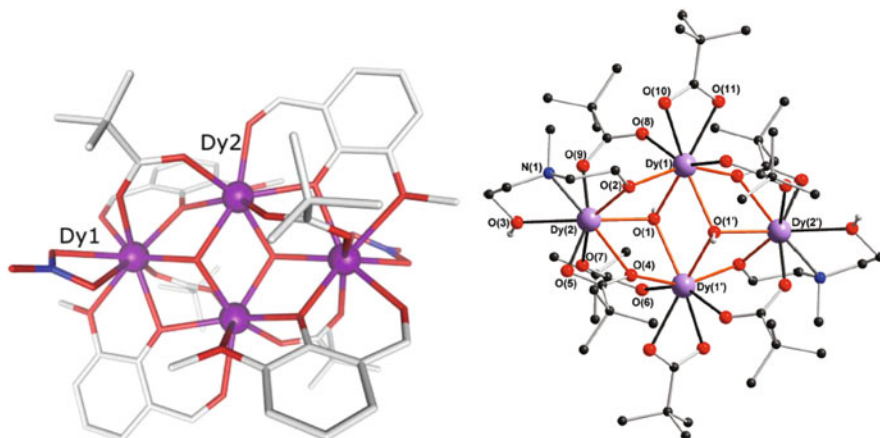
Fig. 6 Structures of [Dy$_4$(μ_3-OH)$_2$(o-van)$_4$(O$_2$C^{t}Bu)$_4$(NO$_3$)$_2$] (*left*) and [Dy$_4$(μ_3-OH)$_2$(mdeaH)$_2$(O$_2$C^{t}Bu)$_8$] (*right*). Reprinted with the permission from [22] Copyright 2011 Royal Society of Chemistry and [23] Copyright 2010 American Chemical Society
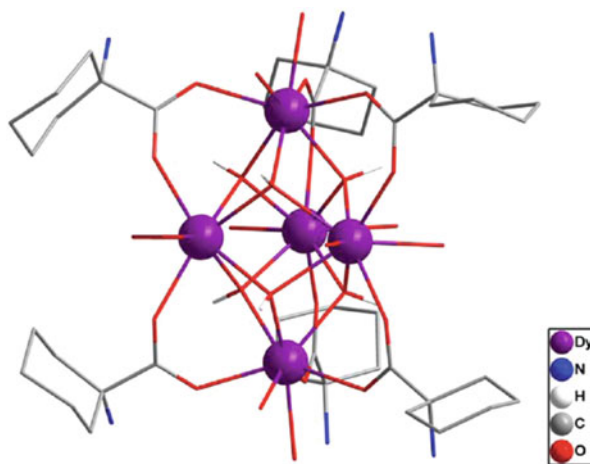
Fig. 7 Structure of [Dy$_5$(μ_3-OH)$_6$(Acc)$_6$(H$_2$O)$_{10}$]$^{9+}$. Reprinted with the permission from [24] Copyright 2012 American Chemical Society

(hydroxymethyl)ethane; tpaH = triphenylacetic acid) [26]. The synthesis was carried out under solvothermal conditions using a mixture of lanthanide nitrate hydrates, thmeH$_3$, tpaH, and triethylamine in acetonitrile. The cluster core consists of seven coplanar Ln^{3+} ions organized into a disc-like hexagon with six peripheral Ln^{3+} ions occupying the vertices of the hexagon and the remaining Ln^{3+} ion sitting at the center of hexagon and connecting the peripheral metal ions through six μ_3-OH groups. Alternatively this cluster core can be viewed as two of the coplanar tetranulcear units, such as those shown in Figs. 5 and 6, joined together by two μ_3-OH groups. In effect, the six μ_3-OH groups are alternatively above and below the

Fig. 8 Structure of [Ln$_7$((μ_3-OH)$_6$(thmeH$_2$)$_5$(thmeH)(tpa)$_6$(MeCN)$_2$]$^{2+}$ (color code: *purple*, Ln; *yellow*, O; *blue*, N; and *skeletal*, C). Reprinted with the permission from [26] Copyright 2011 Royal Society of Chemistry
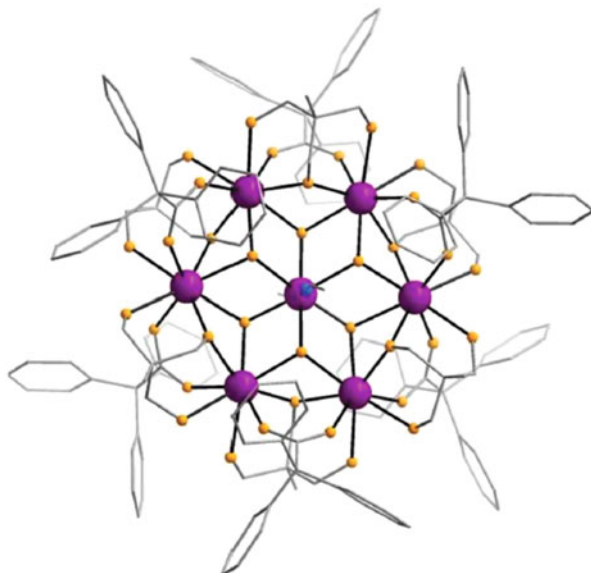
disc plane. In addition to the coordination by these OH groups, the central lanthanide ion is further coordinated with two *trans*-disposed acetonitrile molecules. Each edge of the lanthanide hexagon is bridged by one tpa carboxylate group and one thmeH$_2^-$ or thmeH$_2^-$ ligand (Fig. 8).

2.1.2 Decanuclear and Higher-Nuclearity Clusters

An increasing number of lanthanide hydroxide complexes of even higher nuclearities have also appeared in the literature, although their assembly generally cannot be predicted. A number of factors may be responsible for the formation of such giant cluster species. These include the nature of the ligands, the lanthanide ions, available anionic templates, as well as pH condition. For example, in the aforementioned work by Zhao and coworkers in which tetranuclear cluster complexes were obtained, a decanuclear complex [Dy$_{10}$(μ_3-OH)$_8$(L)$_{22}$(bipy)$_2$(H$_2$O)$_2$]·5H$_2$O·(L = 3-fluoro-4-(trifluoromethyl)benzoate) was also isolated when the reaction pH was adjusted to 10 with NaOH prior to the hydrothermal treatment [21]. The complex structure as shown in Fig. 9 has a formal crystallographic center symmetry. The Dy^{3+} ions are connected by eight μ_3-OH groups and the L carboxylate groups. The coordination spheres are further fulfilled by either chelating bipy or aqua ligands.

It should be noted that a gadolinium complex [Gd$_{10}$(μ_3-OH)$_8$(3-TCA)$_{22}$(H$_2$O)$_4$]·(3-TCAH = thiophene-3-carboxylic acid) with a similar decanuclear core (Fig. 10) had been reported by Bu and his coworkers, but the primarily supporting ligand is different [27]. In addition, no co-ligand was utilized.
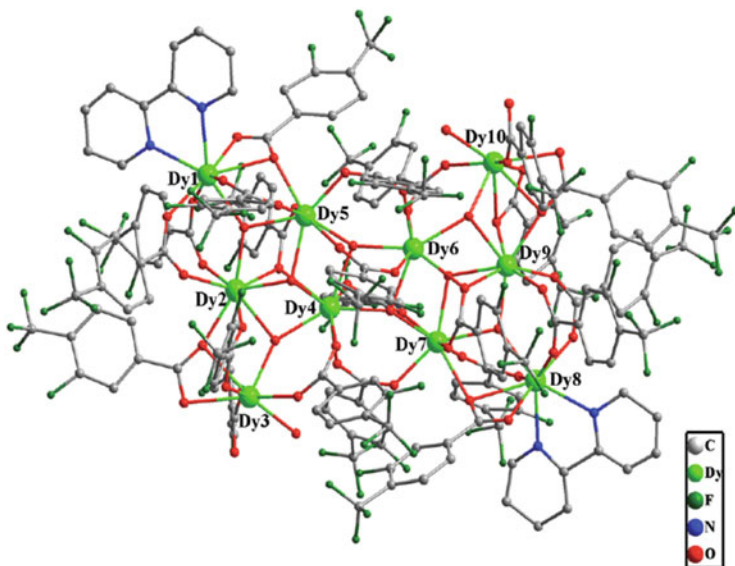
Fig. 9 Structure of $[Dy_{10}(\mu_3\text{-}OH)_8(L)_{22}(bipy)_2(H_2O)_2](L = 3\text{-fluoro-4-(trifluoromethyl)benzoate}.$
Reprinted with the permission from [21] Copyright 2014 Royal Society of Chemistry
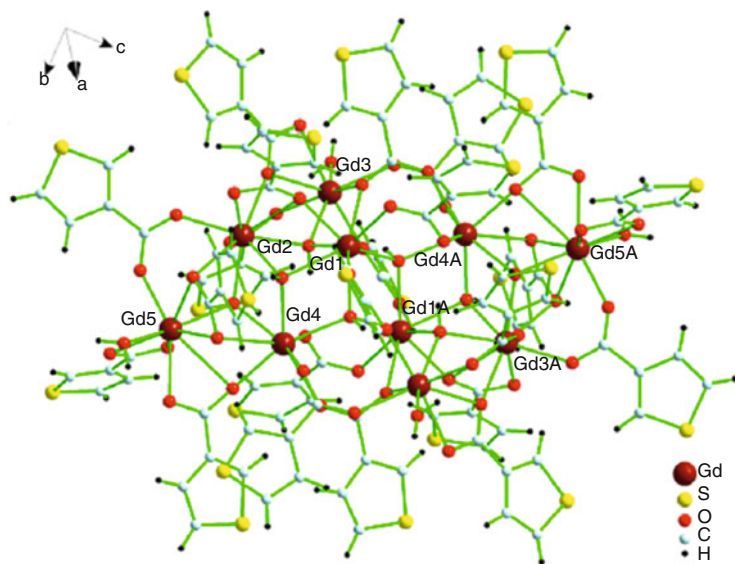
Fig. 10 Structure of $[Gd_{10}(\mu_3\text{-}OH)_8(3\text{-}TCA)_{22}(H_2O)_4]$. Reprinted with the permission from [27]
Copyright 2013 American Chemical Society
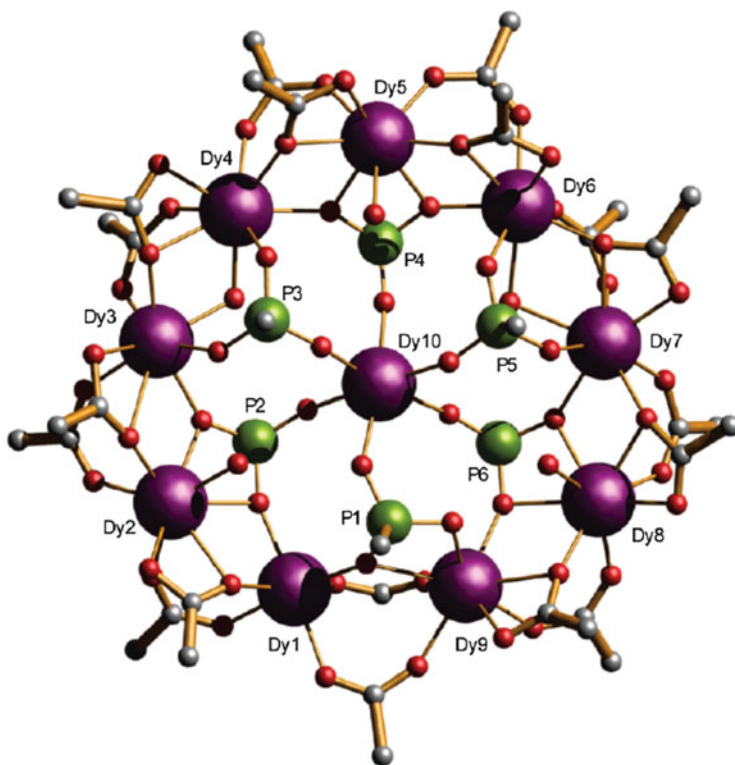
Fig. 11 Structure of $[Dy_{10}(O_2C^tBu)_{18}(O_3P^tBu)_6(OH)(H_2O)_4]^-$. Reprinted with the permission from [28] Copyright 2014 Royal Society of Chemistry

Distinctly different from the above compounds, two lanthanide complexes of the common formula $[Co_3(\mu_3-O)(O_2C^tBu)_6(py)_3][Ln_{10}(O_2C^tBu)_{18}(O_3P^tBu)_6(OH)(H_2O)_4]$ (Ln = Dy, Gd) reported by Winpenny et al. possess a decanuclear cluster core that features a nine-metal ring surrounding a central metal atom in the complex anion [28]. The lanthanide ions are essentially coplanar with those in the ring occupying at the vertices of a nearly regular nonagon, each connecting the central lanthanide ion via an O of the O_3P^tBu ligand. Connection between neighboring metal atoms in the ring is achieved by O_3P^tBu, O_2C^tBu, and bridging aqua and/or OH ligands (Fig. 11).

With isonicotinic acid (Hina) and *o*-vanillin as protecting ligands, Murray et al. obtained a decanuclear complex $[Dy_{10}(\mu_4-O)_2(\mu_3-OH)_6(o\text{-}van)_6(ina)_{13}(H_2O)_2](NO_3)$ that can be viewed as two pentanuclear complex units bridged by one ina carboxylate group [29]. This pentanuclear cluster core has the structure of a distorted trigonal bipyramid similar to the one discussed above [24]. Within each pentanuclear unit, the metal ions are bridged by one μ_4-O group, three μ_3-OH groups, the ina carboxylate, and the O atom of the deprotonated
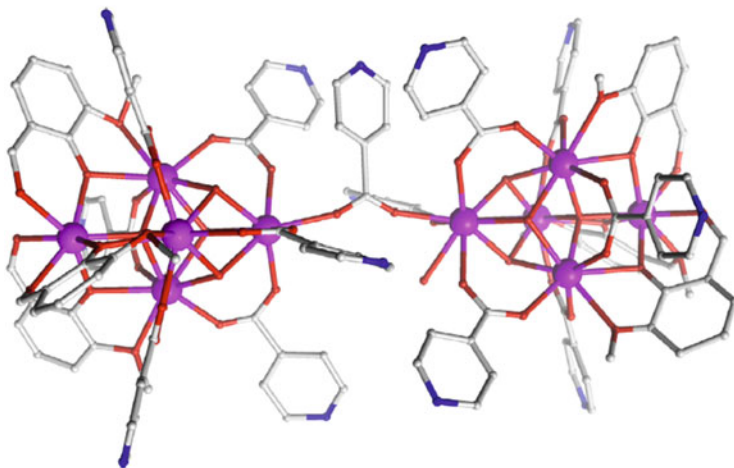
Fig. 12 Structure of $[Dy_{10}(\mu_4\text{-O})_2(\mu_3\text{-OH})_6(o\text{-van})_6(\text{ina})_{13}(H_2O)_2]^+$ cluster. Reprinted with the permission from [29] Copyright 2013 Elsevier

phenol groups of the o-van ligands. The coordination sphere is completed by the OH and MeO groups of the o-van ligand and aqua ligands (Fig. 12).

With the combined use of structurally or functionally more sophisticated ligands, lanthanide hydroxide complexes of even higher nuclearities can be obtained. For example, Ogden et al. reported the use of a tetrazole-functionalized calixarene (**1**) in combination with acetic acid or phenylcarboxylic acid in the controlled assembly of lanthanide cluster complexes [30]. The synthesis was carried out by using a mixture of ligand **1**, $Dy(NO_3)_3(DMSO)_3$, and ammonium acetate or ammonium benzoate in H_2O/ethanol. With the sterically more hindered phenylcarboxylate, they obtained a dodecanuclear complex $[Dy_{12}(\textbf{1}\text{-3H})_3(\textbf{1}\text{-}$ $2H)_3(PhCO_2)_5(\mu_3\text{-OH})_{16}(H_2O)_{21}]$ (**1**-3H and **1**-2H represent, respectively, triply and doubly deprotonated ligand **1**), whereas with acetate, they isolated a nonadecanuclear complex $[Dy_{19}(\textbf{1}\text{-3H})_{11}(\textbf{1}\text{-2H})_{11}(CH_3CO_2)_6(\mu_3\text{-}$ $OH)_{26}(H_2O)_{30}]$. The cluster core of $[Dy_{12}(OH)_{16}]$ in the smaller complex can be viewed as two trigonal bipyramids and one distorted tetrahedron joined together by sharing vertices (Fig. 13a, top) with each of the triangular Dy3 faces being capped by a μ_3-OH group. The cluster core is encapsulated by the organic protecting sphere formed by both the carboxylate and the calixarene ligands (Fig. 13a, bottom). In the larger complex, the core of $[Dy_{19}(\mu_3\text{-OH})_{26}]$ can be conveniently viewed as being elongated by adding one trigonal bipyramid and one distorted tetrahedron to the dodecanuclear core. Alternatively the core may be more straightforwardly viewed as three trigonal bipyramids being sandwiched by two distorted tetrahedra with neighboring polyhedra being joined together by sharing a Dy-vertex (Fig. 13b, top). Corresponding to the larger and elongated cluster core, there are 26 μ_3-OH groups, each capping a triangular metal face. This hydroxide cluster core is protected in an organic sphere composed of acetate ligands and the tetrazole groups of the
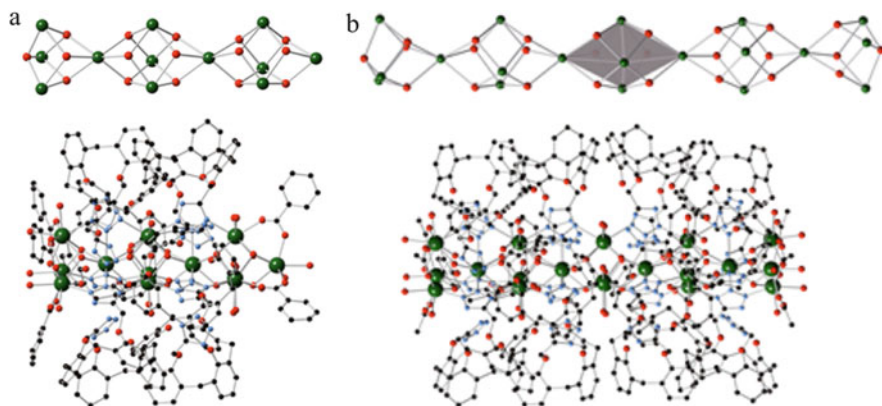
Fig. 13 Structures of the cluster core (*top*) and the complex (*bottom*) of: (**a**) $[Dy_{12}(\mathbf{1}\text{-}3H)_3(\mathbf{1}\text{-}2H)_3(PhCO_2)_5(OH)_{16}(H_2O)_{21}]$ and (**b**) $[Dy_{19}(\mathbf{1}\text{-}3H)(\mathbf{1}\text{-}2H)_{11}-(CH_3CO_2)_6(OH)_{26}(H_2O)_{30}]$. Reprinted with the permission from [30] Copyright 2014 American Chemical Society

calixarene ligand (Fig. 13b, bottom). In both complexes, aqua ligands fulfill the rest of the metal coordination sphere.

Even larger lanthanide hydroxide clusters have also been reported, generally as unintended outcome of reactions originally aiming at different synthetic targets. As an example, three 26-metal lanthanide hydroxide cluster complexes were reported by two different groups. They are $[Er_{26}I(\mu_3\text{-}OH)_{20}(\mu_3\text{-}O)_6(NO_3)_9(ina)_{33}(OH)_3(H_2O)_{33}]$ reported by Xue et al. [31] and $[Ho_{26}(ina)_{28}(CH_3COO)_4(CO_3)_{10}(OH)_{26}(H_2O)_{18}]\cdot 20H_2O$ and $[Er_{26}(ina)_{29}(CH_3COO)_3(CO_3)_{10}(OH)_{26}(H_2O)_{19}]\cdot 26H_2O$ by Xu and his coworkers [32]. The first member of the three was isolated from a hydrothermal reaction using a mixture of Er_2O_3, AgI, isonicotinic acid, and HNO_3, whereas the others were obtained, also under hydrothermal conditions, using a mixture of Ln_2O_3, $Mn(OAc)_2\cdot 4H_2O$, isonicotinic acid, and formic acid.

Surprisingly, despite the different synthetic procedures and the compositions of the final product, the polyhedral arrangement of the core metal atoms is actually the same with the difference being only in the type and the number of bridging ligands. As such, only the representative structure of $[Er_{26}I(\mu_3\text{-}OH)_{20}(\mu_3\text{-}O)_6(NO_3)_9(ina)_{33}(OH)_3(H_2O)_{33}]$ is shown in Fig. 14. All three complexes have the same number (26) of triply bridging oxo/hydroxo groups. Furthermore, in each of the lanthanide-oxo/hydroxo cores there are a total of 42 bridging ligands that connect adjacent lanthanide atoms. These bridging ligands are all O-based with ina being common in all three clusters. The remaining bridging ligands are either inorganic (NO_3^-, CO_3^{2-}) or acetate ion. Coordination of the lanthanide ions is completed by aqua and other small-entity ligands that do not alter the overall complex structures.

In addition to the essential presence of bridging hydroxo group, anion species including O^{2-}, N_3^-, NO_3^-, halides, CO_3^{2-}, and ClO_4^- have frequently been
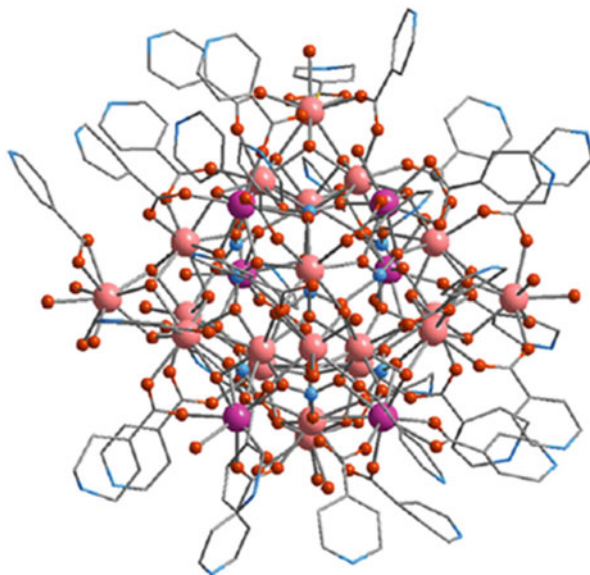
Fig. 14 Structure of $[Er_{26}I(\mu_3\text{-}OH)_{20}(\mu_3\text{-}O)_6(NO_3)_9(ina)_{33}(OH)_3(H_2O)_{33}]$. Reprinted with the permission from [31] Copyright 2008 Elsevier

observed in high-nuclearity lanthanide hydroxide clusters wherein such anions serve presumably to template the assembly of the giant clusters. We note that the genesis of these anions (if they are not from the starting materials) and/or their role (s) constitute an active research topic for which definitive answers remain unclear. In the work reported by Hong et al., two 36-metal cluster complexes formulated as $[Ln_{36}(nic)_{36}(OH)_{49}(O)_6(NO_3)_6(N_3)_3(H_2O)_{20}]\cdot Cl_2 \cdot 28H_2O \cdot (Ln = Gd, \quad Dy)$ were obtained from a hydrothermal reaction using a mixture of lanthanide chloride, NaN_3, nicotinic acid, and HNO_3 [33]. Structural studies by single-crystal X-ray diffraction revealed 36 Ln^{3+} ions organized into a cage-like structure featuring coordination by bridging OH^-, O^{2-}, N_3^-, and NO_3^- groups (Fig. 15a). The distorted cubane units of $[Ln_4(\mu_3\text{-}OH)_4]^{8+}$ are easily recognizable in the core structure, together with other types of Ln-OH motifs that link these cubane units. The Ln^{3+} coordination sphere is completed by aqua ligands, carboxylate O atoms, as well as the nic chelating carboxylate groups (Fig. 15b).

Tong et al. reported two high-nuclearity complexes $[Gd_{38}(\mu\text{-}O)(\mu_8\text{-}ClO_4)_6(\mu_3\text{-}OH)_{42}(caa)_{37}(H_2O)_{36}(EtOH)_6](ClO_4)_{10}\cdot(OH)_{17}\cdot 14DMSO\cdot 13H_2O$ and $[Gd_{48}(\mu_4\text{-}O)_6(\mu_3\text{-}OH)_{84}(caa)_{36}(NO_3)_6(H_2O)_{24}(EtOH)_{12}(NO_3)Cl_2]Cl_3 \cdot 6DMF\cdot 5EtOH\cdot 20H_2O$ (Hcaa = chloroacetic acid) [34]. The profound influence of the nature of the anions on the structure of the resulting clusters is clearly shown here. While the reaction of a mixture containing chloroacetic acid, gadolinium perchlorate, and NaOH in a water/ethanol/DMSO mixed solvent produced the 38-metal cluster complex, the use of gadolinium nitrate or chloride hydrate in place of gadolinium perchlorate afforded the 48-metal complex under nearly identical reaction conditions.
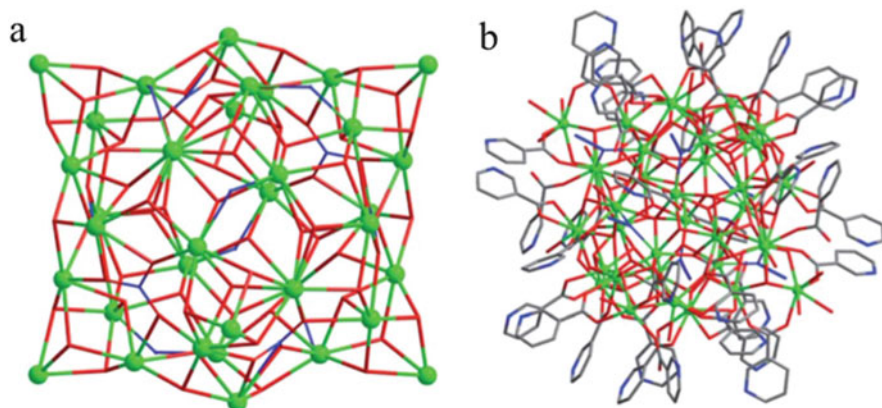
Fig. 15 Structure of: (**a**) $[Ln_{36}(nic)_{36}(OH)_{49}(O)_6(NO_3)_6(N_3)_3(H_2O)_{20}]^{2+}$ and (**b**) the hydroxide cluster core. Reprinted with the permission from [33] Copyright 2013 Royal Society of Chemistry

The 38 Gd^{3+} ions in the smaller complex are organized into a cage-like structure featuring twelve vertex-sharing $\{Gd_4\}$ tetrahedra with the metals joined together by one μ-O, μ_8-ClO_4^-, μ_3-OH, and caa carboxylate groups. The coordination sphere is completed by aqua and ethanol ligands (Fig. 16a). In comparison, the 48 metal atoms in the larger complex are connected by six μ_4-O anions, 84 μ_3-OH groups, and caa carboxylate groups into a barrel-like structure. One NO_3^- anion and two Cl^- anions are imbedded inside the void of the barrel through hydrogen bonding. Aqua and ethanol ligands as well as NO_3^- anions complete the lanthanide coordination (Fig. 16b).

Although nicotinic acid was used, a very similar hydroxide cluster core as in the work by Tong et al. [34] with an identical arrangement of 48 lanthanide ions was reported by Hong and coworkers [35]. Specifically, using a mixture of NaN_3, nicotinic acid, $NaNO_3$, and erbium chloride, a hydrothermal reaction produced $\{[Cl_2\&(NO_3)]@[Er_{48}(nic)_{44}(OH)_{90}(N_3)(H_2O)_{24}]\}\cdot6Cl\cdot35H_2O$ wherein the occlusion of two Cl^- and one NO_3^- ions (Fig. 17b) is also observed. The barrel-like cluster core may alternatively be viewed as an $\{Er_{12}\}$ ring being sandwiched between two $\{Er_{18}\}$ wheels (Fig. 17a). The assembly of the two almost identical cluster cores suggests that this cluster motif, though obtained in different reactions, may be a common one in the family of lanthanide hydroxide complexes.

The significant templating roles played by small anions are further exemplified in the assembly of $[Er_{60}(\text{L-thre})_{34}(\mu_6\text{-}CO_3)_8(\mu_3\text{-}OH)_{96}(\mu_2\text{-}O)_2(H_2O)_{18}]$ $Br_{12}(ClO_4)_{18}(H_2O)_{40}$ (L-thre = L-threonine) by Zheng and his coworkers. This giant complex was prepared by the hydrolysis of Er^{3+} using L-threonine as supporting ligand [36]. The 60 Er^{3+} ions are arranged into a discrete sodalite cage (Fig. 18a) with each of its 24 vertices being occupied by an $[Er_4(\mu_3\text{-}OH)_4]^{8+}$ cubane unit (Fig. 18b). Alternatively, the cage structure can be viewed as being built by using two different yet related cubane-wheel second-building units (SBUs), one being dodecanuclear (composed of four vertex-sharing cubanes) and the other
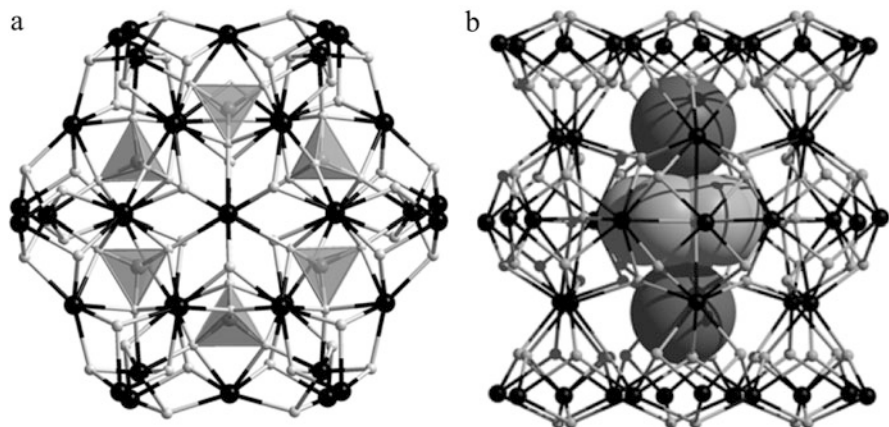
Fig. 16 Structure of: (**a**) $\{Gd_{38}(O)(ClO_4)_6(OH)_{42}\}^{64+}$ and (**b**) $\{Gd_{48}(\mu_4\text{-O})_6(\mu_3\text{-OH})_{84}Cl_2(NO_3)\}$. Reprinted with the permission from [34] Copyright 2013 Wiley-VCH Verlag GmbH & Co
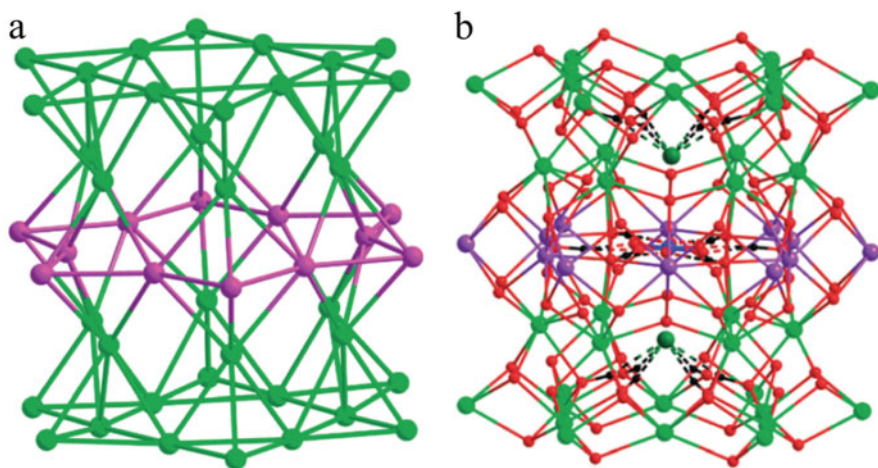
Fig. 17 Structure of: (**a**) the cluster core of $\{[Cl_2\&(NO_3)]@[Er_{48}(nic)_{44}(OH)_{90}(N_3)\text{-}(H_2O)_{24}]\}$ $6Cl\cdot35H_2O$ with the encapsulated anions and bridging atoms displayed and (**b**) the metallic backbone of the cluster core. Reprinted with the permission from [35] Copyright 2013 Royal Society of Chemistry

octadecanuclear (consisting of six vertex-sharing cubanes) with the latter being templated by a $\mu_6\text{-CO}_3^{2-}$ ion. The lanthanide hydroxide cluster core is encapsulated by L-thre$^-$ ligands (Fig. 18c).

More recently, three isostructural cluster complexes with a record-high 104 lanthanide atoms were reported by Long and his coworkers [37]. These complexes, formulated as $[Nd_{104}(ClO_4)_6(CH_3COO)_{60}(\mu_3\text{-OH})_{168}(\mu_4\text{-O})_{30}(H_2O)_{112}]$ $(ClO_4)_{18}\cdot(CH_3CH_2OH)_8\cdot xH_2O$ and $[Ln_{104}(ClO_4)_6(CH_3COO)_{56}(\mu_3\text{-OH})_{168}$
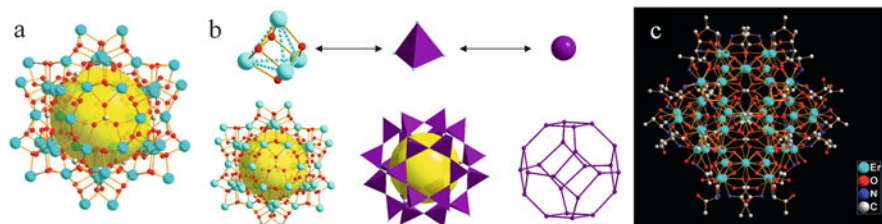
Fig. 18 (**a**) Structure of the 24-cubane cluster core in $[Er_{60}(L\text{-thre})_{34}(\mu_6\text{-}CO_3)_8(\mu_3\text{-OH})_{96}$ $(\mu_2\text{-O})_2(H_2O)_{18}]^{30+}$; (**b**) formal assembly of a discrete sodalite cage by using cluster cubane units as SBUs; and (**c**) structure of the cationic 60-metal complex. Reprinted with the permission from [36] Copyright 2009 American Chemical Society

$(\mu_4\text{-O})_{30}(H_2O)_{112}]\cdot(ClO_4)_{22}\cdot(CH_3CH_2OH)_2\cdot xH_2O$ (Ln = Nd, Gd), were obtained from the reaction of *N*-acetyl-D-glucosamine, $Co(CH_3COO)_2\cdot 4H_2O$, and lanthanide perchlorate in ethanol under either solvothermal or ambient-pressure conditions. It is of note that Co^{2+} was not incorporated into the product, but replacing the transition metal acetate for sodium acetate did not lead to the same cluster species; the role of the transition metal ion remains unclear. The 104 metal ions are organized into an aesthetically pleasing four-shell cage structure with an ideal cubic symmetry (Fig. 19a). An alternative way of looking at the structure is that it can be built by 24 square pyramidal $[Ln_5(\mu_4\text{-O})(\mu_3\text{-OH})_4]^{9+}$ and 8 $[Ln(\mu_3\text{-OH})_6]^{3-}$ units. Every four adjacent units of $[Ln_5(\mu_4\text{-O})(\mu_3\text{-OH})_4]^{9+}$ are joined together by centering around one $\mu_4\text{-O}^{2-}$ anion to form an $[Ln_{16}(\mu_4\text{-O})_5(\mu_3\text{-OH})_{20}]^{18+}$ wheel that occupies one vertex of a perfect octahedron (Fig. 19b). The Ln^{3+} ions are further connected by acetate ligands (Fig. 19c). Water molecules and 6 ClO_4^- anions are encapsulated within the void of the nanoscopic cluster. The 104-Gd complex has been shown to possess one of the largest magnetocaloric effects measured for all lanthanide-exclusive clusters reported. These magnetic lanthanide clusters are of interest in developing energetically more efficient and more environmentally friendly cooling technologies.

2.2 Diketonates

Equally extensively utilized in lanthanide coordination chemistry are diketonate-based ligands [38–43]. Recent years have seen their increasing use in supporting the assembly of lanthanide hydroxide cluster complexes [44, 45]. A number of cluster core motifs have been reported and are collected in Fig. 20 with the planar tetranuclear and square pyramidal pentanuclear motifs being more frequently observed than the rest. We note that lanthanide hydroxide clusters supported by carboxylate-based ligands exhibit a much greater structural variety than those with diketonate ligands.
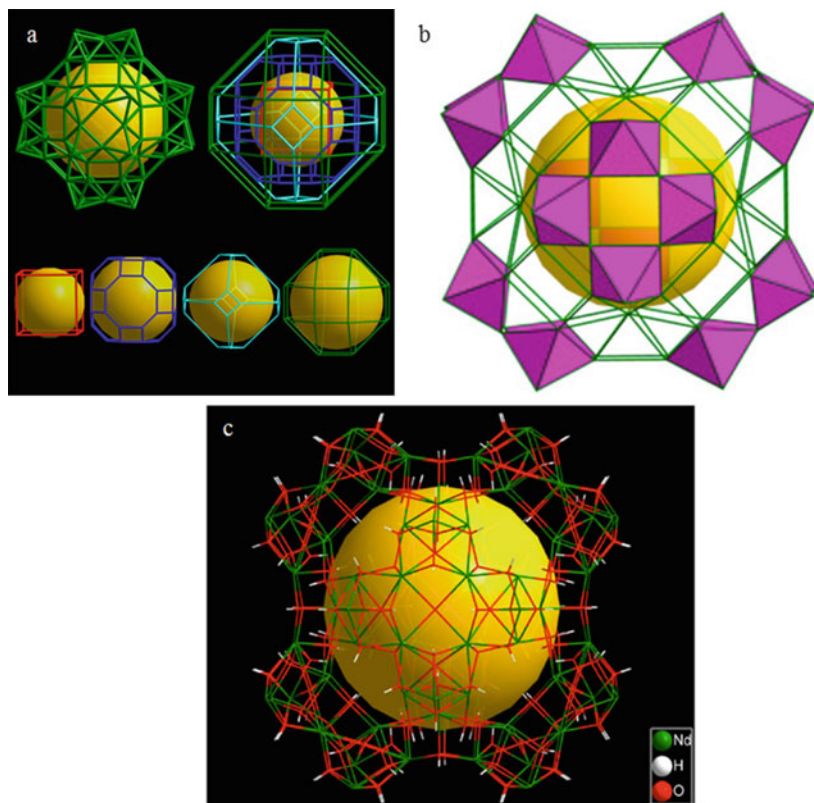
Fig. 19 (**a**) Four-shell organization of the 104 lanthanide atoms; (**b**) building the cluster core by using square pyramidal SBUs; and (**c**) structure of the cationic complex $[Ln_{104}(\mu_3\text{-OH})_{168}(\mu_4\text{-O})_{30}]^{84+}$ showing the coordination/passivation of the cluster core by acetate ligands. Reprinted with the permission from [37] Copyright 2014 American Chemical Society

2.2.1 Clusters with Nuclearity Smaller Than Nine

Trinuclear lanthanide hydroxide cluster complexes are not common. [46] One recent example is $[Dy_3(OH)(teaH_2)_3(paa)_3]Cl_2\cdot MeCN\cdot 4H_2O$ (teaH$_3$ = triethanolamine; paaH = N-(2-pyridyl)-acetoacetamide) wherein deprotonated teaH$_3$ and paaH were used together to support a cuboidal or incomplete cubane core of $[Dy_3(\mu_3\text{-OH})]$ [29]. The three Dy^{3+} ions together with the μ_3-OH group form a pyramid that is encapsulated by the diketonate ligands. Each of the three Dy...Dy edges is bridged by one ethanoxide O atom of one teaH$_2$ ligand that also uses its N atom and the remaining two ethanol OH groups to coordinate the same lanthanide ion. Each lanthanide ion is also chelated by two ketonate O atoms of a paa ligand (Fig. 21).
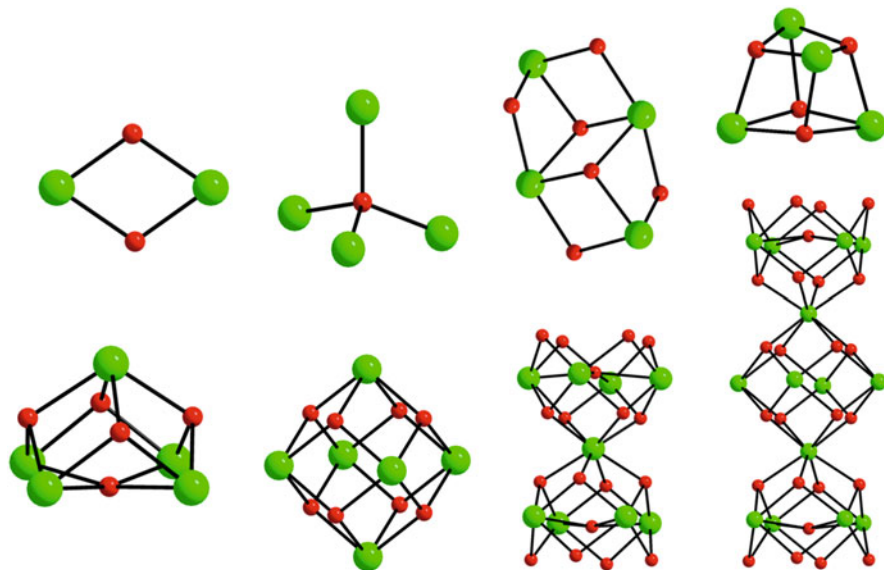
Fig. 20 Structure of representative core motifs in lanthanide-oxo/hydroxo cluster complexes supported by diketonate-based ligands
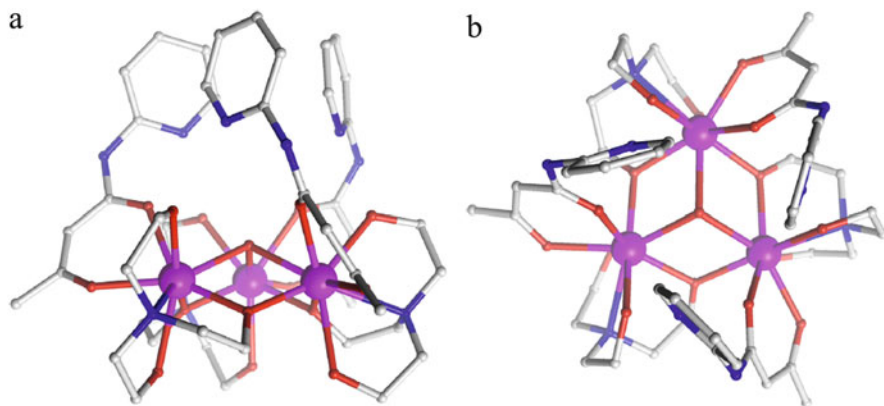
Fig. 21 *Side view* (**a**) and *top view* (**b**) of $[Dy_3(OH)(teaH_2)_3(paa)_3]^{2+}$. Reprinted with the permission from [29] Copyright 2013 Elsevier

Tetranuclear cluster motifs are either a distorted cubane or a planar arrangement of 4 lanthanide ions with two μ_3-OH groups. Both motifs, already discussed above, have seen frequent occurrence in the literature.

Zheng et al. conducted a systematic study on utilizing acetylacetonate (acac) as protecting ligand to support the assembly of hydroxide cluster complexes in organic solution. A structure representing the isostructural tetranuclear complexes $Ln_4(\mu_3\text{-}OH)_2(\mu_3\text{-}OCH_3)_2(CH_3OH)_2(acac)_8$ (Ln $=$ Nd, Sm) is shown in Fig. 22 [47]. The
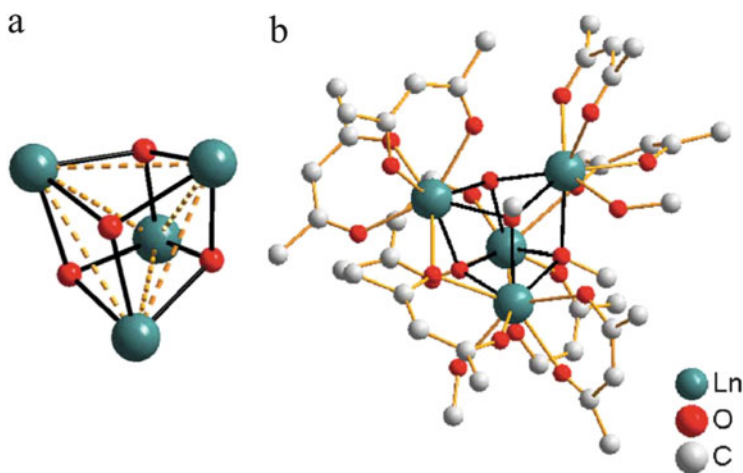
Fig. 22 Structures of: (**a**) the cubane cluster core and (**b**) $[Ln_4(\mu_3\text{-}OH)_2(\mu_3\text{-}OCH_3)_2(CH_3OH)_2(acac)_8]$ [47]. Reprinted with the permission from [47] Copyright 2011 Royal Society of Chemistry

cubane cluster core of $[Ln_4(\mu_3\text{-}OH)_2(\mu_3\text{-}OCH_3)_2]^{8+}$ features coordination by two μ_3-OH and two μ_3-OCH$_3^-$ groups (Fig. 22a). Each Ln^{3+} ion is chelated by two acac ligands with two of the lanthanide ions being also coordinated with one methanol molecule (Fig. 22b).

Using *ortho* ring-functionalized 1-phenylbutane-1,3-dione ligands bearing nitro (Hnpd and Hnmc), methoxy (Hmmc), or fluoro (Hfpp) groups, MacLellan et al. reported a series of tetranuclear hydroxide cluster complexes $[Er_4(\mu_3\text{-}OH)_4(H_2O)_2(npd)_8]$, $[Ln_4(\mu_3\text{-}OH)_4(nmc)_8]\cdot(Ln = Gd, Tb, Dy \text{ and } Er)$, $[Er_4(\mu_3\text{-}OH)_4(mmc)_8]$, and $[Er_4(\mu_3\text{-}OH)_4(H_2O)_2(fpp)_8]$ [48]. These complexes were prepared in methanol using a reaction mixture containing lanthanide chloride hydrates, one of the diketone ligands, and trimethylamine; the organic base is responsible for promoting the hydrolysis of the lanthanide hydrates.

All of these complexes contain the same cubane cluster core, and the structures of $[Er_4(\mu_3\text{-}OH)_4(H_2O)_2(npd)_8]$ and $[Er_4(\mu_3\text{-}OH)_4(nmc)_8]$ are shown in Fig. 23. In both complexes, each of the Er^{3+} ions is chelated by two diketonate ligands (either npd or nmc). In $[Er_4(\mu_3\text{-}OH)_4(H_2O)_2(npd)_8]$, two of the four Er^{3+} ions are also each coordinated by one aqua ligand in addition to two chelating diketonate ligands (Fig. 23a).

A number of tetranuclear complexes with different diketonate ligands but bearing the same planar cluster motif have been reported. Shown in Fig. 24 are the structures of $[Er_4(dbm)_6(O\text{-}btd)_4(\mu_3\text{-}OH)_2]$ and $[Er_4(dbm)_4(O\text{-}btd)_6(\mu_3\text{-}OH)_2]$ (dbm = dibenzoylmethanide; O-btd = 4-hydroxo-2,1,3-benzothiadiazolate) [49]. In both clusters, the planar rhomboid cluster core is encapsulated by a combination of the bridging–chelating O-btd ligands and chelating-only dbm ligands.

Using a combination of Hacac and $H_2L_6 = N,N'$-bis(salicylidene)-1,2-cyclohexanediamine, Sun et al. obtained four isostructural complexes of the
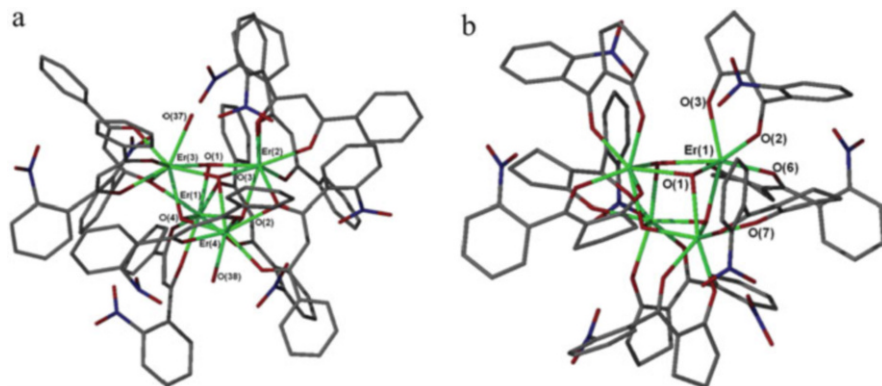
Fig. 23 Structure of: (**a**) [Er$_4$(μ_3-OH)$_4$(H$_2$O)$_2$(npd)$_8$] and (**b**) [Er$_4$(μ_3-OH)$_4$(nmc)$_8$]. Reprinted with the permission from [48] Copyright 2011 Royal Society of Chemistry
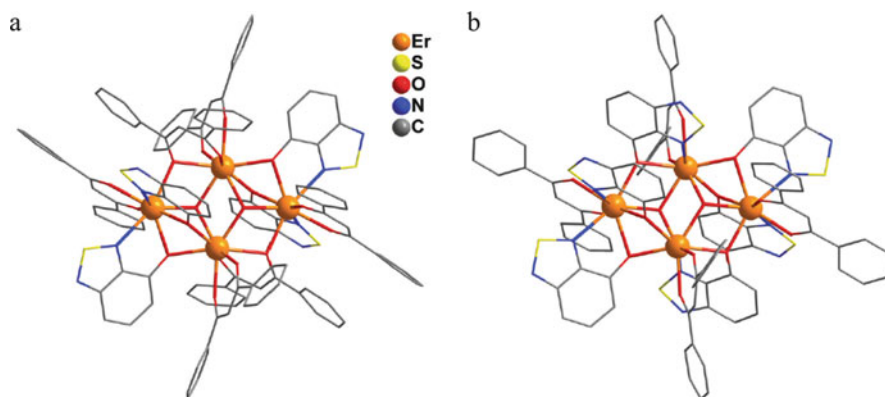
Fig. 24 Structure of: (**a**) [Er$_4$(dbm)$_6$(O-btd)$_4$(OH)$_2$] and (**b**) [Er$_4$(dbm)$_4$(O-btd)$_6$(OH)$_2$]. Reprinted with the permission from [49] Copyright 2015 Royal Society of Chemistry

common formula [Ln$_4$(μ_3-OH)$_2$(L$_6$)$_2$(acac)$_6$]·xH$_2$L$_6$·yCH$_3$CN·zH$_2$O·(Ln = Sm, Gd, Tb, and Dy) [50]. The synthesis was carried out by slowly adding a methanolic solution of a lanthanide acetylacetonate hydrate to an acetonitrile solution of H$_2$L$_6$, followed by reflux of the resulting solution mixture. Two opposite edges of the rhomboid cluster core are each bridged by one L$_6$phenol O, while the other two edges are each bridged by one L$_6$phenol O as well as one O atom of the chelating–bridging acac ligand. Each of the lanthanide ions is further coordinated by one chelating-only acac ligand (Fig. 25).

Lastly, Urbatsch et al. reported two tetranuclear complexes formulated as [Ln$_4$(μ_3-OH)$_2${(μ-O)-k^2-htp}$_2${(μ-O)$_2$-k^2-htp}$_2$(k^2-htp)$_6$] (Ln = Nd, Eu) by using (Z)-3-hydroxy-3-phenyl-1-(thiophen-2-yl)prop-2-en-1-one (Hhtp; Fig. 26a) – a thiophene-containing β-diketone – as supporting ligand [51]. The rhomboid cluster core is coordinated with the diketonate ligands in three different modes: Two
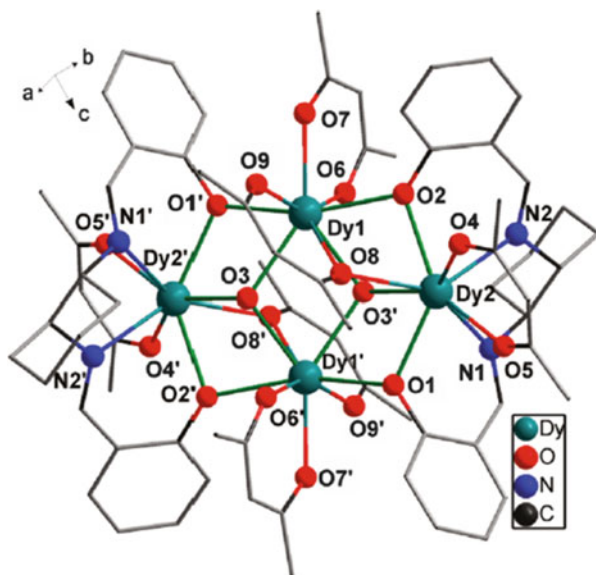
Fig. 25 Structure of $[Dy_4(\mu_3\text{-}OH)_2(L_6)_2(acac)_6]$. Reprinted with the permission from [50] Copyright 2011 American Chemical Society
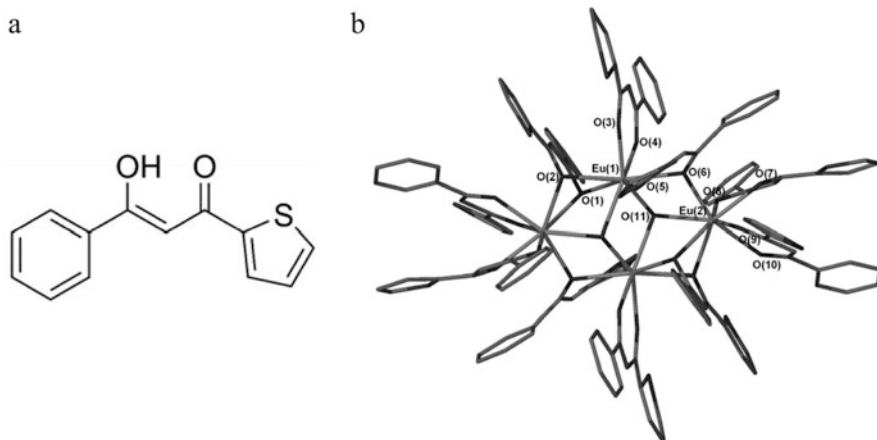
Fig. 26 (**a**) Schematic illustration of the Hhtp ligand and (**b**) structure of $[Eu_4(\mu_3\text{-}OH)_2\{(\mu\text{-}O)\text{-}k^2\text{-}htp\}_2\{(\mu\text{-}O)_2\text{-}k^2\text{-}htp\}_2(k^2\text{-}htp)_6]$. Reprinted with the permission from [51] Copyright 2012 Wiley-VCH Verlag GmbH & Co

opposite edges are each uniquely bridged by the two O atoms from the same htp ligand, while the other two are each bridged by one htpO atom; these latter two htp ligands each chelate one lanthanide ion. The remaining 6 htp ligands are of the chelating-only type to complete the octacoordinate sphere for each lanthanide ion (Fig. 26b).
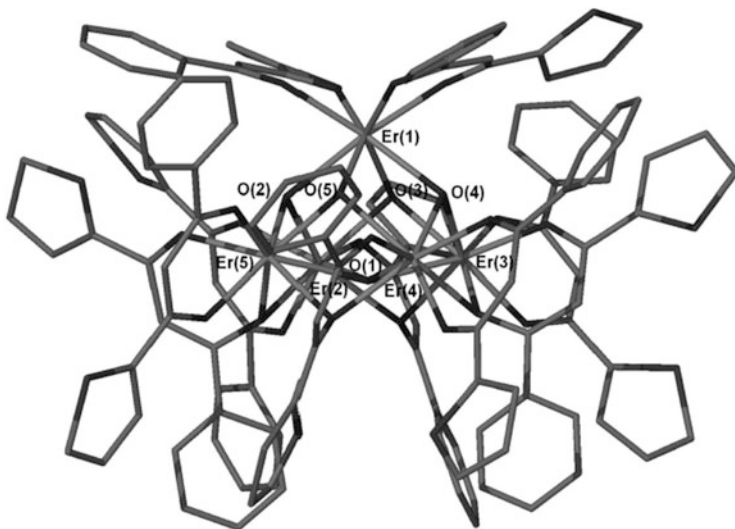
Fig. 27 Structure of [Er$_5$(μ_3-OH)$_4$(μ_4-OH)(μ-η^2-htp}$_4$(η^2-htp)$_6$). Reprinted with the permission from [51] Copyright 2012 Wiley-VCH Verlag GmbH & Co

Together with the above tetranuclear complexes, a pentanuclear complex Er$_5$(μ_3-OH)$_4$(μ_4-OH)(μ-η^2-htp}$_4$(η^2-htp)$_6$ was also isolated [51]. Though not entirely clear, the formation of a larger cluster under otherwise identical reaction conditions may be due to the difference in the lanthanide ion size (Er^{3+} versus Nd^{3+}/ Eu^{3+}). The five Er^{3+} ions are organized into a square pyramid with a μ_4-OH group situated at the center of its basal plane and coordinating all four basal Er^{3+} ions. Each of the four triangular faces of the square pyramid is capped by a μ_3-OH group. This [Er$_5$(μ_3-OH)$_4$(μ_4-OH)]$^{10+}$ core is encapsulated in the coordination sphere formed by 10 htp ligands, of which four are bridging–chelating that uses one of its two ketonate O atoms to bridge one basal Er. . .Er linkage while using the very same O atom together with the other ketonate O to chelate one of the Er^{3+} ions. Each basal Er^{3+} is also coordinated by a second chelating-only htp ligand. The Er^{3+} ion at the axial position is unique; it is coordinated by two chelating-only htp ligands (Fig. 27).

It appears that such coordinating modes are prevalent. Despite the different diketonate ligands used, the same coordination modes have been observed in the six isostructural pentanuclear complexes Ln$_5$(dbm)$_{10}$(μ_3-OH)$_4$(μ_4-OH)·n(solvent) (Ln = Nd, Eu, Gd, Tb, Er, Yb; solvent = acetonitrile or toluene) independently reported by Holiday, Luneau, and their respective coworkers [52, 53], as well as in Ln$_5$(μ_3-OH)$_4$(μ_4-OH)(Iphacac)$_{10}$ (Ln = Tb, Dy, Yb; bis(*para*-iododibenzoyl)-methanide = Iphacac) by Thielemann et al. [54], and in Ln$_5$(μ_3-OH)$_4$(μ_4-OH) (L$_7$)$_{10}$ (Ln = Eu, Ho; 1,3-bis(4-ethoxyphenyl)propane-1,3-dione = HL$_7$) by Silberstein and his coworkers [55].
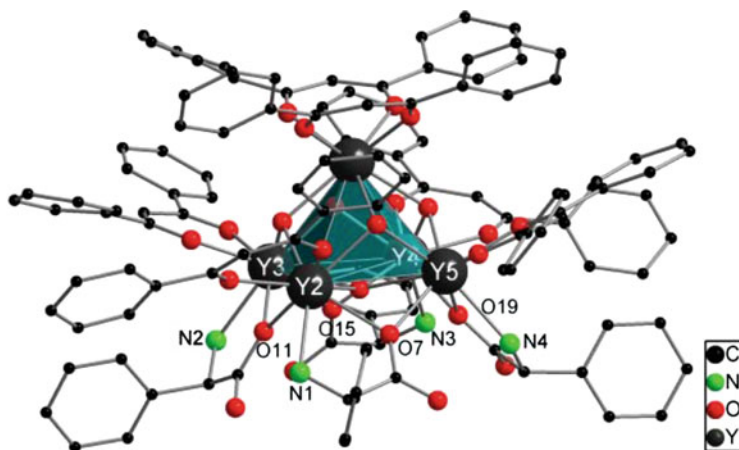
Fig. 28 Structure of $[Y_5(\mu_3\text{-OH})_4(\mu_4\text{-OH})(\text{D-PhGly})_4(\text{dbm})_6]$. Reprinted with the permission from [56] Copyright 2010 Royal Society of Chemistry

Interestingly, some of the diketonate ligands can be replaced by other types of ligands that are capable of both bridging and chelating metal ions. Roesky et al. reported four pentanuclear yttrium complexes of the general formula $[Y_5(\mu_3\text{-OH})_4(\mu_4\text{-OH})(\alpha\text{-AA})_4(\text{dbm})_6]$ (α-AA = D-phenyl glycine; L-proline; L-valine; and L-tryptophan) in which the amino acids can be viewed as a diketonate surrogate [56]. Each of the amino acid ligands uses one of its carboxylate O atom to bridge one basal Ln. . .Ln linkage while using this very same O atom together with the amino N atom to chelate one of the four basal lanthanide ions; the other carboxylate O remains uncoordinated (Fig. 28).

Using *o*-hydroxydibenzoylmethane (HO-Hdbm) as supporting ligand, Baskar et al. were able to obtain a hexanuclear complex $[Y_6(\text{O-dbm})_6(\text{HO-dbm})_4(\mu_3\text{-}OH)_2(\text{MeOH})_4]$ with a rare core motif (Fig. 29) [57]. The six Y^{3+} ions are nearly coplanar and can be viewed as being constructed by adding one Y^{3+} ion on each side of the planar tetranulcear motif. This is made possible by the coordination of the phenoxide O of 6 doubly negatively charged O-dbm ligands. The four Y^{3+} ions in the central rhomboid are bridged by two μ_3-OH groups with each of its edges being bridged by one O-dbm O atom. This very O atom, together with the phenoxide O of the same ligand, chelates one of the four Y^{3+} ions, while the same phenoxide O also bridges the added terminal Y^{3+} ion. Each of these two added Y^{3+} ions is additionally coordinated by two chelating HO-dbm whose phenol moiety remains neutral and uncoordinated (Fig. 29).

When in assessing the influence of ligand sterics on the structure of the resulting hydroxide clusters, Luneau et al. obtained two octanuclear complexes $[Ln_8(\text{thd})_{10}(\mu_4\text{-}O)(\mu_3\text{-OH})_{12}]$ (Ln = Eu, Y) with 2,2,6,6-tetramethylheptane-3,5-dione (Hthd), while pentanuclear clusters were isolated when dbm was the hydrolysis-limiting ligand under otherwise identical conditions [52]. The eight Ln^{3+} ions in the cluster
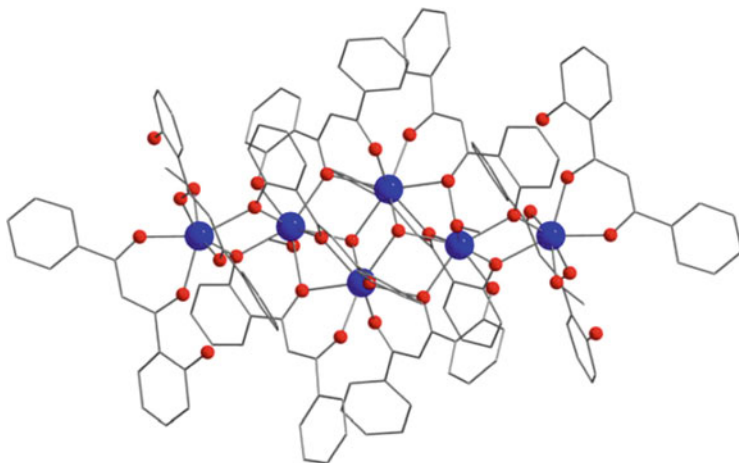
Fig. 29 Structure of $[Y_6(O\text{-}dbm)_6(HO\text{-}dbm)_4(\mu_3\text{-}OH)_2(MeOH)_4]$. Reprinted with the permission from [57] Copyright 2009 Elsevier
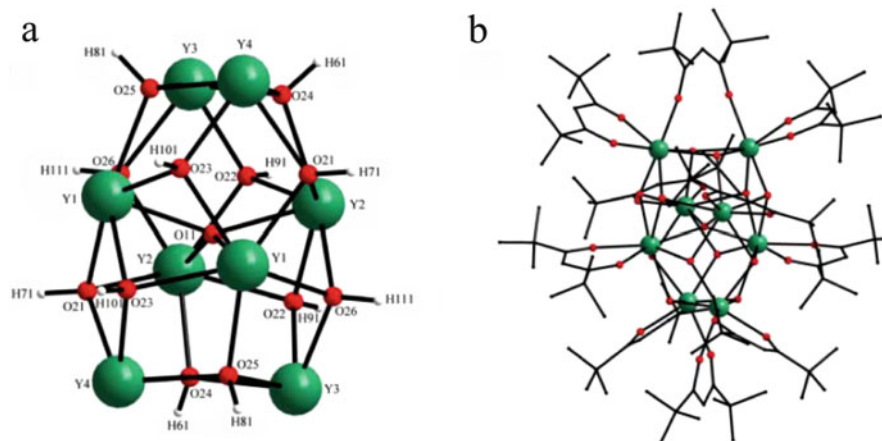
Fig. 30 Structure of: (**a**) the octanuclear cluster core with bridging oxo/hydroxo groups displayed and (**b**) $[Y_8(thd)_{10}(\mu_4\text{-}O)(\mu_3\text{-}OH)_{12}]$. Reprinted with the permission from [52] Copyright 2009 Royal Society of Chemistry

core are bridged by one μ_4-O group and twelve μ_3-OH groups (Fig. 30a). The structure may be viewed as two distorted cubanes joined together by the μ_4-O group with the Ln...Ln linkages (Y1...Y2) at the juncture disposed orthogonally with each other. Each lanthanide ion is chelated by one thd ligand. There are two additional ligands, each bridging a pair of "external" lanthanide ions that are not associated with the μ_4-O group (Fig. 30b).
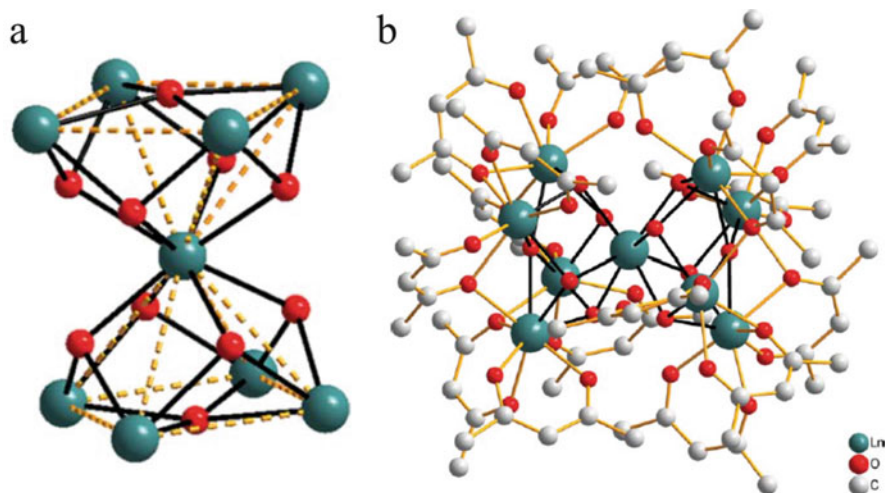
Fig. 31 Structure of: (**a**) the nonanuclear cluster core with bridging oxo/hydroxo groups displayed and (**b**) [Ln$_9$(acac)$_{16}$(μ_3-OH)$_8$(μ_4-O)(μ_4-OH)]. Reprinted with the permission from [47] Copyright 2011 Royal Society of Chemistry

2.2.2 Nonanuclear or Higher-Nuclearity Clusters

From the hydroxide complexes presented above, it becomes clear that higher-nuclearity cluster core motifs can be formally constructed by using smaller polyhedral units as SBUs. If two pentanuclear square pyramids are joined by sharing the non-basal vertex lanthanide ion, an hourglass-shaped nonanuclear motif is produced (Fig. 31a). Such a core motif is present in [Ln$_9$(acac)$_{16}$(μ_3-OH)$_8$(μ_4-O)(μ_4-OH)]·H$_2$O (Ln = Eu, Gd, Tb, Dy, Er, Yb, Y), prepared independently by Luneau, Zheng, and their respective coworkers [47, 52, 58]. The two recognizable pentanuclear units are disposed 90° with respect to each other. One of the basal planes is capped by a μ_4-O group, while the other one by a μ_4-OH group. Each of the triangular faces is capped by a μ_3-OH to give the core formula of [Ln$_9$(μ_3-OH)$_8$(μ_4-O)(μ_4-OH)]$^{16+}$. The acac ligands provide the coordination sheath with 8 being chelating only for each of the basal lanthanide ions and the remaining 8 being both chelating and bridging (Fig. 31b). It should be noted that the ligand coordination mode for the basal lanthanide ions is the same as exhibited by ketonate ligands in the pentanuclear cluster complexes discussed above.

The vertex-sharing can occur between other types of SBUs that are of the same or different kinds. Shown in Fig. 32 is the structure of a tetradecanuclear complex [Dy$_{14}$(μ_4-OH)$_2$(μ_3-OH)$_{16}$(μ-η^2-acac)$_8$(η^2-acac)$_{16}$] [59]. The cluster core can be formally built by sandwiching a hexanuclear octahedral hydroxide unit between two pentanuclear square pyramids via vertex-sharing. The two terminal square basal faces are each capped by a μ_4-OH group. The coordination modes of the acac ligands for the basal lanthanide ions are exactly the same as seen above in the
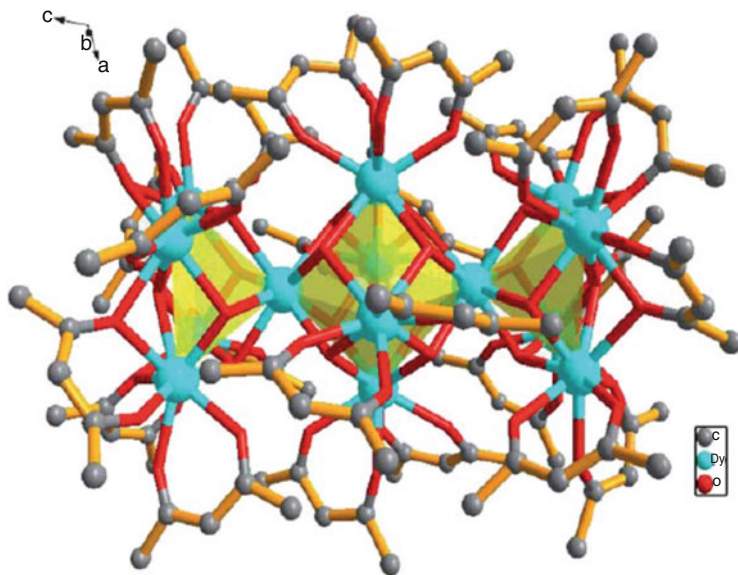
Fig. 32 Structure of $[Dy_{14}(\mu_4\text{-OH})_2(\mu_3\text{-OH})_{16}(\mu\text{-}\eta^2\text{-acac})_8(\eta^2\text{-acac})_{16}]$. Reprinted with the permission from [59] Copyright 2011 Royal Society of Chemistry

nonanuclear complex. The remaining eight acac ligands are chelating only, two on each of the four equatorial lanthanide ions of the central octahedral unit.

Pentadecanuclear hydroxide complexes with tyrosinate as supporting ligand are arguably one of the more notable high-nuclearity lanthanide clusters whose core motif features five cubane units joined together by sharing two vertex lanthanide ions with the assistance of a templating halide ion [11]. More recently, Roesky et al. reported a series of isostructural cluster complexes of the general formula $[Ln_{15}(\mu_3\text{-OH})_{20}(PepCO_2)_{10}(dbm)_{10}Cl]\cdot Cl_4\cdot(PepCO_2 = 2\text{-}[\{3\text{-}(((tert\text{-butoxycarbonyl})$ amino)methyl)benzyl}-amino]acetate; $Ln = Eu$, Tb, Dy, Y) that contain the same pentadecanuclear core (Fig. 33) [60, 61]. The Eu^{3+} and Tb^{3+} complexes have been shown to luminesce in cellular structures and are therefore potentially useful for biological imaging and immunoassay.

2.3 Phosphonates and Sulfonates

Inspired by the great success of utilizing carboxylate and diketonate ligands as supporting ligands for the assembly of high-nuclearity lanthanide hydroxide clusters, chemists have also turned to other O-based ligands such as phosphonates and sulfonates with the hopes of creating cluster complexes with novel structures and properties. Such ligands can be used alone or in combination with other type(s) of ligands.
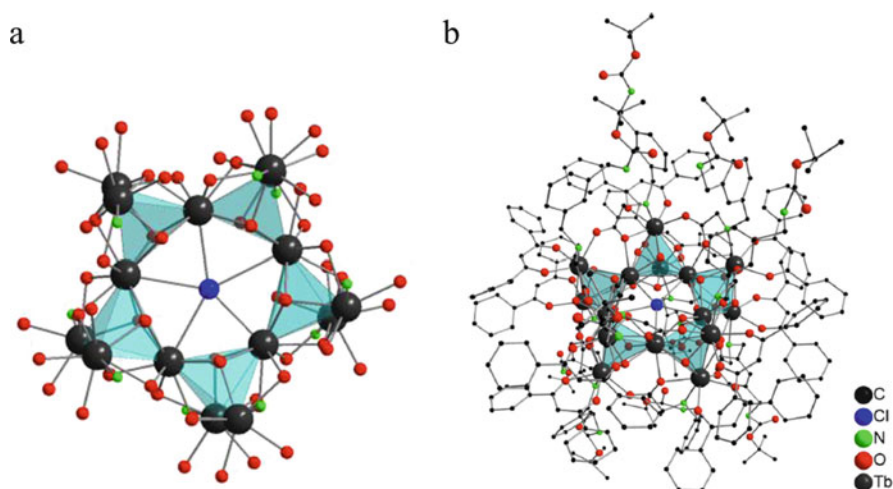
Fig. 33 Structure of: (**a**) the pentadecanuclear core with a templating chloride ion and (**b**) $[Tb_{15}(\mu_3\text{-OH})_{20}(PepCO_2)_{10}(dbm)_{10}Cl]^{4+}$. Reprinted with the permission from [60] Copyright 2013 American Chemical Society

Treating lanthanide nitrate hydrates with pyridine in the presence of pivalic acid and *t*-butyl phosphonic acid in isobutanol under reflux led to the production of a series of tetranuclear lanthanide hydroxide complexes of the formula $[pyH]_4[Ln_4(\mu_3\text{-OH})(O_3P^tBu)_3(HO_3P^tBu)(O_2C^tBu)_2(NO_3)_6]\cdot(Ln = Gd, Tb, Dy, Ho, Er)$ [62]. The representative structure of the Gd^{3+} complex is shown in Fig. 34. The tetranuclear core may be viewed as a μ_3-OH-bridged trinuclear cuboidal unit being connected to the fourth metal through the bridging of three $\mu_3\text{-}O_3P^tBu^{2-}$ ligands; each of the phosphate ligands uses one of its O atom to coordinate this fourth metal, the second to bridge two adjacent lanthanide ions within the cuboidal units, and the third, together with the second one, to chelate one of the three metals in the cuboidal unit. In addition, there are one $\mu_2\text{-}HO_3P^tBu^-$ and two $\mu_2\text{-}O_2C^tBu^-$ ligands along the edge of the cuboidal unit, each bridging a pair of adjacent lanthanide ions. Each lanthanide ion within the cuboidal unit is also chelated by an NO_3^- anion, whereas the coordination sphere of the fourth metal atom is completed with three chelating NO_3^- anions (Fig. 34).

With the same ligand set but using isopropylamine in place of pyridine to promote hydrolysis, Winpenny et al. were able to obtain three isostructural octanuclear complexes of the formula $[Ln_8(O_3P^tBu)_6(\mu_3\text{-OH})_2(H_2O)_2(HO^iBu)(O_2C^tBu)_{12}](NH_3$ $^iPr)_2\cdot(Ln = Gd, Dy, Tb; {}^iPrNH_2 = isopropylamine; HO^iBu = isobutyl alcohol)$ [63]. The eight Ln^{3+} ions are arranged into a horseshoe-like structure (Fig. 35a) with the component lanthanide ions bridged together by six $O_3P^tBu^{2-}$ ligands, two $\mu_2\text{-}O_2C^tBu^-$, and four $\mu\text{-}\eta^2\text{-}O_2C^tBu^-$ ligands (Fig. 35b). The coordination spheres are completed by bidentate chelating $O_2C^tBu^-$ ligands, HO^iBu molecules, and aqua ligands. Alternatively, the cluster motif can be viewed as two μ_3-OH-containing cuboidal units joined together by two $O_3P^tBu^{2-}$ and one $\mu\text{-}\eta^2\text{-}O_2C^tBu^-$ ligands with an add-on lanthanide ion on each side of the double-cuboidal arrangement.
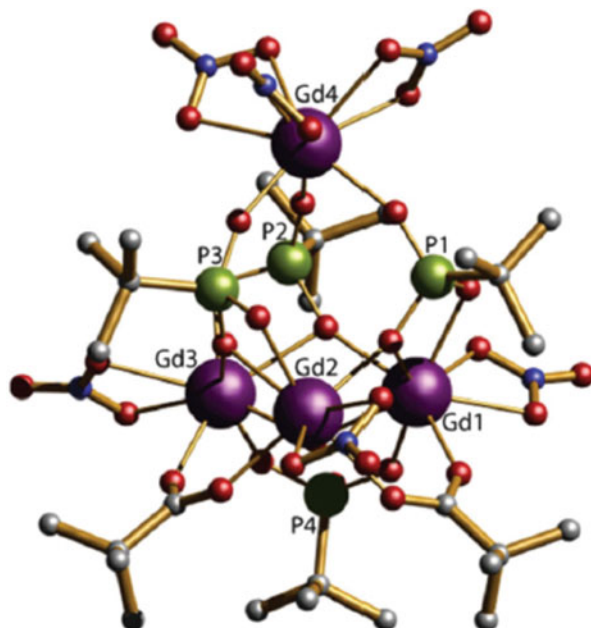
Fig. 34 Structure of the anionic cluster complex $[Gd_4(\mu_3\text{-}OH)(O_3P^tBu)_3(HO_3P^tBu)(O_2C^tBu)_2(NO_3)_6]^{4-}$. Reprinted with the permission from [62] Copyright 2014 Royal Society of Chemistry
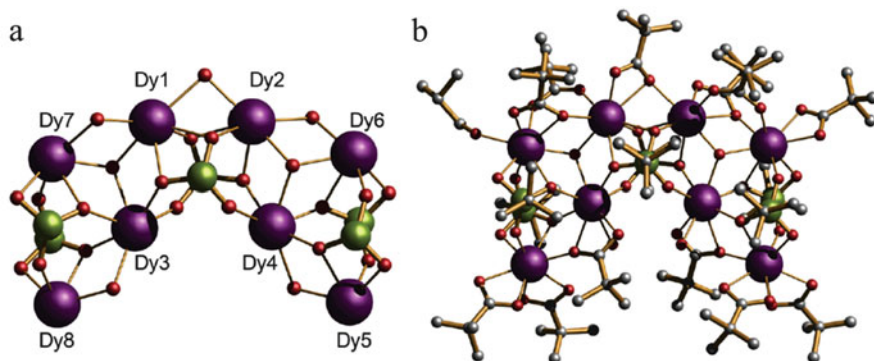
Fig. 35 Structure of: (**a**) the octanuclear core with bridging atoms displayed and (**b**) $[Ln_8(O_3P^tBu)_6(\mu_3\text{-}OH)_2(H_2O)_2(HO^iBu)(O_2C^tBu)_{12}](NH_3^iPr)_2$. Reprinted with the permission from [63] Copyright 2013 Royal Society of Chemistry

Cao et al. reported two isostructural nonanuclear complexes $[Ln_9(\mu_2\text{-}OH)(Hpmp)_{12}(ClO_4)(H_2O)_{26}](ClO_4)_{13}\cdot 18H_2O$ (Ln = Nd, Pr) by using N-piperidinomethane-1-phosphonic acid (H$_2$pmp) as supporting ligand [64]. The synthesis was carried out by adding NaOH into an aqueous solution containing H$_2$pmp·HCl and lanthanide perchlorate salt until pH reached about 6.2. The nine Ln^{3+} ions are
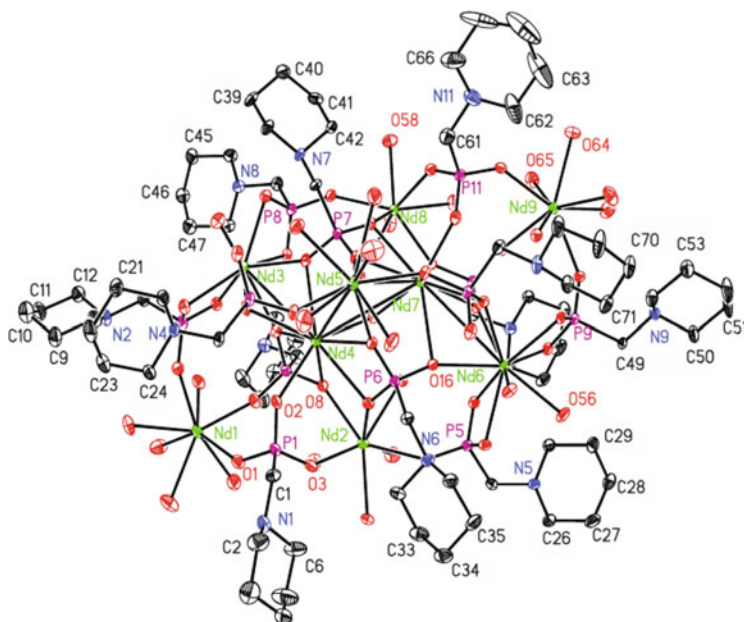
Fig. 36 Structure of cationic complex of $[Nd_9(\mu_2\text{-}OH)(Hpmp)_{12}(ClO_4)(H_2O)_{26}]^{13+}$. Reprinted with the permission from [64] Copyright 2009 Elsevier

organized into a unique lotus-leaf-shaped arrangement with one μ_2-OH group and 12 phosphonate bridging ligands. The coordination spheres are completed with ClO_4^- anion and aqua ligands (Fig. 36).

Phosphate can also be used as a second or ancillary ligand to support the assembly of polynuclear lanthanide hydroxide complexes. As an example, Hong et al. reported two isostructural decanuclear complexes $[Ln_{10}(TBC8A)_2(PhPO_3)_4(OH)_2(HCO_3)(HCOO)(DMF)_{14}] \cdot (H_6TBC8A) \cdot xDMF \cdot yCH_3OH \cdot (Ln = Pr, Nd; H_8TBC8A = p\text{-}tert\text{-}$butylcalix[8]arene; $H_2PhPO_3 = $ phenylphosphonic acid) using a mixture of lanthanide nitrate hydrate, H_8TBC8A, and H_2PhPO_3 in DMF/methanol [65]. The ten Ln^{3+} ions are encapsulated by two $TBC8A^{8-}$ ligands that are in their cup-conformation with their lower-rim phenoxide O atoms coordinating the lanthanide ions (Fig. 37). Four $PhPO_3^{2-}$ ligands, two OH^- groups, one HCO_3^- anion, and one $HCOO^-$ ligand help further stabilize the multinuclear arrangement of the core. In the crystal lattice, the $[Ln_{10}(TBC8A)_2(PhPO_3)_4(OH)_2(HCO_3)(HCOO)(DMF)_{14}]^{2+}$ cations and $(H_6TBC8A)^{2-}$ anions are arranged alternatively to the stable crystalline bulk phase.

There is one report of lanthanide hydroxide cluster complex featuring a sulfonate supporting ligand. Zhang et al. isolated a hexanuclear complex $[Yb_6(\mu_6\text{-}O)(\mu_3\text{-}OH)_8(mds)_4(H_2O)_6]$ by reacting Yb_2O_3 with methylenedisulfonic acid (H_2mds) under hydrothermal conditions [66]. As shown in Fig. 38, the six Yb^{3+} ions are organized into a μ_6-O-centered regular octahedron with each of the triangular faces being capped by one μ_3-OH group. The complex unit is not a discrete one, however.
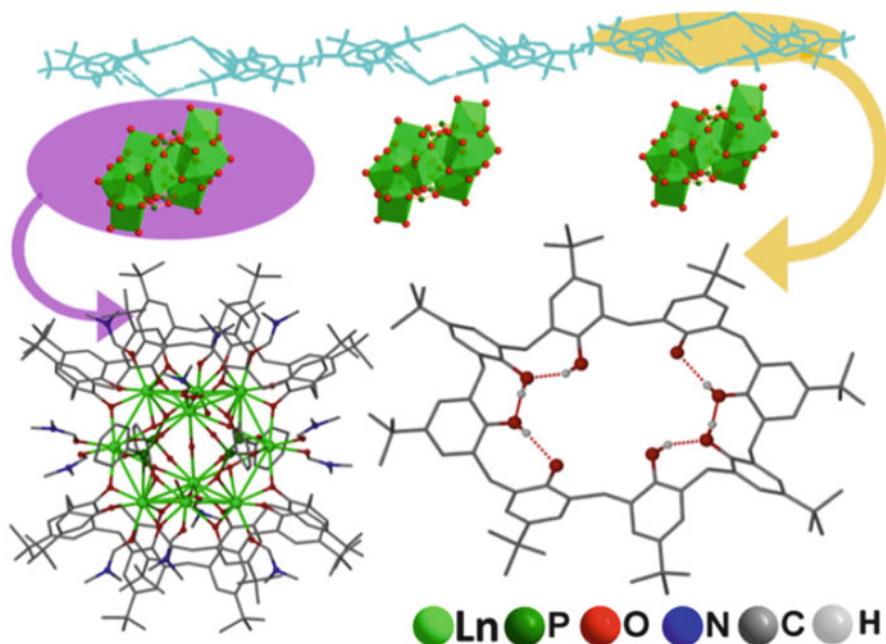
Fig. 37 Structure of $[Ln_{10}(TBC8A)_2(PhPO_3)_4(OH)_2(HCO_3)(HCOO)(DMF)_{14}](H_6TBC8A)$. Reprinted with the permission from [65] Copyright 2015 Elsevier

They are instead connected into a one-dimensional column structure via two opposite Yb^{3+} ions by way of mds coordination. Specifically, the disulfonate ligand is bridging with each of its two sulfonate groups contributing one O for the coordination of one Yb^{3+} from different cluster unit. This unit-connecting Yb^{3+} is also coordinated by two aqua ligands. The remaining four Yb^{3+} ions are of two different types in terms of their coordination spheres: Both are coordinated by one chelating mds ligand with one of them also coordinated by an aqua ligand but not the other.

2.4 Polyoxometalates

Another emerging class of ligands to support the assembly of lanthanide hydroxide complexes are POMs. POMs are known for their facile synthesis and tunable chemical composition [67–69], and have been found to be valuable for promoting many organic transformations [70, 71], catalyzing water-splitting process [72], and making novel memory devices [73, 74].

The increasing use of POMs in lanthanide coordination is due presumably to two reasons. First, POMs are anions with a large number of O atoms on the surface. The
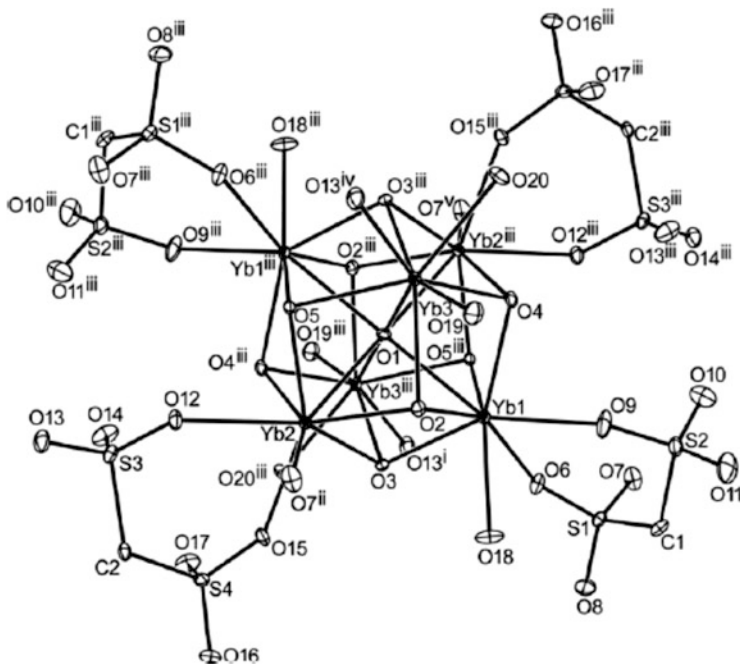
Fig. 38 Structure of $Yb_6(\mu_6\text{-}O)(\mu_3\text{-}OH)_8(mds)_4(H_2O)_6$. Reprinted with the permission from [66] Copyright 2008 IUCr Journals

electrostatic attractions between lanthanide ions and a POM, together with the desirable hard Lewis acid/base match, make POMs an attractive class of protecting ligands and/or templating anions for the assembly of lanthanide clusters. We must note that: (1) not all the examples shown below have the polyhedral Ln-O/OH motif to be qualified as "lanthanide oxide or hydroxide clusters"; the hydroxo groups in some cases are in fact associated with the metal ion in the POM ligands rather than a lanthanide ion and (2) many of the species actually contain lanthanide atoms that are separated by a distance beyond what is anticipated for a conventional cluster motif. Second, as POMs are generally weakly coordinating, the Lewis acidity of lanthanide ions is enhanced in an Ln-POM combination with respect to the complexes with more strongly coordinating ligands. This feature may help enhance the catalytic efficiency when Ln-POM complexes are used in Lewis acid-promoted reactions.

Zhang et al. reported three isostructural lanthanide tungstobismuthate complexes $Na_xH_{22-x}\{(BiW_9O_{33})_4(WO_3)[Bi_6(\mu_3\text{-}O)_4(\mu_2\text{-}OH)_3][Ln_3(H_2O)_6(CO_3)]\}\cdot nH_2O\cdot$ (Ln = Pr, Nd, La) from an aqueous reaction involving $Na_{12}[Bi_2W_{22}O_{74}(OH)_2]\cdot$ 44H_2O, a lanthanide chloride hydrate, $Na_9[BiW_9O_{33}]\cdot16H_2O$, and Na_2CO_3 [75]. As shown in Fig. 39, the three Ln^{3+} ions are organized into a trigonal planar arrangement around a $\mu_3\text{-}CO_3^{2-}$ that uses each of its O atoms to link two lanthanide ions along the edge of the triangle. Each Ln^{3+} ion is further coordinated with two aqua ligands. This $[Ln_3(H_2O)_6(CO_3)]^{7+}$ motif is then encapsulated by four
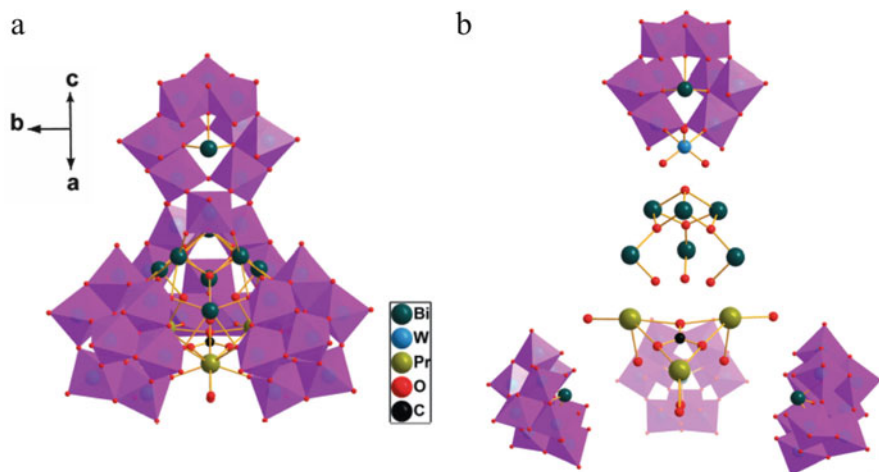
Fig. 39 (**a**) Structure of $\{(BiW_9O_{33})_4(WO_3)[Bi_6(\mu_3\text{-}O)_4(\mu_2\text{-}OH)_3][Pr_3(H_2O)_6(CO_3)]\}^{22-}$ and (**b**) building blocks for the cluster (H atoms and lattice solvent molecules were omitted for clarity). Reprinted with the permission from [75] Copyright 2012 Royal Society of Chemistry

$[BiW_9O_{33}]^{9-}$ anions, three of which being directly connected to the $[Ln_3(H_2O)_6(CO_3)]^{7+}$ core with the fourth one through one $[Bi_6(\mu_3\text{-}O)_4(\mu_2\text{-}OH)_3]^{7+}$ unit.

By reacting $Na_2WO_4 \cdot 2H_2O$, oxalic acid, and lanthanide chloride, without or with the presence KCl in an aqueous solution at pH 7.5, Chen et al. obtained $Na_{10}[Ln_2(C_2O_4)(H_2O)_4(\mu_2\text{-}OH)(W_4O_{16})]_2 \cdot 30H_2O$ and $K_4Na_{16}[Ln(C_2O_4)(W_5O_{18})]_4 \cdot 60H_2O \cdot (Ln = Eu, Ho, Er, Tb)$, respectively [76]. As shown in Fig. 40a, the core of the former consists of a rectangular arrangement of four lanthanide ions with its two longer sides each being bridged by a $C_2O_4^{2-}$ ligand and the shorter side by a $\mu_2\text{-}OH$ group. In addition, there are two aqua ligands on each of the lanthanide ions. This core motif is then sandwiched along the direction of the longer side by two $W_4O_{16}^{8-}$ units via O-Ln coordination to bridge the two lanthanide ions along the shorter side.

In the latter cluster complex, the four lanthanide ions are arranged into a square with each of its sides being bridged by a $C_2O_4^{2-}$ ligand; there are no aqua ligands or hydroxo groups (Fig. 40b). Each of the lanthanide ions is then coordinated via O-coordination to one $W_5O_{18}^{6-}$ capping ligand.

Another series of tetranuclear Ln-POM complexes, formulated as $[PMo^V_8Mo^{VI}_4O_{36}[Ln(H_2O)_4(OH)]_4] \cdot Cl_5 \cdot xH_2O \cdot (Ln = La, Ce, Nd, Sm)$, were reported by Dolbecq and coworkers [77]. The $[PMo^V_8Mo^{VI}_4O_{36}]^{11-}$ anion in these compounds serves as a support or platform for the attachment of four $[Ln(H_2O)_4(OH)]^{2+}$ units into a tetrahedral arrangement (Fig. 41).

It is clear from the above examples, POM ligands can be used to protect lanthanide ions by encapsulation and to support the attachment of lanthanide ions onto their surface. In a rare example provided by Wang et al., these two coordination
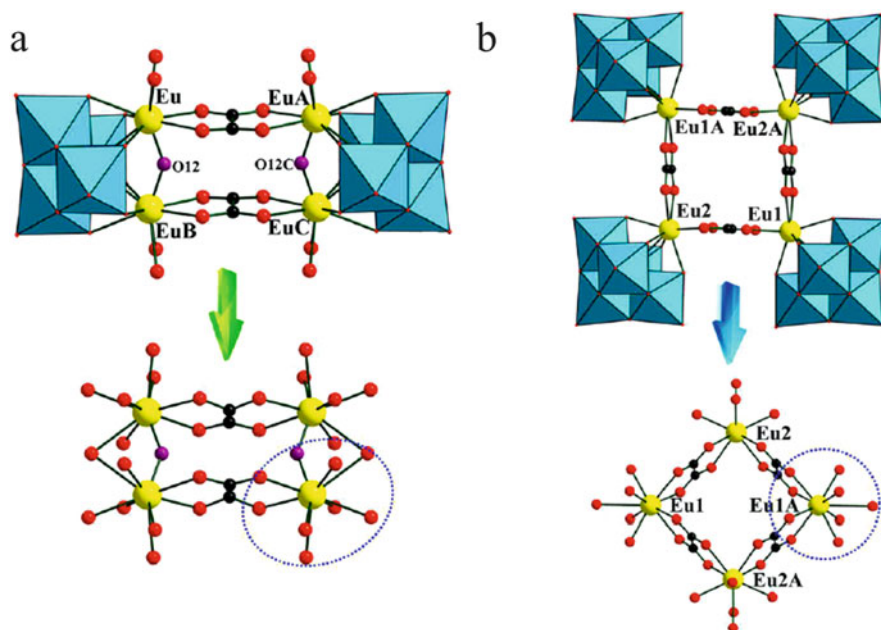
Fig. 40 Structure of: (**a**) $\{[Eu_2(C_2O_4)(H_2O)_4(\mu_2\text{-}OH)(W_4O_{16})]_2\}^{10-}$ (*top*) and cluster core (*bottom*) and (**b**) $\{[Eu(C_2O_4)(W_5O_{18})]_4\}^{20-}$ (*top*) and the cluster core (*bottom*). Reprinted with the permission from [76] Copyright 2014 American Chemical Society
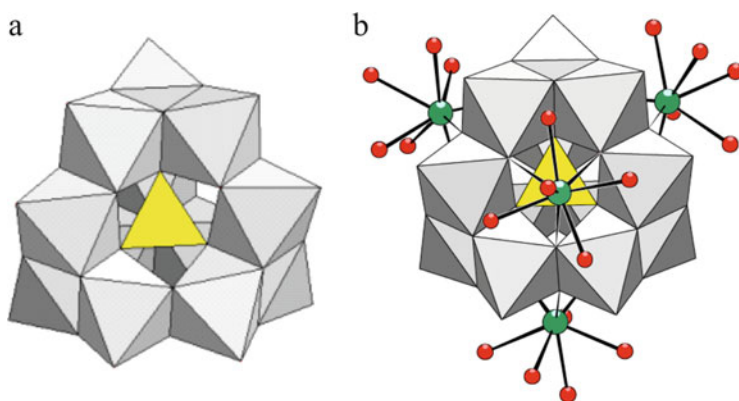
Fig. 41 (**a**) Structure of $[PMo^V_8Mo^{VI}_4O_{36}]^{11-}$ illustrating the triangular face used for the coordination of the $[Ln(H_2O)_4(OH)]^{2+}$ unit and (**b**) structure of $\{PMo^V_8Mo^{VI}_4O_{36}[Ln(H_2O)_4(OH)]_4\}^{5+}$. Reprinted with the permission from [77] Copyright 2011 Wiley-VCH Verlag GmbH & Co
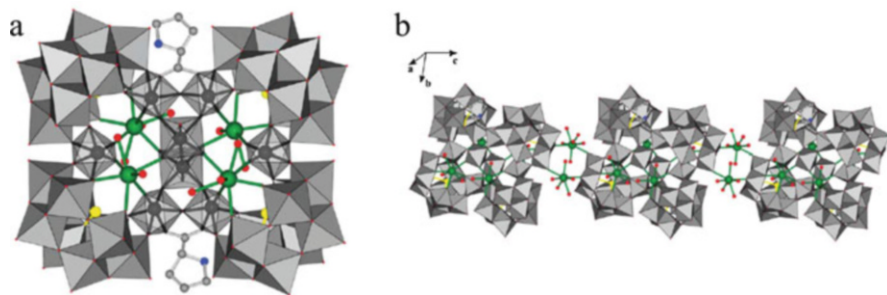
Fig. 42 Structure of: (**a**) the $[Ln_4(H_2O)_{16}\{As_4W_{44}(OH)_2(proline)_2O_{151}\}]^{16-}$ building block and (**b**) $[Ln_6(H_2O)_x\{As_4W_{44}(OH)_2(proline)_2O_{151}\}]^{10-}$. Reprinted with the permission from [78] Copyright 2013 Royal Society of Chemistry
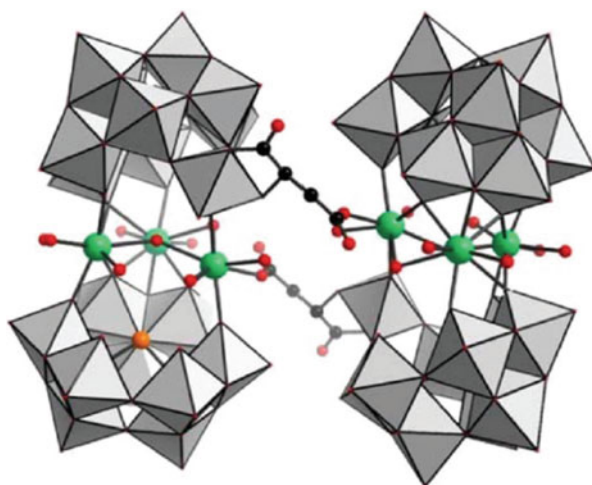
Fig. 43 Structure of $\{[Ln_3(\mu_3\text{-}OH)(H_2O)_8(AsW_9O_{33})(AsW_{10}O_{35})(mal)]_2\}^{22-}$. Reprinted with the permission from [79] Copyright 2015 Royal Society of Chemistry

modes of the POM ligands are demonstrated. Shown in Fig. 42 is the chain structure of the anionic complex in $Na_{10}[Ln_6(H_2O)_x\{As_4W_{44}(OH)_2(proline)_2O_{151}\}] \cdot nH_2O \cdot$ (Ln = Tb, Dy, Nd) linked through hydrated Ln^{3+} ions [78].

Linkages can also be provided by organic ligands that serve to coordinate metal ions from different Ln-POM SBUs. Shown in Fig. 43 is the structure of the anionic complex unit in $K_{20}Li_2[Ln_3(\mu_3\text{-}OH)(H_2O)_8(AsW_9O_{33})(AsW_{10}O_{35})(mal)]_2 \cdot 17H_2O \cdot$ (Ln = Dy, Tb, Gd, Eu, Sm, mal = malate) [79]. It can be viewed as two μ_3-OH group-bridged cuboidal building blocks connected by two mal ligands. This complex motif is then sandwiched in between one $\{AsW_9O_{33}\}$ and one $\{AsW_{10}O_{35}\}$ unit with the latter being also coordinated by one mal ligand. The coordination sphere of the Ln^{3+} ion chelated by the mal ligand is completed by two aqua ligands while that of the other two Ln^{3+} ions is each completed by three aqua ligands.

Using an aqueous mixture of samarium chloride, Na_2CO_3, KCl, and $Na_{10}[A$-α-$SiW_9O_{34}]\cdot xH_2O$, Davoodi et al. obtained $[(A$-α-$SiW_9O_{34})_2(H_2OSm)_3CO_3]^{13-}$ which decomposed slowly in a concentrated solution to afford an anionic octanuclear complex $[(SiW_{10}Sm_2O_{38})_4(W_3O_8)(OH)_4(H_2O)_2)]^{26-}$ as the final product [80]. The complex unit can be viewed as eight Sm^{3+} ions wrapping around one $[W_3O_8(OH)_4(H_2O)_2]^{2-}$ template anion. This arrangement is then encapsulated by four $[SiW_{10}O_{38}]^{12-}$ ligands (Fig. 44).

Lastly, Patzke et al. reported a series of hexadecanuclear lanthanide polyoxotungstate complexes with the core formulated as $[Ln_{16}As_{16}W_{164}O_{576}(OH)_8(H_2O)_{42}]^{80-}\cdot(Ln = Eu, Gd, Tb, Dy, Ho)$ [81]. The product was obtained from an aqueous reaction of $K_{14}[As_2W_{19}O_{67}(H_2O)]$, lanthanide nitrate hydrate, NaCl, and CsCl. Each of the 16 Ln^{3+} ions is capped by one $\{AsW_9O_{33}\}$ unit, and the 16 $\{LnAsW_9O_{33}\}$ units are connected by 20 tungstate anions, eight OH^- groups, and four Cs^+ cations. The coordination spheres of Ln^{3+} ions are completed by aqua ligands (Fig. 45).

2.5   Miscellaneous Ligands

There are also some structurally interesting lanthanide hydroxide cluster complexes supported by ligands that do not belong to the types discussed above. For example, Alikberova et al. reported two hexanuclear complexes $[Ln_6(H_2O)_{23}(OH)_{10}]$ $I_8\cdot8H_2O\cdot(Ln = La, Nd)$ by directly reacting $La_2(CO_3)_3\cdot6H_2O$ and Nd_2O_3 with an aqueous solution of HI [82]. We note that a very similar octahedral hexanuclear cluster complex with exclusively H_2O-based ligands was previously reported by direct hydrolysis of simple lanthanide salts [83]. The cluster core is essentially the same as in $Yb_6(\mu_6$-$O)(\mu_3$-$OH)_8(mds)_4(H_2O)_6$ discussed above [66] with six Ln^{3+} ions arranged into an octahedron centering around a μ_6-OH rather than a μ_6-O group. Each face of the octahedron was capped by one μ_3-OH group. The coordination spheres of five of the six Ln^{3+} ions are each completed by four aqua ligands, while that of the sixth one is fulfilled by three aqua ligands and one OH^- group (Fig. 46).

Complexes with similar hexanuclear core have also been reported with the use of a triazole ligand 4-amino-3,5-dimethyl-1,2,4-triazole (L_8) [84]. Cheng et al. reported a series of hexanuclear complexes of the common formula $[Ln_6(\mu_6$-$O)(\mu_3$-$OH)_8(L_8)_4(H_2O)_{14}]Cl_8\cdot2\ L_8\cdot6H_2O\cdot(Ln = Er, Ho, Dy)$. As shown in Fig. 47, ligand L_8 bridges four equatorial Ln…Ln edges of the octahedral core. The rest of the coordination sphere is fulfilled by either aqua ligands or an aqua/chloro ligand combination.

Batten et al. reported two tetradecanuclear lanthanide hydroxide complexes, $[Gd_{14}(CO_3)_{13}(ccnm)_9(OH)(H_2O)_6(phen)_{13}(NO_3)](CO_3)_{2.5}\cdot(phen)_{0.5}$ and $[Dy_{14}(CO_3)_{13}(ccnm)_{10}(OH)(H_2O)_6(phen)_{13}](CO_3)_{2.5}\cdot(phen)_{0.5}$ by using a combination of 1,10-phenanthroline (phen) and carbamoylcyanonitrosomethanide (ccnm) as the protecting ligands [85]. They share the same cluster core, differing only
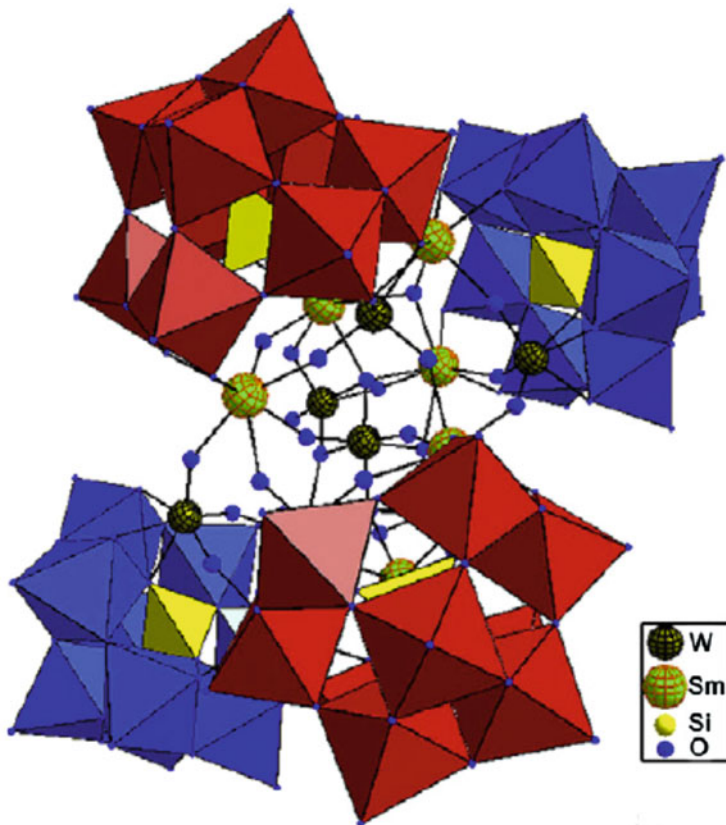
Fig. 44 Structure of the $[(SiW_{10}Sm_2O_{38})_4(W_3O_8)(OH)_4(H_2O)_2)]^{26-}$ cluster core. Reprinted with the permission from [80] Copyright 2012 Elsevier

slightly in the peripheral coordination ligands and anions. The structures of the core and the cationic Gd^{3+} complex are shown in Fig. 48. The 14 Gd^{3+} ions are bridged by one μ_3-OH group and 13 CO_3^{2-} anions (Fig. 48a). The coordination spheres of Gd^{3+} ions are completed by ccnm, phen, aqua, and chelating NO_3^- ligands (Fig. 48b).
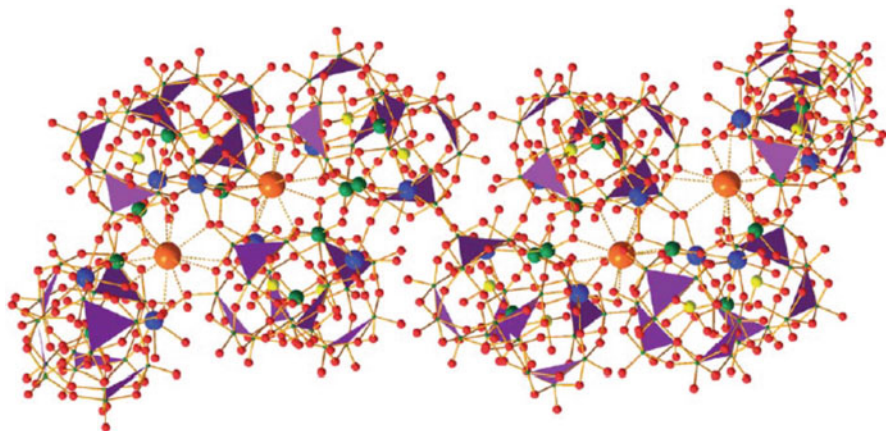
Fig. 45 Structure of the $[Ln_{16}As_{16}W_{164}O_{576}(OH)_8(H_2O)_{42}]^{80-}$ cluster core (color code: *blue*, Ln; *yellow*, As; *green*, W; *red*, O; *orange*, Cs; and *purple triangular planes*, W_3O_{13} triads of the $\{AsW_9O_{33}\}$ units). Reprinted with the permission from [81] Copyright 2011 Royal Society of Chemistry
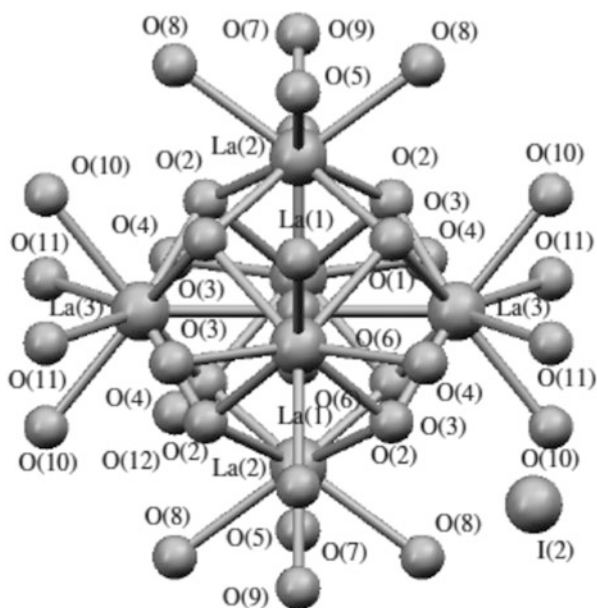
Fig. 46 Structure of $[La_6(H_2O)_{23}(OH)_{10}]^{8+}$. Reprinted with the permission from [82] Copyright 2009 Springer
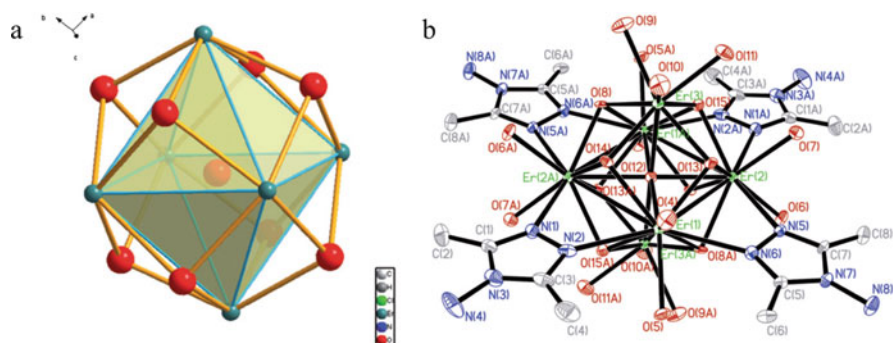
Fig. 47 Structure of: (**a**) the hexanuclear $[Ln_6(\mu_6\text{-O})(\mu_3\text{-OH})_8]^{8+}$ cluster core and (**b**) $[Er_6(\mu_6\text{-O})(\mu_3\text{-OH})_8(L_8)_4(H_2O)_{14}]^{8+}$. Reprinted with the permission from [84] Copyright 2009 Royal Society of Chemistry
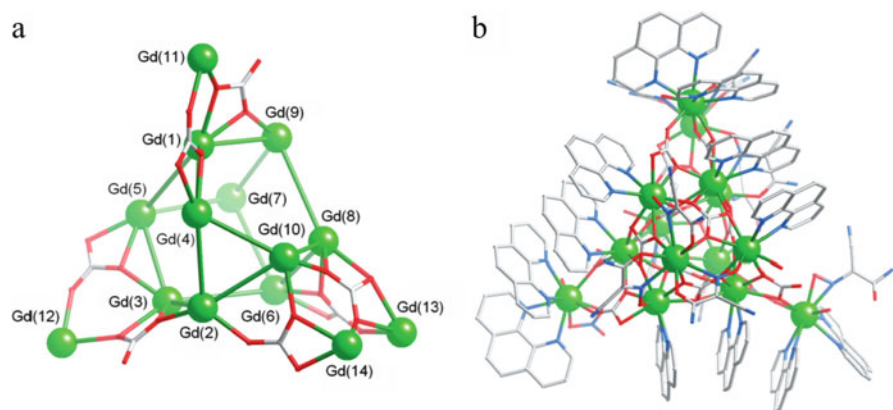
Fig. 48 Structure of: (**a**) the cluster core $[Gd_{14}(CO_3)_{13}(OH)(NO_3)]^{14+}$ and (**b**) $[Gd_{14}(CO_3)_{13}(ccnm)_9(OH)(H_2O)_6(phen)_{13}(NO_3)]^{5+}$. Reprinted with the permission from [85] Copyright 2012 Royal Society of Chemistry

3 Summary and Perspectives

In this chapter, we survey the lanthanide hydroxide cluster complexes that are supported by carboxylate, diketonate, phosphate, sulfonate, and POM ligands. The synthetic procedures leading to the production of the cluster species and the unique cluster core motifs are the focus of the discussion. The extensive scope in terms of the variety of ligands to control the lanthanide hydrolysis as well as the diverse structures of the cluster motifs indicates that this sub-area of lanthanide coordination chemistry is full of potential for further synthetic development and materials discovery. The following are the key conclusions drawn from the work summarized in this chapter and that prior to this review:

1. It is the high pH at which a reaction is conducted that makes the critical difference in the complex products when compared with lanthanide coordination with the same types of ligands at a lower pH. The assembly of the cluster species hinges upon the formation of the hydroxo intermediate produced upon deprotonation of aqua ligand(s).

2. Hydrolysis can occur in either aqueous or organic media, using hydrated lanthanide complexes or salts, or oxides, promoted by using an inorganic or organic base, and under ambient-pressure or hydro/solvothermal conditions.

3. The supporting ligands, most of which being organic with O-based functional groups, should support a reasonable degree of water solubility of their complexes if the hydrolysis is to be executed in an aqueous solution. This is exemplified by the results obtained by using amino acids as supporting ligands for lanthanide hydrolysis. In comparison, hydrated complexes with simple carboxylic acids are generally insoluble, and therefore precipitate out before any hydrolysis may occur.

4. Supporting ligands can be used alone or in combination with other ligands. The accompanying use of an O-based ligand, inorganic ones included, is generally required if the other supporting ligand does not carry any O-based functional groups. The nature (nuclearity and structure) of the lanthanide hydroxide clusters is critically dependent on the ancillary ligands used.

5. A number of factors other than the supporting ligand are also significant in determining the reaction outcome. These include the nature of the lanthanide ions (contrary to the common perception of lanthanide chemistry being similar among different lanthanide ions due to lanthanide contraction), the template effects of certain small anions, and the participation of transition metal ions (not discussed herein).

6. Highly sophisticated lanthanide-containing clusters can be formally constructed by using smaller and recognizable cluster units as formal secondary building units (SBUs).

One should not be surprised that the research activities of lanthanide hydroxide clusters will continue to grow with high possibility of finding interesting materials with useful applications that have not yet been realized or even contemplated. Rapid progress notwithstanding, questions such as the scope of the chemistry, the robustness of the synthetic approach, and effects of experimental conditions, and any structure–property relationship remain to be answered. Thus, the primary goal of any future efforts is to systematically assess the effects of factors such as the nature of supporting ligands and metal ions, and experimental conditions on the reaction outcome, with the hopes of developing a robust and generally applicable approach to these unique lanthanide-containing substances. The ultimate goal is to discover lanthanide-containing materials for catalysis, magnetic, optical, biomedical, and other advanced technological applications.

References

1. Demars T, Boltoeva M, Vigier N, Maynadié J, Ravaux J, Genre C, Meyer D (2012) From coordination polymers to doped rare-earth oxides. Eur J Inorg Chem 2012:3875–3884
2. Wang D, Zhang J, Lin Q, Fu L, Zhang H, Yang B (2003) Lanthanide complex/polymer composite optical resin with intense narrow band emission, high transparency and good mechanical performance. J Mater Chem 13:2279–2284
3. Woodruff DN, Winpenny REP, Layfield RA (2013) Lanthanide single-molecule magnets. Chem Rev 113:5110–5148
4. Zheng YZ, Zhou GJ, Zheng Z, Winpenny REP (2014) Molecule-based magnetic coolers. Chem Soc Rev 43:1462–1475
5. New K, Andolina CM, Morrow JR (2008) Tethered dinuclear europium(III) macrocyclic catalysts for the cleavage of RNA. J Am Chem Soc 130:14861–14871
6. Aime S, Castelli DD, Crich SG, Gianolio E, Terreno E (2009) Pushing the sensitivity envelope of lanthanide-based magnetic resonance imaging (MRI) contrast agents for molecular imaging applications. Acc Chem Res 42:822–831
7. Mikkelsen M, Jørgensen J, Krebs FC (2009) The teraton challenge. A review of fixation and transformation of carbon dioxide. Energy Environ Sci 3:43–81
8. Cotton FA (1966) Transition-metal compounds containing clusters of metal atoms. Q Rev Chem Soc 20:389–401
9. Zheng Z (2010) Cluster compounds of rare-earth elements. In: Handbook of physics and chemistry of rare earths, vol 40. Elsevier, pp 109–239. ISBN 978-0-444-53220-6
10. Zheng Z (2001) Ligand-controlled self-assembly of polynuclear lanthanide-oxo/hydroxo complexes: from synthetic serendipity to rational supramolecular design. Chem Commun 2521–2529
11. Wang R, Zheng Z, Jin T, Staples RJ (1999) Coordination chemistry of lanthanides at "high" pH: synthesis and structure of the pentadecanuclear complex of europium(III) with tyrosine. Angew Chem Int Ed 38:1813–1815
12. Wang R, Liu H, Carducci MD, Jin T, Zheng C, Zheng Z (2001) Lanthanide coordination with α-amino acids under near physiological pH conditions: polymetallic complexes containing the cubane-like $[Ln_4(\mu_3-OH)_4]^{8+}$ cluster core. Inorg Chem 40:2743–2750
13. Xu F, Miras HN, Scullion RA, Long DL, Thiel J, Cronin L (2012) Correlating the magic numbers of inorganic nanomolecular assemblies with a {Pd84} molecular-ring Rosetta Stone. Proc Natl Acad Sci U S A 109:11609–11612
14. Peng JB, Zhang QC, Kong XJ, Zheng YZ, Ren YP, Long LS, Huang RB, Zheng LS, Zheng Z (2012) High-nuclearity 3d-4f clusters as enhanced magnetic coolers and molecular magnets. J Am Chem Soc 134:3314–3317
15. Peng JB, Zhang QC, Kong XJ, Ren YP, Long LS, Huang RB, Zheng LS, Zheng Z (2011) A 48-metal cluster exhibiting a large magnetocaloric effect. Angew Chem Int Ed 50:10649–10652
16. Tasiopoulos AJ, Vinslava A, Wernsdorfer W, Abboud KA, Christou G (2004) Giant single-molecule magnets: a {Mn84} torus and its supramolecular nanotubes. Angew Chem Int Ed 43:2117–2121
17. Kong X, Ren Y, Chen W, Long L, Zheng Z, Huang R, Zheng L (2008) A four-shell, nesting doll-like 3d-4f cluster containing 108 metal ions. Angew Chem Int Ed 47:2398–2401

18. Peng JB, Ren YP, Kong XJ, Long LS, Huang RB, Zheng LS (2011) A series of di-, tri- and tetranuclear lanthanide clusters with slow magnetic relaxation for Dy_2 and Dy_4. CrystEngComm 13:2084–2090

19. Kong XJ, Long LS, Zheng LS, Wang R, Zheng Z (2009) Hydrolytic synthesis and structural characterization of lanthanide hydroxide clusters supported by nicotinic acid. Inorg Chem 48:3268–3273

20. Gao Y, Xu GF, Zhao L, Tang J, Liu Z (2009) Observation of slow magnetic relaxation in discrete dysprosium cubane. Inorg Chem 48:11495–11497

21. Wu ZL, Dong J, Ni WY, Zhang BW, Cui JZ, Zhao B (2014) pH-induced Dy_4 and Dy_{10} cluster-based 1D chains with different magnetic relaxation features. Dalton Trans 43:16838–16845

22. Langley SK, Chilton NF, Gass IA, Moubaraki B, Murray KS (2011) Planar tetranuclear lanthanide clusters with the Dy_4 analogue displaying slow magnetic relaxation. Dalton Trans 40:12656–12659

23. Abbas G, Lan Y, Kostakis GE, Wernsdorfer W, Anson CE, Powell AK (2010) Series of isostructural planar lanthanide complexes $[Ln^{III}_4(\mu_3\text{-}OH)_2(mdeaH)_2(piv)_8]$ with single molecule magnet behavior for the Dy_4 analogue. Inorg Chem 49:8067–8072

24. Peng JB, Kong XJ, Ren YP, Long LS, Huang RB, Zheng LS (2012) Trigonal bipyramidal Dy_5 cluster exhibiting slow magnetic relaxation. Inorg Chem 51:2186–2190

25. Wang R, Selby HD, Liu H, Carducci MD, Jin T, Zheng Z, Anthis JW, Staples RJ (2002) Halide-templated assembly of polynuclear lanthanide-hydroxo complexes. Inorg Chem 41:278–286

26. Sharples JW, Zheng YZ, Tuna F, McInnes EJL, Collison D (2011) Lanthanide discs chill well and relax slowly. Chem Commun 47:7650–7652

27. Liu SJ, Zhao JP, Tao J, Jia JM, Han SD, Li Y, Chen YC, Bu XH (2013) An unprecedented decanuclear Gd(III) cluster for magnetic refrigeration. Inorg Chem 52:9163–9165

28. Zangana KH, Pineda EM, Mclnnes EJL, Schnack J, Winpenny REP (2014) Centred nine-metal rings of lanthanides. Chem Commun 50:1438–1440

29. Langley SK, Moubaraki B, Murray KS (2013) Trinuclear, octanuclear and decanuclear dysprosium(III) complexes: Synthesis, structural and magnetic studies. Polyhedron 64:255–261

30. D'Alessio D, Sobolev AN, Skelton BW, Fuller RO, Woodward RC, Lengkeek NA, Fraser BH, Massi M, Ogden MI (2014) Lanthanoid "bottlebrush" clusters: remarkably elongated metal-oxo core structures with controllable lengths. J Am Chem Soc 136:15122–15125

31. Gu X, Clérac R, Houri A, Xue D (2008) Slow relaxation of the magnetization in high-nuclearity Ln-complexes. Inorg Chim Acta 361:3873–3876

32. Chen L, Huang L, Wang C, Fu J, Zhang D, Zhu D, Xu Y (2012) Hydrothermal synthesis, structure, and properties of two new nanosized Ln_{26} (Ln = Ho, Er) clusters. J Coord Chem 65:958–968

33. Wu M, Jiang F, Kong X, Yuan D, Long L, Al-Thuabaiti SA, Hong M (2013) Two polymeric 36-metal pure lanthanide nanosize clusters. Chem Sci 4:3104–3109

34. Guo FS, Chen YC, Mao LL, Lin WQ, Leng JD, Tarasenko R, Orendáč M, Prokleška J, Sechovský V, Tong ML (2013) Anion-templated assembly and magnetocaloric properties of a nanoscale {Gd_{38}} cage versus a {Gd_{48}} barrel. Chem Eur J 19:14876–14885

35. Wu M, Jiang F, Yuan D, Pang J, Qian J, Al-Thuabaiti SA, Hong M (2014) Polymeric double-anion template Er_{48} nanotubes. Chem Commun 50:1113–1115

36. Kong XJ, Wu Y, Long LS, Zheng LS, Zheng Z (2009) A chiral 60-metal sodalite cage featuring 24 vertex-sharing $[Er_4(\mu_3\text{-}OH)_4]$ cubanes. J Am Chem Soc 131:6918–6919

37. Peng JB, Kong XJ, Zhang QC, Orendáč M, Prokleška J, Ren YP, Long LS, Zheng Z, Zheng LS (2014) Beauty, symmetry, and magnetocaloric effect–four-shell Kelperates with 104 lanthanide atoms. J Am Chem Soc 136:17938–17941

38. Halverson F, Brinen JS, Leto JR (1964) Photoluminescence of lanthanide complexes. III. Synergic agent complexes involving extended chromophores. J Chem Phys 41:2752–2760

39. de Sa GF, Alves S, da Silva BJP, da Silva EF (1998) A novel fluorinated Eu(III) β-diketone complex as thin film for optical device applications. Opt Mater 11:23–28

40. Wang J, Wang R, Yang J, Zheng Z, Carducci MD, Cayou T, Peyghambarian N, Jabbour GE (2001) First oxadiazole-functionalized terbium(III) β-diketonate for organic electroluminescence. J Am Chem Soc 123:6179–6180

41. Bunzli JCG (2010) Lanthanide luminescence for biomedical analyses and imaging. Chem Rev 110:2729–2755

42. Eliseeva SV, Bunzli JCG (2010) Lanthanide luminescence for functional materials and bio-sciences. Chem Soc Rev 39:189–227

43. Bunzli JCG, Piguet C (2005) Taking advantage of luminescent lanthanide ions. Chem Soc Rev 34:1048–1077

44. Barash EH, Coan PS, Lobkovsky EB, Streib WE, Caulton KG (1993) Anhydrous yttrium acetylacetonate and the course of thermal "dehydration" of $Y(acac)_3 \cdot 3H_2O$. Inorg Chem 32:497–501

45. Plakatouras JC, Baxter I, Hursthouse MB, Malik KMA, McAleese J, Drake SR (1994) Synthesis and structural characterization of two novel GdIII β-diketonates $[Gd_4(\mu_3\text{-}OH)_4(\mu_2\text{-}H_2O)_2(H_2O)_4(hfpd)_8] \cdot 2C_6H_6 \cdot H_2O$ **1** and $[Gd(hfpd)_3(Me_2CO)(H_2O)]$ **2** (hfpd-H = 1,1,1,5,5,5-hexafluoropentane-2,4-dione). J Chem Soc Chem Commun 1994:2455–2456

46. Evans WJ, Rabe GW, Ziller JW (1994) Utility of N-methylimidazole in isolating crystalline lanthanide iodide and hydroxide complexes: crystallographic characterization of octasolvated $[Sm(N\text{-}MeIm)_8]I_3$ and polymetallic $[SmI(\mu\text{-}I)(N\text{-}MeIm)_3]_2$, $[(N\text{-}MeIm)_5Sm(\mu\text{-}OH)]_2I_4$, and $\{[(N\text{-}MeIm)_4Sm(\mu\text{-}OH)]_3(\mu_3\text{-}OH)_2\}I_4$. Inorg Chem 33:3072–3078

47. Wu Y, Morton S, Kong X, Nichol GS, Zheng Z (2011) Hydrolytic synthesis and structural characterization of lanthanide-acetylacetonato/hydroxo cluster complexes–a systematic study. Dalton Trans 40:1041–1046

48. Andrews PC, Gee WJ, Junk PC, MacLellan JG (2011) Systematic study of the formation of the lanthanoid cubane cluster motif mediated b steric modification of diketonate ligands. Dalton Trans 40:12169–12179

49. Sukhikh TS, Bashirov DA, Kuratieva NV, Smolentsev AI, Bogomyakov AS, Burilov VA, Mustafina AR, Zibarev AV, Konchenko SN (2015) New NIR-emissive tetranuclear Er(III) complexes with 4-hydroxo-2,1,3-benzothiadiazolate and dibenzoylmethanide ligands: synthesis and characterization. Dalton Trans 44:5727–5734

50. Yan PF, Lin PH, Habib F, Aharen T, Murugesu M, Deng ZP, Li GM, Sun WB (2011) Planar tetranuclear Dy(III) single-molecule magnet and its Sm(III), Gd(III), and Tb(III) analogues encapsulated by salen-type and β-diketonate ligands. Inorg Chem 50:7059–7065

51. Andrews PC, Deacon GB, Gee WJ, Junk PC, Urbatsch A (2012) Synthesis and characterization of thiophene-functionalised lanthanoid diketonate clusters with solvent-modulated europium luminescence. Eur J Inorg Chem 2012:3273–3282

52. Petit S, Baril-Robert F, Pilet G, Reber C, Luneau D (2009) Luminescence spectroscopy of europium(III) and terbium(III) penta-, octa- and nonanuclear clusters with β-diketonate ligands. Dalton Trans 2009:6809–6815

53. Chen XY, Yang X, Holliday BJ (2010) Metal-controlled assembly of near-infrared-emitting pentanuclear lanthanide β-diketone clusters. Inorg Chem 49:2583–2585

54. Andrews PC, Hennersdorf F, Junk PC, Thielemann DT (2014) Variable nuclearity in lanthanoid coordination chemistry. Eur J Inorg Chem 2014:2849–2854

55. Andrews PC, Beck T, Fraser BH, Junk PC, Massi M, Moubaraki B, Murray KS, Silberstein M (2009) Functionalised β-diketonate polynuclear lanthanoid hydroxo clusters: synthesis, characterization, and magnetic properties. Polyhedron 2009:2123–2130

56. Thielemann DT, Fernández I, Roesky PW (2010) New amino acid ligated yttrium hydroxyl clusters. Dalton Trans 39:6661–6666

57. Jami AK, Kishore PVVN, Baskar V (2009) Functionalized β-diketone assisted self-assembly of a hexanuclear yttrium oxo-hydroxo cluster. Polyhedron 2009:2284–2286

58. Baril-Robert F, Petit S, Pilet G, Chastanet G, Reber C, Luneau D (2010) Site-selective lanthanide doping in a nonanuclear yttrium(III) cluster revealed by crystal structures and luminescence spectra. Inorg Chem 49:10970–10976

59. Li XL, He LF, Feng XL, Song Y, Hu M, Han LF, Zheng XJ, Zhang ZH, Fang SM (2011) Two chiral tetradecanuclear hydroxo-lanthanide clusters with luminescent and magnetic properties. CrystEngComm 13:3643–3645

60. Thielemann DT, Wagner AT, Rösch E, Kölmel DK, Heck JG, Rudat B, Neumaier M, Feldmann C, Schepers U, Bräse S, Roesky PW (2013) Luminescent cell-penetrating pentadecanuclear lanthanide clusters. J Am Chem Soc 135:7454–7457

61. Thielemann DT, Wagner AT, Lan Y, Oña-Burgos P, Fernández I, Rösch ES, Kölmel DK, Powell AK, Bräse S, Roesky PW (2015) Peptoid-ligated pentadecanuclear yttrium and dysprosium hydroxyl clusters. Chem Eur J 21:2813–2820

62. Zangana KH, Pineda EM, Winpenny REP (2014) Tetrametallic lanthanide(III) phosphonate cages: synthetic, structural and magnetic studies. Dalton Trans 43:17101–17107

63. Zangana KH, Pineda EM, Schnack J, Winpenny REP (2013) Octametallic 4f-phosphonate horseshoes. Dalton Trans 42:14045–14048

64. Li X, Liu Q, Lin J, Li Y, Cao R (2009) Phosphonate supported assembly of nanoscale lotus-leaf-shaped nonanuclear lanthanide clusters. Inorg Chem Commun 12:502–505

65. Su K, Jiang F, Qian J, Pang J, Hu F, Bawaked SM, Mokhtar M, AL-Thabaiti SA, Hong M (2015) Synthesis and characterization of decanuclear Ln(III) cluster of mixed calix[8]arene-phosphonate ligands (Ln = Pr, Nd). Inorg Chem Commun 54:34–37

66. Zhang ZC (2008) Poly[hexaaquaocta-μ_3-hydroxido-tetrakis(μ_3-methylenedisulfo-nato)-μ_6-oxido-hexaytterbium(III)]: the first lanthanide sulfonate containing a hexanuclear Ln-hydroxide/oxide cluster synthesized via 'ligand-controlled acidolysis' of lanthanide oxide. Acta Crystallogr C64:m381–m383

67. Nyman M, Bonhomme F, Alam TM, Rodriguez MA, Cherry BR, Krumhansl JL, Nenoff TM, Sattler AM (2002) A general synthetic procedure for heteropolyniobates. Science 297:996–998

68. Liu T, Langston MLK, Li D, Pigga JM, Pichon C, Todea AM, Müller A (2011) Self-recognition among different polyprotic macroions during assembly processes in dilute solution. Science 331:1590–1592

69. Sadeghi O, Zakharov LN, Nyman M (2015) Aqueous formation and manipulation of the iron-oxo Keggin ion. Science 347:1359–1362

70. Kamata K, Yonehara K, Sumida Y, Yamaguchi K, Hikichi S, Mizuno N (2003) Efficient epoxidation of olefins with $\geq 99\%$ selectivity and use of hydrogen peroxide. Science 300:964–966

71. Kozhevnikov IV (1998) Catalysis by heteropoly acids and multicomponent polyoxometalates in liquid-phase reactions. Chem Rev 98:171–198

72. Rausch B, Symes MD, Chisholm G, Cronin L (2014) Decoupled catalytic hydrogen evolution from a molecular metal oxide redox mediator in water splitting. Science 345:1326–1330

73. Busche C, Vilà-Nadal L, Yan J, Miras HN, Long DL, Georgiev VP, Asenov A, Pedersen RH, Gadegaard N, Mirza MM, Paul DJ, Poblet JM, Cronin L (2014) Design and fabrication of memory devices based on nanoscale polyoxometalate clusters. Nature 515:545–549

74. Lehmann J, Gaita-Ariño A, Coronado E, Loss D (2007) Spin qubits with electrically gated polyoxometalate molecules. Nat Nanotechnol 2:312–317

75. Cui K, Li F, Xu L, Xu B, Jiang N, Wang Y, Zhang J (2012) Lanthanide-tungstobismuthate clusters based on $[BiW_9O_{33}]^{9-}$ building units: synthesis, crystal structures, luminescent and magnetic properties. Dalton Trans 41:4871–4877

76. Zhao J, Li H, Li Y, Li C, Wang Z, Chen L (2014) Rectangle versus square oxalate-connective tetralanthanide cluster anchored in lacunary Lindqvist isopolytungstates: syntheses, structures, and properties. Cryst Growth Des 14:5495–5505

77. Moll HE, Nohra B, Mialane P, Marrot J, Dupré N, Riflade B, Malacria M, Thorimbert S, Hasenknopf B, Lacôte E, Aparicio PA, López X, Poblet JM, Dolbecq A (2011) Lanthanide

polyoxocationic complexes: experimental and theoretical stability studies and Lewis acid catalysis. Chem Eur J 17:14129–14138

78. Feng XJ, Han HY, Wang YH, Li LL, Li YG, Wang EB (2013) Assembly of chainlike polyoxometalate-based lanthanide complexes in one-pot reaction system. CrystEngComm 15:7267–7273

79. Ma P, Wan R, Si Y, Hu F, Wang Y, Niu J, Wang J (2015) Double-malate bridging tri-lanthanoid cluster encapsulated arsenotungstates: Syntheses, structures, luminescence and magnetic properties. Dalton Trans 44:11514–11523

80. Khoshnavazi R, Bahrami L, Davoodi H (2012) Decomposition of the lanthanide-containing sandwich-type polyoxometalates: synthesis and characterization of new multi samarium-containing polyoxometalates. Inorg Chim Acta 382:158–161

81. Hussain F, Patzke GR (2011) Self-assembly of dilacunary building blocks into high-nuclear $[Ln_{16}As_{16}W_{164}O_{576}(OH)_8(H_2O)_{42}]^{80-}$ (Ln = Eu^{III}, Gd^{III}, Tb^{III}, Dy^{III}, and Ho^{III}) polyoxotungstates. CrystEngComm 13:530–536

82. Rukk NS, Al'bov DV, Skryabina AY, Osipov RA, Alikberova LY (2009) Deca(hydroxo)-23-aqua-hexa(lanthanum(III)) iodide octahydrate and deca(hydroxo)-23-aqua-hexa(neodymium (III)) iodide octahydrate: syntheses and structures. Russ J Coord Chem 35:12–14

83. Wang R, Carducci MD, Zheng Z (2000) Direct hydrolytic route to molecular oxo-hydroxo lanthanide clusters. Inorg Chem 39:1836–1837

84. Tong YZ, Wang QL, Yang G, Yang GM, Yan SP, Liao DZ, Cheng P (2010) Hydrolytic synthesis and structural characterization of five hexanuclear oxo-hydroxo lanthanide clusters. CrystEngComm 12:543–548

85. Chesman ASR, Turner DR, Moubaraki B, Murray KS, Deacon GB, Batten SR (2012) Tetradecanuclear polycarbonatolanthanoid clusters: diverse coordination modes of carbonate providing access to novel core geometries. Dalton Trans 41:10903–10909

Synthesis and Structures of Lanthanide–Transition Metal Clusters

Xiu-Ying Zheng, Xiang-Jian Kong, and La-Sheng Long

Abstract Based on the inherent contribution of the d–f electrons and the unique exchange interactions between different metal ions, heterometallic lanthanide–transition metal (d–f) clusters have received substantial attention in modern chemistry. In the past two decades, numerous lanthanide–transition metal clusters with diverse molecular structures have been obtained. Various synthetic approaches have been developed by analyzing the crystal structures and reaction conditions. In this chapter, we discussed synthetic methodology based on hard and soft acids and bases (HSAB) theory and the resulting structures. In addition, personal perspectives and outlooks regarding the future research directions of d–f molecular clusters are provided at the end of this chapter.

Keywords Clusters • Crystal structure • Heterometallic lanthanide-transition metal (d–f) • Synthetic methodology

Contents

X.-Y. Zheng, X.-J. Kong (✉), and L.-S. Long (✉)
State Key Laboratory of Physical Chemistry of Solid Surfaces and Department of Chemistry,
College of Chemistry and Chemical Engineering, Xiamen University, Xiamen 361005, China
e-mail: xjkong@xmu.edu.cn; lslong@xmu.edu.cn

1   Introduction

Heterometallic lanthanide–transition metal (d–f) clusters have received substantial attention in the last two decades not only for the inherent contribution of their d and f electrons but also the unique exchange interactions between different metal ions. The unique topological arrangement of the different metal ions within these clusters often leads to interesting optical, electrical, magnetic, and catalytic properties [1–5]. Recently, d–f cluster-based molecular magnetic materials have attracted substantial attention for their great potential in high-density information-storage devices, quantum computers, spintronics and magnetocaloric materials [6–11].

Numerous lanthanide-transition metal clusters have been obtained in the past two decades. Crystal structure studies show that these d–f clusters exhibit diverse molecular structures, such as cage-like, ring-like, ball-like, and disc-like structures. By analyzing the crystal structure and reaction conditions, various synthetic approaches, including the anion-template method, cationic-template method, metalloligand method, and ligand-controlled hydrolytic method, have been developed. According to hard and soft acids and bases (HSAB) theory, the choice of ligands is very important for constructing d–f polynuclear clusters. Polydentate ligands, such as Schiff base ligands, amino acids, amino polyalcohols, oxime ligands, and polyoxometalate (POM), are considered good candidates [12–15].

This chapter focuses on the synthetic methodology and structural descriptions. In addition, personal perspectives and outlooks regarding the future research directions of d–f molecular clusters are provided at the end of this chapter. We hope that this account will contribute to the booming research focusing on d–f clusters.

2   Synthesis of d–f Clusters

The design and synthesis of high-nuclearity 3d–4f heterometallic clusters remain challenging because of the different coordination geometries of 3d and 4f metal ions and the instability caused by the overaggregation of metal ions. A number of efficient methods have been utilized to synthesize 3d–4f clusters. One typical

method is the self-assembly of mixed metal ions and ligands containing mixed donor atoms, such as Schiff bases, amino acids, and carboxylate ligands. Another effective synthetic method relies on the use of a metalloligand. This strategy can reduce some uncertainty in the reaction and simplify the synthesis of the target product. Recent studies have demonstrated that the anion template strategy, especially the mixed-anion template and multi-anion template approaches, is an effective synthetic method to construct high-nuclearity metal clusters. Reported complexes have also confirmed the potential of the cationic-template method.

2.1 Ligand-Controlled Assembly of d–f Clusters

Lanthanide ions and transition metal ions have different coordinative behaviors: Lanthanide ions behave as hard acids and prefer to bind to oxygen donors, whereas transition metal ions are borderline acids and have a strong tendency to coordinate to N-donors and O-donors. A chelate ligand containing N and O atoms is therefore the best choice. Under high pH conditions, the ligands can also limit the degree of lanthanide hydrolysis, forming structurally well-defined hydroxide clusters. Here, we summarize several types of ligands used in the assembly of d–f clusters.

2.1.1 Schiff Bases

Salen-type Schiff base ligands (Scheme 1) consisting of an N_2O_2 donor set are frequently used to construct 3d–4f clusters. By varying the amines or substituent groups on the aromatic rings, different Schiff base ligands with more coordination donor atoms have been prepared. Using different Salen-type Schiff base ligands, series of binuclear (MLn) [16], trinuclear (M$_2$Ln) [17–20], and tetranuclear (M$_2$Ln$_2$) [21–24] clusters have been obtained. Other Schiff base ligands created
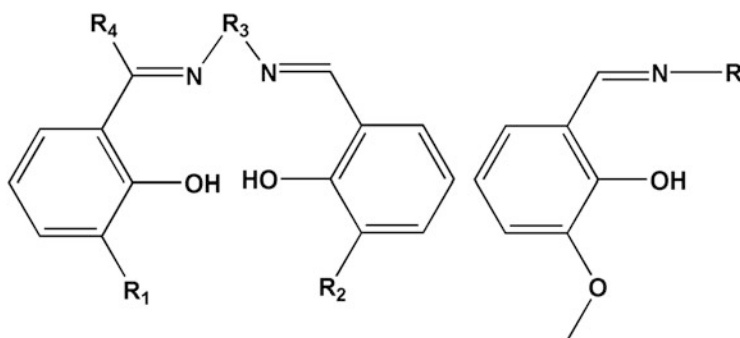
Scheme 1 Schiff base ligands derived from salicylaldehyde and diamines and other Schiff base ligands (R: aliphatic alkyl or aryl substituent)

by reacting aldehydes and amines are also ideal candidates for assembling 3d–4f clusters. Different Schiff base ligands with more coordination donor atoms have been used to produce series of d–f clusters, such as M_2Ln [25], M_2Ln_2 [26, 27], Ni_4Ln_2 [28], Mn_4Dy_3 and Mn_4Dy_5 [29], and $Dy_{10}Co_2$ [30]. These works have shown that the 3d/4f/L molar ratios, co-ligands, and other external physical stimuli (such as temperature, pH, and pressure) can strongly influence the structures of related 3d–4f clusters.

2.1.2 Amino Acids

Amino acids are the building blocks of proteins (Scheme 2). The interactions between amino acids and metal ions have been studied extensively to elucidate the functions of metals in biomolecules. Because of the flexible and various coordination modes of their carboxylate group with lanthanide ions and their amino group with transition metal ions, amino acids have been widely studied in relation to 3d–4f clusters.

α-Amino acid-supported 3d–4f clusters have been extensively studied because of their commercial availability in both enantiomeric forms, such as $LnNi_6$ [31], Ln_3Cr_2 [32], Ln_2Ni_9 [33], $Cu_{12}Gd_6$ [34], $Cu_{24}Gd_6$ [35–38], and $Cu_{26}Tb_6$ [36]. Amino polycarboxylic acids are also excellent ligands for the synthesis of polynuclear 3d–4f clusters or extended complexes. Many higher-nuclearity aggregates, such as Ni_6La_3 [39], $Ni_{30}La_{20}$ [40], $Ni_{54}Gd_{54}$ [41], and $Ni_{76}La_{60}$ [42], have been prepared through self-assembly based on ligands containing –NH and –COOH groups. Because of the flexible coordination mode of the amino acids, different structural 3d–4f clusters have been obtained by varying the reaction conditions, such as the molar ratio, anion template, solvent, and temperature.

2.1.3 Amino Polyalcohols

Amino polyalcohols are another ideal ligand for constructing 3d–4f polynuclear complexes because they contain multiple N- and O-donor atoms (Scheme 3). The triethanolamine (H_3tea) ligand has been extensively studied and used to create a series of 3d–4f clusters with novel core topologies. In 2006, Christou's group synthesized the 3d–4f cluster of Ln_2Fe_2 [43] using the $teaH_3$ ligand. Subsequently, very similar analogues of Ln_2Co_2 [44] and Ln_2Mn_2 [45] have been reported based on the same ligand. To date, the metallo-ring $Fe_{16}Ln_4$ [46] and Fe_4Dy_4 [4], the metallo-disc Mn_3Ln_4 [29], the metallo-star Mn_3Ln and Fe_3Ln [47], and the metallo-

Scheme 2 α-Amino acid and aminoacetic acid derivatives (R: variable substituent)
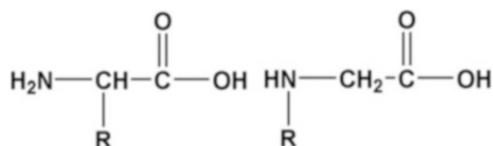
Scheme 3 Triethanolamine (H₃tea) and functionalized diethanolamine (RH₂dea) ligands
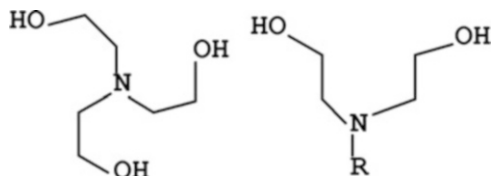
Scheme 4 Pyridine oxime and salicyl hydroxamic acid ligands (R: variable substituent)
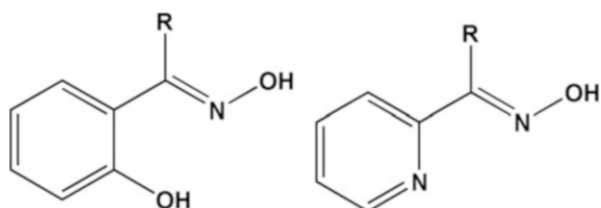
cage Fe_7Ln_4 [48], Mn_9Dy_8 [49], Mn_4Ln_2 [50], and Cu_5Ln_4 [51] have been prepared based on the H_3tea ligand.

Diethanolamine (H_2dea) and functionalized diethanolamines (RH_2dea, where R=Me, ^nBu, and ^tBu) are important amino polyalcohol ligands for the preparation of 3d–4f clusters. For example, with the use of H_2dea and RH_2dea, Co_2Ln_2 [52], Mn_2Ln_2 [53], Mn_2Ln_3 [54], Cr_4Dy_4 [55], Mn_4Ln_4 [56], Mn_5Ln_4 [57], Fe_7Dy_3 [58], $Mn_{12}Ln_6$ [59], Mn_2Ce_8 [60], $MnCe_9$ [60], Mn_2Ce_4 [60], and M_5Ln_8 [61, 62] have been created using different reaction conditions.

2.1.4 Oxime Ligand

Oxime ligands, such as pyridine oxime and salicyl hydroxamic acid, have also been extensively studied in relation to 3d–4f clusters (Scheme 4). By varying the substituent group of the salicyl hydroxamic acid ligands, many Mn–Ln clusters, such as Mn_4Ln_3 [29], Mn_6Ln_2 [63], Mn_4Ln_4 [64], and Mn_5Ln_5 [63, 65], can be obtained. In their structures, the salicyl hydroxamic acid ligands display various coordination modes. Pecoraro and coworkers synthesized a family of metallacrown (MC)-like complexes, such as Cu_5Ln [66–68], Mn_6Ln_4 [69], Mn_4Ln_2 [70, 71], and Mn_8Ln_4 [72], using salicyl hydroxamic acid ligands.

Pyridine oxime ligands have also been utilized to synthesize 3d–4f clusters. The two N atoms from the pyridine and NO groups can chelate one transition metal ion, and the outer O atom can link another 4f ion. Pyridine and its derivatives have been used to create a family of 3d–4f clusters, including $CuLn$ [73] or $NiLn$ [74], M_2Ln_2 [75], Ni_2Ln [76], and Ni_8Dy_8 [77] complexes.

Scheme 5 Lacunary
polyanions of XW_9, X_2W_{15}
and P_2W_{12}
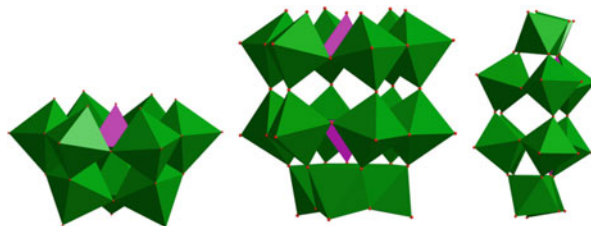
2.1.5 POM

POMs are a well-known class of anionic clusters composed of oxo-bridged transition metals. They show remarkable structural diversity and have numerous potential applications .A significant number of lacunary POMs have been proven to have well-defined metal cation-binding sites (Scheme 5). Although the classes of 3d-substituted POMs and 4f-containing POMs have grown significantly, less work has been dedicated to heterometallic 3d–4f POMs. Trilacunary Keggin subunits (XW_9, X=P, Ge, As, or Sb) have shown great potential for the design of heterometallic clusters with O-bridged 3d–4f atoms. For example, Ce_2Mn_2-GeW_9 [78], $CeCu_3$-GeW_9 [79], LnV_2AsW_9 [80], $DyCu_3$-GeW_9 [81], and Dy_3Co_2-GeW_9 [82] have been obtained using XW_9 POM units. Monolacunary (XW_{11}) and dilacunary Keggin subunits (XW_{10}) have also been used to produce several 3d–4f clusters, such as $FeCe$-AsW_{10} [83], Ln_6Fe_6-SiW_{10} [84], and $LnCu_3$-SiW_{11} [85]. The trilacunary $[P_2W_{15}O_{46}]^{12-}$ Wells–Dawson species is another important building block for assembling 3d–4f heterometallic clusters. Fang and Kögerler obtained a $CeMn_6$-P_2W_{15} cluster using preformed heterometallic complexes $[CeMn_6O_9(OAc)_9(NO_3)(H_2O)_2]$ as precursors in the reaction with lacunary P_2W_{15} POMs under normal bench conditions [86]. They also prepared a Ce_3Mn_2 cluster based on the P_2W_{15} POMs [87]. In addition, the P_2W_{12} building block was used to construct a series of 3d–4f clusters, such as Ce_3Mn_2 [88].

2.2 Anion-Template Methods

Anions can act not only as templates to induce the formation of the cluster skeletons but also as negative charges to balance the positive charges of metal ions (Scheme 6). In this chapter, an overview of hydrogen bonding- and coordination bonding-based anions as templates is provided.

2.2.1 CO_3^{2-}

The carbonate anion is a very common anion template for 3d–4f clusters because of its versatile coordination modes (Scheme 7) and the relatively strong coordination bonding between CO_3^{2-} and metal ions. The first example of a carbonato-bridged
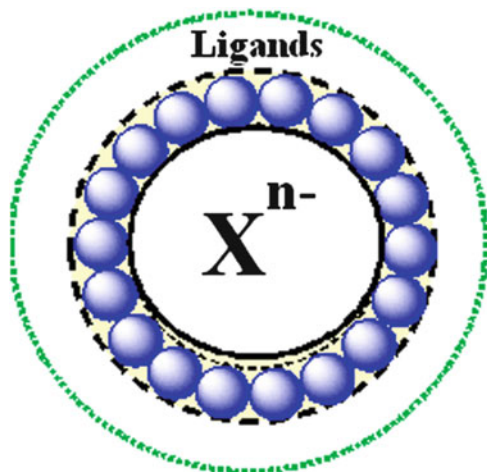
Scheme 6 Scheme of metal clusters based on anion-template methods. *Blue spheres*: metal atoms
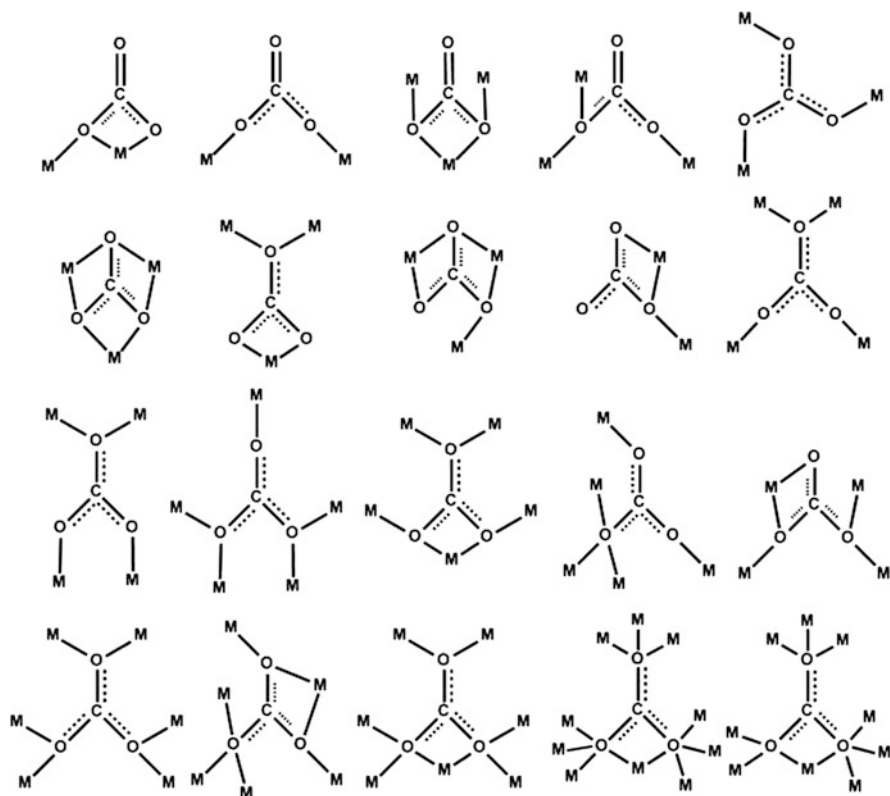
Scheme 7 Reported bridging modes of the CO_3^{2-} ion
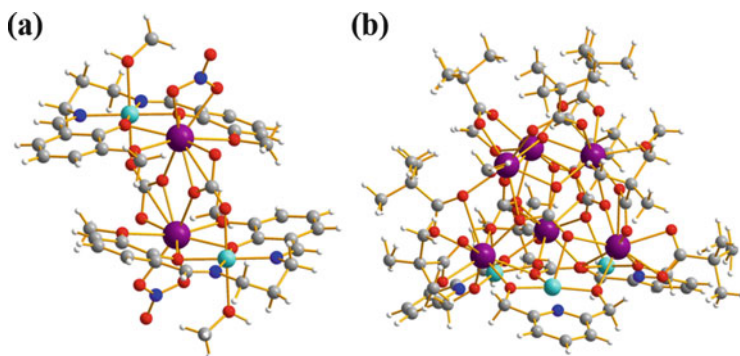
Fig. 1 (**a**) Crystal structure of tetranuclear Gd$_2$Ni$_2$. (**b**) Crystal structure of the complex Gd$_6$Cu$_3$. *Purple*: Ln (lathanide metal). *Light blue*: M (transition metal). *Gray*: C. *Blue*: N. *Red*: O. *White*: H

3d–4f complex generated by atmospheric CO_2 fixation was reported by Sakamoto et al. [90]. Ni$_2$Ln$_2$ tetranuclear compounds were obtained by the reaction of [Ni (3-MeOsaltn)(H$_2$O)$_2$], Gd(NO$_3$)$_3 \cdot$ 6H$_2$O, and triethylamine (Fig. 1a) [89]. Subsequently, the syntheses of Zn$_2$Ln$_2$ and Ni$_2$Ln$_2$ were reported by adopting similar ligands [80, 91–93]. Two octanuclear compounds with Ni$_4$Ln$_4$ structures obtained through the coordination of atmospheric CO_2 were recently reported by Pasatoiu et al. [94]. The carbonato ligand is presumably generated from the fixation of atmospheric CO_2 in a basic medium through the nucleophilic attack of the hydroxo species bound to the Ln ions on the electrophilic C atom of CO_2. Employing pyridine-2,6-dimethanol afforded a new Cu$_5$Gd$_7$ cage-like molecule with a beautiful structure built by fused triangular subunits. The CO_3^{2-} ions are presumably derived from the fixation of atmospheric CO_2. Identification of the CO_3^{2-} ions (vs NO_3^-) was achieved based on X-ray diffraction data and IR absorption bands [95]. A similar fixation of atmospheric CO_2 for the slow formation of CO_3^{2-} has been observed in Zn$_4$Eu$_4$ [96], Ni$_8$Ln$_4$ [97], and Wells–Dawson Fe$_6$Ln$_6$P$_6$ [98].

Interestingly, a CO_3^{2-}-paneled Gd$_6$Cu$_3$ cage (Fig. 1b) with a tridiminished icosahedral structure can be synthesized by bubbling CO_2 through a solution of Gd and Cu ions [99]. Although Na$_2$CO$_3$ or NaHCO$_3$ can be deliberately added either initially or to improve the yield of a serendipitously obtained product, the direct use of CO_2 as a starting material has only been reported a few times.

2.2.2 2NO$_3^-$

The coordination mode of the nitrate anion is very similar to that of the carbonate anion. Winpenny and coworkers observed that the reaction of [Cu$_6$Na(mhp)$_{12}$] [NO$_3$] (mhp=6-methyl-2-pyridone) with hydrated lanthanum nitrate leads to a high-nuclearity complex with a Cu$_{12}$La$_8$ core [100]. A disordered nitrate anion is encapsulated inside a polymetallic core. These authors also reported heterometallic clusters of Cu$_{24}$Ln$_8$ cages. The structure of Cu$_{24}$Ln$_8$ consists of eight Dy^{III} centers at the vertices of a cube with 12 coppers inside and 12 coppers outside the cube.
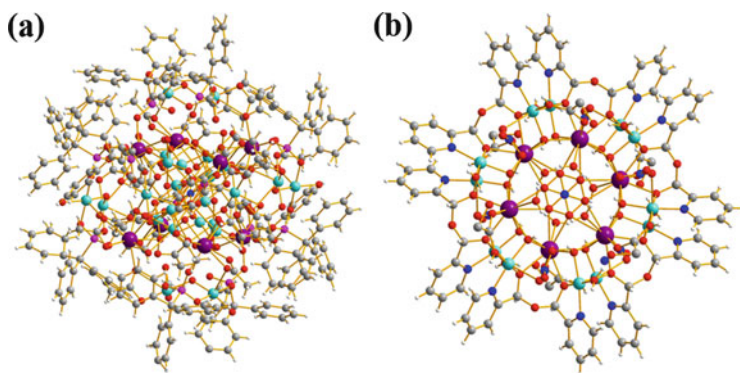
Fig. 2 (**a**) Crystal structure of $Cu_{12}La_8$; (**b**) crystal structure of Gd_6Cu_{12}. *Purple*: Ln. *Light blue*: M. *Gray*: C. *Blue*: N. *Red*: O. *White*: H

The 12 inner coppers are arranged in the form of a cuboctahedron and are connected by one NO_3^- [101] (Fig. 2a).

By introducing PF_6^- anions into the betaine reaction system, Chen et al. reported a $Cu_{12}Nd_6$ cluster. In the center of the octahedral $Cu_{12}Nd_6$ cage, an encapsulated NO_3^- anion exists that exhibits a multi-coordinating mode, with each of its O atoms weakly ligating three or four Cu^{II} atoms of the cage [102].

Reacting picolinaldehyde and acetylpyridine with $Gd(NO_3)_3$ and $Cu(OAc)_2$, Tong et al. synthesized varieties of 3d–4f clusters of S-shaped Ln_9Cu_8, featuring eight vertex-sharing Ln_2Cu triangles arranged around two NO_3^- [103]. Through a two-step in situ reaction of picolinaldehyde, they obtained a hexagonal wheel of Gd_6Cu_{12} featuring six vertex-sharing Gd_2Cu_2 units. The central NO_3^- anion may act as a template in the construction of the hexagon (Fig. 2b) [104]. Tong et al. reported wheel-shaped nanoscale 3d–4f $Co_{16}Ln_{24}$ clusters (Ln=Dy and Gd). Four internal nitrates coordinated in a u_3-η^1: η^1: η^1 mode may play a template role in the formation of the wheel-like structure [105].

2.2.3 $C_2O_4^{2-}$

Because of the insolubility of lanthanide oxalates, only a few oxalate templated 3d–4f clusters have been reported. To avoid the formation of lanthanide oxalate precipitate, the slow introduction/release of oxalate by ligand decomposition is necessary. One of the first oxalate-bridged $Cu^{II}Ln^{III}$ complexes was reported by Kahn et al., with the oxalate ions resulting from the decomposition of a bis(oxalate) ligand [106]. Two types of oxalate-bridged heterometallic 3d–4f compounds, Ni_6Ln_6 (Fig. 3a) and Ni_4Gd_2 (Fig. 3b), have been obtained by connecting six
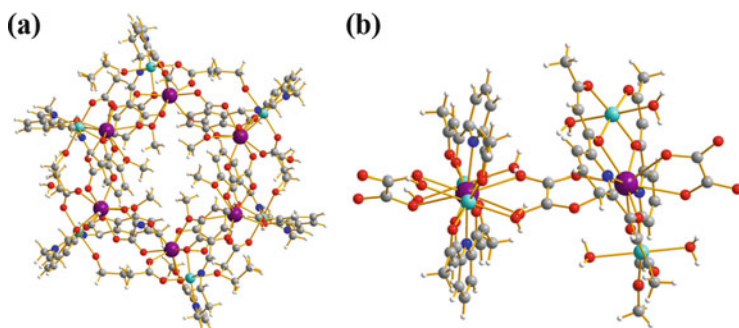
Fig. 3 (**a**) Dodecanuclear structures of Dy_6Ni_6; (**b**) molecular structure of Gd_2Ni_4. *Purple*: Ln. *Light blue*: M. *Gray*: C. *Blue*: N. *Red*: O. *White*: H

binuclear and two trinuclear moieties through oxalate bridges arising from the slow decomposition of L-ascorbic acid [107].

Utilizing 3d-oxalates as a reaction precursor is another method to avoid creating insoluble lanthanide oxalates. By selecting the complex ligand Λ-Na[Cr (acac)$_2$(ox)] as the precursor, Kaizaki et al. prepared a series of chiral hetero-metal dinuclear Cr-ox-Ln complexes [108].

Yamada and coworkers used the divalent mononuclear complex anion [Co(nta) (ox)]$_2$(nta=nitrilotriacetate) as an effective building block for the construction of oxalate-bridged heteropolynuclear lanthanide complexes. The reaction of [Co(nta) (ox)]$_2$ with the Dy^{3+} ion in a molar ratio of 1:1 was used to form a dinuclear CoDy complex, whereas a similar reaction with a ratio of 2:1 results in the formation of the trinuclear species of $DyCo_2$ [109].

2.2.4 ClO_4^-

In 1995, Chen and Hendrickson et al. reported a polynuclear $Cu_{12}Ln_6$(Ln=Y, Nd, or Gd) complex encapsulating a u_{12}-ClO_4^- anion [110]. The cation core may be described as having a pseudocubic O_h symmetry, with the six Gd^{3+} ions positioned at the vertices of a regular nonbonding octahedron and the 12 Cu^{2+} ions located at the midpoints of the 12 octahedral edges (Fig. 4a). Subsequently, Huang et al. reported a similar cluster using different ligands [111]. Wu et al. synthesized a series of Ln_6Cu_{24} with different amino acids as ligands [37]. The encapsulated ClO_4^- anion is at the center of the Ln_6Cu_{12} octahedral inner metal cage (Fig. 4b).

Kong and Long et al. reported two heterometallic cage-like $Dy_{24}M_2$ (M=Ni, Mn) cluster compounds obtained through the self-assembly of the metal ions and myo-inositol ligands. Structural analysis revealed that three ClO_4^- anions, acting as templates, are immobilized in the cages of the clusters through hydrogen bonding [112].
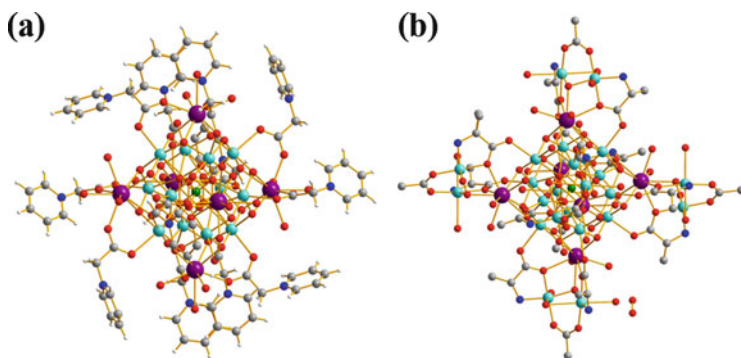
Fig. 4 (**a**) Stereoview of the $Gd_6Cu_{12}ClO_4$ core inscribed inside an octahedron; (**b**) stereoview of the structure of one of the vertices of the octahedron of Ln_6Cu_{24}. *Purple*: Ln. *Light blue*: M. *Gray*: C. *Blue*: N. *Red*: O. *White*: H. *Green*: Cl

2.2.5 SO_4^{2-} and PO_4^{3-}

As simple tetrahedral oxo-anions, sulfates and phosphates have versatile coordination modes. However, few 3d–4f clusters with sulfate or phosphate anions as templates have been reported because of the insolubility of lanthanide sulfates and phosphates. Winpenny and McInnes et al. reported a 3d–4f phosphonate Co_4Ln_{10} cage with two μ_6-bridging phosphates located in the center of the cage. The phosphates may have resulted from hydrolysis, and the phosphonate may have arose under solvothermal reaction conditions. These authors attempted to improve the yields of Co_4Ln_{10} by introducing Na_3PO_4 as a phosphate source. However, under otherwise identical reaction conditions, Co_6Ln_4 clusters without PO_4^{3-} were obtained [113].

2.2.6 $X^-(X=F^-, Cl^-, Br^-)$

Because of the precipitation of insoluble LnF_3, the synthesis of F^--based 3d–4f clusters is difficult. Similar to other insoluble lanthanide complexes, using the 3d–F complex as a reaction precursor is a successful method to construct F^--based 3d–4f clusters. Using $\{Cr_6F_{11}(O_2CtBu)_{10}\}_3]_2$ as a ligand, Winpenny and Prozorov et al. reported a series of $\{(Cr_6)Ln_x\}_n$ (Fig. 5a) [114]. Bendix et al. also showed that robust chromium(III)-F complexes are a convenient route to heterometallic complexes with fluoride bridges, such as Dy_2Cr [115], Ln_2Cr_2 (Fig. 5b) and Ln_3Cr_2 (Fig. 5c) [32], and Gd_3M_2 (M=Cr, Fe, or Ga) [116].

A bridge based on Cl^- in 3d–4f clusters has also been reported. Some μ_3-Cl atoms are observed in series of MnLn clusters, such as Mn_4La [117], Ce_3Mn_6 [118], Ce_3Mn_8 [118], $Ce_{10}Mn_4$ [118], and $CeMn_{11}$ [118]. Br^--supported 3d–4f clusters are rare. Qiu and Powell et al. adopted a pre-designed Schiff base tripodal ligand and synthesized a hepta nuclear CuGd cluster. In this cluster, two μ_3-Br ligands occupy axial sites on the Cu centers and bridge between three Cu atoms [119].
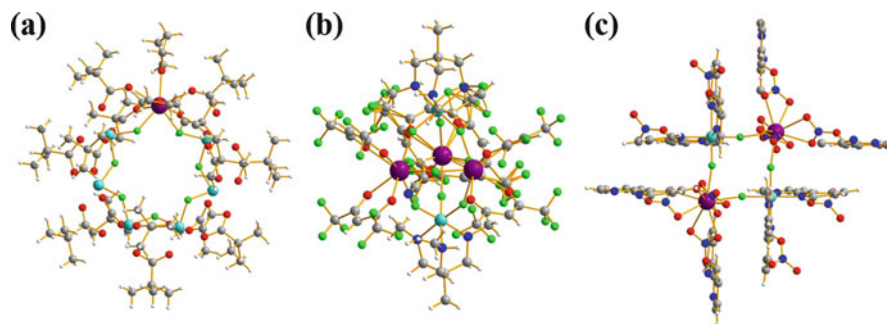
Fig. 5 Molecular structures of (**a**) CeCr$_6$; (**b**) Ln$_3$Cr$_2$; (**c**) Ln$_2$Cr$_2$. *Purple*: Ln. *Light blue*: M. *Gray*: C. *Blue*: N. *Red*: O. *White*: H. *Light green*: F

2.2.7 Mixed-Anion Template

The use of a simple single anion as a template has been studied most extensively. However, compared with the single-anion template, a multiple-anion template would be a better approach to construct high-nuclearity 3d–4f metal clusters because of its dispersion of the clusters' positive charge.

In 2007, Long and Zheng et al. reported a dual-shell Keplerate cluster of La$_{20}$Ni$_{30}$ under hydrothermal conditions using a mixture of Ni(NO$_3$)$_2$, La(NO$_3$)$_3$, and iminodiacetic acid (IDA) [40]. In the two-shell cage clusters, six CO$_3^{2-}$ and six NO$_3^-$ acted as templates and were located on the 12 pentagonal faces of a dodecahedron. The CO$_3^{2-}$ is a putative product of IDA decomposition under hydrothermal conditions. Notably, under hydrothermal reactions, the IDA also can decompose into C$_2$O$_4^{2-}$, in addition to CO$_3^{2-}$. The decomposed C$_2$O$_4^{2-}$ was captured in sandwich-like Ln$_{20}$Ni$_{21}$ clusters [120], in which three C$_2$O$_4^{2-}$ and nine NO$_3^-$ anions play templating roles in the cage-like structures. The slow release of these template anions is important for the formation of high-nuclearity metal clusters.

Based on the mixed-anion template strategy, Kong and Long et al. reported one 48-metal 3d–4f cluster of Gd$_{36}$Ni$_{12}$ based on simple acetate ligands [121]. In this cluster, 48 metal ions were assembled into a tube-like structure, with one NO$_3^-$ and two Cl$^-$ ions confined inside the tube (Fig. 6a). The presence of both the Cl$^-$ and NO$_3^-$ anions in the cluster cation is believed to be critical for the formation of the final product. Interestingly, by changing the anions, four 52-metal-ion 3d–4f cluster complexes featuring a common core of Ln$_{42}$M$_{10}$ (Ln=Gd^{3+}, Dy^{3+}; M=Co$^{2+/3+}$, Ni^{2+}) were obtained through the self-assembly of the metal ions templated by mixed anions (ClO$_4^-$ and CO$_3^{2-}$) (Fig. 6b). The CO$_3^{2-}$ is thought to be formed through the absorption of atmospheric CO$_2$ [122].
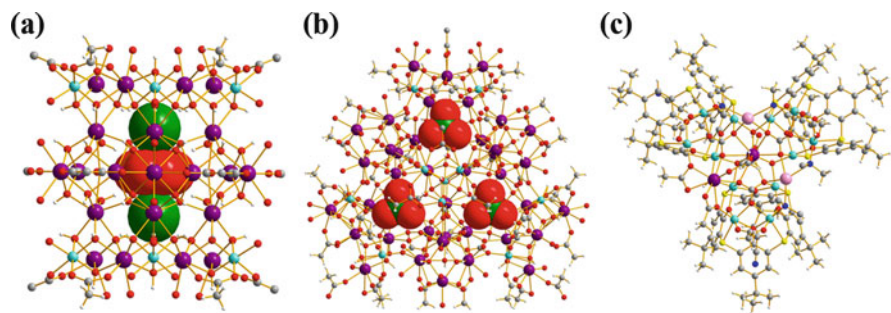
Fig. 6 (**a**) Ball-and-stick view of the cluster cation in $Ln_{36}Ni_{12}$; (**b**) ball-and-stick view of the cationic $Ln_{42}Co_{10}$ cluster; (**c**) molecular structure of the $Na_2Ni_{12}Ln_2$ complex. *Purple*: Ln. *Light blue*: M. *Gray*: C. *Blue*: N. *Red*: O. *White*: H. *Green*: Cl. *Yellow*: S. *Pink*: Na

Hong et al. reported thiacalix [4] arene-supported $Na_2Ni_{12}Ln_2$ clusters with vertex-fused tricubane cores (Fig. 6c).Three u_7-CO_3^{2-} anions and two u_3-Cl^- anions acted as mixed templates [123].

2.3 Cationic Template Methods

Compared with the anion template method, cationic template-based d–f clusters are difficult to design and synthesize. Only a few cationic-templating 3d–4f clusters have been reported and were incidentally discovered.

The lanthanide ion is the most common cationic template able to induce the formation of 3d–4f clusters. Yukawa et al. reported an $SmNi_6$ cluster based on the reaction of bis(l-pralinato)nickel(ii) ligands and $Sm(ClO_4)_3$ [124, 125]. Six Ni and one Sm form a Sm^{3+}-centered octahedron. The 12-coordinate Sm may play an important role in the formation of the octahedral structure (Fig. 7a). A similar heptanuclear octahedral $LnNi_6$ was obtained by Wu et al. using different amino acids as ligands in aqueous media [126]. Interestingly, Gao and Li et al. found that six transition metals and one lanthanide can also forma lanthanide-centered wheel structure based on N-carboxymethyl-N-(2-carboxyphenyl) glycine acid (Fig. 7b) [127] and lanthanide-centered trigonal prismatic clusters based on the IDA ligand [128]. The Schröder group reported the $\{M@[Ni(L)]_6\}^{3+}$ cationic octahedral cage (M=La, Ce, Pr, or Nd). Interestingly, the templating metal can be replaced by Sror Ba [31].

Pecoraro reported a metallacrown-like $LnCu_5$ (Ln=Nd, Eu, Gd, or Sm) using an appropriate hydroxamic acid and an appropriate chiral MC building block. ALn^{3+} ion is encapsulated in the center of the complex through the ligation of the oxime oxygen atoms [66, 67, 129–131].

Christou et al. accidentally obtained a $CeMn_6$ cluster via the reaction of [Mn $(O_2CMe)_2]\cdot 4H_2O$ in aqueous acetic acid with Ce^{4+}. $CeMn_6$ consists of a wheel of Mn_6 with a central lanthanide ion [132]. For targeted syntheses of large metal loops,
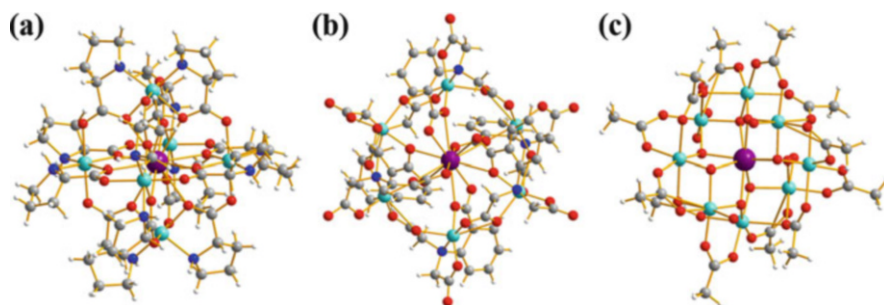
Fig. 7 (**a**) Molecular structure of the SmNi$_6$ metal cluster; (**b**) stereoview of the wheel-like cluster core of the PrCu$_6$ complex; (**c**) molecular structure of CeMn$_8$ complex. *Purple*: Ln. *Light blue*: M. *Gray*: C. *Blue*: N. *Red*: O. *White*: H

Christou et al. used the oxophilic Ce^{4+} ion as a template to warp the linear Mn^{III} polymer {[Mn(OH)(O$_2$CMe)$_2$] and generated a CeMn$_8$ cluster (Fig. 7c) [133]. The lanthanide ion can also be trapped in a well-designed macrocyclic ligand, forming tetranuclear macrocyclic 3d–4f complexes of Zn$_3$Ln and Cu$_3$Ln [134, 135].

2.4   Metal Ligand Method

Lanthanide ions and transition metal ions have different coordinative behaviors: The lanthanide ions behave as hard acids, preferring O- to N-donors, while transition metal ions, such as nickel(II), are borderline acids and have a strong tendency to coordinate to N-donors and O-donors. The metalloligand strategy can reduce some uncertainty in the reaction, simplifying the reaction process needed to successfully synthesize the target product. First the ligand and the transition metal ions form a metal ligand, and then, the lanthanide ions are added to construct the d–f metal clusters. The many reported 3d–4f clusters have demonstrated that the metal ligand strategy is an effective synthetic method to construct 3d–4f clusters.

Iminodiacetate anions form complexes with transition metal centers in which four noncoordinated oxygen atoms can act as potential donors for lanthanide ions. Series of 3d–4f clusters, including LnNi$_6$ [128, 136], Ln$_2$Ni$_9$ [33], Ln$_5$Ni$_{12}$ (Fig. 8a) [33], Ln$_{20}$Ni$_{30}$ [116], Ln$_{20}$Ni$_{21}$ [116], Ln$_{52}$Ni$_{56}$ [41], and Ln$_{60}$Ni$_{76}$ [42], have been obtained based on the iminodiacetic acid ligand.

IDA derivatives are also efficient chelators for transition metals and the construction 3d–4f clusters. Gao et al. reported series of tetranuclear clusters of Ln$_2$Co$_2$ [137] and heptanuclear clusters of LnCu$_6$ [127] using H$_4$CDTA (*trans*-1,2-cyclohexanedinitrilotetra acetic acid) as a ligand. Using *N*-(phosphonomethyl) iminodiacetic acid and L-alanine-*N*-monoacetic acid as ligands, Kong and Long et al. synthesized a Gd$_6$Ni$_3$ cluster (Fig. 8b) [138] and Ln$_6$Cu$_{24}$Na$_{12}$ (Ln=Gd, Dy) clusters (Fig. 8c) [38], respectively.
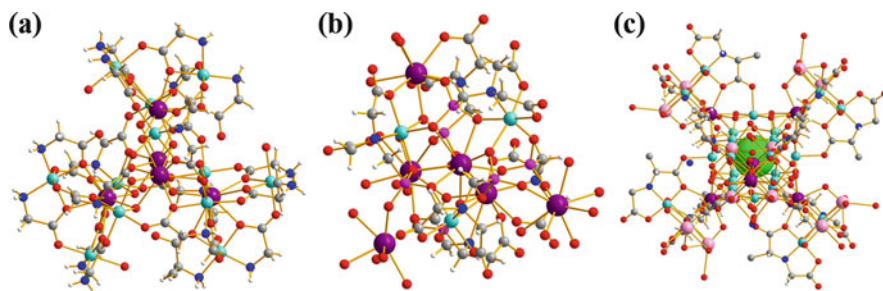
Fig. 8 (**a**) Overall structure of the Gd_5Ni_{12} cation cluster; (**b**) molecular structure of Gd_6Ni_3; (**c**) cation core of $Gd_6Cu_{24}Na_{12}$. *Purple*: Ln. *Light blue*: M. *Gray*: C. *Blue*: N. *Red*: O. *White*: H. *Green*: Cl. *Pink*: Na. *Rose red*: P

3 Structural Characterization

The past 30 years have witnessed the development of a new area of d–f coordination chemistry featuring a large number of d–f complexes with structurally and compositionally well-defined cluster-type core motifs. The history of clusters begins in 1985, when the Italian chemist Gateschi reported the first lanthanide-transition heteronuclear complex, Gd-Cu [139]. To date, many different configurations of d–f clusters with nuclearities up to 136 have been reported in the literature. The characterization of their crystal structures would undoubtedly form a basis for interpreting some of their properties. In this chapter, we divide discrete d–f complexes into types defined by the number of metal centers. By gathering and comparing complexes with similar structural topologies, we wish to inspire future designs of polynuclear d–f clusters.

3.1 Trinuclear d–f Clusters

Linear arrangements and triangular configurations are the main metal alignments in trinuclear 3d–4f clusters.

3.1.1 Linear trinuclear Alignments

Many different types of linear trinuclear 3d–4f clusters have been reported. In 2008, Chandrasekhar et al. reported the linear Mn–Ln–Mn 3d–4f cluster, in which the two Mn^{II} ions are present in a distorted octahedral arrangement, and the central lanthanide ion is surrounded by 12 oxygen atoms. The arrangement of the three metal ions in these heterometallic complexes is nearly linear, featuring Mn–Ln–Mn bond angles near 180° (Fig. 9a) [140]. Analogous linear trinuclear clusters were
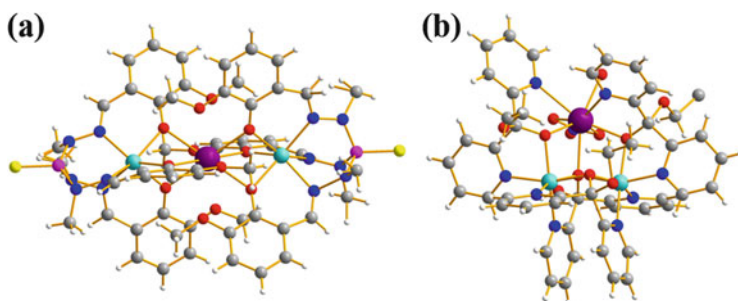
Fig. 9 (**a**) Molecular structure of LnMn$_2$; (**b**) plot of the heterometallic cation present in TbNi$_2$. *Purple*: Ln. *Light blue*: M. *Gray*: C. *Blue*: N. *Red*: O. *White*: H. *Yellow*: S. *Rose red*: S.

synthesized with other transition metals, such as Fe–Ln–Fe [141], Co–Ln–Co [142–144], Ni–Ln–Ni [56, 76], and Zn–Ln–Zn [145]. Another type of linear trinuclear 3d–4f Ln–M–Ln cluster was observed in two-fluoride-bridged Dy$_2$Cr [115], Dy$_2$Fe [146], Ln$_2$Ni [147] and Dy$_2$Cu [148]. Nonlinear alignments have also been noted in some M–Ln–M and M–M–Ln compounds, such as Fe–Ln–Fe [19], Co–Ln–Co [149], Mn–Ln–Mn [150], and Mn–Mn–Ce [151].

3.1.2   Triangular Configurations

Most trinuclear complexes are triangular, with the three metal ions bridged by a μ_3-O^{2-} ion [152–156]. For example, the crystal cation [Ni$_2$Tb{(py)$_2$C(OEt) (O)}$_3${(py)$_2$C(OH)(O)}(NO$_3$)(H$_2$O)]$^{2+}$ consists of one Tb^{III} and two Ni^{II} atoms in a triangular arrangement, capped by a central μ_3-O^{2-} atom. Each edge of the Ni$_2$Tb triangle is bridged by the deprotonated O atom of the ligand, and pyridyl nitrogen and the alkoxide oxygen atom each chelate a metal ion, forming two five-membered chelating rings (Fig. 9b) [156].

3.2   Tetranuclear 3d–4f Clusters

The tetranuclear complexes constitute one of the largest families of d–f clusters. The reported tetranuclear 3d–4f complexes show different structural topologies, including cubane-like, ring-shaped, propeller-shaped (or star-shaped), and co-planar arrangements.

3.2.1   Cubane-Like Topology

M$_2$Ln$_2$ and M$_3$Ln tetranuclear complexes exhibit versatile metallic topologies and molecular structures. Among the complexes with a planar M$_2$Ln$_2$ arrangement, one

type of metallic core topology can be described as a "defective dicubane" or "butterfly" structure. In contrast, others have a tetrahedral M_2Ln_2 or M_3Ln topology that can be called a "cubane-like" structure [157].

In the "defective dicubane" structure, the four metal ions are linked together by two μ_3-O and are further bridged by four μ_2-O, forming an $M_2Ln_2O_6$ core. The two 3d ions and two 4f ions can be regarded as being in the same plane, and the six oxygen atoms are located above and below the plane in acentrosymmetric arrangement. In the reported $[(NO_3)_2Gd(ovan)_2(HO)Co_2(OH)(ovan)_2Gd(NO_3)_2]$ (ovan=orthovanillin) [158] (Fig. 10a), the vertices of the common face of the defect dicubane are occupied by the two cobalt ions and the two hydroxo groups, which form a double bridge between the Co ions. Each μ_3-OH group is also linked to a Gd^{3+} ion. Around the cobalt ion, the phenoxo oxygen atoms are in a *trans* arrangement, whereas they take on a *cis* arrangement for the Gd ion. In addition to Gd_2Co_2, the family of tetranuclear M_2Ln_2 clusters with a defective dicubane structure includes many other examples, such as Ln_2Mn_2 [45, 53], Ln_2Fe_2 [45, 159], and Dy_2Co_2 [27].As shown in Fig. 10b, $[Ni_2Ln_2(L)_4(NO_3)_2(DMF)_2]$ [26] and $[Fe_2Ln_2(\mu_3\text{-}OH)_2(teg)_2(N_3)_2(piv)_4]$ [44] (teg=triethylene glycol, piv=pivalate) have butterfly-shaped structures. In Ni_2Ln_2, the core can be described as possessing a defect dicubane or butterfly topology, with the two Ni^{II} ions in the body positions and the Dy^{III} ions in the wing positions. In one Fe_2Ln_2 compound, the Fe centers occupy the wing tip positions, whereas in the second, these positions are occupied by the Ln ions. LnM_3 tetranuclear complexes also have butterfly-shaped structures [43].

In addition to the various defective dicubane structures, M_2Ln_2 and M_3Ln clusters often exhibit tetrahedral topologies. The complex $[Ni_2Gd_2(\mu_3\text{-}OH)_2(L)_2(OAc)_4(H_2O)_{3.5}](ClO_4)_2$ possesses a distorted $[Ni_2Gd_2O_4]$ cubane core with two μ_3-OH^- and two μ_3-$O_{phenolate}$ groups as the vertices [160]. The complexes $[Co_2Ln_2(pdmH)_4(Piv)_6]$ [52] (pdmp = 2,6-pyridinedimethanol), $[M_2Ln_2(hmp)_4(PhCO_2)_5(ROH)_2](ClO_4)(M=Ni/Zn,$ $Ln=Dy/Gd/Y)$ (hmp=2-hydroxymethylpyridine) [161], $[Ln_2Ni_2(\mu_3\text{-}OH)_2(OH)(OAc)_4(HL)_2(MeOH)_3]$ (ClO_4) [162] (HL=2-(benzothiazol-2-ylhydrazonomethyl)-6-methoxyphenol), and $(Et_3NH)[LnCu_3L_3Cl(hfac)_3](L=1,1,1\text{-trifluoro-7-hydroxy-4-methyl-5-aza-hept-e-}$
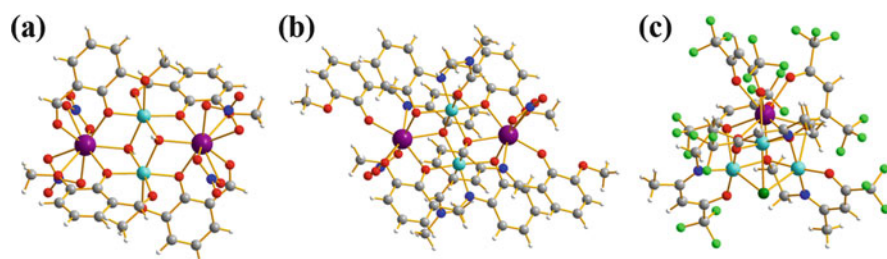
Fig. 10 (**a**) Molecular structure of Gd_2Co_2 complex; (**b**) molecular structure of the Ln_2Ni_2 coordination cluster; (**c**) view of the cubane core of the $GdCu_3$ complex. *Purple*: Ln. *Light blue*: M. *Gray*: C. *Blue*: N. *Red*: O. *White*: H. *Green*: Cl. *Light green*: F

en-2-one, hfac=hexafluoroacetylacetone) (Fig. 10c) [163] have almost the same tetrahedral metallic topology $[M_2Ln_2(O)_4]$ as that described above.

3.2.2 Ring-Shaped Topology

In one type of topology, two M–L–Ln parts are linked via bridging ligands to form a tetranuclear strand. As shown in Fig. 11a, in the ring-like $[CuLGd(hfac)_2]_2$ tetranuclear structure, the Cu^{II} complex functions as an electrically mononegative "bridging ligand complex" for the two Gd^{III} ions [23]. Similar ring-like complexes of Ln_2Cu_2 have also been prepared [24, 163, 164]. Another topology of this type is the quadrilateral complex, examples of which include Gd_2Ni_2 [165], Cr_2Ln_2 [166], Ni_2Ln_2 [167], Fe_2Ln_2 [168], Mn_2Gd_2 [169], and Co_2Gd_2 [170].

3.2.3 Propeller-Shaped Topology

Tetranuclear M_3Ln or MLn_3-type complexes with propeller-shaped or star-shaped structures consist of one central metal ion and three terminal ones connected by three pairs of bridges, with examples including $[Fe_3Ln(acac)_6(tea)_2]$ [47], $[Ni_3Gd(pyCHOpy)_6](ClO_4)_3$ [171] and $[MDy_3(HBpz_3)_6(dto)_3]$ (M=Fe/Co) $(HBpz_3$=hydrotri(pyrazolyl)borate) [172]. The propeller-type tetranuclear MDy_3 complexes comprise three eight-coordinated Dy^{III} centers in a square antiprismatic coordination environment that are connected to a central octahedral trivalent Fe or Co ion (Fig. 11b).

3.2.4 Co-planar Arrangements

Complexes with co-planar arrangements are usually seen in M_3Ln compounds. In the planar M_3Ln-type complex $[Cu_3Tb(L^{Pr})(NO_3)_2(MeOH)_3](NO_3)$, the
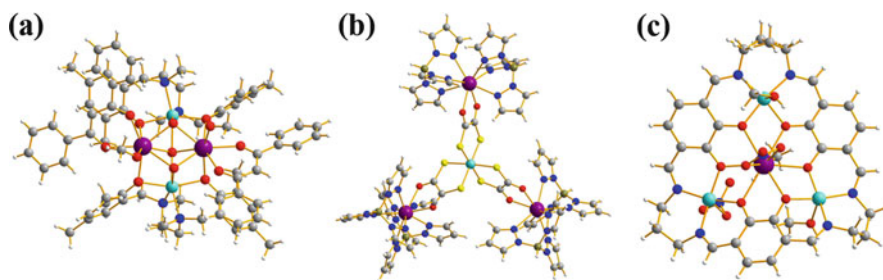
Fig. 11 (**a**) Molecular structure of cyclic tetranuclear Gd_2Cu_2 complex; (**b**) molecular structure of Ln_3Fe complex; (**c**) crystal structure of $TbCu_3$. *Purple*: Ln. *Light blue*: M. *Gray*: C. *Blue*: N. *Red*: O. *White*: H. *Yellow*: S

macrocycle coordinates one Tb^{III} ion in the central and three smaller Cu^{II} ions in the outer N_2O_2 sites, with approximate three-fold symmetry. As a result, the macrocycle adopts a slightly curved conformation (Fig. 11c) [134]. By modifying the ligand and varying the spin carriers, a series of tetranuclear complexes with similar structures were synthesized [173–175].

3.2.5   Other Topological Structures

Other topological structures can be classified as M–Ln–Ln–M [75, 91, 176–179] and M_3Ln [135]. The complex $[Dy_2Zn_2L_2(OAc)_2(CO_3)_2]$ can be considered to result from the coupling of two [ZnDy] units through the loss of the terminal nitrate and bridge in acetate groups and the formation of a bridging carbonate via the fixation of atmospheric CO_2 [92]. A similar topology, $[Co_2Dy_2(L)_2(OAc)_4(OH)_2(H_2O)_2]$ $(ClO_4)_2$, has a core that can be described as nearly linear Co-Dy-Dy-Co centers. The two central lanthanide ions are surrounded by nine oxygen atoms, exhibiting a tricapped trigonal prism geometry. The chelating and bridging capacities of the Schiff base ligand together with the hydroxo and acetate groups consolidate this linear tetranuclear Dy_2Co_2 cluster. Complex $[Mn_2Dy_2(LH)_4(\mu\text{-OAc})_2](NO_3)_2$ possesses an arch-like tetrametallic core, where Mn^{III} ions are present in the periphery and Ln^{III} ions in the central positions [75].

3.3   Pentanuclear 3d–4f Clusters

Relatively few pentanuclear 3d–4f clusters have been reported. In [Cu $(dmg)_2\{Ln_4(hfac)_8\}(AcO)_4](Ph_4P)_2$ (Ln=Gd/Dy) complexes, the Cu ion is surrounded by rectangularly arrayed Ln ions with N–O bridges. For the longer edge, an acetate anion bridges two Ln ions (Fig. 12a) [180]. Another complex, $[(CuL)_3\{CuL(C_2H_5OH)\}Eu(H_2O)](ClO_4)_3$, has a similar geometric configuration to that described above [181]. The central europium and external copper ions are bridged by macrocyclic oxamide groups. The central europium atom resides in a distorted tricapped trigonal prismatic environment. The complex $[Mn^{III}_2Ln_3(n\text{-}$ $bdeaH)_3(n\text{-}bdea)_2(piv)_8]$ (Ln=Y/Tb/Dy/Ho/Er) (bdeaH2=N-butyldiethanolamine, piv=pivalate) exhibits a semicircular Ln–Mn–Ln–Mn–Ln strand, in which adjacent pairs of metals are bridged by two alkoxide O atoms (Fig. 12b) [54]. Indeed, still other topologies, such as discrete $Gd_2Mn_3(CH_2C(CH_3)COO)_{12}(bipy)_2$(bipy=2,2 $'$-bipyridine) [182], the square-based pyramid cluster $[Ln_3Fe_2(\mu_5\text{-O})\text{-}$ $L_2(NO_3)_5(H_2O)(MeOH)] \cdot 0.5MeOH$(Ln=Gd/Dy)   (L = N,N,N',N'-tetrakis-(2-hydroxyethyl)-ethylenediamine) [183], and the ladder-type $\{Ln_2[Cu(opba)]_3\}$ (opba=$ortho$-phenylenebis(oxamato) [184] and $[LaMn_4(OPiv)_3(cat)_4(py)_6Cl]$ (cat=catecholate) complexes [118], exist.
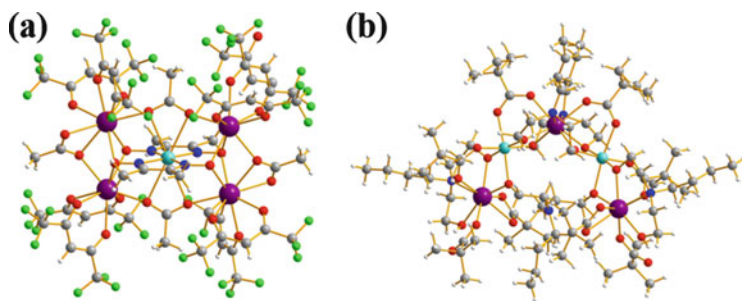
Fig. 12 (**a**) Crystal structure of Eu_4Cu; (**b**) semicircular molecular structure of Dy_3Mn_2. *Purple*: Ln. *Light blue*: M. *Gray*: C. *Blue*: N. *Red*: O. *White*: H. *Light green*: F

3.4 Hexanuclear 3d–4f Clusters

3.4.1 Cubane or Butterfly-Shaped Topology

Structures with tetranuclear cores with a cubane or butterfly-shaped configuration of units and two extra metal ions linked to the core via bridging ligands constitute a large portion of the heterometallic hexanuclear M_2Ln_4 or M_4Ln_2 clusters. For example, the complexes $[Mn_4Ln_2O_2(O_2CBut)_6(edteH_2)_2(NO_3)_2]$ [50] and $[Fe_2Dy_4(\mu_4\text{-}O)_2(\mu_3\text{-}OH)_{2.36}(\mu_3\text{-}OMe)_{1.64}(O_2CCH_2CN)_{10}(MeOH)_5(H_2O)]$ [185] have similar geometric configurations. The $[Mn_4Gd_2]$ core consists of a face-fused double cubane comprising four Mn and two Gd atoms bridged by two $\mu_4\text{-}O^{2-}$ and four μ_3-OR-groups (Fig. 13a). In the $[Mn_2Tb_4L_2(\mu_4\text{-}O)_2(N_3)_2$ $(CH_3O)_2(CH_3OH)_4(NO_3)_2]$ complex, the four Tb^{III} ions are nearly coplanar and are connected by the two $\mu_4\text{-}O^{2-}$ atoms and four phenoxo oxygen atoms, yielding a butterfly Tb_4 structure or a so-called defective dicubane structure. The two Mn^{III} atoms are located on opposite sides of the Tb_4 plane [186]. The similar cubane or butterfly-shaped arrangement of the hexanuclear 3d–4f cluster core has also been observed in complexes of $[Mn_4La_2(H_2L)_2(HL)_2 (OAc)_4(CH_3O)_2(CH_3OH)_4]$ [187], $[Mn_2Ln_4(\mu_4\text{-}O)_2(hmp)_4(pic)_2(piv)_6(\mu\text{-}N_3)_2]$ [188], $[Fe_4Ln_2(\mu_4\text{-}O)_2(NO_3)_2(piv)_6$ $(Hedte)_2]$ [189], $[Mn^{II}_2Mn^{III}_2Ln_2(Piv)_8(thme)_2 (H_2tea)_2]$ $(H_3thme=1,1,1\text{-tris}$ (hydroxymethyl)ethane, piv=pivalic) [190], $[Mn_4Ln_2 (\mu_3\text{-}O)_2(Hbe\text{-}emp)_2(OAc)_8$ $(OMe)_2(H_2O)_2]$ (Ln=Gd/Tb/Y)(H_3beemp=2,6-bis[((2-(2-hydroxyethoxy)ethyl) imino)methyl]-4-methylphenol) [191], and $[Ni_4Ln_2 (\mu_3\text{-}OH)_2(L)_4(OAc)_2(NO_3)_2$ $(H_2O)_2]$ [28].

The complex $\{[Ln_2Ni_4L_2Cl_2(OH)_2(CH_3O)_2(CH_3OH)_6]^{4+}$, whose core can be described as two Ni_2DyO_3Cl defective cubane subunits held together by two hydroxyl groups and two phenoxo bridging oxygen atoms, differs from those described above (Fig. 13b) [192].
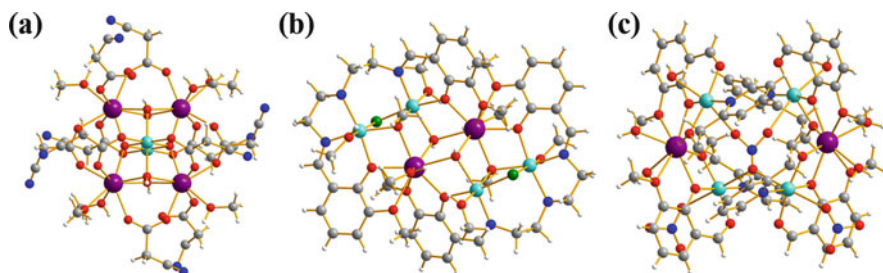
Fig. 13 Molecular structures of (**a**) Gd_2Mn_4; (**b**) Dy_2Ni_2; (**c**) Ln_2Cu_4. *Purple*: Ln. *Light blue*: M. *Gray*: C. *Blue*: N. *Red*: O. *White*: H. *Green*: Cl

3.4.2 Propeller-Shaped Topology

The cluster of $[Cu_4Ln_2L_4L'_4(NO_3)_2(OH_2)_2]^{3+}$ (Ln=Dy/Gd) (L=o-vanillin; L' = 2-(hydroxyethyl)pyridine) can be described as a novel "pseudo-double propeller"-shaped cluster and is composed of a μ_6-NO_3^- and two trinuclear units, where two Cu^{II} ions and one Ln^{III} ion are bridged through two pairs of double oxygen atoms (Fig. 13c) [193]. A similar propeller structure has been observed in $[(\mu_3$-$C_9H_3O_6)\{LCuLn(NO_3)_2\}_3]$ (Ln=Gd/Tb/Dy). The complex contains three dinuclear CuDy units based on the Schiff base ligand [194].

3.4.3 Ring-Shaped Topology

Complexes $[Ln(OAc)(NO_3)_2][14$-$MC_{Mn(III)Ln(O)(OH)N(shi)}5]$ are members of the MC family and contain a unique 14-MC-5 moiety incorporating an extra Ln^{III} ion (Fig. 14a) [70, 71]. The structures of complexes $Ln(NO_3)_3[15$-$MC_{CuN(L-pheha)}$-5] [48] and $Nd(NO_3)_2(OH)[15$-$MC_{CuN(D-alaha)}$-5] [130] are similar to those described above. Other complexes have also been noted to exhibit ring-shaped structures, including $[Pr_2Cu_4(fsaaep)_4(NO_3)_6]$ [195].

3.4.4 Other Configurations

The complex $[Cr_2Dy_4(\mu_4-O)_2(\mu_3$-$OH)_4(H_2O)_{10}(SO_4)_4(SO_4)_2]$, which is a unique compressed octahedral C_2Dy_4 aggregate, has been reported (Fig. 14b) [196]. Hexanuclear $[Fe_4Dy_2(H_2L)_2(HL)_2(L)_2(MeOH)_2(piv)_2(NO_3)_2]$ shows an "S" shape along the backbone of the cluster [197]. Some other hexanuclear topologies also exist but are not detailed here [198, 199].
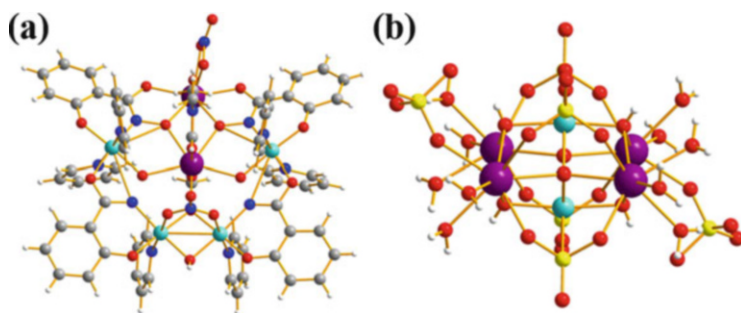
Fig. 14 (**a**) Molecular structure of Dy$_2$Mn$_4$ complex; (**b**) molecular structure of Dy$_4$Cr$_2$, which has an octahedral metallic skeleton. *Purple*: Ln. *Light blue*: M. *Gray*: C. *Blue*: N. *Red*: O. *White*: H. *Green*: Cl. *Yellow*: S

3.5 Heptanuclear 3d–4f Clusters

According to the metal core classification, heptanuclear 3d–4f clusters can be divided into M$_6$Ln-type, M$_5$Ln$_2$-type and M$_4$Ln$_3$-type; the M$_6$Ln-type is the most common and has many different configurations.

3.5.1 Trigonal Prism Structure

The reported complexes [Co$_6$Eu(aib)$_6$(OH)$_3$(NO$_3$)$_3$]$^{3+}$ (aib=2-amino-isobutyric) [200] and [Cu$_6$Ln(aib)$_6$(OH)$_3$(OAc)$_3$(NO$_3$)$_3$] [201] have the same metallic core configuration. In Co$_6$Eu, a Co$^{II}_6$ trigonal prism encapsulates the Eu^{III} center to form a cage-shaped structure (Fig. 15a). A similar M$_6$Ln metallic core was also observed in [Co$_6$La(aib)$_6$(OH)$_3$(NO$_3$)$_2$(H$_2$O)$_4$(CH$_3$CN)$_2$]$^{4+}$ [202], [LnCu$_6$(OH)$_3$(HL)$_2$(L)$_4$]$^{2+}$ [128], [Mn$_6$LnO$_3$(OMe)$_3$(SALO)$_6$(SALOH)$_3$] [203], and [Mn$^{III}_3$Mn^{IV}O$_3$Ln$_3$(OH) (piv)$_6$(EtO)$_3$(EtOH)$_3$(Et-sao)$_3$] [204].

3.5.2 Octahedral Structure

The metal core of the complex (NMe$_4$)[LnNi$_6$(pro)$_{12}$]$^{4+}$ (Ln=Gd, La; Hpro=proline) consists of a Ln^{III}-centered cage of six symmetry-equivalent Ni^{II} ions that form a perfect octahedron. The nickel centers are equatorially *cis*-chelated by two prolinate ligands. The oxygen donor of the chelate rings is also connected to the central lanthanide, creating dodeca coordination around this ion (Fig. 15b) [205]. Similar structures in heptanuclear 3d–4f clusters have also been reported by other groups [31].
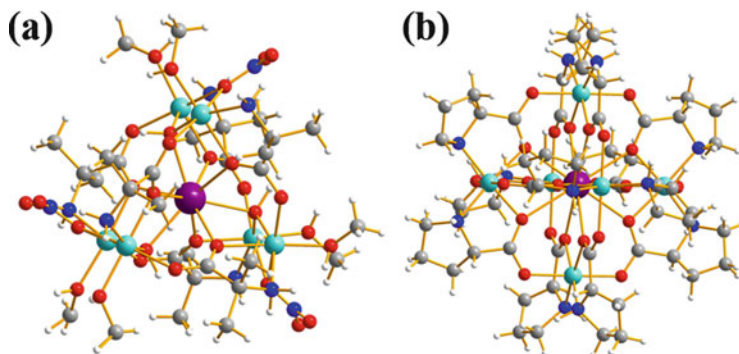
Fig. 15 (**a**) "Generic" structure of the compound EuCo$_6$; (**b**) molecular drawing of the cluster cation of GdNi$_6$. *Purple*: Ln. *Light blue*: M. *Gray*: C. *Blue*: N. *Red*: O. *White*: H
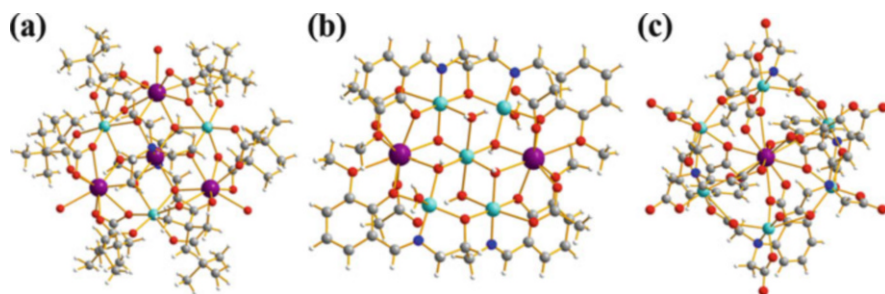
Fig. 16 (**a**) Molecular structure of Nd$_4$Mn$_3$; (**b**) structure of Dy$_2$Cu$_5$ complex; (**c**) molecular structure of the wheel-like cluster core of PrCu$_6$. *Purple*: Ln. *Light blue*: M. *Gray*: C. *Blue*: N. *Red*: O. *White*: H

3.5.3 Disc-Like Topology

Another family of heptanuclear clusters, [Mn$^{II}_3$Ln$_4$(piv)$_{12}$(tea)$_2$(H$_2$O)$_3$], has disc-like [Mn$_3$Ln$_4$(μ_3-O)$_6$(μ_2-O)$_6$] cores, as shown in Fig. 16a. Here, the core is composed of a central Ln^{III} ion encircled by a ring of alternating Mn^{II} and Ln^{III} ions [206]. The [Cu$_5$Ln$_2$(L)$_2$(μ_3-OH)$_4$(μ_3-OAc)$_2$(μ-OAc)$_2$](NO$_3$)$_2$ complexes also display disc-like topologies [207]. The heptanuclear aggregates possessed a centrosymmetrical molecular wheel structure, as shown in Fig. 16b. A similar metal topology structure was also found in the compound [Cu$_6$PrL$_6$][Pr(H$_2$O)$_{10}$] (Fig. 16c) [127].

3.6   Octanuclear 3d–4f Clusters

3.6.1   Square-in-Square Topology

The "square-in-square" configuration is often observed in octanuclear 3d–4f clusters of the M_4Ln_4 type. In this configuration, four Ln^{III} ions assemble a square bridging ligand and further link four 3d ions on each edge of the square. The structure of the $[Mn_4Ln_4(OH)_4(X)_4(O_2CBu^t)_8(t\text{-bdea})_4]$ complex is shown in Fig. 17a. The central core contains four Dy cations arranged to form an approximate square. Each pair of adjacent Dy cations is bridged by a hydroxo ligand, which also coordinates with a Mn^{III} cation [56]. Similar structures have also been obtained in other octanuclear complexes of $[Mn^{III}_4Ln^{III}_4(OH)_4(Calix)_4(NO_3)_2(DMF)_6(H_2O)_6]$ [208], $[Cr_4Dy_4(\mu_3\text{-OH})_4(\mu\text{-N}_3)_4(mdea)_4(piv)_4]$ [55], and $[Fe_4Dy_4(\mu_3\text{-OH})_4(n\text{-bdea})_4(CH_3C_6H_4CO_2)_{12}]$ [4]. The "square-in-square" M_4Ln_4-type topology also exhibits another configuration, as shown in Fig. 17b [208]. The Mn_4Gd_4 cluster comprises a near-planar octametallic core with a square of Gd^{III} ions inside a square of Mn^{III} ions [209].

3.6.2   Double Tetrahedral Structure

The double tetrahedral structure is rare in octanuclear 3d–4f clusters. The compound $[Et_4N][Gd_2Ni_6(val)_{12}(MeCN)_6(H_2O)_3]^{7+}$ consists of two $[GdNi_3]$ tetrahedra that are linked through the vertices by three water molecules. The water molecules act as bridging ligands, connecting two Gd^{III} ions and forming an unprecedented $[Gd(\mu\text{-H}_2O)_3Gd]$ coordination moiety (Fig. 17c) [210]. The M_6Ln_2-type double tetrahedral structure was also observed in $[Cu_6Ln_2Cl_2\{(py)_2CO_2\}_5\{(py)_2CO(OH)\}_2(OTf)_2(H_2O)_4]$ [211].
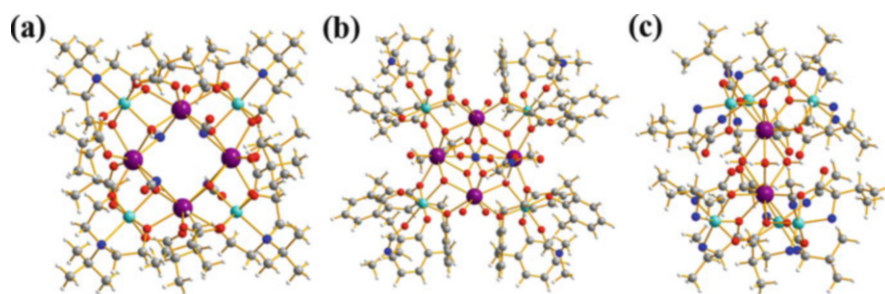
Fig. 17 (**a**) Molecular structure of Dy_4Mn_4 complex; (**b**) molecular structure of Gd_4Mn_4 complex; (**c**) representation of the complex cation of Gd_2Ni_6. *Purple*: Ln. *Light blue*: M. *Gray*: C. *Blue*: N. *Red*: O. *White*: H
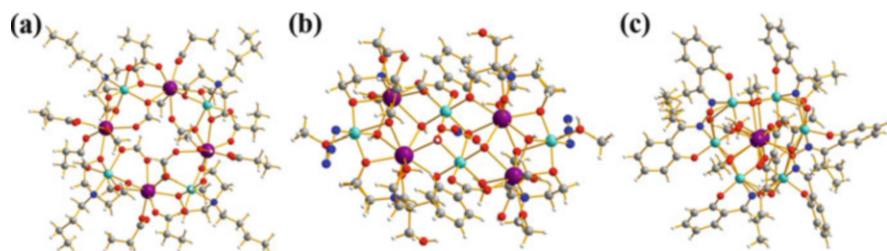
Fig. 18 (**a**) Molecular structure of Ln_4Mn_4 through *top view*; (**b**) molecular structure of Dy_4Mn_4; (**c**) molecular structure of Gd_2Mn_6 viewed parallel to the Mn_6 wheel. *Purple*: Ln. *Light blue*: M. *Gray*: C. *Blue*: N. *Red*: O. *White*: H

3.6.3 Other Topologies

In addition to the structures as described above, different central cores with other types of metallic topology have been synthesized and characterized, such as octanuclear wheel complexes, formulated as $Mn_4Ln_4(^nBu\text{-}dea)_4(\mu_3\text{-}HCOO)_4(\mu\text{-}OMe)_4(\mu\text{-}O_2CEt)_4(O_2CEt)_4(MeOH)_4$ (Fig. 18a) [212]. The Mn_4Ln_4 cores possess an eight-member saddle-like $[Mn_4Dy_4]$ ring, with four Mn^{III} and four Dy^{III} ions arranged in an alternating fashion. The same molecular configuration was also reported by another research group [213]. The complexes $[Mn_4Ln_4(OH)_6(H_2bis\text{-}tris)_2(H_3bis\text{-}tris)_2(PhCO_2)_2(N_3)_2(MeOH)_4]^{3+}$ (Ln=Gd/Tb/Dy/Ho/Er) showed an unusual planar centrosymmetric core that consisted of six fused triangles of four Mn^{III} and four Ln^{III} ions. All the metal centers were held together through eight μ_3-O and eight μ_2-O bridges (Fig. 18b) [214]. Two M_6Ln_2-type octanuclear clusters, $[Gd_2Mn_6O_3(OMe)_4(Et\text{-}sao)_6(acac)_2(MeOH)_4]$ [65] and $[Ln_2Mn_6O_3(saO)_6(OCH_3)_6Ln_2(CH_3OH)_4(H_2O)_2]$ [63], featuring hexagonal prisms, were also prepared. The metallic core contains a chair-like wheel of six Mn^{III} ions capped on the top and bottom by a Gd(III) ion, described as a distorted hexagonal prism (Fig. 18c).

3.7 Nonanuclear 3d–4f Clusters

According to the number of lanthanide and transition metals in the complexes, nonanuclear 3d–4f clusters can be divided into the following types: Mn_8Ln, [215], M_6Ln_3 [216], M_5Ln_4 [50], and M_4Ln_5 [29]. The metallic core of the compound $[Dy_3Cu_6L_6(\mu_3\text{-}OH)_6(H_2O)_{10}]^{3+}$ can be described as resulting from the condensation of three distorted $Dy_2Cu_2O_4$ cubane-like moieties that share the Dy^{III} ions in a triangular fashion, as shown in Fig. 19a [217].

The complex $Mn_5Ln_4(O)_6(mdea)_2\text{-}(mdeaH)_2(Piv)_6(NO_3)_4(H_2O)_2$] Ln=Tb/Dy/Ho/Y) consists of a centrosymmetric $[Mn_5Dy_4]$ core held together by four μ_3-O and two μ_4-O ligands [57] (Fig. 19b). The complex
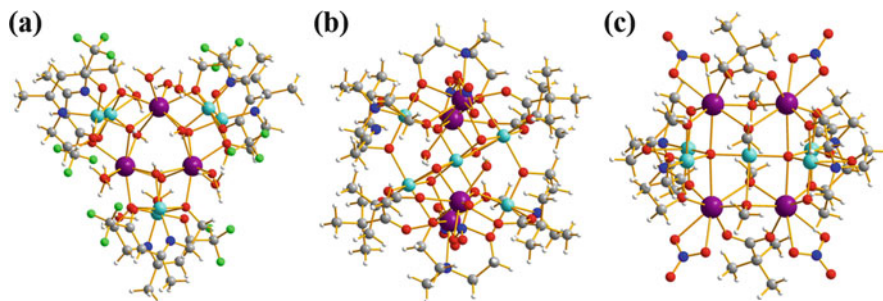
Fig. 19 (**a**) Cation core structure of Dy_3Cu_6; (**b**) molecular structure of Dy_4Mn_5; (**c**) Molecular structure of Gd_4Cu_5. *Purple*: Ln. *Light blue*: M. *Gray*: C. *Blue*: N. *Red*: O. *White*: H. *Light green*: F.

$[Cu_5Gd_4O_2(OMe)_4(teaH)_4(O_2CC(CH_3)_3)_2(NO_3)_4]$ is another configuration of M_5Ln_4-type nanocluster [218]. This complex contains five Cu^{II} and four Gd^{III} ions; the Cu^{II} ions form a planar "bow tie" arrangement, whereas the four Gd^{III} ions form a perpendicular rectangle. The metallic skeleton thus includes four vertex and face-sharing $\{GdCu_3\}$ tetrahedra. Two central trigonal bipyramidal μ_5-O^{2-} ions link the perpendicular Cu_5 and Gd_4 frameworks together (Fig. 19c). The M_6Ln_3-type of nonanuclear cluster includes sandwich-type [163] and cage-like [39] configurations.

3.8 Decanuclear 3d–4f Clusters

The decanuclear aggregate $[Mn^{II}_2Mn^{III}_2Dy_6(\mu_3\text{-}OH)_2(Hgly)_4(H_2gly)_2(PhCO_2)_{16}(H_2O)_2]$ was synthesized using a glycerol ligand. The structure was built up from two Mn_2Dy_2 hetero-cubane units linked through a central $[Dy_2(PhCO_2)_4]^{2+}$ paddle wheel dimer (Fig. 20a) [219]. For the complex $[Dy_3Fe_7(\mu_4\text{-}O)_2(\mu_3\text{-}OH)_2$-$(mdea)_7(\mu\text{-}benzoate)_4(N_3)_6]$, the two $(\mu_4\text{-}O)^{2-}$ ligands bridge between two Fe and Dy centers (Fig. 20b) [58]. The decanuclear $Ln_4Mn^{III}_6(H_2shi)_2(shi)_6(sal)_2(OAc)_4(OH)_2(MeOH)_8]$ (Ln=Dy/Ho) can be described as a 22-MC-8 that contains all of the Mn^{III} ions and two of the Ln^{III} ions (Fig. 20c) [69]. Other topologies, such as M_5Ln_5 [63, 65], M_8Ln_2 [220, 221], and cage-like M_4Ln_6 [222, 223], are not detailed here.

3.9 High-Nuclearity 3d–4f Clusters from 11 to 20

A large number of polynuclear 3d–4f clusters with nuclearity ranging from 11 to 20 have been reported. These polynuclear clusters do not exhibit regular metallic topologies or rational synthetic routes.
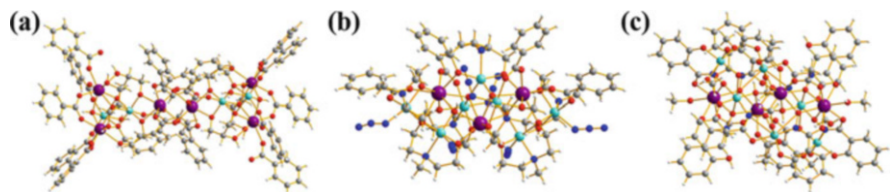
Fig. 20 (**a**) Structure of the decanuclear aggregate Dy_6Mn_4; (**b**) molecular structure of Dy_3Fe_7; (**c**) crystal structure of Ln_4Mn_6. *Purple*: Ln. *Light blue*: M. *Gray*: C. *Blue*: N. *Red*: O. *White*: H
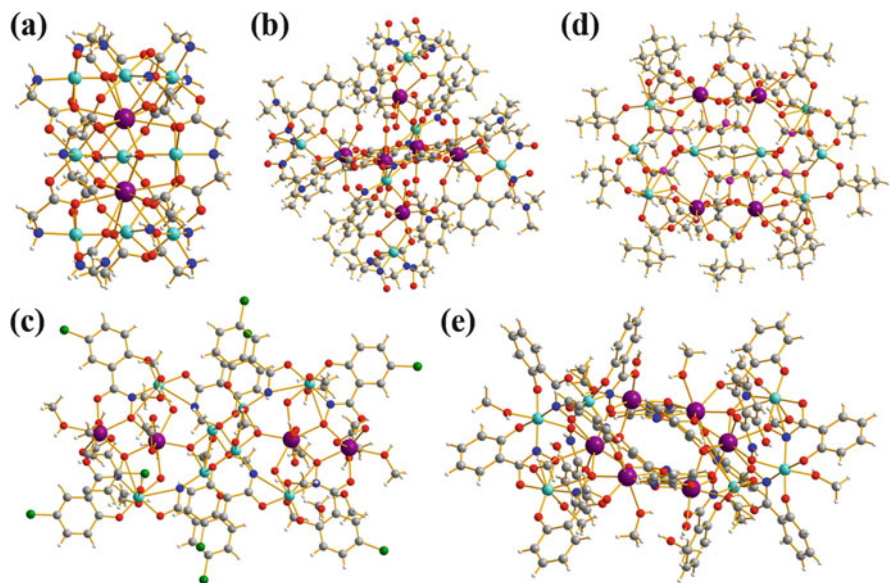
Fig. 21 (**a**) Cationic core of La_2Ni_9; (**b**) Gd_6Cu_6 cluster; (**c**) metal skeleton of Dy_4Mn_8; (**d**) molecular structure of the Gd_4Cu_8 cation; (**e**) molecular structure of Dy_6Mn_6. *Purple*: Ln. *Light blue*: M. *Gray*: C. *Blue*: N. *Red*: O. *White*: H. *Green*: Cl

The undecanuclear cationic cluster $[La_2Ni_9(Gly)_{12}(IDA)_3(\mu_3\text{-}OH)_3]^{3+}$ features a face-shared and La-centered dioctahedral structural motif [33]. The 11 metal atoms are arranged in an interesting topology: The nine Ni^{2+} ions form two octahedrons sharing one face, and the two La^{3+} ions are located in the centers of the two octahedrons (Fig. 21a). Another set of undecanuclear clusters with the general formula $[Mn_5Ln_6(O)_4(OH)_4(OMe)_2(bemp)_2(OAc)_{10}(NO_3)_4]$ (Ln=Gd/Tb) (H_3bemp=2,6-bis[*N*-(2-hydroxyethyl)iminomethyl]-4-methylphenol) has been prepared [224]. The Mn_5Ln_6 cationic core consisted of two corner-sharingoxo-bridged M_2Ln_2 cubes, and the compounds were capped by two pentadentate bemp ligands that bridge between the outer Mn centers and the two cubane motifs.

Many types of dodecanuclear 3d–4f clusters exist, such as the dodecanuclear wheel $Dy_{10}Co_2$ [30], double-propeller dimer of hexanuclear $[Cu_3Dy_3]_2$ [194],
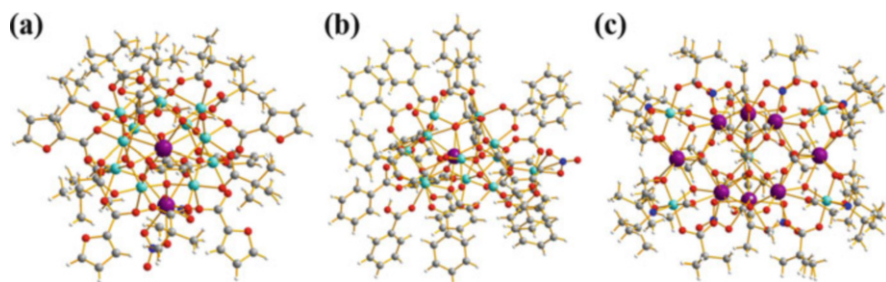
Fig. 22 (**a**) Cationic core of Gd_2Mn_{11} complex; (**b**) molecular structure of $GdMn_{12}O_9$; (**c**) crystal structure of the Gd_8Fe_5 complex. *Purple*: Ln. *Light blue*: M. *Gray*: C. *Blue*: N. *Red*: O. *White*: H

octahedral Cu_6Gd_6 (Fig. 21b) [225], bell-shaped $Mn_{11}Ln$ [226], dimeric 14-metallacrown-5 compound Mn_8Dy_4 (Fig. 21c) [71], square-like (or wheel) Cu_8Gd_4 (Fig. 21d) [227], Co_8Gd_4 [228], and Dy_6Mn_6 (Fig. 21e) [229]. For example, the neutral dodecanuclear cluster $[\{(HL)(L)(DMF)Cu^{II}Gd^{III}(DMF)(H_2O)\}_6]$ consists of six Cu^{II} and six Gd^{III} ions. The six Gd^{III} ions form an octahedron that is inscribed in the octahedron created by the Cu ions [225]. The complex $[Gd^{III}_4Cu^{II}_8(OH)_8(L)_8(O_2CR)_8](ClO_4)_4$ has a core that consists of a square of four corner-sharing $[Gd^{III}_2Cu^{II}_2O_4]^{6+}$ cubanes. The shared corners are the Gd ions, which thus form an inner Gd_4 square, each edge of which is occupied by two μ_3-OH^- ions that further bridge to an M^{II} ion [227].

Three 3d–4f clusters containing 13 metal ions have been reported: $[Mn^{III}_9Mn^{II}_2Gd_2(O)_8(OH)_2(piv)_{10.6}(fca)_{6.4}(NO_3)_2(H_2O)]$ (fcaH=2-furan-carboxylic acid) (Fig. 22a) [230], $[Mn_{12}GdO_9(O_2CPh)_{18}(O_2CH)(NO_3)(HO_2CPh)]$ (Fig. 22b) [231], and $[Fe^{III}_5Gd_8(\mu_3$-$OH)_{12}(L)_4(piv)_{12}(NO_3)_4(OAc)_4]$ (Fig. 22c) [61, 62]. The core of the $Mn_{11}Ln_2$ complex can be described as bell-shaped, with the Mn^{III} and Mn^{II} centers forming the shell of the bell and the two Gd centers forming the bell's clapper. Interestingly, $Mn_{11}Ln_2$ is the first mixed-valence $Mn^{II,III}$-Ln^{III} d/f complex. The core of the centrosymmetric tridecanuclear cluster M_5Ln_8 can be viewed as consisting of two distorted dinner heterometallic $[FeGd_3(\mu_3$-$OH)_4]^{8+}$ cubane units sharing a common vertex Fe, flanked by four edge-sharing heterometallic $[FeGd_2(OH)_4]^{5+}$ partial cubane units. Six of the eight Gd ions are arranged in a planar hexagonal ring capped above and below the plane by the other two Gd ions. All five Fe^{III} ions are nearly coplanar, with four Fe atoms located at the vertices of a rectangle and the fifth at the center.

There are two heterometallic d–f clusters containing fourteen metal ions. The first is the thiacalix [4] arene-supported complex $[Na_2Ni^{II}_{12}Ln^{III}_2(BTC^4A)_3(CO_3)_3(\mu_3$-$OH)_4(\mu_3$-$Cl)_2$-$(OAc)_6(dma)_4]\cdot2OAc$(Ln=Dy and Tb)(dma=dimethylamine) (Fig. 23a). The $Na_2Ni_{12}Ln_2$ complex possesses a trinary cubane core composed of one $[Ni_2Ln_2]$ cubane unit and two $[NaNi_2Ln]$ cubane units sharing one Ln ion, which is unprecedented [123]. The heterometallic cluster of $Ni_{12}Ln_2$ can be viewed as a tricubane connecting six peripheral Ni ions through three carbonato anions. Three ligands are located on the trigonal plane of the tricubane core. The second d–f
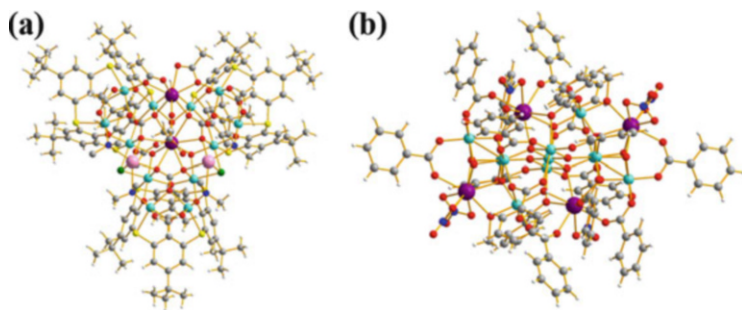
Fig. 23 (**a**) Molecular structure of $Ln_2Ni_{12}Na_2$ complex; (**b**) structure of the centrosymmetric core of Dy_4Mn_{11} complex. *Purple*: Ln. *Light blue*: M. *Gray*: C. *Blue*: N. *Red*: O. *White*: H. *Green*: Cl. *Yellow*: S

cluster containing fourteen metal ions is phosphonate cages of $[Co_4Dy_{10}(O_2C^t$ $Bu)_{12}(O_3PC_6H_{10}NH_2)_8(PO_4)_2(O_2CMe)_2(O_3PC_6H_{10}NH_3)_2]$ [61]. In this cluster, the $Dy_{10}P_{12}$ core can be described as being based on two centered 12-vertex polyhedra sharing a face. The two atoms at the center of each polyhedron are from μ_6-bridging phosphates. The four Co^{II} ions cap the $Ln_{10}P_{12}$ core.

Only one d–f cluster containing 15 metal ions has been prepared and was formulated as $[Mn_{11}Dy_4O_8(OH)_6(OMe)_2(O_2CPh)_{16}(NO_3)_5(H_2O)_3]$. The core contains two distorted $[DyMn_3O_4]$ cubanes that are each linked by an Mn and Dy atom to a central linear Mn_3 unit [232]. The Mn and Dy atoms are six and nine coordinate, respectively (Fig. 23b).

Four types of d–f clusters containing 16 metal ions have been reported, Ni_8Dy_8. Co_8Gd_8, $Fe_{12}Ln_4$ and Mo_4Ln_{12}. The core-shell complex $[Ni_8Dy_8O(OH)_4(pao)_{28}]$ $(ClO_4)_5(NO_3)$ (paoH=2-pyridinealdoxime) consists of eight octahedral Ni and eight 8-coordinate Dy atoms [77]. The 16 metal atoms are arranged in an inner Dy_8 core and an outer Ni_8 shell. The Dy_8 core comprises a central $[Dy_4(\mu_4$-$O)]$ tetrahedron, four of whose edges are each fused with an edge of a $[Dy_3(\mu_3$-$OH)]$ triangular unit. The outer Ni_8 shell has a nonplanar square-based topology that can be described as comprising a Ni_4 square and a concentric Ni_4 tetrahedron (Fig. 24a). The square-shaped $[Co_8Gd_8(\mu_3$-$OH)_4(NO_3)_4(O_3P^tBu)_8(O_2C^tBu)_{16}]$ has a distorted grid structure [227]. As shown in Fig. 24b, the center of the molecule features a $[2 \times 2]$ Co_4 square grid in which six-coordinate cobalt (II) ions are bridged by four nitrates that are disordered about the C_2 axis with alternating up and down orientations. The outer Gd_8Co_4 frame can be viewed as four $[CoGd_2(\mu_3$-$OH)]$ triangles linked by phosphonate ligands.

The structure of the $[Fe_{12}Ln_4(\mu_4$-$O)_6(\mu_3$-$O)_4(\mu_3$-$OH)_4(PhCO_2)_{24}]$ complex [233, 234] can be viewed as two $Fe_4O_2(OH)_2$ cubane units and one "sandwich" of four central Fe^{III} ions linked together by four Gd^{III} ions (Fig. 24c). For Mo_4Ln_{12}, the Gd_{12} core can be conveniently viewed as a distorted truncated tetrahedron with each of its 12 vertices occupied by one Gd atom. Each of the triangular faces is
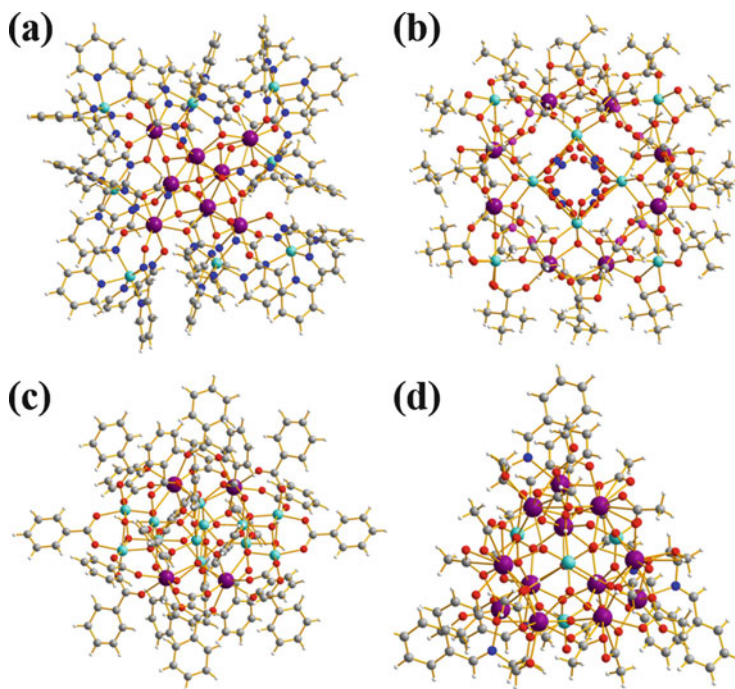
Fig. 24 (**a**) Molecular structure of the inner Dy_8 cage and the outer Ni_8 shell of the Dy_8Ni_8 complex; (**b**) crystal structure of Gd_8Co_8 complex; (**c**) cationic core of Sm_4Fe_{12} complex; (**d**) demonstration of the Gd_{12} unit capped by four MoO_4^{2-} ions. *Purple*: Ln. *Light blue*: M. *Gray*: C. *Blue*: N. *Red*: O. *White*: H

capped by a triply bridging OH^- group, whereas each of the hexagonal faces is capped by a MoO_4^{2-} anion (Fig. 24d)[235].

A heptadecanuclear d–f cluster, formulated as $[Mn_9Dy_8O_8(OH)_8(tea)_2(teaH)_2(-teaH_2)_4(Ac)_4(NO_3)_2(H_2O)_4](NO_3)_7$, was reported by Murray and coworkers [49]. The core can be described as two edge-sharing $Mn^{III}{}_5Dy^{III}$ supertetrahedra with the apical vertices of the shared edge containing Dy^{III} ions with the center position containing a Mn^{III} ion (Fig. 25a). For the complex $[Gd_5Ni_{12}(Gly)_{12}(IDA)_6(\mu_3\text{-}OH)_9(H_2O)_3] \cdot (ClO_4)_6$, the 17 metal ions were assembled into an onion-like $Gd_5 \subset Ni_{12}$ structure (Fig. 25b) [33]. The central Gd_5 units exhibit a trigonal bipyramidal structure, whereas the outer Ni_{12} shell possesses a triangular orthobicupola framework. The Gd_5 core and Ni_{12} shell are bridged by μ_3-OH^- groups and carboxylate oxygen atoms. $[Dy_9Cu^{II}{}_8(NO_3)_2(OH)_{10}(L_3)_4(OAc)_{18}(H_2O)_4](NO_3)_2(OH)_3$ is another heptadecanuclear d–f cluster (Fig. 26a, b) [103].

Five types of octadecanuclear d–f cluster have been reported to date, including octahedral $Cu_{12}Ln_6$ [109], fan-shaped $Cu_{12}Gd_6$ [34], wheel-like $Cu_{12}Gd_6$ [103], and two Mn–Ln clusters of $Mn_{12}Dy_6$ [59] and Mn_9Gd_9 [236]. Octahedral $Cu_{12}Ln_6$ is very common, as described above. The six Ln^{3+} ions are positioned at the vertices
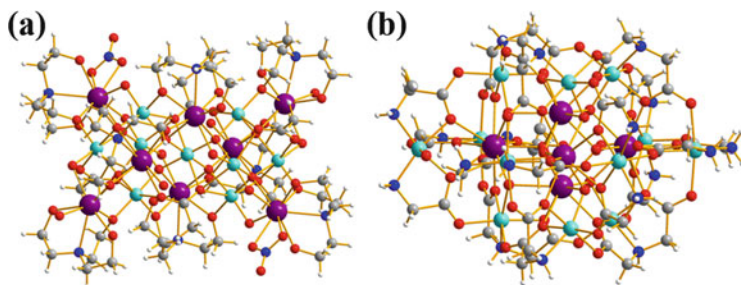
Fig. 25 (**a**) Molecular structure of Dy_8Mn_9 complex; (**b**) crystal structure of the Gd_5Ni_{12} complex. *Purple*: Ln. *Light blue*: M. *Gray*: C. *Blue*: N. *Red*: O. *White*: H
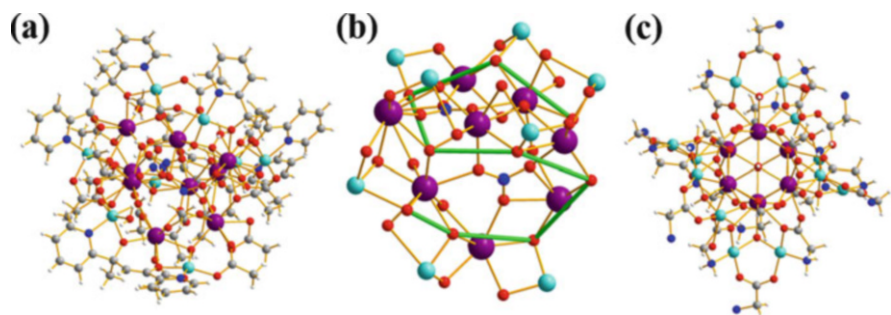
Fig. 26 (**a**) Cationic core of Ln_9Cu_8 complex; (**b**) metallic skeleton of Ln_9Cu_8; (**c**) Gd_6Cu_{12} cluster cation with an axial-fan shape viewed along the *c*-axis. *Purple*: Ln. *Light blue*: M. *Gray*: C. *Blue*: N. *Red*: O. *White*: H

of a regular nonbonding octahedron, and the 12 Cu^{2+} ions are located at the midpoints of the 12 octahedral edges [60]. Wu and coworkers reported a fan-shaped Gd_6Cu_{12} complex $[Gd(H_2O)_8][Gd_6Cu_{12}(OH)_{14}(Gly)_{15}(HGly)_3(H_2O)_6]$ •16ClO_4 [34]. Six symmetry-related Gd atoms form a homometal octahedral cluster $[Gd_6(OH)_8]$ (Fig. 26c). The $[Gd_6]$ core is encapsulated by six symmetry-related $[Cu_2]$ fragments, leading to the axial-fan-shaped cation $[Gd_6Cu_{12}]$, which has a different topology from the octahedral $Cu_{12}Ln_6$. The wheel structure is another type of octadecanuclear 3d–4f cluster. In the complex $[Gd^{III}_6Cu^{II}_{12}(OH)_{12}(L_3)_6$ $(NO_3)_7(OAc)_3(H_2O)_{12}](OH)_8$, six vertex-sharing Gd_2Cu_2 units can form a beautiful hexagonal wheel of $[Gd_6Cu_{12}]$, and the edges of the perfect hexagon are 4.3 Å [55]. The central NO_3^- anion may act as a template in the construction of the hexagon. The highly symmetric trigonal bipyramidal compound $[Mn^{II}_9Gd^{III}_9$ $(O_3PMe)^{12}(O_2CtBu)_{18}(L)]$ [236] was synthesized using the smallest organophosphonate and has D_{3h} symmetry. Three Mn^{II} sites lie near the trigonal plane of a trigonal bipyramid, whereas the remaining six manganese centers form two triangles near the apical positions. Six of the Gd^{III} centers lie on the nonequatorial edges of the trigonal bipyramid, and the other three Gd^{III} sites form a triangle.
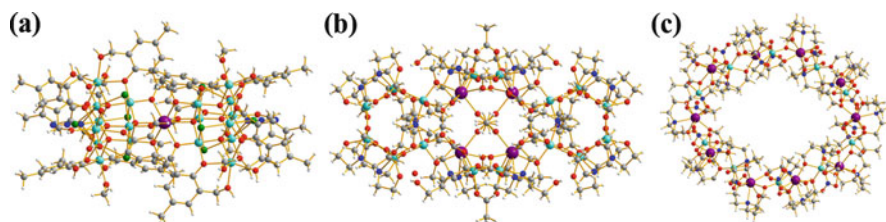
Fig. 27 Molecular structure of (**a**) $DyMn_{18}$; (**b**) $Fe_{16}Dy_4$ ring; (**c**) $Yb_{10}Fe_{10}$. *Purple*: Ln. *Light blue*: M. *Gray*: C. *Blue*: N. *Red*: O. *White*: H. *Green*: Cl

Only one d–f cluster containing 19 metal ions has been reported. The Mn–Ln cluster $[Mn^{III}_{12}Mn^{II}_6Dy^{III}(\mu_4\text{-}O)_8(\mu_3\text{-}Cl)_{6.5}(\mu_3\text{-}N_3)_{1.5}(HL)_{12}(MeOH)_6]Cl_3$ can be formed when the central Mn^{II} cation of Mn_{19} is replaced by Dy^{III} with the same core topology [237]. The structure of the $Mn_{19}Dy$ cluster can be viewed as two $[M_9Dy]$ supertetrahedral units that share one vertex Dy ion (Fig. 27a).

Three cases of 20-membered heterometallic d–f clusters have been reported: ring-like $Fe_{16}Ln_4$ [46] and $Fe_{10}Yb_{10}$ [238] and cage-like Ln_8Cu_{12} [100]. In $[Fe_{16}Ln_4(tea)_8(teaH)_{12}(\mu\text{-}OAc)_8](NO_3)_4$ (Ln=Sm/Eu/Gd/Tb/Dy/Ho) [46], 20 metal ions are linked by a tea ligand, forming a $Fe_{16}Dy_4$ ring. Within the ring, the four Dy centers are situated between two Fe_2 units and two Fe_6 chains, which can be designated as sub-chains (Fig. 27b).The complex $[Fe_{10}Yb_{10}(Me\text{-}tea)_{10}(Me\text{-}teaH)_{10}(NO_3)_{10}]$ is another type of ring-shaped structure and is constructed from ten $\{FeYb(Me\text{-}tea)(MeteaH)(NO_3)\}$ units that form an elliptical $Fe_{10}Yb_{10}$ ring with alternating Fe and Yb ions [238]. The elliptical ring is approximately 2.8 nm across the major axis and 2.6 nm across the minor axis, with a thickness of approximately 1.3 nm (Fig. 27c).

3.10 Higher-Nuclearity 3d–4f Clusters to 136

Using pyridine-2,6-dimethanol to form 3d–4f clusters afforded a cage-like $[Cu_{15}Gd_7(OH)_6(CO_3)_4(O_2CPh)_{19}(pdm)_9(pdmH_2)_3(H_2O)_2]$ cluster with C_3 crystallographic symmetry [95]. As shown in Fig. 28a, the complicated core of $Cu_{15}Gd_7$ can be conveniently described as consisting of a central, nonplanar μ_6-carbonato-bridged Cu_3Gd_3 unit, four bridging Gd^{3+} ions, and three extrinsic Cu_4 subunits. The CO_3^{2-} ions are presumably derived from the fixation of atmospheric CO_2.

The compound $[Mn_{21}DyO_{20}(OH)_2(Bu^tCO_2)_{20}(HCO_2)_4(NO_3)_3(H_2O)_7]$ consists of a $[Mn^{IV}_3Mn^{III}_{18}Dy(\mu_4\text{-}O)_2(\mu_3\text{-}O)_{18}]$ core comprising a $[DyMn^{IV}_3O_4]^{7+}$ cubane [239], on the top of which is a nonplanar Mn_7 loop attached by oxide ions and on the bottom of which is a nonplanar Mn_8 loop and additional Mn atoms (Fig. 28b).
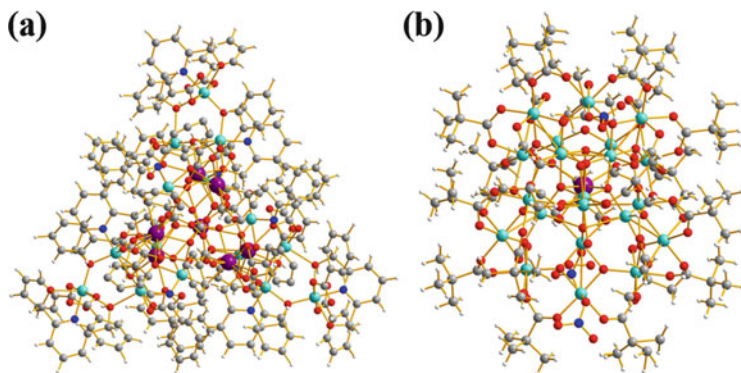
Fig. 28 Molecular structures of (**a**) Gd_7Cu_{15}; (**b**) $Mn_{21}DyO_{20}$. *Purple*: Ln. *Light blue*: M. *Gray*: C. *Blue*: N. *Red*: O. *White*: H
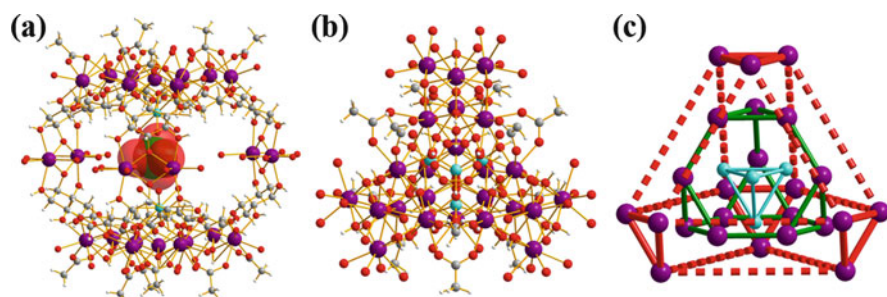
Fig. 29 (**a**) Crystal structure of $Dy_{24}Ni_2$; (**b**) molecular structure of Zn_4Gd_{24} complex; (**c**) three-shell nesting structures with tetrahedron@pseudo-truncated-tetrahedron@pseudo-cuboctahedron of $Gd_{24}Zn_4$. *Purple*: Ln. *Light blue*: M. *Gray*: C. *Blue*: N. *Red*: O. *White*: H. *Green*: Cl

Two heterometallic cage-like clusters $[Dy_{24}M_2(OH)_8(CH_3COO)_{12}(C_6H_{10}O_6)_6(C_6H_9O_6)_6(H_2O)_{51}][Dy(H_2O)_9](ClO_4)_{29}(M=Ni/Mn)$ have been synthesized through the self-assembly of metal ions and the myo-inositol ligand [112]. The cage-like cluster core can be viewed as being constructed from two bowl-like Dy_9Ni units and three Dy_2 units. The bowl-like structure of Dy_9Ni is formed by three $[Dy_3OH]^{8+}$ ions connected by one OH^- and one Ni^{2+} ion. Three templating ClO_4^- anions are found in the center of the cage (Fig. 29a).

Two $[Ln_{24}Zn_4(\mu_6\text{-}O)_4(\mu_4\text{-}O)(OH)_{44}(CH_3COO)_{12}(H_2O)_{48}]\bullet14ClO_4(Ln=Gd/Sm)$ clusters were reported by Kong and Long et al. The cationic core consists of four $[Gd_6(\mu_6\text{-}O)(\mu_3\text{-}OH)_8]^{8+}$ octahedral units and one $[Zn_4(\mu_4\text{-}O)]^{6+}$ tetrahedron unit as building blocks (Fig. 29b, c) [240]. This $Gd_{24}Zn_4$ metal core can be considered a fascinating three-shell structure. Moving outward, the innermost shell contains four Zn^{2+} forming a tetrahedron and is followed by shell 2, which includes 12 Gd^{3+} forming a pseudo-truncated tetrahedral structure with four triangular and four pentagonal faces. The outermost shell of 12 Gd^{3+} is a pseudo-cuboctahedron with eight triangular and six rectangular faces.
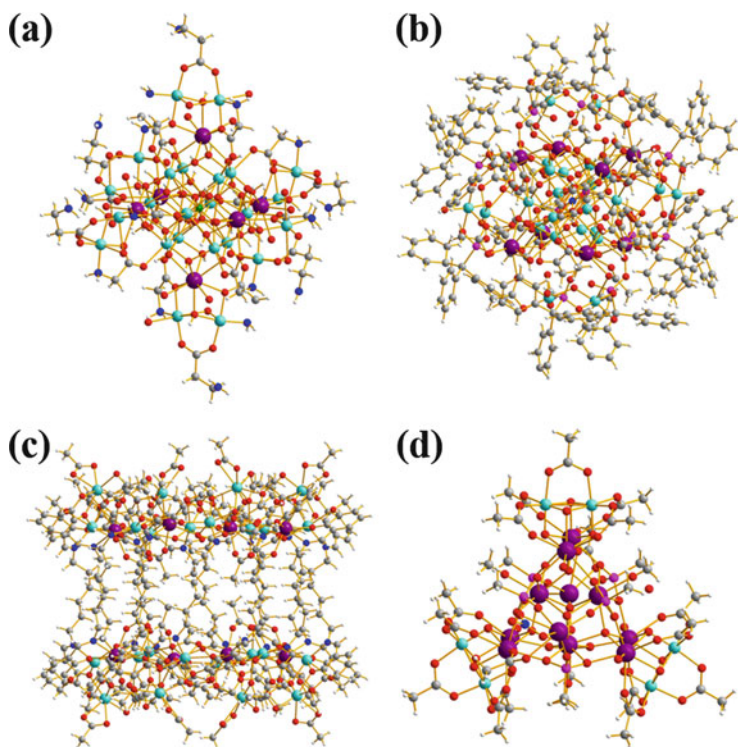
Fig. 30 (**a**) Molecular structure of $Gd_6Cu_{24}OH_{30}$ complex; (**b**) view of the Dy_8 cube encapsulating a Cu_{12} cuboctahedron of Dy_8Cu_{24}; (**c**) crystal structure of Ln_8Cd_{24}; (**d**) molecular structure of $Ce_{22}Mn_{12}$ complex. *Purple*: Ln. *Light blue*: M. *Gray*: C. *Blue*: N. *Red*: O. *White*: H. *Green*: Cl

As shown in Fig. 30a, the $[Gd_6Cu_{24}(\mu_3-OH)_{30}(Gly)_{12}(\beta-Ala)_6(ClO_4)$ $(H_2O)_{12}] \cdot (ClO_4)_{17}$ complex is composed of a $[Gd_6Cu_{12}]$ octahedral core and six outer $[Cu_2]$ units. The inner $[Gd_6Cu_{12}]$ core can be described as a huge octahedron with pseudocubic O_h symmetry. One particularly interesting structural feature of this Gd_6Cu_{24} cluster is that a distorted ClO_4^- anion, which may act as a template, is captured in the cage [35]. Similar structures have been described previously [36–38, 241].

A cage-like complex $[H_3O][Cu_{24}Dy_8(Ph_3CPO_3)_6(Ph_3CPO_3H)_6(MeCO_2)_{12}(-MeCO_2H)_6(OH)_{42}(NO_3)(OH_2)_6]$ bridged by phosphonates and acetates was reported by Winpenny and coworkers. That structure consists of eight Dy^{III} centers at the vertices of a cube with 12 coppers inside and 12 coppers outside the cube [101], as shown in Fig. 30b. The 12 inner coppers are arranged in the form of a cuboctahedron and are connected by one NO_3^- and 24 OH^- bridges.

Two series of high-nuclearity 4d–4f heterometallic clusters, $[Ln_8Cd_{24}L_{12}(OAc)_{48}]$ and $[Ln_6Cd_{18}L_9Cl_8(OAc)_{28}])$ ($H_2L = N,N'$-bis(3-methoxy-

salicylidene)hexane-1,6-diamine), were constructed using a flexible Schiff base ligand [242]. These complexes exhibit drum-like structures with the Ln^{III} centers shielded within the nanoscale structures and protected from outside solvent molecules. The self-assembly process of the drum-like structures appears to be anion dependent (Fig. 30c).

The $Ce_{22}Mn_{12}O_{34}$ unit of the $Ce_{22}Mn_{12}O_{34}(MePO_3)_{12}(O_2CMe)_{33}(OMe)_6(NO_3)$ complex is constituted by two centrosymmetric $Ce_9^{IV}Ce_2^{III}Mn_6^{IV}O_{17}$ subunits [243], which feature three identical distorted cubanes $Ce^{IV}_2Mn^{IV}_2O_4$ connected to a central trigonal-bipyramidal unit $\{Ce^{IV}_3O_2\}$ and two additional Ce^{III} ions capping the top and bottom of the central trigonal bipyramid (Fig. 30d).

The $[\{(GeW_9O_{34})_2Dy_3(OH)_3(H_2O)_2\}_6\{Co_2Dy_3(OH)_6(OH_2)_6\}_4]^{56-}$ polyanionic cluster contains 30 Dy, 8 Co, and 108 W metal centers [82]. The structure of the nanocluster polyanion is composed of six anionic sandwich-type building blocks $[(GeW_9O_{34})_2Dy_3(OH)_3(H_2O)_2]$ and four cationic trigonal-bipyramidal $[Co^{II}_2Dy^{III}_3(OH)_6(OH_2)_6]^{7+}$ clusters. The planar triangular $[Dy_3(OH)_3(OH_2)]^{6+}$ unit is sandwiched by two trilacunary $[GeW_9O_{34}]^{10-}$ anions. This assembly of four $Co^{II}_2Dy^{III}_3$ and six $Dy_3(GeW_9)_2$ subunits results in a hollow heterometallic tetrahedral cluster with a side length of ca. 3.2 nm and a central cavity with a diameter of approximately 1.3 nm.

Two unprecedented wheel-shaped nanoscale clusters $[Co_{16}Ln_{24}(OH)_{50}(pyacac)_{16}(NO_3)_{18}(H_2O)_{12}][Ln(H_2O)_8]_2(NO_3)_{16}(OH)_{10}$(Ln=Gd/Dy) (pyacacH=1,3-di(2-pyridyl)-1,3-propanedione), with a diameter and thickness of 3.0 nm and 2.0 nm, respectively, were obtained by Tong et al. [105]. The metallo-core of $Co_{16}Dy_{24}$ is constructed from a super-square Dy_{24} and an octagonal prism Co_{16}. The $16Co^{II}$ ions form a flat octagonal prism, as shown in the metallic skeleton of the $Co_{16}Dy_{24}$ metallo-wheel (Fig. 31a).The super-square Dy_{24} consists of two types of subunits: a "butterfly" $[Dy_4(\mu_3\text{-}OH)_2(\mu\text{-}O)_5]$ and a distorted tetrahedron $[Dy_4(\mu_3\text{-}OH)_2(\mu\text{-}O)_5]$. Four I subunits and four II subunits are joined together to form the super-square Dy_{24} with shared Dy vertices.
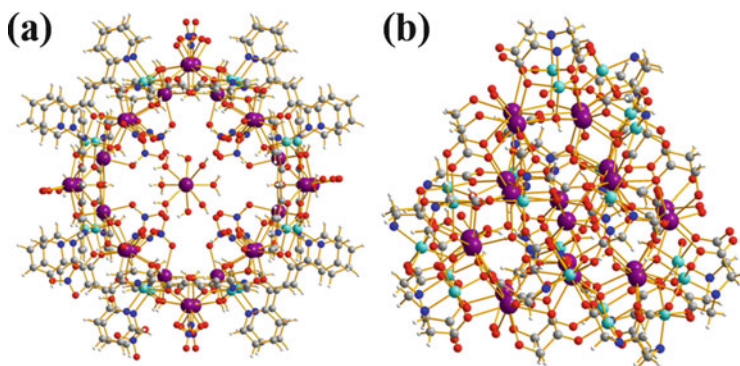
Fig. 31 (a) Molecular structure of $Ln_{24}Co_{16}$ complex, (b) cluster core structure of $Ln_{20}Ni_{21}$ showing an outer Ni_{21} framework encapsulating an inner Ln_{20}. *Purple*: Ln. *Light blue*: M. *Gray*: C. *Blue*: N. *Red*: O. *White*: H

Dual shell-like nanoscopic clusters $[Ln_{20}Ni_{21}(IDA)_{21}(OH)_{24}(C_2H_2O_3)_6(C_2O_4)_3(NO_3)_9(H_2O)_{12}](NO_3)_9$ featuring a polynuclear Ni^{II} framework encapsulating that of the lanthanide ions were synthesized by Long and Zheng et al. [120]. The dual-shell framework structure may be viewed as being constructed from two identical bowl-shaped fragments (Fig. 31b), each featuring an Ln_{10} bowl stacked in an outer Ni_9 bowl. The two Ni_9 bowls are joined together by three Ni^{II} ions and bridging NO_3^- and oxalate ligands. Thus, a closed-shell structure is formed inside the Ln_{20} unit. The cluster core features an outer shell of 21 Ni^{II} ions encapsulating an inner shell of 20 Ln^{III} ions.

Kong and Long et al. reported a tube-like cluster of $[Gd_{36}Ni_{12}(CH_3COO)_{18}(\mu_3\text{-}OH)_{84}(\mu_4\text{-}O)_6(H_2O)_{54}(NO_3)Cl_2](NO_3)_6Cl_9$, which can be viewed as a "sandwich" of two different types of cluster wheel [121]. The outer "bread" layer is a wheel of six vertex-sharing $[Gd_3Ni(\mu_3\text{-}OH)_4]^{7+}$ units (Fig. 6a), and each of these cubane-like clusters is connected to two identical neighbors by sharing two Gd atoms, producing an 18-metal hexagonal wheel. The sandwiched cluster wheel is composed of six $[Gd_5(\mu_4\text{-}O)(\mu_3\text{-}OH)_4]^{9+}$ units joined with two identical neighbors by sharing two basal Gd atoms, generating a hexagonal 24-metal assembly of Gd_{24}. The outer 18-metal cubane assemblies and the sandwiched 24-metal assembly of square-pyramidal clusters are connected by sharing six Gd atoms between adjacent wheels, producing the tube-like structure. The 48 metal ions themselves are organized into 12 Gd_3Ni tetrahedrons and six Gd_5 square pyramids.

The stunningly beautiful structure of the $La_{20}Ni_{30}$ cluster is formulated as $[La_{20}Ni_{30}(IDA)_{30}(CO_3)_6(NO_3)_6(OH)_{30}(H_2O)_{12}](CO_3)_6$ [120]. As shown in Fig. 32a, the metal cluster core features a fascinating double sphere, Keplerate-type structure with an outer sphere formed by 30 Ni^{II} ions encapsulating the inner sphere of 20 La^{III} ions. The 30 Ni^{II} ions span an icosidodecahedron, an Archimedean solid formed by 12 pentagonal and 20 triangular faces, whereas the 20 La^{III} ions occupy the vertices of a perfect dodecahedron, a Platonic solid featuring
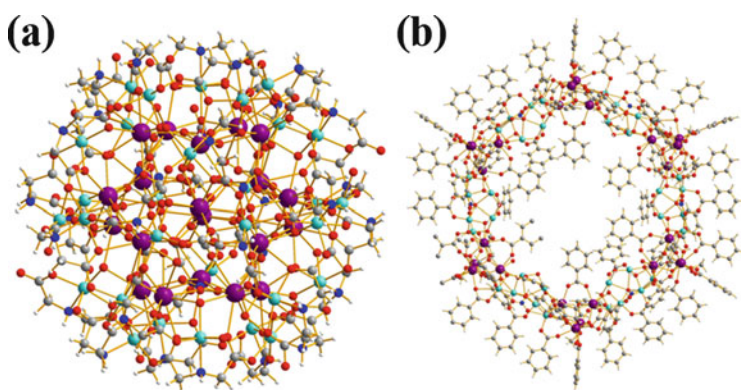
Fig. 32 (**a**) Cluster structure of $La_{20}Ni_{30}$, showing an outer Ni_{30} icosidodecahedron encapsulating an inner La_{20} dodecahedron; (**b**) structure of the $Dy_{24}Cu_{36}$ ring. *Purple*: Ln. *Light blue*: M. *Gray*: C. *Blue*: N. *Red*: O. *White*: H

12 pentagonal faces. The cage-like arrangement of the two distinct sets of metal ions manifests the beauty of symmetry because both ideally possess icosahedral (I_h) symmetry, the highest molecular symmetry possible.

The bowl-like complex $Gd_{42}Co_{10}$, formulated as $[Gd_{42}Co^{II}_9Co^{III}(\mu_3\text{-}OH)_{68}(CO_3)_{12}(CH_3COO)_{30}(H_2O)_{70}](ClO_4)_{25}$ [122], was obtained through self-assembly of metal ions templated by mixed anions (ClO_4^- and CO_3^{2-}). The $Gd_{42}Co_{10}$ core can be viewed as being constructed from three different types of cluster unit (Fig. 6b). Type I, $[Gd_8(\mu_3\text{-}OH)_9]^{15+}$, is made up of one $[Gd_5(\mu_3\text{-}OH)_5]^{10+}$ square pyramid and one cubane-like $[Gd_4(\mu_3\text{-}OH)_4]^{8+}$ unit that share one Gd^{3+}. Type II, $[Gd_6Co_2(\mu_3\text{-}OH)_{12}]^{10+}$, can be viewed as two distorted cubane-like $[Gd_3Co(\mu_3\text{-}OH)_4]^{7+}$ units and one $[Gd_3(\mu_3\text{-}OH)_4]^{5+}$ unit joined together through the sharing of three Gd^{3+} ions. Type III, $[Co^{III}Co^{II}_3(\mu_3\text{-}OH)(CO_3)_3]^{2+}$, is a distorted tetrahedron. Three type I, three type II, and one type III units are joined together in an alternating fashion through nine CO_3^{2-} anions and three ClO_4^- anions.

Two unprecedented 3d–4f hexagonal metallo-rings, $Ln_{24}Cu_{36}(Ln=Dy/Gd)$, with a diagonal dimension of approximately 4.6 nm were facilely synthesized by the self-assembly of Cu^{II} and Ln^{III} nitrates and benzoate in the presence of triethylamine[244]. The metallic ring consisted of two types of alternating subunit – a cubane-like $[Dy_4(OH)_4]$ commonly and an unexpected boat-shaped $[Cu_6(OH)_8(NO_3)]$ – which act as the vertices and sides of the hexagon (Fig. 32b), respectively.

A giant heterometallic cluster $[Gd_{54}Ni_{54}(ida)_{48}(OH)_{144}(CO_3)_6(H_2O)_{25}](NO_3)_{18}$ containing 108 metal ions was reported by Long and Zheng et al. [41]. The four-shell, nesting doll-like structure of the cationic core is shown in Fig. 33a. Moving outward, the innermost shell contains six Ni^{II} and two Gd^{III} ions and is followed by shell 2 with 20 Gd^{III} ions, shell 3 with 32 Gd^{III} ions, and the outermost shell with 48 Ni^{II} ions. The geometry of the shells approximates that of a cube. Inter-shell connections are primarily provided by triply bridging hydroxo groups, affording a highly compact brucite-like core structure.
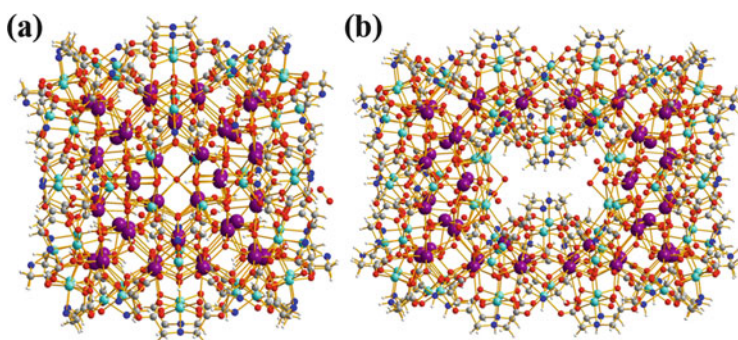
Fig. 33 (**a**) Four-shell presentation of $Gd_{54}Ni_{54}$ complex; (**b**) ball-and-stick plot of the $La_{60}Ni_{76}$ framework with its four shells distinctly shown. *Purple*: Ln. *Light blue*: M. *Gray*: C. *Blue*: N. *Red*: O. *White*: H

To date, the largest member of the 3d–4f cluster is the complex $[La_{60}Ni_{76}(IDA)_{68}(\mu_3\text{-}OH)_{158}(NO_3)_4(H_2O)_{44}](NO_3)_{34}$, which contains 60 La^{III} and 76 Ni^{II} ions and also has a four-shell, nest-like framework structure. As shown in Fig. 33b, the cationic core approximates a rectangular parallelepiped. The structure of $La_{60}Ni_{76}$ can be viewed as an elongation along one of the axes of the cube-shaped $Gd_{54}Ni_{54}$ cluster with its 136 metal ions organized in four distinct shells. Moving outward from the innermost shell, the 8Ni(II) ions in shell 1 are encaged by shell 2 of $La_{20}Ni_4$, followed by shell 3 of La_{40}, and then shell 4 of Ni_{64} [42].

4   Perspectives and Outlooks

In the last two decades, the synthesis and investigation of heterometallic d–f polynuclear compounds have attracted intense interest because of their fascinating architecture and potential applications in various research fields. A large number of d–f clusters with novel topologies (such as ball-like, cage-like, disc-like, and ring-like structures) have been reported.

To date, chemists have developed several synthesis strategies. Based on HSAB theory, the most efficient technique is the polydentate ligand method. Appropriate organic ligands containing N and O atoms can combine 3d and 4f metal ions within a single molecular entity. The ligand-controlled hydrolytic approach is relatively beneficial for the construction of d–f hydroxide complexes. Some structurally well-defined hydroxide cluster species can be rationally synthesized via a ligand-controlled hydrolytic approach with the use of judiciously chosen ancillary ligands to limit the degree of lanthanide hydrolysis. The anion template method is more useful for the assembly of the high-nuclearity d–f clusters because of its dispersion of the clusters' positive charge. Until now, the use of a single anion as a template has been studied most extensively. Compared with the single-anion template, the multiple-anion template is a better approach to construct high-nuclearity d–f metal clusters. Cationic-template-based d–f clusters are difficult to design and synthesize. Only a few cationic templating d–f clusters have been reported and were accidental discoveries. The metalloligand strategy can reduce the uncertainty in the reaction and simplify the reaction process to design and synthesize the target product.

Nano-sized d–f clusters with nuclearity as high as 136 have been reported in the literature. The observed heterometallic clusters display different structural topologies, such as ring-like, cage-like, tube-like, ball-like, and disc-like structures. In this chapter, we summarized and compared these discrete d–f clusters with similar structural topologies based on the number of metal centers. We hope that this summary will facilitate the design and synthesis polynuclear 3d–4f clusters with different structures.

Despite the large numbers of d–f clusters prepared in the last two decades, the development of d–f clusters with different nuclearities continues to attract substantial interest. First, the design and synthesis of d–f heterometallic clusters remain challenging because of the different coordination geometries of d and f metal ions

and the instability caused by the overaggregation of the metal ions. High-nuclearity clusters containing 30 metal ions are particularly rare. In the next few years, it will be necessary to develop additional novel heterometallic clusters to elucidate the effects of the reaction conditions on their structures. Our ultimate goal is the directed synthesis of a molecule with a specific composition and structure. Clearly, however, we are still far from that goal. Second, although the properties (especially the magnetism) of d–f clusters have been studied extensively, the property-structural correlations of these fascinating systems remain unclear. A deeper under-standing of the property-structural correlations will be a very interesting research topic in the future. In addition, the synergistic effects of transition metal and lanthanide ions can likely be used to obtain some special properties, such as the synergism catalytic property. However, little research has been conducted in this area. Therefore, investigating the synergistic effects of heterometallic atoms in these clusters or nanoparticles derived from these clusters will likely be very rewarding.

References

1. Chen QY, Luo QH, Hu XL, Shen MC, Chen JT (2002) Chem Eur J 8:3984
2. Wong WK, Liang H, Wong WY, Cai Z, Li KF, Cheah KW (2002) New J Chem 26:275
3. Maity M, Majee MC, Kundu S, Samanta SK, Sanudo EC, Ghosh S, Chaudhury M (2015) Inorg Chem 54:9715
4. Chen S, Mereacre V, Prodius D, Kostakis GE, Powell AK (2015) Inorg Chem 54:3218
5. Benelli C, Gatteschi D (2002) Chem Rev 102:2369
6. Sakamoto M, Manseki K, Ōkawa H (2001) Coord Chem Rev 219:379
7. Christou G, Gatteschi D, Hendrickson DN, Sessoli R (2000) MRS Bull 25:66
8. Corradini V, Ghirri A, Candini A, Biagi R, del Pennino U, Dotti G, Otero E, Choueikani F, Blagg RJ, McInnes EJ, Affronte M (2013) Adv Mater 25:2816
9. Zhang S, Li H, Duan E, Han Z, Li L, Tang J, Shi W, Cheng P (2016) Inorg Chem. doi:10.1021/acs.inorgchem.5b02378
10. Liu K, Shi W, Cheng P (2015) Coord Chem Rev 74:289
11. Winpenny REP (1998) Chem Soc Re 27:447
12. Sharples JW, Collison D (2014) Coord Chem Rev 260:1
13. Huang YG, Jiang FL, Hong MC (2009) Coord Chem Rev 253:2814
14. Kong XJ, Long LS, Zheng ZP, Huang RB, Zheng LS (2010) Acc Chem Res 43:201
15. Kajiwara T, Iki N, Yamashita M (2007) Coord Chem Rev 251:1734
16. Koner R, Lin HH, Wei HH, Mohanta S (2005) Inorg Chem 44:3524
17. Costes JP, Donnadieu B, Gheorghe R, Novitchi G, Tuchagues JP, Vendier L (2008) Eur J Inorg Chem 17:5235
18. Towatari M, Nishi K, Fujinami T, Matsumoto N, Sunatsuki Y, Kojima M, Mochida N, Ishida T, Re N, Mrozinski J (2013) Inorg Chem 52:6160
19. Gheorghe R, Andruh M, Costes JP, Donnadieu B, Schmidtmann M, Müller A (2007) Inorg Chim Acta 360:4044
20. Xu L, Zhang Q, Hou G, Chen P, Li G, Pajerowski DM, Dennis CL (2013) Polyhedron 52:91

21. Costes JP, Shova S, Wernsdorfer W (2008) Dalton Trans 37:1843
22. Costes JP, Auchel M, Dahan F, Peyrou V, Shova S, Wernsdorfer W (2006) Inorg Chem 45:1924
23. Hamamatsu T, Yabe K, Towatari M, Osa S, Matsumoto N, Re N, Pochaba A, Mrozinski J, Gallani JL, Barla A, Imperia P, Paulsen C, Kappler JP (2007) Inorg Chem 46:4458
24. Osa S, Kido T, Matsumoto N, Re N, Pochaba A, Mrozinski J (2004) J Am Chem Soc 126:420
25. Nemec I, Machata M, Herchel R, Boˇca R, Trávníˇcek Z (2012) Dalton Trans 41:14603
26. Mondal KC, Kostakis GE, Lan Y, Wernsdorfer W, Anson CE, Powell AK (2011) Inorg Chem 50:11604
27. Mondal KC, Sundt A, Lan Y, Kostakis GE, Waldmann O, Ungur L, Chi botaru LF, Anson CE, Powell AK (2012) Angew Chem Int Ed 51:7550
28. Ke H, Zhao L, Guo Y, Tang J (2012) Inorg Chem 51:2699
29. Alexandropoulos MI, Nguyen TN, Cunha-Silva L, Zafiropoulos TF, Escuer A, Christou G, Stamatatos TC (2013) Inorg Chem 52:1179
30. Zou LF, Zhao L, Guo YN, Yu GM, Guo Y, Tang JK, Li YH (2011) Chem Commun 47:8659
31. Lin X, Dan MJD, Alexander JB, Andrew H, Claire W, Martin S (2003) J Am Chem Soc 125:9476
32. Birk T, Pedersen KS, Thuesen CA, Weyhermuller T, Magnussen MS, Piligkos S, Weihe H, Mossin S, Evangelisti M, Bendix J (2012) Inorg Chem 51:5435
33. Li ZY, Zhu J, Wang XQ, Ni J, Zhang JJ, Liu SQ, Duan CY (2013) Dalton Trans 42:5711
34. Xiang SC, Hu SM, Sheng TL, Fu RB, Wu XT, Zhang X (2007) J Am Chem Soc 129:15144
35. Shen CJ, Hu SM, Sheng TL, Xue ZZ, Wu XT (2015) Dalton Trans 44:6510
36. Zhang JJ, Hu SM, Xiang SC, Sheng TL, Wu XT, Li YM (2006) Inorg Chem 45:7173
37. Zhang JJ, Sheng TL, Xia SQ, Leibeling G, Meyer F, Hu SM, Fu RB, Xiang SC, Wu XT (2004) Inorg Chem 43:5472
38. Zhuang GL, Chen WX, Zhao HX, Kong XJ, Long LS, Huang RB, Zheng LS (2011) Inorg Chem 50:3843
39. Zhuang GL, Sun XJ, Long LS, Huang RB, Zheng LS (2009) Dalton Trans 4640
40. Kong XJ, Ren YP, Long LS, Zheng Z, Huang RB, Zheng LS (2007) J Am Chem Soc 129:7016
41. Kong XJ, Ren YP, Chen WX, Long LS, Zheng Z, Huang RB, Zheng LS (2008) Angew Chem Int Ed 47:2398
42. Kong XJ, Long LS, Huang RB, Zheng LS, Harris TD, Zheng Z (2009) Chem Commun (Camb) 4354
43. Peng G, Kostakis GE, Lan Y, Powell AK (2013) Dalton Trans 42:46
44. Langley SK, Chilton NF, Ungur L, Moubaraki B, Chibotaru LF, Murray KS (2012) Inorg Chem 51:11873
45. Murugesu M, Mishra A, Wernsdorfer W, Abboud KA, Christou G (2006) Polyhedron 25:613
46. Baniodeh A, Hewitt IJ, Mereacre V, Lan Y, Novitchi G, Anson CE, Powell AK (2011) Dalton Trans 40:4080
47. Chilton NF, Langley SK, Moubaraki B, Murray KS (2010) Chem Commun (Camb) 46:7787
48. Mereacre V, Prodius D, Lan Y, Turta C, Anson CE, Powell AK (2011) Chem A Eur J 17:123
49. Langley SK, Moubarakia B, Murray KS (2010) Dalton Trans 39:5066
50. Saha A, Thompson M, Abboud KA, Wernsdorfer W, Christou G (2011) Inorg Chem 50:10476
51. Langley SK, Ungur L, Chilton NF, Moubaraki B, Chibotaru LF, Murray KS (2011) Chem A Eur J 17:9209
52. Zhao XQ, Lan YH, Zhao B, Cheng P, Ansona CE, Powell AK (2010) Dalton Trans 39:4911
53. Akhtar MN, Lan Y, Mereacre V, Clérac R, Anson CE, Powell AK (2009) Polyhedron 28:1698
54. Akhtar MN, Zheng YZ, Lan Y, Mereacre V, Anson CE, Powell AK (2009) Inorg Chem 48:3502

55. Rinck J, Novitchi G, Van den Heuvel W, Ungur L, Lan Y, Wernsdorfer W, Anson CE, Chibotaru LF, Powell AK (2010) Angew Chem Int Ed 49:7583
56. Mereacre V, Akhtar MN, Lan YH, Ako AM, Cl´ R, Ansona CE, Powell AK (2010) Dalton Trans 39:4918
57. Mereacre V, Ako AM, Clerac R, Wernsdorfer W, Hewitt IJ, Anson CE, Powell AK (2008) Chem Eur J 14:3577
58. Abbas G, Lan Y, Mereacre V, Wernsdorfer W, Clerac R, Buth G, Sougrati MT, Grandjean F, Long GJ, Anson CE, Powell AK (2009) Inorg Chem 48:9345
59. Liu JL, Guo FS, Meng ZS, Zheng YZ, Leng JD, Tong ML, Ungur L, Chibotaru LF, Heroux KJ, Hendrickson DN (2011) Chem Sci 2:1268
60. Mereacre V, Ako AM, Akhtar MN, Lindemann A, Anson CE, Powell AK (2009) Helv Chim Acta 92:2507
61. Ako AM, Mereacre V, Clérac R, Hewitt IJ, Lan Y, Anson CE, Powell AK (2007) Dalton Trans 5245
62. Ako AM, Mereacre V, Clerac R, Hewitt IJ, Lan Y, Buth G, Anson CE, Powell AK (2009) Inorg Chem 48:6713
63. Rigaux G, Inglis R, Morrison S, Prescimone A, Cadiou C, Evangelisti M, Brechin EK (2011) Dalton Trans 40:4797
64. Hallier K, Hołyńska M, Dehnen S (2011) Z Anorg Allg Chem 637:2093
65. Hallier K, Hołyńska M, Rouzières M, Clérac R, Dehnen S (2012) Inorg Chem 51:3929
66. Cutland AD, Halfen JA, Kampf JW, Pecoraro VL (2001) J Am Chem Soc 123:6211
67. CutlandVan Noord AD, Kampf JW, Pecoraro VL (2002) Angew Chem Int Ed 41:4667
68. Zaleski CM, Depperman EC, Kampf JW, Kirk ML, Pecoraro VL (2006) Inorg Chem 45:10022
69. Zaleski CM, Kampf JW, Mallah T, Kirk ML, Pecoraro VL (2007) Inorg Chem 46:1954
70. Boron TT III, Kampf JW, Pecoraro VL (2010) Inorg Chem 49:9104
71. Deb A, Boron TT 3rd, Itou M, Sakurai Y, Mallah T, Pecoraro VL, Penner-Hahn JE (2014) J Am Chem Soc 136:4889
72. Cao F, Wang S, Li D, Zeng S, Niu M, Song Y, Dou J (2013) Inorg Chem 52:10747
73. He F, Tong ML, Chen XM (2005) Inorg Chem 44:8285
74. Colacio E, Ruiz-Sanchez J, White FJ, Brechin EK (2011) Inorg Chem 50:7268
75. Chandrasekhar V, Bag P, Speldrich M, van Leusen J, Kogerler P (2013) Inorg Chem 52:5035
76. Singh SK, Tibrewal NK, Rajaraman G (2011) Dalton Trans 40:10897
77. Papatriantafyllopoulou C, Stamatatos TC, Efthymiou CG, Cunha-Silva L, Paz FA, Perlepes SP, Christou G (2010) Inorg Chem 49:9743
78. Reinoso S, Galan-Mascaros JR (2010) Inorg Chem 49:377
79. Reinoso S, Galan-Mascaros JR, Lezama L (2011) Inorg Chem 50:9587
80. Merca A, Mueller A, Slageren J, Laege M, Krebs B, Cluster J (2007) Science 18:711
81. Wang WD, Li XX, Fang WH, Yang G-Y, Cluster J (2011) Science 22:87
82. Ibrahim M, Mereacre V, Leblanc N, Wernsdorfer W, Anson CE, Powell AK (2015) Angew Chem Int Ed 54:15574
83. Chen W, Li Y, Wang Y, Wang E, Zhang Z (2008) Dalton Trans 865
84. Zhang ZM, Li YG, Yao S, Wang EB (2011) Dalton Trans 40:6475
85. Nohra B, Mialane P, Dolbecq A, Rivière E, Marrot J, Sécheresse F (2009) Chem Commun 45:2703
86. Fang X, Koegerler P (2008) Chem Commun (Cambridge, U.K.) 3396
87. Fang X, Kogerler P (2008) Angew Chem Int Ed 47:8123
88. Li YW, Li YG, Wang YH, Feng XJ, Lu Y, Wang EB (2009) Inorg Chem 48:6452
89. Cristovao B, Miroslaw B, Klak J, Rams M (2015) Polyhedron 85:697
90. Sakamoto S, Yamauchi S, Hagiwara H, Matsumoto N, Sunatsuki Y, Re N (2012) Inorg Chem Commun 26:20
91. Zhang P, Zhang L, Lin SY, Tang J (2013) Inorg Chem 52:6595

92. Ruiz J, Lorusso G, Evangelisti M, Brechin EK, Pope SJA, Colacio E (2014) Inorg Chem 53:3586

93. Ehama K, Ohmichi Y, Sakamoto S, Fujinami T, Matsumoto N, Mochida N, Ishida T, Sunatsuki Y, Tsuchimoto M, Re N (2013) Inorg Chem 52:12828

94. Pasatoiu TD, Ghirri A, Madalan AM, Affronte M, Andruh M (2014) Dalton Trans 43:9136

95. Dermitzaki D, Lorusso G, Raptopoulou CP, Psycharis V, Escuer A, Evangelisti M, Perlepes SP, Stamatatos TC (2013) Inorg Chem 52:10235

96. Zhang B, Zheng X, Su H, Zhu Y, Du C, Song M (2013) Dalton Trans 42:8571

97. Ke H, Zhang S, Zhu W, Xie G, Chen S (2015) J Coord Chem 68:808

98. Pineda EM, Tuna F, Zheng Y-Z, Teat SJ, Winpenny REP, Schnack J, McInnes EJL (2014) Inorg Chem 53:3032

99. Hooper TN, Inglis R, Palacios MA, Nichol GS, Pitak MB, Coles SJ, Lorusso G, Evangelisti M, Brechin EK (2014) Chem Commun (Cambridge, U.K.) 50:3498

100. Blake AJ, Gould RO, Grant CM, Milne PEY, Parsons S, Winpenny REP (1997) J Chem Soc Dalton Trans 485

101. Baskar V, Gopal K, Helliwell M, Tuna F, Wernsdorfer W, Winpenny REP (2010) Dalton Trans 39:4747

102. Yang YY, Huang ZQ, He F, Chen XM, Ng SW (2004) Z Anorg Allg Chem 630:286

103. Liu JL, Lin WQ, Chen YC, Coca SG, Aravena D, Ruiz E, Leng JD, Tong ML (2013) Chem Eur J 19:17567

104. Liu JL, Chen YC, Li QW, Coca SG, Aravena D, Ruiz E, Lin WQ, Leng JD, Tong ML (2013) Chem Commun (Cambridge, U.K.) 49:6549

105. Zhang ZM, Pan LY, Lin WQ, Leng JD, Guo FS, Chen YC, Liu JL, Tong ML (2013) Chem Commun (Cambridge, U.K.) 49:8081

106. Guillou O, Oushoorn RL, Kahn O, Boubekeur K, Batail P (1992) Angew Chem Int Ed 31:626

107. Dinca AS, Shova S, Ion AE, Maxim C, Lloret F, Julve M, Andruh M (2015) Dalton Trans 44:7148

108. Subhan MA, Suzuki T, Kaizaki S (2002) J Chem Soc Dalton Trans 1416

109. Yamada Y, Tanabe M, Miyashita Y, Okamoto KI (2003) Polyhedron 22:1455

110. Chen XM, Aubin SMJ, Wu YL, Yang YS, Mak TCW, Hendrickson DN (1995) J Am Chem Soc 117:9600

111. Cui Y, Chen JT, Huang JS (1999) Inorg Chim Acta 293:129

112. Liu DP, Peng JB, Lin XP, Huang Q, Kong XJ, Long LS, Huang RB, Zheng LS (2014) CrystEngComm 16:5527

113. Moreno Pineda E, Tuna F, Pritchard RG, Regan AC, Winpenny REP, Zheng Y-Z, McInnes EJL (2013) Chem Commun (Cambridge, U.K.) 49:3522

114. McRobbie A, Sarwar AR, Yeninas S, Nowell H, Baker ML, Allan D, Luban M, Muryn CA, Pritchard RG, Prozorov R, Timco GA, Tuna F, Whitehead GFS, Winpenny REP (2011) Chem Commun (Cambridge, U.K.) 47:6251

115. Dreiser J, Pedersen KS, Piamonteze C, Rusponi S, Salman Z, Ali ME, Magnussen MS, Thuesen CA, Piligkos S, Weihe H, Mutka H, Waldmann O, Oppeneer P, Bendix J, Nolting F, Brune H (2012) Chem Sci 3:1024

116. Pedersen KS, Lorusso G, Morales JJ, Weyhermueller T, Piligkos S, Singh SK, Larsen D, Magnussen MS, Rajaraman G, Evangelisti M, Bendix J (2014) Angew Chem Int Ed 53:2394

117. Reynolds RA, Coucouvanis D (1998) J Am Chem Soc 120:209

118. Romanenko GV, Yu Fursova E, Ovcharenko VI (2009) Russ Chem B Int Ed 58:1

119. Wu G, Hewitt IJ, Mameri S, Lan Y, Clerac R, Anson CE, Qiu S, Powell AK (2007) Inorg Chem 46:7229

120. Kong XJ, Ren YP, Long LS, Zheng Z, Nichol G, Huang RB, Zheng LS (2008) Inorg Chem 47:2728

121. Peng JB, Zhang QC, Kong XJ, Ren YP, Long LS, Huang RB, Zheng LS, Zheng Z (2011) Angew Chem Int Ed 50:10649

122. Peng JB, Zhang QC, Kong XJ, Zheng YZ, Ren YP, Long LS, Huang RB, Zheng LS, Zheng Z (2012) J Am Chem Soc 134:3314
123. Xiong K, Wang X, Jiang F, Gai Y, Xu W, Su K, Li X, Yuan D, Hong M (2012) Chem Commun (Cambridge, U.K.) 48:7456
124. Yukawa Y, Igarashi S, Yamano A, Sato S (1997) Chem Commun (Cambridge) 711
125. Igarashi S, Hoshino Y, Masuda Y, Yukawa Y (2000) Inorg Chem 39:2509
126. Zhang JJ, Xiang SC, Hu SM, Xia SQ, Fu RB, Wu XT, Li YM, Zhang HS (2004) Polyhedron 23:2265
127. Zhang YJ, Ma BQ, Gao S, Li JR, Liu QD, Wen GH, Zhang XX (2000) J Chem Soc Dalton Trans 2249
128. Liu QD, Gao S, Li JR, Zhou QZ, Yu KB, Ma BQ, Zhang SW, Zhang XX, Jin TZ (2000) Inorg Chem 39:2488
129. Stemmler AJ, Barwinski A, Baldwin MJ, Young V, Pecoraro VL (1996) J Am Chem Soc 118:11962
130. Stemmler AJ, Kampf JW, Kirk ML, Atasi BH, Pecoraro VL (1999) Inorg Chem 38:2807
131. Cutland AD, Malkani RG, Kampf JW, Pecoraro VL (2000) Angew Chem Int Ed 39:2689
132. Tasiopoulos AJ, O'Brien T, Abboud KA, Christou G (2004) Angew Chem Int Ed 43:345
133. Tasiopoulos AJ, Wernsdorfer W, Moulton B, Zaworotko MJ, Christou G (2003) J Am Chem Soc 125:15274
134. Feltham HLC, Clerac R, Powell AK, Brooker S (2011) Inorg Chem 50:4232
135. Feltham HLC, Lan Y, Kloewer F, Ungur L, Chibotaru LF, Powell AK, Brooker S (2011) Chem Eur J 17:4362
136. Liu QD, Li JR, Gao S, Ma BQ, Kou HZ, Ouyang L, Huang RL, Zhang XX, Yu KB (2003) Eur J Inorg Chem 731
137. Ma BQ, Gao S, Bai O, Sun HL, Xu GX (2000) J Chem Soc Dalton Trans 1003
138. Zhuang GL, Jin YC, Zhao HX, Kong XJ, Long LS, Huang RB, Zheng LS (2010) Dalton Trans 39:5077
139. Bencini A, Benelli C, Caneschi A, Carlin RL, Dei A, Gatteschi D (1985) J Am Chem Soc 107:8128
140. Chandrasekhar V, Pandian BM, Boomishankar R, Steiner A, Clerac R (2008) Dalton Trans 5143
141. Liu JL, Wu JY, Chen YC, Mereacre V, Powell AK, Ungur L, Chibotaru LF, Chen XM, Tong ML (2014) Angew Chem Int Ed 53:12966
142. Yamaguchi T, Costes JP, Kishima Y, Kojima M, Sunatsuki Y, Brefuel N, Tuchagues JP, Vendier L, Wernsdorfer W (2010) Inorg Chem 49:9125
143. Chandrasekhar V, Das S, Dey A, Hossain S, Kundu S, Colacio E (2014) Eur J Inorg Chem 2014:397
144. Chandrasekhar V, Pandian BM, Jagadese RC, Vittal J (2009) Inorg Chem 48:1148
145. Liu JL, Chen YC, Zheng YZ, Lin WQ, Ungur L, Wernsdorfer W, Chibotaru LF, Tong ML (2013) Chem Sci 4:3310
146. Pointillart F, Bernot K, Sessoli R, Gatteschi D (2007) Chemistry 13:1602
147. Mori F, Ishida T, Nogami T (2005) Polyhedron 24:2588
148. Mori F, Nyui T, Ishida T, Nogami T, Yong Choi K, Nojiri H (2006) J Am Chem Soc 128:1440
149. Liu CM, Zhang DQ, Hao X, Zhu DB (2014) Chem An Asian J 9:1847
150. Bhunia A, Gamer MT, Ungur L, Chibotaru LF, Powell AK, Lan Y, Roesky PW, Menges F, Riehn C, Niedner-Schatteburg G (2012) Inorg Chem 51:9589
151. Tasiopoulos AJ, Paul J, Milligan L, Abboud KA, O'Brien TA, Christou G (2007) Inorg Chem 46:9678
152. Bhunia A, Yadav M, Lan Y, Powell AK, Menges F, Riehn C, Niedner-Schatteburg G, Jana PP, Riedel R, Harms K, Dehnen S, Roesky PW (2013) Dalton Trans 42:2445
153. Lampropoulos C, Stamatatos TC, Abboud KA, Christou G (2009) Inorg Chem 48:429

154. Georgopoulou AN, Adam R, Raptopoulou CP, Psycharis V, Ballesteros R, Abarca B, Boudalis AK (2011) Dalton Trans 40:8199
155. Efthymiou CG, Georgopoulou AN, Papatriantafyllopoulou C, Terzis A, Raptopoulou CP, Escuer A, Perlepes SP (2010) Dalton Trans 39:8603
156. Georgopoulou AN, Efthymiou CG, Papatriantafyllopoulou C, Psycharis V, Raptopoulou CP, Manos M, Tasiopoulos AJ, Escuer A, Perlepes SP (2011) Polyhedron 30:2978
157. Gao Y, Zhao L, Xu X, Xu GF, Guo YN, Tang J, Liu Z (2011) Inorg Chem 50:1304
158. Costes JP, Vendier L, Wernsdorfer W (2011) Dalton Trans 40:1700
159. Baniodeh A, Lan Y, Novitchi G, Mereacre V, Sukhanov, Ferbinteanu M, Voronkova V, Anson CE, Powell AK (2013) Dalton Trans 42:8926
160. Mereacre V, Prodius D, Turta C, Shova S, Filoti G, Bartolomé J, Clérac R, Anson CE, Powell AK (2009) Polyhedron 28:3017
161. Meng ZS, Guo FS, Liu JL, Leng JD, Tong ML (2012) Dalton Trans 41:2320
162. Yu WR, Lee GH, Yang EC (2013) Dalton Trans 42:3941
163. Aronica C, Chastanet G, Pilet G, Guennic BL, Robert V, Wernsdorfer W, Luneau D (2007) Inorg Chem 46:6108
164. Andruh M, Costes JP, Diaz C, Gao S (2009) Inorg Chem 48:3342
165. Igarashi S, Kawaguchi S, Yukawa Y, Tuna F, Winpenny RE (2009) Dalton Trans 3140
166. Thuesen CA, Pedersen KS, Schau-Magnussen M, Evangelisti M, Vibenholt J, Piligkos S, Weihe H, Bendix J (2012) Dalton Trans 41:11284
167. Abtab SM, Maity M, Bhattacharya K, Sanudo EC, Chaudhury M (2012) Inorg Chem 51:10211
168. Sanz S, Ferreira K, McIntosh RD, Dalgarno SJ, Brechin EK (2011) Chem Commun (Camb) 47:9042
169. Bi YF, Li YL, Liao WP, Zhang HJ, Li D (2008) Inorg Chem 47:9733
170. Abtab SM, Majee MC, Maity M, Titis J, Boca R, Chaudhury M (2014) Inorg Chem 53:1295
171. Efthymiou CG, Stamatatos TC, Papatriantafyllopoulou C, Tasiopoulos AJ, Wernsdorfer W, Perlepes SP, Christou G (2010) Inorg Chem 49:9737
172. Xu GF, Gamez P, Tang J, Clerac R, Guo YN, Guo Y (2012) Inorg Chem 51:5693
173. Feltham HL, Clerac R, Ungur L, Chibotaru LF, Powell AK, Brooker S (2013) Inorg Chem 52:3236
174. Feltham HL, Klower F, Cameron SA, Larsen DS, Lan Y, Tropiano M, Faulkner S, Powell AK, Brooker S (2011) Dalton Trans 40:11425
175. Feltham HL, Clerac R, Ungur L, Vieru V, Chibotaru LF, Powell AK, Brooker S (2012) Inorg Chem 51:10603
176. Pasatoiu TD, Etienne M, Madalan A, Andruh M, Sessoli R (2010) Dalton Trans 39:4802
177. Benelli C, Caneschi A, Gatteschi D, Guillou O, Pardi L (1990) Inorg Chem 29:1750
178. Zhao L, Wu J, Xue S, Tang J (2012) Chem An Asian J 7:2419
179. Chesman AS, Turner DR, Berry KJ, Chilton NF, Moubaraki B, Murray KS, Deacon GB, Batten SR (2012) Dalton Trans 41:11402
180. Fujiwara K, Okazawa A, Kojima N, Tanaka G, Yoshii S, Nojiri H, Ishida T (2012) Chem Phys Lett 530:49
181. Sun YQ, Liang M, Dong W, Yang GM, Liao DZ, Jiang ZH, Yan SP, Cheng P (2004) Eur J Inorg Chem 2004:1514
182. Wu B (2006) Dalton Trans 5113
183. Li H, Shi W, Niu Z, Zhou JM, Xiong G, Li LL, Cheng P (2015) Dalton Trans 44:468
184. Myrtil LK, Corine M, Kahn O (1999) Inorg Chem 38:3692
185. Polyzou CD, Baniodeh A, Magnani N, Mereacre V, Zill N, Anson CE, Perlepes SP, Powell AK (2015) RSC Adv 5:10763
186. Xie QW, Cui AL, Tao J, Kou HZ (2012) Dalton Trans 41:10589
187. Ke H, Zhao L, Guo Y, Tang J (2012) Dalton Trans 41:2314
188. Feuersenger J, Prodius D, Mereacre V, Clérac R, Anson CE, Powell AK (2011) Inorg Chem Commun 14:1851

189. Akhtar MN, Mereacre V, Novitchi G, Tuchagues JP, Anson CE, Powell AK (2009) Chemistry 15:7278
190. Liu J, Ma C, Chen H, Hu M, Wen H, Cui H, Song X, Chen C (2013) Dalton Trans 42:2423
191. Shiga T, Hoshino N, Nakano M, Nojiri H, Oshio H (2008) Inorg Chim Acta 361:4113
192. Zhao L, Wu J, Ke H, Tang J (2014) Inorg Chem 53:3519
193. Chaudhari AK, Joarder B, Riviere E, Rogez G, Ghosh SK (2012) Inorg Chem 51:9159
194. Novitchi G, Wernsdorfer W, Chibotaru LF, Costes JP, Anson CE, Powell AK (2009) Angew Chem 48:1614
195. Andruh M, Ramade I, Codjovi E, Guillou O, Kahn O, Trombe JC (1993) J Am Chem Soc 115:1822
196. Xiang H, Lu WG, Zhang WX, Jiang L (2013) Dalton Trans 42:867
197. Nayak S, Roubeau O, Teat SJ, Beavers CM, Gamez P, Reedijk J (2010) Inorg Chem 49:216
198. Bi Y, Wang XT, Wang BW, Liao W, Wang X, Zhang H, Gao S, Li D (2009) Dalton Trans 2250
199. Milios CJ, Wood PA, Parsons S, Foguet-Albiol D, Lampropoulos C, Christou G, Perlepes SP, Brechin EK (2007) Inorg Chim Acta 360:3932
200. Orfanoudaki M, Tamiolakis I, Siczek M, Lis T, Armatas GS, Pergantis SA, Milios CJ (2011) Dalton Trans 40:4793
201. Sopasis GJ, Canaj AB, Philippidis A, Siczek M, Lis T, O'Brien JR, Antonakis MM, Pergantis SA, Milios CJ (2012) Inorg Chem 51:5911
202. Sopasis GJ, Orfanoudaki M, Zarmpas P, Philippidis A, Siczek M, Lis T, O'Brien JR, Milios CJ (2012) Inorg Chem 51:1170
203. Ledezma Gairaud M, Grangel L, Aromi G, Fujisawa T, Yamaguchi A, Sumiyama A, Sanudo EC (2014) Inorg Chem 53:5878
204. Liu CM, Zhang DQ, Zhu DB (2010) Dalton Trans 39:11325
205. Yukawa Y, Aromi G, Igarashi S, Ribas J, Zvyagin SA, Krzystek J (2005) Angew Chem 44:1997
206. Liu J, Ma C, Chen H, Hu M, Wen H, Cui H, Chen C (2013) Dalton Trans 42:3787
207. Chandrasekhar V, Dey A, Das S, Rouzieres M, Clerac R (2013) Inorg Chem 52:2588
208. Karotsis G, Kennedy S, Teat SJ, Beavers CM, Fowler DA, Morales JJ, Evangelisti M, Dalgarno SJ, Brechin EK (2010) J Am Chem Soc 132:12983
209. Karotsis G, Evangelisti M, Dalgarno SJ, Brechin EK (2009) Angew Chem Int Ed 48:9928
210. Hosoi A, Yukawa Y, Igarashi S, Teat SJ, Roubeau O, Evangelisti M, Cremades E, Ruiz E, Barrios LA, Aromi G (2011) Chem Eur J 17:8264
211. Sheng E, Yu W, Li X (2008) Inorg Chem Commun 11:418
212. Li M, Ako AM, Lan Y, Wernsdorfer W, Buth G, Anson CE, Powell AK, Wang Z, Gao S (2010) Dalton Trans 39:3375
213. Li M, Lan Y, Ako AM, Wernsdorfer W, Anson CE, Buth G, Powell AK, Wang Z, Gao S (2010) Inorg Chem 49:11587
214. Khan A, Lan Y, Kostakis GE, Anson CE, Powell AK (2012) Dalton Trans 41:8333
215. Mishra A, Tasiopoulos AM, Wernsdorfer W, Moushi EE, Moulton B, Zaworotko MJ, Abboud KA, Christou G (2008) Inorg Chem 47:4832
216. Zheng Y, Kong XJ, Long LS, Huang RB, Zheng LS (2011) Dalton Trans 40:4035
217. Aronica C, Pilet G, Chastanet G, Wernsdorfer W, Jacquot JF, Luneau D (2006) Angew Chem Int Ed 45:4659
218. Langley SK, Chilton NF, Moubaraki B, Hooper T, Brechin EK, Evangelisti M, Murray KS (2011) Chem Sci 2:1166
219. Majeed Z, Mondal KC, Kostakis GE, Lan YH, Ansona CE, Powell AK (2010) Dalton Trans 39:4740
220. Zhang H, Zhuang GL, Kong XJ, Ren YP, Long LS, Huang RB, Zheng LS (2013) Cryst Growth Des 13:2493
221. Wang SN, Pang JZ, Wagner MJ (1992) Inorg Chem 31:5381
222. Kizas CM, Papatriantafyllopoulou C, Manos MJ, Tasiopoulos AJ (2013) Polyhedron 52:346

223. Zheng Y, Pan YY, Ren YP, Long LS, Huang RB, Zheng L-S (2014) Chem Comm 50:14728
224. Shiga T, Onuki T, Matsumoto T, Nojiri H, Newton GN, Hoshino N, Oshio H (2009) Chem Commun (Camb) 3568
225. Dinca AS, Ghirri A, Madalan AM, Affronte M, Andruh M (2012) Inorg Chem 51:3935
226. Mereacre V, Lan Y, Wernsdorfer W, Anson CE, Powell AK (2012) Comptes Rendus Chimie 15:639
227. Zheng YZ, Evangelisti M, Winpenny REP (2011) Chem Sci 2:99
228. Hooper TN, Schnack J, Piligkos S, Evangelisti M, Brechin EK (2012) Angew Chem Int Ed 51:4633
229. Zaleski CM, Depperman EC, Kampf JW, Kirk ML, Pecoraro VL (2004) Angew Chem 43:3912
230. Mereacre VM, Ako AM, Clerac R, Wernsdorfer W, Filoti G, Anson CE, Powell AK (2007) J Am Chem Soc 129:9248
231. Stamatatos TC, Teat SJ, Wernsdorfer W, Christou G (2009) Angew Chem Int Ed 48:521
232. Mishra A, Wernsdorfer W, Abboud KA, Christou G (2004) J Am Chem Soc 126:15648
233. Zeng YF, Xu GC, Hu X, Chen Z, Bu XH, Gao S, Sanudo EC (2010) Inorg Chem 49:9734
234. Liu SJ, Zeng YF, Xue L, Han SD, Jia JM, Hu TL, Bu XH (2014) Inorg Chem Front 1:200
235. Zheng Y, Zhang QC, Long LS, Huang RB, Müller A, Schnack J, Zheng LS, Zheng Z (2013) Chem Commun 49:36
236. Zheng YZ, Mo Pineda E, Helliwell M, Winpenny REP (2012) Chem Eur J 18:4161
237. Ako AM, Mereacre V, Clerac R, Wernsdorfer W, Hewitt IJ, Anson CE, Powell AK (2009) Chem Commun (Camb) 544
238. Baniodeh A, Anson CE, Powell AK (2013) Chem Sci 4:4354
239. Papatriantafyllopoulou C, Wernsdorfer W, Abboud KA, Christou G (2011) Inorg Chem 50:421
240. Zheng XY, Wang SQ, Tang W, Zhuang GL, Kong XJ, Ren YP, Long LS, Zheng LS (2015) Chem Commun (Camb) 51:10687
241. Hu SM, Dai J, Wu X, Wu L, Cui C, Fu Z, Hong M, Liang Y, Cluster J (2002) Science 13:33
242. Yang X, Schipper D, Jones RA, Lytwak LA, Holliday BJ, Huang S (2013) J Am Chem Soc 135:8468
243. Wang M, Yuan DQ, Ma CB, Yuan MJ, Hu MQ, Li N, Chen H, Chen CN, Liu QT (2010) Dalton Trans 39:7276
244. Leng JD, Liu JL, Tong ML (2012) Chem Commun (Camb) 48:5286

Hydrothermal Synthesis of Lanthanide and Lanthanide-Transition-Metal Cluster Organic Frameworks via Synergistic Coordination Strategy

Jian-Wen Cheng and Guo-Yu Yang

Abstract The study of polynuclear lanthanide (Ln) complexes has been a field of rapid growth in coordination chemistry. Lanthanide clusters synthesized via a ligand-controlled hydrolytic approach using different flexible α-amino acids have been well summarized. In this chapter, we describe efforts to synthesize lanthanide and lanthanide-transition-metal (Ln-TM) cluster organic frameworks using rigid ligands of isonicotinic acid (HIN), 4-pyridin-4-ylbenzoic acid (HL), nicotinic acid (HNA), and 4-(3-pyridyl)benzoic acid (HL$'$) under hydrothermal condition. In addition, the synergistic coordination between these rigid ligands with other organic/inorganic ligands has also been discussed.

Keywords Heterometallic compounds • Hydrothermal synthesis • Lanthanide cluster organic framework • Rigid ligands • Synergistic coordination

Contents

J.-W. Cheng and G.-Y. Yang (✉)
MOE Key Laboratory of Cluster Science, School of Chemistry, Beijing Institute of Technology, Beijing 100081, China

Key Laboratory of the Ministry of Education for Advanced Catalysis Materials, Institute of Physical Chemistry, Zhejiang Normal University, Jinhua, Zhejiang 321004, China
e-mail: ygy@bit.edu.cn

Abbreviations

2,5-pdc	2,5-Pyridinedicarboxylic acid
H_2bdc	1,2-Benzenedicarboxylic acid
HIN	Isonicotinic acid
HL	4-Pyridin-4-ylbenzoic acid
HL$'$	4-(3-Pyridyl)benzoic acid
HNA	Nicotinic acid
HOAc	Acetic acid
Ln	Lanthanide
ox	Oxalate
TM	Transition metal

1 Introduction

Lanthanide (Ln) and lanthanide-transition-metal (Ln-TM) clusters and coordination polymers are of great interest because of their fascinating structures and a variety of applications ranging from luminescent and magnetic materials to their use in homogeneous catalysis [1–7]. At present, hydroxo lanthanide clusters can be synthesized via a ligand-controlled hydrolytic approach with the judiciously chosen supporting ligands to limit the degree of lanthanide hydrolysis and the aggregation of the hydroxo intermediates [8, 9]. To date, a large number of lanthanide clusters from Ln_3 to Ln_{104} have been reported [10–25], in which most of the reported high-nuclearity hydroxo lanthanide clusters are discrete. Obviously, novel lanthanide clusters with interesting structures and exciting properties strongly rely on the innovations in synthetic methodology, developing new synthetic methods continue to be of great importance in this field. Hydrothermal synthesis represents a kind of milder and softer synthetic techniques by employing water as reaction media at relatively low temperature. Hydrothermal synthesis has been widely used in the synthesis of coordination polymers or metal–organic frameworks [26, 27], and extended to grow crystalline lanthanide cluster organic frameworks very recently [28]. Under hydrothermal process, lanthanide oxides can be used as the source of lanthanides in the presence of acid at low pH value, rather than using lanthanide salts in aqueous solution at high pH value.

The coordination chemistry of the copper(I) halides has been of great interest due to their large structural variation and rich electronic/optical properties. Copper (I) halides are inclined to form a variety of inorganic CuX clusters generally based on corner or edge sharing of trigonal planar $\{CuX_3\}$ or tetrahedral $\{CuX_4\}$ subunits, various copper halide cluster motifs from rhomboid Cu_2X_2 dimers, cubane or stepped cubane Cu_4X_4 tetramers to $Cu_{36}X_{56}$ have been well documented [29]. Therefore, it should be rational to introduce CuX clusters into the Ln cluster organic framework to construct fascinating 3D hetero-Ln-TM structures. Linear and rigid ligands with oxygen and nitrogen donors, such as isonicotinic acid (HIN)

Scheme 1 Pyridyl benzoate ligands discussed in this chapter

HIN   HL   HNA   HL'
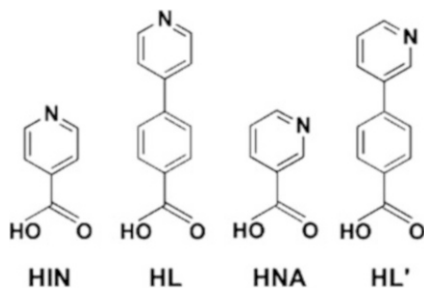
and 4-pyridin-4-ylbenzoic acid (HL) were selected to make lanthanide and Ln-TM cluster organic frameworks based on the following considerations: (1) They are rigid ligands with oxygen and nitrogen donors on opposite sides, enabling these ligands to act as a linear bridge for the formation of the extended structures. (2) The carboxy group may induce the oxophilic lanthanide ions to undergo hydroxo lanthanide cluster aggregation, while the nitrogen atoms can coordinate to TM ions, and thus extended solids containing hydroxo lanthanide cluster cores and TM ions might be obtained. The hetero-Ln-TM structures consist of both Ln^{3+} and d ^{10} TM ions (Cu/Ag/Zn), which may expand their applications in photovoltaic and optoelectronic devices, based on their luminescent properties [4]. In addition, the synergistic coordination between HIN/HL and other organic/inorganic ligands also gives rise to a new series of lanthanide cluster organic frameworks. Lanthanide cluster organic frameworks constructed by the analogue nicotinic acid (HNA) and 4-(3-pyridyl)benzoic acid (HL′) have also been discussed (Scheme 1).

2 Lanthanide and Lanthanide-Transition-Metal Cluster Organic Frameworks

2.1 Cluster Organic Frameworks Constructed by Isonicotinic Acid

Hydrothermal reaction of Ln_2O_3, HIN, and $CuCl_2 \cdot 2H_2O$ in water in the presence of $HClO_4$ (pH 2) leads to three lanthanide cluster organic frameworks: $[Ln_{14}(\mu_6\text{-}O)(\mu_3\text{-}OH)_{20}(IN)_{22}Cu_6Cl_4 (H_2O)_8] \cdot 6H_2O$ (Ln = Y, Gd, Dy) [30]. These structures contain the high-nuclearity hydroxo lanthanide cluster $[Ln_{14}(\mu_6\text{-}O)(\mu_3\text{-}OH)_{20}(H_2O)_8]^{20+}$, which acts as a building block that combines with copper ions through linear IN^- ligands to form a 3D framework. The Gd_{14} core consists of one octahedral $[Gd_6(\mu_6\text{-}O)(\mu_3\text{-}OH)_8]^{8+}$ unit that shares two opposing Gd1 apexes with two novel $[Gd_5(\mu_3\text{-}OH)_6]^{4+}$ trigonal bipyramids. The linkages between the Gd_{14} cores and two different types of copper centers through IN^- ligands give rise to an unusual 3D cluster organic framework (Fig. 1).
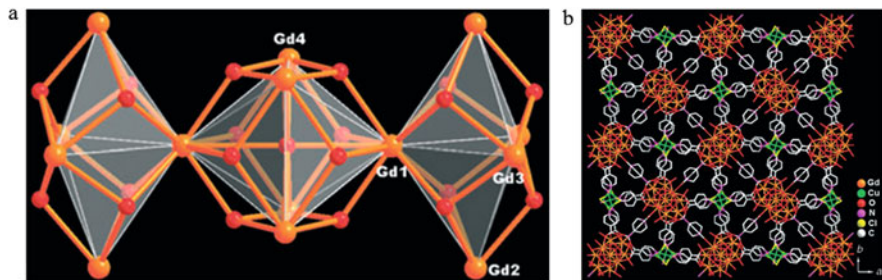
Fig. 1 (**a**) Polyhedral representation of the structure of $[Gd_{14}(\mu_6-O)(\mu_3-OH)_{20}]^{20+}$ core; (**b**) the overall 3D structure showing the unusual framework. Reproduced from [30] by permission of John Wiley & Sons Ltd

The I^- ion has a larger ionic radius than Cl^- and Br^-, and may favor higher coordination numbers and versatile coordination modes, resulting in a larger copper-iodide cluster. Hydrothermal reactions of Ln_2O_3, CuI, HIN, and 2-pyrazinecarboxylic acid in water in the presence of $HClO_4$ (pH 2) give the sandwich frameworks: $[Ln_6(\mu_3-O)_2](IN)_{18}[Cu_8(\mu_4-I)_2(\mu_2-I)_3] \cdot H_3O$ (FJ-4, Ln = Y, Nd, Dy, Gd, Sm, Eu, Tb) [31]. Two unusual trinuclear $[Ln_3(\mu_3-O)]$ and tetranuclear $[Cu_4(\mu_4-I)]$ cores are successfully used as secondary building units to make two different nanosized wheels $[Ln_{18}(\mu_3-O)_6(CO_2)_{48}]^{6-}$, Ln_{18}, and $[Cu_{24}(\mu_4-I)_6(\mu_2-I)_{12}]^{6+}$, Cu_{24}, with 12-membered rings and a diameter of 26.7 and 26.4 Å, respectively. The wheels are further assembled into 2D Ln_{18} and Cu_{24} networks, the linkages between two distinct layered networks of Ln_{18} and Cu_{24} wheels by IN^- pillars along the c axis giving a series of unprecedented 3D sandwich frameworks (Fig. 2).

$Dy_{30}I(\mu_3-OH)_{24}(\mu_3-O)_6(NO_3)_9(IN)_{41}(OH)_3(H_2O)_{38}$ and $Dy_{104}I_4(\mu_3-OH)_{80}$ $(\mu_3-O)_{24}(NO_3)_{36}(IN)_{125}(OH)_{19}(H_2O)_{167}$ have been obtained under hydrothermal conditions by incorporation of IN^- and NO_3^- ligands [32]. $[Dy_{26}(\mu_3-OH)_{20}$ $(\mu_3-O)_6(NO_3)_9I]^{36+}$ cluster core motif has been observed in their crystal structures, nine NO_3^- ligands are incorporated into the cluster core backbone by Dy–O coordination bonds. The size of the Dy_{26} cluster is 20.47×17.20 Å^2. The synergistic coordination between the IN^- ligands and the trigonal planar geometry NO_3^- ligands as surface modifiers inserted into the lanthanide cluster core backbone remarkably improves the dimension of cluster cores.

$Dy_{30}I(\mu_3-OH)_{24}(\mu_3-O)_6(NO_3)_9(IN)_{41}(OH)_3(H_2O)_{38}$ consists of two Dy_{26} and two Dy_4 clusters, these clusters are further linked by IN^- linkers to form the final structure, while $Dy_{104}I_4(\mu_3-OH)_{80}(\mu_3-O)_{24}(NO_3)_{36}(IN)_{125}(OH)_{19}(H_2O)_{167}$ is the first tetramer assembled by the Dy_{26} clusters and IN linkers (Fig. 3).

Compared with the reported discrete Ln_{26} cluster of $[Dy_{26}(\mu_3-OH)_{20}$ $(\mu_3-O)_6(NO_3)_9I]^{36+}$ [32], Xu et al. replaced NO_3^- by CO_3^{2-} to reinforce the huge Ln_{26} cluster and introduced a third ligand CH_3COO^- to reduce the steric restriction.
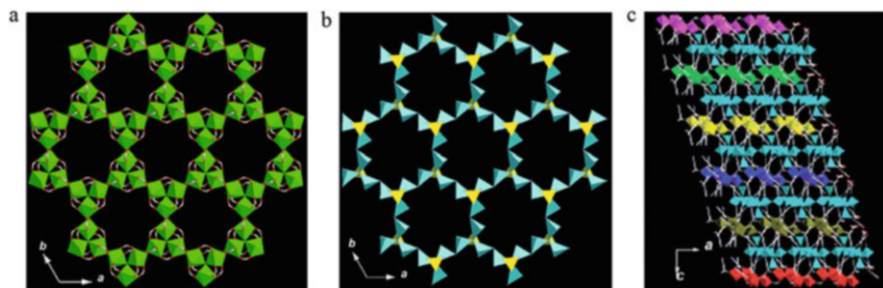
Fig. 2 (**a**) Polyhedral view of layered network of Dy_{18} wheels; (**b**) polyhedral view of layered network of Cu_{24} wheels; and (**c**) view of the layered networks of Dy_{18} and Cu_{24} wheels linked by IN^- ligands. Reproduced from [31] by permission of John Wiley & Sons Ltd
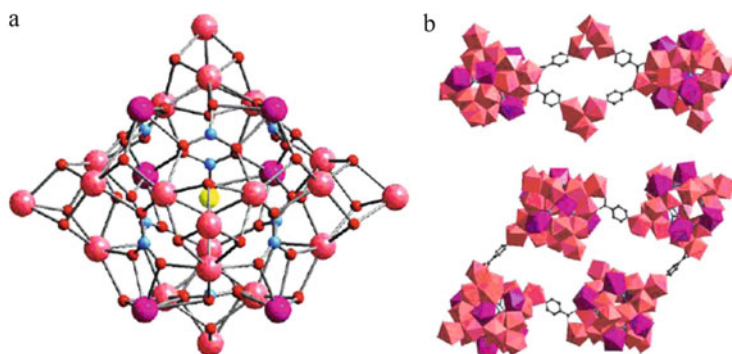
Fig. 3 (**a**) View of the structure of Dy_{26} core; (**b**) view of the structures of tetramer constructed by lanthanide clusters and IN^- linkers. Reprinted with the permission from [32]. Copyright 2007 American Chemical Society

Two 3D coordination polymers $Zn_{1.5}Dy_{26}(IN)_{25}(CH_3COO)_8(CO_3)_{11}(OH)_{26}(H_2O)_{29}$ and $Zn_{1.5}Gd_{26}(IN)_{26}(CH_3COO)_7(CO_3)_{11}(OH)_{26}(H_2O)_{28}$ have been hydrothermally synthesized [33]. Structural analysis indicates that the ligands IN^-, CH_3COO^-, and CO_3^{2-} anion make the Ln_{26} cluster stable. The linkages between nanosized Ln_{26} cluster and Zn centers through IN ligands result in two novel 3D open framework topologies (Fig. 4).

A novel 2D coordination polymer $K_2[Ho_{48}(IN)_{46}(\mu_3\text{-OH})_{84}(\mu_4\text{-OH})_4$ $(\mu_5\text{-O})_2(OAc)_4(H_2O)_{14}(CO_3)Br_2] \cdot 2HIN \cdot 20H_2O$ [34] which contains nanosized Ho_{48} clusters was synthesized and structurally characterized by Xu et al. At the top or bottom of the core structure of Ho_{48}, each cubane-like $[Ho_4(\mu_3\text{-OH})_4]^{8+}$ unit (Fig. 5a) can be described as a tetrahedron, while the middle Ho_5 (Fig. 5b) units can be depicted as square pyramids. Six Ho_5 units surround the equatorial ring of the
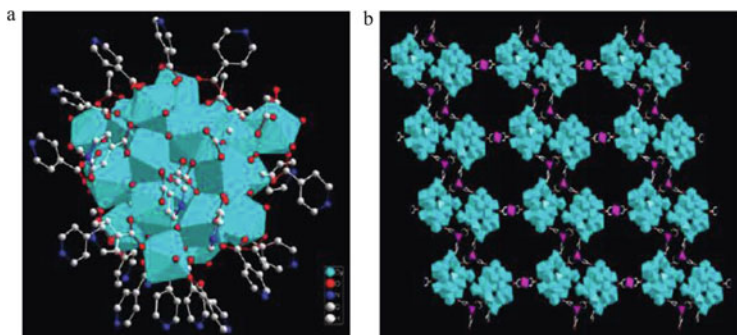
Fig. 4 (**a**) View of the Ln_{26} core; (**b**) the linkages of nanosized Ln_{26} clusters and zinc centers by IN^- ligands. Reprinted with the permission from [33]. Copyright 2010 American Chemical Society
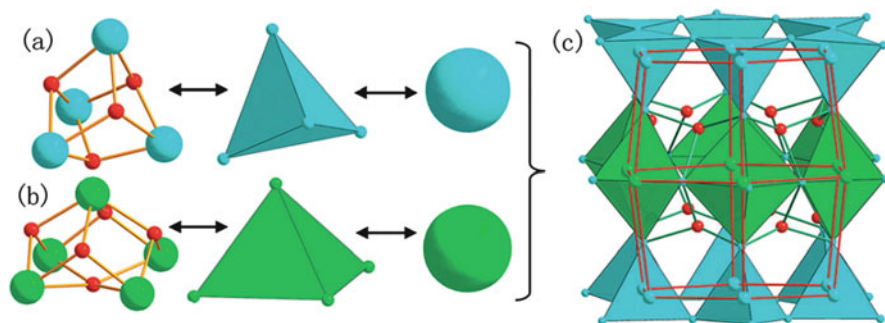
Fig. 5 (**a**) The $\{Ho_4\}$ cluster unit. (**b**) The $\{Ho_5\}$ cluster unit. (**c**) The drum-like core structure of $\{Ho_{48}\}$ cluster. Reproduced from [34] by permission of The Royal Society of Chemistry

Ho_{48} core via six corner sharing Ho atoms to form the barrel of the drum (Fig. 5c). Each Ho_{48} cluster is simultaneously bridged to four adjacent Ho_{48} cores by the IN^- ligands to form a large rhombic ring with a length of 26.57 Å (Fig. 6). Similar nanosized Ln_{48} cluster is also observed in $\{[Cl_2\&(NO_3)]@[Er_{48}(NA)_{44}(OH)_{90}(N_3) (H_2O)_{24}]\}_n \cdot 6nCl \cdot 35nH_2O$ [35], in which Er_{48} clusters are linked by NA^- ligands and N_3^- anions to give a square layer, Cl^- and NO_3^- anions act as templates.

Xue et al. obtained two 3D heterometallic coordination polymers, $Ln_4 (\mu_3\text{-}OH)_2Cu_6I_5(IN)_8(OAc)_3$ (Ln = Nd, Pr; HOAc = acetic acid) under hydrothermal conditions [36]. The Ln_6 and Ln_2 cores are connected alternately to form a nanosized Ln_{16} wheel with an eight-membered ring with the size of 12.59 and
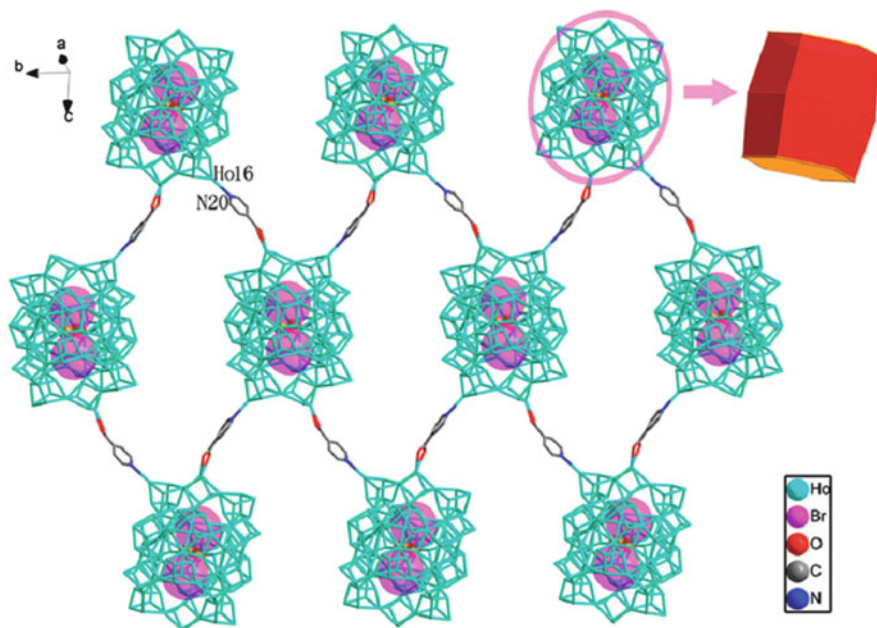
Fig. 6 The layered structure connected by IN ligands. Reproduced from [34] by permission of The Royal Society of Chemistry
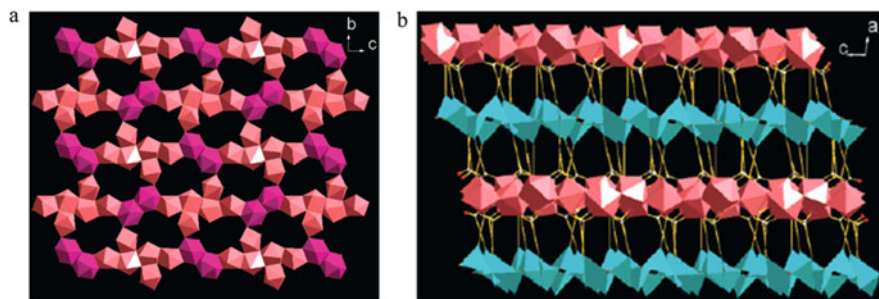
Fig. 7 (**a**) View of the 2D cluster network constructed by lanthanide wheel clusters with an eight-membered ring; (**b**) view of the 3D coordination framework based on the linkage of 2D neodymium cluster layers and 1D copper-iodine cluster chains by IN^- linkers. Reprinted with the permission from [36]. Copyright 2007 American Chemical Society

9.13 Å, OAc^- ligand shows two different coordination modes. The transition-metal cluster moiety is the 1D chain formed by Cu_6I_5 clusters. It is interesting that the linkage between the 2D lanthanide wheel cluster layers and the 1D copper halide cluster chains by IN^- ligands gives rise to a 3D coordination framework (Fig. 7).

If a second ligand 1,2-benzenedicarboxylic acid (H_2bdc) were to be introduced, the synergistic coordination between IN and bdc ligands leads to two new lanthanide cluster organic frameworks, $[Er_7(\mu_3\text{-O})(\mu_3\text{-OH})_6(bdc)_3](IN)_9[Cu_3X_4]$ (X = Cl/Br, FJ-2a/b) [37]. The Er_4 and the Er_2 cores are alternately linked from a nanosized $[Er_{36}(\mu_3\text{-OH})_{30}(\mu_3\text{-O})_6(bdc)_6]^{54+}$ (Er_{36}), this wheel-shaped building block of Er_{36} with an 18-membered ring is currently the largest lanthanide wheel (Fig. 8a). Remarkably, six bdc^{2-} ligands are trapped in the inner of the 18-membered ring (Fig. 8a). Each Er_{36} cluster is linked to surrounding clusters and forming a highly ordered layered cluster network with hexagonal, honeycomb arrays (Fig. 8b). The linkages between 2D hybrid cluster polymers and copper clusters by IN^- ligands give rise to an unprecedented 3D sandwich framework (Fig. 8c).

The synergistic coordination between IN^- and 2,5-pyridinedicarboxylic acid gives a new lanthanide cluster organic framework, $Er_4(OH)_4Cu_5I_4(IN)_6(NA)$ (2,5-pdc)·0.3H_2O (HNA = nicotinic acid, 2,5-pdc = 2,5-pyridinedicarboxylic acid) [38]. This compound consists of two distinct building blocks of inorganic 1D $[Ln_4(OH)_4]_n^{8n+}$ cluster polymers and $[Cu_{10}I_8]^{2+}$ clusters. The inorganic 1D $[Ln_4(OH)_4]_n^{8n+}$ chains are further connected to each other by 2,5-pdc^{2-} into 2D
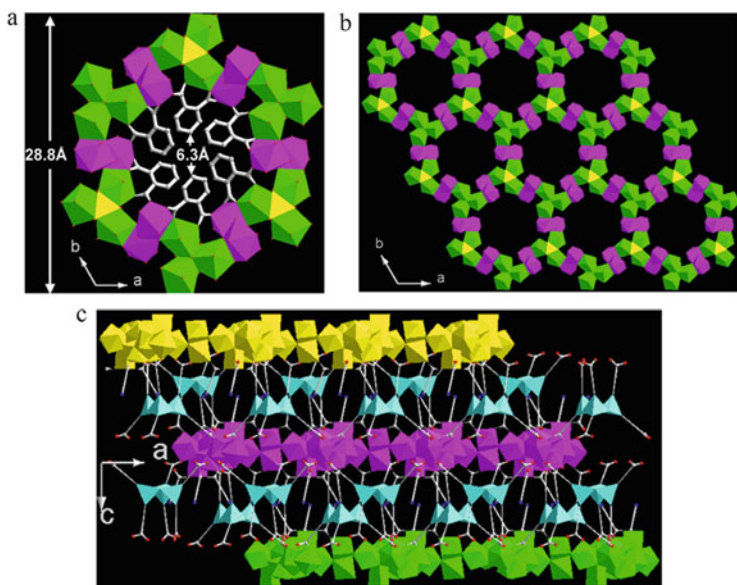
Fig. 8 (**a**) View of the Er_{36} wheel; (**b**) view of giant wheel clusters linked to form layered cluster network; and (**c**) view of sandwich framework based on linkages of 2D cluster layers and Cu cluster pillars by IN^- ligands. Reproduced from [37] by permission of John Wiley & Sons Ltd

layers in the *ab* plane. The linkage between layered Ln networks and $[Cu_{10}I_8]^{2+}$ clusters by IN^- and NA^- pillars along the *c* axis forms an unprecedented 3D framework (Fig. 9). It is interesting that decarboxylation occurred in the ortho position and 2,5-pdc^{2-} was partially transformed into NA^- under hydrothermal conditions.

Fig. 9 (**a**) View of the inorganic $[Ln_4(OH)_4]_n^{8n+}$ chain; (**b**) 2D Ln–organic layer; and (**c**) the 3D framework. Reprinted with the permission from [38]. Copyright 2008 American Chemical Society
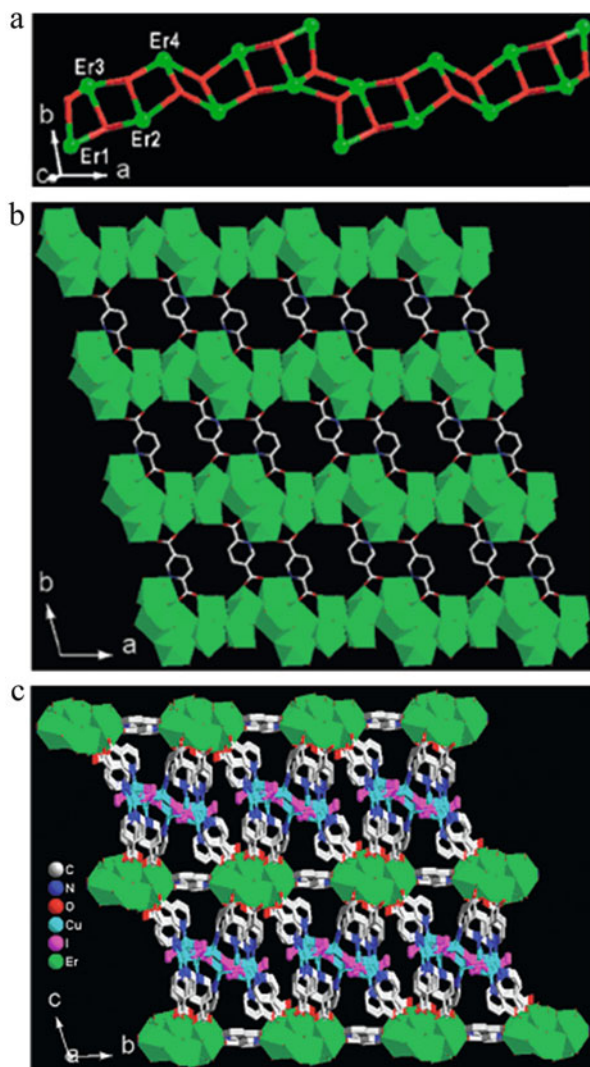
2.2   Cluster Organic Frameworks Constructed by 4-(4-Pyridyl)benzoic Acid

To make new Ln cluster organic frameworks for potential applications, an expanded ligand with a benzene spacer between the two coordinating moieties of HIN, 4-pyridin-4-ylbenzoic acid (HL), is employed, with the expectation that this lengthened ligand is capable of avoiding steric crowding around metal clusters. Heptanuclear trigonal-prismatic Ln clusters derived from HL, $[Ln_7(\mu_3\text{-}OH)_8L_9(H_2O)_6] \cdot 4ClO_4 \cdot 3HL \cdot nH_2O$ (Ln = Y, La, Gd, Yb, $n = 6$; Ln = Dy, Er, $n = 4$), were made by the hydrothermal treatment of Ln_2O_3 and HL at 190°C for 7 days in the presence of $HClO_4$ (pH 2) [39]. The heptanuclear cluster core, $[Y_7(\mu_3\text{-}OH)_8]^{13+}$ (Y_7) core, can be described as two $Y_4(OH)_4$ cubanes sharing a Y atom, in contrast to previously reported trigonal antiprismatic Ln_7 cores [40]. In the structure, each Y_7 core connects six nearest neighbors with a distance of 16.955 Å by the ligands to produce a 2D Ln cluster organic layer possessing a thickness about 10.92 Å along the b axis (Fig. 10).

Two pillared-layer cluster organic frameworks, $[Ln_5(\mu_3\text{-}OH)_4(\mu\text{-}H_2O)Cu_8I_8L_{11}] \cdot H_2O$ (Ln = Dy, Eu), have been made by employing lanthanide oxide and copper(I) halide as the source of lanthanide and transitional metal under hydrothermal condition [41]. There are two distinct nanoscale crown-like clusters in the structure, one is hydroxo lanthanide $[Dy_{10}(\mu_3\text{-}OH)_8]^{22+}$ (Dy_{10}) cluster and the other is copper(I) halide $[Cu_{16}I_{16}]$ (Cu_{16}) cluster. The Dy_{10} cluster can be intuitively regarded as a slightly slipped sandwich configuration. Each half of the sandwich contains a roughly planar set of five Dy^{3+} ions in a trapezoid arrangement, which can be viewed as three edge-sharing triangles with each bearing a capped μ_3-OH group. The Dy_{10} core has an external diameter of 1.2 nm and an inner olive-shaped 4-ring with a diameter of 0.7 nm. The Dy_{10} cores are bridged by water molecules to
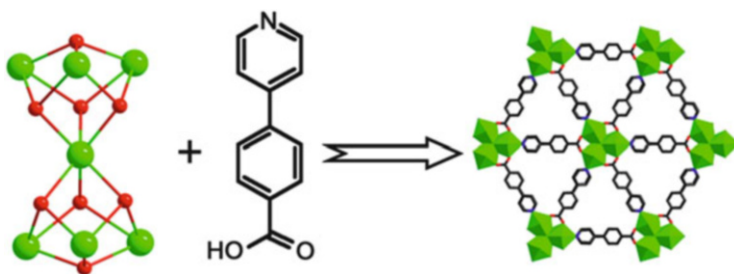
Fig. 10 View of the 2D Ln cluster organic layer constructed by Y_7 cluster and L^-. Reprinted with the permission from [39]. Copyright 2013 American Chemical Society

be a ribbon-like chain along the [0 1 0] direction. The adjacent inorganic chains with reverse orientation are extended via L^- ligands to generate Ln cluster organic layer on the bc plane. The Cu_{16} cores and the Ln cluster organic layers are pillared by the L^- ligands to generate a fascinating 3D pillared-layer cluster organic framework. From the topological point of view, these compounds represent an intriguing example of a binodal (8,14)-connected net considering the Dy_{10} and Cu_{16} connectors as the nodes, revealing that they are typical high dimensional frameworks with high connected net based on high-nuclearity nodes (Fig. 11).

The synergistic coordination between two different organic ligands, as well as inorganic and organic ligands, leads to two types of cluster organic frameworks: $[La_6(\mu_3\text{-}OH)_2(ox)_3L_{12}Cu_{11}(\mu_3\text{-}X)_6(\mu_2\text{-}X)_3] \cdot 8H_2O$ (X = Br/Cl, FJ-21 a/b; ox = oxalate); $[Ln_4(OAc)_3(H_2O)_4L_9][Cu(\mu_3\text{-}I)]@[Cu_{10}(\mu_3\text{-}I)\ (\mu_4\text{-}I)_6(\mu_5\text{-}I)_3] \cdot 7H_2O$ (Ln = Pr/Nd/Sm/Eu, FJ-22 a/b/c/d; OAc = acetate) [42]. FJ-21 a/b were made by hydrothermal treatment of lanthanum oxalate, CuX_2 (X = Br/Cl), and HL at 200°C for 5 days in the presence of $HClO_4$ (pH 2). The secondary building unit (SBU) of Ln wheel in FJ-21a is edge-sharing trinuclear unit $[La_3(\mu_3\text{-}OH)]^{8+}$ (La_3). Every La_3 core is linked by three ox ligands and nine L ligands. Six La_3 cores with reverse orientation are alternately linked by six ox ligands to form an $[La_{18}(\mu_3\text{-}OH)_6(ox)_6]^{36+}$ (La_{18}) wheel having a diagonal dimension of about 2.3 nm and a thickness of 0.4 nm, respectively. The SBU of CuI wheel in FJ-21a is Cu-centered edge-sharing truncated cubane $[Cu_4(\mu_3\text{-}Br)_6]^{2-}$. Six Cu_4 cores are connected by halide bridges into a nanosized neutral $[Cu_{24}(\mu_3\text{-}Br)_{18}(\mu_2\text{-}Br)_6]$ (Cu_{24}) wheel with 12-ring and a diameter of 2.0 nm. Two different kinds of the wheel cluster layers of La_{18} and Cu_{24} are pillared by L^- ligands to give rise to a 3D sandwich framework.

FJ-22 was made by hydrothermal reaction of Ln_2O_3, CuI, sodium acetate, and HL at low pH value under the same reaction conditions as FJ-21. The SBUs of Ln wheel in FJ-22d are edge-sharing tetranuclear $[Eu_4(OAc)_3]^{9+}$ (Eu_4) cores in
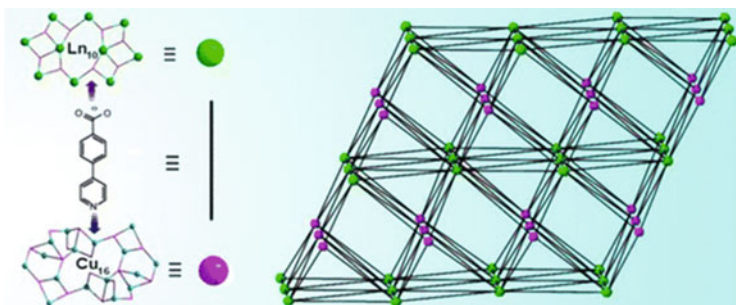
Fig. 11 View of the framework constructed by Dy_{10} and Cu_{16} clusters. Reprinted with the permission from [41]. Copyright 2014 American Chemical Society

compressed tetrahedral geometry. Six Eu_4 cores are alternately linked edge-to-edge by twelve L ligands to generate an $[Eu_{24}(OAc)_{18}(COO)_{12}]^{42+}$ (Eu_{24}) wheel with a diameter of 3.0 nm and a thickness of 0.4 nm. Six Cu_4 cores are linked alternately to form a nanosized $[Cu_{24}(\mu_4\text{-}I)_{12}(\mu_5\text{-}I)_6]^{6+}$ (Cu_{24}) wheel with 6-ring and a diameter of 2.8 nm. Therefore, the 3D sandwich framework of FJ-22d can be understood as the strictly alternating of Eu_{24} and Cu_{24} wheel cluster layers pillared by L ligands. Obviously, the synergistic coordination between organic ligands, L and oxalate/acetate, leads to the formation of La_{18} and Ln_{24} wheels, while the synergistic coordination between organic L and inorganic Br/I ligands results in Cu wheels for FJ-21 and FJ-22, respectively (Fig. 12).

Two sandwiched cluster organic frameworks, $Eu_6(OH)_2Cu_9I_6L_{12}(ox)_3 \cdot H_2O \cdot ClO_4$ (FJ-23, ox = oxalate) and $Eu_6Cu_7I_7L_{12}(OAc)_6(H_2O)_2 \cdot 2H_2O$ (FJ-24, OAc = acetate),
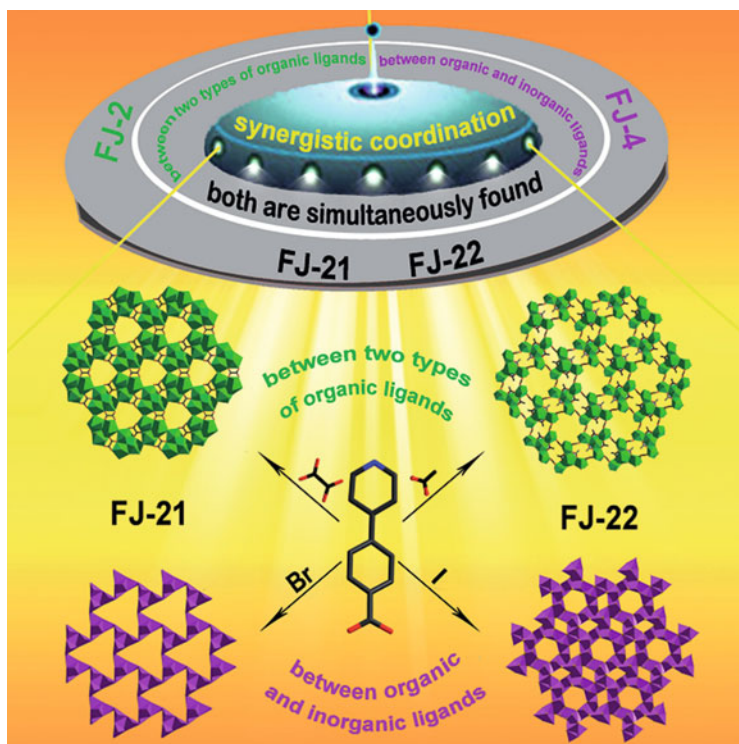
Fig. 12 The frameworks of FJ-21 and FJ-22 consist of two different kinds of nanosized Ln and Cu wheel cluster units. Reproduced from [42] by permission of John Wiley & Sons Ltd

have been successfully made [43]. In FJ-23, the $[Eu_{18}(\mu_3\text{-}OH)_6(ox)_6]^{36+}$ wheel contains six edge-to-edge equilateral triangles $[Eu_3(\mu_3\text{-}OH)]8+$ SBUs. While in FJ-24, the $[Eu_{18}(OAc)_{18}]^{36+}$ wheel is made up of six vertex-sharing compressed tetrahedral $[Eu_4(OAc)_3]^{9+}$ SBUs. In FJ-23 and FJ-24, the graphene-like wheel cluster layers are linked through shape-matching trigonal prism metalloligands into 5-connected BN nets (Figs. 13 and 14). The second harmonic generation (SHG) measurements show
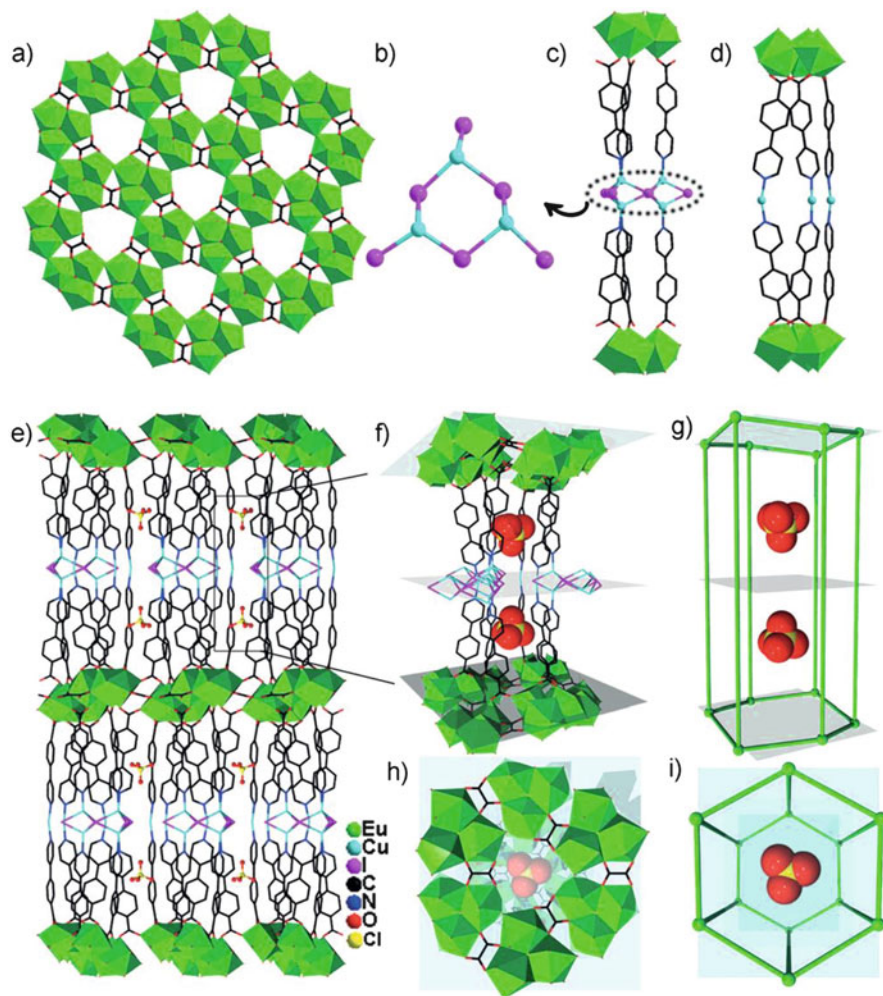
Fig. 13 (**a**) Polyhedral view of the graphene-like Eu_{18} wheel cluster layer in FJ-23; (**b**) ball/stick view of the Cu_3 SBU; (**c, d**) the coordinate environment of the Cu_3L_6 and $3(CuL_2)$ metalloligands in FJ-23; (**e**) the overall pillared-layer framework of FJ-23. (**f–i**) Zoomed images at the left show the side and top view of the ClO_4^- ions located in the narrow hexagonal channels. Reproduced from [43] by permission of John Wiley & Sons Ltd
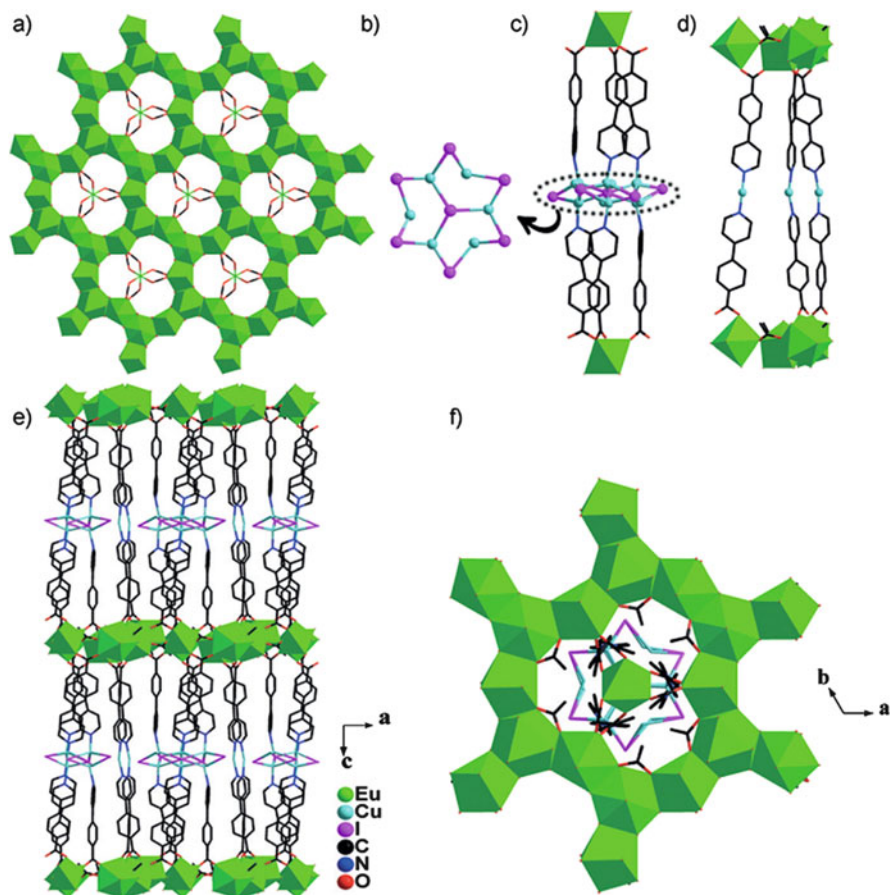
Fig. 14 (**a**) Polyhedral view of the Eu@Eu18 wheel cluster layer in FJ-24; (**b**) ball/stick view of the star-shape I@Cu$_6$ SBU; (**c**, **d**) the coordinate environment of the I@Cu$_6$L$_6$ and 3(CuL$_2$) metalloligands in FJ-24; (**e**) the overall pillared-layer framework of FJ-24; and (**f**) top view of the FJ-24. Reproduced from [43] by permission of John Wiley & Sons Ltd

that the SHG coefficients of FJ-23 and FJ-24 are about 0.15 and 0.2 times as large as that of KH$_2$PO$_4$ (KDP).

Two supertetrahedral cluster organic frameworks (SCOFs), 2(Ln$_4$Cu$_{10}$I$_8$L$_{18}$) ·8H$_3$O·9H$_2$O (Ln = Sm, Gd) were made by hydrothermal reaction of Ln$_2$O$_3$, CuI, and HL ligands at 180°C for 3 days [44]. A prominent structural feature of these two compounds is the presence of tetrahedral [Sm$_4$(COO)$_6$] (Sm$_4$) and supertetrahedral

T_3-[$Cu_{10}I_8$] (Cu_{10}) clusters. Each Sm_4 tetrahedron is linked to six adjacent Cu_{10} supertetrahedra via 18 carboxyl groups, and each Cu_{10} supertetrahedron is bridged to six nearest Sm_4 tetrahedra by 18 pyridine nitrogen atoms, the overall framework exhibits a twofold interpenetrated pcu net (Fig. 15). The proton conductivity at 30°C is 7.1×10^{-6} S/cm at 30% RH. When the temperature increases to 80°C, the conductivity dramatically rises to 1.4×10^{-3} S/cm (Fig. 16).
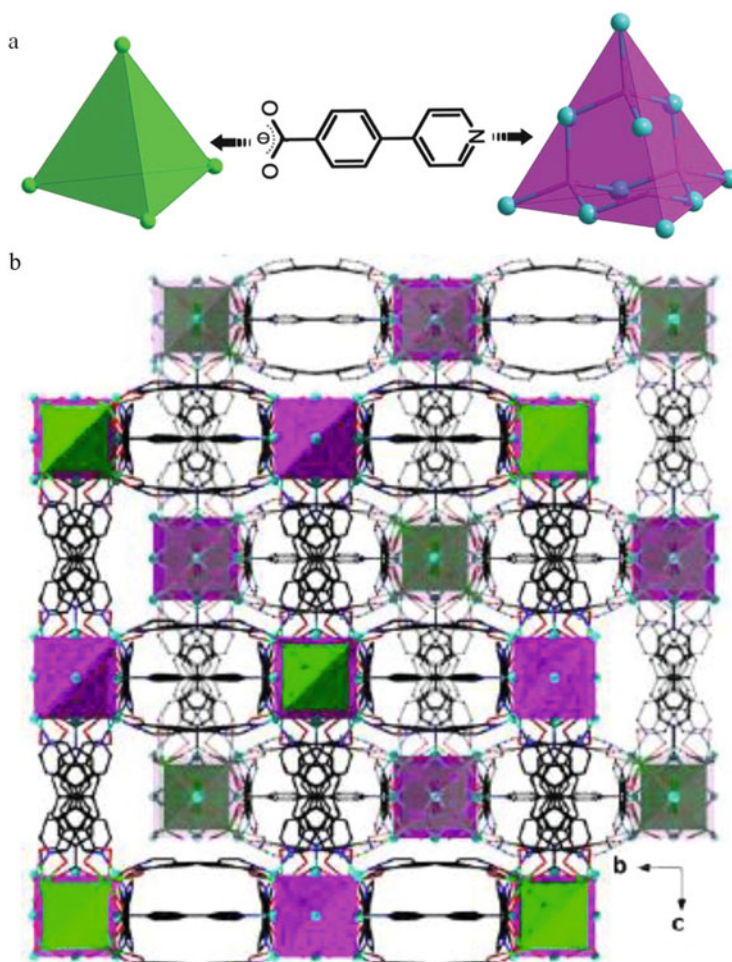
Fig. 15 (**a**) View of the inducement of Ln(III) tetrahedral and Cu(I) supertetrahedral clusters; (**b**) 3D framework along the *a*-axis. Reproduced from [44] by permission of John Wiley & Sons Ltd

Fig. 16 Arrhenius plots of
the proton conductivity
under 95% RH. Reproduced
from [44] by permission of
John Wiley & Sons Ltd
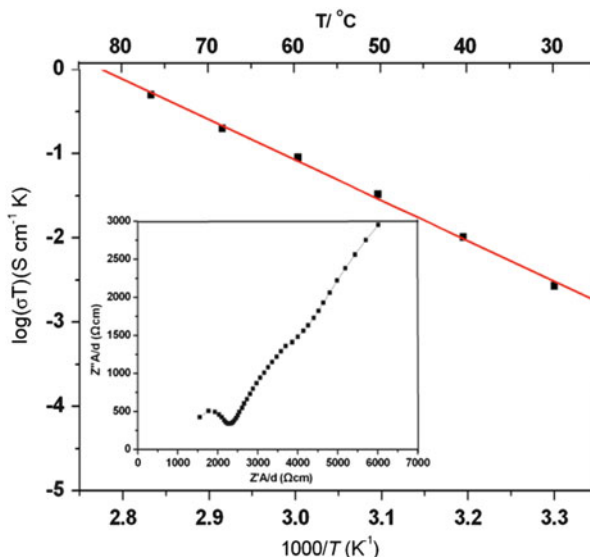
2.3 Cluster Organic Frameworks Constructed by Nicotinic Acid

Koner et al. obtained a new Gd_{26} cluster based 3D framework, $\{[Gd_{26}(\mu_6\text{-}CO_3)_9(NA)_{32}(\mu_3\text{-}OH)_{26}](NO_3)_2 \cdot 3(H_2O)\}_n$ via hydrothermal synthesis [45]. Five distorted cubane cores are attached to each other through six Gd^{3+} ions to give the Gd_{26} clusters. The dimension of Gd_{26} cluster shell including the organic ligands is around 2.32(4) nm. The Gd_{26} clusters are then connected to each other by NA^- ligands forming a 3D framework. The compound catalyzes the heterogeneous epoxidation of olefinic substrates including α,β-unsaturated ketones (Fig. 17). Similar nanosized Ln_{26} clusters have been observed in lanthanide-transition-metal–organic frameworks, $[Dy_{26}Cu_3(NA)_{24}(CH_3COO)_8(CO_3)_{11}(OH)_{26}(H_2O)_{14}]$ $Cl \cdot 3H_2O$ and $[Tb_{26}NaAg_3(NA)_{27}(CH_3COO)_6(CO_3)_{11}(OH)_{26}Cl(H_2O)_{15}] \cdot 7.5H_2O$ [46]. In these compounds, Ln_{26} clusters and $Cu^+/[Ag_3Cl]^{2+}$ centers are connected by NA^- bridges to give rise to 3D perovskite-like and 2D structures, respectively (Fig. 18).

Hong et al. reported two 2D coordination polymers based on huge 36-metal pure lanthanide clusters, $\{[Ln_{36}(NA)_{36}(OH)_{49}(O)_6(NO_3)_6(N_3)_3(H_2O)_{20}]Cl_2 \cdot 28H_2O\}_n$
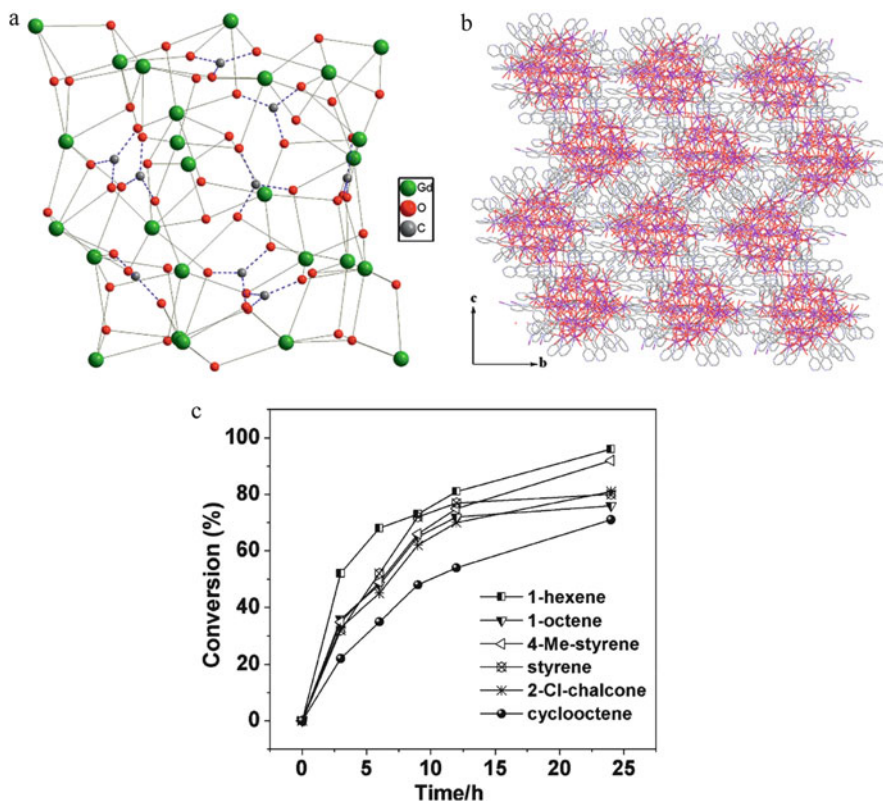
Fig. 17 (**a**) The structure of Gd_{26} cluster; (**b**) 3D framework along the *a*-axis; and (**c**) reaction profile for the epoxidation of olefins with *t*BuOOH catalyzed in acetonitrile media. Reproduced from [45] by permission of John Wiley & Sons Ltd

(Ln = Gd, Dy) [47]. Six tetrahedral Ln_4 clusters adopt an up and down arrangement and form a cyclohexane chair-like Ln_{24} cluster. The Ln_{36} cluster can be viewed as the aggregation of two types of cluster units of one wheel-like Ln_{24} unit and two identical tripod-like Ln_6 units (Fig. 19). The nanosized Ln_{36} clusters are then connected to each other by NA^- ligands to form a square layer. These compounds show a large MCE of 39.66 J kg^{-1} K^{-1} and slow relaxation of the magnetization, respectively.
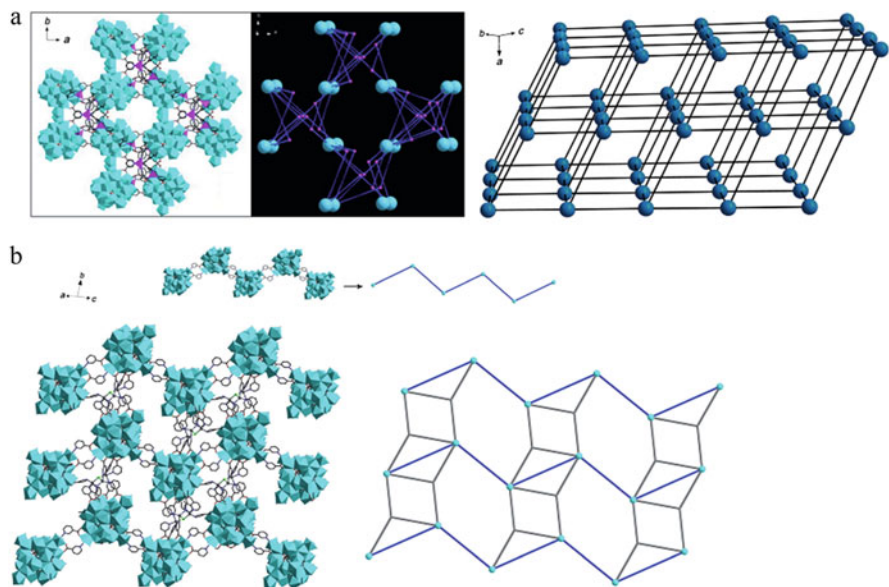
Fig. 18 (**a**) The 3D coordination structure constructed by {Dy_{26}} clusters and Cu centers and its perovskite-like topological structure; (**b**) the 2D coordination layer constructed by {Tb_{26}} clusters and [Ag_3Cl]$^{2+}$ bridges and its topological structure. Reproduced from [46] by permission of John Wiley & Sons Ltd
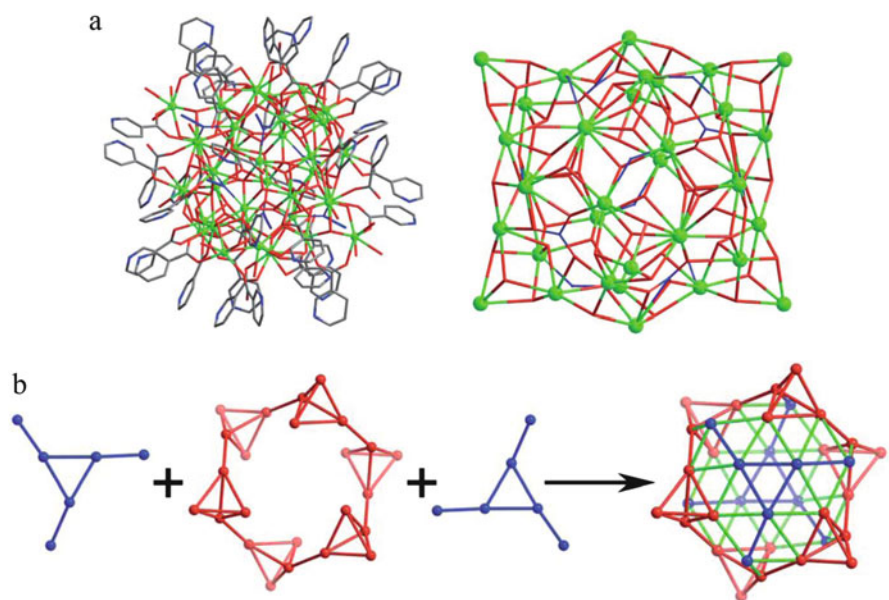
Fig. 19 (**a**) The 36-metal Gd(III) cluster; (**b**) illustration of the structure of Ln_{36} cluster. Reproduced from [47] by permission of The Royal Society of Chemistry
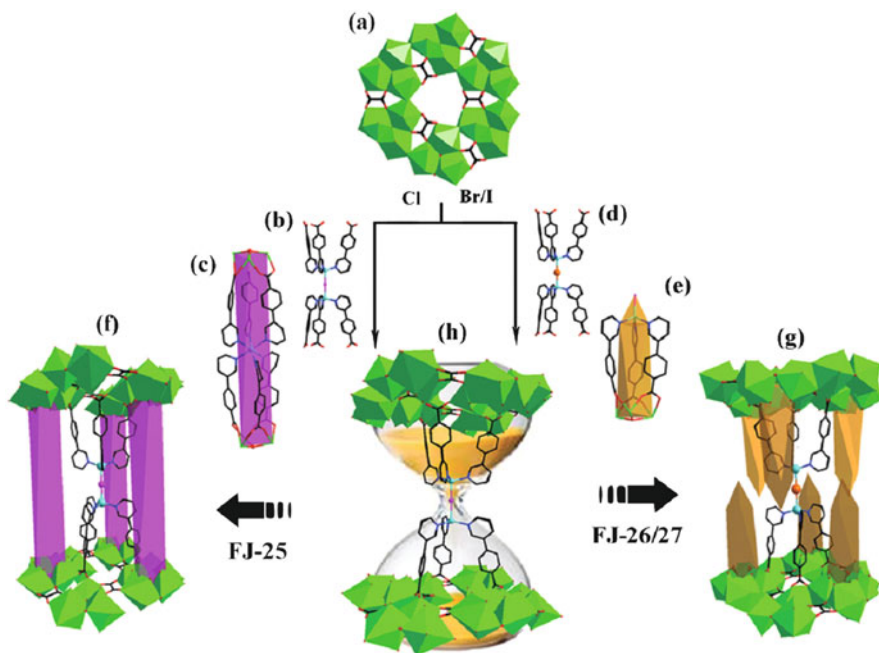
Fig. 20 View of the La_{18} TBU and auxiliary pillars in FJ-25 and FJ-26/27. Reproduced from [48] by permission of The Royal Society of Chemistry

2.4 Cluster Organic Frameworks Constructed by 4-(3-Pyridyl)benzoic Acid

Two series of wheel cluster organic frameworks (WCOFs), $La_6Cu_3ClL'_{12}(ox)_3(OH)_2 \cdot 8H_2O$ (FJ-25; ox = oxalate) and $La_6Cu_4X_3L'_{12}(ox)_3(OH)_2 \cdot H_3O$ (FJ-26/27; X = Br/I), are successfully made using 4-(3-pyridyl)benzoic acid (HL') as ligands [48]. In these compounds, μ_3-OH bridge three La^{3+} ions to form edge-sharing trinuclear $[La_3(\mu_3\text{-}OH)]^{8+}$ (La_3) secondary building units (SBUs). The La_3 SBUs are linked by ox^{2-} ligands into a 6^3 graphene-like La_{18} wheel TBUs, TBUs are further linked by different kinds of pillars to give the whole frameworks (Fig. 20).

3 Summary

This chapter has provided a brief overview of the preparation and structures of lanthanide and Ln-TM cluster organic frameworks using rigid ligands under hydro-thermal condition. These compounds show intriguing architectures with several structural types: (1) lanthanide clusters and coordination polymers linked via both Ln–O and Ln–N bonds and (2) Ln-TM heterometallic compounds constructed by lanthanide and different transition metal clusters/ions, in which these rigid ligands act as a linear bridge to form the heterometallic Cluster organic frameworks. The chapter broadens the research from discrete clusters to extended frameworks, which are different to the reported high-nuclearity Ln-TM clusters constructed by flexible ligands of Schiff-base and amino acids, in which the formation of mixed Ln-TM nanosized discrete clusters is usually observed with an investigation on the nature of the magnetic exchange interactions between 3d and 4f ions [3, 49]. The second ligand also plays an important role in the synthetic procedures, the inorganic anions can be used as templates or employed as surface modifiers inserted into the lanthanide cluster core backbone and improve the dimension of cluster cores. To date, the application of these compounds is mainly focused on magnetism and less involved in other aspects [50]. Further investigations in this area are necessary to use these large lanthanide and transition metal clusters to obtain porous cluster organic frameworks, and extend their uses in catalysis and adsorption processes.

References

1. Chen L, Jiang FL, Zhou K, Wu MY, Hong MC (2015) Metal–organic frameworks based on lanthanide clusters. Struct Bond 163:145–184
2. Zhang Z, Zheng Z (2015) Nanostructured and/or nanoscale lanthanide metal-organic frameworks. Struct Bond 163:297–368
3. Kong XJ, Long LS, Zheng ZP, Huang RB, Zheng LS (2010) Keeping the ball rolling: fullerene-like molecular clusters. Acc Chem Res 43:201–209
4. Zhang SW, Cheng P (2015) Recent advances in the construction of lanthanide–copper heterometallic metal–organic frameworks. CrystEngComm 17:4250–4271
5. Roesky PW, Canseco-Melchor G, Zulys A (2004) A pentanuclear yttrium hydroxo cluster as an oxidation catalyst. Catalytic oxidation of aldehydes in the presence of air. Chem Commun 738–739
6. Bünzli J-CG, Piguet C (2002) Lanthanide-containing molecular and supramolecular polymetallic functional assemblies. Chem Rev 102:1897–1928
7. Shi W, Liu K, Cheng P (2015) Transition–lanthanide heterometal–organic frameworks: synthesis, structures, and properties. Struct Bond 163:231–264

8. Wang RY, Zheng ZP, Jin TZ, Staples RJ (1999) Coordination chemistry of lanthanides at "high" pH: synthesis and structure of the pentadecanuclear complex of europium(III) with tyrosine. Angew Chem Int Ed 38:1813–1815

9. Ma BQ, Zhang DS, Gao S, Jin TZ, Yan CH, Xu GX (2000) From cubane to supercubane: the design, synthesis, and structure of a three-dimensional open framework based on a Ln_4O_4 cluster. Angew Chem Int Ed 39:3644–3646

10. Wang WH, Tian HR, Zhou ZC, Feng YL, Cheng JW (2012) Two unusual chiral lanthanide-sulfate frameworks with helical tubes and channels constructed from interweaving two double-helical chains. Cryst Growth Des 12:2567–2571

11. Guo FS, Chen YC, Mao LL, Lin WQ, Leng JD, Tarasenko R, Orendáč M, Prokleška J, Sechovský V, Tong ML (2013) Anion-templated assembly and magnetocaloric properties of a nanoscale $\{Gd_{38}\}$ cage versus a $\{Gd_{48}\}$ barrel. Chem Eur J 19:14876–14885

12. Hu FL, Jiang FL, Zheng J, Wu MY, Pang JD, Hong MC (2015) Magnetic properties of 3D heptanuclear lanthanide frameworks supported by mixed ligands. Inorg Chem 54:6081–6083

13. Guo PH, Liu J, Wu ZH, Yan H, Chen YC, Jia JH, Tong ML (2015) Single-molecule-magnet behavior in a $[2 \times 2]$ grid Dy^{III}_4 cluster and a dysprosium-doped Y^{III}_4 cluster. Inorg Chem 54:8087–8092

14. Thielemann DT, Wagner AT, Rösch E, Kölmel DK, Heck JG, Rudat B, Neumaier M, Feldmann C, Schepers U, Bräse S, Roesky PW (2013) Luminescent cell-penetrating pentadecanuclear lanthanide clusters. J Am Chem Soc 135:7454–7457

15. Zhang L, Zhao L, Zhang P, Wang C, Yuan SW, Tang JK (2015) Nanoscale $\{Ln^{III}_{24}Zn^{II}_6\}$ triangular metalloring with magnetic refrigerant, slow magnetic relaxation, and fluorescent properties. Inorg Chem 54:11535–11541

16. Chang LX, Xiong G, Wang L, Cheng P, Zhao B (2013) A 24-Gd nanocapsule with a large magnetocaloric effect. Chem Commun 49:1055–1057

17. Canaj AB, Tzimopoulos DI, Philippidis A, Kostaki GE, Millios CJ (2012) A strongly blue-emitting heptametallic $[Dy^{III}_7]$ centered-octahedral single-molecule magnet. Inorg Chem 51:7451–7453

18. Joarder B, Mukherjee S, Xue SF, Tang JK, Ghosh SK (2014) Structures and magnetic properties of two analogous Dy_6 wheels with electron-donation and -withdrawal effects. Inorg Chem 53:7554–7560

19. Alexandropoulos DI, Fournet A, Cunha-Silva L, Mowson AM, Bekiari V, Christou G, Stamatatos TC (2014) Fluorescent naphthalene diols as bridging ligands in Ln^{III} cluster chemistry: synthetic, structural, magnetic, and photophysical characterization of Ln^{III}_8 "Christmas Stars". Inorg Chem 53: 5420–5422

20. Ren YX, Zheng XJ, Li LC, Yuan DQ, An M, Jin LP (2014) Three-dimensional frameworks based on dodecanuclear Dy − hydroxo wheel cluster with slow relaxation of magnetization. Inorg Chem 53:12234–12236

21. Addamo M, Bombieri G, Foresti E, Grillone MG, Volpe M (2004) Assembling process of charged nonanuclear cationic lanthanide(III) clusters assisted by dichromium decacarbonyl hydride. Inorg Chem 43:1603–1605

22. Sang RL, Xu L (2013) Unprecedented infinite lanthanide hydroxide ribbons $[Ln_3(\mu_3\text{-}OH)_3]_n^{6n+}$ in a 3-D metal-organic framework. Chem Commun 49:8344–8346

23. Dong J, Cui P, Shi PF, Cheng P, Zhao B (2015) Ultrastrong alkali-resisting lanthanide-zeolites assembled by $[Ln_{60}]$ nanocages. J Am Chem Soc 137:15988–15991

24. Kong XJ, Wu Y, Long LS, Zheng LS, Zheng Z (2009) A chiral 60-metal sodalite cage featuring 24 vertex-sharing $[Er_4(\mu_3\text{-}OH)_4]$ cubanes. J Am Chem Soc 131:6918–6919

25. Peng JB, Kong XJ, Zhang QC, Orendáč M, Prokleška J, Ren YP, Long LS, Zheng ZP, Zheng LS (2014) Beauty, symmetry, and magnetocaloric effect-four-shell keplerates with 104 lanthanide atoms. J Am Chem Soc 136:17938–17941

26. Cui Y, Yue Y, Qian G, Chen B (2012) Luminescent functional metal-organic frameworks. Chem Rev 112:1126–1162

27. Sun YQ, Zhang J, Chen YM, Yang GY (2005) Porous lanthanide-organic open frameworks with helical tubes constructed from interweaving triple-helical and double-helical chains. Angew Chem Int Ed 44:5814–5817

28. Zheng XJ, Jin LP, Gao S (2004) Synthesis and characterization of two novel lanthanide coordination polymers with an open framework based on an unprecedented $[Ln_7(\mu_3\text{-}OH)_8]^{13+}$ cluster. Inorg Chem 43:1600–1602

29. Lu JY (2003) Crystal engineering of Cu-containing metal–organic coordination polymers under hydrothermal conditions. Coord Chem Rev 246:327–347

30. Zhang MB, Zhang J, Zheng ST, Yang GY (2005) A 3D coordination framework based on linkages of nanosized hydroxo lanthanide clusters and copper centers by isonicotinate ligands. Angew Chem Int Ed 44:1385–1388

31. Cheng JW, Zhang J, Zheng ST, Yang GY (2008) Linking two distinct layered networks of nanosized $\{Ln_{18}\}$ and $\{Cu_{24}\}$ wheels through isonicotinate ligands. Chem Eur J 14:88–97

32. Gu XJ, Xue DF (2007) Surface modification of high-nuclearity lanthanide clusters: two tetramers constructed by cage-shaped $\{Dy_{26}\}$ clusters and isonicotinate linkers. Inorg Chem 46:3212–3216

33. Huang L, Han LJ, Feng WJ, Zheng L, Zhang ZB, Xu Y, Chen Q, Zhu DR, Niu SY (2010) Two 3D coordination frameworks based on nanosized huge Ln_{26} (Ln = Dy and Gd) spherical clusters. Cryst Growth Des 10:2548–2552

34. Chen L, Guo JY, Xu X, Ju WW, Zhang D, Zhu DR, Xu Y (2013) A novel 2-D coordination polymer constructed from high-nuclearity waist drum-like pure Ho_{48} clusters. Chem Commun 49:9728–9730

35. Wu M, Jiang F, Yuan D, Pang J, Qian J, AL-Thabaiti SA, Hong M (2014) Polymeric double anion template Er48 nanotubes. Chem Commun 50:1113–1115

36. Gu XJ, Xue DF (2007) 3D coordination framework $[Ln_4(\mu_3\text{-}OH)_2Cu_6I_5(IN)_8(OAc)_3]$ (IN = Isonicotinate): employing 2D layers of lanthanide wheel clusters and 1D chains of copper halide clusters. Inorg Chem 46:5349–5353

37. Cheng JW, Zhang J, Zheng ST, Zhang MB, Yang GY (2006) Lanthanide-transition-metal sandwich framework comprising $\{Cu_3\}$ cluster pillars and layered networks of $\{Er_{36}\}$ wheels. Angew Chem Int Ed 45:73–77

38. Cheng JW, Zheng ST, Yang GY (2008) Incorporating distinct metal clusters to construct diversity of 3D pillared-layer lanthanide-transition-metal frameworks. Inorg Chem 47:4930–4935

39. Fang WH, Cheng L, Huang L, Yang GY (2013) A series of lanthanide-based cluster organic frameworks made of heptanuclear trigonal-prismatic cluster units. Inorg Chem 52:6–8

40. Canaj AB, Tsikalas GK, Philippidis A, Spyros A, Milios CJ (2014) Heptanuclear lanthanide $[Ln_7]$ clusters: from blue-emitting solution-stable complexes to hybrid clusters. Dalton Trans 43:12486–12494

41. Fang WH, Yang GY (2014) Pillared-layer cluster organic frameworks constructed from nanoscale Ln_{10} and Cu_{16} clusters. Inorg Chem 53(11):5631–5636

42. Fang WH, Cheng JW, Yang GY (2014) Two series of sandwich frameworks based on two different kinds of nanosized lanthanide(III) and copper(I) wheel cluster units. Chem Eur J 20:2704–2711

43. Fang WH, Zhang L, Zhang J, Yang GY (2015) Construction of cluster organic frameworks with bnn hexagonal BN topologies. Chem Eur J 21:15511–15515

44. Fang WH, Zhang L, Zhang J, Yang GY (2016) Water stable homochiral cluster organic frameworks built by two kinds of large tetrahedral cluster units. Chem Eur J 22:2611–2615

45. Sen R, Hazra DK, Mukherjee M, Koner S (2011) Gd_{26} cluster consisting of distorted cubane cores: synthesis, structure and heterogeneous catalytic epoxidation of olefins. Eur J Inorg Chem 2826–2831

46. Zhang Y, Huang L, Miao H, Wan HX, Mei H, Liu Y, Xu Y (2015) Hydrothermal synthesis, structure, and optical properties of two nanosized $Ln_{26}@CO_3$ (Ln = Dy and Tb) cluster-based lanthanide–transition-metal–organic frameworks (Ln MOFs). Chem Eur J 21:3234–3241

47. Wu M, Jiang F, Kong X, Yuan D, Long L, Al-Thabaiti SA, Hong M (2013) Two polymeric 36-metal pure lanthanide nanosized clusters. Chem Sci 4:3104–3109
48. Fang WH, Zhang L, Zhang J, Yang GY (2016) Halogen dependent symmetry change in two series of wheel cluster organic frameworks built from La_{18} tertiary building units. Chem Commun 52:1455–1457
49. Zhou Y, Hong M, Wu X (2006) Lanthanide–transition metal coordination polymers based on multiple N and O-donor ligands. Chem Commun 135–143
50. Huang Y, Jiang F, Hong M (2009) Magnetic lanthanide–transition-metal organic–inorganic hybrid materials: from discrete clusters to extended frameworks. Coord Chem Rev 253:2814–2834

Oxo Clusters of 5*f* Elements

Sarah Hickam and Peter C. Burns

Abstract The chemistry of the 5*f* elements has been studied for decades, primarily driven by nuclear security and the nuclear-fuel cycle. A young subset of this field, the synthesis of actinide clusters, is rapidly developing and providing new insight into actinide chemistry and environmental behavior, with possible applications for the nanoscale control of these elements. The electronic character and oxidation states of the actinides strongly influence the types and diversity of structures that may be achieved. Hexavalent actinide clusters in particular have structural variety paralleling that of transition metal polyoxometalates. This is exemplified by uranyl peroxide cage clusters, which have more structural topologies than any other cluster-type examined here. This text provides an update on this still-emerging field, building on previous review articles, with a focus on oxygen-coordinated actinide clusters and the commonalities and trends between them.

Keywords Actinides • Actinyl ion • Cluster synthesis • Oxo bridges • Polynuclear

Contents

S. Hickam
Department of Civil and Environmental Engineering and Earth Sciences, University of Notre Dame, Notre Dame, IN 46556, USA

P.C. Burns (✉)
Department of Civil and Environmental Engineering and Earth Sciences, University of Notre Dame, Notre Dame, IN 46556, USA

Department of Chemistry and Biochemistry, University of Notre Dame, Notre Dame, IN 46556, USA
e-mail: pburns@nd.edu

1 Introduction

The actinide elements are a transition series generated by filling of the 5*f* orbitals.
The 5*f* and 6*d* orbitals are both capable of contributing to bonding for the actinides
[1], and the behavior of the 5*f* orbitals greatly influences the properties of these
elements, yielding a diverse chemistry. The elements thorium through plutonium
have characteristics in common with d-block elements, including covalent bonding
and multiple oxidation states [1, 2]. Actinium and the actinide elements heavier
than plutonium have properties that commonly link them to the lanthanide series,
such as ionic character and the prevalence of the trivalent oxidation state
[1]. Diverging characteristics are observed for californium and heavier elements,
including that they more readily achieve the divalent oxidation state [3, 4] and
californium has displayed covalent bonding [3, 5].

Actinides are radioactive heavy metals that are the fuels for nuclear reactors and
atomic weapons. More than 400 nuclear plants in the world produce about 13% of
all electricity, and more than 70 new plants are under construction. Actinides fuel
reactors used for medical isotope production, as well as many industrial applica-
tions. They are also major constituents of irradiated nuclear fuel and various types
of radioactive waste, are environmental contaminants in uranium mine and mill
tailings [6], and are widespread contaminants at sites used for nuclear weapon
production and testing [7, 8].

Owing at least in part to their radioactivity and strategic importance, studies of
actinides have generally lagged behind those of other areas of the periodic table.
Synthesis and characterization of actinide oxo clusters also lagged behind
corresponding studies of the transition metals, but it is an area of substantial growth
over the past decade. Such polynuclear species are of considerable interest because
they can impact transport and migration behavior of actinides in the environment,
related to hydrolysis and condensation [9], especially for Pu(IV) and Th(IV).

Actinide clusters, such as uranyl peroxides, have several potential applications in the nuclear-fuel cycle [10]. Furthermore, actinide oxo clusters allow for a degree of control at the nanoscale, and the probing of size-property relations.

Actinide (An) clusters have been isolated for An(IV), An(V), and An(VI) and usually exhibit characteristics that are oxidation-state specific, such as the details of the termination of the cluster structure. An(IV)-bearing clusters are typically terminated by organic ligands, but many An(VI) clusters are terminated by O atoms that are strongly bound to An(VI) cations, as part of actinyl ions (see below). Although covalent interactions between An(IV) and ligands have been observed [1], O atoms are generally not terminal ligands in An(IV) clusters, owing to their tendency to bridge to other metals, which favors extended solids. When specific ligands, usually organic, are used to passivate the surface of an An (IV) oxo cluster, clusters can be isolated. Some of the An(IV) oxo clusters have the well-known fluorite-type structure, where the An(IV) cation is coordinated to eight O atoms and each O atom is coordinated to four An(IV) cations [11].

Thorium and plutonium oxo clusters are only known to occur with tetravalent cations. Thorium is stable only in the tetravalent oxidation state in aqueous solution [2], and although plutonium occurs in multiple oxidation states in solution, only Pu (IV) clusters have been obtained, although Pu(VI) has been incorporated into a polyoxometalate sandwich complex [12]. Uranium oxo clusters have been isolated that contain U(IV), U(V), or U(VI), and in some cases combinations of U(IV) and U (V). U(V) is unstable toward disproportionation to U(IV) and U(VI) in most aqueous solutions [2].

Actinyl ions dominate the chemistry of An(V) and An(VI). In the actinyl ion, two oxygen atoms are multiply bonded to the actinide in a *trans* configuration, giving a linear $(AnO_2)^{+1,+2}$ species. The most studied actinyl ion is $(UO_2)^{2+}$, in which $5f_\sigma$-$6p_\sigma$ hybridization and $6d_\pi$ overlap with O $2p$ orbitals create a covalent metal–oxygen bond with a linear geometry [13, 14]. The average U(VI)-O_{yl} bond length is ~1.78 Å and bonding requirements of the uranyl O atoms are largely satisfied by bonds with U(VI) alone [15]. Thus, the –*yl* O atoms tend not to form strong bonding interactions with other atoms; instead, they are the terminal ligands of many U(VI) clusters, where they only participate in weaker hydrogen bonds or bonds to low-valence cations in most cases.

The preference of –*yl* O atoms to adopt a *trans* arrangement in actinyl structures has been attributed to an inverse *trans* influence (ITI) [16]. For transition metals, a strongly bound ligand weakens the bond *trans* to it, which is known as the *trans* influence, but the opposite occurs for actinide structures. The *trans* and inverse *trans* influences have been studied for MZY_5^{n-} complexes, where M is a transition metal or actinide, Z is the strongly bound oxo or nitrido group, and Y denotes a halide. The M-Y_{trans} bond is longer than M-Y_{cis} bonds for transition metals, whereas the M-Y_{trans} bond is shorter than the M-Y_{cis} bonds in actinide structures [14]. Computational studies have given insight into these observations. The polarization of the $6p$ orbitals due to the metal-oxo bond results in good parity and mixing of the $6p$ the $5f$ orbitals and quadrupolar polarization of the metal core

electrons [17, 18], and this contributes significantly to the ITI [17]. Several studies have demonstrated that the ITI is also influenced by the 5f orbitals [19, 20], as the ITI increases with the lowering of 5f orbital energy, and La Pierre et al. [17] showed that the decreased energy of 5f orbitals results in better parity with O 2p orbitals relative to N 2p orbitals.

Ligand attachment and polymerization occur in the equatorial plane of bipyramids about the uranyl ion, where it is coordinated to four, five, or six ligands, resulting in square, pentagonal, and hexagonal bipyramids, respectively. Typically, these units polymerize to form one- and two-dimensional structures, but in recent years many clusters have resulted from linkages of these polyhedra. For hexagonal bipyramids, the average bond length from the U(VI) cation to an equatorial O atom is significantly longer and more variable than the U-O_{yl} bond, with an average length of about 2.36–2.46 Å [21]. Sheet structures of U(VI) often contain polyhedra that share several or all equatorial edges [21] as the bonding requirements of equatorial O atoms are not entirely met by bonding to only two U(VI) cations.

Np(VI) coordination environments are very similar to U(VI), although the average Np(VI)-O_{yl} bond in inorganic structures published prior to 2008 is slightly shorter at about 1.74 Å [22]. The Np(V) neptunyl ion also displays similar coordinations; however, the difference in valence leads to significant structural differences. At 1.84 Å, the Np(V)-O_{yl} bond length is slightly longer than Np(VI)-O_{yl} and U-O_{yl} bonds, and the Np(V)-O bonds within the neptunyl ion are noticeably weaker than those in Np(VI) or U(VI) actinyl ions [22]. Often, $(NpO_2)^+$ ions are linked through the so-called cation–cation interactions (CCIs), where one –yl oxygen is also the equatorial oxygen atom coordinated to a neighboring actinyl ion. CCIs are pervasive in Np(V) structures – approximately 50% contain them, often as part of a framework structure [22, 23].

The first actinyl polyoxometalate cluster was reported in 2001 and contains six U(V) ions [24]. The field has experienced phenomenal growth in the last decade, starting in 2005 with the emergence of uranyl peroxide cage clusters that have been compared to the transition metal polyoxometalates [25, 26]. Highlights such as these will be discussed in this text, proceeding from tetravalent to hexavalent oxidation states. The focus here is oxo clusters published subsequent to a review by Qiu and Burns [11], with selected references to earlier structures that demonstrate a significant contribution to actinide cluster chemistry.

2 Tetravalent Actinide Clusters

Clusters with four An(IV) cations have been reported [27–29] and are examined in an earlier review [11]. The emphasis here is on clusters containing six or more An (IV) cations and, more specifically, the clusters reported since the review by Qiu and Burns [11] and those with unique terminal ligands (i.e., ligands that are not organic).

2.1 Clusters with Six An(IV) Cations

Hexanuclear clusters dominate tetravalent actinide clusters [30–39], and some have argued that these structures could be fundamental units in hydrolysis and condensation reactions of An(IV) [33]. A series of An(IV) clusters has been described that generally have the same $An_6(O,OH)_8$ composition and often have a total core composition of $[An_6(OH)_4O_4(H_2O)_6]^{12+}$, including the previously reviewed clusters containing Th(IV), [31, 33, 35], Np(IV) [34], and U(IV) [35, 38, 39], although the structure of the Np(IV) cluster was assumed on the basis of UV-vis and X-ray absorption studies of solutions [40]. Four Th(IV) and eight similar U(IV) $An_6(O,OH)_8$ clusters were reviewed previously. A fifth Th(IV) hexanuclear cluster with a $Th_6(O,OH)_8$ core has since been reported [37].

Carboxylate ligands are often used in the synthesis of hexanuclear An (IV) clusters and are incorporated as bridging and terminal ligands. A typical structure is represented in Fig. 1 and contains An(IV) cations coordinated by four bridging μ_3-O or μ_3-OH anions to form an $[An_6\{\mu_3$-$O,OH)_8\}]$ core. The An (IV) cations are additionally coordinated to four O atoms from a bridging ligand and an O atom from a water molecule. In the most recently reported cluster, the bridging ligand was formate [37]. Other ligands have included acetate and chloroacetate, which have been incorporated in the clusters of Knope et al. [33]. An_6O_8 structures have been obtained without carboxylate ligands, such as those by Berthet et al. [38], which were synthesized by reacting uranocene with uranyl(VI) salts, activating the strong actinyl O bonds and reducing uranium to form structures with $U_6(\mu_3$-$O)_8$ cores in conformations that are analogous to those described above.

The series of $An_6(O,OH)_8$ clusters has been expanded with the first Pu(IV) compound, $Li_6[Pu_6(OH)_4O_4(H_2O)_6(HGly)_{12}]Cl_{18} \cdot 10.5H_2O$ (Fig. 1) [40]. The crystals were synthesized by complexation of Pu(IV) with glycine ligands. The
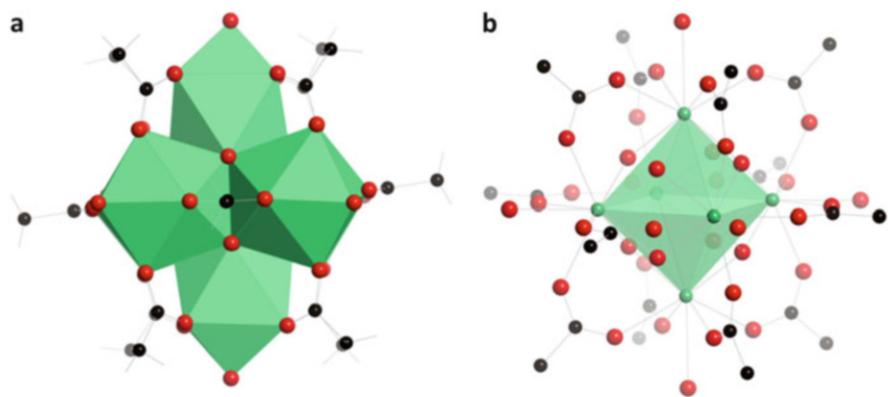
Fig. 1 (**a**) Polyhedral representation of Pu_6O_8; (**b**) the geometric arrangement of Pu atoms indicated is by a *green octahedron*. Pu is *green*, O is *red*, and carbon is *black*.

core, with composition $[Pu_6O_4(OH)_4]^{12+}$, contains Pu(IV) coordinated by nine O atoms: four are from μ_3-O/OH groups of the core, whereas the outer edges are bound to one water group and four O atoms from the glycine ligands. Cl ions balance the net +12 charge of the cluster as well as the positive charges from Li cations associated with the structure.

The $An_6(O,OH)_8$ clusters display similarities to Zr(IV) [41], Ce(IV) [42], and Bi (III) [43] clusters. For example, a Zr(IV) cluster contains atoms that are arranged at the vertices of an octahedron, are linked by μ_3-OH groups, and are bridged by glycine ligands, like many of the hexanuclear An(IV) clusters. Furthermore, a similar series of Th(IV), U(IV), Np(IV), and Pu(IV) clusters has been described that contains bridging disphosphonate ligands [30, 44]. The $An_6(O,OH)_8$ cores have also been incorporated as building units in other structures, such as U(IV) hexanuclear clusters that are identifiable in MOF-type structures [45] and Th(IV) clusters that have been linked into 3D structures through SeO_4 tetrahedra [46]. The prevalence of the An_6O_8 structural unit and variety of synthetic routes indeed seems to indicate a fundamental importance of these structures in the hydrolysis and condensation chemistry of tetravalent actinides.

2.2   Clusters with 10 or More An(IV) Ions

Two decanuclear An(IV) clusters have been reported that have $U_{10}O_{14}$ core compositions and that are terminated by organic ligands [47]. Structurally, the cores of both clusters are made up of two U_6O_8 cages that share two U(IV) cations and two O anions. With a distinct topology, the largest and only decanuclear Th (IV) compound to date, $[Th_{10}(\mu\text{-}F_{16})(\mu_3\text{-}O_4)(\mu_4\text{-}O_4)(NH_3)_{32}](NO_3)_8 \cdot 19.6\ NH_3$, was recently reported by Woidy and Kraus [48]. The core of the cluster is $[Th_{10}O_4]$ $^{32+}$ with a topology consisting of four corner-sharing tetrahedra with Th(IV) cations at the vertices. The four μ_4-O atoms bridge Th(IV) cations in the core, which are further connected on the exterior by μ_3-O atoms. The Th(IV) cations are in three different coordination environments: four are 10-coordinate in a $[ThO_4F_3(NH_3)_3]^{7-}$ unit, and two other Th(IV) cations are coordinated to eight atoms in a $[ThO_4F_2(NH_3)_2]^{6-}$ unit. The remaining four Th(IV) cations are nine-coordinate as $[ThOF_4(NH_3)_4]^{2-}$.

While most An(IV) oxo clusters are truncated by organic ligands, four related Th(IV) octanuclear clusters and a large Pu(IV) cluster are truncated in a different fashion. In the Th(IV) structures, all of which feature a $[Th_8O_4(OH)_8]^{16+}$ core, Th(IV) cations are coordinated to nine O atoms from μ_3-O or μ_2-OH groups, water molecules, and monodentate selenate anions (Fig. 2) [9]. Selenate tetrahedra are the terminal ligands in these structures, and their additional roles include occupying "voids" in the core structures and linking multiple metal centers. The authors noted that $[Th_8(\mu_3\text{-}O)_4(\mu_2\text{-}OH)_8(SeO_4)_2]^{12+}$ and a dodecanuclear U(IV/V) cluster, $[U_{12}(\mu_3\text{-}OH)_8(\mu_3\text{-}O)_{12}]^{16+}$ [49], have structural units that are remarkably similar,
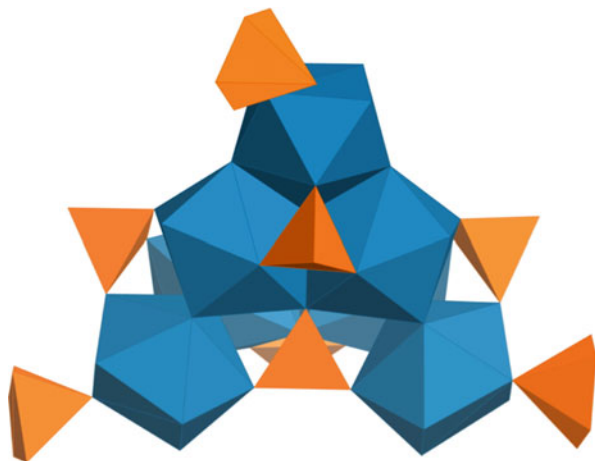
and the limited redox chemistry of Th or the influence of selenate ligands may prevent the formation of a larger Th complex.

Hydrolyzed Pu(IV) forms multinuclear metal oligomers that are of interest in Pu colloid chemistry. Crystals of $[Pu_{38}O_{56}]^{40+}$, the first oxo Pu cluster, were obtained by two different methods: (1) acidifying an alkaline peroxide solution and passing it through an anion-exchange column followed by a combination of heating and treatment with HCl and LiCl [50] and (2) recrystallizing $Li_{12}[Pu_{38}O_{56}Cl_{54}(H_2O)_8]$ $(H_2O)_x$ that was made by boiling a solution of Pu(IV) and HCl, adding LiOH, and allowing the solution to evaporate [51]. The first method produced crystals with composition $Li_{14}(H_2O)_n[Pu_{38}O_{56}Cl_{54}(H_2O)_8]$, and those from the second contain 42 Cl anions and 20 structural H_2O molecules, for a total composition of $Li_2[Pu_{38}O_{56}Cl_{42}(H_2O)_{20}] \cdot 15H_2O$. The clusters have a distorted *Fm3m* fluorite-type structure yielding a pseudocubic shape. In the first structure, H_2O groups truncate the corners and each of the six faces is terminated by Cl ions, 54 in total. The center of the cluster contains six Pu(IV) cations that are coordinated by eight shared O atoms. An additional eight Pu(IV) cations are arranged around the corners of the core, coordinated by seven O atoms and one H_2O group. The faces of the cluster contain 24 Pu(IV) cations coordinated to four O atoms and four Cl anions. In the second structure, water molecules replace 12 Cl anions.

Pu environmental transport and sorption has been extensively studied by Powell et al., who have observed Pu complexation with organic compounds in solution and nanocolloid formation on mineral surfaces [52–55]. Aqueous Pu(IV) interacts strongly with a goethite surface and forms a Pu_4O_7 nanocolloid with a distorted fluorite-type structure, as determined by HRTEM and electron diffraction [56].

Controlling the rate of hydrolysis of uranium has led to the isolation of U(IV) structures containing 10, 12, and 16 U(IV) cations [47, 49]. Utilizing this approach has more recently yielded the largest U(IV) cluster synthesized to date, $U_{38}O_{56}Cl_{18}(THF)_8(bz)_{24} \cdot 8THF$ (Fig. 3), which notably has the same nuclearity as $[Pu_{38}O_{56}]^{40+}$ [57]. The structure is related to the Pu(IV)$_{38}$ structure with a
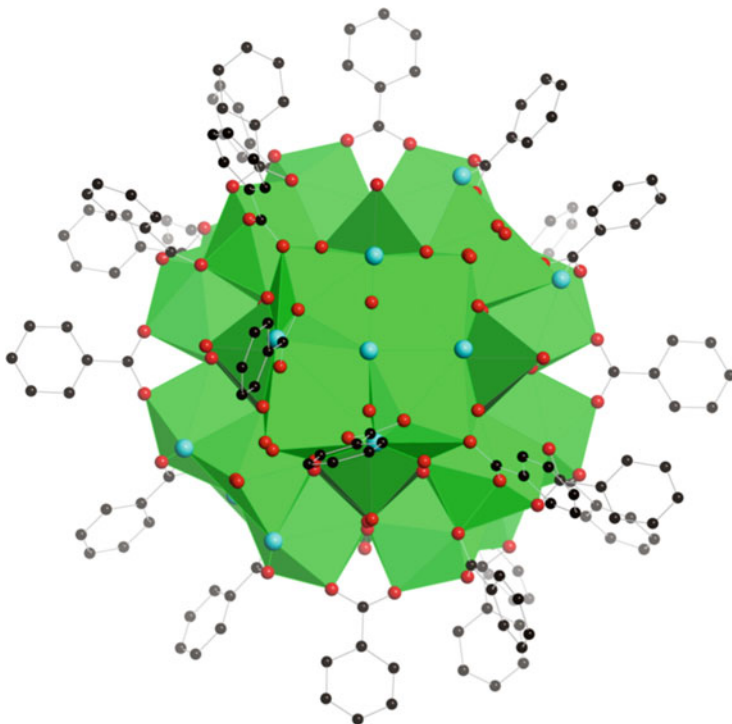
Fig. 3 Polyhedral representation of the U(IV)$_{38}$ cluster. Core U polyhedra are *dark green,* faces are *green*, Cl is *teal,* and O is *red*. Each core uranium is coordinated by a disordered benzoate molecule that is shown

fluorite-type core composed of 14 U(IV) cations in UO_8 polyhedra with cubic coordination geometry. The polyhedra are linked through edge-sharing via μ_4-O atoms. The exterior of the structure consists of six faces, each containing four U atoms. Four of the faces are identical, with two U(IV) cations in $UO_4O^{bz}Cl_3$ coordination, where *bz* indicates a benzoate ligand, and two as $UO_4O^{bz}{}_2Cl_2$. The two remaining faces have uranium atoms in $UO_4O^{bz}{}_4Cl$ coordination. Unlike $[Pu_{38}O_{56}]^{40+}$, this U(IV) cluster has benzoate terminal ligands, which occur as bidentate linkers between polyhedra and distort the structure from ideal *Fm3m* symmetry.

3 Actinide(V/VI) Actinyl Clusters

We know of only one cluster that contains Np(V) cations, a tetrameric compound with composition $[\{NpO_2(salen)\}_4(\mu_8\text{-K})_2][K(18C6)Py]_2$ (Fig. 4) [58]. CCIs are a prevalent feature of the structure, where they connect the four Np(V) cations into a cyclic core. CCIs are becoming more important features of uranium oxo-bridged
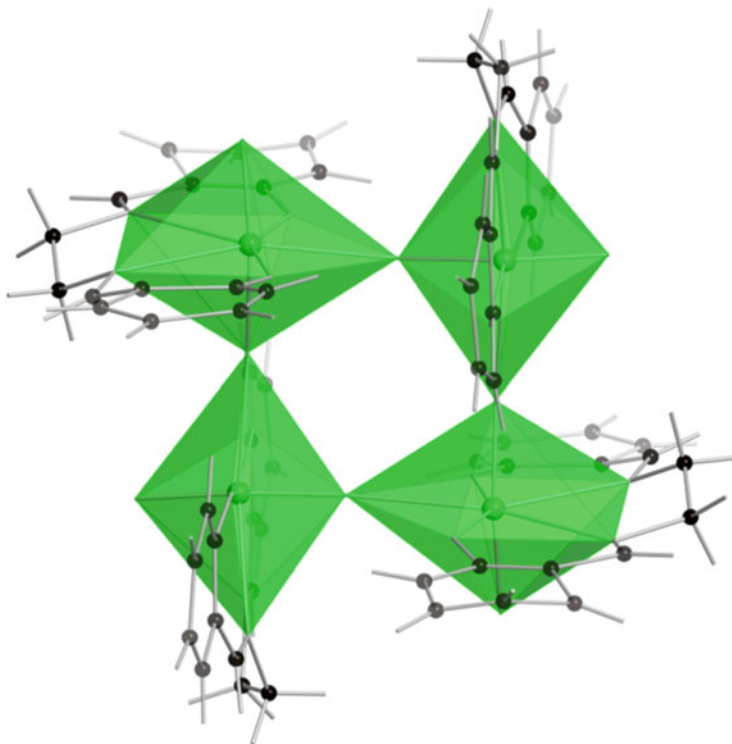
Fig. 4 Cation–cation interactions in Np(V) form a cyclic cluster

clusters as well [11]. For example, $[\{UO_2(salen)\mu\text{-}K(18C6)\}\text{-}\{UO_2(salen)\}_3$ $(\mu_8\text{-}K)_2]$ is the first example of a uranyl cluster with CCIs between U(V) and U(VI) [59]. More discussion about CCIs in uranyl structures is provided in an earlier review [60].

Pentavalent uranium often disproportionates to U(VI) and U(IV) or oxidizes to U(VI) in solution, and as a result, the literature contains relatively few structures with U(V). One example is the largest U(V) cluster reported to date, $[Cp^*_4(bpy)_2]$ $[U_6O_{13}]$, $Cp^* = 1,2,4\text{-}^tBu_3C_5H_2$, bpy = bipyridine. The core, U_6O_{13}, is analogous to the Lindqvist-type structures of molybdenum and tungsten polyoxometalates [24]. No additional U(V) clusters have been reported since the review in 2013 [11].

A large family of U(VI) peroxide cage clusters has been described in reviews published in 2011 and in 2013 [11, 61]. The focus here is an overview of uranyl peroxide cage clusters, with more detailed structural descriptions for some recently reported clusters and those with novel topological features. The Qiu and Burns [11] review indicated that all actinide clusters containing 18 or more actinide ions, with the sole exception of $Pu_{38}O_{56}$, were actinyl peroxide clusters [11]. This is no longer the case owing to the report of $U_{38}O_{56}$ and a new wheel-shaped cluster that contains 20 uranyl cations [62, 63]. The following sections explore these and other new developments.

The uranyl peroxide clusters are designated with the notation $U_xV_yW_z$, where U is the number of uranyl (or neptunyl in one case) ions within a cage. V and W designate structural components of the cage in addition to the uranyl ions, such as *Ox* for oxalate, *Pp* for pyrophosphate, *PCP* for methylenediphosphonate, and *L* for etidronic ligands. Finally, x, y, and z denote the number of each unit contained within a cluster as well as any relevant alphanumeric descriptors of topology, such as "R" for ring.

4 Uranyl Peroxide Cage Clusters

The first actinyl peroxide cage clusters were reported in 2005 and were U_{24}, U_{28}, U_{32}, and Np_{24} (Fig. 5) [25]. After a decade of exhaustive exploratory syntheses, about 60 uranyl peroxide clusters have been published that demonstrate a remarkably diverse family: some have fullerene topologies, including U_{60} (Fig. 5e) [64] that is topologically identical to C_{60} [65], others are incomplete cages with open bowl-shapes [66], and additional topologies include core-shell structures [67, 68] and one cluster with multiple, fused cages [69]. The smallest member of this family contains 16 uranyl polyhedra, whereas the largest has 124 [69]. These topologies
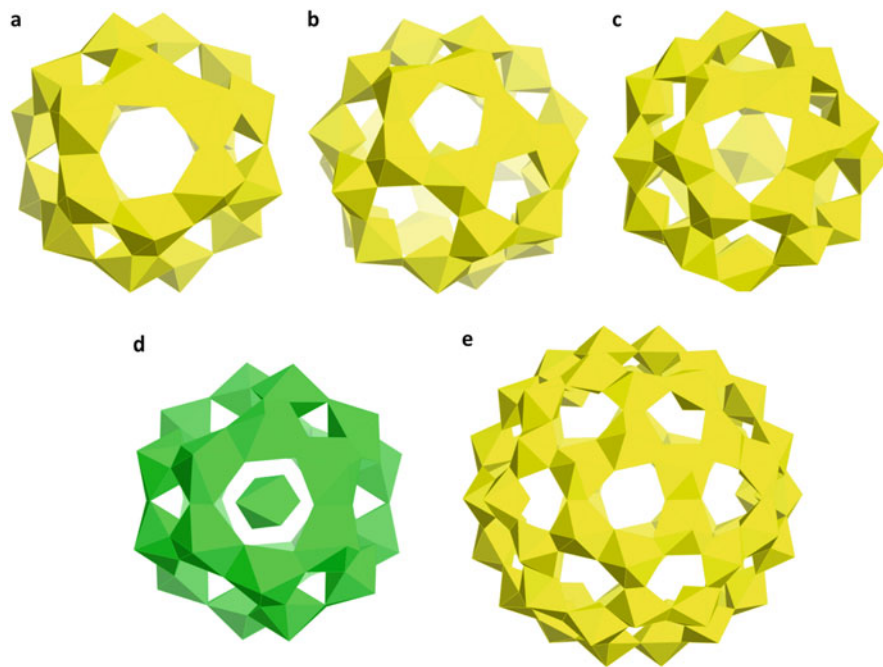
Fig. 5 The first actinyl peroxide cage clusters and those with typical topologies, including fullerene topologies. (**a**) U_{24}, (**b**) U_{28}, (**c**) U_{32}, (**d**) Np_{24}, and (**e**) U_{60}

have generally resulted by mixing uranyl nitrate and excess hydrogen peroxide, followed by the addition of other solvents and cations, and clusters have formed in solutions with pH ranges of 4–11.5 [70]. Normally, these steps are completed under ambient conditions; only U_{50} and U_{40} were crystallized after exposure to nonambient conditions by heating the solutions to 80°C in sealed Teflon-lined vials [71].

Expansion of the uranyl peroxide cage cluster family may lead to applications and new understanding, such as in the nanoscale control of materials in the nuclear-fuel cycle [10] and transport of actinides in the environment [72]. Mass-based separation of uranium peroxide cage cluster species from solutions has been achieved using ultrafiltration [10] and mesoporous silica (SBA-15) material sequestration [73]. As much as 95% rejection of U is achieved via ultrafiltration when the uranyl ions are contained in clusters, and SBA-15 extracts uranyl peroxide cage clusters from solution with an extraction capacity of 6.77 mg g^{-1}, corresponding to 97.1% efficiency.

4.1 *Actinyl Coordination and Arrangement*

Uranium atoms in cage clusters are strongly bonded to *trans-yl* O atoms, forming the linear dioxo cation $(UO_2)^{2+}$ that lies approximately perpendicular to the cluster surface. The *–yl* oxygen atoms passivate both the inner and outer surfaces of the structure. Five or six additional oxygen atoms are coordinated equatorially to the U(VI) cation, yielding pentagonal and hexagonal bipyramids, although hexagonal bipyramids are far more common in uranyl peroxide clusters. In most uranyl peroxide clusters, four, five, or six uranyl hexagonal bipyramids are arranged in rings by sharing equatorial edges, yielding topological square, pentagonal, and hexagonal units in the cluster structures (Fig. 6). These units are linked by edge-sharing, such that each uranyl polyhedron shares edges with three other uranyl polyhedra. However, as new structures have continued to emerge, novel topologies have been established. For example, uranyl polyhedra have been linked into belts instead of rings (Fig. 6) [60, 74] and crown- and ring-shaped clusters such as U_{20R} and U_{24R} contain hexagonal bipyramids with both two and three shared edges [66].

4.2 *Peroxide Bridges*

Peroxide bridges appear to be essential in cage clusters as bridging ligands between uranyl polyhedra, where two or three of the shared edges of polyhedra are peroxo groups that are bidentate to the uranyl ions. The peroxo edges of uranyl polyhedra are ~1.45 Å long, much shorter than the ~2.8 Å length typical in the absence of peroxide, resulting in distorted hexagonal or pentagonal bipyramids. U_{20}, U_{28}, and U_{44} are rare examples of clusters that contain only triperoxide polyhedra [25, 64,
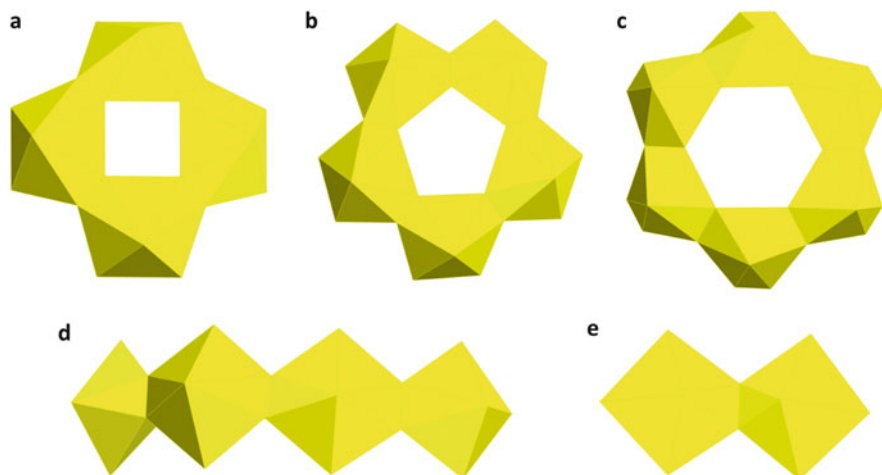
Fig. 6 Arrangements of actinyl polyhedra found in uranyl peroxide cage clusters, including (**a**) square faces, (**b**) pentagonal faces, (**c**) hexagonal faces, (**d**) belts, and (**e**) dimers

75], and polyhedra with one peroxo group have also been reported [76] but are rare. The influence of peroxide on the cage cluster topology is related to two properties: the bonding requirements of peroxide limit the number of connections between uranyl polyhedra, and the $U-O_2-U$ bridge is highly pliable. The formal valence of peroxide is 2-, and each peroxo O atom that forms bonds to two U(VI) atoms contributes ~1 *valence unit*, satisfying the bond valence requirement [71]. Thus, connectivity in the cage clusters is limited to one, two, or three shared edges between uranyl polyhedra, and the resulting porous nature is conducive to forming a cage structure.

The characteristic curvature of the cage clusters is a result of the bent $U-O_2-U$ dihedral angles, which range from ~130° to 155° [77]. A prevalent hypothesis has been that peroxide bridges are inherently bent and thus facilitate cage cluster formation [75]. Density function theory (DFT) studies of the $U-O_2-U$ bridges found only a modest, 0.5 kcal mol^{-1} energy advantage of a bent dihedral angle compared to 180° in the absence of counterions [78]. Qiu et al. [79] further probed the role of hydrogen peroxide in cage cluster formation by synthesizing a variety of uranyl peroxide dimers coordinated by various organic ligands. Six of the 15 dimers had $U-O_2-U$ dihedral angles of 180°, inconsistent with the hypothesis that the peroxide bridge is inherently bent. Nevertheless, the $U-O_2-U$ bridge is certainly flexible and thus is an ideal ligand for the formation of cage clusters.

4.3   Roles of Alkali Ions

Counterions are essential components of uranyl peroxide cage structures that balance the large negative charges of the structural units. Although the full extent of their role in directing cluster formation is still not well understood, different

counterions are generally associated with specific rings of uranyl polyhedra [78]. K, Li, and Na are the most common counterions in the synthesis of uranyl peroxide clusters and are typically located both on the exterior of the clusters and as encapsulated species in the solid state. Unfortunately, understanding their roles is complicated by the difficulty of locating Li in X-ray structures and cation disordering in general. Two-dimensional ^{7}Li-^{7}Li magic angle spinning nuclear magnetic resonance (MAS NMR) exchange experiments indicate that Li can be highly mobile in these clusters in the solid state, exchanging between encapsulated and other lattice sites [80]. Li has only been located in the structures of Np_{24} and a LiK salt of U_{24} to date [25, 80].

DFT calculations combined with multiconfigurational methods (CASSCF/ CASPT2) indicate that the U-O_2-U dihedral angle is affected by intermolecular interactions with, and the sizes of, the countercations, with a correlation between increasing angle and increasing ionic radius of the cations [77, 79]. Additionally, the U-O_2-U angle for a $[(UO_2)_2(O_2)_5]^{6-}$ cluster optimized to 180° without the addition of cations and to 145° with the addition of Na cations [77]. Counterions thus seem to favor bent U-O_2-U configurations, and may even result in different angles and therefore curvature in the resulting cages.

Cations can influence the topology of uranyl peroxide clusters by their associations with four-, five-, or six-membered rings, either by templating or by stabilizing the rings of polyhedra [78]. In general, the smaller alkali cations, Li and Na, are associated experimentally with square faces, or four-membered rings of polyhedra, while medium-size alkalis favor pentagonal faces and large alkalis occupy sites of hexagonal faces [70, 81]. DFT calculations by Miro et al. [78] support these observations. The calculations indicate that topological squares and pentagons provide bonding environments that both favor Na when it is present but, when Na is absent, Li is most suitable for square sites and K fits the topological pentagons. In the Na and Li salts of U_{24}, the encapsulated cations are located under the square face, while the larger K cations in the LiK salt are located under the hexagonal face [25, 80]. These observations are consistent with the general trends because K cations prefer the larger available sites of the cluster [80]. Due to the nature of the experiment, more specifically that the cations were exchanged after the anions were assembled, the results do not imply that K cations template six-membered rings of polyhedra. In U_{60}, for example, K occupies sites of the five-membered rings although the cluster contains both pentagonal and hexagonal faces [64]; thus, the observations from the U_{24} experiments are merely an example of the trend.

Miro et al. [78] noted that the six-membered rings of uranyl ions in uranyl peroxide cages are typically linkages between the more stable tetramers and pentamers. DFT calculations indicate that alkali cations do not have a significant stabilizing affect on hexagonal rings; nevertheless, Cs and Rb are the most suitable cations for these sites. Experimentally, less evidence exists for the influence of Cs and Rb compared to the smaller alkali cations, but two clusters, U_{24R} and U_{28}, have been published with the larger cations in the expected sites [66, 82]. Nyman et al. [82] have accomplished a more comprehensive study in which U_{28} was synthesized with combinations of K, Rb, and Cs cations. Indeed, Rb and Cs cations exclusively occupied sites of the six-membered rings of uranyl polyhedra.

4.4   Hydroxyl and Functionalized Bridging Ligands

Select shared polyhedral edges in numerous cage clusters correspond to two hydroxyl groups, forming U-(OH)$_2$-U bridges. These bridges are typically slightly bent in cage clusters, although computational studies find that the lowest energy is achieved for a U-(OH)$_2$-U dihedral angle of 180° [77]. The authors noted that a bent angle is not prohibited, and cations that bridge uranyl O atoms may encourage such bending. Many studies of uranyl peroxide cage clusters have focused on the incorporation of other ligands, including pyrophosphate, phosphite, nitrate, methylenediphosphonate, and oxalate (Fig. 7) [67, 70, 74, 83, 84]. Of these, pyrophosphate and oxalate have been extremely fruitful, because they assume "side-on," bidentate configurations with lengths that are suitable for coordination to the uranyl ion [70]. In several cases, these ligands replace hydroxyl bridges in a topologically identical cluster, such as the pyrophosphate ligands in $U_{24}Pp_{12}$, which is topologically identical to U_{24} [25, 70]. Similarly, oxalate ligands in $U_{60}Ox_{30}$ are in the place of hydroxyl bridges in U_{60} [64, 84]. $U_{30}Pp_{10}Ox_5$ contains both pyrophosphate and oxalate ligands [83]. In $U_{30}Pp_{12}P_1$, two pyrophosphate groups share all six available vertices with four different hexagonal bipyramids instead of the typical coordination of four O atoms shared with two hexagonal bipyramids [74].

Recent studies report incorporation of carboxyphosphonate [85] and (1-hydroxyethane 1,1-diphosphonic) etidronic acid [86] into uranyl peroxide cage clusters. Etidronic acid bridges uranyl ions in a fashion that is analogous to pyrophosphate and methylenediphosphonate; however, the use of this ligand,
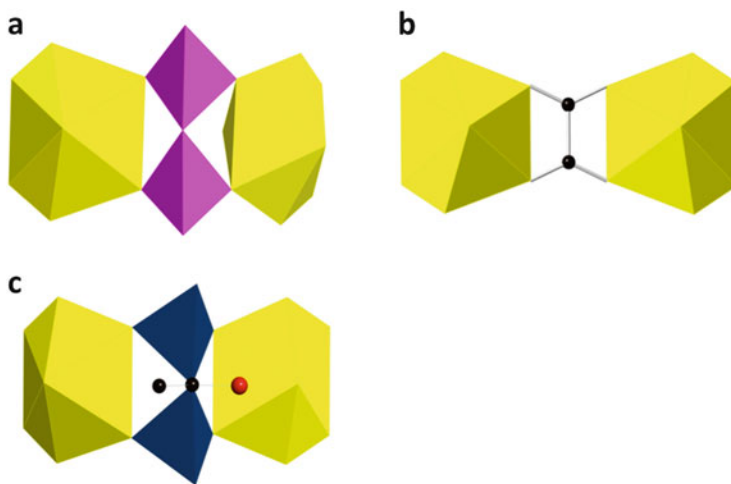
Fig. 7 Typical ligand coordination to uranyl ions is shown as (**a**) pyrophosphate, (**b**) oxalate, and (**c**) etidronic ligands

which contains larger functional groups on the bridging C atom, has yielded novel topologies discussed below.

4.5   Novel and Complex Topologies in Uranyl Peroxide Cage Clusters

$U_{22}PO_3$ and $U_{28}PO_3$ are the first reported chiral uranyl peroxide clusters [60]. The composition of the $U_{22}PO_3$ cage is $[(UO_2)_{22}(O_2)_{15}(HPO_3)_{20}(H_2O)_{10}]^{26-}$ (Fig. 8a, b), and the cage is charge balanced by disordered K counter cations or both K and Na cations. $U_{28}PO_3$ has composition $[(UO_2)_{28}(O_2)_{20}(HPO_3)_{24}(H_2O)_{12})]^{32-}$ (Fig. 8c, d) and has only been reported with K countercations. The syntheses of these crystals are similar to those reported for other uranyl peroxide cage clusters, except that ethylenediaminetetraacetic acid dipotassium salt and $NaNO_3$ are the sources of cations. $U_{22}PO_3$ and $U_{28}PO_3$ crystallize across the limited pH range of
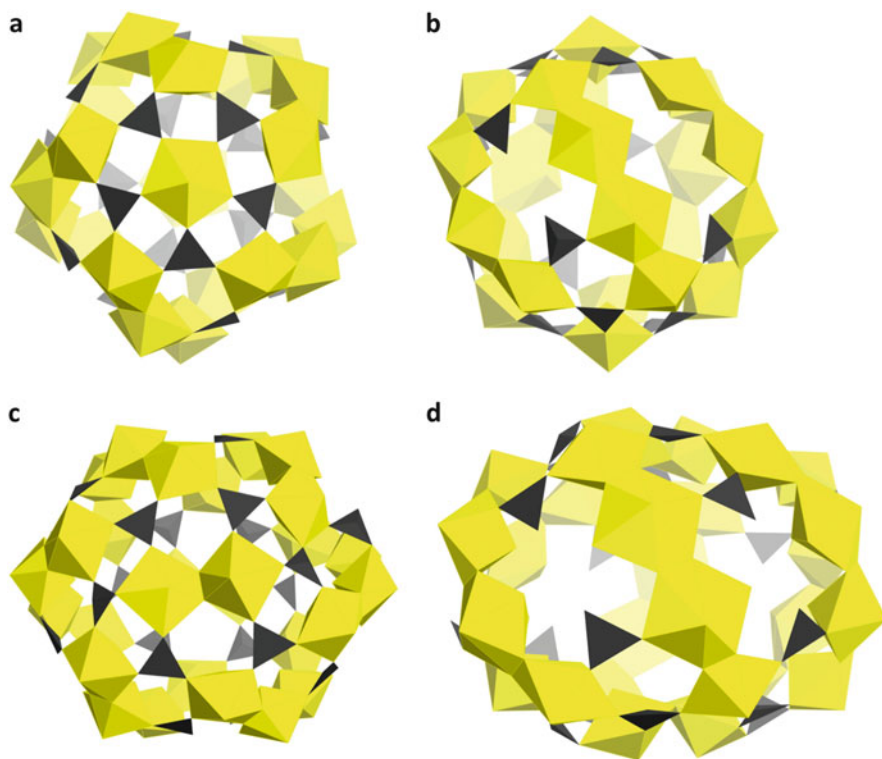
Fig. 8 Chiral uranyl peroxide cage clusters are shown containing belts of polyhedra that are linked to the poles by phosphite groups, shown in *black*. (**a**) and (**b**) are the poles and equatorial regions of $U_{22}PO_3$, respectively. (**c**) and (**d**) are the equivalent features in $U_{28}PO_3$

5.2–6.5. They are the first cage clusters to contain hexagonal bipyramids with bidentate peroxide ligands in a *trans* configuration. The *trans* configuration of peroxide polyhedra gives belts of polyhedra, rather than rings, in both clusters. The belts consist of four polyhedra arranged with two pentagonal bipyramids at the ends and two hexagonal bipyramids toward the center, which are all bridged by bidentate peroxide ligands. The pentagonal bipyramids of the belt are also coordinated to three $(HPO_3)^{2-}$ ligands, one of which links the belt to the pole and two that connect adjacent belts. $U_{22}PO_3$ contains five of these belts and has poles terminated by pentagonal bipyramids coordinated by five $(HPO_3)^{2-}$ ligands. $U_{28}PO_3$ has six belts bridged in the same manner and poles consisting of dimers in the form of two bidentate peroxo-bridged pentagonal bipyramids, which are coordinated to a total of six $(HPO_3)^{2-}$ ligands.

$U_{22}PO_3$ and $U_{28}PO_3$ crystallize as enantiomorphic pairs of right- and left-handed structures. The *trans* configuration of peroxo ligands is also found in the infinite chains in studtite, although it had not been reported in a uranyl peroxide cage cluster [87]. The two pole configurations are also novel: $U_{22}PO_3$ is the first uranyl peroxide cluster to contain pentagonal bipyramids with no peroxide ligands, and $U_{28}PO_3$ is the first to contain uranyl pentagonal bipyramids linked through peroxo bridges. Interestingly, no relationships between the Na or K cations and the belts of polyhedra were observed, and the authors suggested that these clusters might assemble by a different mechanism than those containing rings, for which the cations play a significant role.

Some of the most complex uranyl peroxide cage clusters consist of core-shell units. $U1 \subset U28 \subset U40R$ contains a core cage of 28 triperoxide and diperoxide uranyl hexagonal bipyramids with fullerene topology that has a U atom at the center [68] (Fig. 9a). Surrounding this core, 40 uranyl polyhedra occur as pentamers that are linked, along with nitrate groups, into a bent ring-shaped shell. 40 K cations are located between and connect the two units by coordinating to –*yl* and peroxo O atoms. The authors suggested that the shell is templated by the core structure, because topological pentagons of the shell are located above pentagons of the core structure. Additionally, the assembly of the shell is delayed by 2 weeks compared to the core, as indicated by electrospray ionization mass spectrometry (ESI-MS) and small-angle X-ray scattering (SAXS) data.

$U_{120}Ox_{90}$ [67] has a core that is identical to $U_{60}Ox_{30}$ [84]. Instead of a fully connected shell structure, 12 separate five-membered rings of uranyl hexagonal bipyramids, terminated by oxalate groups coordinated to each uranyl ion, are arranged around the core (Fig. 9b). Similarly to $U1 \subset U28 \subset U40R$, K cations connect the core structure to the five-membered rings of the shell, and the core most likely templates the shell structure.

The largest uranyl peroxide cage cluster synthesized to date is $U_{124}P_{32}$, which has a composition $K_xLi_y[(UO_2)_{124}(O_2)_{152}(PO_4)_{16}(HPO_4)_8(H_2PO_4)_8(OH)_4(H_2O)_{24}]$ H_2O_n (Fig. 9c). Compared to previously published uranyl peroxide cage clusters, the high degree of complexity of $U_{124}P_{32}$ is unequivocal: it is composed of five cages within a single cluster. Four of the five cages are symmetrically identical, and
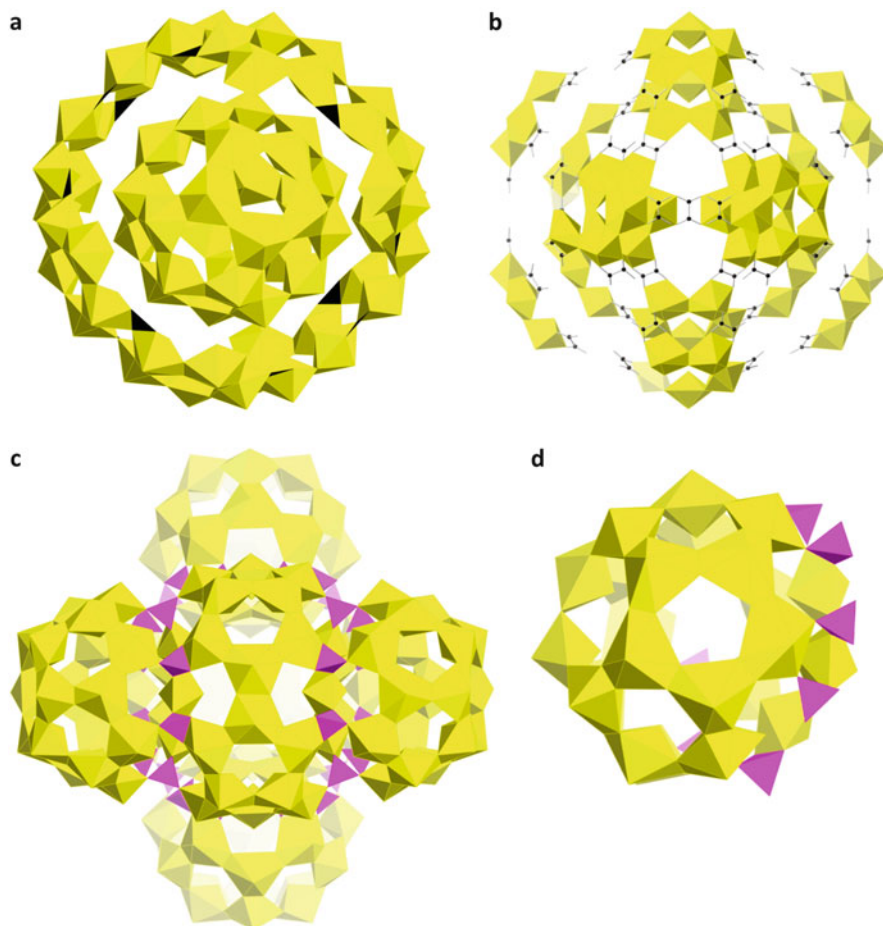
Fig. 9 Complex topologies in uranyl peroxide cage clusters including (**a** and **b**) core-shell clusters and (**c**) the multi-cage cluster containing 124 uranyl ions. One of the cages from the multi-cage structure is shown in (**d**). Nitrate groups are *black triangles,* C atoms are *black spheres*, and phosphate tetrahedra are *pink*

each contains 23 uranyl hexagonal bipyramids that are arranged into five-membered rings and one six-membered ring (Fig. 9d). One of the pentamers is connected by phosphate tetrahedra to the rest of the cage. These four cages are arranged geometrically as vertices of a tetrahedron. Two separate units of four five-membered rings of polyhedra fuse the four "vertices" together, forming a fifth cage in the center of the structure.

4.6 Expanding the Family of Cage Clusters with Organic Ligands

Inclusion of organic ligands has yielded uranyl peroxide-based structures, including one that contains two uranyl peroxide tetramers linked by ethylenediaminetetraacetate (EDTA) ligands [88]. Several cage clusters incorporate oxalate or methylenediphosphonate [70]. In recent years, new topologies of uranyl peroxide cage clusters have been achieved using carboxyphosphonate and etidronic ligands. Although –yl O atoms quite often passivate the surfaces of uranyl peroxide cage clusters, the addition of larger organic ligands into the structural units of these cage clusters provides the opportunity for organic ligands to act as terminal ligands.

Two uranyl-carboxyphosphonate cage clusters have been synthesized: $\{[K_{18}Li_4]$ $[(UO_2)_{20}(HO_2CC_6H_4PO_3)_{10}(O_2)_{20}(OH)_{10}](H_2O)_n\}^{8-}$ and $\{[K_3][(UO_2)_{24}(HO_2CC_6$ $H_4PO_3)_8(O_2)_{24}(OH)_8]\cdot(H_2O)_n\}^{21-}$ [85], with disordered counterions required for charge balance. $\{[K_{18}Li_4][(UO_2)_{20}(HO_2CC_6H_4PO_3)_{10}(O_2)_{20}(OH)_{10}](H_2O)_n\}^{8-}$ contains two five-membered rings of hexagonal bipyramids and a belt of uranyl polyhedra (Fig. 10a). A topological belt was earlier reported for $U_{22}PO_3$ and $U_{28}PO_3$ (see above), but it is unique in this cluster because it consists of 10 uranyl ions in a closed ring around the equatorial region. Carboxyphosphonate groups connect the belt to the two rings of uranyl polyhedra through the phosphonate moiety, whereas the carboxylate units donate oxygen atoms to uranyl polyhedra of the tetramers. The carboxylate moieties project outward in this structure and decorate the elongated exterior edges. In doing so, they act as terminal ligands for the elongated faces, while –yl O atoms terminate the poles.

$\{[K_3][(UO_2)_{24}(HO_2CC_6H_4PO_3)_8(O_2)_{24}(OH)_8]\cdot(H_2O)_n\}^{21-}$ also has belts of polyhedra (Fig. 10b); however, the connectivity of the belts is different from those previously described. The belt is a ring with a circumference of eight
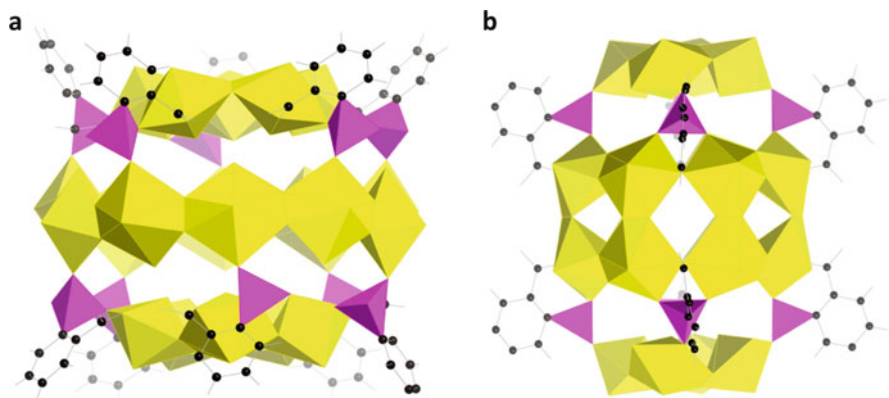

Fig. 10 The uranyl peroxide cage clusters with carboxyphosphonate ligands, (**a**) $\{[K_{18}Li_4]$ $[(UO_2)_{20}(HO_2CC_6H_4PO_3)_{10}(O_2)_{20}(OH)_{10}](H_2O)_n\}^{8-}$ and (**b**) $\{[K_3][(UO_2)_{24}(HO_2CC_6H_4PO_3)_8$ $(O_2)_{24}(OH)_8]\cdot(H_2O)_n\}^{21-}$. Carboxyphosphonate ligands are shown as phosphonate moieties in *pink* and carbon of the carboxyl moieties in *black*

corner-sharing polyhedra that is two polyhedra wide, formed by edge-sharing of peroxo groups. Both poles of the cluster are four-membered rings of polyhedra connected to the belt by oxygen atoms of the phosphonate groups. Instead of donating oxygen to the uranyl polyhedra of the four-membered ring, as in the previous structure, the carboxylate moieties donate oxygen atoms that connect polyhedra of the belt, linking the dimers of polyhedra to each other through corner-sharing [85].

Six cages contain (1-hydroxyethane 1,1-diphosphonic) etidronic acid ligands: $U_{24}L_{12}$, $U_{40}L_{20}$, $U_{64}L_{32}$, $U_{16}L_8$, $U_{20}L_{10}$, and $U_{16}L_8P_4$, where L indicates $[(PO_3)_2C(OH)CH_3)]^{4-}$ and P is PO_4^{3-} [86]. The use of etidronic ligands yields both known and novel topologies. Etidronic acid ligands are coordinated to a uranyl ion by two oxygen atoms and provide the linkages between rings of polyhedra in the cage structures.

$U_{16}L_8$ and $U_{20}L_{10}$ may be compared with $\{[K_{18}Li_4][(UO_2)_{20}(HO_2CC_6H_4PO_3)_{10}(O_2)_{20}(OH)_{10}](H_2O)_n\}^{8-}$ and $\{[K_3][(UO_2)_{24}(HO_2CC_6H_4PO_3)_8(O_2)_{24}(OH)_8]-(H_2O)_n\}^{21-}$ [85], because a belt of polyhedra forms a ring around the equatorial region of the cluster, whereas rings of polyhedra are at the poles (Fig. 11a, b). Two uranyl configurations define the elongated structure of $U_{16}L_8$: four-membered rings and an eight-membered belt. The belt of uranyl hexagonal bipyramids forms a ring around the equatorial region of the cluster and polyhedra are connected by edge-sharing of peroxide in a *cis* arrangement, creating a zig-zag pattern. The belt is connected to the terminating four-membered rings through the side-on etidronic ligands. Like $U_{16}L_8$, $U_{20}L_{10}$ is capped at either end by rings of uranyl polyhedra and has a belt around the center of the cluster; however, the units in $U_{20}L_{10}$ are larger, as it has two pentamers and a 10-membered belt. This cage has a fullerene topology and is isostructural to $U_{20}Py_{10}$ [70]. K cations are associated with the five-membered rings of polyhedra. Lithium hydroxide was used in the synthesis of all of the uranyl-etidronic ligand clusters and Li is assumed to be in the structures, although the cations were not identified.

$U_{24}L_{12}$, $U_{40}L_{20}$, and $U_{64}L_8$ contain four-membered rings of uranyl polyhedra formed by edge-sharing via U-O_2-U bridges in a *cis* arrangement. $U_{24}L_{12}$ is topologically identical to $U_{24}Pp_{12}$ with etidronic ligands in the place of pyrophosphate (Fig. 11c). One of the rings in $U_{24}L_{12}$ is concave outwards, whereas all rings are concave inwards in $U_{24}Pp_{12}$. Ten four-membered rings of polyhedra connected by etidronic ligands define the novel $U_{40}L_{32}$ cage (Fig. 11d). $U_{64}L_{32}$ also has a novel configuration with 16 rings (Fig. 11e, f). Na cations are located on the concave inwards side of each of the four-membered rings, with half inside and half outside the cluster.

The cluster $U_{16}L_8P_4$ has several unique features (Fig. 11g). Similar to $U_{16}L_8$, $U_{16}L_8P_4$ is terminated at two ends by four-membered rings of polyhedra; however, the central region of $U_{16}L_8P_4$ is quite different from $U_{16}L_8$ and $U_{20}L_{10}$ because it contains dimers of uranyl pentagonal bipyramids. These dimers do not contain peroxide and, instead, are bridged by the sharing of edges defined by two hydroxyl groups. The dimers are connected by $(PO_4)^{3-}$ tetrahedra. Another unique feature of $U_{16}L_8P_4$ is a tetramer occupied by K, an observation that is a departure from the
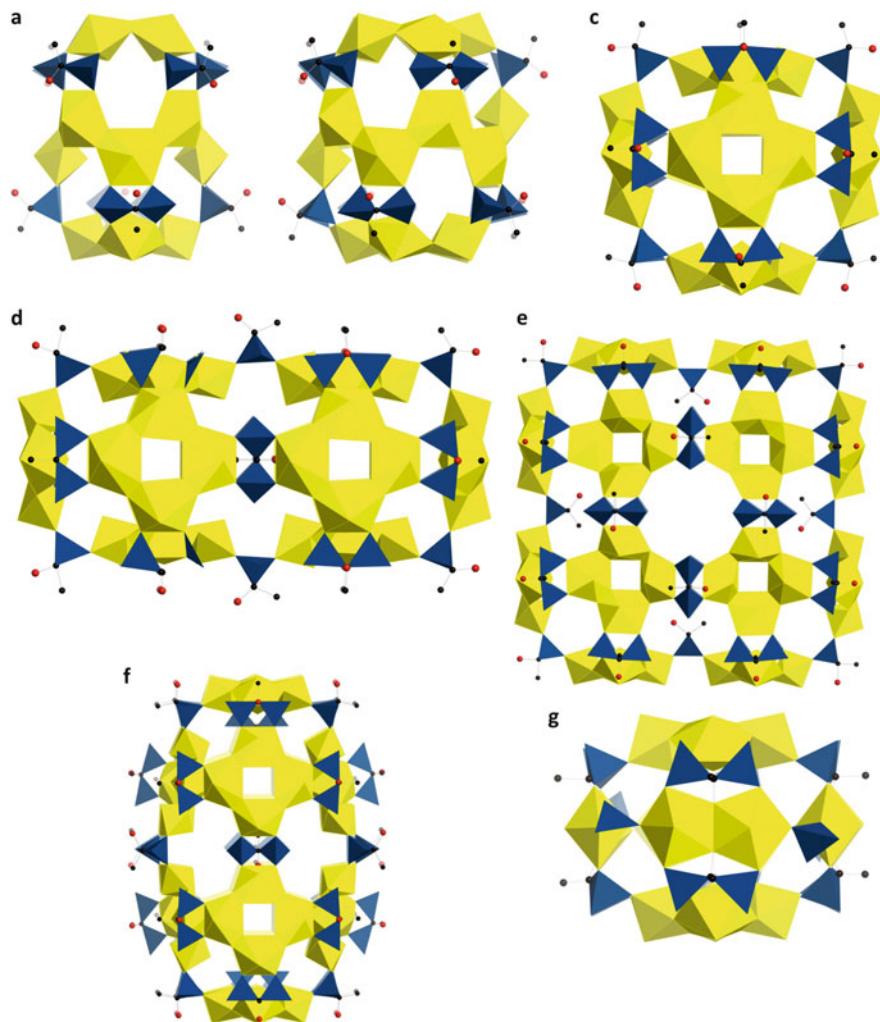
Fig. 11 The clusters (**a**) $U_{16}L_8$, (**b**) $U_{20}L_{10}$, (**c**) $U_{24}L_{12}$, (**d**) $U_{40}L_{20}$, (**e** and **f**) $U_{64}L_{32}$, and (**g**) $U_{16}L_8P_4$ that contain etidronic ligands, shown in *blue*

general trend for uranyl peroxide cage clusters. Other four-membered rings are either vacant or are occupied by Li.

4.7   Uranyl Cage Clusters Without Peroxide

The incorporation of peroxo ligands has proven to be an indispensable tool for the synthesis of large An(VI) clusters. Recently, however, several clusters were synthesized that have broadly similar structures but without peroxide ligands.
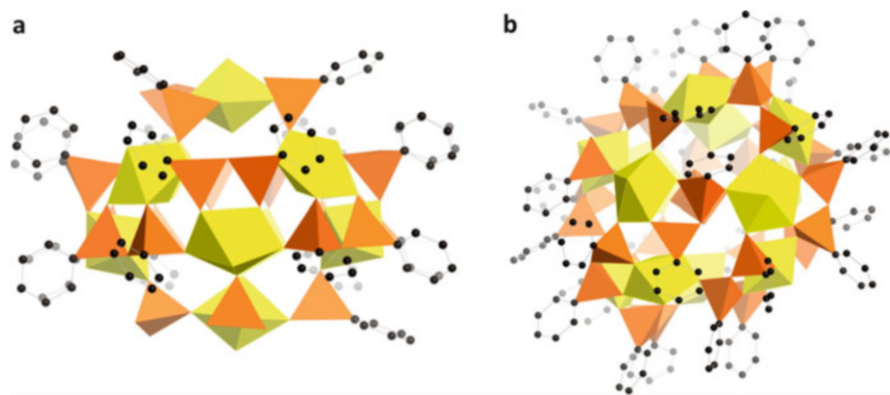
Fig. 12 Uranyl clusters containing monomers of (**a**) 10 and (**b**) 12 uranyl polyhedra connected by pyroarsonate and phenylarsonate groups, in *orange*

Adelani et al. [89] explored the use of pyroarsonate ligands in uranyl cage cluster formation with the strategy of synthesizing pyroarsenate in situ to enhance the flexibility of the ligand. From these studies, two clusters were formed: $[H_3O]_6$ $\{(UO_2)_{10}[(C_6H_5)_2As_2O_5]_8(C_6H_5AsO_3)_2(C_6H_5AsO_3H)_2(H_2AsO_4)_4(H_2O)_3\} \cdot 2H_2O$ and $[H_3O]_6\{(UO_2)_{12}[(C_6H_5)_2As_2O_5]_{12}(C_6H_5AsO_3H)_6(H_2O)_5[H_2AsO_4(H_2O)_2]$ $[H_3O]\} \cdot H_2O$ [89] (Fig. 12a, b). In both structures the uranyl polyhedra are monomeric, and the first structure contains ten of these uranyl cations, eight of which are bound by eight pyroarsonate ligands. Two hydrogen arsenates and two phenylarsonates coordinate the remaining two polyhedra. Indeed, pyroarsonate is pliable and conducive with cage cluster formation. Similar to the carboxylate moieties in the uranyl-carboxyphosphonate clusters, the phenyl rings of the phenylarsonate groups project outwards on the periphery of the structures, while the arsonate unit is bound to the uranyl cations as part of the core cage structure.

The second structure, $[H_3O]_6\{(UO_2)_{12}[(C_6H_5)_2As_2O_5]_{12}(C_6H_5AsO_3H)_6(H_2O)_5$-$[H_2AsO_4(H_2O)_2][H_3O]\} \cdot H_2O$, also has two distinct coordination environments for uranyl polyhedra: six uranyl cations bound by 12 pyroarsonate groups and two unique triangular units, where three uranyl cations are connected by three phenylarsonates. The cage encapsulates a hydrogen arsenate in octahedral coordination. These structures have only been observed crystallographically, and their assembly in solution prior to crystallization and persistence in solution subsequent to dissolution has not been demonstrated.

Two uranyl calixarene carboxylate cage structures were reported by Pasquale et al. [63] that contain 8 and 20 uranyl polyhedra (Fig. 13a). The calixarene carboxylates are located on the faces of the cages. The first cage is in the space group *Fm-3m* and contains 6 calixarene units and 8 uranyl hexagonal bipyramids. The second contains 12 calix[5]arene units and 20 uranyl ions. Also, octanuclear cages, dodecanuclear rings, and hexadecanuclear cages have been synthesized with Cu(II) or Ni(II) and Kemp's triacid (Fig. 13b) [90, 91].
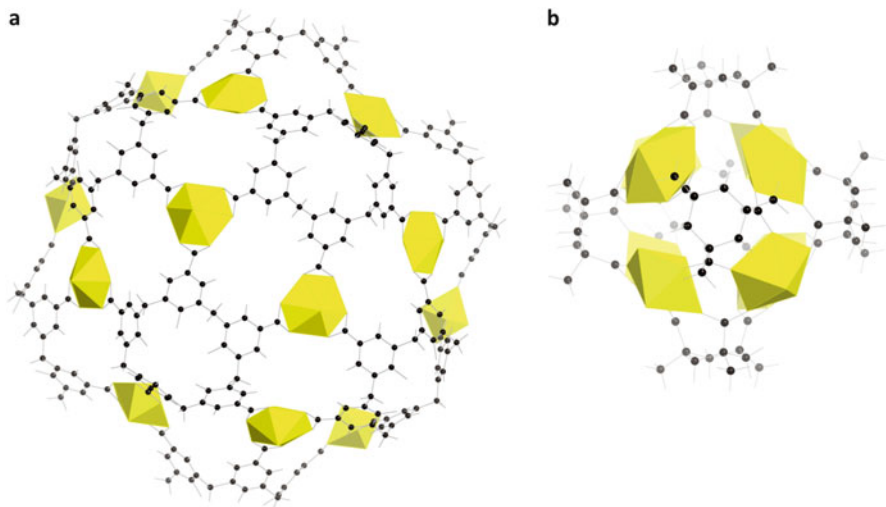
Fig. 13 (**a**) The dodecanuclear uranyl calixarene carboxylate cage cluster and (**b**) an octanuclear Kemp's triacid cluster

5 Hybrid Actinide and Transition Metal Clusters

The science of transition metal oxide clusters, commonly referred to as polyoxometalates (POMs), began long before the actinide clusters – the first POM, ammonium 12-molybdophosphate or $(NH_4)_3PMo_{12}O_{40}$aq, was described nearly 240 years ago, although it was not until much later that it was understood [92]. This field continues to advance centuries later, as an abundance of new structures with potentially useful properties are continuously discovered. Recently, actinyl peroxide cage clusters have emerged and have been compared to transition metal polyoxometalates in detail by Nyman and Burns [26]. Similarities between actinides and the d-block elements include the ability to attain multiple oxidation states and, perhaps most importantly, multiply bonding to terminal –*yl* O atoms. Like An(V) and An(VI), d^0 closed shell transition metals V(V), Nb(V), Ta(V), Mo (VI), and W(VI) may possess one or two –*yl* oxygen atoms. In contrast to actinyl O atoms, –*yl* oxygen atoms bound to transition metals are usually in a *cis* arrangement; therefore, –*yl* oxygen atoms terminate only one surface of a transition metal cluster.

The Keplerates are perhaps the most structurally similar transition metal POMs to the actinyl peroxide cage [93, 94]. These spherical POMs exist as two types: $\{M_{72}M'_{30}\}$ where M = Mo, M' = V(IV), Cr(III), Fe(III), Mo(V) and $\{M_{72}Mo_{60}\}$ where M = Mo, W [95]. Like Keplerate structures, uranyl peroxide cage clusters have similar properties such as stability in solution and the ability to exchange encapsulated cations [93]. Both have also been observed to further assemble into blackberry structures in solution [96, 97].

Nyman and Burns [26] expanded the comparison of actinyl clusters to transition metal POMs by including the broader acidic and alkaline groups of transition metals. Uranyl clusters display similarities with both groups, such as self-assembly in basic conditions and forming stable bonds with peroxide, like the alkaline transition metals. On the other hand, they also display alkali ion-associated solubility trends that are akin to the acidic transition metals. The authors also observed that Nb and Ta both form stable bonds with peroxide, but only $Nb/Ta(O_2)_4$ centered U clusters have been published. Commonalities such as these promote the idea that the two fields may meet and that hybrid structures may be realized [26].

The first transition metal polyoxometalate containing uranium was $[Na_2(UO_2)_2(PW_9O_{34})_2]^{12-}$, published by Kim et al. [98]. Other studies have reported structures of transition metal polyoxometalates that incorporate actinide cations as addenda atoms, such as sandwich complexes bridged by actinide cations. Examples include tri-lacunary heteropolyoxotungstates, which have been bridged by U, Np, and Pu cations [12, 99–104]. Previous reviews have described other hybrid actinyl-transition metal structures including a large transition metal and thorium cluster that has a core composition of $[Th_6Mn_{10}O_{22}(OH)_2]^{18+}$ [105]. Uranyl peroxide units were first incorporated into polyoxometalate structures with the synthesis of the U-shaped 36-tungsto-8-phosphate cluster containing two uranyl peroxide units, which has the total cluster composition $LiK_4\{(UO_2)_4 (\mu-O_2)_4(H_2O)_2(PO_3OH)_2P_6W_{36}O_{136}\}^{25-}$ [106].

5.1 Wheel-Shaped Structures

The wheel-shaped uranyl peroxide tungstometalate $\{[W_5O_{21}]_3[UO_2)_2(\mu-O_2)]_3\}^{30-}$, published by Miro et al. [107], is an example of a hybrid transition metal-actinide POM (Fig. 14a). Very recently, a peroxide-free wheel-shaped cluster, $(EMIm)_{15} Na_5[(UO_2)_{20}(V_2O_7)_{10}-(SO_4)_{10}]\cdot80H_2O$ (EMIm is 3-ethyl-1-methylimidazolium), was obtained using ionic liquids (Fig. 14b, c) [62]. U(VI) is in pentagonal bipyramidal geometry, and vanadium(V) is in square pyramidal coordination. The structure also includes 10 sulfate tetrahedra. Typical of POMs, vanadyl O atoms terminate the cluster, as do the uranyl O atoms. The wheel consists of two 10-membered rings of uranyl bipyramids linked by vertex-sharing to the two adjacent polyhedra. Five sulfate tetrahedra on the top and bottom of the wheel connect three uranyl polyhedra by vertex-sharing, giving the ten-membered rings rigidity. Edge-sharing dimers of vanadate polyhedra link the two uranyl sulfate rings by sharing two additional edges each with adjacent uranyl polyhedra. The dimers are also linked to each other by vertex-sharing. Na and 10 H_2O groups are encapsulated in the cluster and the exterior contains EMIm cations and disordered H_2O.
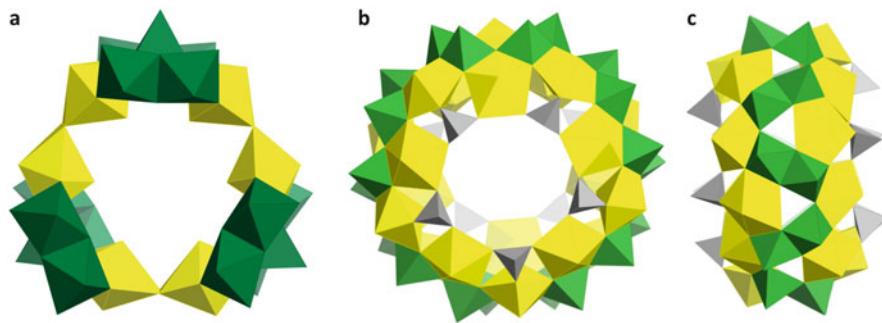
Fig. 14 Wheel-shaped hybrid transition metal clusters synthesized to date, including (**a**) $\{[W_5O_{21}]_3[U^{VI}O_2]_2(\mu\text{-}O_2)]_3\}^{30-}$ and (**b** and **c**) $U_{20}V_{20}$, with vanadium or tungsten polyhedra in *green*, and sulfate in *gray*

5.2   Hybrid Closed-Cage Structures

In the past few years, progress has been made toward transition metal incorporation into uranyl peroxide cages, where uranyl polyhedra and transition metal polyhedra are both essential components of the cage wall. Adelani et al. [108] used Ni to synthesize the first complete hybrid cage, $[H_3O]_4[Ni(H_2O)_3]_4\{Ni[(UO_2)\text{-}(PO_3C_6H_4CO_2)]_3(PO_4H)\}_4 \cdot 2.72H_2O$, although its presence in solution was not demonstrated. In contrast to the hexagonal bipyramids in most uranyl peroxide cage clusters, this cluster has only pentagonal bipyramids that share edges to form dimers (Fig. 15). It contains six dimers of uranyl pentagonal bipyramids in addition to eight Ni(II) octahedra, four of which are included in the core structure by sharing three vertices with uranyl bipyramids and phosphonate groups. The remaining Ni (II) polyhedra are located on the exterior of the cluster, where they are held onto the structure by the 2-carboxyphenyl phosphonate ligands. The phenyl groups of the 2-carboxyphenylphosphonate ligands extend from the core structure and are the terminal ligands.

More recently, Ling et al. [76] reported several hybrid uranyl-transition metal cage clusters ($U_{50}W_6P_{20}$, $U_{44}Mo_2P_{16}$, $U_{28}W_4P_{12}$, $U_{28}Mo_4P_{12}$, $U_{18}W_2P_{12}$, and $U_{48}W_6P_{48}$) containing uranyl peroxide polyhedra, tungsten or molybdenum units, and phosphate tetrahedra. Compared to previously described cage clusters, these six clusters have novel topologies and configurations of U(VI), including rings of polyhedra containing 7, 8, 10, and 12 members. These rings are the largest in uranyl peroxide cage clusters that do not form equatorial belts around their clusters, a configuration that is possible because select peroxo ligands are in a *trans* arrangement. This was only previously reported for belts of uranyl polyhedra in $U_{22}PO_3$ and $U_{28}PO_3$ [60]. Tungsten and molybdenum may play the role of stabilizing rings of polyhedra, where they share vertices with uranyl polyhedra. All of these structures contain Li counterions that, although not resolved in the crystal
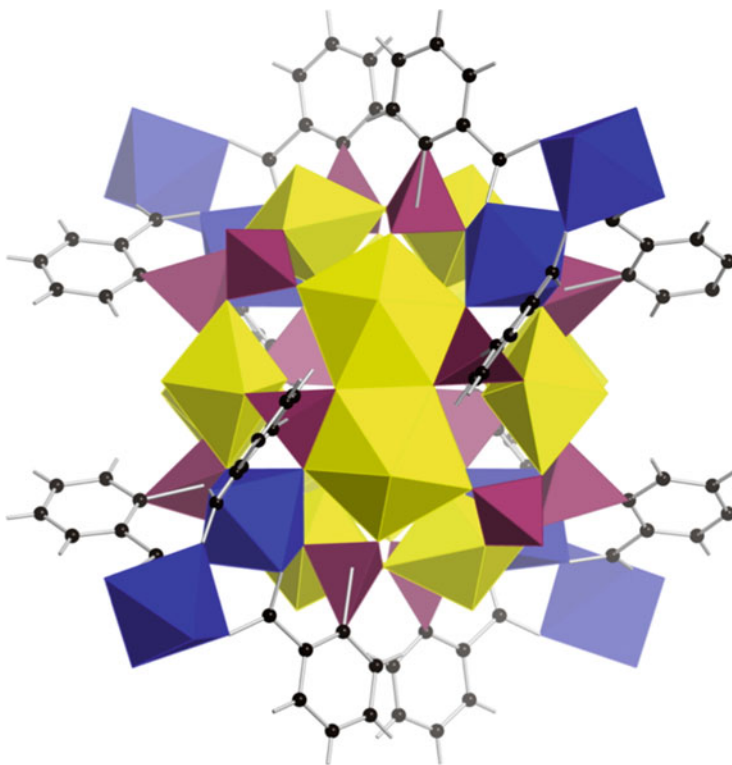
Fig. 15 The hybrid closed-cage structure $[H_3O]_4[Ni(H_2O)_3]_4\{Ni[(UO_2)-(PO_3C_6H_4CO_2)]_3$ $(PO_4H)\}_4 \cdot 2.72H_2O$. Ni(II) polyhedra are *blue* and phosphonate groups are in *pink*

structures, are presumed to be encapsulated by and located on the outside of the clusters to balance negative charges.

$U_{50}W_6P_{20}$ and $U_{44}Mo_2P_{16}$ [76] contain uranyl in hexagonal bipyramidal coordination (Fig. 16a, b). The majority of the hexagonal bipyramids are analogous to those found in most uranyl peroxide cage clusters: three edges are shared with adjacent polyhedra and two of the shared edges are peroxide bridges in a *cis* configuration. $U_{44}Mo_2P_{16}$ also has hexagonal bipyramids with only one bidentate peroxide group. $U_{50}W_6P_{20}$ and $U_{44}Mo_2P_{16}$ have an additional 18 and 14 uranyl hexagonal bipyramids, respectively, that share edges with only two other polyhedra through peroxide bridges in *trans* configuration. Two of these polyhedra in $U_{44}Mo_2P_{16}$ are unique because they also share vertices with each other, resulting in tetramers formed by vertex- and edge-sharing. Both clusters have six-membered rings of edge-sharing polyhedra that are analogous to those described previously for uranyl peroxide cage clusters, and $U_{44}Mo_2P_{16}$ also has five-membered rings of polyhedra.

Fig. 16 (**a**) $U_{50}W_6P_{20}$, (**b**) $U_{44}Mo_2P_{16}$, (**c**) $U_{28}W_4P_{12}$, (**c**) $U_{28}Mo_4P_{12}$, (**d**) $U_{18}W_2P_{12}$, and (**e**) $U_{48}W_6P_{48}$ are shown. W and Mo tetrahedra are both *green* and phosphate are *red*

The *trans* configuration of peroxide groups about uranyl allows the formation of novel seven- and eight-membered rings of uranyl polyhedra in both $U_{50}W_6P_{20}$ and $U_{44}Mo_2P_{16}$. Each of the eight-membered rings features two $(H_2PO_4)^-$ tetrahed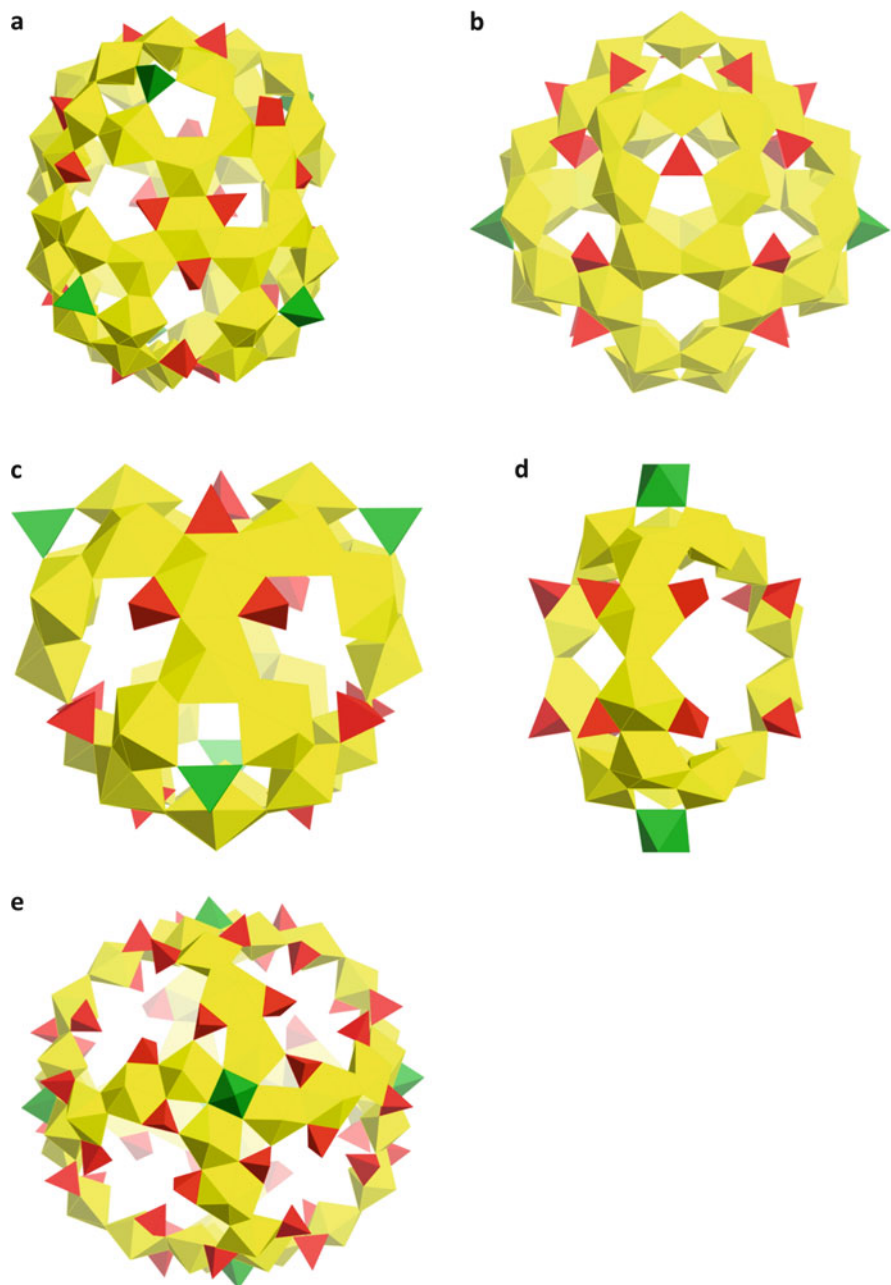ra that are bidentate to the uranyl polyhedra and extend into the voids of the rings. The voids of the seven-membered rings contain the transition metal polyhedra, $(WO_3OH)^-$ and $(MoO_3OH)^-$ for $U_{50}W_6P_{20}$ and $U_{44}Mo_2P_{16}$, respectively. The tetrahedra share vertices with three uranyl polyhedra of the ring, dividing the seven-membered rings into two topological squares and a pentagon. $U_{44}Mo_2P_{16}$ has four seven-membered rings but only two $(MoO_3OH)^-$ tetrahedra – the two remaining seven-membered rings have $(HPO_4)^{2-}$ tetrahedra located at the center.

$U_{28}W_4P_{12}$ and $U_{28}Mo_4P_{12}$ [76] are isostructural clusters that contain $(WO_3OH)^-$ or $(MoO_3OH)^-$ tetrahedra, respectively (Fig. 16c). *Trans* $U\text{-}O_2\text{-}O$ bridges in the structure yield eight-membered rings analogous to those in $U_{50}W_6P_{20}$ and $U_{44}Mo_2P_{16}$, with two bidentate $(H_2PO_4)^-$ tetrahedra that extend into the void of the ring. In contrast to the previously described clusters, $(WO_3OH)^-$ or $(MoO_3OH)^-$ tetrahedra are coordinated to uranyl ions at the center of six-membered rings instead of seven-membered rings. These six-membered rings contain alternating two-edge-sharing polyhedra, with peroxide in *trans* configuration, and three-edge-sharing polyhedra.

A more definitive departure from typical uranyl peroxide cage cluster topologies is displayed by the cluster $U_{18}W_2P_{12}$, which has two $(WO_3(OH)_3)^{3-}$ octahedra and 12 $(H_2PO_4)^-$ tetrahedra in addition to uranyl hexagonal bipyramids (Fig. 16d). The majority of uranyl polyhedra make up three 10-membered rings of polyhedra that extend from pole to pole, unlike any previously reported configuration for uranyl peroxide cage clusters. The polar regions are terminated by two six-membered rings of uranyl polyhedra that are topologically identical to those in $U_{28}W_4P_{12}$ and $U_{28}Mo_4P_{12}$; however, $(WO_3(OH)_3)^{3-}$ octahedra share three vertices with uranyl polyhedra, dividing the ring into three topological squares. $U_{18}W_2P_{12}$ is the first example of a uranyl peroxide cage cluster that has direct linkages between clusters. $(WO_3(OH)_3)^{3-}$ octahedra share faces with $(WO_3(OH)_3)^{3-}$ octahedra of the neighboring cluster, connecting the $U_{18}W_2P_{12}$ clusters into chains.

The remaining hybrid uranyl-transition metal peroxide cage cluster synthesized by Ling et al. [76] is $U_{48}W_6P_{48}$, which has 6 $(WO_4OH)^{3-}$ square pyramids, 24 $(HPO_4)^{2-}$ tetrahedra, and 24 $(H_2PO_4)^-$ tetrahedra (Fig. 16e). The uranyl configuration of this cluster is similar to $U_{22}PO_3$ [60] in that it contains $U\text{-}O_2\text{-}U$ bridged hexagonal bipyramids that share exclusively two edges and that are incorporated into four-membered belts terminated by pentagonal bipyramids. Unlike $U_{22}PO_3$, where peroxide bridges the hexagonal and pentagonal bipyramids, the hexagonal bipyramids in $U_{48}W_6P_{48}$ share edges with pentagonal bipyramids through O atoms donated by bidentate $(H_2PO_4)^-$ tetrahedra. The uranyl pentagonal bipyramids also share two vertices with adjacent pentagonal bipyramids. This cluster is the first cage cluster to have 12-membered rings of uranyl polyhedra although it has a relatively simple topology composed of only 4- and 12-membered rings. The six tetramers are made up of four vertex-sharing pentagonal bipyramids coordinated at the center by

the $(WO_4OH)^{3-}$ square pyramids. Each of the polyhedra in the four-membered ring is shared with the two of the four adjacent 12-membered rings.

6 Conclusions

Despite being a relatively new field of study, there is already an extensive library of actinide oxo clusters, especially in the case of uranyl peroxide cage clusters. It is now apparent that the topological and compositional complexity of actinide oxo clusters rivals that found for transition metal polyoxometalates over the past several decades. Many more variations in actinide oxo clusters will likely be described over the next few years. Efforts focused on potential applications in the nuclear-fuel cycle may also be fruitful, as the behavior of actinide oxo clusters in solution will in many cases be markedly different from that of simple species. Conditions in nuclear accident scenarios, such as where water is interacting with the damaged reactor cores at Fukushima, Japan, and in geologic repositories for nuclear waste, are potentially conducive to formation of actinide oxo clusters, in which case they may be important for environmental transport of actinides and repository performance.

References

1. Neidig ML, Clark DL, Martin RL (2013) Covalency in f-element complexes. Coord Chem Rev 257(2):394–406
2. Morss LR et al (2006) In: Morss LR, Edelstein NM, Fuger J, Katz JJ (ed) The chemistry of the actinide and transactinide elements, 3rd edn. Springer, Dordrecht
3. Cary SK et al (2015) Emergence of californium as the second transitional element in the actinide series. Nat Commun 6:8
4. Maly J et al (1968) Nobelium - tracer chemistry of divalent and trivalent ions. Science 160 (3832):1114
5. Polinski MJ et al (2014) Unusual structure, bonding and properties in a californium borate. Nat Chem 6(5):387–392
6. Abdelouas A (2006) Uranium mill tailings: geochemistry, mineralogy, and environmental impact. Elements 2(6):335–341
7. Kersting AB et al (1999) Migration of plutonium in ground water at the Nevada Test Site. Nature 397(6714):56–59
8. Stubbs JE et al (2009) Newly recognized hosts for uranium in the Hanford Site vadose zone. Geochimica Et Cosmochimica Acta 73(6):1563–1576
9. Knope KE et al (2012) Thorium(IV)-selenate clusters containing an octanuclear Th (IV) hydroxide/oxide core. Inorg Chem 51(7):4239–4249

10. Wylie EM et al (2014) Ultrafiltration of URANYL PEROXIDE NANOCLUSTERS FOR THE SEPARATION OF URANIUM FROM AQUEOUS SOLUTION. ACS Appl Mater Interfaces 6(1):473–479

11. Qiu J, Burns PC (2013) Clusters of actinides with oxide, peroxide, or hydroxide bridges. Chem Rev 113(2):1097–1120

12. Copping R et al (2009) Probing the 5f electrons in a plutonyl(VI) cluster complex. Dalton Trans 29:5609–5611

13. Denning RG et al (2002) Covalency in the uranyl ion: a polarized x-ray spectroscopic study. J Chem Phys 117(17):8008–8020

14. Denning RG (2007) Electronic structure and bonding in actinyl ions and their analogs. J Phys Chem A 111(20):4125–4143

15. Burns PC, Ewing RC, Hawthorne FC (1997) The crystal chemistry of hexavalent uranium: polyhedron geometries, bond-valence parameters, and polymerization of polyhedra. Can Mineral 35:1551–1570

16. Denning RG (1992) Electronic-structure and bonding in actinyl ions. Struct Bond 79:215–276

17. La Pierre HS et al (2015) Charge control of the inverse trans-influence. Chem Commun 51 (93):16671–16674

18. La Pierre HS, Meyer K (2013) Uranium-ligand multiple bonding in uranyl analogues, L=U=L (n+), and the inverse trans influence. Inorg Chem 52(2):529–539

19. O'Grady E, Kaltsoyannis N (2002) On the inverse trans influence. Density functional studies of MOX(5) (n-) (M=Pa, n=2; M=U, n=1; M=Np, n=0; X=F, Cl or Br). J Chem Soc Dalton Trans 2002(6):1233–1239

20. Chermette H, Rachedi K, Volatron F (2006) Trans effect and inverse trans effect in MLX5 complexes (M=Mo, U; L=O, S; X=Cl, Br): a rationalization within density functional theory study. J Mol Struct THEOCHEM 762(1–3):109–121

21. Burns PC (2005) U6+ minerals and inorganic compounds: insights into an expanded structural hierarchy of crystal structures. Can Mineral 43:1839–1894

22. Forbes TZ, Wallace C, Burns PC (2008) Neptunyl compounds: polyhedron geometries, bond-valence parameters, and structural hierarchy. Can Mineral 46:1623–1645

23. Krot NN, Grigoriev MS (2004) Cation-cation interaction in crystalline actinide compounds. Uspekhi Khimii 73(1):94–106

24. Duval PB et al (2001) Synthesis and structural characterization of the first uranium cluster containing an isopolyoxometalate core. Angew Chem Int Ed 40(18):3358

25. Burns PC et al (2005) Actinyl peroxide nanospheres. Angew Chem Int Ed 44(14):2135–2139

26. Nyman M, Burns PC (2012) A comprehensive comparison of transition-metal and actinyl polyoxometalates. Chem Soc Rev 41(22):7354–7367

27. Salmon L, Thuery P, Ephritikhine M (2006) Polynuclear uranium(IV) compounds with (mu (3)-oxo)U-3 or (mu(4)-oxo)U-4 cores and compartmental Schiff base ligands. Polyhedron 25 (7):1537–1542

28. Rogers RD, Bond AH, Witt MM (1991) Macrocycle complexation chemistry 34. Polyethylene-glycol and glycolate complexes of Th^{4+}. Preparation and structural characterization of ThCl$_3$(Pentaethylene glycol) Cl.CH$_3$CN and the (Th^{4+})$_4$ cluster, [Th$_4$Cl$_8$(O) (Tetraethylene glycolate)$_3$].3CH$_3$CN. Inorg Chim Acta 182(1):9–17

29. Brianese N et al (1989) Reactivity of dicyclopentadienyluranium(IV) derivatives: formation and structural characterization of an oxygen bridged cluster containing both inorganic and organometallic uranium atoms. J Organomet Chem 365(3):223–232

30. Diwu J, Wang S, Albrecht-Schmitt TE (2012) Periodic trends in hexanuclear actinide clusters. Inorg Chem 51(7):4088–4093

31. Hennig C et al (2012) Structure and stability range of a hexanuclear Th(IV)-glycine complex. Dalton Trans 41(41):12818–12823

32. Hu YJ et al (2013) Understanding the ligand-directed assembly of a hexanuclear Th-IV molecular cluster in aqueous solution. Eur J Inorg Chem 2013(24):4159–4163

33. Knope KE et al (2011) Thorium(IV) molecular clusters with a hexanuclear Th core. Inorg Chem 50(19):9696–9704
34. Takao K et al (2012) Formation of soluble hexanuclear neptunium(IV) Nanoclusters in aqueous solution: growth termination of actinide(IV) hydrous oxides by carboxylates. Inorg Chem 51(3):1336–1344
35. Takao S et al (2009) First hexanuclear UIV and ThIV formate complexes – structure and stability range in aqueous solution. Eur J Inorg Chem 2009(32):4771–4775
36. Vasiliu M et al (2012) Spectroscopic and energetic properties of thorium(IV) molecular clusters with a hexanuclear core. J Phys Chem A 116(25):6917–6926
37. Zhang Y et al (2015) Synthesis, spectroscopic characterization and crystal structures of thorium(IV) mononuclear lactato and hexanuclear formato complexes. Polyhedron 87:377–382
38. Berthet J-C, Thuery P, Ephritikhine M (2010) Formation of uranium(IV) oxide clusters from uranocene U(eta(8)-C8H8)(2) and uranyl UO2X2 compounds. Inorg Chem 49(17):8173–8177
39. Nocton G et al (2010) Ligand assisted cleavage of uranium oxo-clusters. Chem Commun 46(16):2757–2759
40. Knope KE, Soderholm L (2013) Plutonium(IV) cluster with a hexanuclear Pu-6(OH)(4)O-4 (12+) core. Inorg Chem 52(12):6770–6772
41. Pan L et al (2008) Synthesis and structural determination of a hexanuclear zirconium glycine compound formed in aqueous solution. Inorg Chem 47(13):5537–5539
42. Lundgren G (1956) The crystal structure of Ce6O4(OH)4(SO4)6. Ark Kemi 10(2):183–197
43. Miersch L et al (2010) A novel water-soluble hexanuclear bismuth oxido cluster - synthesis, structure and complexation with polyacrylate. Eur J Inorg Chem 30:4763–4769
44. Diwu J et al (2011) Self-assembly of hexanuclear clusters of 4f and 5f elements with cation specificity. Eur J Inorg Chem 2011(9):1374–1377
45. Falaise C et al (2013) Three-dimensional MOF-type architectures with tetravalent uranium hexanuclear motifs (U6O8). Chemistry 19(17):5324–5331
46. Xiao B et al (2015) Chemical and structural evolution in the Th-SeO32-/SeO42- system: from simple selenites to cluster-based selenate compounds. Inorg Chem 54(6):3022–3030
47. Biswas B et al (2011) Base-driven assembly of large uranium oxo/hydroxo clusters. Angew Chem Int Ed 50(25):5744–5747
48. Woidy P, Kraus F (2014) Th-10(mu-F-16)(mu(3)-O-4)(mu(4)-O-4)(NH3)(32) (NO3)(8) center dot 19.6 NH3 - the largest thorium complex from solution known to date. Zeitschrift Fur Anorganische Und Allgemeine Chemie 640(8–9):1547–1550
49. Nocton G et al (2007) Self-assembly of polyoxo clusters and extended frameworks by controlled hydrolysis of low-valent uranium. Angew Chem Int Ed 46(40):7574–7578
50. Soderholm L et al (2008) The structure of the plutonium oxide nanocluster Pu38O56Cl54 (H2O)(8) (14-). Angew Chem Int Ed 47(2):298–302
51. Wilson RE, Skanthakumar S, Soderholm L (2011) Separation of plutonium oxide nanoparticles and colloids. Angew Chem Int Ed 50(47):11234–11237
52. Powell BA et al (2004) Pu(V)O-2(+) adsorption and reduction by synthetic magnetite (Fe3O4). Environ Sci Technol 38(22):6016–6024
53. Powell BA et al (2005) PU(V)0(2)(+) adsorption and reduction by synthetic hematite and goethite. Environ Sci Technol 39(7):2107–2114
54. Zimmerman T, Zavarin M, Powell BA (2014) Influence of humic acid on plutonium sorption to gibbsite: determination of Pu-humic acid complexation constants and ternary sorption studies. Radiochim Acta 102(7):629–643
55. Hixon AE, Powell BA (2014) Observed changes in the mechanism and rates of Pu (V) reduction on hematite as a function of total plutonium concentration. Environ Sci Technol 48(16):9255–9262
56. Powell BA et al (2011) Stabilization of plutonium nano-colloids by epitaxial distortion on mineral surfaces. Environ Sci Technol 45(7):2698–2703

57. Falaise C et al (2013) Isolation of the large {Actinide}(38) poly-oxo cluster with uranium. J Am Chem Soc 135(42):15678–15681
58. Copping R et al (2012) A tetrameric neptunyl(v) cluster supported by a Schiff base ligand. Dalton Trans 41(36):10900–10902
59. Mougel V et al (2009) Stable pentavalent uranyl species and selective assembly of a polymetallic mixed-valent uranyl complex by cation-cation interactions. Angew Chem Int Ed 48(45):8477–8480
60. Qiu J et al (2013) Time-resolved assembly of chiral uranyl peroxo cage clusters containing belts of polyhedra. Inorg Chem 52(1):337–345
61. Burns PC (2011) Nanoscale uranium-based cage clusters inspired by uranium mineralogy. Mineral Mag 75(1):1–25
62. Senchyk GA et al (2015) Hybrid uranyl-vanadium nano-wheels. Chem Commun 51 (50):10134–10137
63. Pasquale S et al (2012) Giant regular polyhedra from calixarene carboxylates and uranyl. Nat Commun 3:785
64. Sigmon GE et al (2009) Symmetry versus minimal pentagonal adjacencies in uranium-based polyoxometalate fullerene topologies. Angew Chem Int Ed 48(15):2737–2740
65. Kroto HW et al (1985) C-60 - buckminsterfullerene. Nature 318(6042):162–163
66. Sigmon GE et al (2009) Crown and bowl-shaped clusters of uranyl polyhedra. Inorg Chem 48 (23):10907–10909
67. Ling J, Qiu J, Burns PC (2012) Uranyl peroxide oxalate cage and core-shell clusters containing 50 and 120 uranyl ions. Inorg Chem 51(4):2403–2408
68. Qiu J et al (2012) Time-resolved self-assembly of a fullerene-topology core-shell cluster containing 68 uranyl polyhedra. J Am Chem Soc 134(3):1810–1816
69. Qiu J et al (2014) Water-soluble multi-cage super tetrahedral uranyl peroxide phosphate clusters. Chem Sci 5(1):303–310
70. Ling J et al (2010) Uranium pyrophosphate/methylenediphosphonate polyoxometalate cage clusters. J Am Chem Soc 132(38):13395–13402
71. Forbes TZ et al (2008) Metal-oxygen isopolyhedra assembled into fullerene topologies. Angew Chem Int Ed 47(15):2824–2827
72. Burns PC, Ewing RC, Navrotsky A (2012) Nuclear fuel in a reactor accident. Science 335 (6073):1184–1188
73. Liu Y et al (2015) Extraction of uranyl peroxo clusters from aqueous solution by mesoporous silica SBA-15. J Radioanal Nucl Chem 303(3):2257–2262
74. Unruh DK et al (2011) Complex nanoscale cage clusters built from uranyl polyhedra and phosphate tetrahedra. Inorg Chem 50:5509–5516
75. Sigmon GE et al (2009) Uranyl-peroxide interactions favor nanocluster self-assembly. J Am Chem Soc 131(46):16648
76. Ling J et al (2014) Hybrid uranium-transition-metal oxide cage clusters. Inorg Chem 53 (24):12877–12884
77. Vlaisavljevich B, Gagliardi L, Burns PC (2010) Understanding the structure and formation of uranyl peroxide nanoclusters by quantum chemical calculations. J Am Chem Soc 132 (41):14503–14508
78. Miro P et al (2010) On the origin of the cation templated self-assembly of uranyl-peroxide nanoclusters. J Am Chem Soc 132(50):17787–17794
79. Qiu J et al (2015) Cation templating and electronic structure effects in uranyl cage clusters probed by the isolation of peroxide-bridged uranyl dimers. Inorg Chem 54(9):4445–4455
80. Alam TM et al (2014) Solid-state dynamics of uranyl polyoxometalates. Chemistry 20 (27):8302–8307
81. Liao ZL, Deb T, Nyman M (2014) Elucidating self-assembly mechanisms of uranyl peroxide capsules from monomers. Inorg Chem 53(19):10506–10513
82. Nyman M, Rodriguez MA, Alam TM (2011) The U-28 nanosphere: what's inside? Eur J Inorg Chem 14:2197–2205

83. Ling J et al (2012) Uranyl peroxide pyrophosphate cage clusters with oxalate and nitrate bridges. Dalton Trans 41(24):7278–7284
84. Ling J et al (2010) Hybrid uranium-oxalate fullerene topology cage clusters. Angew Chem Int Ed 49(40):7271–7273
85. Adelani PO et al (2013) Hybrid uranyl-carboxyphosphonate cage clusters. Inorg Chem 52 (13):7673–7679
86. Liao ZL et al (2013) Cage clusters built from uranyl ions bridged through peroxo and 1-hydroxyethane-1,1-diphosphonic acid ligands. Dalton Trans 42(19):6793–6802
87. Burns PC, Hughes KA (2003) Studtite, (UO2)(O-2)(H2O)(2) (H2O)(2): the first structure of a peroxide mineral. Am Mineral 88(7):1165–1168
88. Qiu J et al (2014) Expanding the crystal chemistry of uranyl peroxides: four hybrid uranyl-peroxide structures containing EDTA. Inorg Chem 53(22):12084–12091
89. Adelani PO, Sigmon GE, Burns PC (2013) Hybrid uranyl arsonate coordination nanocages. Inorg Chem 52(11):6245–6247
90. Thuery P (2014) Increasing complexity in the Uranyl Ion-Kemp's Triacid System: from one- and two-dimensional polymers to uranyl-copper(II) dodeca- and hexadecanuclear species. Cryst Growth Des 14(5):2665–2676
91. Thuery P (2014) A highly adjustable coordination system: nanotubular and molecular cage species in uranyl ion complexes with Kemp's triacid. Cryst Growth Des 14(3):901–904
92. Berzelius JJ (1826) Poggend. Ann Phys Chem 6:369
93. Muller A et al (1998) Organizational forms of matter: an inorganic super fullerene and Keplerate based on molybdenum oxide. Angew Chem Int Ed 37(24):3360–3363
94. Kortz U et al (2009) Polyoxometalates: fascinating structures, unique magnetic properties. Coord Chem Rev 253(19–20):2315–2327
95. Muller A, Gouzerh P (2012) From linking of metal-oxide building blocks in a dynamic library to giant clusters with unique properties and towards adaptive chemistry. Chem Soc Rev 41(22):7431–7463
96. Liu TB (2002) Supramolecular structures of polyoxomolybdate-based giant molecules in aqueous solution. J Am Chem Soc 124(37):10942–10943
97. Li D et al (2014) Evolution of actinyl peroxide clusters U-28 in dilute electrolyte solution: exploring the transition from simple ions to macroionic assemblies. Chemistry 20 (6):1683–1690
98. Kim K-C, Pope MT (1999) Cation-directed structure changes in polyoxometalate chemistry. Equilibria between isomers of Bis(9-tungstophosphatodioxouranate(VI)) complexes. J Am Chem Soc 121(37):8512–8517
99. Berg JM et al (2015) Unexpected actinyl cation-directed structural variation in neptunyl (VI) A-type tri-lacunary heteropolyoxotungstate complexes. Inorg Chem 54(9):4192–4199
100. Kim KC, Gaunt A, Pope MT (2002) New heteropolytungstates incorporating dioxouranium (VI). Derivatives of alpha- SiW9O34 (10-), alpha- AsW9O33 (9-), gamma- SiW10O36 (8-), and As4W40O140 (28-). J Clust Sci 13(3):423–436
101. Khoshnavazi R et al (2007) Syntheses and structural determination of new bis (9-tungstoarsenato)tris(dioxouranate(VI)) and its mono oxovanadate(IV) derivative com- plexes. Inorg Chim Acta 360(2):686–690
102. Tan RX et al (2006) Polyoxotungstates containing uranyl group: Germanotungstates with Keggin sandwich structure. Inorg Chem Commun 9(12):1331–1334
103. Khoshnavazi R et al (2006) Syntheses and structures determination of new polytungstoarsenates Na2As2W18U2O72 (12-) and MAs2W18U2O72 (13-) (M=NH4+ and K+). Polyhedron 25(9):1921–1926
104. Gaunt AJ et al (2002) The first structural and spectroscopic characterization of a neptunyl polyoxometalate complex. J Am Chem Soc 124(45):13350–13351
105. Mishra A et al (2007) High-nuclearity Ce/Mn and Th/Mn cluster chemistry: preparation of complexes with Ce4Mn10O10(OMe)(6) (18+) and Th6Mn10O22(OH)(2) (18+) cores. Inorg Chem 46(8):3105–3115

106. Mal SS, Dickman MH, Kortz U (2008) Actinide polyoxometalates: incorporation of uranyl-peroxo in U-shaped 36-tungsto-8-phosphate. Chemistry 14(32):9851–9855
107. Miro P et al (2012) Experimental and computational study of a new wheel-shaped {W5O21 (3) ((UO2)-O-VI)(2)(mu-O-2) (3)}(30-) polyoxometalate. Inorg Chem 51(16):8784–8790
108. Adelani PO, Oliver AG, Albrecht-Schmitt TE (2012) Uranyl heteropolyoxometalate: synthesis, structure, and spectroscopic properties. Inorg Chem 51(9):4885–4887

Construction and Luminescence Properties of 4f and d-4f Clusters with Salen-Type Schiff Base Ligands

Xiaoping Yang, Shiqing Wang, Chengri Wang, Shaoming Huang, and Richard A. Jones

Abstract The synthesis, crystal structures, and photophysical properties of twenty-three 4f and d-4f clusters based on eight salen-type Schiff base ligands are described in this chapter. Most of these lanthanide-based clusters exhibit interesting "enclosed" structures, such as multi-decker, "twisted," and drum-like structures. In these polynuclear complexes, the multidentate salen-type ligands can efficiently sensitize lanthanide emissions by serving as antennas that absorb excitation light and transfer the energy to the lanthanide centers. With the lanthanide ions encapsulated by chromophoric salen-type ligands and shielded from solvent molecules which can quench the emissions from lanthanide ions, those lanthanide-based clusters with "enclosed" structures show impressive luminescence properties.

Keywords 4f and d-4f clusters • Crystal structures • Luminescence properties • Salen-type Schiff base ligands • Synthesis

Contents

X. Yang (✉), S. Wang, C. Wang, and S. Huang (✉)
College of Chemistry and Materials Engineering, Wenzhou University, Wenzhou 325035, China
e-mail: xpyang@wzu.edu.cn; smhuang@wzu.edu.cn

R.A. Jones (✉)
Department of Chemistry and Biochemistry, The University of Texas at Austin, 1 University Station A5300, Austin, TX 78712, USA
e-mail: rajones@cm.utexas.edu

1   Introduction

Metal clusters have emerged as a new class of materials and have recently attracted considerable interest [1–7]. Polynuclear lanthanide (4f) homometallic and d-block transition metal–lanthanide (d-4f) heterometallic clusters with well-defined structures and interesting properties are currently of interest for their potential applications in magnetism, optoelectronics, and as porous materials [8–10]. Self-assembly by metal–ligand coordination is one of the most efficient processes whereby individual molecular components organize into higher nuclearity or polymeric species. However, compared to coordination frameworks of the d-block transition metals, the construction of polynuclear lanthanide complexes is more challenging. This may be due to the difficulty in controlling the coordination environment of Ln (III) ions which often display high and variable coordination numbers [11, 12]. A general strategy for the synthesis of lanthanide-based clusters is to control the hydrolysis of lanthanide ions by organic ligands. Several reports have also focused on polynuclear 4f and 3d-4f clusters (i.e., Cu/Ln [13], Mn/Ln [14–16], and Ni/Ln [17–19]) with small rigid ligands such as multicarboxylic acids, iminodiacetic acids, pyridinecarboxylate, and carbonyl ligands in order to obtain single-molecule magnets with large values of the magnetocaloric effect (MCE). In contrast, luminescent polynuclear 4f and d-4f systems have received much less attention. Lanthanide-based clusters with distinct luminescent properties have potential use in applications involving the fabrication of novel materials and as probes in biological systems [20]. Due to the core nature of 4f electrons, which are shielded from the coordination environment by the $5s^2 5p^6$ electrons, the emission bands of Ln^{III} ions based on f–f transitions are narrow and ion-specific, leading to pure colors and potentially high emission efficiencies [21]. In d-4f clusters, light-absorbing d-block metal chromophores (i.e., Pt^{II} [22, 23], Ru^{II} [24, 25], Zn^{II} [26, 27], Cr^{II} [28, 29], and Cd^{II} [30, 31]) can act as sensitizers for visible and NIR luminescence from Ln(III) centers following ligand $\rightarrow$ f and d $\rightarrow$ f energy-transfers. For example, as shown in Scheme 1, indirect excitation (called sensitization or antenna effect) has to be used and proceeds in three steps. First, light is absorbed by the immediate environment of the Ln(III) ion through the attached organic ligands (chromophores). Energy is then transferred onto one or several excited states of the metal ion. Finally, the metal ion emits light.

Compartmental Schiff bases with two dissimilar metal-binding sites, one being specific for the d metal ion and another for the f metal ion, are classical ligands which have been employed to synthesize lanthanide-based complexes [32, 33]. Recent studies in our laboratories have focused on the construction of

Scheme 1 Simplified diagram showing the main energy flow paths during sensitization of lanthanide luminescence via its surroundings (ligands)
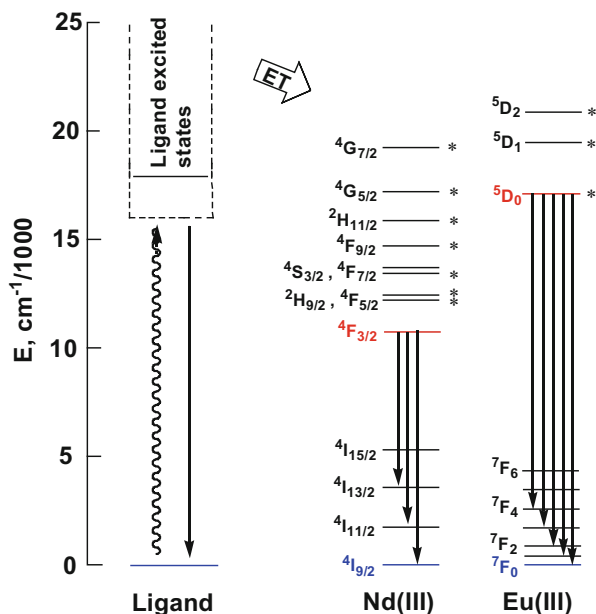
luminescent polynuclear lanthanide complexes with various Schiff base ligands (Scheme 2). For example, it has been found that rigid conjugated Schiff base ligands with phenylene backbones, such as $H_2L^{1,2}$ (Scheme 2), tended to form "multi-decker" 4f and d-4f complexes, while the use of Schiff base ligands with flexible carbon–carbon backbones, for example, H_2L^{3-8} (Scheme 2), resulted in various 4f and d-4f polynuclear complexes (d = Ni^{2+}, Cu^{2+}, Zn^{2+}, and Cd^{2+}). In this chapter, we describe the synthesis, crystal structures, and luminescence properties of twenty-three 4f and d-4f clusters based on salen-type Schiff base ligands H_2L^{1-8}. In these lanthanide-based clusters, the salen-type ligands not only stabilize lanthanide centers in the formation of polynuclear assemblies but also act as antennas that sensitize the luminescence of lanthanide ions. The overall fluorescence quantum yields were determined by using $[Ru(bipy)_3]Cl_2$ (bipy = 2,2'-bipyridine, $\Phi_{em} = 0.028$ in water) and quinine sulfate ($\Phi_{em} = 0.546$ in 0.5 M H_2SO_4) as standard for the Tb(III) and Eu(III) clusters, respectively.

2 Luminescent Lanthanide Clusters with Salen-Type Ligands

Some lanthanide ions, such as Nd^{3+}, Eu^{3+}, Tb^{3+}, Er^{3+}, and Yb^{3+}, are attractive luminescent centers due to their long-lived excited states and their large Stokes' Shifts. However, the photophysical properties of these ions depend markedly on their environments. For efficient emissions, chromophoric ligands are often
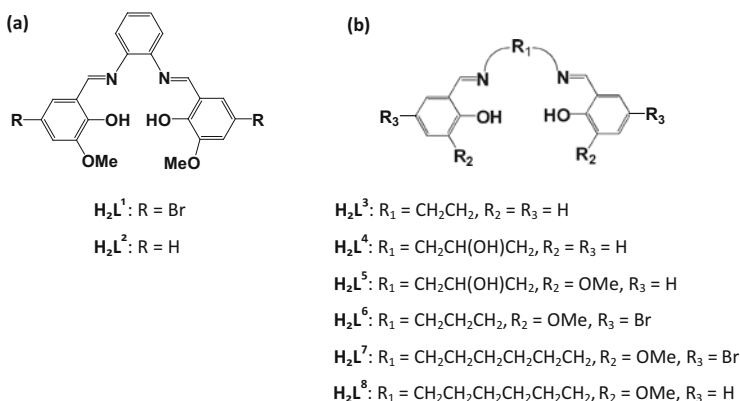
Scheme 2 Conjugated (**a**) and flexible (**b**) Schiff base ligands H_2L^{1-8}

employed to transfer absorbed energy efficiently to the lanthanide ion. They should also be capable of protecting the Ln(III) center from solvent molecules which can quench emissions [34, 35]. In this section, we describe the formation and properties of 11 lanthanide clusters (**1–11**) with the rigid ligand H_2L^1 and flexible ligands H_2L^{3-5}.

2.1 Lanthanide Clusters with Rigid Conjugated Salen-Type Ligands

In our studies, the rigid ligand N,N'-bis(5-bromo-3-methoxysalicylidene) phenylene-1,2-diamine (H_2L^1) has been used in the construction of luminescent lanthanide clusters. An interesting emerging feature exhibited by these polynuclear lanthanide complexes is the self-assembly of stacked "multi-decker" structures in which Ln^{III} ions are sandwiched between alternating layers of the rigid conjugated salen-type ligand. Our initial results with triple-decker materials raised the possibility of larger multi-decker multi-metallic lanthanide-Schiff base assemblies by careful adjustment of stoichiometry, anion selection, and reaction conditions. Since a multi-decker framework could be effective in keeping solvent and water molecules away from Ln^{III} center, it seemed reasonable to assume that enhanced luminescent properties could be achieved with these types of architectures.

Reaction of H_2L^1 with $TbCl_3 \cdot 6H_2O$ (4:3) in an acetonitrile/methanol mixture resulted in the formation of the trimetallic tetradecker complex $[Tb_3(L^1)_4(H_2O)_2]Cl$ (**1**) [36, 37]. A view of the cationic moiety of **1** and skeletal view of the N,O donor framework are shown in Fig. 1. The two outer Tb^{3+} ions, Tb(2) and Tb(3), have similar nine-coordinate environments comprising the N_2O_2 donor set of the outer L^1 group, the O_2O_2 set of one inner L^1 group, and one H_2O molecule. The central Tb (1) ion has an eight-coordinate pseudo-square-based antiprismatic geometry

Fig. 1 A view of the
molecular structure of **1**
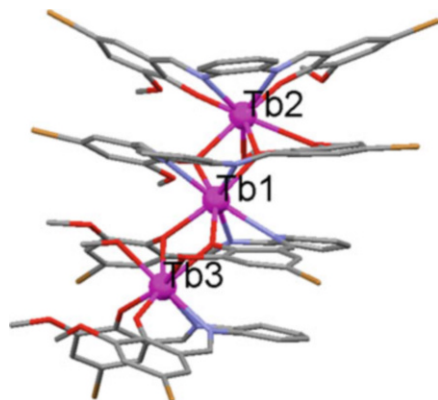
formed by the two N_2O_2 donor sets of the internal L^1 ligands. The phenolic oxygen atoms of the interior L^1 group are bridging while those of the outer L^1 are monodentate. The Tb–Tb separations are similar at 3.884 and 3.872 Å for Tb(1)–Tb(2) and Tb(1)–Tb(3), respectively. The valence requirements for **1** are satisfied by the presence of a single uncoordinated Cl^- anion.

The self-assembly process of Tb^{3+}/L^1 multi-decker systems appears to be anion dependant. Thus, if the reaction between $TbCl_3 \cdot 6H_2O$ and H_2L^1 is conducted in the presence of $Zn(OAc)_2 \cdot 2H_2O$, the triple-decker complex $[Tb_3(L^1)_3(OAc)_2Cl]$ (**2**) is produced (Fig. 2) [36, 37]. We assume that OAc^- groups are able to coordinate effectively to one Tb^{3+} ion and prevent coordination of the fourth L^1 ligand. A key feature in both **1** and **2** is the presence of intramolecular π–π stacking interactions between phenylene units. The distances range from 3.491 to 3.962 Å. These interactions may add to the stability of these multi-decker architectures. In order to coordinate effectively to two Tb^{3+} ions the inner L^1 ligands in both **1** and **2** are virtually planar. In contrast the outer L^1 ligands adopt angular configurations in which the two salicylaldehyde rings of the Schiff base are pinned back into a wing-like formation. The dihedral angles between these rings in **1** are 116.7 and 121.3°. In **2**, where the steric restraints are less severe, the dihedral angle for the analogous outer L^1 is 146.5°.

Both **1** and **2** exhibit green luminescence in the solid state. In solutions of CH_3CN, CH_3OH, and CD_3OD, the free ligand H_2L^1 exhibits strong absorption bands at 235, 280, and 335 nm. These maxima are all red-shifted on metal ion coordination. Excitation of the ligand-centered absorption bands of both **1** and **2** produces the typical emission bands of the Tb(III) ion ($^5D_4 \rightarrow {}^7F_n$ transitions, $n = 6$, 5, 4, and 3; Fig. 3) while the ligand-centered ^{1}π–π* emission was not detected. The fluorescence quantum yields (Φ_{em}) of **1** and **2** in CH_3CN are 0.153 and 0.181, respectively [36, 37]. The quantum yield of **1** is slightly lower than that of **2** probably due to the coordination of two water molecules which can quench lanthanide luminescence. With the same absorbance value of 255 nm for both **1** and **2**, the emission intensities in CH_3CN and CD_3OD are much higher than those in CH_3OH (Fig. 3).

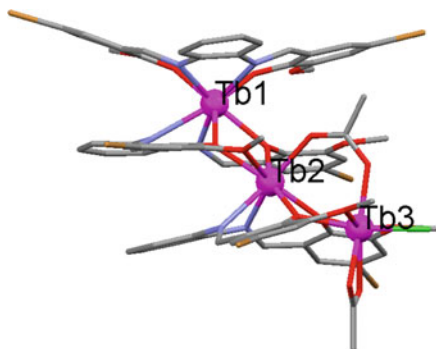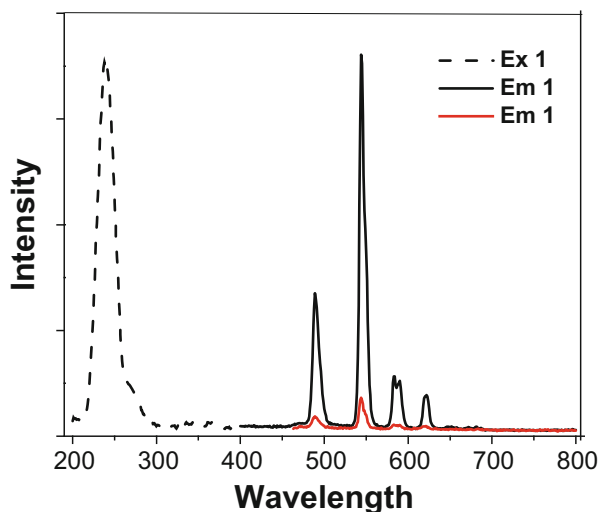**Fig. 2** A view of the molecular structure of **2**

Fig. 3 Excitation spectrum of **1** in CD$_3$OD (*dashed lines*). Emission spectrum of **1** in CH$_3$OH (*red lines*) and CD$_3$OD (*lines*). Reprinted with the permission from ref. [36]. Copyright 2005 American Chemical Society

Interestingly, the reaction conditions and the nature of counter anions used for the synthesis of these kinds of materials are critical. With the addition of Et$_3$N the reaction of H$_2$L^1 with Eu(NO$_3$)$_3 \cdot$ 6H$_2$O and Eu(CF$_3$SO$_3$)$_3$ in refluxing MeOH gave the pentanuclear tetra-decker lanthanide Schiff base complexes [Eu$_5$(L^1)$_4$(OH)$_2$ (NO$_3$)$_4$(H$_2$O)$_2$] $\cdot$ NO$_3$ (**3**) and [Eu$_5$(L^1)$_4$(CF$_3$SO$_3$)$_4$(MeO)$_2$(H$_2$O)$_4$] $\cdot$ CF$_3$SO$_3$ (**4**) [38]. A view of the cationic moiety of **3** is shown in Fig. 4. The two outer Eu^{3+} ions, Eu(1) and Eu(5), have similar nine-coordinate environments and each is bound to the O$_2$O$_2$ cavities of the outer Schiff base ligand and surrounded by nine oxygen atoms from one L^1 group, one bidentate NO$_3^-$ anion, one bridged NO$_3^-$ anion, one OH$^-$ anion, and one H$_2$O molecule. The two inner Eu^{3+} ions, Eu(2) and Eu(4), also have similar nine-coordinate environments comprising the N$_2$O$_2$ donor set of one outer L^1 group, the O$_2$O$_2$ set of one inner L^1 group, and one bridged NO$_3^-$ anion. The central Eu(3) ion has an eight-coordinate pseudo-square-based antiprismatic geometry formed by the two N$_2$O$_2$ donor sets of the internal L^1 ligands. The Eu–Eu separations range from 3.700 Å to 3.925 Å.

Fig. 4 Crystal structure of **3** showing general ligand configurations. Coordinated NO_3^- and OH^- anions, H_2O molecules, and H atoms have been omitted for clarity. Reprinted with the permission from ref. [38]. Copyright 2008 Royal Society of Chemistry
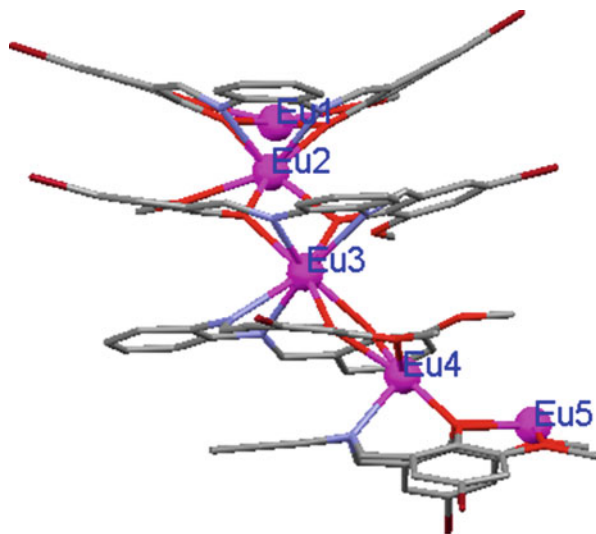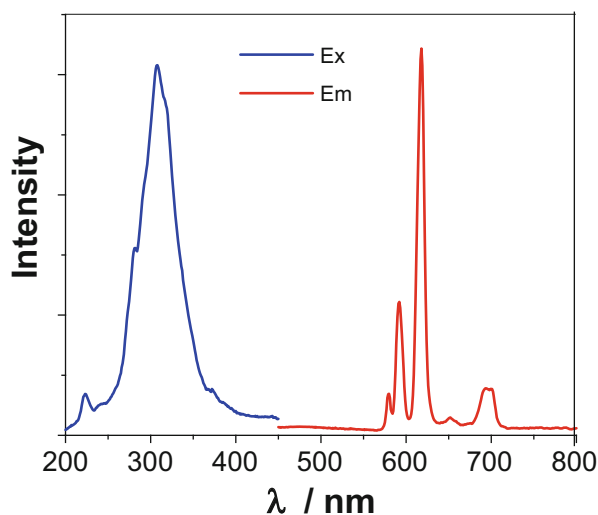
A view of the cationic moiety of **4** is shown in Fig. 5. The framework contains a C_2 axis running through the central Eu(3) ion which has an eight-coordinate environment similar to that in **3**. For each of the equal inner eight-coordinate Eu^{3+} ions (Eu(2) and Eu(2)*), one bridged MeO^- anion replaces the bridging NO_3^- anion in **4**. For each of the equal outer nine-coordinate Eu^{3+} ions (Eu(1) and Eu(1)*), two monodentate $CF_3SO_3^-$ anions and one H_2O molecule replace the NO_3^- and OH^- anions in **3**. The distances of Eu(1)-Eu(2) and Eu(2)-Eu(3) are 3.636 Å and 4.037 Å, respectively. In all three complexes, the phenolic oxygen atoms of the Schiff base ligands are bridging and the methoxy oxygen atoms and nitrogen atoms of L^1 group are monodentate.

In both **3** and **4**, the inner two L^1 ligands are virtually planar while the outer two L^1 ligands display a curved bowl-like configuration. The dihedral angles between these rings range from 121.9 to 149.5°. Intramolecular π–π stacking interactions between phenylene units are found in both **3** and **4**. The distances between adjacent aryl units range from 3.389 Å to 3.721 Å. Upon excitation of the ligand-centered (L^1) absorption band, **3** and **4** show visible emission bands typical of the Eu^{3+} ion ($^5D_0 \rightarrow {}^7F_j$ transitions, $j = 1$, 2, 3, and 4) (Fig. 6). The ligand-centered $^1\pi$–π^* emission was not detected in either **3** or **4**. The fluorescence quantum yields (Φ_{em}) of **3** and **4** in CH_3CN are 0.084 and 0.077, respectively,

The nuclearity of lanthanide Schiff base complexes can be manipulated by the introduction of different linkers which can bridge lanthanide moieties. Thus, 1,4-benzenedicarboxylate (BDC) is a convenient bidentate linker used for the construction of polynuclear complexes. In our hands an octanuclear lanthanide cluster $[Eu_8(L^1)_4(1,4\text{-BDC})_2Cl_8(MeOH)_{12}] \cdot 4Cl$ (**5**) was formed which contained two linking BDC groups [39] As shown in Fig. 7, the overall structure of **5** comprises two crystallographically equivalent $Eu_4(L^1)_2$ units related by a center of
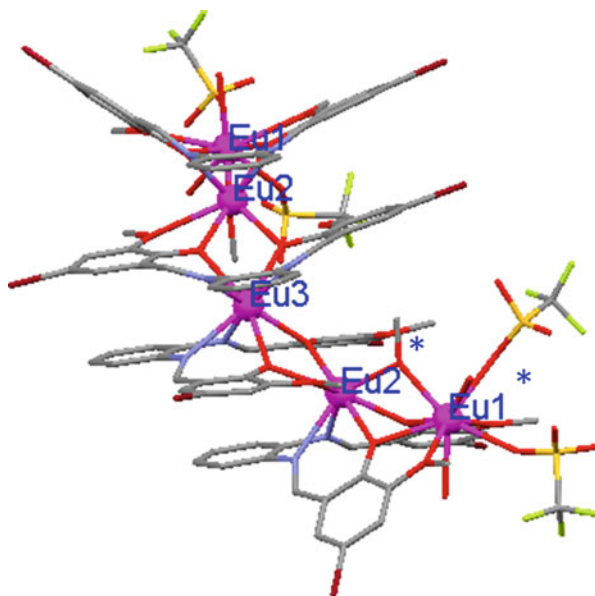
symmetry and linked by two 1,4-BDC groups. The 1,4-BDC units are virtually perpendicular to each other which results in the cage-like structure. The cluster is of nanoscale proportions ($17.5 \times 17.3 \times 10.8$ Å). Each $Eu_4(L^1)_2$ unit consists of two similar Eu_2L^1 moieties bridged by two μ–Cl groups. For each Eu_2L^1 moiety the two Eu^{3+} ions are coordinated to the N_2O_2 and O_2O_2 binding sites, and they are also located outside of the overall plane of the ligand ($Eu\cdots N_2O_2$ 1.440 Å and $Eu\cdots O_2O_2$ 0.973 Å (*av.*)).
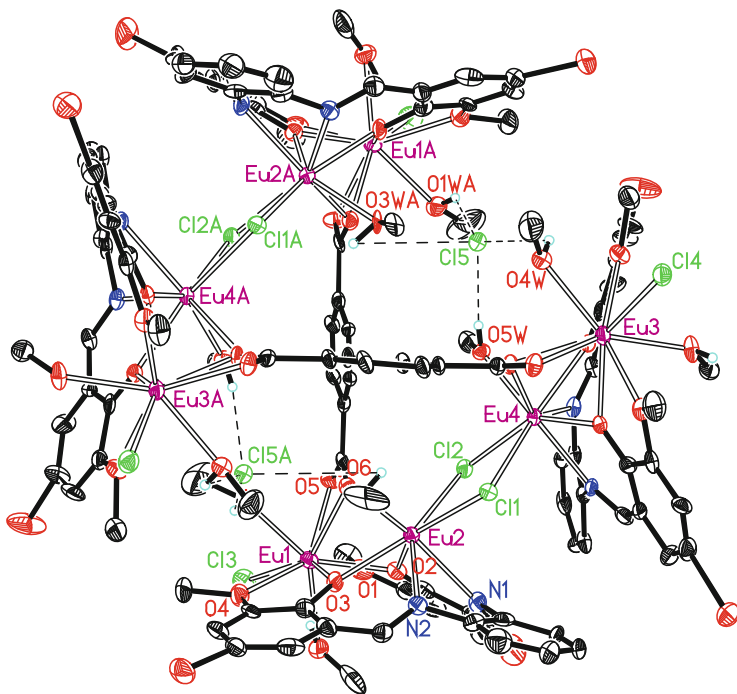
Fig. 7 A view of the molecular structure of **5**. Reprinted with the permission from ref. [39]. Copyright 2007 American Chemical Society

In the solid state **5** has an open, porous 3D-framework architecture formed by supramolecular interactions between neighboring $Eu_8(L^1)_4$ moieties (Fig. 8). The porous structure has extended channels running along both the *a*- and *c*- axes. These channels measure approximately 8×15 Å and 7×18 Å, respectively, and accommodate guest molecules of MeOH and H_2O. Hydrogen-bonded interactions are present between the entrapped molecules and the surrounding supramolecular framework.

The reversible host-guest binding of MeOH by **5** has been studied using the gas phase quartz crystal microbalance (QCM) technique. Figure 9 is a plot of the apparent partition coefficient vs. normalized partial pressure and shows binding site saturation, qualitatively consistent with the Langmuir isotherm model. The partition coefficient of **5** at saturation is approximately 13.7, which is significantly lower than K_{app} values of many other host materials.

The photophysical properties of **5** have been studied in solution. The emission spectrum of the free ligand H_2L^1 and the excitation and emission spectra of **5** are shown in Fig. 10. Excitation of the absorption band at 279 nm of the free H_2L^1 produces a broad emission band at $\lambda_{max} = 468$ nm [39]. Upon excitation of ligand-centered absorption bands, **5** shows typical visible emission bands of the Eu^{3+} ion
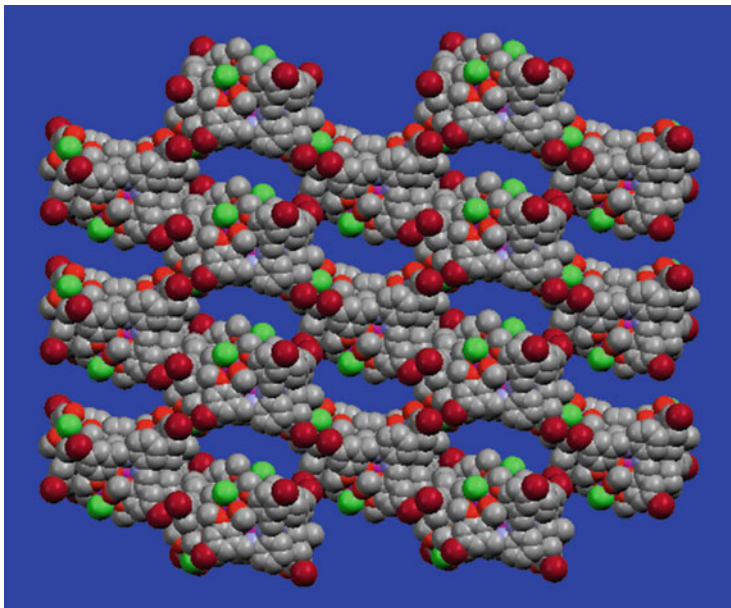
Fig. 8 Space filling view of **5** along the *a*-axis showing the open mesoporous structure. Reprinted with the permission from ref. [39]. Copyright 2007 American Chemical Society
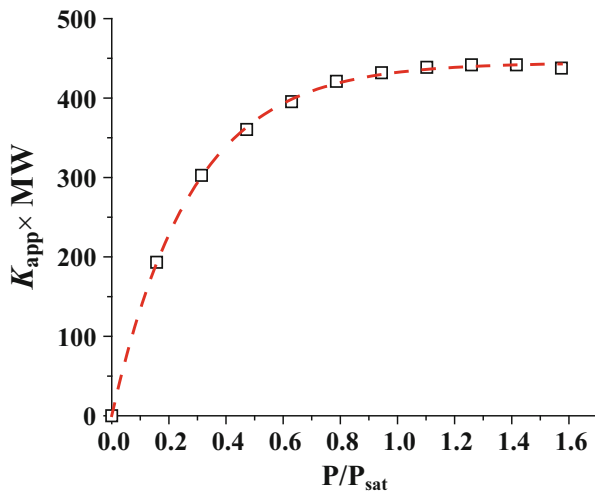

Fig. 9 Apparent partition coefficient vs. normalized partial pressure of MeOH for **5**. Reprinted with the permission from ref. [39]. Copyright 2007 American Chemical Society

($^5D_0 \rightarrow {}^7F_j$ transitions, $j = 0, 1, 2, 3$ and 4), while the ligand-centered (L[1] or 1,4-BDC) $^1\pi–\pi^*$ emissions are not detected. The absence of typical Eu^{3+} ion excitation bands in the excitation spectra and the ligand-centered luminescence in the emission spectra of **5** indicates that the ligand-to-metal energy transfer takes place efficiently [40].
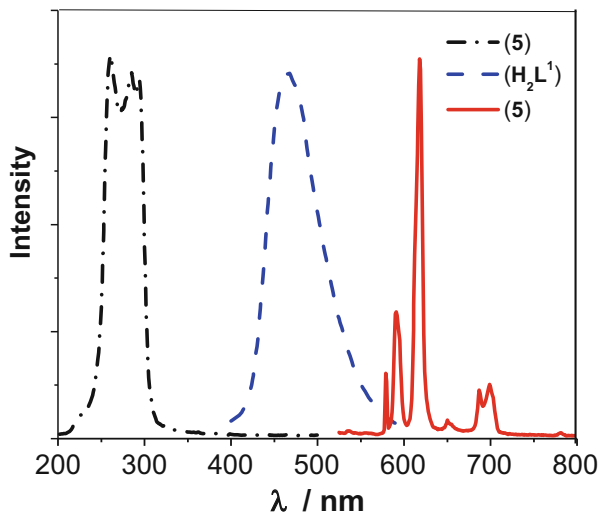
2.2 Lanthanide Clusters with Flexible Salen-Type Ligands

While the majority of lanthanide clusters have been synthesized by the use of rigid ligands, such as multicarboxylic acids and carboxyphenyl porphyrin [41, 42], relatively few studies involving more flexible ligands have been reported. However, the skeletal adaptability of flexible ligands enables them to form many different molecular systems and extended network materials. Here we describe the use of flexible Schiff base ligands H_2L^{3-5} (Scheme 2) to synthesize lanthanide clusters.

The neutral homoleptic lanthanide salen complex $[Tb_4(L^3)_6]$ (**6**) was prepared from the reaction of H_2L^3 (*N,N'*-ethylene bis(salicylideneimine)) with Tb $(OAc)_3 \cdot 4H_2O$ [43]. A view of the crystal structure of **6** is shown in Fig. 11, and reveals a tetranuclear centrosymmetric core with two equivalent $Tb_2(L^3)_3$ moieties linked by two μ-O phenoxide atoms. Interestingly, none of the MeOH or H_2O molecules found in the structure are bound to a metal center. The unique outer Tb ion (Tb(1)) is 8-coordinate and bound by the inner N_2O_2 cavities of two salen groups. The inner Tb ion (Tb(2)) is bound by the N_2O_2 core of just one salen group in addition to phenoxide O atoms from three other ligands resulting in a 7-coordinate geometry. The two unique Tb–Tb distances are similar at 3.857 and 3.869 Å for Tb(1)-Tb(2) and Tb(2)-Tb(2A), respectively. It is noted that each salen group is bound to a Tb(III) center through its N_2O_2 core with only one of its phenoxide O atoms adopting a bridging role. The molecular structure of **6** also features π–π stacking between aryl groups which may add to the overall stability of the compound. The distances between adjacent aryl units range from 3.805 to 3.994 Å (Fig. 11).

Excitation of the ligand-centered absorption bands in complex **6** results in typical visible emission bands for the Tb^{3+} ion ($^5D_4 \rightarrow {}^7F_n$ transitions, $n = 6, 5, 4$
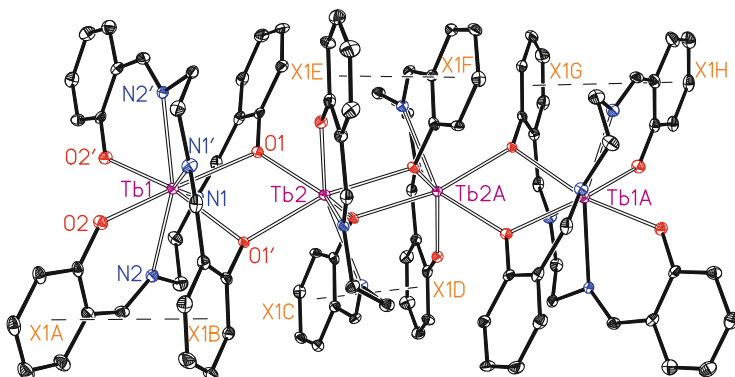
Fig. 11 A view of the molecular structure of **6**. Intramolecular π–π stacking interactions: X1A···X1B and X1G···X1H: 3.805 Å, X1C···X1D and X1E···X1F: 3.994 Å. Reprinted with the permission from ref. [43]. Copyright 2008 Royal Society of Chemistry
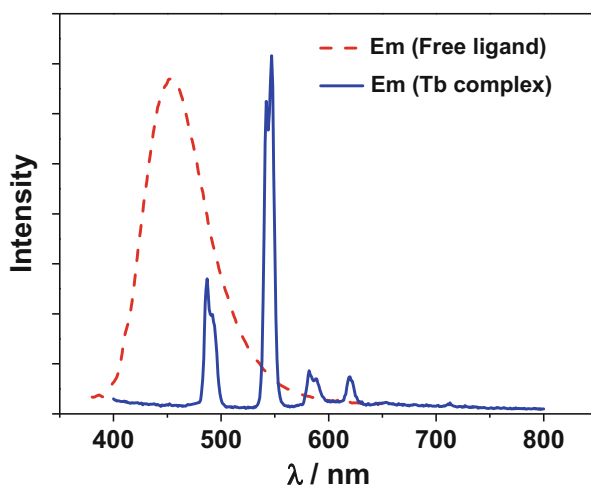

Fig. 12 Emission spectra of free H_2L^3 (*red line*) and Tb(III) complex **6** (*blue line*). Reprinted with the permission from ref. [43]. Copyright 2008 Royal Society of Chemistry

and 3), while the ligand-centered $^1\pi$–π^* emissions were not detected (Fig. 12). The fluorescence quantum yields (Φ_{em}) for **6** is 0.230 in MeOH.

The structures of lanthanide salen complexes are often influenced by a variety of factors such as lanthanide ionic radius, the nature of counter ions, and pH value of the environment. Thus, the reactions of H_2L^3 with $Yb(CF_3SO_3)_3$, $Yb(OAc)_3 \cdot 4H_2O$, and $Yb(NO_3)_3 \cdot 6H_2O$ resulted in complexes $[Yb_6(L^3)_9(H_2L^3)_2]$ (**7**), $[Yb_3(L^3)_3(HL^3)(OH)_2]$ (**8**), and $[Yb_2(L^3)_2(H_2L^3)_2(NO_3)(MeOH)_2] \cdot NO_3$ (**9**), respectively [44]. A view of the crystal structure of **7** is shown in Fig. 13, and reveals a centrosymmetric core with two equivalent $Yb_3(L^3)_5$ moieties linked by a salen ligand. The complex **7** has a "twisted" structure, in which no MeOH or H_2O molecules are bound to the
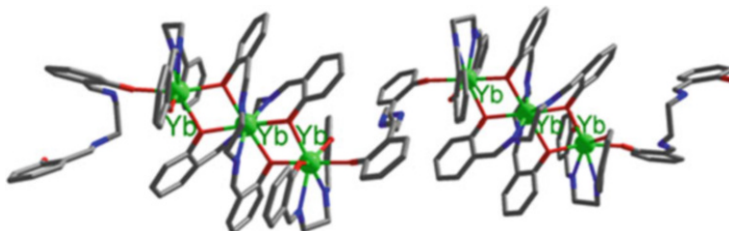
Fig. 13 A view of the crystal structure of **7**. Reprinted with the permission from ref. [44]. Copyright 2013 Royal Society of Chemistry
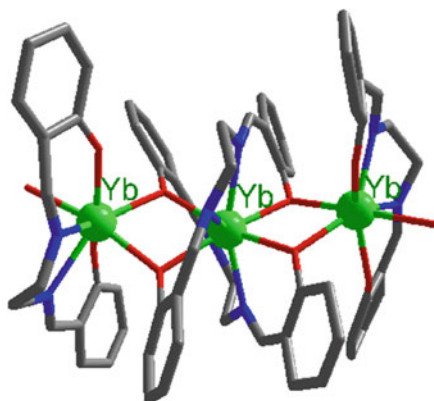

Fig. 14 A view of the crystal structure of **8**. Reprinted with the permission from ref. [44]. Copyright 2013 Royal Society of Chemistry

metal centers. Meanwhile, there are no $CF_3SO_3^-$ anions coordinated to the Yb^{3+} ions, probably due to steric factors.

The complex **8** displays a trinuclear structure which is similar to the $Yb_3(L^3)_5$ moiety in **7**, with two monodentate OH^- anions replacing two coordinated salen ligands of **7** (Fig. 14). The counter OAc^- anions may play a key role in the formation of **8**. Acetate can serve as a weak base in the reaction system to deprotonate H_2O (introduced in $Yb(OAc)_3 \cdot 4H_2O$), giving OH^- ions which lead to the formation of **8**. The Yb–Yb distances in **7** and **8** are approximately 3.7 Å.

The geometry of **9** is somewhat different from those of **7** and **8**. As shown in Fig. 15, **9** has a more flattened structure. In **9**, two Yb^{3+} ions are bridged by one salen ligand with a separation of 11.166 Å, significantly longer than the Yb–Yb distances in **7** and **8**. The "twisted" structures of **7** and **8** feature intramolecular π–π stacking (3.870–3.999 Å) and C–H···π interactions (2.566–2.782 Å) between salen ligands, while these interactions are not found in the flattened structure of **9**.

Upon excitation of the ligand-centered absorption band either at 275 or 330–360 nm, complexes **7–9** show the typical NIR emission bands of Yb^{3+} assigned to the $^2F_{5/2} \rightarrow {}^2F_{7/2}$ transitions (Fig. 16). The relative NIR emission intensity at 979 nm in CH_3CN was estimated to be 5.1:1.8:1 for **7:8:9**, indicating that **7** has superior luminescence properties compared to **8** and **9**. This may due to the fact that
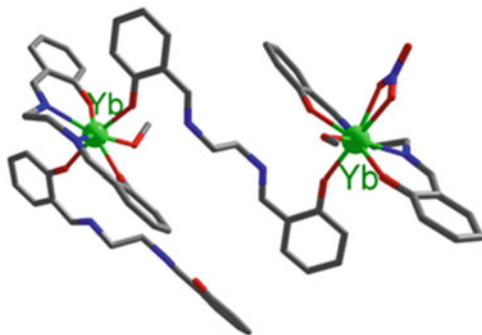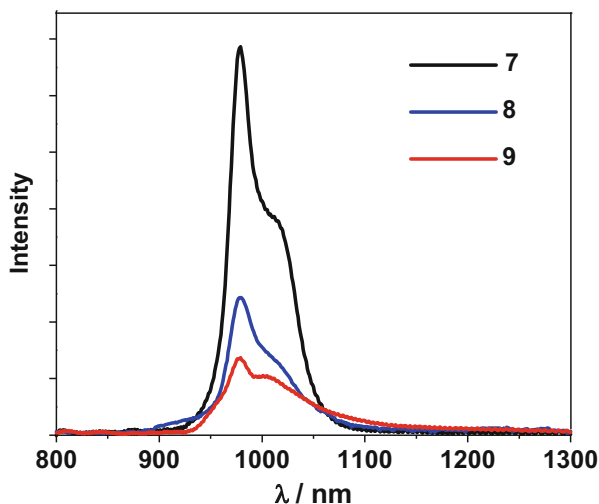
the coordinated CH_3OH molecules and OH^- anions in **8** and **9** can efficiently quench the luminescence of lanthanide ions through non-radiative exchange of electronic energy of Ln^{3+} to the high vibrational modes of OH-groups ($v = 3,700$ cm^{-1}) [44]. Meanwhile, the influence of the structural differences in **7–9** on the photophysical properties was investigated by comparing their NIR emission intensities in CH_3CN and CH_3OH. All three complexes display weaker NIR emissions in CH_3OH than in CH_3CN. However, the intensities of **7** and **8** are reduced much less than that of **9**, indicating that the "twisted" structures of complexes **7** and **8** may help to shield the metal centers from the outside solvent environment and improve their luminescent properties [44].

The modification of a given salen-type ligand may affect the formation of polynuclear assemblies. For example, the ligands H_2L^4, and H_2L^5 feature a backbone hydroxyl group. Two hexanuclear lanthanide complexes $[Eu_6(L^4)_4$ $(OH)_4(MeOH)_2(EtOH)_2(H_2O)_2] \cdot 2Cl$ (**10**) and $[Nd_6(L^5)_4(OH)_4(MeOH)_4] \cdot 2Cl$ (**11**) were synthesized from H_2L^4 and H_2L^5, respectively [45]. Interestingly, both
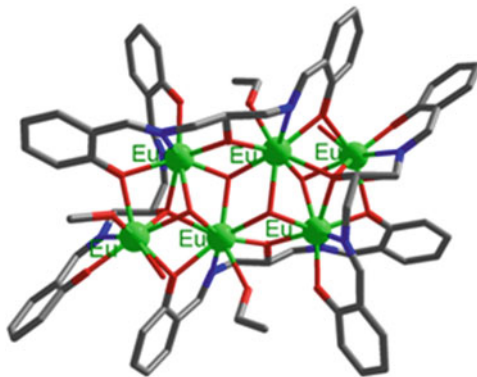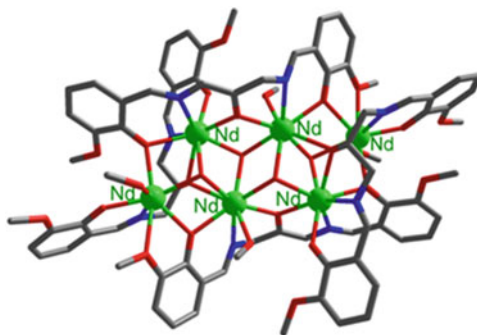
10 and **11** have similar hexanuclear structures with six lanthanide ions enclosed by four Schiff base ligands. A view of the cationic complex **10** is shown in Fig. 17. The X-ray structure of **10** reveals a centrosymmetric core with two equivalent $Eu_3(L^4)_2$ moieties linked by two μ_3-OH$^-$ anions, in which two Eu^{3+} ions are coordinated with three Schiff base ligands, while one Eu^{3+} is coordinated with two Schiff base ligands. In **10**, each μ_3-OH$^-$ anion links three Eu^{3+} ions.

A view of the crystal structure of **11** is shown in Fig. 18. Although H_2L^5 has two more methoxy groups than H_2L^4, **11** has a hexanuclear structure which is similar to that observed in **10**. It also reveals a centrosymmetric core with two equivalent $Nd_3(L^5)_2$ moieties that are bridged by two μ_3-OH$^-$ anions. For each $Nd_3(L^5)_2$ moiety, the Nd^{3+} ions have coordination environments similar to the Eu^{3+} ions in **10**. One methoxy group of the Schiff base ligand bonds to one Nd^{3+} ion in the $Nd_3(L^5)_2$ moiety. The Schiff base ligands in **10** and **11** have a formal -3 charge resulting from the deprotonation of two phenolic hydroxyls and one backbone hydroxyl group.

For lanthanide complexes, excitations of the ligand-centered absorption bands in **10** and **11** result in visible emission bands for the Eu^{3+} ion ($^5D_0 \rightarrow {}^7F_j$ transitions, $j = 1$, 2, 3, and 4; Fig. 19) and NIR emission bands of Nd^{3+} ion ($^4F_{3/2} \rightarrow {}^4I_{j/2}$ transitions, $j = 9$, 11, and 13; Fig. 20), respectively.

Fig. 19 Excitation spectra and visible emission spectra of the free ligand H_2L^4 (*dashed line* and *blue line*) and the Eu(III) complex **10** (*dashed with dot line* and *red line*) in CH_3CN. Reprinted with the permission from ref. [45]. Copyright 2012 American Chemical Society
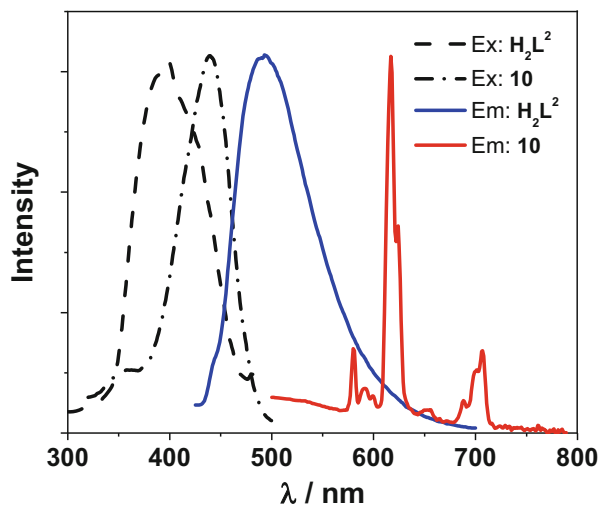
Fig. 20 The NIR luminescence of the Nd(III) complex **11** in CH_3CN. Reprinted with the permission from ref. [45]. Copyright 2012 American Chemical Society
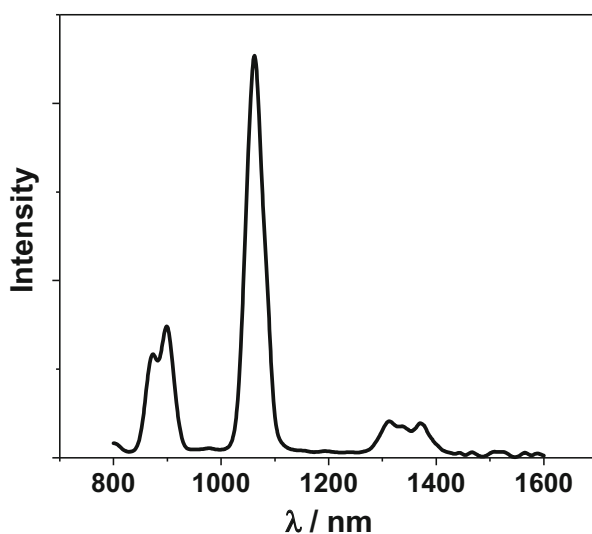
3   Luminescent d-4f Clusters with Salen-Type Ligands

Long-lived transition metal ions, such as Cr^{III}, Ru^{II}, and Pt^{II}, have been explored as sensitizers to extend the emissive lifetime of lanthanide ions in d-f heterobimetallic complexes [22–25, 28, 29]. For example, the lifetime of lanthanide ions in Cr-Ln (Ln = Nd, Yb) heterobimetallic complexes could be extended from the microsecond to millisecond timescale at 10 K, due to the $Cr^{III} \rightarrow Ln^{III}$ intramolecular energy transfer [28, 29].

Salen-type Schiff base ligands have two dissimilar metal-binding sites N_2O_2 and O_2O_2 (Scheme 2). The N_2O_2 site has a higher affinity for the d metal ion and the O_2O_2 site for the f metal ion. A number of bi-metallic 3d-4f Schiff base complexes have been prepared in order to study their magnetic properties in the past few years [32, 33, 46, 47]. In this section, we describe the construction of 12 luminescent d-4f clusters (**12–23**) with the rigid ligand H_2L^2 and flexible ligands H_2L^{6-8}. In these d-4f clusters, light-absorbing d-block metal chromophores (i.e., Zn^{II} and Cd^{II}) can be used as sensitizers for visible and NIR luminescence from Ln(III) centers following ligand $\rightarrow$ f and d $\rightarrow$ f energy-transfers.

3.1   d-4f Clusters with Rigid Conjugated Salen-Type Ligands

Three multinuclear Zn–Nd Schiff base complexes $[Nd(ZnL^2)_2(NO_3)_2(H_2O)_2] \cdot NO_3$ (**12**), $[Nd(ZnL^2)_2Cl_2(H_2O)_3] \cdot Cl$ (**13**), and $[Nd_2(ZnL^2)_2Cl_6(MeOH)_2]$ (**14**) have been prepared from the reactions of ZnL^2 ($H_2L^2 = N,N'$-bis(3-methoxy-salicylidene)phenylene-1,2-diamine) with $Nd(NO_3)_3 \cdot 6H_2O$ and $NdCl_3 \cdot 6H_2O$ [48] All these Zn–Nd clusters show interesting "double-decker" structures. The stoichiometry and structures of these complexes are dependent on the ZnL^2:Nd ratio employed in their syntheses as well as the nature of the anion present (Cl^- *vs* NO_3^-). In trinuclear Zn_2Nd complexes **12** and **13**, the Nd^{3+} ion is sandwiched between the two ZnL^2 units which are virtually parallel to each other (Figs. 21 and 22). Although there is an Nd^{3+} ion sandwiched between two ZnL^2 moieties, the planar aromatic groups of each ligand are sufficiently close to each other to form intramolecular π–π stacking interactions in both molecules (the shortest distance between aryl units is 3.498 Å). The structure of the tetranuclear Zn_2Nd_2 complex **14** comprises two $ZnNdL^2$ units linked together by two bridging Cl atoms bound to both Nd^{3+} ions (Fig. 23). The Zn^{2+} and Nd^{3+} ions in this complex are located in the inner N_2O_2 and O_2O_2 cavities of each Schiff base ligand, respectively. The Nd–Nd separation is 4.477 Å which effectively rules out the possibility of any π–π stacking between the aromatic groups of the ligands.

For all these three complexes, excitation of the ligand-centered absorption bands results in Nd^{3+} NIR emission bands assigned to the $^4F_{3/2} \rightarrow {}^4I_{j/2}$ ($j = 9$, 11, 13) transitions (Scheme 1 and Fig. 24). The luminescence properties of lanthanide complexes are dependent on both coordination structures and outside solvent environment. In these "double-decker" structures, the Nd^{3+} ion is sandwiched between two ZnL^2 units and protected from outside solvent environment, so their photophysical properties are less affected by outside solvent molecules which may quench lanthanide luminescence.
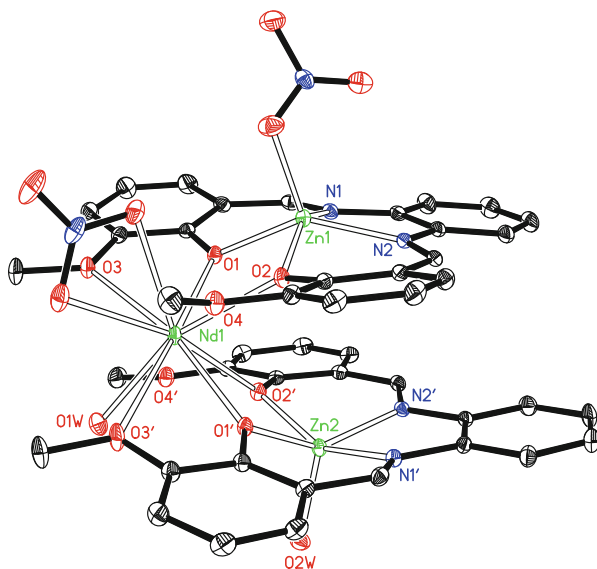
Fig. 21 Crystal structure of trinuclear $[Nd(ZnL^2)_2(NO_3)_2(H_2O)_2] \cdot NO_3$ (**12**). Reprinted with the permission from ref. [48]. Copyright 2006 American Chemical Society
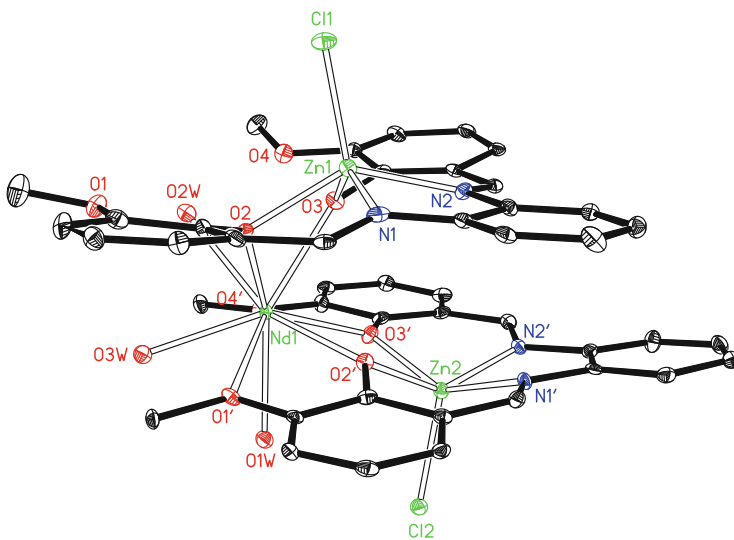
Fig. 22 Crystal structure of trinuclear $[Nd(ZnL^2)_2Cl_2(H_2O)_3] \cdot Cl$ (**13**). Reprinted with the permission from ref. [48]. Copyright 2006 American Chemical Society

Fig. 23 Crystal structure of tetranuclear Zn_2Nd_2 complex $[Nd_2(ZnL^2)_2 Cl_6(MeOH)_2]$ (**14**). Reprinted with the permission from ref. [48]. Copyright 2006 American Chemical Society

Fig. 24 NIR luminescence of **12** in CH_3OH at room temperature. Reprinted with the permission from ref. [48]. Copyright 2006 American Chemical Society

3.2 d-4f Clusters with Flexible Salen-Type Ligands

The design and construction of polynuclear d-f complexes has received extensive attention due to the remarkable *physical* and *chemical* properties associated with

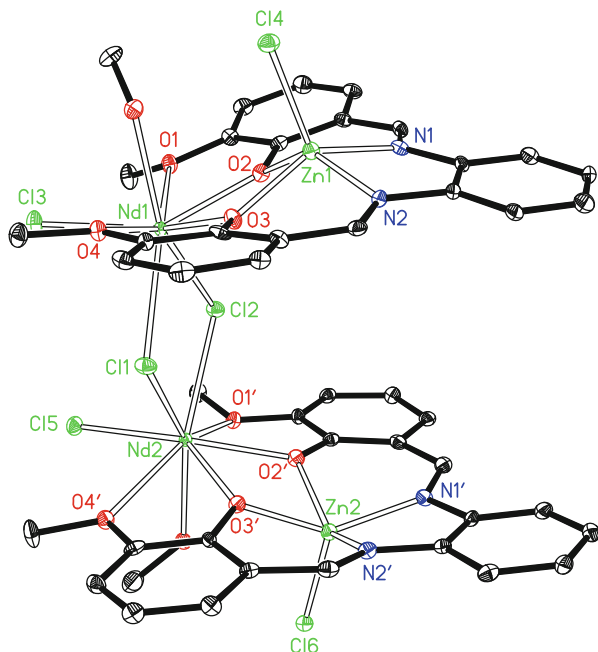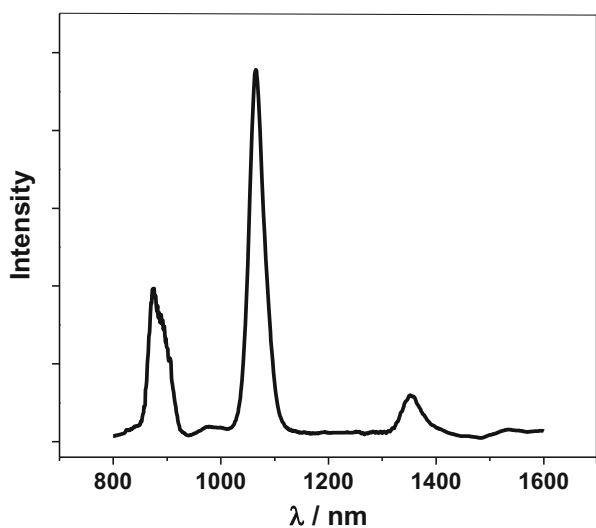this class of materials [49–52]. For example, research on polynuclear d-f complexes of Yb(III), Nd(III), and Er(III) with near-infrared (NIR) emission in the 900–1,600 nm range has become a hot topic due to potential applications in bioassays and laser systems [53–55]. Light-absorbing d-block metal chromophores (i.e., Pt^{II}, Ru^{II}, Zn^{II}, and Cd^{II}) have been used as sensitizers for NIR luminescence from Ln(III) centers following ligand $\rightarrow$ f and d $\rightarrow$ f energy-transfers [22–25, 28, 29, 30, 31].

A tetrametallic Zn–Yb complex $[Zn_2Yb_2(L^6)_2(OH)_2Cl_4]$ (**15**) was synthesized from the reaction of H_2L^6 (N,N'-bis(5-bromo-3-methoxysalicylidene)propylene-1,3-diamine) with $Zn(NO_3)_2 \cdot 6H_2O$ and $YbCl_3 \cdot 6H_2O$ in the presence of Et_3N [56]. A view of the crystal structure of **15** is shown in Fig. 25. Each Zn atom is five-coordinate and sits slightly above the N_2O_2 plane of each ligand by 0.555 Å. The Yb–Yb separation is 3.588 Å, and each Yb^{3+} ion is seven-coordinate from the four-oxygen atoms of L^6, two bridging hydroxides and a terminal chloride. The molecule sits on a crystallographically imposed inversion center. The unique Zn–Yb distance is 3.481 Å. The two central bridging hydroxides give the molecule an overall slipped sandwich configuration. The typical emission band of Yb^{3+} assigned to the $^2F_{5/2} \rightarrow {}^2F_{7/2}$ transition is observed at 977 nm upon excitation of the ligand-centered absorption band either at 275 or 350 nm (Fig. 26).

As described in **5**, 1,4-BDC groups may act as convenient bidentate linkers in the formation of lanthanide complexes with higher nuclearity. Thus, a hexanuclear Zn–Nd complex $[Zn_4Nd_2(L^6)_4(1,4\text{-BDC})_2] \cdot [Nd(NO_3)_5(H_2O)]$ (**16**) was formed which contained two linking BDC groups [57]. As shown in Fig. 27, two BDC groups bridge the Zn_2Nd moieties such that each carboxylate group spans a Zn–Nd set. The ^1H NMR spectrum of **16** shows that this kind of bridged structure is very stable in solution at room temperature [57].

The complex **16** shows typical NIR emission bands of Nd^{III} ($^4F_{3/2} \rightarrow {}^4I_{j/2}$ transition, $j = 9$, 11, 13) upon excitation of the ligand-centered absorption bands both in the solid state and MeCN solution (Fig. 28). It is noticeable that, with the central metal ion encapsulated by four chromophoric ligands and shielded from solvent interactions, this complex shows superior luminescence properties compared to the related simple dinuclear Zn–Nd complex $[ZnNdL^6(OAc)(NO_3)_2]$. With the same absorbance value at the excitation wavelength (275 nm), the emission intensity at 1,068 nm in **16** is 5.5 times as strong as that in $[ZnNdL^6(OAc)(NO_3)_2]$ [57].

As with Ln(III) ions, the Cd(II) ion can have high coordination numbers (6–8) and display various coordination geometries, and high-nuclearity Cd-Ln clusters are possible. Two flexible salen-type ligands H_2L^7 (N,N'-bis(5-bromo-3-methoxysalicylidene)hexane-1,6-diamine) and H_2L^8 (N,N'-bis(3-methoxysalicylidene)hexane-1,6-diamine), which have six methylene (-CH$_2$-) groups in their backbones, were employed to construct d-4f complexes. Interestingly, increasing the number of CH_2 units in the backbone of the salen ligands results in the formation of a series of high-nuclearity d-4f nanoclusters.

Fig. 25 A view of the crystal structure of **15**

Fig. 26 The NIR luminescence of **15** in CH$_3$CN. Reprinted with the permission from ref. [56]. Copyright 2005 Royal Society of Chemistry
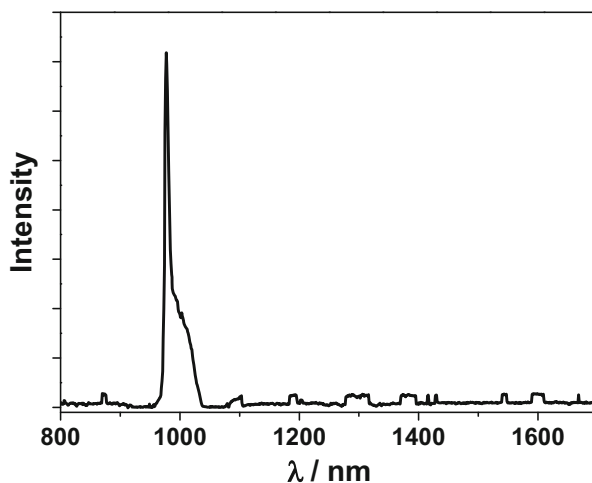
Fig. 27 A view of the crystal structure of **16**
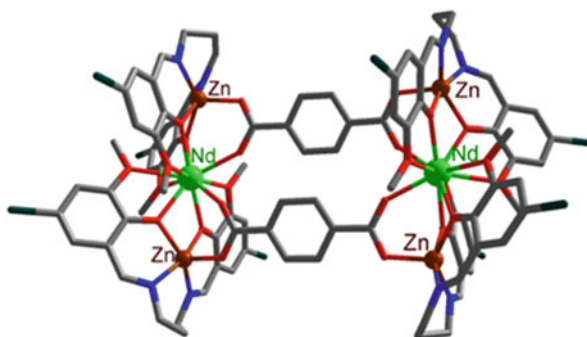
Two classes of Cd-Ln nanoclusters can be prepared from the reactions of H$_2$L^7 with Cd(OAc)$_2 \cdot$4H$_2$O and LnX$_3 \cdot$nH$_2$O (X = OAc$^-$ and Cl$^-$). They are [Ln$_8$Cd$_{24}$(L^7)$_{12}$(OAc)$_{48}$] (Ln = Nd (**17**) and Yb (**18**)) and [Ln$_{12}$Cd$_{44}$(L^7)$_{20}$ Cl$_{30}$(OAc)$_{54}$] (Ln = Nd (**19**) and Yb (**20**)) [58]. **17** and **18** are isomorphous and have 32-metal single-drum-like structures. Two views of the crystal structure of
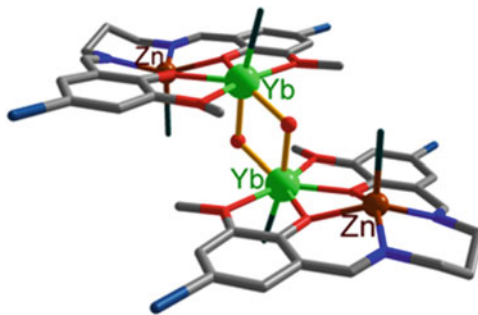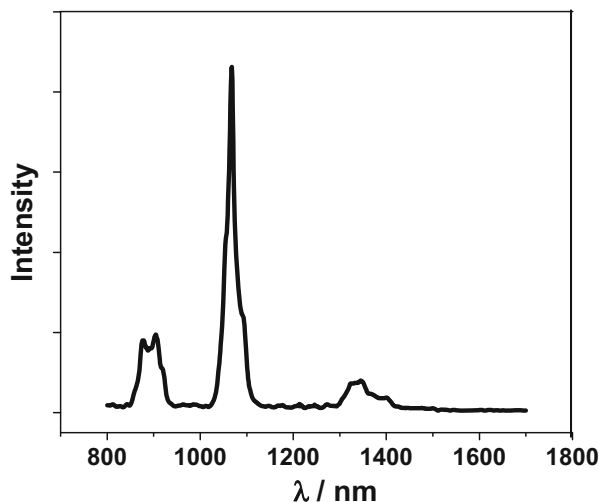
Fig. 28 The NIR luminescence of **16** in CH$_3$CN. Reprinted with the permission from ref. [57]. Copyright 2006 Royal Society of Chemistry

Fig. 29 (**a**) Two views of the nano-drum-like structure of **17**: viewed along the *b*-axis (*top*) and *a*-axis (*lower*) (Nd^{3+}: *green*; Cd^{2+}: *blue*; and Br: *brown*); (**b**, **c**) TEM and SEM images of **17**. Reprinted with the permission from ref. [58]. Copyright 2014 Royal Society of Chemistry

17 are shown in Fig. 29a. The left one is essentially a side-on view while the right one is looking down into the top of the drum. The ends of the drum are created by two rings of 16 metals (4 Nd(III) and 12 Cd(II)) coordinated to half of the N, O

binding groups of the 12 Schiff base ligands plus 24 OAc^- ions, while the sides of the drum are formed by the $-(CH_2)_6-$ linkers of the Schiff base ligands.

It is noticeable that the H_2L^{1-6} ligands exhibit the classical "salen" type of coordination modes with the 3d-metal ions bound in the N_2O_2 cavities and the 4f-metal ions in the O_2O_2 cavities, while complexes formed using the long-chain Schiff base ligand H_2L^7 exhibit "stretched" coordination modes resulting in very large architectures. The X-ray crystallographic data reveal that the molecular dimensions of **17** are approximately $22 \times 27 \times 27$ Å. It is also possible to obtain images of these molecular nanoparticles using transmission electron microscopy (TEM). Dilute solutions of **17** in MeCN were contacted with a Cu grid and the solvent carefully evaporated under vacuum. The TEM images obtained (Fig. 29b) show uniform nanoparticles with diameters measuring approximately 2.72 nm which corresponds well with the diameter of the 16-metal ring end of the nano-drum found in the crystal structure. In Fig. 29c a panoramic scanning electron microscopy (SEM) image shows the crystalline nature of **17**.

The self-assembly process of nano-drum-like structures appears to be anion dependent. Thus, if Cl^- anions are introduced into the reactions with the use of $LnCl_3 \cdot 6H_2O$, unprecedented 56-metal clusters **19** and **20** are produced which have linked nano-double-drum-like architectures. Two views of the crystal structure of **19** are shown in Fig. 30a. The X-ray structure of **19** reveals a centrosymmetric core with two equivalent 28-metal single-drum $Nd_6Cd_{22}(L^7)_{10}Cl_{15}(OAc)_{27}$ moieties linked by four Cl^- anions. In each 28-metal moiety, two rings of 14 metals (3 Nd (III) and 11 Cd(II)) are linked by 10 Schiff base ligands. In **19**, each Ln^{3+} ion and its closest two Cd^{2+} ions are linked by phenolic oxygen atoms of $(L^7)^{2-}$, OAc^- anions and/or Cl^- anions. The distances between Ln^{3+} and Cd^{2+} ions range from 3.645 Å to 3.907 Å. The molecular dimensions of **19** (ca. $44 \times 27 \times 27$ Å) are, of course, significantly larger than those of **17** or **18**. A TEM image of **19** (Fig. 30b) shows 4.45-nm sized nanoparticles, in agreement with the dimensions found in the crystal structure. An SEM image of **19** is shown in Fig. 30c.

Cd(II) chromophores with visible emissions can be used to sensitize the luminescence of Ln(III) ions [30, 31]. The luminescence properties of these Cd-Ln nanoclusters were studied in CH_3CN. The photophysical properties of **17–20** were studied in CH_3CN and the solid state. For **17–20**, the absorption bands in the UV-vis region are all red-shifted compared to those of the free ligand H_2L^7. The absorptions of **17–20** are about 10 times stronger than the free ligand [30, 31], which enhances the ability of the ligand-center to absorb energy for sensitizing the lanthanide luminescence. It is noticeable that the absorptions of **19** and **20** are stronger than **17** and **18**. For these Cd–Ln nanoclusters, upon excitation of the ligand-centered absorption bands, **17** and **19** show typical NIR emission spectra for Nd^{3+} ($^4F_{3/2} \rightarrow {}^4I_{j/2}$ transitions, $j = 9$, 11 and 13), and **18** and **20** show those for Yb^{3+} ($^2F_{5/2} \rightarrow {}^2F_{7/2}$ transition) in both solution and the solid state (Fig. 31). The excitation spectra of **17–20** show two bands at approximately 290 nm and 380 nm (Fig. 31), in agreement with their absorption spectra. We were naturally interested in the influence of structural differences in the Cd–Ln nanoclusters on their
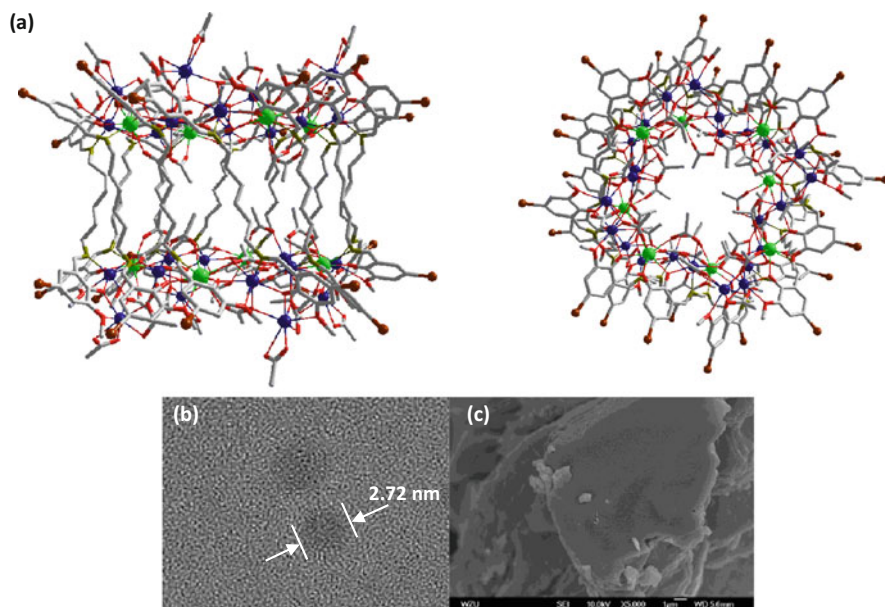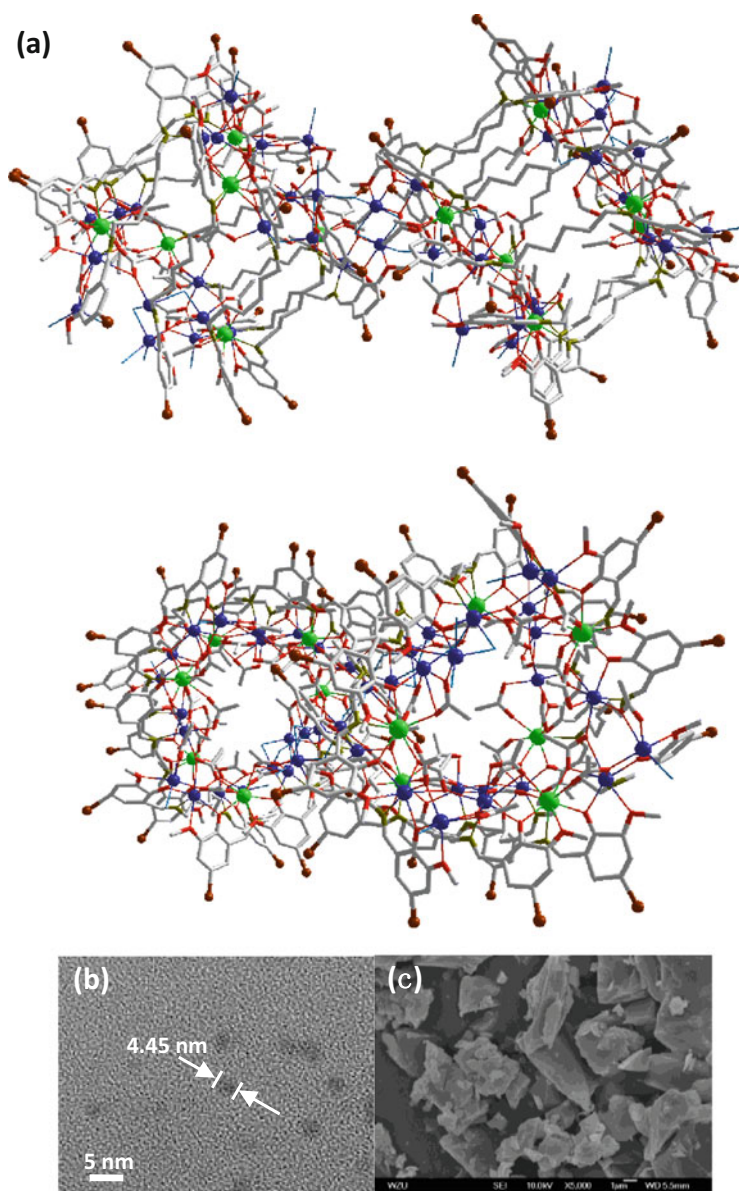
Fig. 30 (**a**) Two views of the nano-double-drum structure of **19**: viewed along the *b*-axis (*top*) and *a*-axis (*lower*) (Nd^{3+}: *green*; Cd^{2+}: *blue*; and Br: *brown*); (**b**, **c**) TEM and SEM images of **19**. Reprinted with the permission from ref. [58]. Copyright 2014 Royal Society of Chemistry

photophysical properties. The relative emission intensities of **19** vs. **17** and **20** vs. **18** were determined under the same experimental conditions in CH$_3$CN with the same absorbance value at 380 nm, respectively. The relative NIR emission intensities were

Fig. 31 The excitation and NIR emission spectra of **19** and **20** in CH_3CN at 298 K. Reprinted with the permission from ref. [58]. Copyright 2014 Royal Society of Chemistry
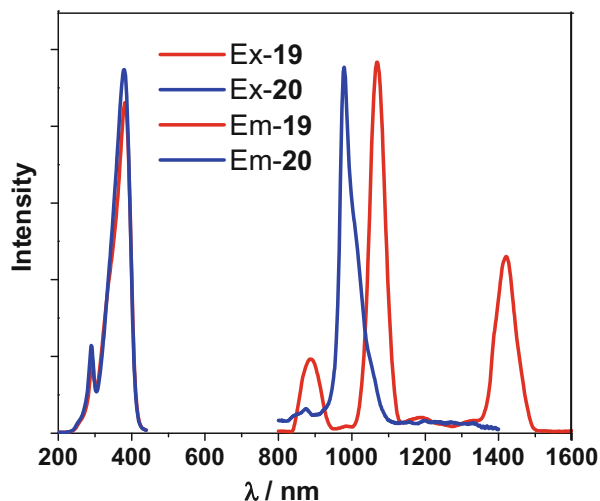
estimated to be 3.3 and 2.5 for **19**:**17** (measured at 1,068 nm) and **20**:**18** (measured at 979 nm), respectively, indicating that nanoclusters with double-drum-like structures have superior luminescence properties compared to those with single-drum-like structures. This can also be confirmed by comparing their luminescence lifetimes. The emission lifetimes (τ) of **17** and **19** are 2.6 μs and 3.8 μs, respectively. The intrinsic quantum yields (Φ_{Ln}) of Nd^{3+} emission in **17** and **19** are calculated as 1.04 % and 1.52 %, respectively, using $\Phi_{Ln} = \tau/\tau_0$ ($\tau_0 = 250$ μs, the natural lifetime of Nd^{3+}). The emission lifetimes of **18** and **20** are 9.5 μs and 12.3 μs, respectively. So the intrinsic quantum yields of Yb^{3+} emission in **18** and **20** are calculated as 0.48 % and 0.62 %, respectively ($\tau_0 = 2,000$ μs for the natural lifetime of Yb^{3+}).

Compared with Cd(II), the Zn(II) ion tends to have lower coordination numbers (4–6) and exhibits some common coordination geometries such as square-planar, trigonal pyramid, and octahedral. Thus, reactions of H_2L^7 with $Zn(OAc)_2 \cdot 4H_2O$ and $Ln(OAc)_3 \cdot 4H_2O$ under the same experimental conditions as above produced 12-metal Zn-Ln clusters $[Ln_4Zn_8(L^7)_2(OAc)_{20}(OH)_4]$ (Ln = Nd (**21**) and Yb (**22**)) [59]. They are isomorphous and have rectangular-like structures. Two views of the crystal structure of **21** are shown in Fig. 32. The left view is looking right in front of the rectangle while the right one is essentially a side-on view. The X-ray structure of **21** reveals a centrosymmetric core with two equivalent $Nd_2Zn_4(OAc)_{10}(OH)_2$ moieties linked by two Schiff base ligands. Interestingly, the rectangular form of **21** is like a vertical strip cut from the drum-like structure of **17**. In each $Nd_2Zn_4(OAc)_{10}(OH)_2$ moiety, two Nd^{3+} ions have similar coordination environments, surrounded by nine oxygen atoms from one L^7 ligand, two OH^-, and five OAc^- ions. They are bridged by two OH^- groups with a separation of 4.191 Å. All four Zn^{2+} ions have tetrahedral geometries. In **21** and **22**, each Ln^{3+} ion and its closest three Zn^{2+} ions are linked by phenolic oxygen atoms of the L^7 ligand, OAc^- anions, and/or OH^- anions. The distances between Ln^{3+} and Zn^{2+} ions range from 3.648 Å to 3.800 Å.
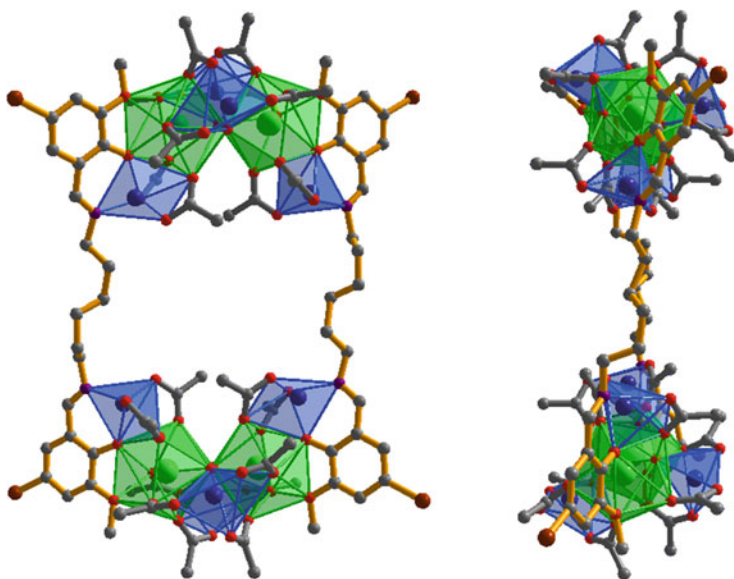
Fig. 32 Two views of the square-like structure of **21**: viewed along the *b*-axis (*left*) and *ac*-axis (*right*). (Nd^{3+}: *green* and Zn^{2+}: *blue*). Reprinted with the permission from ref. [59]. Copyright 2014 Royal Society of Chemistry
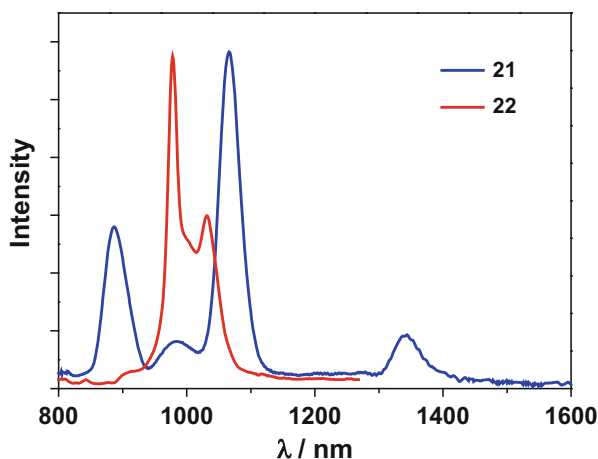
Fig. 33 Excitation (**a**) and emission (**b**) spectra of **21** and **22** in CH_3CN. Reprinted with the permission from ref. [59]. Copyright 2014 Royal Society of Chemistry

Upon excitation of the ligand-centered absorption bands, **21** and **22** show the NIR luminescence of Nd^{3+} ($^4F_{3/2} \rightarrow {}^4I_{j/2}$ transitions, $j = 9$, 11 and 13) and Yb^{3+} ($^2F_{5/2} \rightarrow {}^2F_{7/2}$ transition), respectively (Fig. 33). The emission lifetimes (τ) of **21** and **22** are 1.2 µs and 8.1 µs, respectively.

Fig. 34 Views of the crystal structure of **23**. Viewed along the *a*-axis (*top*) and *c*-axis (*lower*). (Eu^{3+}: *green* and Cd^{3+}: *brown*). Reprinted with the permission from ref. [60]. Copyright 2015 Royal Society of Chemistry
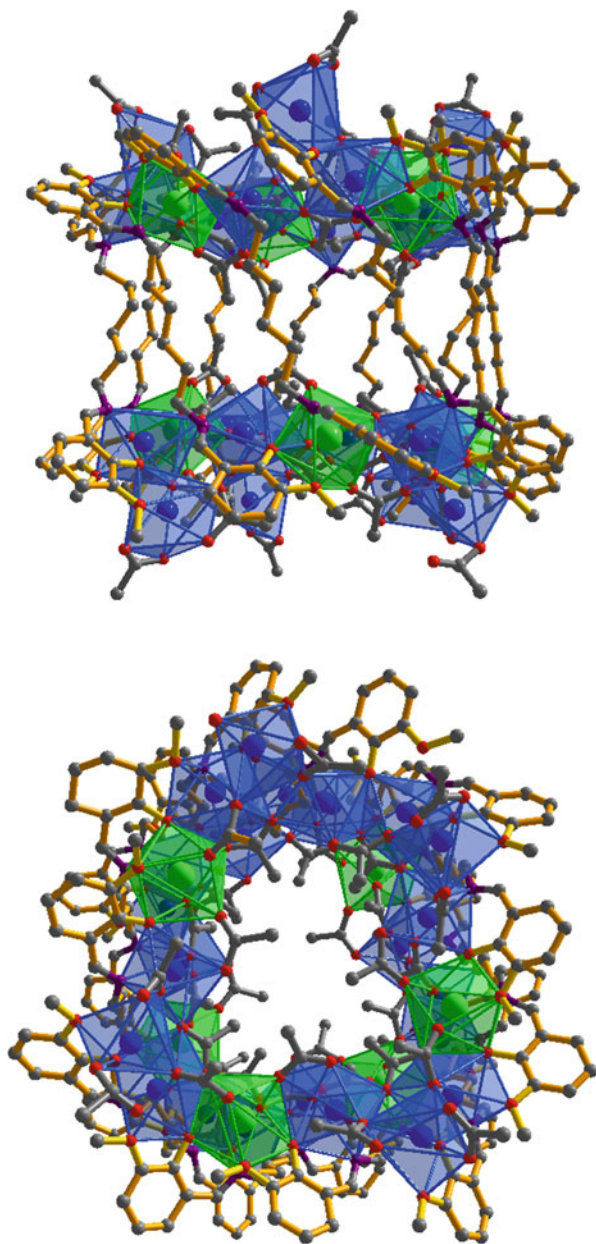
Reaction of H$_2$L^8 with Cd(OAc)$_2 \cdot$ 4H$_2$O and Eu(OAc)$_3 \cdot$ 4H$_2$O produced the Cd-Eu heterometallic cluster [Eu$_8$Cd$_{24}$(L^8)$_{12}$(OAc)$_{48}$] (**23**) [60]. This cluster possesses the 32-metal drum-like structure similar to those observed in **17** and **18**. Two views of the crystal structure of **23** are shown in Fig. 34. The top view is essentially

Fig. 35 Emission spectra of the free H_2L^8 and **23** in CH_3CN. Reprinted with the permission from ref. [60]. Copyright 2015 Royal Society of Chemistry
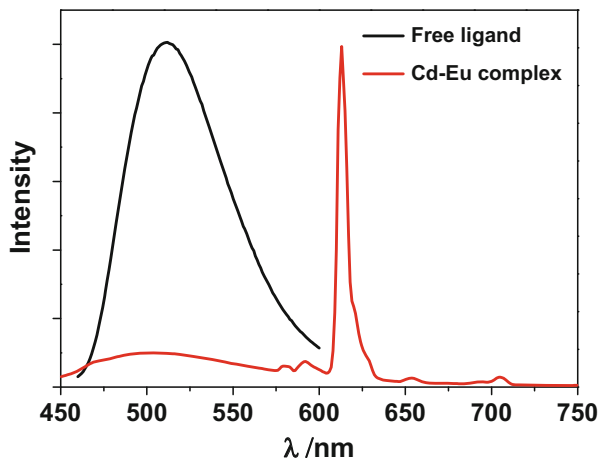
a side-on view while the lower one is looking down into the top of the drum. The complex is of nanoscale proportions ($19 \times 26 \times 26$ Å). The ends of the drum are created by two rings of 16 metals (4 Eu(III) and 12 Cd(II)). The sides of the drum are formed by the -(CH$_2$)$_6$- linkers of 12 Schiff base ligands.

For **23**, the typical narrow emission bands of the Eu^{3+} ion ($^5D_0 \rightarrow {}^7F_j$ transitions, $j = 0, 1, 2, 3$ and 4) can be detected upon excitation of the ligand-centered absorption bands in both solution and the solid state at room temperature (Fig. 35). The appearance of the symmetry-forbidden emission $^5D_0 \rightarrow {}^7F_0$ at 578 nm indicates that the Eu^{3+} ions in the complex occupy sites with low symmetry and have no inversion center, in agreement with the solid state structure.

The initial studies of the use of **23** as a bioprobe for biological imaging applications have been investigated [60]. Crosslinked polystyrene beads (6-μm) containing **23** were visualized using epifluorescence, TIRF, and two-photon microscopy by observing emission in the visible spectrum. Evidence that the nano-drum is incorporated intact into the pores of the beads was provided by XPS studies which revealed an Eu:Cd ratio of 1:3 consistent with the ratio found in the crystal structure. Beads loaded with **23** can be excited with an illumination source filtered by a DAPI filter and show high signal to background intensity ratio as well as high mean intensity under the DAPI, FITC, TRITC, and Cy5 emission filter channels (Fig. 36a) [60]. The use of longer wavelength excitation filters appeared to only slightly excite this sample. Using the TIRF imaging platform, beads loaded with **23** exhibited a high fluorescence when excited with a 405-nm laser using identical filter settings and controlled for the same exposure time of 1 frame/s (Fig. 36b). The two-photon fluorescence images shown in Fig. 37 were acquired at constant laser power and detector sensitivity. Beads were excited at 760 nm, and images shown obtained by PMT with a 535/50-nm emission filter. Control beads lacking **23** did not display significant fluorescence in any of the microscopy studies presented here.
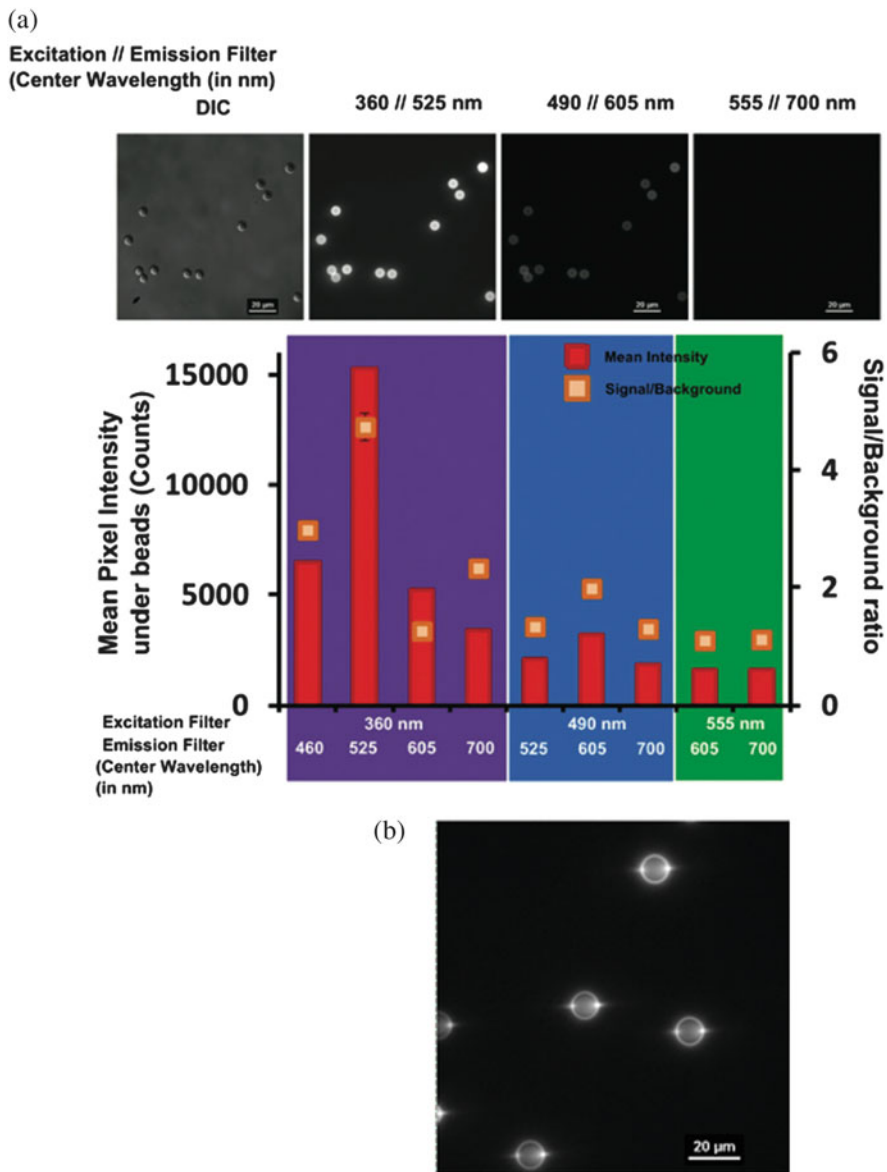
Fig. 36 Luminex beads doped with **23** show bright fluorescence under epifluorescent (**a**) and total internal reflection fluorescence (**b**) microscopy. Reprinted with the permission from ref. [60]. Copyright 2015 Royal Society of Chemistry

To determine the inherent cytotoxicity of complexes towards potential tumor targets, cell proliferation assays were conducted using an A549 lung cancer cell line. As shown in Fig. 38, the nano-drum **23** displayed an IC_{50} value of
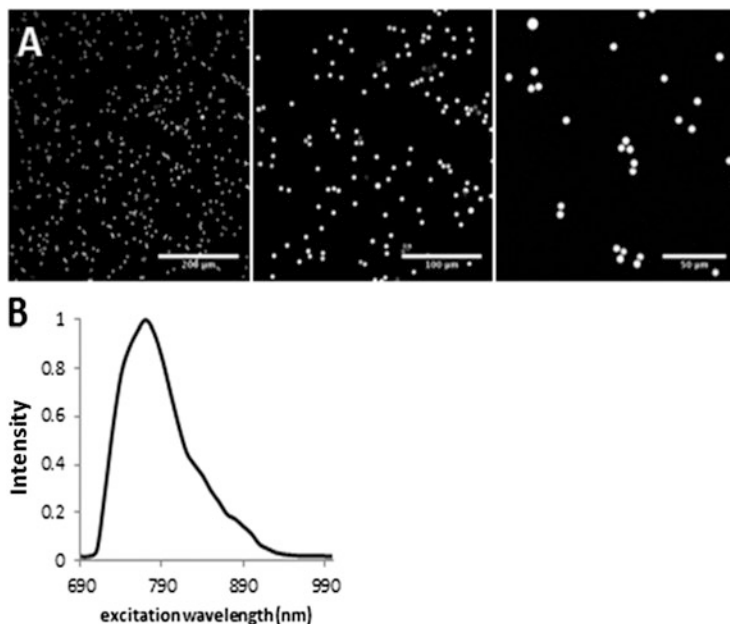
Fig. 37 Polystyrene beads loaded with **23** imaged by two-photon fluorescence microscopy. (**a**) Beads were excited at 760 nm, with signal detected in blue emission PMT shown at 20× (*left panel*), 40× (*middle panel*), and 63× (*right panel*) magnification. (**b**) Two-photon excitation spectra for **23** in visible emission range. Reprinted with the permission from ref. [60]. Copyright 2015 Royal Society of Chemistry
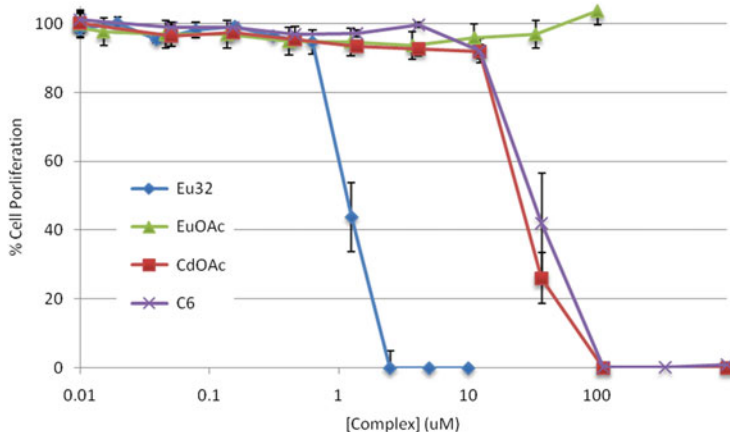
Fig. 38 Dose responsive cell proliferation curves of A549 lung cells treated with **23**. *Error bars* represent standard deviation. Reprinted with the permission from ref. [60]. Copyright 2015 Royal Society of Chemistry

1.37 ± 0.43 μM in an A549 lung cancer cell line and 2.0 μM in an AGS gastric cancer cell line. At this point, it is unknown whether the observed cytotoxicity is due to the complex as a whole or due to individual entities within the supramolecular drum assembly (i.e., Cd, Eu, and H_2L^8 ligand). In this particular cellular assay, the cytotoxicity (antiproliferative activity) of the free metal acetates and ligand (i.e., $Eu(OAc)_3$, $Cd(OAc)_2$, and the H_2L^8 ligand) were significantly lower than that of the corresponding nano-drum complex **23**. The cadmium salt $Cd(OAc)_2$ and the H_2L^8 ligand provided IC_{50} values of 31.0 ± 7.0 and 29.7 ± 1.2 μM, respectively, while $Eu(OAc)_3$ displayed no inhibition of cell proliferation under the concentrations tested. These observations suggest that the supramolecular drum assembly is facilitating transport of the ligand and metal components into the cell using an endocytotic mechanism [61]. Our current studies are aimed at further optimization of photophysical properties and cell bioimaging.

From the structures of these drum-like architectures, we can conclude that the key to the construction of these high-nuclearity Ln/Cd nanoclusters is that both Ln (III) and Cd(II) ions have the potential for high coordination numbers (6–8) with variable coordination geometries. The adaptability of flexible ligands enables them to form different molecular systems and extended network materials.

4 Conclusions

Eight salen-type Schiff base ligands have been used in the synthesis of 4f and d-4f clusters. The stoichiometry and structures of these lanthanide-based clusters are dependent on the Schiff base ligands employed in their syntheses as well as the types of d-block metal ions, lanthanide ionic radius, counter ions, and reaction conditions. Most of these multi-metallic lanthanide-based complexes have interesting "enclosed" structures, such as multi-decker, "twisted," and drum-like structures. Of the polynuclear complexes described in this chapter, one octanuclear Eu (III) complex and one hexanuclear Zn-Nd complex have been constructed by the use of two different ligands (one is a Schiff base ligand and the other a bridging ligand 1,4-BDC).

In these lanthanide-based complexes, the salen-type ligands can stabilize Ln^{III} centers and act as antenna sensors for lanthanide luminescence. In d-4f complexes, Zn^{2+} and Cd^{2+} may enhance the luminescence via $d \rightarrow f$ energy transfer. With the Ln^{3+} centers protected by the Schiff base ligands from solvent and water molecules, those lanthanide-based complexes with "enclosed" structures show impressive visible and NIR emissions.

Overview

The synthesis, structures and luminescence properties of twenty-three 4f and d-4f clusters which are formed from eight salen-type Schiff base ligands are described in this chapter.

References

1. Jin R (2010) Nanoscale 2:343–362
2. Maity P, Xie S, Yamauchi M, Tsukuda T (2012) Nanoscale 4:4027–4037
3. Jiang D-E (2013) Nanoscale 5:7149–7152
4. Pei Y, Zeng XC (2012) Nanoscale 4:4054–4072
5. Wang B, Zang Z, Wang H, Dou W, Tang X, Liu W, Shao Y, Ma J, Li Y, Zhou J (2013) Angew Chem Int Ed 52:3756–3760
6. Stamatatos TC, Foguet-Albiol D, Wernsdorfer W, Abboud KA, Christou G (2011) Chem Commun 47:274–276
7. Langley SK, Stott RA, Chilton NF, Moubaraki B, Murray KS (2011) Chem Commun 47:6281–6283
8. Müller A (2007) Nature 447:1034–1035
9. Müller A, Kögerler P, Dress AWM (2001) Coord Chem Rev 222:193–218
10. Mednikov EG, Jewell MC, Dahl LF (2007) J Am Chem Soc 129:11619–11630
11. Bünzli J-CG (1989) Lanthanides probes in life, chemical and earth sciences, vol 1989. Elsevier, Amsterdam
12. Piguet C, Bünzli J-CG (1999) Chem Soc Rev 28:347–358
13. Xiang S-C, Hu S-M, Sheng T-L, Fu R-B, Wu X-T, Zhang X-D (2007) J Am Chem Soc 129:15144–15146
14. Zaleski CM, Depperman EC, Kampf JW, Kirk ML, Pecoraro VL (2004) Angew Chem Int Ed 43:3912–3914
15. Mereacre VM, Ako AM, Clerac R, Wernsdorfer W, Filoti G, Bartolome J, Anson CE, Powell AK (2007) J Am Chem Soc 129:9248–9249
16. Mishra A, Wernsdorfer W, Abboud KA, Christou G (2004) J Am Chem Soc 126:15648–15649
17. Yukawa Y, Aromi G, Igarashi S, Ribas J, Zvyagin SA, Krzystek J (2005) Angew Chem Int Ed 44:1997–2001
18. Kong X-J, Ren Y-P, Long L-S, Zheng Z, Huang R-B, Zheng L-S (2007) J Am Chem Soc 129:7016–7017
19. Peng J-B, Zhang Q-C, Kong X-J, Zheng Y-Z, Ren Y-P, Long L-S, Huang R-B, Zheng L-S, Zheng Z-P (2012) J Am Chem Soc 134:3314–3317
20. Lehn J-M (1995) Supramolecular chemistry. VCH, Weinheim
21. Hasegawa Y, Nakagawa T, Kawai T (2010) Coord Chem Rev 254:2643–2651
22. Li X-L, Shi L-X, Zhang L-Y, Wen HM, Chen ZN (2007) Inorg Chem 46:10892–10900
23. Xu H-B, Shi L-X, Ma E, Zhang L-Y, Wei Q-H, Chen Z-N (2006) Chem Commun 1601–1603
24. Baca SG, Adams H, Grange CS, Smith AP, Sazanovich I, Ward MD (2007) Inorg Chem 46:9779–9789
25. Davies GM, Pope SJA, Adams H, Faulkner S, Ward MD (2005) Inorg Chem 44:4656–4665
26. Yin M, Lei X, Li M, Yuan L, Sun J (2006) J Phys Chem Solids 67:1372–1378
27. Wong W-K, Liang H, Wong W-Y, Cai Z, Li K-F, Cheah K-W (2002) New J Chem 26:275–278
28. Torelli S, Imbert D, Cantuel M, Bernardinelli G, Delahaye S, Hauser A, Bünzli J-CG, Piguet C (2005) Chem Eur J 11:3228–3242
29. Piguet C, Bünzli J-CG, Bernardinelli G, Hopfgartner G, Petoud S, Schaad O (1996) J Am Chem Soc 118:6681–6682
30. Chi Y-X, Niu S-Y, Jin J, Wang R, Li Y (2009) J Chem Soc Dalton Trans 47:7653–7659

31. Chi Y-X, Niu S-Y, Wang Z-L, Jin J (2008) Eur J Inorg Chem 2336–2343
32. Ermolaev VL, Sveshnikova EB (1994) Russ Chem Rev 63:905–922
33. Cortes J-P, Dahan F, Dupuis A (2000) Inorg Chem 39:165–168
34. Richardson FS (1982) Chem Rev 82:541–552
35. Yanagida S, Hasegawa Y, Murakoshi K, Wada Y, Nakashima N, Yamanaka T (1998) Coord Chem Rev 171:461–480
36. Yang X-P, Jones RA (2005) J Am Chem Soc 127:7686–7687
37. Yang X-P, Jones RA, Oye MM, Holmes A, Wong W-K (2006) Crystal Growth Des 2122–2125
38. Yang X-P, Jones RA, Wong W-K (2008) Dalton Trans 1676–1678
39. Yang X-P, Hahn B, Jones RA, Wong W-K, Stevenson K (2007) Inorg Chem 46:7050–7054
40. Petoud S, Cohen SM, Bünzli J-CG, Raymond KN (2003) J Am Chem Soc 125:13324–13325
41. Sabbatini N, Guardigli M, Lehn JM (1993) Coord Chem Rev 123:201–228
42. Guerriero P, Tamburini S, Vigato PA (1995) Coord Chem Rev 139:17–243
43. Yang X-P, Jones RA, Wong W-K (2008) Chem Commun 3266–3268
44. Yang X-P, Michael MO, Jones RA, Huang S-M (2013) Chem Commun 49:9579–9581
45. Liao S, Yang X-P, Jones RA (2012) Crystal Growth Des 12:970–976
46. Lin P-H, Sun W-B, Yu M-F, Li G-M, Yan P-F, Murugesu M (2011) Chem Commun 47:10993–10995
47. Hernandez I, Tan RHC, Pearson JM, Wyatt PB, Gillin WP (2009) J Phys Chem B 113:7474–7480
48. Wong W-K, Yang X-P, Jones RA, Rivers J, Lynch V, Lo W-K, Xiao D, Oye MM, Holmes A (2006) Inorg Chem 45:4340–4345
49. Kong X-J, Ren Y-P, Chen W-X, Long L-S, Zheng Z, Huang R-B, Zheng L-S (2008) Angew Chem Int Ed 47:2398–2401
50. Müller A, Krickemeyer E, Bögge H, Schmidtmann M, Peters F (1998) Angew Chem Int Ed 37:3359–3363
51. Fenske D, Persau C, Dehnen S, Anson CE (2004) Angew Chem Int Ed 43:305–308
52. Fenske D, Anson CE, Eichhöfer A, Fuhr O, Ingendoh A, Persau C, Richert C (2005) Angew Chem Int Ed 44:5242–5246
53. Bünzli J-CG (2004) Metal ions in biological systems, vol 42. Marcel Dekker, New York
54. Hemmila I, Webb S (1997) Drug Discov Today 2:373–375
55. Stouwdam JW, Hebbink GA, Huskens J, Van Veggel FCJM (2003) Chem Mater 15:4604–4616
56. Yang X-P, Jones RA, Lynch V, Oye MM, Holmes A (2005) Dalton Trans 5:849–851
57. Yang X-P, Jones RA, Wong W-K, Lynch V, Oye MM, Holmes A (2006) Chem Commun 1836–1838
58. Yang X-P, Schipper D, Zhang L-J, Yang K-Q, Huang S-M, Jiang J-J, Su C-Y, Jones RA (2014) Nanoscale 6:10569–10572
59. Yang X-P, Li Z-P, Wang S-Q, Huang S-M, Schipper D, Jones RA (2014) Chem Commun 50:15569–15572
60. Brown K, Yang X-P, Schipper D, Hall J, DePue L, Gnanam A, Arambula J, Jones J, Swaminathan J, Dieye Y, Vadivelu J, Chandler D, Marcotte E, Sessler J, Ehrlich L, Jones RA (2015) Dalton Trans 44:2667–2675
61. Canton I, Battaglia G (2012) Chem Soc Rev 41:2718–2739

4f-Clusters for Cryogenic Magnetic Cooling

Yan-Cong Chen, Jun-Liang Liu, and Ming-Liang Tong

Abstract Based on the magnetocaloric effect (MCE), cryogenic magnetic cooling is one of the most promising applications of molecule-based magnets. In recent years, 4f-clusters played important roles and set up several records in such area, some of which exhibit large and promising cryogenic MCE catching up the commercial coolant GGG. Here in this chapter, we focus on the structure–magnetocaloric correlations of 4f-clusters and 4f-cluster-based coordination polymers for use as cryogenic magnetic coolants. The assembly strategies are introduced and discussed on the purpose of obtaining high performance 4f-clusters for cryogenic magnetic cooling. Then, the recent development is summarized and accompanied by the discussion on representative examples. Finally, the outlooks about the future research directions in this area are made.

Keywords Cluster compounds • Lanthanide • Magnetic coolant • Magnetocaloric effect • Magnetocaloric material

Contents

Y.-C. Chen, J.-L. Liu, and M.-L. Tong (✉)
Key Laboratory of Bioinorganic and Synthetic Chemistry of Ministry of Education, School of Chemistry and Chemical Engineering, Sun Yat-sen University, Guangzhou 510275, Peoples Republic of China
e-mail: tongml@mail.sysu.edu.cn

Abbreviations

|	
3-TCA	Thiophene-3-carboxylic acid
CAA	Chloroacetic acid
DMC	N,N'-dimethylcarbamic acid anions
H_2DPA	Diphenic acid
H_3dhpimp	(E)-2-(2,3-dihydroxypropylimino)methyl)-phenol
H_4bmhcp	2,6-Bis[(3-methoxysalicylidene)hydrazinecarbonyl]pyridine
HNA	Nicotinic acid
mvandeta	N,N',N''-Trimethyl-N,N''-bis(2-hydroxy-3-methoxy-5-methylbenzyl)-diethylenetriamine
thmeH$_3$	Tris(hydroxymethyl)ethane
tpaH	Triphenylacetic acid

1 Introduction

The history of cryogenic MCE began in the early 1930s using paramagnetic salts to obtain ultra-low temperature down to the sub-Kelvin level by adiabatic demagnetization [1, 2]. Many different kinds of materials have been studied in the following years, including metals, alloys and intermetallic compounds, and the gadolinium gallium garnet ($Gd_3Ga_5O_{12}$, GGG) is chosen nowadays as the commercial cryogenic magnetic coolant.

As a major field in molecular magnetism, cryogenic magnetic cooling using molecule-based materials grew rapidly in the last decade [3–10]. The adventure began with the 3d metal clusters with high spin (S); however, their performance was limited by strong magnetic coupling and/or large magnetic anisotropy. Later, 4f ions, especially the Gd(III) ions, were intensively studied in both 3d-4f systems and pure 4f systems, leading to significant breakthroughs on not only the molecular clusters but also the cluster-based coordination polymers with large cryogenic MCE, catching up the commercial coolant GGG.

Here in this chapter, we focus on the 4f-clusters for cryogenic magnetic cooling. Firstly, the basic theory and assembly strategies are introduced, followed by the case study on the structure–magnetocaloric correlations on recent development of discrete 4f-clusters and the 4f-cluster-based coordination polymers. Finally, the prospect and challenges are concluded.

2 Basic Theory

The MCE of a magnetic coolant can be evaluated by two key parameters, namely –ΔS_M (isothermal magnetic entropy change) and ΔT_{ad} (adiabatic temperature change). For a magnetic insulator with negligible electronic entropy, the total
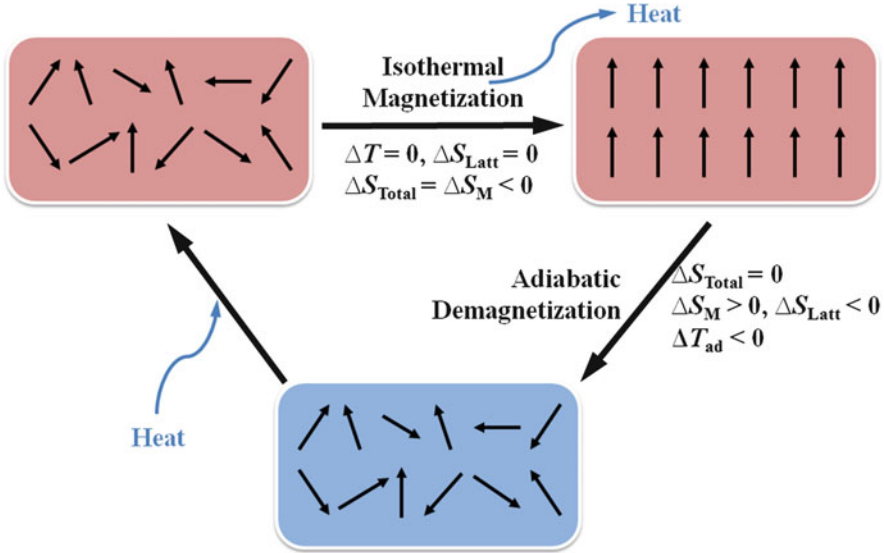
Scheme 1 The isothermal magnetization process and adiabatic demagnetization process in magnetic cooling

entropy (S_{Total}) only comprises the field-dependent magnetic entropy (S_M) and the field-independent lattice entropy (S_{Latt}) [11, 12].

$$S_{Total}(T,H) = S_M(T,H) + S_{Latt}(T) \tag{1}$$

During an isothermal magnetization process, the temperature and the lattice entropy are unchanged ($\Delta T = 0$, $\Delta S_{Latt} = 0$) whereas the increasing magnetic field removes the degeneracies of the energy levels and leads to a decrease in the magnetic entropy ($\Delta S_{Total} = \Delta S_M < 0$), and the heat produced in this process should be released to environment.

Then, during an adiabatic demagnetization process, the total entropy is unchanged ($\Delta S_{Total} = 0$), whereas the degeneracies of the energy levels are restored and lead to an increase in the magnetic entropy ($\Delta S_M > 0$). As compensation, the lattice entropy must decrease ($\Delta S_{Latt} < 0$) and appear as a temperature drop ($\Delta T_{ad} < 0$). By running such a system in reversible magnetothermal cycles, heat can be pumped out continuously and achieve the magnetic cooling (Scheme 1).

To evaluate a given material for magnetic cooling, the $-\Delta S_M$ and ΔT_{ad} parameters can be calculated from isothermal magnetization using the Maxwell equation, $[\partial S_M(T,H)/\partial H]_T = [\partial M(T,H)/\partial T]_H$, and from heat capacity applying the integration either from absolute zero or from the high-temperature end [10]. In addition, the ΔT_{ad} can also be directly measured by running a pseudo-adiabatic magnetization/demagnetization process.

3 Assembly Strategies

To obtain high performance 4f-clusters for cryogenic magnetic cooling, the most primary requirement is the high spin, because the full magnetic entropy is defined as $S_M = R\ln(2S + 1)$ for a magnetic system with a well-isolated spin-only S, and this will act as the upper limit of the maximum ΔS_M. Since the zero-field splitting, spin–orbit coupling and magnetic interactions can largely reduce the degeneracies, Gd(III) is the most promising candidate owing to the large $S = \frac{7}{2}$ single-ion spin from the $4f^7$ electron configuration and the negligible anisotropy without orbital contribution. In addition, the magnetic interactions between Gd(III) ions are usually weak and thus extremely suitable for a large MCE. If the complex is properly designed, a maximum $-\Delta S_m$ value of $R\ln(8)$ or $2.08R$ can be obtained for each Gd(III).

However, things are not so simple as the Gd(III) ion cannot form a compound all on its own – ligands and/or counter ions are necessary to balance the charge and provide the coordination environment. Although these nonmagnetic components do not have direct influence on magnetic cooling, they inevitably take up weight and space, thus lowering the performances when evaluating the MCE in the practical units, such as the gravimetric (J kg^{-1} K^{-1}) and volumetric (mJ cm^{-3} K^{-1}) ones.

The most straightforward and also successful strategy is to select small and light bridging ligands, which increase the metal-to-ligand ratio in the compound. These include the carboxyl groups ($-COO^-$) and most inorganic anions such as OH^-, CO_3^{2-} and SO_4^{2-}. However, such a strategy is a double-edged sword as the magnetic interactions will become stronger with small bridging ligands, which hinder the full exploitation of magnetic entropy. For the polymeric materials, the long-range magnetic ordering temperature may also be increased.

Combining organic and inorganic ligands in 4f-clusters and 4f-cluster-based coordination polymers is another successful approach to strike a balance between dense structures and strong magnetic interactions. The inorganic core inside the cluster can maximize the density of spin carriers; while the organic ligands on the shell (or as linkers) separate neighbouring clusters and keep the ordering temperature below the working region.

Finally, if the magnetic interactions are inevitable, choosing suitable bridging ligands such as F^- ions to achieve ferromagnetic interactions is much better than antiferromagnetic ones. Indeed, although weak ferromagnetic interactions lower the maximum approachable value of $-\Delta S_m$ compared with paramagnetic cases, the performance at a high temperature and in lower fields can be improved. This is of great significance to practical application as the working field can be provided by the convenient permanent magnets instead of superconducting electromagnets.

4 Recent Development

4.1 4f-Clusters for Cryogenic Magnetic Cooling

The disc-like $\{Gd_7\}$ (Fig. 1), $[Gd_7(OH)_6(thmeH_2)_5(thmeH)(tpa)_6(MeCN)_2](NO_3)_2$ (**1**) [13], was solvothermally synthesized from $Ln(NO_3)_3 \cdot 5H_2O$, the tripodal alcohol tris(hydroxymethyl)ethane (thmeH_3) and triphenylacetic acid (tpaH). The central Gd(III) was surrounded by a Gd_6 hexagon with six μ_3-OH groups alternating above and below the plane, and the outer shell is constructed by $thmeH_2^-$, $themH^{2-}$ and tpa^-.

The magnetic interactions between Gd(III) are antiferromagnetic, but the frustrated topology leads to low-lying excited states, thereby yielding a comparable $-\Delta S_M = 23$ J kg^{-1} K^{-1} at 3 K with $\Delta H = 70$ kOe. Although the $-\Delta S_M$ value was quite large at that time, however, it is only equivalent to $10.6R$ compared with the full entropy of $14.6R$ for seven uncoupled Gd(III), thereby demonstrating the need to reduce antiferromagnetic coupling.

Subsequently, the simple and well-known ferromagnetic $\{Gd_2\}$ dimer (Fig. 2) of gadolinium acetate tetrahydrate, $[\{Gd(OAc)_3(H_2O)_2\}_2] \cdot 4H_2O$ (**2**) [14], was evaluated by magnetization, heat capacity and direct measurements to assess its MCE.
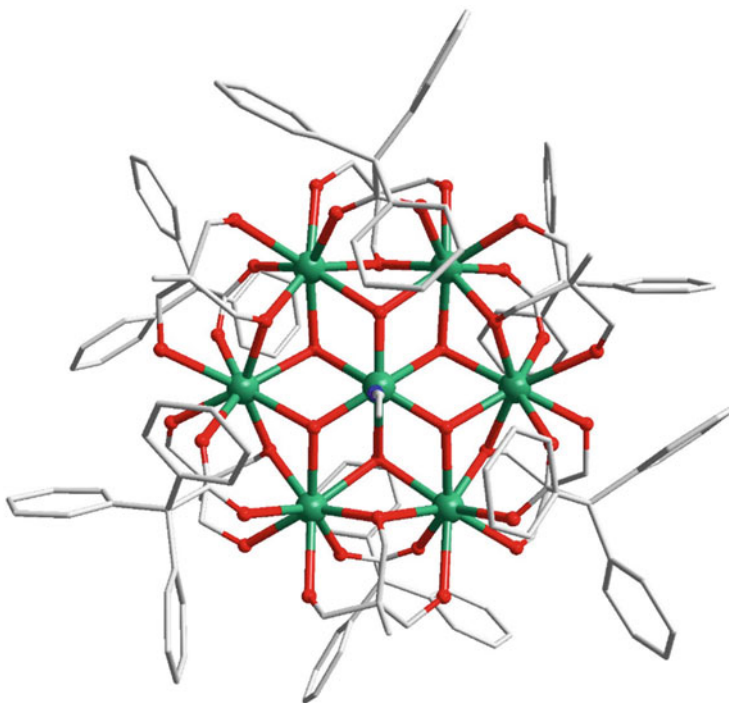

Fig. 1 Crystal structure of $[Gd_7(OH)_6(thmeH_2)_5(thmeH)(tpa)_6(MeCN)_2](NO_3)_2$ (**1**)
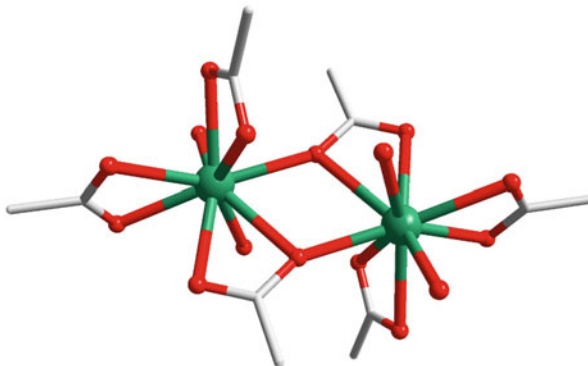
Fig. 2 Crystal structure of $[\{Gd(OAc)_3(H_2O)_2\}_2] \cdot 4H_2O$ (**2**)

The ferromagnetic interactions in this compound lead to nice performance with a relatively modest $\Delta H = 10$ kOe, namely $-\Delta S_M = 27$ J kg^{-1} K^{-1} at 0.5 K and $\Delta T_{ad} = 3.5$ K. For larger ΔH, the maximum value of $-\Delta S_M$ exceeds 40 J kg^{-1} K^{-1} at 1.8 K with $\Delta H = 70$ kOe, approaching the upper limit of 42.5 J kg^{-1} K^{-1} corresponding to $4.16R$. Finally, the magnetic ordering T_c was estimated by a Metropolis Monte Carlo simulation as 0.18 K, far below the working region. Although this complex is somewhat similar to the gadolinium sulphate octahydrate, $Gd_2(SO_4)_3 \cdot 8H_2O$, used at the very first age of cryogenic magnetic cooling, it is believed that this $\{Gd_2\}$ dimer possesses quite an advantage owing to the intramolecular ferromagnetic coupling ($J = 0.068(2)$ K). Recently, a Zn–Gd cluster complex, $[Zn_2Gd_2(mvandeta)_2(CO_3)_2(NO_3)_2] \cdot 4CH_3OH$ (**3**) [15], was reported with similar Gd–Gd bridging fragments. A weak intra-dimer ferromagnetic interaction of $J = 0.038(2)$ K was found. Similarly, the maximal value of $-\Delta S_M = 18.5$ J kg^{-1} K^{-1} at 1.9 K with $\Delta H = 70$ kOe was close to the full entropy content; however, the diamagnetic Zn^{2+} and bulky ligands lead to the large difference in the performance between $\{Zn_2Gd_2\}$ and $\{Gd_2\}$.

The following dimer $[Gd_2(OAc)_2(Ph_2acac)_4(MeOH)_2]$ (**4**) and tetranuclear $[Gd_4(OAc)_4(acac)_8(H_2O)_4]$ (**5**) clearly demonstrated how the metal-to-ligand ratio can affect the MCE properties (Fig. 3) [16]. Both complexes are ferromagnetically coupled, namely $J = 0.04$ cm^{-1} for **4** and $J_1 = J_2 = 0.02$ cm^{-1} for **5**. The maximum values of $-\Delta S_M$ reach $1.98R$ and $1.96R$, respectively, very close to the full entropy of $2.08R$. However, the difference arises from the Mw/N_{Gd}, namely 695 g mol^{-1} for **4** and 432.5 g mol^{-1} for **5**. Therefore, the $-\Delta S_M$ values are largely differed as 23.7 J kg^{-1} K^{-1} at 2.4 K with $\Delta H = 70$ kOe for **4** and 37.7 J kg^{-1} K^{-1} at 2.4 K with $\Delta H = 70$ kOe for **5**, respectively.

The square-based pyramid $[Gd_5O(O^iPr)_{13}]$ (**6**, Fig. 4) was obtained from reactions between anhydrous $LnCl_3$ and isopropanol (^iPrOH) and belongs to the $\{Ln_5\}$ family [17]. The μ_5-O and μ_3-O^iPr provide efficient routes for intramolecular antiferromagnetic coupling with a frustrated $J = -0.085$ cm^{-1}. Although the maximum $-\Delta S_M$ of 34 J kg^{-1} K^{-1} can be achieved at 3 K with $\Delta H = 70$ kOe, it is well

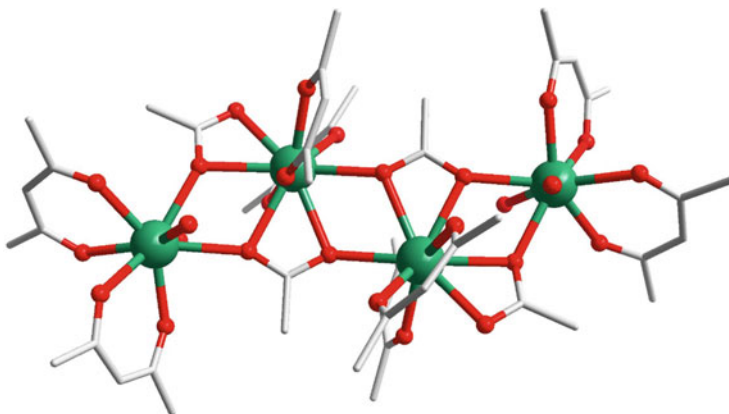**Fig. 3** Crystal structure [Gd$_4$(OAc)$_4$(acac)$_8$(H$_2$O)$_4$] (**5**)
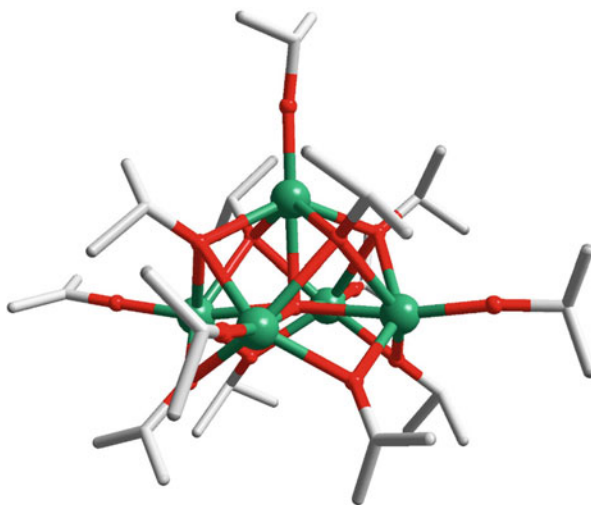
Fig. 4 Crystal structure of [Gd$_5$O(O^{i}Pr)$_{13}$] (**6**)

below the limit value of 55 J kg^{-1} K^{-1}. Apart from the relatively strong magnetic coupling, the high magnetic anisotropy that leads to nice SMM behaviour for Dy and Ho derivatives actually plays a negative role for Gd as a magnetic coolant.

By the reaction of Ln(NO$_3$)$_3 \cdot$ 6H$_2$O, HO$_2$C^{t}Bu, H$_2$O$_3$P^{t}Bu and a mild base ^{i}PrNH$_2$ in ^{t}BuOH, the "horseshoe" 4f-phosphonate clusters, (NH$_3$^{i}Pr)$_2$ [Gd$_8$(O$_3$P^{t}Bu)$_6$(μ_3-OH)$_2$(H$_2$O)$_2$(HO^{i}Bu)(O$_2$C^{t}Bu)$_{12}$] (**7**) [18], can be isolated. The structure of this complex comprises a {Gd$_8$P$_6$} core (Fig. 5), while the outer shell is encapsulated by hydrophobic *tert*-butyl groups. The clusters are well isolated with weak but antiferromagnetic interactions among Gd(III) ions, which were evaluated based on

Fig. 5 Crystal structure of $[Gd_8(O_3P^tBu)_6(\mu_3\text{-OH})_2(H_2O)_2(HO^iBu)(O_2C^tBu)_{12}](NH_3{}^iPr)_2$ (**7**)

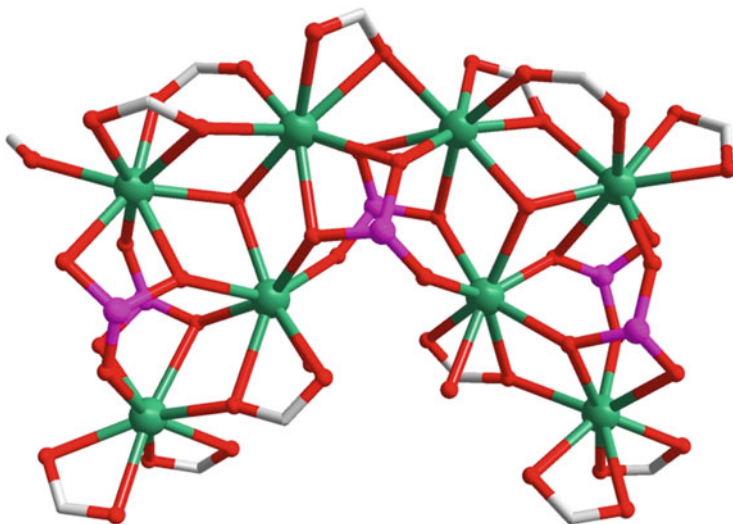an equivalent neighbouring exchange parameter of $J = -0.03$ cm^{-1}. The maximum value of $-\Delta S_M$ is 32.3 J kg^{-1} K^{-1} at 3 K with $\Delta H = 70$ kOe, which is lower than the expected value of 45.9 J kg^{-1} K^{-1} for eight uncoupled Gd(III). Although the $-\Delta S_M$ value itself is moderate, this case was the first magnetic entropy study on the 4f-phosphonate clusters and opened a new category thereafter.

An unprecedented {Gd$_{10}$} cluster comprising the $[Gd_{10}(\mu_3\text{-OH})_8]^{22+}$ core, $[Gd_{10}(3\text{-TCA})_{22}(\mu_3\text{-OH})_8(H_2O)_4]$ (**8**, Fig. 6) [19], is formed via a hydrothermal reaction between Gd_2O_3 and 3-TCA. The Gd_2O_3 acts as both a slow-release Gd(III) source and a pH regulator of the system, leading to an inorganic core surrounded by the organic shell of 3-TCA. The weak antiferromagnetic interaction with $\theta = -1.78$ K yields $\Delta T_{ad} = 8.7$ K at 2 K and $-\Delta S_M = 31.2$ J kg^{-1} K^{-1} at 3 K with $\Delta H = 70$ kOe, which is close to the calculated value of 37.8 J kg^{-1} K^{-1}, despite the relatively high inorganic component of such compound.

Another decanuclear 4f-cluster, $[Gd_{10}(bmhcp)_5(\mu\text{-OH})_6(H_2O)_{22}](Cl)_4 \cdot 7H_2O$ (**9**, Fig. 7), can be synthesized using a hydrazine-based ligand H$_4$bmhcp [20]. The cage can be regarded as a $2 \times [1 \times 5]$ rectangular array, with five ligands categorized into three "rungs" and two "rails". The rung locks were acted by six Gd(III) ions, while each discrete molecule encapsulates three Cl$^-$ ions at the centre by hydrogen bonds. The magnetic interactions between Gd(III) are antiferromagnetic, and the maximum $-\Delta S_M$ is moderate as 37.4 J kg^{-1} K^{-1} at 3 K with $\Delta H = 70$ kOe.

The truncated tetrahedral cluster {Gd$_{12}$} (Fig. 8), $[Gd_{12}Mo_4O_{16}(Hdhpimp)_6(\mu_3\text{-OH})_4 (MeCO_2)_{12}] \cdot 12MeOH \cdot 8H_2O$ (**10**), was solvothermally synthesized with the presence of $(n\text{-Bu}_4N)_4Mo_8O_{26}$ [21]. Four oxometalate ions, MoO$_4{}^{2-}$,

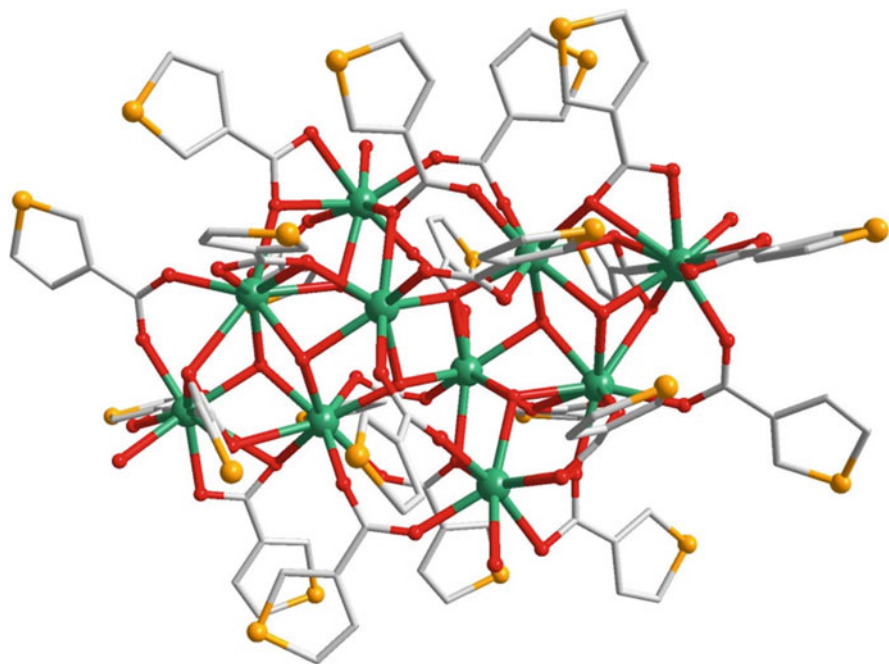**Fig. 6** Crystal structure of $[Gd_{10}(3\text{-}TCA)_{22}(\mu_3\text{-}OH)_8(H_2O)_4]_2$ (**8**)

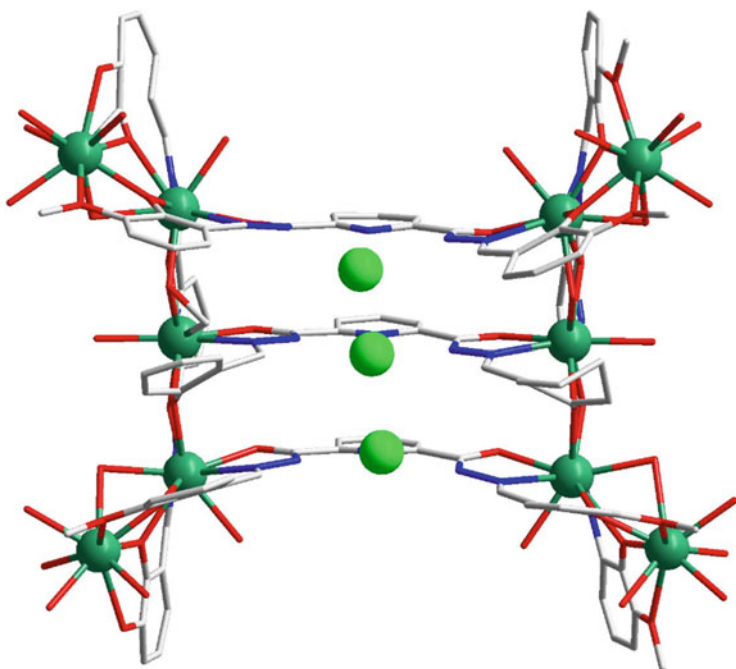**Fig. 7** Crystal structure of $[Gd_{10}(bmhcp)_5(\mu\text{-}OH)_6(H_2O)_{22}]Cl_4 \cdot 7H_2O$ (**9**)
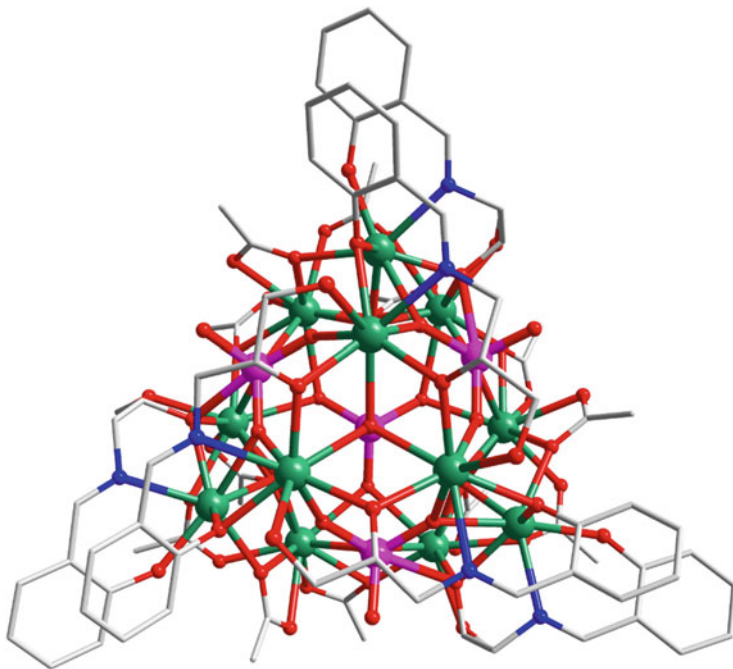
Fig. 8 Crystal structure of $[Gd_{12}Mo_4O_{16}(Hdhpimp)_6(\mu_3\text{-OH})_4(MeCO_2)_{12}] \cdot 12MeOH \cdot 8H_2O$ (**10**)

were found in the final cluster and served as the templates for the assembly. The magnetic interactions are antiferromagnetic with the exchange constant J estimated as -0.04 K using a Monte Carlo simulation and the finite temperature Lanczos method. The highest $-\Delta S_M$ value reached 35.3 J kg^{-1} K^{-1} at 3 K with $\Delta H = 70$ kOe, close to the calculated value of 41.6 J kg^{-1} K^{-1}.

The capsule-like $\{Gd_{24}\}$, $[Gd_{24}(DMC)_{36}(\mu_4\text{-CO}_3)_{18}(\mu_3\text{-H}_2O)_2] \cdot 6H_2O$ (**11**) [22], comprises DMC and CO_3^{2-} anions which are both in situ generated from DMF and act as coats and bridges, respectively (Fig. 9). It is a rare case of high-nuclearity lanthanide clusters without bridging OH$^-$ groups, thus the antiferromagnetic interactions between Gd(III) ions are quite weak with a small Weiss constant $\theta = -0.16$ K. This combined with the low molecular weight normalized per Gd(III) as 340.39 g mol^{-1} leads to a maximum $-\Delta S_M$ value of 46.1 J kg^{-1} K^{-1} at 2.5 K with $\Delta H = 70$ kOe, approaching the theoretical limit of 52.1 J kg^{-1} K^{-1}. For an anisotropic Dy(III) analogue, however, the maximum $-\Delta S_M$ value declines to only 13.8 J kg^{-1} K^{-1} at 7 K with $\Delta H = 70$ kOe mainly owing to the magnetic anisotropy of Dy(III) ions.

The nanoscale $\{Gd_{38}\}$ cage and $\{Gd_{48}\}$ barrel, i.e., $[Gd_{38}(\mu\text{-O})(\mu_8\text{-ClO}_4)_6(\mu_3\text{-OH})_{42}(CAA)_{37}(H_2O)_{36}(EtOH)_6](ClO_4)_{10}(OH)_{17} \cdot 14DMSO \cdot 13H_2O$ (**12**) and $[Gd_{48}(\mu_4\text{-O})_6(\mu_3\text{-OH})_{84}(CAA)_{36}(NO_3)_6(H_2O)_{24}(EtOH)_{12}(NO_3)Cl_2]$ $Cl_3 \cdot 6DMF \cdot 5EtOH \cdot 20H_2O$ (**13**) [23], demonstrated the anion-templated synthesis of high-nuclearity lanthanide clusters with large MCEs (Fig. 10). The basic units are
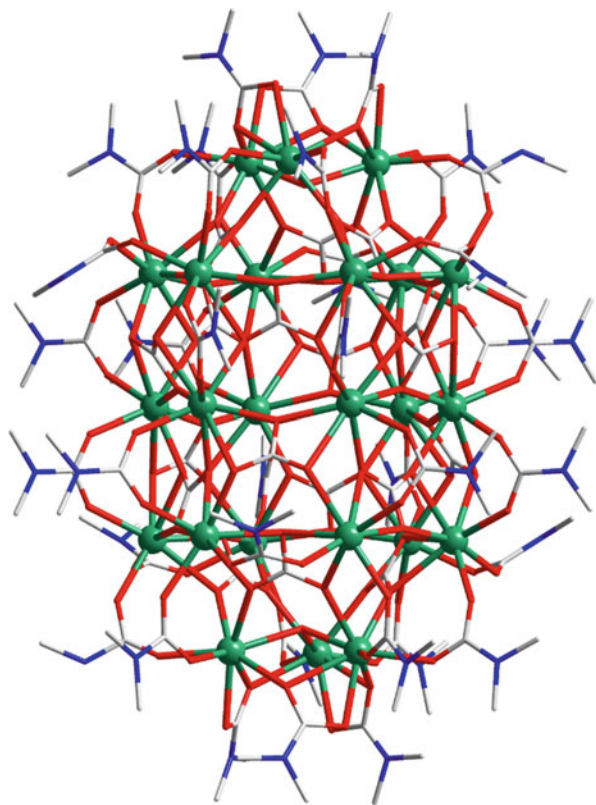
Fig. 9 Crystal structure of $[Gd_{24}(DMC)_{36}(\mu_4\text{-}CO_3)_{18}(\mu_3\text{-}H_2O)_2]\cdot 6H_2O$ (**11**)
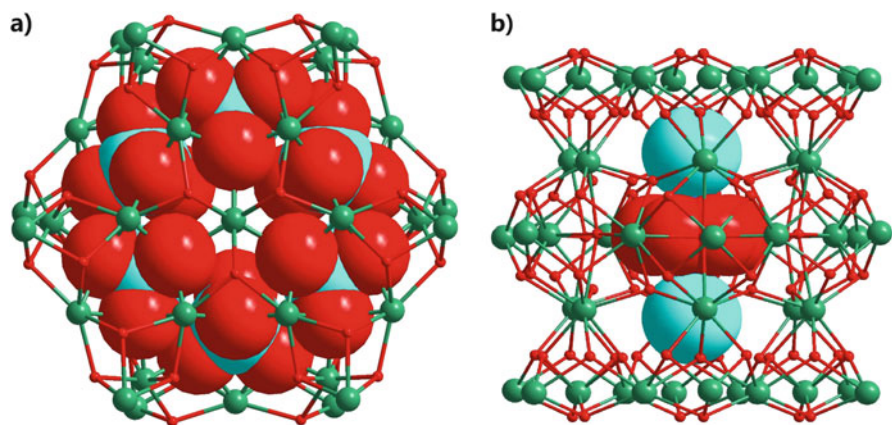
Fig. 10 Crystal structures of **12** (a) and **13** (b)

tetrahedral $\{Gd_4\}$ and/or pyramidal $\{Gd_5\}$, which connected with the anion template and hydroxyl groups into $\{Gd_{38}(ClO_4)_6\}$ for **12** and $\{Gd_{48}Cl_2(NO_3)\}$ for **13**. Both complexes exhibit antiferromagnetic interactions among Gd(III) ions: for **12**, the Weiss constant is $\theta = -2.99$ K and the maximum $-\Delta S_M$ value is 37.9 J kg^{-1} K^{-1} at 1.8 K with $\Delta H = 70$ kOe, while for **13**, $\theta = -3.57$ K and $-\Delta S_M$ increases to 43.6 J kg^{-1} K^{-1} at 1.8 K with $\Delta H = 70$ kOe. Although these are still less than the upper limit of 42 and 50.4 J kg^{-1} K^{-1}, respectively, their relatively high mass densities of 2.689 and 2.769 g cm^{-3} serve as a compensation. When evaluating the values in the volumetric unit, they exhibit much more competitive $-\Delta S_M$ of 102 and 120.7 mJ cm^{-3} K^{-1}, respectively.

The giant 104-Gd complex, $[Gd_{104}(ClO_4)_6(CH_3COO)_{56}(\mu_3\text{-OH})_{168}(\mu_4\text{-O})_{30}$ $(H_2O)_{112}](ClO_4)_{22} \cdot 2CH_3CH_2OH \cdot 140H_2O$ (**14**), is the largest known lanthanide-exclusive cluster [24]. This high-nuclearity cluster is synthesized from the hydrolysis of Gd(ClO$_4$)$_3$ with the presence of acetate, forming a four-shell $Gd_8@Gd_{48}@Gd_{24}@Gd_{24}$ arrangement (Fig. 11). The magnetic interactions are
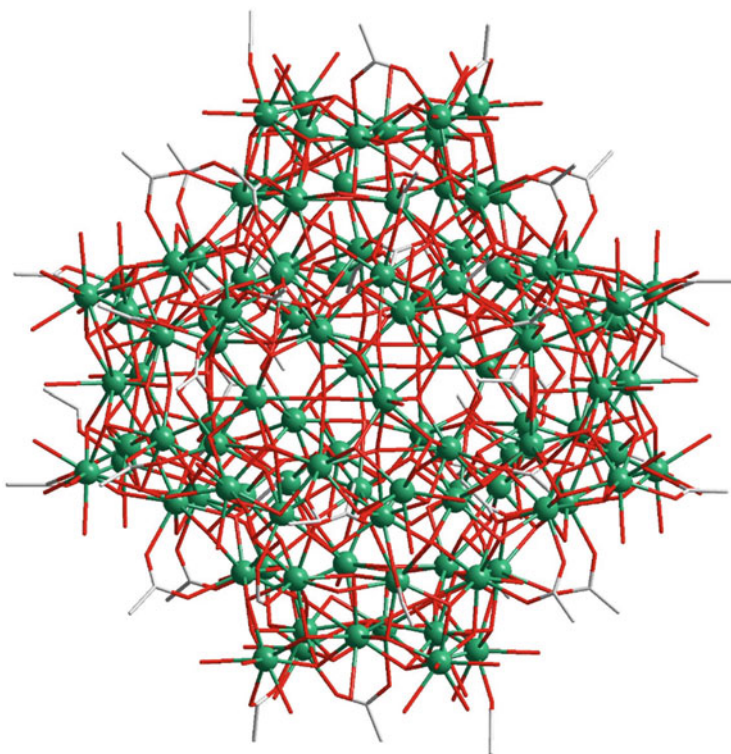
Fig. 11 Crystal structures of $[Gd_{104}(ClO_4)_6(CH_3COO)_{56}(\mu_3\text{-OH})_{168}(\mu_4\text{-O})_{30}$ $(H_2O)_{112}](ClO_4)_{22} \cdot$ $2CH_3CH_2OH \cdot 140H_2O$ (**14**)

also antiferromagnetic with the Weiss constant of $\theta = -4.11$ K, and the maximum $-\Delta S_M$ value is 46.9 J kg^{-1} K^{-1} at 2 K with $\Delta H = 70$ kOe, lower than the anticipated 59.1 J kg^{-1} K^{-1}. However, the large density of 2.945 g cm^{-3} leads to nice $-\Delta S_M$ of 137.2 mJ cm^{-3} K^{-1}, the largest one among 4f-clusters.

4.2   4f-Cluster-Based Coordination Polymers for Cryogenic Magnetic Cooling

The sulphate-based network with distorted cubic $\{Gd_4(\mu_3\text{-}OH)_4\}$ building units, $[Gd_4(SO_4)_4(\mu_3\text{-}OH)_4(H_2O)_4]_n$ (**15**), was synthesized comprising the tetranuclear clusters as 12-connected nodes and the SO_4^{2-} as 4-connected nodes, which lead to a unique (3,12)-connected topological network (Fig. 12) [25]. The magnetic interactions are weakly antiferromagnetic with a negative Weiss constant θ of -1.57 K, and the maximum $-\Delta S_M$ reaches quite a significant value of 51.3 J kg^{-1} K^{-1} (198.9 mJ cm^{-3} K^{-1}) at 2 K with $\Delta H = 70$ kOe owing to the low Mw/N_{Gd} of 288.3 g mol^{-1} and the large density of 3.877 g cm^{-3}.

A similar (3,11)-connected network based on the $\{Gd_4(\mu_3\text{-}OH)_4\}$ building units, $[Gd_4(\mu_4\text{-}SO_4)_3(\mu_3\text{-}OH)_4(\mu\text{-}C_2O_4)(\mu\text{-}H_2O)(H_2O)_4]_n \cdot nH_2O$ (**16**), was synthesized with the in situ generated sulphate and oxalate [26]. This inorganic–organic hybrid framework also exhibits antiferromagnetic interaction with $\theta = -1.57$ K, and the maximum $-\Delta S_M$ value is 51.5 J kg^{-1} K^{-1} (190.5 mJ cm^{-3} K^{-1}) at 2 K with $\Delta H = 70$ kOe, also among the highest ones.
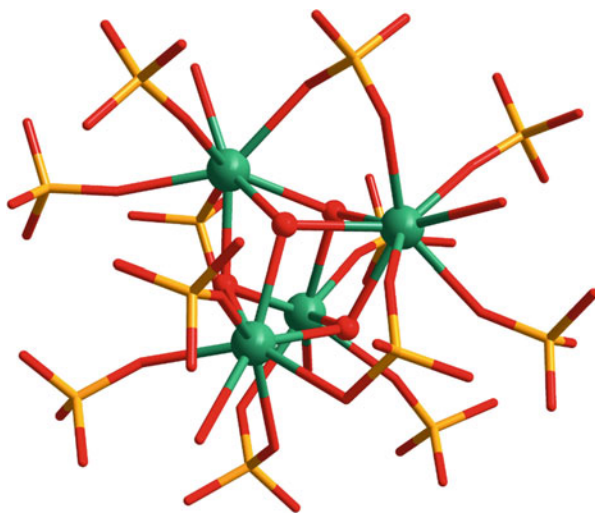
Fig. 12   Crystal structure of $[Gd_4(SO_4)_4(\mu_3\text{-}OH)_4(H_2O)_4]_n$ (**15**)
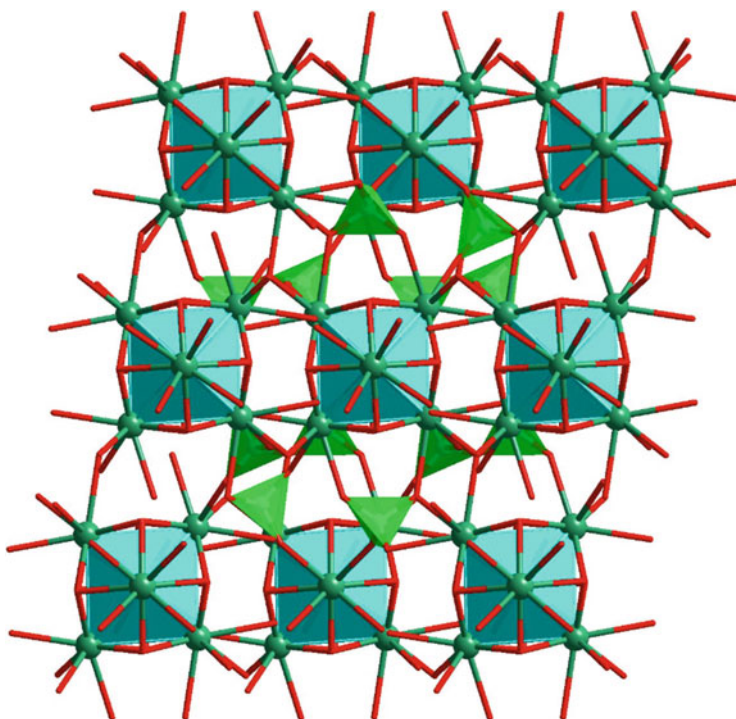
Fig. 13 Crystal structure of $[Gd_4(SO_4)_4(\mu_3\text{-}OH)_4(H_2O)_4]_n$ (**17**)

Based on the well-known octahedral $[Gd_6(\mu_6\text{-}O)(\mu_3\text{-}OH)_8]^{8+}$ nodes, a (3,12)-connected coordination polymer was solvothermally synthesized with the formula of $\{[Gd_6(\mu_6\text{-}O)(\mu_3\text{-}OH)_8(\mu_4\text{-}ClO_4)_4(H_2O)_6](OH)_4\}_n$ (**17**, Fig. 13) [27]. The large amount of inorganic component of this complex yields a very low Mw/N_{Gd} of 278.25 g mol^{-1}, which can lead to an upper limit for the $-\Delta S_M$ value of 62.13 J kg^{-1} K^{-1}. Unfortunately, the experimental value is much lower, namely 46.6 J kg^{-1} K^{-1}, at 2.5 K with $\Delta H = 70$ kOe and far from saturation with increasing fields. This is due mainly to the strong antiferromagnetic interactions between Gd(III) in this complex, characterized by a relatively large $\theta = -5.50$ K. However, the volumetric $-\Delta S_M$ value of up to 215.6 mJ cm^{-3} K^{-1} is still the largest among the 4f-clusters and 4f-cluster-based coordination polymers owing to the high mass density of 4.627 g cm^{-3}.

By hydrothermal reaction of Gd_2O_3, HNA and H_2DPA, the three-dimensional lanthanide framework, $[Gd_7(DPA)_5(NA)_3(\mu_3\text{-}OH)_8(H_2O)_3] \cdot 2.5H_2O$ (**18**), can be obtained [28]. Each heptanuclear $\{Gd_7(\mu_3\text{-}OH)_8\}$ core is formed by two vertex-sharing tetrahedral $\{Gd_4(\mu_3\text{-}OH)_4\}$ units, and the organic ligands further link them
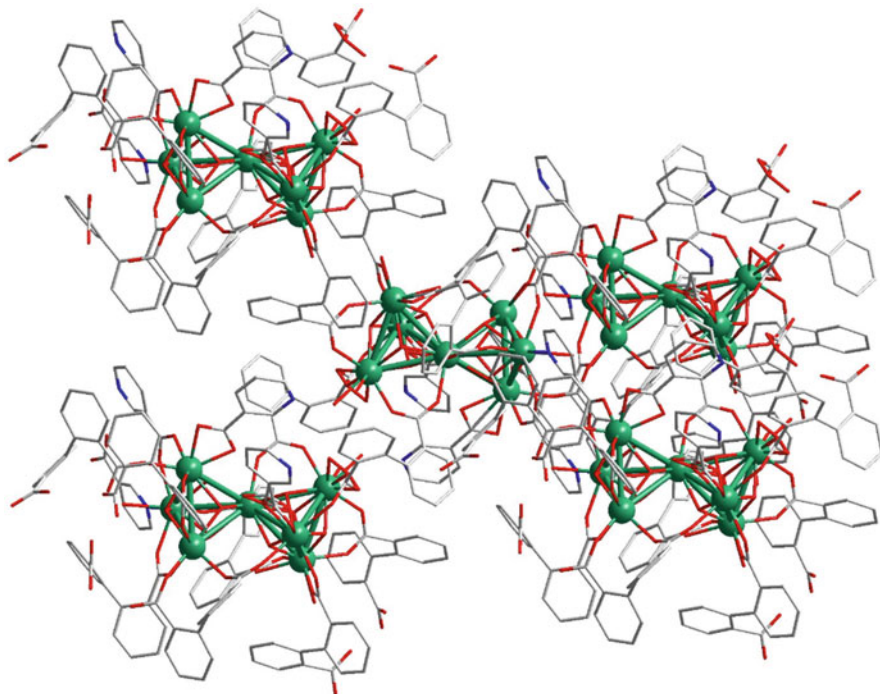
Fig. 14 Crystal structure of $[Gd_7(DPA)_5(NA)_3(\mu_3\text{-}OH)_8(H_2O)_3] \cdot 2.5H_2O$ (**18**)

into a four-connected **dia** net (Fig. 14). The magnetic interactions are antiferromagnetic with $\theta = -0.89$ K, and the maximum value of $-\Delta S_M$ is 34.2 J kg^{-1} K^{-1} at 2.5 K with $\Delta H = 70$ kOe.

The high-nuclearity clusters can also be connected by suitable ligands and extended into cluster-based coordination polymers. A novel two-dimensional coordination polymer, $[Gd_{36}(NA)_{36}(OH)_{49}(O)_6(NO_3)_6(N_3)_3(H_2O)_{20}]_nCl_{2n} \cdot 28nH_2O$ (**19**), is based on the {Gd$_{36}$} clusters (Fig. 15) [29]. The maximum $-\Delta S_M$ value is 39.7 J kg^{-1} K^{-1} at 2.5 K with $\Delta H = 70$ kOe, lower than the limiting 49.64 J kg^{-1} K^{-1}, which is owing to the efficient antiferromagnetic interactions mediated by the OH$^-$ and O^{2-} bridges with $\theta = -2.43$ K. Nevertheless, it provided a rare example of coordination polymers based on high-nuclearity clusters, and such types of compounds still have potential for the further improvement on their MCE (Table 1).
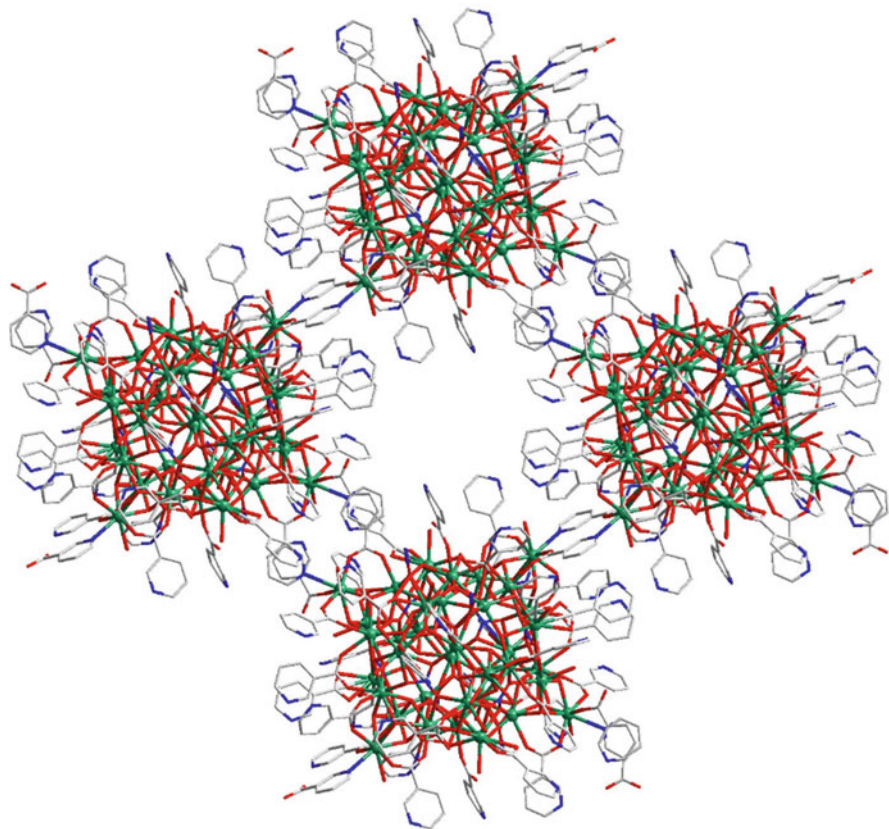
Fig. 15 Crystal structure of $[Gd_{36}(NA)_{36}(OH)_{49}(O)_6(NO_3)_6(N_3)_3(H_2O)_{20}]_nCl_{2n} \cdot 28nH_2O$ (**19**)

5 Conclusion and Outlook

As demonstrated above, a number of 4f-clusters for cryogenic magnetic cooling were reported just in the recent years, ranging from a simple dimer to a huge 104-nuclear cluster. However, most of them exhibit antiferromagnetic interactions between Gd(III) ions, with only a few exceptions [14–16]. Although the intra-cluster magnetic interactions are inevitable in these cluster compounds, they usually exhibit relatively weak inter-cluster magnetic interactions compared with most of the polymeric complexes with higher dimensionalities. As a result, the magnetic ordering temperature can be kept well below the working region for use as cryogenic magnetic coolants.

Many lessons on the magnetostructural correlations have been learned during the design and synthesis of these compounds, and the successful assembly strategies have been generalized and validated. Rational design and targeted synthesis shall

Table 1 $-\Delta S_M$ data at a given temperature with $\Delta H = 70$ kOe

Complex	$-\Delta S_M$		T/K	References
	J kg^{-1} K^{-1}	mJ cm^{-3} K^{-1}		
[Gd$_7$(OH)$_6$(thmeH$_2$)$_5$(thmeH)(tpa)$_6$(MeCN)$_2$](NO$_3$)$_2$ (**1**)	23	41.3	3	[13]
[{Gd(OAc)$_3$(H$_2$O)$_2$}$_2$]·4H$_2$O (**2**)	40.6	82.8	1.8	[14]
[Zn$_2$Gd$_2$(mvandeta)$_2$(CO$_3$)$_2$(NO$_3$)$_2$]·4CH$_3$OH (**3**)	18.5	31.0	1.9	[15]
[Gd$_2$(OAc)$_2$(Ph$_2$acac)$_4$(MeOH)$_2$] (**4**)	23.7	60.1	2.4	[16]
[Gd$_4$(OAc)$_4$(acac)$_8$(H$_2$O)$_4$] (**5**)	37.7	70.2	2.4	[16]
[Gd$_5$O(O^{i}Pr)$_{13}$] (**6**)	34	60.6	3	[17]
[Gd$_8$(O$_3$P^{t}Bu)$_6$(OH)$_2$(H$_2$O)$_2$(HO^{i}Bu)(O$_2$C^{t}Bu)$_{12}$](NH$_3$^{i}Pr)$_2$ (**7**)	32.3	45.0	3	[18]
[Gd$_{10}$(3-TCA)$_{22}$(μ$_3$-OH)$_8$(H$_2$O)$_4$] (**8**)	31.2	68.8	3	[19]
[Gd$_{10}$(bmhcp)$_5$(μ-OH)$_6$(H$_2$O)$_{22}$](Cl)$_4$·7H$_2$O (**9**)	37.4	43.0	3	[20]
[Gd$_{12}$Mo$_4$O$_{16}$(Hdhpimp)$_6$(OH)$_4$(OAc)$_{12}$]·12MeOH·8H$_2$O (**10**)	35.3	77.0	3	[21]
[Gd$_{24}$(DMC)$_{36}$(CO$_3$)$_{18}$(H$_2$O)$_2$]·6H$_2$O (**11**)	46.1	89.9	2.5	[22]
[Gd$_{38}$O(OH)$_{42}$(ClO$_4$)$_6$(CAA)$_{37}$(H$_2$O)$_{36}$(EtOH)$_6$](ClO$_4$)$_{10}$(OH)$_{17}$·14DMSO·13H$_2$O (**12**)	37.9	102	1.8	[23]
[Gd$_{48}$O$_6$(OH)$_{84}$(CAA)$_{36}$(NO$_3$)$_6$(H$_2$O)$_{24}$(EtOH)$_{12}$(NO$_3$)Cl$_2$]Cl$_3$·6DMF·5EtOH·20H$_2$O (**13**)	43.6	120.7	1.8	[23]
[Gd$_{104}$(ClO$_4$)$_6$(CH$_3$COO)$_{56}$(μ$_3$-OH)$_{168}$(μ$_4$-O)$_{30}$(H$_2$O)$_{112}$](ClO$_4$)$_{22}$·2CH$_3$CH$_2$OH·140H$_2$O (**14**)	46.9	137.2	2	[24]
[Gd$_4$(SO$_4$)$_4$(μ$_3$-OH)$_4$(H$_2$O)]$_n$ (**15**)	51.3	198.9	2	[25]
[Gd$_4$(μ$_4$-SO$_4$)$_3$(μ$_3$-OH)$_4$(μ-C$_2$O$_4$)(μ-H$_2$O)(H$_2$O)$_4$]$_n$·nH$_2$O (**16**)	51.5	190.5	2	[26]
{[Gd$_6$O(OH)$_8$(ClO$_4$)$_4$(H$_2$O)$_6$](OH)$_4$}$_n$ (**17**)	46.6	215.6	2.5	[27]
[Gd$_7$(DPA)$_5$(NA)$_3$(μ$_3$-OH)$_8$(H$_2$O)$_3$]·2.5H$_2$O	34.2	74.7	2.5	[28]
[Gd$_{36}$O$_6$(OH)$_{49}$(NA)$_{36}$(NO$_3$)$_6$(N$_3$)$_3$(H$_2$O)$_{20}$]$_n$Cl$_{2n}$·28nH$_2$O (**19**)	39.7	91.3	2.5	[29]

be adopted in the future for high performance cryogenic magnetic coolants. For the 4f-cluster-based coordination polymers, although only a handful of cases have been reported, they have great potential to combine the advantages of discrete clusters and extended frameworks. Indeed, it has been evidenced that the 4f-based coordination polymers and even inorganics can have much superior magnetic cooling performance than any other kinds of materials ever reported [30–34], especially when there are ferromagnetic interactions such as in GdF_3 [35].

References

1. Debye P (1926) Ann Phys 386:1154
2. Giauque WF (1927) J Am Chem Soc 49:1864
3. Evangelisti M, Luis F, de Jongh LJ, Affronte M (2006) Magnetothermal properties of molecule-based materials. J Mater Chem 16(26):2534–2549
4. Evangelisti M, Brechin EK (2010) Recipes for enhanced molecular cooling. Dalton Trans 39:4672–4676
5. Gutfleisch O, Willard MA, Brück E, Chen CH, Sankar S, Liu JP (2011) Magnetic materials and devices for the 21st century: stronger, lighter, and more energy efficient. Adv Mater 23 (7):821–842
6. Sessoli R (2012) Chilling with magnetic molecules. Angew Chem Int Ed 51(1):43–45
7. Zheng Y-Z, Zhou G-J, Zheng Z, Winpenny RE (2014) Molecule-based magnetic coolers. Chem Soc Rev 43(5):1462–1475
8. Sharples JW, Collison D (2013) Coordination compounds and the magnetocaloric effect. Polyhedron 54:91–103
9. Shi PF, Xiong G, Zhang ZY, Zhao B (2013) Recent advance on molecule-based magnetic refrigeration materials at low temperatures. Scientia Sinica Chimica 43(10):1262–1271
10. Liu J-L, Chen Y-C, Guo F-S, Tong M-L (2014) Recent advances in the design of magnetic molecules for use as cryogenic magnetic coolants. Coord Chem Rev 281:26–49
11. Pecharsky VK, Gschneidner KA Jr (1999) Magnetocaloric effect and magnetic refrigeration. J Magn Magn Mater 200:44–56
12. Tishin AM, Spichkin YI (2003) The magnetocaloric effect and its applications. Institute of Physics, London
13. Sharples JW, Zheng Y-Z, Tuna F, McInnes EJ, Collison D (2011) Lanthanide discs chill well and relax slowly. Chem Commun 47(27):7650–7652
14. Evangelisti M, Roubeau O, Palacios E, Camon A, Hooper TN, Brechin EK, Alonso JJ (2011) Cryogenic magnetocaloric effect in a ferromagnetic molecular dimer. Angew Chem Int Ed 50 (29):6606–6609
15. Ruiz J, Lorusso G, Evangelisti M, Brechin EK, Pope SJ, Colacio E (2014) Closely-related Zn^{II} $_2Ln^{III}_2$ complexes (Ln^{III} = Gd, Yb) with either magnetic refrigerant or luminescent single-molecule magnet properties. Inorg Chem 53(7):3586–3594
16. Guo F-S, Leng J-D, Liu J-L, Meng Z-S, Tong M-L (2011) Polynuclear and polymeric gadolinium acetate derivatives with large magnetocaloric effect. Inorg Chem 51(1):405–413
17. Blagg RJ, Tuna F, McInnes EJL, Winpenny REP (2011) Pentametallic lanthanide-alkoxide square-based pyramids: high energy barrier for thermal relaxation in a holmium single molecule magnet. Chem Commun 47(38):10587–10589
18. Zangana KH, Pineda EM, Schnack J, Winpenny RE (2013) Octametallic 4f-phosphonate horseshoes. Dalton Trans 42(39):14045–14048
19. Liu S-J, Zhao J-P, Tao J, Jia J-M, Han S-D, Li Y, Chen Y-C, Bu X-H (2013) An unprecedented decanuclear GdIII cluster for magnetic refrigeration. Inorg Chem 52(16):9163–9165

20. Adhikary A, Jena HS, Khatua S, Konar S (2014) Synthesis and characterization of two discrete Ln10 nanoscopic ladder-type cages: magnetic studies reveal a significant cryogenic magnetocaloric effect and slow magnetic relaxation. Chem Asian J 9(4):1083–1090
21. Zheng Y, Zhang Q-C, Long L-S, Huang R-B, Müller A, Schnack J, Zheng L-S, Zheng Z (2013) Molybdate templated assembly of Ln 12 Mo 4-type clusters (Ln = Sm, Eu, Gd) containing a truncated tetrahedron core. Chem Commun 49(1):36–38
22. Chang L-X, Xiong G, Wang L, Cheng P, Zhao B (2013) A 24-Gd nanocapsule with a large magnetocaloric effect. Chem Commun 49(11):1055–1057
23. Guo F-S, Chen Y-C, Mao L-L, Lin W-Q, Leng J-D, Tarasenko R, Orendáč M, Prokleška J, Sechovský V, Tong M-L (2013) Anion-templated assembly and magnetocaloric properties of a nanoscale {Gd$_{38}$} cage versus a {Gd$_{48}$} barrel. Chem Eur J 19(44):14876–14885
24. Peng J-B, Kong X-J, Zhang Q-C, Orendáč M, Prokleška J, Ren Y-P, Long L-S, Zheng Z, Zheng L-S (2014) Beauty, symmetry, and magnetocaloric effect—four-shell keplerates with 104 lanthanide atoms. J Am Chem Soc 136(52):17938–17941
25. Han S-D, Miao X-H, Liu S-J, Bu X-H (2014) Magnetocaloric effect and slow magnetic relaxation in two dense (3,12)-connected lanthanide complexes. Inorg Chem Front 1 (7):549–552
26. Han S-D, Miao X-H, Liu S-J, Bu X-H (2014) Large magnetocaloric effect in a dense and stable inorganic–organic hybrid cobridged by in situ generated sulfate and oxalate. Chem Asian J 9 (11):3116–3120
27. Hou Y-L, Xiong G, Shi P-F, Cheng R-R, Cui J-Z, Zhao B (2013) Unique (3, 12)-connected coordination polymers displaying high stability, large magnetocaloric effect and slow magnetic relaxation. Chem Commun 49(54):6066–6068
28. Hu F-L, Jiang F-L, Zheng J, Wu M-Y, Pang J-D, Hong M-C (2015) Magnetic properties of 3D heptanuclear lanthanide frameworks supported by mixed ligands. Inorg Chem 54 (13):6081–6083
29. Wu M, Jiang F, Kong X, Yuan D, Long L, Al-Thabaiti SA, Hong M (2013) Two polymeric 36-metal pure lanthanide nanosize clusters. Chem Sci 4(8):3104–3109
30. Meng Y, Liu J-L, Zhang Z-M, Lin W-Q, Lin Z-J, Tong M-L (2013) Ionothermal synthesis of two oxalate-bridged lanthanide(iii) chains with slow magnetization relaxation by using a deep eutectic solvent. Dalton Trans 42(36):12853–12856
31. Chen Y-C, Guo F-S, Zheng Y-Z, Liu J-L, Leng J-D, Tarasenko R, Orendac M, Prokleska J, Sechovsky V, Tong M-L (2013) Gadolinium(III)-hydroxy ladders trapped in succinate frameworks with optimized magnetocaloric effect. Chem Eur J 19(40):13504–13510
32. Chen Y-C, Qin L, Meng Z-S, Yang D-F, Wu C, Fu Z, Zheng Y-Z, Liu J-L, Tarasenko R, Orendac M, Prokleska J, Sechovsky V, Tong M-L (2014) Study of a magnetic-cooling material Gd(OH)CO$_3$. J Mater Chem A 2(25):9851–9858
33. Meng Y, Chen Y-C, Zhang Z-M, Lin Z-J, Tong M-L (2014) Gadolinium oxalate derivatives with enhanced magnetocaloric effect via ionothermal synthesis. Inorg Chem 53 (17):9052–9057
34. Qiu JZ, Wang LF, Chen YC, Zhang ZM, Li QW, Tong ML (2016) Magneto-caloric properties of heterometallic 3d-Gd complexes based on the [Gd(oda)$_3$]$^{3-}$ metalloligand. Chem Eur J 22 (2):802–808. doi:10.1002/chem.201503796
35. Chen Y-C, Prokleška J, Xu W-J, Liu J-L, Liu J, Zhang W-X, Jia J-H, Sechovský V, Tong M-L (2015) A brilliant cryogenic magnetic coolant. Magnetic and magnetocaloric study of the ferromagnetically coupled GdF$_3$. J Mater Chem C 3(47):12206–12211

Lanthanide Clusters Toward Single-Molecule Magnets

Tian Han, You-Song Ding, and Yan-Zhen Zheng

Abstract Single-molecule magnets (SMMs) have attracted increasing attention for their potential applications in high-density information storage and quantum computing. Thereinto, polynuclear $4f$ complexes are excellent candidates to create high-performance SMMs for the advantages of significant single-ion magnetic anisotropy arising from $4f$ ions and manipulable magnetic exchange couplings via tunable arrangement of the metal ions, which promotes the rapid development of this area in the last decade. In this chapter we present a comprehensive review focusing on cluster-based lanthanide SMMs and their correlations between the molecular structures and magnetic behaviors and further highlight some novel strategies for enhancing SMMs.

Keywords Lanthanide • Magnetic relaxation • Polynuclear $4f$ complexes • Single-molecule magnets

Contents

T. Han, Y.-S. Ding, and Y.-Z. Zheng (✉)
Frontier Institute of Science and Technology (FIST), State Key Laboratory for Mechanical Behavior of Materials and MOE Key Laboratory for Nonequilibrium Synthesis and Modulation of Condensed Matter, Xi'an Jiaotong University, Xi'an 710054, P. R. China
e-mail: zheng.yanzhen@xjtu.edu.cn

1   Introduction

Molecular nanomagnets, which mainly include paramagnetic coordination complexes with metal aggregation at nanometric level, have been considered as futuristic device components for high-density information storage, quantum computer, and miniatured spintronics, due to the blocked magnetic momentum and significant quantum effects with manipulable features [1]. The first molecular nanomagnet was identified in 1993 by Gatteschi and coworkers, in a 0D structure $[Mn_{12}O_{12}(OAc)_{16}(H_2O)_4]$ ($Mn_{12}Ac$) [2, 3], and such individual molecules that can function as magnets have since been called single-molecule magnets (SMMs).

If one SMM is magnetized by an applied magnetic field, it relaxes its magnetization very slowly to return to the equilibrium by overcoming the anisotropic barrier, giving one of the characteristic properties for SMMs known as magnetic relaxation. For $Mn_{12}Ac$, the relaxation time at 2 K is a few months. Under the condition of well-known double-well energy potential, the relaxation time (τ) strongly depends on the temperature and increases exponentially on decreasing the temperature, according to the Arrhenius law, $\tau = \tau_0 \exp(U_{eff}/k_B T)$, where τ_0 is a pre-factor, U_{eff} represents the effective spin reversal barrier, k_B is the Boltzmann constant, and T is the temperature. As a result, $Mn_{12}Ac$ has a relaxation time of the order of years below 1 K. In this respect, the SMM behaves like a classical magnet and therefore potential application in very high-density information storage where each individual molecule is stored as one bit of information [4, 5].

SMMs can feature hysteresis loop, but with steps which are not usually observed in classical magnets. This phenomenon results from the quantum tunneling of the magnetization (QTM), another characteristic property for SMMs. It occurs when there is an energy coincidence of the levels on the opposite parts of the double-well potential, leading to a fast relaxation without climbing the barrier but tunneling. The fact that the relaxation time of the magnetization does not exactly follow an exponential law is often caused by QTM. Although quantum tunneling relaxation process results in the loss of remnant magnetization, which is a disadvantage in the application of information storage, it may provide quantum superposition states of magnetization suitable for quantum information processing [6].

Generally, SMMs require large-spin ground state (S) and uniaxial magnetic anisotropy ($|D|$), giving rise to an energy barrier U defined as $|D|S^2$ and $|D|(S^2 - 1/4)$ for integer or half-integer spins, respectively. This relationship applies well to transition metal systems, and hence, for high energy barrier, the initial study of SMMs focused on large $3d$-oxo clusters where S can be increased significantly

[7, 8]. However, the accompanying D values of many clusters with large S values tend to be low, resulting in poor SMMs or even no SMM behavior [9]. The lack of coexistence of giant ground-spin state and high magnetic anisotropy is also suggested by theoretical studies [10–12], challenging the approach of increasing S for maximizing the relaxation barrier in polynuclear SMMs.

Instead, recent efforts have been devoted toward enhancing uniaxial anisotropy in small molecules containing several or even just one spin carrier. Particularly, the lanthanides are the promising candidates, because their large unquenched orbital moments and significant inherent spin–orbit coupling can give strong single-ion anisotropies. Although the limited radial extension of the 4f orbital corresponds to very weak or even no exchange interactions, increasing the magnetic anisotropy could partially compensate for this exchange, facilitating the slow relaxation of magnetization. Indeed, lanthanide SMMs have received considerable research attention and shown high performance with breakthrough progress in SMMs [13–20].

The first example of a lanthanide SMM was reported in 2003 in mononuclear complexes of the general formula $[LnPc_2]^-$ with a double-decker structure [21–23], which fully embodies the huge contribution of single-ion anisotropy to SMM behavior and questions the relationship of U, S, and D in transition metal systems. This discovery has sparked the intensive interest in the SMMs containing lanthanide metals. Since a triangular Dy_3 cluster reported in 2006 featuring toroidal arrangement of magnetic moments on the dysprosium sites shows SMM behavior [24], polynuclear lanthanide SMMs with various topologies have been greeted with great enthusiasm. By investigating such systems, one could expect to understand not only the dominant single-ion effect but also the magnetic interaction between lanthanide ions and hence the alignments of anisotropy axes and spin vectors. Moreover, the weak but operational magnetic exchange couplings between the lanthanide ions could mitigate the quantum tunneling relaxation accompanied for many lanthanide SMMs at zero dc field, thereby preventing the loss of magnetization [25]. In this context, we focus on the lanthanide clusters designed for SMMs [26–28].

By exploring a large number of polynuclear 4f systems as far as January 2016, we provide an overview of the cluster-based lanthanide SMMs and their relationship between the structures and SMM behaviors, including the structural factors such as the lanthanide ion, coordination environment, bridging mode, molecular symmetry and even the secondary environment, and slow magnetic relaxation as well as quantum tunneling effect. Theoretical results for some interesting SMMs are shared to better understand the intrinsic nature.

From the view of the number of lanthanide ions in the molecular structure, this chapter of polynuclear lanthanide SMMs is divided into sections from dinuclear 4f clusters to higher-nuclearity 4f clusters. For dinuclear SMMs, it is clear to subdivide the section by the μ-bridging motifs. For trinuclear and higher-nuclearity SMMs, each section is subdivided based on the geometries with respect to the metal centers. Hence, a complete summary and thorough analysis for the cluster-based lanthanide SMMs are presented here with the aim of shedding light on further rational design of better SMMs.

2   Survey of 4*f* SMMs in Clusters

2.1   *Dinuclear 4*f* Clusters*

Dinuclear 4*f* SMMs present the simplest models for the study of the magnetic nature including the single-ion effect and the magnetic interaction between two spin carriers. Concerning the impact of structural factors on SMM behavior, 4*f* metal, coordination environment and bridging ligand, and the corresponding SMM parameters for {Ln$_2$} SMMs are surveyed. Bridging moieties in the dinuclear 4*f* SMMs are quite broad and range from monatomic bridges including hydrogen, carbon, nitrogen, oxygen, chloride, and sulfur atoms to polyatomic bridges like $\mu_{1,3}$-carboxylate and pyrazine and radical bridges.

2.1.1   Dinuclear 4*f* Clusters with Monatomic Bridges

Compound [Dy(HMe$_6$tren)(μ-H)$_3$Dy(Me$_6$tren)][B{C$_6$H$_3$(CF$_3$)$_2$}$_4$]$_2$ (**1**) is the first and the only known example of hydride-bridged SMM [29]. Asymmetrical {Dy$_2$} contains two different coordination numbers: one in a seven-coordinate environment described as monocapped octahedral and the other in an eight-coordinate environment with very low symmetry. Two relaxation processes can be identified, with $U_{\text{eff}} = 65$ cm^{-1} and 15 cm^{-1}, respectively. Ab initio calculation suggests an Ising-type exchange interaction and antiferromagnetic exchange coupling in **1** and allows the process with $U_{\text{eff}} = 65$ cm^{-1} to be assigned to the eight-coordinate dysprosium, while fast QTM within seven-coordinate dysprosium prevents detection of a blocking process (Fig. 1).

Monatomic bridge can expand to the carbon atom in the form of aromatic rings, leading to an efficient overlap between the 4*f* orbitals and π electron cloud from sp^2 carbon atoms. Dinuclear triple-decker sandwich complex [Dy$_2$(COT$''$)$_3$] (**2-Dy**)

Fig. 1 Molecular structure of **1**. Hydrogen atoms are omitted, except μ-hydrides. Color codes: *pink*, Dy; *blue*, N; *gray*, C; and *orange*, H
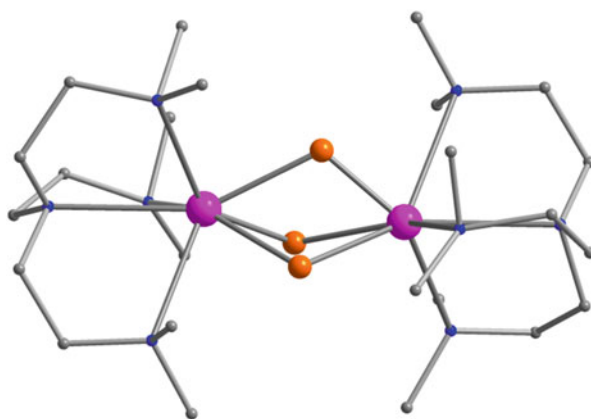
contains two Dy^{III} centers that coordinate to COT″ ligands in η^8 manner, whereas the central ring bridges two Dy^{III} ions in μ-η^8:η^8 mode [30]. A weak direct Dy^{III}–Dy^{III} covalent interaction is detected through DFT calculation and magnetic measurements. Ac susceptibility data show that both compound **2-Dy** and its monomeric unit [Dy(COT″)$_2$] behave as SMMs, with $U_{eff} = 6$ cm^{-1} and 17 cm^{-1}, respectively. Ab initio calculations reveal the direction of the magnetic anisotropic axis on each Dy^{III} ion is not perpendicular to the planar COT″ rings for both [Dy$_2$(COT″)$_3$] and [Dy(COT″)$_2$], which is mainly influenced by the trimethylsilyl groups.

Replacing Dy^{III} ion with Er^{III} ion results in isostructural compound [Er$_2$(COT″)$_3$] (**2-Er**) [31]. The ground and first-excited Kramers-doublet states on each Er^{III} ion are magnetically extremely axial, and these main magnetic axes at different Er^{III} sites are almost parallel to each other, as determined by ab initio calculation. Complex **2-Er** is thus an SMM and exhibits magnetic hysteresis at 12 K in solid state and up to 14 K in solution, the highest blocking temperature observed for a nonradical-bridged SMM. In contrast to its mononuclear analogue [Er(COT″)$_2$], in which single-ion blocking temperature is 8 K, SMM property for **2-Er** is obviously enhanced due to the coupling spin of the SMM [32] (Fig. 2).

Two series of lanthanide complexes [(NN^{TBS})Ln]$_2$(μ-biphenyl)[K(solvent)]$_2$ (NN^{TBS} = 1,1′-fc(NSi^{t}BuMe$_2$)$_2$; Ln = Dy(**3-Dy**), Er(**3-Er**)) and ([(NN^{TBS})

Fig. 2 Molecular structure of **2**. Color codes: *pink*, Ln (Dy for **2-Dy** and Er for **2-Er**); *green*, Si; and *gray*, C
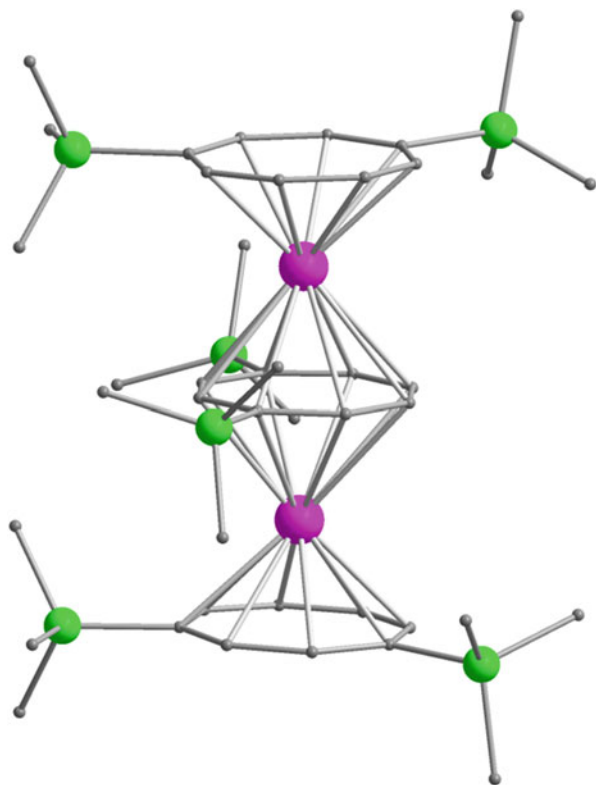
Ln]$_2$(μ-biphenyl))[K(18-C-6)(THF)$_{1.5}$]$_2$ (Ln = Dy(**4-Dy**), Er(**4-Er**)) provide an inverse sandwich type of Ln(III) ion bridging by biphenyl ligand, where the coordination environment around each Ln(III) ion is similar regardless of whether potassium coordinates to the neighboring phenyl ring or not [33]. Interestingly, **3-Dy** acts as an SMM with an energy barrier of 24 cm^{-1} under zero dc field or 37 cm^{-1} at a dc field of 900 Oe, whereas only a significant QTM relaxation process occurs for **3-Er** without clear blocking of magnetization at H_{dc} = 900 Oe. In contrast, both **4-Dy** and **4-Er** display multiple relaxation dynamics at H_{dc} = 900 Oe, namely a thermal relaxation process and a secondary QTM relaxation process. Ab initio calculations reveal main magnetic axes for individual metal sites, as shown in Fig. 3. Different magnetic couplings between the lanthanide ions could be
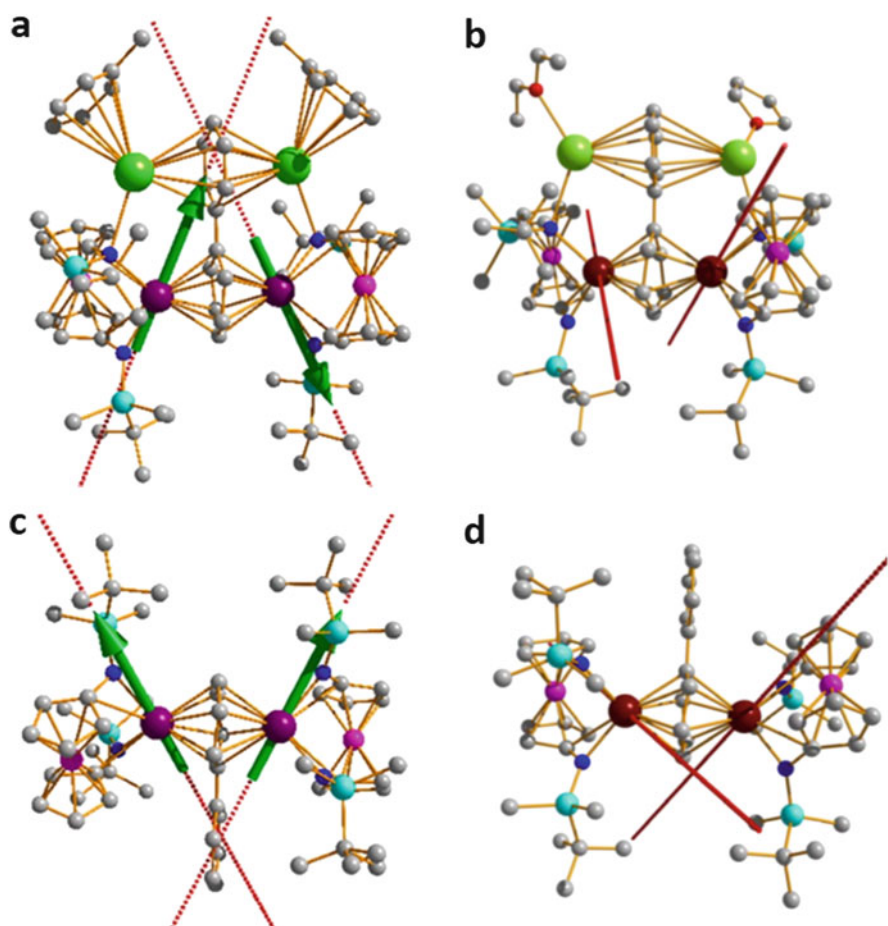
Fig. 3 Molecular structures and main local anisotropy axes on Ln sites for **3-Dy** (**a**), **3-Er** (**b**), **4-Dy** (**c**), and **4-Er** (**d**). Color codes: *purple*, Dy; *wine*, Er; *pink*, Fe; *light green*, K; *cyan*, Si; *gray*, C; and *blue*, N. Reprinted with permission from [33]. Copyright @ 2015, American Chemical Society

responsible for various SMM behaviors: a ferromagnetic interaction in **3-Er**, **4-Dy**, and **4-Er** and antiferromagnetic coupling for **3-Dy**. When Dy(III) and Er(III) ions are coupled ferromagnetically, the observed barriers are reduced due to significant QTM because ferromagnetic coupling of the two half-integer spins leads to an integer ground-spin-state.

The monatomic nitrogen bridge is characterized by μ-phthalocyanine ligand in triple-decker-type SMMs. These sandwich-type di-rare-earth complexes involve homodinuclear and heterodinuclear compounds according to metal ions and pure phthalocyanine and mixed phthalocyanine/porphyrin complexes on the basis of ligands. In fact, the lanthanide SMM era began with the mononuclear double-decker phthalocyanine complexes. The lanthanide ions are placed along the four-fold symmetric axis in the triple-decker molecules with a metal–metal interatomic distance of about 3.6 Å, allowing the effect of intramolecular f–f interaction on dynamic magnetism to be investigated. The first report is on a series of Ln–Pc complexes $(Pc)Ln(Pc)Ln'(obPc)$ (referred to as [Ln,Ln']) [34]. A "monomer +dimer" synthetic method has been used to synthesize [Y, Tb] (**5a**), [Tb, Y] (**5b**), and [Tb, Tb] (**5c**) complexes, in which, [Y, Tb] complex, for example, there was no contamination by [Tb, Y] or [Tb, Tb] complexes [21, 35, 36]. Temperature dependence of ac susceptibilities under a zero dc field shows that relaxation of the magnetization for bis-Tb complex is at a higher temperature range than those of mono-Tb complexes, indicating an increase of relaxation time via f–f interaction. If a dc magnetic field is applied, positions of the single peak for both [Y, Tb] and [Tb, Y] complexes shift to higher temperature and almost coincide with the two peaks of [Tb, Tb] at 27 K and 20 K. This suggests that double-peak appearance of [Tb, Tb] corresponds to the relaxations that occur at sites A and B, respectively, and the two sites are certainly coupled by an f–f interaction, resulting in the greatly reduced dc-field dependence of the ac susceptibility (Fig. 4).

Contrary to the asymmetric Tb sites, symmetric Tb–Pc triple-decker complex, $(obPc)Tb(obPc)Tb(obPc)$ (**6**), exhibits a single peak at 24 K in the $\chi'' T$ versus T plot with $U_{eff} = 230$ cm^{-1} under a zero dc field [37]. However, the relaxation splits from a one-component system into a two-component system (temperature-independent and temperature-dependent regimes) with increasing the dc field in the range of 0.1–0.7 T and then combines into a one-component system again at ~1 T dc field. This transition of the magnetic properties by a dc field gives a new magnetic relaxation phenomenon for an Ising dimer. Isostructural $(obPc)Dy(obPc)Dy(obPc)$ (**7a**) also shows two magnetic relaxation processes in the low-temperature region under a dc magnetic field [38]. These relaxation mechanisms are related to the energy gap of the doublet ground state and QTM. Its mono-Dy complex, $(obPc)Y(obPc)Dy(obPc)$ (**7b**), with the same octacoordination environment, shows similar SMM behavior to those of **7a**, but with a magnetic relaxation time one order of magnitude smaller than that of **7a**. Thus, it is presumably feasible to control the relaxation time by using f–f interactions [39].

When porphyrin was incorporated into sandwich-type complexes, that is, to mix phthalocyanine/porphyrin triple-decker complexes, geometries of the coordination
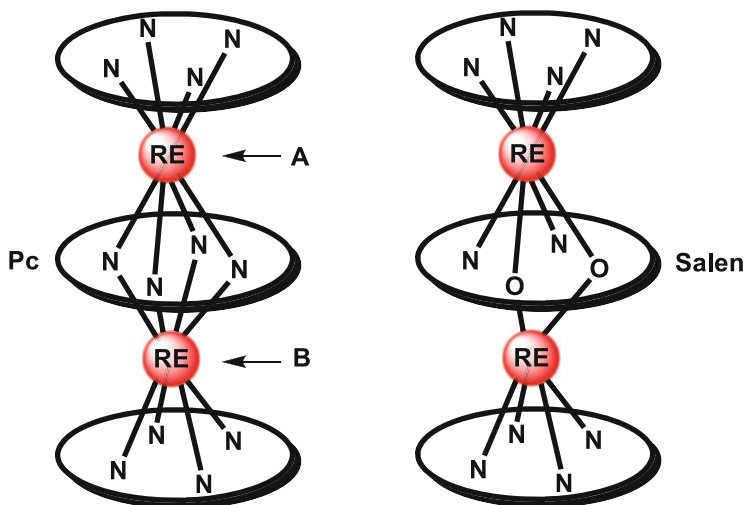
Fig. 4 Schematic illustration of triple-decker single-molecule magnet bridged by phthalocyanine or Schiff base

sites present not only square-antiprismatic (SAP) coordination site but also a square-prismatic (SP) site [40, 41]. Crystal structures of (Pc)Ln(Pc)Ln′(TOMePP) ([Y, Tb] (**8a**), [Tb, Y] (**8b**), and [Tb, Tb] (**8c**)) reveal that two Pc ligands are repelling to each other by nearly 45°, giving a SAP coordination site, while coordination nitrogen atoms of the central Pc and those of TOMePP ligands are in eclipsed positions, making a SP coordination site. Monoterbium complex **8b** with a SAP site acts as a SMM regardless of the presence or absence of H_{dc}, whereas **8a** with a SP site exhibits faster relaxation in the absence of H_{dc}. Magnetic relaxation of diterbium complex **8c** occurs in two steps in the absence of H_{dc} with a relaxation time in the SP site much longer than that of **8a**, which implies that the fast quantum tunneling relaxation process in the SP site is hindered by magnetic–dipolar coupling between the f-electronic systems. Another series of mixed tetrapyrrole sandwich complexes (TClPP)Ln(oPhPc)Ln′(oPhPc)([Y, Dy] (**9a**), [Dy, Y] (**9b**), [Dy, Dy] (**9c**)) contains one metal ion locating between the central phthalocyanine and outer porphyrin ligands with a twisting angle of 9.64–9.90° and the other between two phthalocyanine ligands of 25.12–25.30°. That the SMM, non-SMM, and magnetic-field-induced SMM nature observed for **9a**, **9b**, and **9c**, respectively, indicates the dominant effects of ligand field and coordination geometry of the spin carrier, instead of the f–f interaction, on the magnetic properties.

Apart from monatomic nitrogen bridge via phthalocyanine ligand, rare-earth sandwich triple-decker complexes extend to include salen-type ligands with phenoxo bridge, i.e., mixed phthalocyaninato–Schiff-base dinuclear lanthanide complex, $Dy_2(Pc)_2(BMBDA)H_2O$ (**10**), and triple-decker analogues with pure Schiff-base ligand, $Dy_2(BMBDA)_3H_2O$ (**11**) and $[Dy_2(BSCDA)_3(CH_3OH)]$ (**12**) [42, 43]. Compound **10** is constructed by two phthalocyanine ligands, one Schiff-base ligand shared by two dysprosium ions, and one coordinated water molecule.

One Dy^{III} ion is located in a twisted SAP geometry comprised of isoindole nitrogen atoms of phthalocyanine and two nitrogen and two oxygen atoms of Schiff-base ligand, and the other one is coordinated by N_4O_3 cavity of phthalocyanine, two oxygen atoms of Schiff-base ligand, and one oxygen atom of water molecule (Fig. 4). Compounds **11** and **12** are composed of two Dy^{III} ions, three salen-type ligands, and one water or methanol molecule. One Dy^{III} ion is eight-coordinate with four oxygen atoms and four nitrogen atoms from two neighboring salen-type ligands, and the other one adopts an eight-/seven-coordinate geometry constructed by one outer salen-type ligand, three/two oxygen atoms of the inner salen-type ligand, and one oxygen atom of water or methanol molecule. The dynamic magnetic properties of **10**, **11**, and **12** under 2000 Oe external dc magnetic field were investigated, showing field-induced slow relaxation of the magnetization (Table 1).

Table 1 Dinuclear $4f$ SMMs with monatomic bridges of hydrogen, carbon, and nitrogen

SMMs	CN of $4f$ ions	Bridging moieties	U_{eff}/cm^{-1} (H_{dc}/Oe)	hys (K)	References
$[Dy(HMe_6tren)(\mu\text{-}H)_3Dy$ $(Me_6tren)][B\{C_6H_3(CF_2)_2\}_4]_2$ (**1**)	$7(H_3N_4)$, 8 (H_3CN_4)	$(\mu\text{-}H)_3$	65,15	–	[29]
$[Dy_2(COT'')_3]$ (**2-Dy**)	$16(C_{16})$	$\mu\text{-}\eta^8{:}\eta^8$ COT''	6	–	[30]
$[Er_2(COT'')_3]$ (**2-Er**)	$16(C_{16})$	$\mu\text{-}\eta^8{:}\eta^8$ COT''	231	12	[31]
$[(NN^{TBS})Dy]_2(\mu\text{-biphenyl}[K$ (solvent)]$_2$ (**3-Dy**)	$8(C_6N_2)$	μ-biphenyl	24	–	[33]
$[(NN^{TBS})Er]_2(\mu\text{-biphenyl}[K(sol\text{-}$ vent)]$_2$ (**3-Er**)	$8(C_6N_2)$	μ-biphenyl	11(900)	–	[33]
$[(NN^{TBS})Er]_2(\mu\text{-biphenyl})[K$ $(18\text{-}C\text{-}6)(THF)_{1.5}]_2$ (**4-Er**)	$8(C_6N_2)$	μ-biphenyl	17(900)	–	[33]
(Pc)Y(Pc)Tb(obPc) (**5a**)	$8(N_8)$	μ-Pc	–	–	[34]
(Pc)Tb(Pc)Y(obPc) (**5b**)	$8(N_8)$	μ-Pc	–	–	[34]
(Pc)Tb(Pc)Tb(obPc) (**5c**)	$8(N_8)$	μ-Pc	–	–	[34]
(obPc)Tb(obPc)Tb(obPc) (**6**)	$8(N_8)$	μ-obPc	230	1.5	[37]
(obPc)Dy(obPc)Dy(obPc) (**7a**)	$8(N_8)$	μ-obPc	–	–	[38]
(obPc)Y(obPc)Dy(obPc) (**7b**)	$8(N_8)$	μ-obPc	–	–	[39]
(Pc)Y(Pc)Tb(TOMePP) (**8a**)	$8(N_8)$	μ-Pc	–	–	[40]
(Pc)Tb(Pc)Y(TOMePP) (**8b**)	$8(N_8)$	μ-Pc	–	–	[40]
(Pc)Tb(Pc)Tb(TOMePP) (**8c**)	$8(N_8)$	μ-Pc	–	–	[40]
(TClPP)Y(oPhPc)Dy(oPhPc) (**9a**)	$8(N_8)$	μ-oPhPc	17.3(2000)	–	[41]
(TClPP)Dy(oPhPc)Dy(oPhPc) (**9c**)	$8(N_8)$	μ-oPhPc	–(2000)	–	[41]
$Dy_2(Pc)_2(BMBDA)H_2O$ (**10**)	$7(N_4O_3)$, 8 (N_6O_2)	μ-salen type	19.8(2000)	–	[42]
$Dy_2(BMBDA)_3H_2O$ (**11**)	$8(N_4O_4)$, 8 (N_2O_6)	μ-salen type	10.1(2000)	–	[42]
$[Dy_2(BSCDA)_3(CH_3OH)]$ (**12**)	$7(N_2O_5)$, 8 (N_4O_4)	μ-salen type	–	–	[43]

Double oxygen-bridging motif is the most popular bridge type in dinuclear lanthanide SMMs. Compound $\{[Dy(hfac)_3(H_2O)]_2(4\text{-styr})_2\}$ (**13**)(4-styr = 4-styrylpyridine) presents a simplest and shortest way that two dysprosium ions are linked by water oxygen in μ-bridging mode [44]. Each Dy^{III} ion in this dimer is coordinated to six oxygen atoms of three $hfac^-$ and two $\mu\text{-}H_2O$ in a nearly SAP polyhedron geometry. Static magnetic measurement shows that the $\chi_M T$ value increases very rapidly upon cooling at low temperatures, an indication of ferromagnetic interaction between the two Dy^{III} ions. Single-crystal rotating magnetometry demonstrates that the Dy^{III} ion possesses Ising-type anisotropy, and its easy magnetization axis coincides with the pseudo-C_4 axis of D_{4d} coordination polyhedron. From the dynamic point of view, **13** shows slow relaxation of the magnetization with $U_{eff} = 64$ cm^{-1} in a thermally activated regime, which is close to the energy barrier calculated from the separation between the ground ($\pm 15/2$) and first-excited ($\pm 1/2$) states. The ferromagnetic interaction slows down zero-field magnetic relaxation but accelerates the infield one as suggested by Y^{III} magnetic dilution study (Figs. 5 and 6).
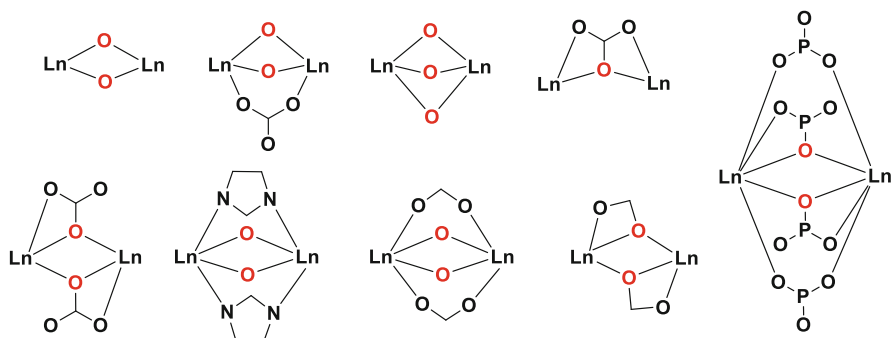

Fig. 5 Schematic illustration for oxygen-bridged dinuclear lanthanide complexes
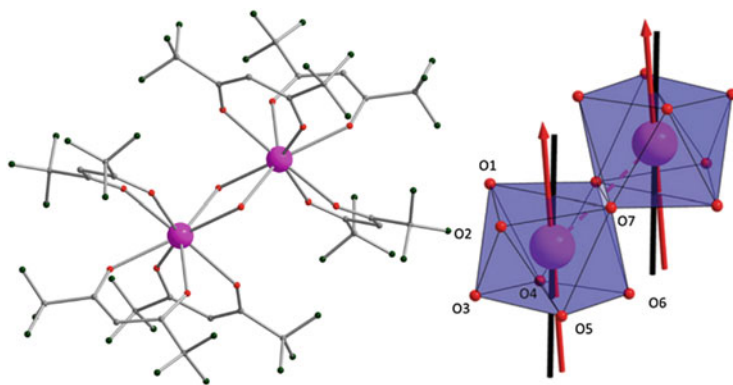

Fig. 6 Molecular structure for **13** (*left*) and schematic orientation of the C_4 (*black*) and easy magnetization axis extracted from rotating single-crystal measurement (*red*) (*right*). Color codes: *pink*, Dy; *gray*, C; *dark green*, F; and *red*, O. Reprinted with permission from [44]. 2013, Royal Society of Chemistry

Heterodinuclear and homodinuclear lanthanide cores in polyoxometalates (POMs), $[Dy(\mu_2\text{-}OH)_2Ln]^{4+}$ (Ln = Eu (**14a = DyEu**), Dy(**14b = DyDy**), Yb (**14c = DyYb**), and Lu(**14d = DyLu**)) that are sandwiched by two $[\gamma\text{-}SiW_{10}O_{36}]^{8-}$ units, have been prepared through the stepwise incorporation of two types of lanthanide cations into the vacant sites of POMs [45, 46]. Both Dy^{3+} and Ln^{3+} ions in this core are six-coordinate by four oxygen atoms of lacunary sites of $[\gamma\text{-}SiW_{10}O_{36}]^{8-}$ units and two μ-OH ligands, and these cations are bridged by two μ-OH ligands with the separation increasing in the order **DyLu**(3.60 Å) < **DyYb** (3.61 Å) < **DyDy**(3.65 Å) < **DyEu** (3.67 Å). These compounds show SMM behavior under zero (**DyEu**, **DyDy**, and **DyLu**) and an applied external magnetic field (**DyYb**). The energy barriers for magnetization reversal are found to increase in the order **DyLu** (33 cm^{-1}) < **DyYb** (37 cm^{-1}) < **DyDy**(46 cm^{-1}) < **DyEu** (51 cm^{-1}), with increasing ionic radius of the Ln^{3+} cation adjacent to the Dy^{3+} ion in the dinuclear $[Dy(\mu_2\text{-}OH)_2Ln]^{4+}$ core, suggesting the maneuverable barriers via adjacent Ln^{3+} ion (Fig. 7).

Aroylhydrazones, R-CO-NH-N=CH-R′, formed by the reaction between aldehydes/ketones and hydrazine derivatives, are excellent ligands to construct dinuclear oxygen-bridging systems for the following two reasons: (1) This kind of multidentate Schiff-base ligand has oxygen and nitrogen donors with suitable relative positions that can coordinate to several lanthanide ions. (2) These ligands
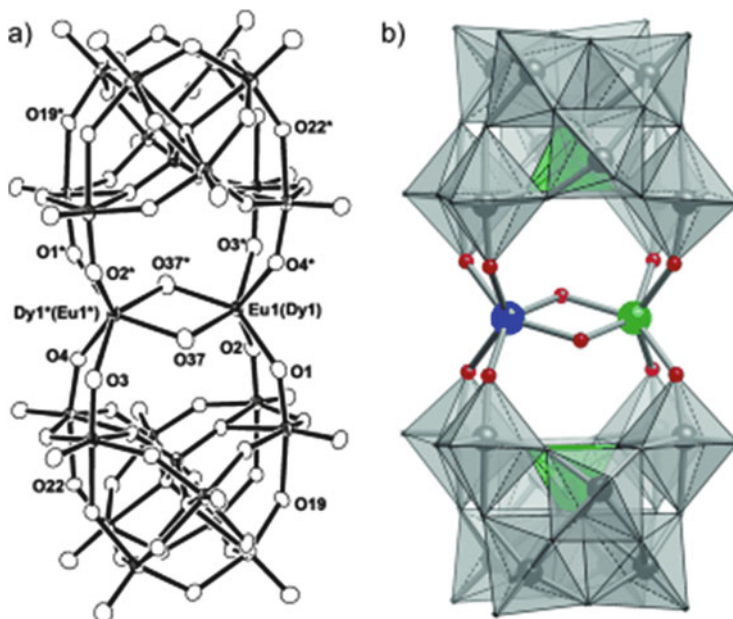

Fig. 7 (**a**) ORTEP view of **14**; thermal ellipsoids are set at 50% probability. (**b**) Polyhedral and ball-and-stick representation of **14a**. The structures of **14c** and **14d** are intrinsically identical to that of **14**. Color codes: Dy, *blue*; Ln', *dark green*; W, *gray*; O, *red*; and Si, *green*. Reprinted with permission from [45]. Copyright 2013 WILEY-VCH Verlag GmbH & Co. KGaA, Weinheim

could functionalize as a monodeprotonated or a dideprotonated ligand (keto and enol form) to bridge two lanthanide ions with μ-$O_{phenoxide}$ and/or μ-$O_{hydrazone}$ features depending on the different reaction conditions. H_2ovph ligand (pyridine-2-carboxylic acid [(2-hydroxy-3-methoxyphenyl)methylene] hydrazide), for example, enables access to a range of didysprosium SMMs. Dinuclear $[Dy_2(ovph)_2Cl_2(MeOH)_3] \cdot MeCN$ (**15**) forms when H_2ovph was reacted with $DyCl_3 \cdot 6H_2O$ in the presence of $NaHCO_3$ in methanol/acetonitrile, where the Dy^{III} ions in the dinuclear core are bridged by the phenoxido groups of two $ovph^{2-}$ ligands [47]. This asymmetric Dy_2 core contains an eight-coordinate dysprosium center in a hula-hoop-like geometry and a seven-coordinate dysprosium center in a nearly perfect pentagonal–bipyramidal coordination environment. Ab initio calculations reveal that two strongly axial and almost parallel magnetic axes on the dysprosium sites lie approximately in the plane formed by the two dysprosium ions and the bridging oxygen atom. Hence, **15** exhibits strong ferromagnetic interactions with $J_{dip} = 5.36$ cm^{-1} and $J_{exch} = 0.52$ cm^{-1}, that is, mostly from dipolar interaction, which originates from the two parallel magnetic axes of the nearest dysprosium ions. Ac susceptibility measurement reveals that two relaxation processes occur at high temperature arising from two distinct anisotropic centers, which affords the effective barriers of 104 and 138 cm^{-1} for the fast and slow relaxation processes, respectively. Also, zero-field tunneling magnetization here is suppressed efficiently, which is related to the high axiality and Ising exchange interaction. At low temperature, **15** enters the exchange-blocking regime, a sluggish relaxation with a characteristic time of $\tau_{QTM} = 35$ s. Such a tunneling rate is crucial, allowing an increase of the relaxation time by three orders of magnitude.

When H_2ovph ligand was reacted with $Dy(NO_3)_3 \cdot 6H_2O$ in methanol/acetonitrile in the presence of Et_3N, crystals of $[Dy_2(ovph)_2(NO_3)_2(H_2O)_2] \cdot 2H_2O$ (**16**) were obtained. If only Et_3N was replaced by pyridine, both monodeprotonated $Hovph^-$ and dideprotonated $ovph^{2-}$ are incorporated into complex **17** ($[Dy_2(Hovph)(ovph)(NO_3)_2(H_2O)_4] \cdot NO_3 \cdot 2CH_3OH \cdot 3H_2O$) [48]. For complex **16**, two $ovph^{2-}$ ligands coordinate to two Dy^{III} centers, resulting in a centrosymmetric structure with both Dy ions in hula-hoop-like geometry. In contrast, noncentrosymmetric $Dy_2(\mu\text{-}O)_2$ core in complex **17** is composed of two dysprosium centers bridged by $O_{hydrazone}$ atom from $ovph^{2-}$ ligand and $O_{phenoxide}$ atom from Hovph ligand, making two Dy ions in a nine-coordinate monocapped square-antiprismatic geometry. Both χ' and χ'' for **16** show frequency-dependent maxima, typical features associated with SMM behavior, giving an effective barrier of 48 cm^{-1}. Upon cooling, the relaxation process undergoes a crossover from a thermally activated mechanism to a direct or phonon-induced tunneling process at ~11 K. However, complex **17** shows only the frequency dependence in χ'' component without maxima, indicating a probable SMM behavior. Thus, the different dynamic magnetic behaviors among **15**–**17** are due to their structure differences induced by local crystal field and magnetic interaction between metal centers (Figs. 8 and 9).

Similar Dy_2 compounds derived from derivatives of H_2ovph ligand with differing aryl substituents could provide more information to understand the correlation between structure and magnetic properties. Two Dy_2 compounds,
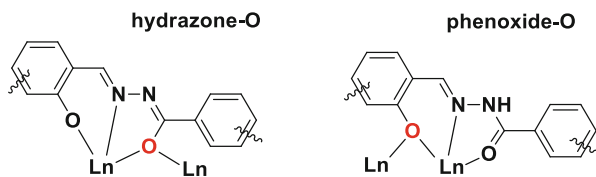
hydrazone-O   **phenoxide-O**

Fig. 8 Schematic illustration for coordinating modes of ovph^{2-} ligand and Hovph$^-$ ligand
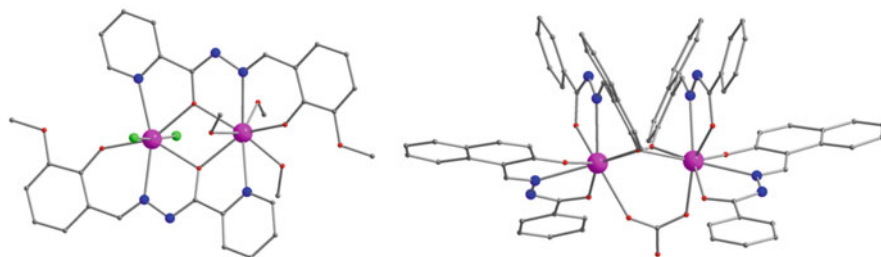

Fig. 9 Molecular structures for **15** (*left*) and **18** (*right*). Color codes: *pink*, Dy; *gray*, C; *blue*, N; *red*, O; and *green*, Cl

[Dy$_2$(Hhnb)$_4$(CO$_3$)]·4H$_2$O (**18**) and [Dy$_2$(hnp)$_2$(NO$_3$)$_2$(CH$_3$OH)$_2$]·4CH$_3$CN (**19**), which were synthesized from H$_2$hnb and H$_2$hnp, respectively, show again that monodeprotonated H$_2$hnb ligands and dideprotonated H$_2$hnp ligands experience keto–enol tautomerism [49]. Each Dy ion of both centrosymmetric dimeric compounds is eight-coordinate in N$_2$O$_6$ coordination environment; however, the metal ions in Dy$_2$ core of **18** are bridged by two phenoxido oxygen atoms of two ligands together with μ$_2$-η^1:η^1 CO$_3$$^{2-}$ (Fig. 9), whereas the Dy ions of **19** are linked by two O$_{hydrazone}$ atoms from two ligands. Hence, distinct magnetic interactions, namely, antiferromagnetic interaction in **18** and obvious ferromagnetic interaction in **19**, are observed. Furthermore, they both exhibit SMM behavior under zero dc field, with energy barriers of 12 cm^{-1} (**18**) and 29 cm^{-1} (**19**), presenting a way to modulate the dynamic behavior.

When H$_2$hmb ligand was applied to accommodate a series of lanthanide ions under similar reaction conditions, drastic structural rearrangement for the dinuclear Ln$_2$ occurs. As the ionic radius of the metal ions is decreased, this series of complexes can be divided into two groups: type I, [M$_2$(Hhmb)$_3$(NCS)$_3$]·2MeOH·py (M = Y, Eu, Gd, Tb, Dy**20-Dy**, Ho), and type II, [M$_2$(Hhmb)$_2$(NCS)$_4$(MeOH)$_2$] (M = Er**20-Er**, Yb **20-Yb**) [50]. Both metal centers in type I compounds are crystallographically independent and nine-coordinate with distorted monocapped square-antiprismatic geometries bridged by three μ-phenoxides of the Hhmb$^-$ ligands, while those in type II are centrosymmetric and eight-coordinate with distorted dodecahedron geometry bridged by two μ-phenoxides of the Hhmb$^-$ ligands. Ac magnetic measurements reveal that {Dy$_2$}, {Er$_2$}, and {Yb$_2$} exhibit slow relaxation of the magnetization under an applied optimum dc field with small

$U_{\text{eff}}(\leq 2 \text{ cm}^{-1})$. Moreover, **20-Yb** is the first example of a dinuclear Yb-based field-induced SMM.

The exception to aroylhydrazone systems is that phenoxido group acts as a bridge in complex $[Dy_2(hmi)_2(NO_3)_2(MeOH)_2]$ (**21**) with dideprotonated H_2hmi ligands [51]. The metal center in this centrosymmetric Dy_2 is coordinated to two hmi^{2-} ligands, one nitrate anion, and one methanol molecule in a NO_7 coordination sphere. The intramolecular ferromagnetic interactions between the metal centers are presented by the ascending $\chi_M T$ product at low temperature, as observed in other dysprosium(III) systems [52]. Ac susceptibility measurements under zero dc field reveal that the relaxation follows a thermally activated mechanism above 2 K, affording an energy barrier of 39 cm^{-1} with a pre-exponential factor of 3×10^{-7} s, signaling the typical SMM behavior, and a pure quantum regime below 2 K with a relaxation time of 3×10^{-3} s.

A similar coordination pockets of ligand H_3hbp in comparison with H_2ovph may lead to a similar dinuclear complex $[Dy_2(hbp)_2(PhCOO)_2(CH_3OH)_2]$ (**22**), which was also characterized with SMM behavior. Both eight-coordinate Dy centers resemble that in compounds **15** and **16** [53]. The two Dy^{III} ions are bridged by the μ-O_{alkoxide} atoms from two hbp^{3-} ligands instead of μ-$O_{\text{hydrazone}}$ atoms, leading to stronger ferromagnetic intramolecular interactions. Slow relaxation of the magnetization and a butterfly-shaped hysteresis loop at 1.65 K is observed for **22**. Typically, the hula-hoop-like configuration may favor persistent axiality of Dy ions, and various interactions might result in different anisotropies of the lowest exchange multiplets, which significantly affect the magnetic relaxation behavior.

Salen-type ligands, as one group of Schiff bases that are usually prepared by the condensation between salicylaldehyde derivatives and diamine, can provide not only multiple coordination sites to chelate poly-lanthanide ions but also phenoxide bridges to strengthen magnetic interactions. As being generally accepted, the SMM behavior of lanthanide complexes is mainly governed by ligand field effect and the magnetic interaction between lanthanide sites. However, the mechanisms behind such as large magnetic anisotropy and high tunneling rates are hard to elucidate due to the lack of model complexes. Here below is one. The reaction of $Dy(NO_3)_3 \cdot 6H_2O$ with $H_2valdien$ ligand under basic conditions yields compounds $[Ln_2(valdien)_2(NO_3)_2]$ (Ln = Eu, Gd, Tb, Dy (**23**), Ho) with SMM behavior in the dysprosium analogue (compound **23**) [54]. The $\{Dy_2\}$ unit in **23** consists of two centrosymmetric eight-coordinate Dy^{III} ions being bridged by phenoxo groups of the valdien^{2-} ligands in an intermediate geometry between square antiprism and dodecahedron. Ab initio calculations reveal weak antiferromagnetic interaction between the two Dy^{III} ions with $J_{\text{Dy-Dy}} = -0.21$ cm^{-1}. The out-of-phase component of the ac susceptibility exhibits a frequency-dependent peak associated with a single relaxation process, in accordance with the presence of a unique crystallographic Dy ion in the dinuclear structure. This indicates SMM behavior with $U_{\text{eff}} = 53$ cm^{-1} from the high-temperature regime where it is a thermally activated relaxation. Although the observed slow magnetic relaxation is mainly due to the single-ion relaxation, the result that an "S-shaped" hysteresis with a large step at $H = \pm 0.3$ T is observed through micro-SQUID experiments on easy axis-oriented
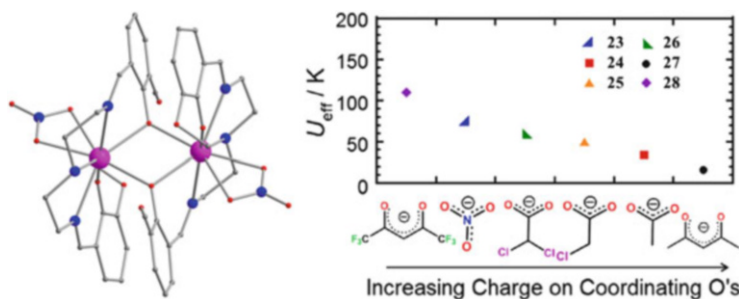
Fig. 10 Molecular structure for **23** (*left*), and plot of U_{eff} vs increasing charge on coordinating Os of the terminal ligands for **23–28** (*right*, reprinted with permission from [56]. Copyright 2013, American Chemical Society). Color codes: *pink*, Dy; *gray*, C; *blue*, N; and *red*, O

single crystals demonstrates a weak exchange coupling between the lanthanide ions affects the QTM (Fig. 10).

Since the method of doping a diamagnetic ion in dinuclear lanthanide SMMs can be employed to elucidate the origin of the slow relaxation of the magnetization, **23** was diluted into the isostructural Y_2 matrix with various Y:Dy ratios (19:1, 9:1, and 1:1). All of the diluted and nondiluted samples exhibit SMM behavior under zero applied dc field, confirming the slow relaxation of the magnetization originates from the single-ion relaxation of Dy^{III} ions. But the single-ion relaxation is found to be entangled with the neighboring Dy^{III} ion relaxation within the molecule via small (typically less than 1 cm^{-1}) but significant intramolecular exchange interactions, as proved by different QTM effects on single-crystal hysteresis loops for diluted samples [55].

By substituting the terminal nitrate ligands in compound **23** with other bidentate ligands bearing different electron-withdrawing abilities while maintaining the geometry of the lanthanide ions, a series of {Dy$_2$} SMMs, [Dy$_2$(valdien)$_2$(L)$_2$] ·solvent (L = CH_3COO^- (**24**), $ClCH_2COO^-$ (**25**), Cl_2CHCOO^- (**26**), $CH_3COCHCOCH_3^-$ (**27**), $CF_3COCHCOCF_3^-$ (**28**)), were prepared to study the correlation between the relaxation barriers and the electronic configurations [56]. For the first system, the sequential addition of Cl atoms, corresponding to coordinating bidentate acetate groups (**24**), chloroacetate (**25**), and dichloroacetate (**26**), leads to an increase of the energy barrier from 34 K (for **24**) to 50 K (for **25**) and 60 K (for **26**). The same trend occurs in the second system from 16 K (for **27**) to 110 K (for **28**) when the acac ligand is replaced by hexafluoroacac (Fig. 10). A correlation thus can be obtained as follows: the more electron deficient the bidentate terminal ligand, the higher the energy barrier of the {Dy$_2$}. Ab initio calculations reveal more axial *g* tensors as well as higher energy of the first-excited Kramers doublets for complexes **26** and **28**.

An asymmetrical dinuclear complex, [Dy$_2$(BSPDA)$_2$(acac)$_2$(H$_2$O)]·2CH$_2$Cl$_2$ (**29-Dy**), with double phenoxo bridge, is assembled from salen-type ligand H$_2$BSPDA and an ancillary β-diketonate ligand [57]. It contains two Dy(III) ions, one in a distorted SAP geometry and the other in a capped -trigonal-prismatic

geometry. Such distinct coordination environments induce two individual relaxation processes regardless of which relaxation corresponds to which ion. The isostructural ytterbium complex, $[Yb_2(BSPDA)_2(acac)_2(H_2O)]\cdot 2CH_2Cl_2$ (**29-Yb**), also exhibits SMM behavior under an applied dc magnetic field with $U_{eff} = 17\ cm^{-1}$ [58]. Strong QTM arising from low magnetic axiality and a large tunneling gap in the ground exchange doublet is responsible for the lack of slow relaxation in zero dc field which is validated by ab initio calculations.

More dinuclear Yb SMMs with salen-type ligands including compounds $[Yb_2(BMBDA)_3(CH_3OH)]\cdot 3CH_3CN$ (**30**), $[Yb_2(BMBDA)(MBP)(o\text{-vanillin})(CH_3OH)(H_2O)_2](ClO_4)_2\cdot CH_3OH\cdot H_2O$ (**31**), and $[Yb_2(BMBDA)(OAc)_4(CH_3OH)_2]\cdot 2CH_3OH$ (**32**) [59] were subsequently reported. It is known that slow relaxation of the magnetization is deeply affected by crystal field as well as bridging moieties. Hence, specifically, different energy barriers ($U_{eff} = 10\ cm^{-1}$ for **30**, $7\ cm^{-1}$ for **32**) under 3000 Oe dc field are observed, which are closely related to their coordination symmetries and bridging modes, i.e., D_{4d}/C_{2v} symmetry with double $\mu\text{-}O_{phenoxide}$ for **30**, D_{3h}/C_{2v} symmetry with triple $\mu\text{-}O_{phenoxide}$ for **31**, and D_{4d}/C_{2v} symmetry with double $\mu\text{-}O_{phenoxide}$ bridges and one acetate group for **32**.

Besides, polydentate Schiff base ligands derived from the condensation of salicylaldehyde derivatives and tetraamines have also produced new 4f compounds displaying SMM behavior. Incorporating the ligand H_3apior or H_3mapi with dysprosium salts results in compounds $[Dy_2api_2]$ (**33**) and $[Dy_2(mapi)_2]\cdot 4CH_3CN$ (**34**), respectively [60, 61]. These symmetric Dy_2 complexes are structurally similar because three methoxy groups of the $mapi^{3-}$ ligands remain free. Thus, both ligands serve as a heptadentate ligand via three phenoxide oxygen atoms and four imine nitrogen atoms, while the lanthanide metals for both compounds are eight-coordinate, with SAP coordination environment, and bridged by two phenoxide oxygen atoms and two imidazolidine groups. Ac susceptibility measurements for both compounds show frequency-dependent behavior, indicating the onset of slow relaxation of the magnetization under zero dc field (Fig. 11).
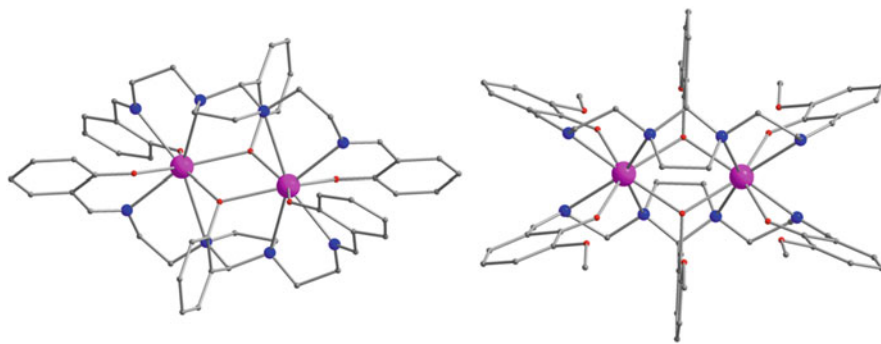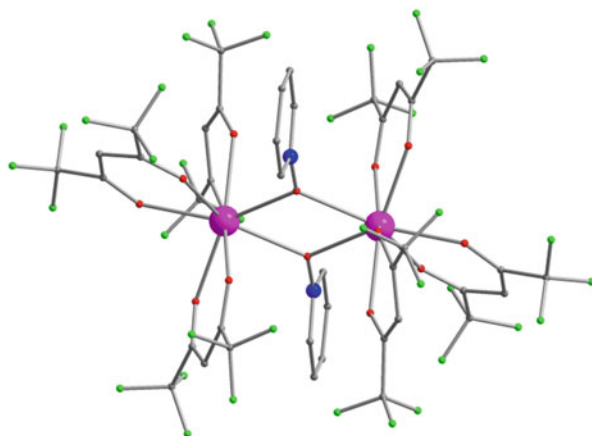

Fig. 11 Molecular structures for **33** (*left*) and **34** (*right*). Color codes: *pink*, Dy; *gray*, C; *blue*, N; and *red*, O

Fig. 12 Molecular structure for **36**. Color codes: *pink*, Dy; *gray*, C; *blue*, N; *red*, O; and *green*, F

Ligands from N-oxide family with lanthanide β-diketonates provide dinuclear complexes [{Dy(tta)$_3$(TTPyNO)}$_2$]·0.5CH$_2$Cl$_2$ (**35**) and [Dy(hfac)$_3$(PyNO)]$_2$ (**36**) [62, 63]. Both compounds have two equivalent Dy^{III} ions locating in a square-antiprismatic geometry of oxygenated coordination sphere; two oxygen atoms from the nitroxide groups bridge two Dy ions in a μ-mode to form the dimers. The intramolecular antiferromagnetic interactions were evidenced by two methods for each compound: (1) an empirical subtraction technique using model mononuclear complexes, [Dy(hfac)$_3$(TTAPyNO)$_2$](TTAPyNO = tetrathiafulvalene-amido-2-pyridine-N-oxide) for **35** and [Dy(hfac)$_3$]·2H$_2$O for **36**, due to their similar coordination sphere, and (2) assuming an Ising model for the Dy^{III} ion with an effective spin $S = 1/2$ and the anisotropic g tensor in the very-low-temperature region, giving negative J values. Both compounds behave as SMMs, with energy barriers as high as 60 cm^{-1} for **35** and 116 cm^{-1} for **36** under zero dc field, especially with an opened hysteresis loop at 1.4 K for **36** (Fig. 12, Table 2).

With the aid of diamagnetic metal ions, heterometallic complexes that contain Dy$^{III}_2$Co$^{III}_2$ "butterfly"-type core, where the two Dy^{III} ions occupy the "body" position with two diamagnetic low-spin Co^{III} ions sitting in the outer "wing tips," can be magnetically considered as dinuclear Dy^{III} complexes. Generally, the two Dy^{III} ions in the Dy$^{III}_2$Co$^{III}_2$-type compounds are eight-coordinate with a distorted SAP geometry and bridged via two μ$_3$-methoxide/hydroxide ligands. Given the different structures built from amine-based polyalcohol, these Dy$^{III}_2$Co$^{III}_2$ SMMs can be classified into two separate families according to whether the coligand is carboxylate or acetylacetonate (acac). The first family was characterized by {Dy$^{III}_2$Co$^{III}_2$}-benzoate complexes, where each benzoate ligand bridges a Co^{III} and a Dy^{III} ion, and two remaining coordination sites around each Dy^{III} ion are completed by two terminal MeOH, or one MeOH and one nitrate ion, or one chelating nitrate ion, as a consequence of varying amine–polyalcohol ligands even with one nonbonding arm in these complexes and different benzoate ligands. These compounds (**37–43**), with general formula of [Dy$_2$Co$^{III}_2$(OMe)$_2$(O$_2$CPh-x)$_4$(RN{(CH$_2$)$_2$O}$_2$)$_2$(L)$_n$]$^{y+}$

Table 2 Dinuclear $4f$ SMMs with monatomic bridges of oxygen

SMMs	CN of $4f$ ions	Bridging moieties	exch.	U_{eff}/cm^{-1} (H_{dc}/Oe)	hys (K)	References
{[Dy(hfac)$_3$(H$_2$O)]$_2$(4-styr)$_2$} (**13**)	8(O$_8$)	(μ-H$_2$O)$_2$	FM	64	–	[44]
TBA$_8$H$_4$[{Dy(μ$_2$-OH)$_2$Eu}(γ-SiW$_{10}$O$_{36}$)$_2$] (**14a**)	6(O$_6$)	(μ-OH)$_2$	–	51	–	[45]
TBA$_8$H$_4$[{Dy(μ$_2$-OH)$_2$Dy}(γ-SiW$_{10}$O$_{36}$)$_2$] (**14b**)	6(O$_6$)	(μ-OH)$_2$	–	46	–	[46]
TBA$_8$H$_4$[{Dy(μ$_2$-OH)$_2$Yb}(γ-SiW$_{10}$O$_{36}$)$_2$] (**14c**)	6(O$_6$)	(μ-OH)$_2$	–	37(1800)	–	[45]
TBA$_8$H$_4$[{Dy(μ$_2$-OH)$_2$Lu}(γ-SiW$_{10}$O$_{36}$)$_2$] (**14d**)	6(O$_6$)	(μ-OH)$_2$	–	33	–	[45]
[Dy$_2$(ovph)$_2$Cl$_2$(MeOH)$_3$]·MeCN (**15**)	7(N$_2$O$_3$Cl$_2$), 8 (N$_2$O$_6$)	(μ-O$_{hydrazone}$)$_2$	FM	104,138	1.5	[47]
[Dy$_2$(ovph)$_2$(NO$_3$)$_2$(H$_2$O)$_2$]·2H$_2$O (**16**)	8(N$_2$O$_6$)	(μ-O$_{hydrazone}$)$_2$	FM	48	–	[48]
[Dy$_2$(Hovph)(ovph)(NO$_3$)$_2$(H$_2$O)$_4$]·NO$_3$·2CH$_3$OH·3H$_2$O (**17**)	9(N$_2$O$_7$), 9 (NO$_8$)	(μ-O$_{phenoxide}$) + (μ-O$_{hydrazone}$)	FM	–	–	[48]
[Dy$_2$(Hhmb)$_4$(CO$_3$)]·4H$_2$O (**18**)	8(N$_2$O$_6$)	(μ-O$_{phenoxide}$)$_2$ + (μ$_2$-η^1:η^{1}CO$_3$)	–	12	–	[49]
[Dy$_2$(hnp)$_2$(NO$_3$)$_2$(CH$_3$OH)$_2$]·4CH$_3$CN (**19**)	8(N$_2$O$_6$)	(μ-O$_{hydrazone}$)$_2$	FM	29	–	[49]
[Dy$_2$(Hhmb)$_3$(NCS)$_3$]·2MeOH·py (**20-Dy**)	9(N$_3$O$_6$)	(μ-O$_{phenoxide}$)$_3$	FM	2(2000)	–	[50]
[Er$_2$(Hhmb)$_2$(NCS)$_4$(MeOH)$_2$] (**20-Er**)	8(N$_3$O$_5$)	(μ-O$_{phenoxide}$)$_2$	–	–	–	[50]
[Yb$_2$(Hhmb)$_2$(NCS)$_4$(MeOH)$_2$] (**20-Yb**)	8(N$_3$O$_5$)	(μ-O$_{phenoxide}$)$_2$	–	2(900)	–	[50]
[Dy$_2$(hmi)$_2$(NO$_3$)$_2$(MeOH)$_2$] (**21**)	8(NO$_7$)	(μ-O$_{phenoxide}$)$_2$	FM	39	–	[51]
[Dy$_2$(hbp)$_2$(PhCOO)$_2$(CH$_3$OH)$_2$] (**22**)	8(NO$_7$)	(μ-O$_{alkoxide}$)$_2$	FM	65	1.65	[53]
[Dy$_2$(valdien)$_2$(NO$_3$)$_2$] (**23**)	8(N$_3$O$_5$)	(μ-O$_{phenoxide}$)$_2$	AFM	53	4	[54]
[Dy$_2$(valdien)$_2$(CH$_3$COO)$_2$] (**24**)	8(N$_3$O$_5$)	(μ-O$_{phenoxide}$)$_2$	AFM	24	–	[56]
[Dy$_2$(valdien)$_2$(ClCH$_2$COO)$_2$] (**25**)	8(N$_3$O$_5$)	(μ-O$_{phenoxide}$)$_2$	AFM	35	–	[56]
[Dy$_2$(valdien)$_2$Cl$_2$CHCOO)$_2$]·0.5MeOH (**26**)	8(N$_3$O$_5$)	(μ-O$_{phenoxide}$)$_2$	AFM	42	–	[56]
[Dy$_2$(valdien)$_2$(acac)$_2$]·2CH$_2$Cl$_2$ (**27**)	8(N$_3$O$_5$)	(μ-O$_{phenoxide}$)$_2$	AFM	11	–	[56]

[Dy$_2$(valdien)$_2$(F$_6$acac)$_2$] (**28**)	8(N$_3$O$_5$)	(μ-O$_{phenoxide}$)$_2$	AFM	76	–	[56]
[Dy$_2$(BSPDA)$_2$(acac)$_2$(H$_2$O)]·2CH$_2$Cl$_2$ (**29-Dy**)	8(N$_2$O$_6$), 7 (N$_2$O$_5$)	(μ-O$_{phenoxide}$)$_2$	FM	25,56(1000)	–	[57]
[Yb$_2$(BSPDA)$_2$(acac)$_2$(H$_2$O)]·2CH$_2$Cl$_2$ (**29-Yb**)	8(N$_2$O$_6$), 7 (N$_2$O$_5$)	(μ-O$_{phenoxide}$)$_2$	FM	17(1600)	–	[58]
[Yb$_2$(BMBDA)$_3$(CH$_3$OH)]·3CH$_3$CN (**30**)	8(N$_4$O$_4$), 8 (N$_2$O$_6$)	(μ-O$_{phenoxide}$)$_2$	–	10(3000)	–	[59]
[Yb$_2$(BMBDA)(MBP)(o-vanillin)(CH$_3$OH)(H$_2$O)$_2$] (ClO$_4$)$_2$·CH$_3$OH·H$_2$O (**31**)	9(N$_2$O$_7$, 8 (O$_8$)	(μ-O$_{phenoxide}$)$_3$	–	-(3000)	–	[59]
[Yb$_2$(BMBDA)(OAc)$_4$(CH$_3$OH)$_2$]·2CH$_3$OH (**32**)	8(N$_2$O$_6$), 8 (O$_8$)	(μ-O$_{phenoxide}$)$_2$ + (μ$_2$-η^1:η^{1}OAc)	–	7(3000)	–	[59]
[Dy$_2$api$_2$] (**33**)	8(N$_4$O$_4$)	(μ-O$_{phenoxide}$)$_2$ + (imidazolidine)$_2$	–	18	–	[60]
[Dy$_2$(mapi)$_2$]·4CH$_3$CN (**34**)	8(N$_4$O$_4$)	(μ-O$_{phenoxide}$)$_2$ + (imidazolidine)$_2$	–	13(800)	–	[61]
[{Dy(tta)$_3$(TTPyNO)}$_2$]·0.5CH$_2$Cl$_2$ (**35**)	8(O$_8$)	(μ-O$_{PyNO}$)$_2$	AFM	60	–	[62]
[Dy(hfac)$_3$(PyNO)]$_2$ (**36**)	8(O$_8$)	(μ-O$_{PyNO}$)$_2$	AFM	116	1.4	[63]

(x = H, Cl, ^{t}Bu, CF$_3$; R = H, Me, Bu, (CH$_2$)$_2$O); L = MeOH and/or NO$_3$), display SMM behaviors in zero dc field with thermally activated barriers in the range of 55–96 cm^{-1} [64–66]. Ab initio calculations reveal that the relaxation mechanism in these complexes is single-ion origin and the magnetic exchange-coupling interactions between the two Dy^{III} ions are antiferromagnetic and derived from the dominant dipolar effects. Thus, changes of coordination sphere of Dy^{III} ions affect the magnitude of anisotropy barrier. Moreover, the diamagnetic ground states coupled with small tunneling gaps result in QTM effect with a time scale between 0.1 and >1.5 s. This was backed up by dilution studies that the relaxation mechanism is of single-ion origin and that the intramolecular magnetic interaction between Dy^{III} ions is indeed vital to the suppression of the QTM effects. Compound **44**, [Dy$_2$Co^{III}$_2$(OMe)$_2$(teaH)$_2$(Piv)$_6$], actually belongs to the type of {Dy^{III}$_2$Co^{III}$_2$}-benzoate complex and also displays SMM behavior with two evident relaxation pathways at zero dc field [67].

The second family is {Dy^{III}$_2$Co^{III}$_2$}-acac complexes, similar butterfly motif but with the replacement of chelating acac ligands, leading to the terminal ligands comprising of one chelating acac and one chelating nitrate or two chelating nitrate/acac ligands. In the case of one chelating acac and one chelating nitrate ligand around Dy^{III} ion, like compounds **45–47**, SMM behaviors are observed in zero dc magnetic field with anisotropy barriers of 18–26 cm^{-1} and quantum tunneling time scales of millisecond [68]. When replacing a chelating acac by a nitrate ligand, SMM properties are significantly enhanced, as shown in compound **48** with a large thermally activated energy barrier (117 cm^{-1}) and reduced quantum tunneling at low temperatures ($\tau_{QTM} > 1.5$ s) [69]. This result, once again, highlights the importance of coordination environment in SMM behavior. Besides, a new Dy^{III}$_2$Co^{III}$_2$ complex, [Dy$_2$Co^{III}$_2$(mdea)$_4$(hfacac)$_3$(O$_2$CCF$_3$)(H$_2$O)]·MeOH(**49**), has identical "butterfly"-type metallic core, but with different Dy environment (eight to nine-coordinate) and bridges between two Dy^{III} ions (three O atoms from three [mdea]$^{2-}$ ligands instead of two OMe$^-$ or OH$^-$ ligands), and displays SMM behavior at zero dc field with $U_{eff} = 23$ cm^{-1} [66] (Fig. 13, Table 3).
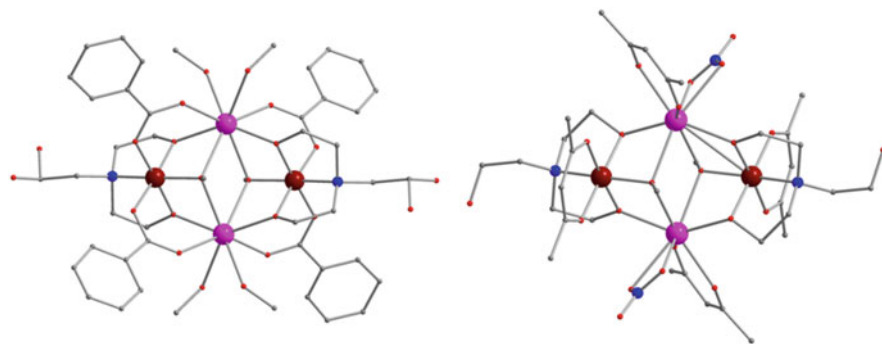

Fig. 13 Molecular structures for {Dy^{III}$_2$Co^{III}$_2$}-benzoate complexes (*left*) and {Dy^{III}$_2$Co^{III}$_2$}-acac complexes (*right*). Color codes: *pink*, Dy; *dark red*, Co; *gray*, C; *blue*, N; and *red*, O

Table 3 "Butterfly"-type Dy$^{III}_2$Co$^{III}_2$ SMMs

SMMs	CN of 4f ions	Bridging moieties	exch.	U_{eff}/cm^{-1} ($H_{dc}/$Oe)	τ_{QTM}, s	References
[Dy$_2$Co$^{III}_2$(OMe)$_2$(O$_2$CPh)$_4$(teaH)$_2$(MeOH)$_4$](NO$_3$)$_2$·MeOH·H$_2$O and [Dy$_2$Co$^{III}_2$(OMe)$_2$(O$_2$CPh)$_4$(teaH)$_2$(NO$_3$)$_2$(MeOH)$_2$]·MeOH·H$_2$O (**37**)	8(O$_8$)	(μ-OMe)$_2$	AFM	62	>1.5	[64]
[Dy$_2$Co$^{III}_2$(OMe)$_2$(O$_2$CPh)$_4$(dea)$_2$(MeOH)$_4$](NO$_3$)$_2$ (**38**)	8(O$_8$)	(μ-OMe)$_2$	AFM	72	0.12	[65]
[Dy$_2$Co$^{III}_2$(OMe)$_2$(O$_2$CPh)$_4$(mdea)$_2$(NO$_3$)$_2$] (**39**)	8(O$_8$)	(μ-OMe)$_2$	AFM	55	0.2	[65]
[Dy$_2$Co$^{III}_2$(OMe)$_2$(O$_2$CPh)$_4$(bdea)$_2$(MeOH)$_4$](NO$_3$)$_2$·0.5MeOH·H$_2$O and [Dy$_2$Co$^{III}_2$(OMe)$_2$(O$_2$CPh)$_4$(bdea)$_2$(MeOH)$_2$(NO$_3$)$_2$]·MeOH·1.5H$_2$O (**40**)	8(O$_8$)	(μ-OMe)$_2$	AFM	80	0.48	[65]
[Dy$_2$Co$^{III}_2$(OMe)$_2$(O$_2$CPh-2-Cl)$_4$(bdea)$_2$(NO$_3$)$_2$] (**41**)	8(O$_8$)	(μ-OMe)$_2$	–	80	0.9	[66]
[Dy$_2$Co$^{III}_2$(OMe)$_2$(O$_2$CPh-4-^{t}Bu)$_4$(bdea)$_2$(NO$_3$)$_3$(MeOH)$_3$](NO$_3$)·H$_2$O·MeOH (**42**)	8(O$_8$)	(μ-OMe)$_2$	AFM	77,96	0.5	[66]
[Dy$_2$Co$^{III}_2$(OMe)$_2$(O$_2$CPh-2-CF$_3$)$_4$(bdea)$_2$(NO$_3$)$_2$] (**43**)	8(O$_8$)	(μ-OMe)$_2$	–	88	~1.5	[66]
[Dy$_2$Co$^{III}_2$(OMe)$_2$(teaH)$_2$(Piv)$_6$] (**44**)	8(O$_8$)	(μ-OMe)$_2$	–	35,88	–	[67]
[Dy$_2$Co$^{III}_2$(OMe)$_2$(teaH)$_2$(acac)$_4$(NO$_3$)$_2$] (**45**)	8(O$_8$)	(μ-OMe)$_2$	–	18	0.00058	[68]
[Dy$_2$Co$^{III}_2$(OH)$_2$(teaH)$_2$(acac)$_4$(NO$_3$)$_2$]·4H$_2$O (**46**)	8(O$_8$)	(μ-OH)$_2$	–	19	0.00058	[68]
[Dy$_2$Co$^{III}_2$(OMe)$_2$(mdea)$_2$(acac)$_4$(NO$_3$)$_2$] (**47**)	8(O$_8$)	(μ-OMe)$_2$	–	26	0.0025	[68]
[Dy$_2$Co$^{III}_2$(OH)$_2$(bdea)$_2$(acac)$_4$(NO$_3$)$_4$] (**48**)	8(O$_8$)	(μ-OH)$_2$	–	117	>1.5	[69]
[Dy$_2$Co$^{III}_2$(mdea)$_4$(hfacac)$_3$(O$_2$CCF$_3$)(H$_2$O)]·MeOH (**49**)	9(O$_9$)	(μ-OR)$_3$	–	23	0.004	[66]

The research of doping another chemically identical ion into a dinuclear lanthanide SMM has been undertaken in a simple system, $[Ln_2(H_2cht)_2Cl_4(H_2O)(MeCN)]\cdot MeCN$ ($Ln = Dy_{0.435}Yb_{0.565}$(**50**), Dy (**51**), Yb (**52**); $H_3cht = 1,3,5$-cyclohexanetriol), to test its impact on the magnetic properties [70]. The dinuclear complex contains two seven-coordinate Ln ions sharing two hydroxyl–O bridges from two $[H_2cht]^-$ ligands. The remaining coordination sites of each Ln ion are completed by two hydroxyl–O atoms of the $[H_2cht]^-$ ligand, two chlorides, and a disordered terminal ligand of H_2O or MeCN molecule. Magnetic studies of compound **50** show a single slow relaxation process in the absence of external field and two relaxation processes with an applied dc field of 3500 Oe. Homospin compound **51** exhibits frequency-dependent behavior in the absence of an external dc field, while this situation occurs on **52** only when an external field is applied. Moreover, the obtained energy barriers of **50** are 70 cm^{-1} at higher temperature and 20 cm^{-1} at lower temperature, which seems to be coherent with respect to their pure analogues ($U_{eff} = 86$ cm^{-1} for Dy_2 and 14 cm^{-1} for Yb_2) but with shifts of the barriers. Hence, the origins of two relaxation processes can be attributed to the different Ln centers. Ab initio calculations for **51** and **52** suggest that the doublet ground state of the Dy ions is strongly axial, resulting the relaxation to occur via the first-excited states, whereas the relaxation on Yb ions occurs via a direct process (Fig. 14).

Incorporating 8-hydroxy-2-methylquinoline(MqH) into dinuclear lanthanide compounds can give anion-induced changes of structures. Specifically, utilizing $Dy(NO_3)_3$ leads to compound $[Dy_2(Mq)_4(NO_3)_6]$ (**53**), while using $DyCl_3$ results in $[Dy_2(Mq)_4Cl_6](EtOH)_2$ (**54**) [71]. Although they contain similar centrosymmetric Dy_2O_2 cores bridged by two oxygen atoms from two Mq ligands, coordination environment of Dy^{III} ion, that is, a distorted nine-coordinate 4,4,4-tricapped trigonal prism in **53** and a highly distorted six-coordinate octahedral environment in **54**, is quite different. Both compounds exhibit SMM behavior, while the thermal energy barrier to magnetization relaxation of **54** is significantly higher than that of **53** ($U_{eff} = 28$ cm^{-1} for **53** and 71 cm^{-1} for **54**).

When using 8-hydroxyquinoline (hqH) as the ligand instead of MqH, an asymmetric lanthanide dimer bridged by three oxygen atoms from three Mq ligands with formula $[hqH_2][Ln_2(hq)_4(NO_3)_3]\cdot MeOH$ was obtained ($Ln_2 = Dy_2$, Lu_2, Y_2, $Dy@Lu_2$, $Dy@Y_2$(**55**)) [72]. For Dy_2, one of two Dy^{III} ions is bound by three bridging hq ligands and a chelating hq ligand, generating an N_4O_4 coordination

Fig. 14 Molecular structure for **51** (*left*) and main species of the heteronuclear dimer for **50** (*right*). Color codes: *pink*, Dy; *purple*, Yb; *green*, Cl; *gray*, C; *blue*, N; and *red*, O
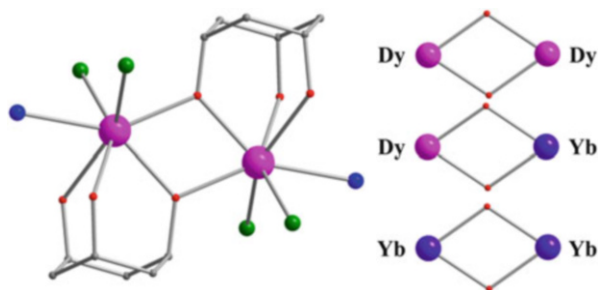
environment (referred to as the "hq pocket"), and the other one binds to three chelating nitrate anions and three O atoms from three bridging hq ligands, yielding a highly distorted O_9 environment (referred to as the "NO_3 pocket"). Since the eight-coordinate hq pocket is significantly smaller than the nine-coordinate NO_3 pocket, doping Dy^{III} ion into Y_2 or Lu_2 could make a different structural response due to the lanthanide contraction effect. It turns out that for a low-level doping of Dy^{III} into Lu_2, hereafter {$Dy@Lu_2$}, Dy^{III} is exclusively in the NO_3 pocket, while for a low-level doping of Dy^{III} into Y_2, hereafter {$Dy@Y_2$}, Dy^{III} is distributed evenly between the two pockets as Y^{III} and Dy^{III} have similar ionic radii. Ac magnetic measurements show no SMM behavior for Dy_2 and {$Dy@Lu_2$}, but pronounced SMM behavior for {$Dy@Y_2$}, suggesting that Dy^{III} in the smaller hq pocket is an SMM, whereas Dy^{III} in the larger NO_3 pocket is not. The SMM behavior is quenched in Dy_2 due to the angle between the principal anisotropy axes and the associated magnetic exchange, evidenced by electron paramagnetic resonance (EPR) spectroscopy, ab initio calculations, and far-infrared (FIR) spectroscopy. This gives the design criterion for enhancing magnetization retention in polymetallic lanthanide SMMs that the magnetic moments of individual spins should be aligned parallel (Fig. 15).

$Dy_2(hfht)_3(phen)_2$ (**56**) is another dinuclear SMM bridged by three oxygen atoms from three hfht ligands ($H_2hfht = 1,1,1,7,7,7$-hexafluoroheptane-2,4,6-trione, phen = 1,10-phenanthrene) [73]. Each Dy ion is eight-coordinate by six
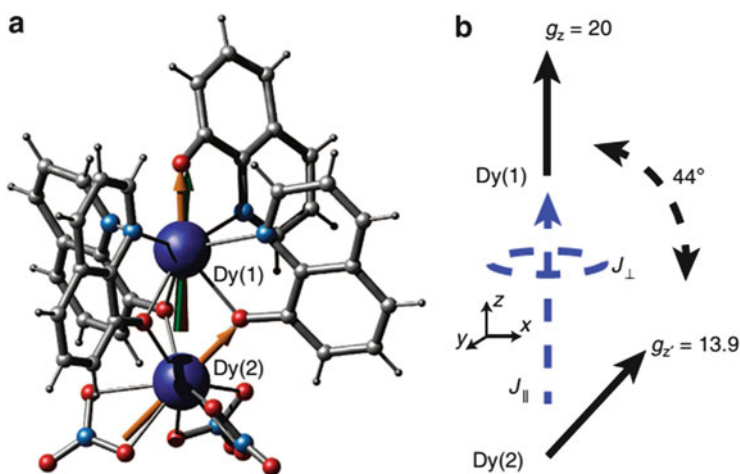
Fig. 15 (**a**) Crystal structure of **55**. Schemes: Dy, *blue*; N, *light blue*; O, *red*; C, *gray*; and H, *dark gray*. Orientation of the principal magnetic axes for Dy(1) and Dy(2) in the ground Kramers doublet from ab initio calculations shown as orange arrows and that for Dy(1) from electrostatic calculations as *green arrow*. (**b**) Schematic of the magnetic model for the EPR simulation. Relative projection of the principal magnetic axes for Dy(1) and Dy(2), along which $g_z = 20$ and 13.9 for Dy(1) and Dy(2), respectively, and the anisotropic exchange interaction between the dysprosium pair. Reprinted with permission from [72]. Copyright 2014, Rights Managed by Nature Publishing Group

oxygen atoms from three hfht ligands and two nitrogen atoms from one capping phen ligand. Each hfht dianion bridging two Dy ions acts as a doubled bidentate ligand. Compound **56** exhibits slow relaxation of the magnetization at low temperature, giving the energy barrier of 60 cm^{-1}.

A series of $Ln^{III}_2Zn^{II}_2$ complexes $[(\mu_3\text{-}CO_3)_2\{Zn(L)Ln(x)\}_2]\cdot$solvent (**57–63**, x = NO_3, OAc, or H_2O; L = salen-type ligands) were synthesized from salen-type ligands incorporating carbonato-bridging ligands derived from atmospheric CO_2 fixation [74–77]. Each $Ln^{III}_2Zn^{II}_2$ structure can be described as dinuclear Ln_2 magnetically bridged by two carbonato CO_3^{2-} ions acting with a μ_3-k^2-O,O′:k-O: k-O″ coordination mode and linking two Ln^{III} ions and one Zn^{II}. The Ln^{III} ion is usually coordinated by four oxygen atoms of two phenoxo and two methoxy/ethoxy O atoms of L^n, three oxygen atoms from the carbonato groups, and two oxygen atoms of bidentate NO_3^- or OAc^- ion, leading to a LnO_9 coordination environment. The Yb^{III} analogue is an exception because it has a H_2O molecule instead of a bidentate NO_3^- or OAc^- ion, resulting in a YbO_8 environment, probably due to the lanthanide contraction. For two $Tb^{III}_2Zn^{II}_2$ complexes, **57** and **59**, obvious frequency dependence in ac susceptibility is observed under 1 kOe dc field, with energy barrier of 27 and 29 cm^{-1}. Moreover, their luminescence spectra show five peaks for the $^5D_4 \rightarrow {}^7F_6$ transition at 77 K, which is correlated to the splitting of the ground-state Stark multiplet [74]. The fine structure assignable to this transition is in agreement with the energy pattern from the magnetic analysis. For four $Dy^{III}_2Zn^{II}_2$ complexes, **58**, **60**, and **61**, with NO_3^- terminal ligand, exhibit field-induced SMM behavior, while **62**, with OAc^- terminal ligand, acts as an SMM under zero dc field, affording the energy barriers of 36, 47, 17, and 24 cm^{-1}, respectively [75, 76]. Magnetic study of diamagnetic dilution demonstrates that the SMM behavior comes from single-ion relaxation of the Dy^{III} ion, as well as the important role of intermolecular interactions in adjusting the QTM process, due to the fact that diluted sample **61′** behaves as an SMM at zero dc field with about three times higher energy barrier than that in **61**. For the $Yb^{III}_2Zn^{II}_2$ complex, **63**, slow relaxation of the magnetization and SMM behavior, is observed under a dc magnetic field [77] (Fig. 16).

Fig. 16 Molecular structure for **62**. Color codes: *pink*, Dy; *dark red*, Zn; *gray*, C; *blue*, N; and *red*, O
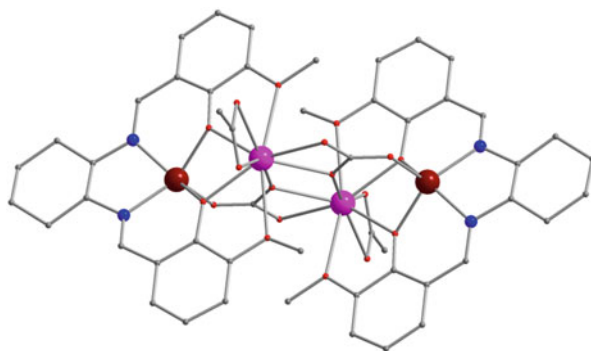
Another carbonato-bridged Dy_2 compound, $[Dy_2(Qda)_6(\mu\text{-}CO_3)]^{8-}$ (**64**), is a typical SMM, in which Dy^{III} ion is in a bicapped triangular prism with six oxygen atoms from three chelating ligands and two oxygen atoms from the bridging bis-bidentate CO_3^{2-} ligand [78]. If CO_3^{2-} was replaced with H_6notp, a phosphonate dimer $\{Dy(notp)(NO_3)(H_2O)\}_2 \cdot 8H_2O$ (**65a**) containing two symmetric Dy^{III} ions with a three-capped trigonal prism environment was obtained. A reversible transformation between **65a** and $\{Dy(notp)(NO_3)(H_2O)\}_2$ (**65b**) through desorption and absorption of solvent water can function at room temperature. Interestingly, both compounds show SMM behavior, and the energy barrier in **65a** can be increased by the removal of lattice water [79].

Mixing ligands of H_3hmmde and pivalic acid with Dy(III) chloride salt leads to a dinuclear $[Dy_2(H_2hmmde)_2(\mu\text{-piv})_2(piv)_2] \cdot 2CHCl_3$ (**66**) bridged by two phenolate oxygen atoms and two $\mu_2\text{-}\eta^1:\eta^1$ pivalate anion, while Hbmd with $Dy(OAc)_3 \cdot 6H_2O$ results in a doubly acetato-bridged dinuclear $[Dy_2(bmd)_2(OAc)_4(MeOH)_2] \cdot 2MeOH$ (**67**)in the form of the $\mu_2\text{-}\eta^1:\eta^2$ mode. Both Dy^{III} ions are nine-coordinate in a distorted monocapped square-antiprismatic geometry, but the coordination sphere of Dy is completed by two bridging phenolate O atoms, two bidentate pivalate O atoms, a unidentate pivalate ligand, one arm ($-$OMe), and the other arm ([N$(CH_2CH_2OH)_2$]) of the H_2hmmde ligands for **66**, while Dy^{III} ion is coordinated to three O atoms from double acetato-bridges, one chelating acetate ion, one methanol molecule, and the NO_2 pocket from the Hbmd for **67**. Magnetic studies reveal that **66** shows a two-step slow relaxation with effective energy barriers of 25 cm^{-1} at high temperatures (HT) and 6 cm^{-1} at low temperatures (LT), while **67** exhibits SMM behavior with energy barrier of 27 cm^{-1} [80, 81].

Employing sulfur donor as a soft-bridge motif would not only enhance the magnetic interaction between Ln^{III} ions but also may influence the crystal-field effect and hence dynamic magnetic properties. The metallocene-based complex $[\{Cp'_2Dy(\mu\text{-}SSiPh_3)\}_2]$ (**68**; $Cp' = C_5H_4Me$), where each Dy^{III} ion is complexed by two η^5-Cp' ligands and two sulfur atoms of two μ-$SSiPh_3$ ligands, is the first sulfur-bridged SMM. Its energy barrier is up to 133 cm^{-1}, one of the highest energy barrier reported for $\{Ln_2\}$ SMMs, proving a successful strategy in better SMMs [82].

Closely related Cl-bridged dinuclear lanthanide compound is $[Cp_2Dy(THF)(\mu\text{-}Cl)]_2$ (**69**) [83]. The structure is similar to **68**, but complexation by THF raises the formal coordination number of each dysprosium to nine, and the type of bridges is changed from S to Cl. **69** features typical of an SMM at zero dc field with lower magnetization reversal barrier of 34 cm^{-1}.

Ab initio calculation was utilized to quantify the magnetic anisotropy and interaction. For **68** and **69**, the g matrices in the ground doublets are very anisotropic ($g_x = 0.0012$, $g_y = 0.0019$, $g_z = 19.3611$ for **68**; $g_x = 0.0224$, $g_y = 0.0479$, $g_z = 18.9208$ for **69**), and the orientation of the main anisotropy axes of the Dy ions is close to perpendicular to the $\{Dy_2S_2\}$ or $\{Dy_2Cl_2\}$ plane. As a result, the intramolecular dipolar interaction ($J_{dipolar}$) is found to be antiferromagnetic coupling between magnetic spins (-2.22550 cm^{-1} for **68**, -1.99075 cm^{-1} for **69**). The other part of magnetic coupling parameter (J) is exchange interaction (J_{exch}), which

can be then derived by fitting the experimental susceptibility data. The J_{dipolar} in **68** and **69** are similar; however, the obtained J_{exch} are significantly different (-2.19475 cm^{-1} for **68**, -0.08550 cm^{-1} for **69**). This is likely due to the more diffuse valence orbitals of sulfur than those of chloride, allowing greater orbital overlap and stronger exchange interaction. The U_{eff} value for **68** agrees well with the calculated energy of the first-excited state on Dy sites (113 cm^{-1}), while this value for **69** is much lower than the calculated energy (96 cm^{-1}), since QTM regime occurs at 5 K for **69** but not approaches even at 2 K for **68**. This accords with the calculated values of transverse g values (g_{x} and g_{y}), which are one order of magnitude larger in **69** relative to **68**. Consequently, a large barrier can be seen in this sulfur-bridged SMM (Table 4).

2.1.2 Dinuclear 4*f* Clusters with Polyatomic Bridges

The monatomic bridges in structural motif [{Cp$_2$Ln(μ-R)}$_2$], like complexes **68** and **69**, can be replaced by other heteroatom groups. A new compound, [{Cp$_2$Dy (μ-bta)}$_2$] (**70**), was thus obtained for incorporating [bta]$^-$ (btaH = 1H-1,2,3-benzotriazole) as the bridging ligand [84]. In **70**, each dysprosium atom is complexed by two terminal η^5-Cp ligands and three nitrogen atoms from double μ_2-[bta]$^-$ ligands, generating a nine-coordinate environment. Ac magnetic susceptibility measurement reveals features associated with SMM below about 12 K, that is, the relaxation process is thermally activated above 6.3 K with energy barrier of 32 cm^{-1} and then enters a pure QTM regime below 4.5 K. This performance is comparable with **69**, but divergent with a paramagnetic complex which contains a similar coordination geometry and a different magnetic interaction, suggesting a controllable SMM behavior through magnetic exchange interaction (Fig. 17).

Utilization of strong electron-withdrawing group to facilitate the coordination of 4*f* ion to a non-chelating pyrazine(pz) ligand leads to a pyrazine-bridged dinuclear dysprosium compound [Dy$_2$(hfac)$_6$(H$_2$O)$_4$pz]·2pz (**71**), in which each Dy$^{\text{III}}$ ion is in a three-capped trigonal prism environment completed by eight oxygen atoms and one nitrogen atom [85]. This Dy$_2$ compound, featuring SMM behavior at low temperature with a relatively large energy barrier of 77 cm^{-1}, presents the first pyrazine-bridged Ln SMM (Fig. 18).

Using a chiral ligand of pyrazine derivative to this kind of Dy$_2$ compound may not only maintain the great SMM properties but also introduce ferroelectric properties. In designing compound [Dy$_2$(dbm)$_6$(bppp)$_{R/S}$]·2H$_2$O (*R*-**72** and *S*-**72** being the complexes containing bppp$_R$ and bppp$_S$ ligands, respectively; dbm = dibenzoylmethanato; bppp = (+)/(−)-2,5-bis(4,5-pinene-2-pyridyl) pyrazine), an important issue is stereoselective to these chiral ligands and homochiral Dy$_2$ compounds [86]. The crystallographic analysis reveals that *R*-**72** and *S*-**72** are pairs of enantiomers with chiral space group *P*2$_1$. Both compounds feature two octacoordinate Dy$^{\text{III}}$ ions bridged by pyrazine ring from bppp, where Dy1 adopts a distorted square-antiprismatic geometry and Dy2 is in a distorted dodecahedron geometry. Magnetic investigation of *R*-**72** finds that it behaves as

Table 4 Dinuclear 4f SMMs with monatomic bridges of oxygen, sulfur, and chlorine

SMMs	CN of 4f ions	Bridging moieties	exch.	U_{eff}/cm^{-1} (H_{dc}/Oe)	hys (K)	References
[Dy$_{0.87}$Yb$_{1.13}$(H$_2$cht)$_2$Cl$_4$(H$_2$O)(MeCN)]·MeCN (**50**)	7(NO$_4$Cl$_2$/O$_5$Cl$_2$)	(μ-OR)$_2$	–	70,20(3500)	–	[70]
[Dy$_2$(H$_2$cht)$_2$Cl$_4$(H$_2$O)(MeCN)]·MeCN (**51**)	7(NO$_4$Cl$_2$/O$_5$Cl$_2$)	(μ-OR)$_2$	–	86	–	[70]
[Yb$_2$(H$_2$cht)$_2$Cl$_4$(H$_2$O)(MeCN)]·MeCN (**52**)	7(NO$_4$Cl$_2$/O$_5$Cl$_2$)	(μ-OR)$_2$	–	14(3500)	–	[70]
[Dy$_2$(Mq)$_4$(NO$_3$)$_6$] (**53**)	9(O$_9$)	(μ-phenoxide)$_2$	–	28	–	[71]
[Dy$_2$(Mq)$_4$Cl$_6$](EtOH)$_2$ (**54**)	6(O$_3$Cl$_3$)	(μ-phenoxide)$_2$	–	71	–	[71]
[hqH$_2$][Ln$_2$(hq)$_4$(NO$_3$)$_3$]·MeOH {Ln$_2$ = Dy@Y$_2$} (**55**)	8(N$_4$O$_4$), 9(O$_9$)	(μ-phenoxide)$_3$	–	41(1000)	–	[72]
Dy$_2$(hfht)$_3$(phen)$_2$ (**56**)	8(N$_2$O$_6$)	(μ-O$_{hfht}$)$_3$	–	60	–	[73]
[(μ$_3$-CO$_3$)$_2${Zn(Mobde)Tb(NO$_3$)$_2$}$_2$]·acetone·H$_2$O (**57**)	9(O$_9$)	(μ$_3$-CO$_3$)$_2$	–	27(1000)	–	[74]
[(μ$_3$-CO$_3$)$_2${Zn(Mobde)Dy(NO$_3$)$_2$}$_2$]·0.5acetone·H$_2$O (**58**)	9(O$_9$)	(μ$_3$-CO$_3$)$_2$	–	36(1000)	–	[74]
[(μ$_3$-CO$_3$)$_2${Zn(Eobde)Tb(NO$_3$)$_2$}$_2$]·2.5H$_2$O (**59**)	9(O$_9$)	(μ$_3$-CO$_3$)$_2$	–	29(1000)	–	[74]
[(μ$_3$-CO$_3$)$_2${Zn(Eobde)Dy(NO$_3$)$_2$}$_2$]·2.5H$_2$O (**60**)	9(O$_9$)	(μ$_3$-CO$_3$)$_2$	–	47(1000)	–	[74]
{(μ$_3$-CO$_3$)$_2$[Zn(Tbda)Dy(NO$_3$)$_2$]$_2$·4CH$_3$OH (**61**)	9(O$_9$)	(μ$_3$-CO$_3$)$_2$	–	17(1000)	–	[75]
{(μ$_3$-CO$_3$)$_2$[Zn(Tbda)Dy$_{0.126}$Y$_{0.874}$(NO$_3$)$_2$]$_2$}· 4CH$_3$OH (**61'**)	9(O$_9$)	(μ$_3$-CO$_3$)$_2$	–	47 54(1000)	–	[75]
[(μ$_3$-CO$_3$)$_2${Zn(BSCDO)Dy(OAc)$_2$}$_2$]·10CH$_3$OH (**62**)	9(O$_9$)	(μ$_3$-CO$_3$)$_2$	FM	24	–	[76]
{(μ$_3$-CO$_3$)$_2$[Zn(Tbda)Yb(H$_2$O)]$_2$}(NO$_3$)$_2$·4CH$_3$OH (**63**)	8(O$_8$)	(μ$_3$-CO$_3$)$_2$	–	13(1000)	–	[77]
(Me$_4$N)$_6${K$_2$(H$_2$O)$_4$[Dy$_2$(Qda)$_6$(μ-CO$_3$)]}·nH$_2$O (**64**)	8(O$_8$)	μ-CO$_3$	–	27	–	[78]

(continued)

Table 4 (continued)

SMMs	CN of 4f ions	Bridging moieties	exch.	U_{eff}/cm^{-1} ($H_{dc}/$ Oe)	hys (K)	References
{Dy(notp)(NO$_3$)(H$_2$O)]$_2$·8H$_2$O (**65a**)	9(O$_9$)	(μ-PO$_3$)$_4$	FM	34(2000)	–	[79]
{Dy(notp)(NO$_3$)(H$_2$O))]$_2$ (**65b**)	9(O$_9$)	(μ-PO$_3$)$_4$	FM	57	–	[79]
[Dy$_2$(H$_2$hmmde)$_2$(μ-piv)$_2$(piv)$_2$]·2CHCl$_3$ (**66**)	9(NO$_8$)	(μ-phenoxide)$_2$ + μ_2-η^1:η^1 COOR)$_2$	–	25,6	–	[80]
[Dy$_2$(bmd)$_2$(OAc)$_4$(MeOH)$_2$]·2MeOH (**67**)	9(NO$_8$)	(μ_2-η^1:η^2 COOR)$_2$	–	27	–	[81]
[{Cp′$_2$-Dy(μ-SSiPh$_3$)}$_2$] (**68**)	12(C$_{10}$S$_2$)	(μ-SSiPh$_3$)$_2$	AFM	133	–	[82]
[Cp$_2$Dy(thf)(μ-Cl)]$_2$ (**69**)	12(C$_{10}$Cl$_2$)	(μ-Cl)$_2$	–	34	–	[83]
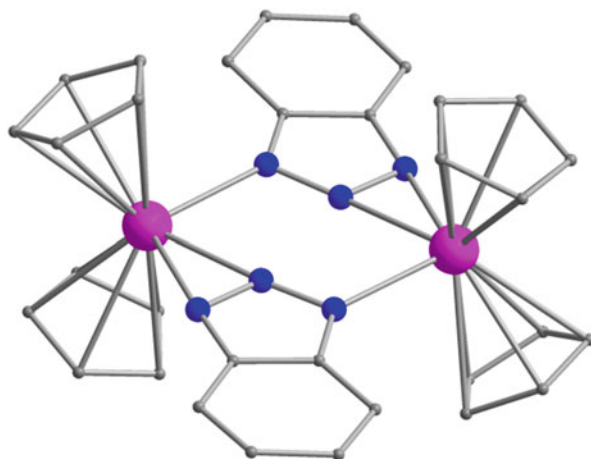
Fig. 17 Molecular structure for **70**. Color codes: *pink*, Dy; *gray*, C; and *blue*, N
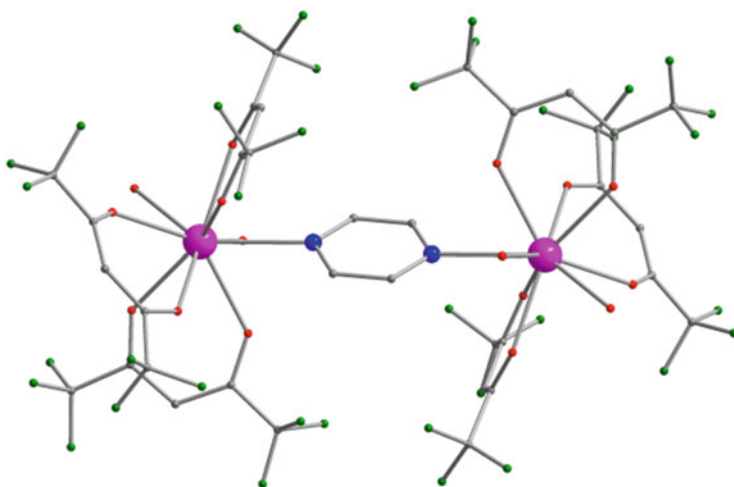
Fig. 18 Molecular structure for **71**. Color codes: *pink*, Dy; *gray*, C; *blue*, N; *red*, O; and *green*, F

SMM with $U_{eff} = 62$ cm^{-1}. Moreover, as the space group $P2_1$ belongs to a polar point group 2, as well as the keto–enol transformation (in β-diketonato molecules), which often triggers the ferroelectricity, ferroelectric study is performed on a single crystal of *R*-**72**. The result is that a well-shaped *P–E* hysteresis loop occurs at room temperature, with a large saturation value of spontaneous polarization. Thus, this is the first example of polynuclear Dy^{III} SMMs with ferroelectric properties (Fig. 19).

Carboxylate-bridged dinuclear Dy$_2$ SMMs in the form of the μ_2-η^1:η^1 mode present a means to adjust the magnetic relaxation from the primary and secondary building blocks. A dinuclear lanthanide complex via in situ hydrothermal synthesis is formulated as [Dy$_2$(3-Htzba)$_2$(3-tzba)$_2$(H$_2$O)$_8$]·4H$_2$O (**73**, 3-H$_2$tzba = 3-(1H-tetrazol-5-yl)benzoic acid) [87]. This centrosymmetric dimer contains eight-
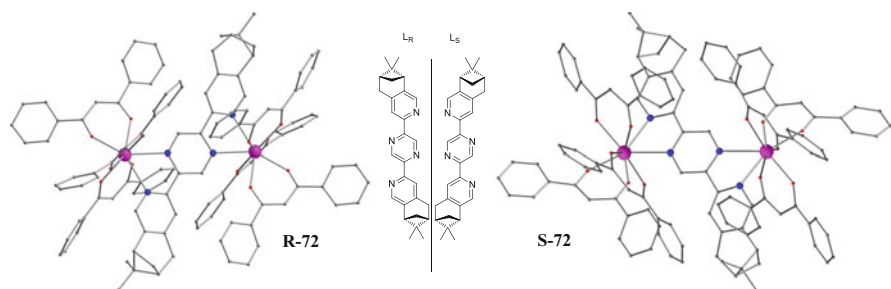
Fig. 19 Molecular structure for **72**. Color codes: *pink*, Dy; *gray*, C; *blue*, N; and *red*, O
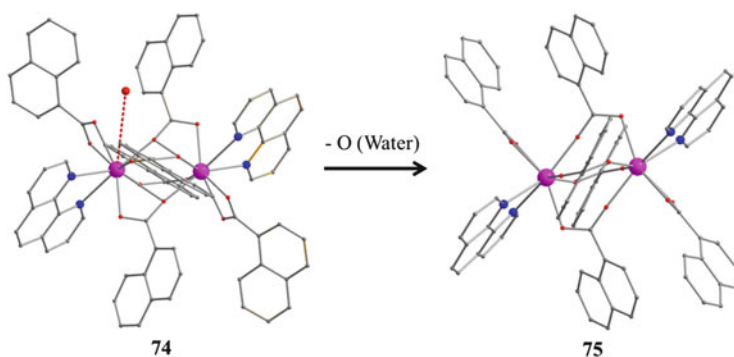
Fig. 20 The detailed structure change of **74** (*left*) and **75** (*right*) involved in this SCSC transformation. Color codes: *pink*, Dy; *gray*, C; *blue*, N; and *red*, O

coordinate Dy^{III} ions in a bicapped trigonal-prismatic DyO_8 coordination geometry that are linked by two carboxylate groups of two 3-Htzba ligands. The dynamic properties show a crossover from a thermally activated to a temperature-independent regime in the relaxation rates. An estimation produces an energy barrier of 37 cm^{-1} at higher temperatures and a saturation of ca. 8 ms at lower temperatures. Under an applied dc magnetic field of 2000 Oe, the obtained quantum relaxation time is much longer than that in the absence of a field, reaching an order of 0.1 s, although the energy barrier is almost unchanged.

Carboxylate-bridged, hydrated phase of $[Dy_2(phen)_2(NaphCO_2)_6]\cdot 2H_2O$ (**74**, NaphCO$_2$H = β-naphthoic acid) and anhydrous phase of $[Dy_2(phen)_2(NaphCO_2)_6]$ (**75**) can undergo a reversible single-crystal-to-single-crystal transformation, accompanied by nine-coordinate monocapped square-antiprismatic coordination geometry in **74** to eight-coordinate square-antiprismatic coordination geometry in **75**, because two of carboxylate bridges switch from $\mu_2:\eta^1:\eta^2$ in **74** to $\mu_2:\eta^1:\eta^1$ coordination mode in **75**. Both compounds present a slow thermally activated relaxation process and an SMM behavior; however, the energy barrier for **74** is 20 cm^{-1}, whereas **75** produces 4 cm^{-1}. This transformation from 0D to 0D in 4*f*-based SMMs is firstly explored, allowing adjustable SMMs via SCSC [88] (Fig. 20).

Employing pivH as the bridging and terminal ligand and phen as the terminal coligand, a dinuclear Dy_2 structure of $[Dy_2(phen)_2(piv)_6]$ (**76**) forms [89]. The molecule consists of one crystallographically independent Dy^{III} ion which is eight-coordinate by six O atoms from four piv ligands and two N atoms of a phen ligand. Two *syn,syn*-carboxylate groups bridge two Dy^{III} ions to a $Dy^{3+} \cdots Dy^{3+}$ separation of 5.391 Å. At zero dc field, a weak frequency-dependent out-of-phase susceptibility appears but without any peaks in the ac susceptibility measurement, whereas at an optimized dc field of 2.0 kOe, relaxation times that can be extracted from the obvious peaks in both the curves give a linear fitting in $U_{eff} = 20$ cm^{-1} and $\tau_0 = 9.64 \times 10^{-7}$ s.

To explore the effect of subtle modification on the SMM behavior in μ_2-η^1:η^1 carboxylate-bridged Dy_2 with N_2O_6 square-antiprismatic coordination geometry, structurally similar dinuclear Dy^{III} complexes, $Dy_2(phen)_2(ClphCO_2)_6$ (**77**), $Dy_2(bpy)_2(ClphCO_2)_6$ (**78**), and $Dy_2(H_2O)_2(bpy)_2(ClphCO_2)_6$ (**79**, ClphCO$_2$H = 4-chlorobenzoic acid), were synthesized [90]. Slight differences are only in coordination environments resulting from various terminal ligands around the Dy^{III} site for each compound, but different magnitudes of energy barriers are obtained, showing relatively fine-tuned SMM properties.

The first lanthanide-based SMM with oxalato-bridge, formulated as $[Dy_2(HBpz_3)_4(\mu\text{-ox})] \cdot 2CH_3CN \cdot CH_2Cl_2$ (**80**), is designed through the rational choice of a capping ligand, namely, hydrotris(pyrazolyl)borate, and of an oxalate as the bridging ligand [91]. With the analysis from dc and ac magnetic measurements, **80** has ferromagnetic interactions between Dy^{III} spin carriers, a relaxation barrier value of over 28 cm^{-1}, and a quantum regime of relaxation below 3 K (Fig. 21, Table 5).

Replacing the ortho-disubstituted phenylene in H_2BMBDA to para-disubstituted phenylene, a biphenyl group or a diphenylmethane group yields a series of ligands H_2bsp, H_2bsbp, and H_2bsbpm, respectively. When reacting with dysprosium salt, rigid ligands H_2bsp and H_2bsbp produce the quadruply-stranded Dy_2 helicates $(NEt_4)_2[Dy_2(bsp)_4]((CH_3)_2CO)_{0.25}$(**81**) and $(NEt_4)_2[Dy_2(bsbp)_4](H_2O)$ (DMF)$_{0.5}$(**82**), whereas the flexible ligand H_2bsbpm results in the mesocate $(NEt_4)_2[Dy_2(bsbpm)_4](Et_2O)_2((CH_3)_2CO)_{1.5}$(**83**) [92]. Each Dy^{III} ion occupies an

Fig. 21 Molecular structure for **80**. Color codes: *pink*, Dy; *gray*, C; *blue*, N; *red*, O; and *black*, B
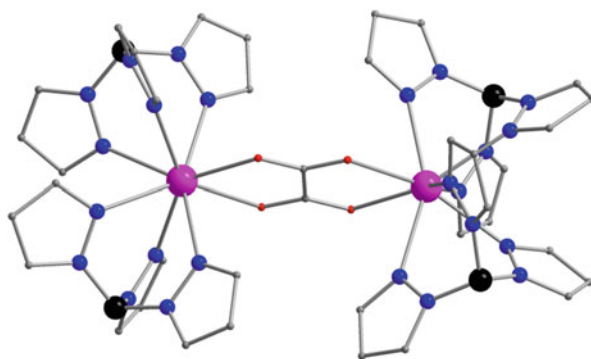
Table 5 Dinuclear $4f$ SMMs with polyatomic bridges (I)

SMMs	CN of $4f$ ions	Bridging moieties	exch.	$U_{\text{eff}}/\text{cm}^{-1}$ ($H_{\text{dc}}/$Oe)	hys (K)	References
[{Cp$_2$Dy(μ-bta)}$_2$] (**70**)	13(N$_3$C$_{10}$)	(μ-bta)$_2$	–	32	–	[84]
[Dy$_2$(hfac)$_6$(H$_2$O)$_4$pz]·2pz (**71**)	9(NO$_8$)	μ-pz	–	77	–	[85]
[Dy$_2$(dbm)$_6$(bppp)$_R$]·2H$_2$O (*R*-**72**)	8(N$_2$O$_6$)	μ-pz	–	62	–	[86]
[Dy$_2$(3-Htrzba)$_2$(3-tzba)$_2$(H$_2$O)$_8$]·4H$_2$O (**73**)	8(O$_8$)	(μ_2-η^1:η^1 COOR)$_2$	FM	37	–	[87]
[Dy$_2$(phen)$_2$(NaphCO$_2$)$_6$]·2H$_2$O (**74**)	9(N$_2$O$_7$)	(μ_2-η^1:η^2 COOR)$_2$ + (μ_2-η^1:η^1 COOR)$_2$	FM	20	–	[88]
[Dy$_2$(phen)$_2$(NaphCO$_2$)$_6$] (**75**)	8(N$_2$O$_6$)	(μ_2-η^1:η^1 COOR)$_4$	FM	4	–	88
[Dy$_2$(phen)$_2$(piv)$_6$] (**76**)	8(N$_2$O$_6$)	(μ_2-η^1:η^1 COOR)$_2$	–	20(2000)	–	[89]
Dy$_2$(phen)$_2$(ClphCO$_2$)$_6$ (**77**)	8(N$_2$O$_6$)	(μ_2-η^1:η^1 COOR)$_4$	FM	46	–	[90]
Dy$_2$(bpy)$_2$(ClphCO$_2$)$_6$ (**78**)	8(N$_2$O$_6$)	(μ_2-η^1:η^1 COOR)$_4$	FM	11	–	[90]
Dy$_2$(H$_2$O)$_2$(bpy)$_2$(ClphCO$_2$)$_6$ (**79**)	8(N$_2$O$_6$)	(μ_2-η^1:η^1 COOR)$_4$	FM	29(2000)	–	[90]
[Dy$_2$(HBpz$_3$)$_4$(μ-ox)]·2CH$_3$CN·CH$_2$Cl$_2$ (**80**)	8(N$_6$O$_2$)	μ-ox	FM	>28	–	[91]
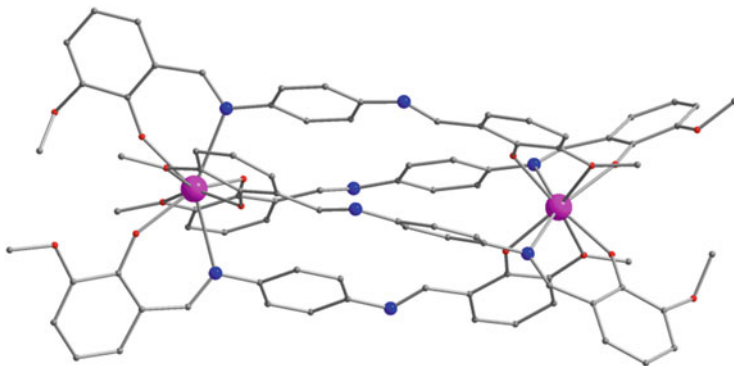
Fig. 22 Molecular structure for **81**. Color codes: *pink*, Dy; *gray*, C; *blue*, N; and *red*, O

eight-coordinate environment consisting of six O and two N atoms, which adopts an intermediate geometry between a square antiprism (D_{4d}) and a dodecahedron (D_{2d}). However, subtle but significant differences appear between the two Dy^{III} ions. At zero dc field, all three complexes do not show maxima in $\chi''(T)$ curves as a result of QTM. Under an optimum dc field of 1600 Oe for **81** and **83** and 1200 Oe for **82**, two relaxation processes are observed in **81** with $U_{eff} = 9$ cm^{-1} and 70 cm^{-1}, and only one process is evident in **82** and **83** with $U_{eff} = 49$ and 14 cm^{-1}, respectively. Ab initio calculations imply that the calculated energies of the first-excited Kramers doublets on two Dy sites differ significantly for **81** but do not differ much in **82** and **83**, thus explaining the presence of two distinct thermally activated processes in **81**. The angle between the two orientations of the anisotropic axes on two Dy centers is calculated as 55.10° (**81**), 52.14° (**82**), and 85.14° (**83**), respectively, indicating a possible way to modify the orientation of the axes by controlling the helical twist exerted in the ligand, although a single-ion mechanism operates in this system (Fig. 22).

Combining tetrathiafulvalene (TTF)-based ligands with lanthanides presents a π–f approach for elaboration of multifunctional materials, such as the applications in electronic conductivity, magnetism, and luminescence. From a magnetic point of view, functionalization of the TTF cores with groups to guarantee the coordination with the lanthanide ions performs magneto-structural correlation. For ttdt, two Dy$_2$ compounds [Dy$_2$(hfac)$_6$(H$_2$O)$_2$(ttdt)] (**84**) and [Dy(tta)$_3$(ttdt)$_{0.5}$]$_2$·3CH$_2$Cl$_2$ (**85**) are reported [93]. Each Dy^{III} ion in **84** is surrounded by nine O atoms from three hfac$^-$ ligands, one water molecule, and one ttdt ligand in a tricapped trigonal-prismatic geometry (D_{3h} symmetry), while in **85** bigger tta$^-$ reduces the coordination number to eight with a bicapped square-face trigonal-prismatic geometry (C_{2v} symmetry). Interestingly, **84** behaves as an SMM, while **85** does not show any slow relaxation of the magnetization in zero field, which should be attributable to a single-ion feature, especially to their local symmetries around the lanthanides, rather than the intramolecular and intermolecular interactions. With bpoe, compound [Dy$_2$(hfac)$_6$(bpoe)$_2$] (**86**) that consists of two Dy^{III} ions in C_{2v} and D_{4d} symmetries
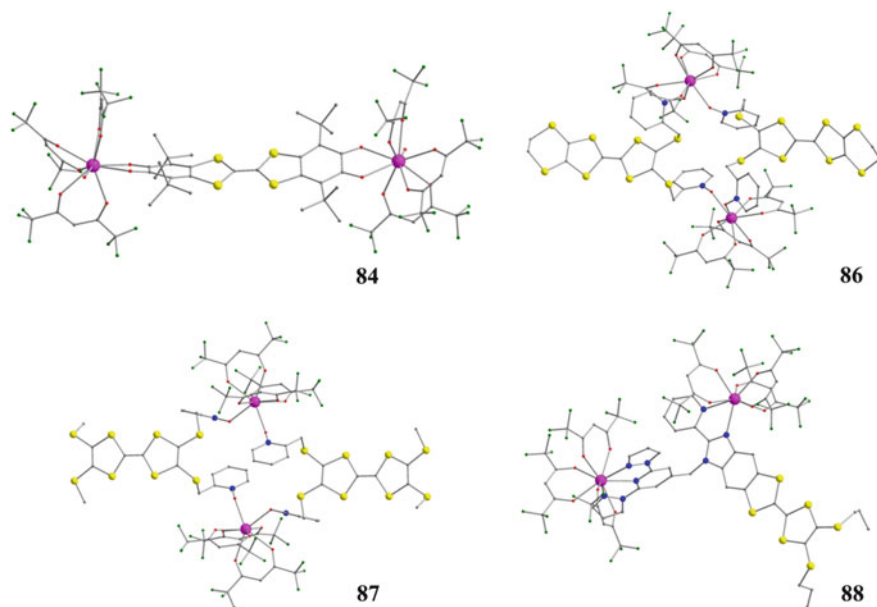
Fig. 23 Molecular structures for **84**, **86**, **87**, and **88**. Color codes: *pink*, Dy; *gray*, C; *blue*, N; *red*, O; *green*, F; and *yellow*, S

was synthesized and shows no out-of-phase signal [94]. The change of ligand from bpoe to bpom leads to a similar dinuclear compound $[Dy(hfac)_3(bpom)]_2$ (**87**) but induces a change of coordination sphere symmetry [94]. This increases the energy between the ground and first-excited states and thus an SMM behavior with $U_{eff} = 9$ cm^{-1}. For bpdp, two dinuclear Dy$_2$ compounds $[Dy_2(hfac)_6(bpdp)]$· $(CH_2Cl_2)_2 \cdot C_6H_{14}$ (**88**) and $[Dy_2(hfac)_3(tta)_3(bpdp)]$ (**89**) were synthesized [95]. Their crystal structures reveal that there are two crystallographically independent Dy^{III} centers, one of which coordinated to the bis-chelating moiety of ligand adopts a D_{4d} coordination geometry and the other of which coordinated to the tris-chelating moiety of ligand is in a D_{3h} sphere. Both compounds act as SMM, and the application of an external dc field induces multiple relaxation dynamics. Each relaxation is attributed to different coordination sites. Specifically, the slow relaxation and fast relaxation should belong to the Dy^{III} ion in D_{4d} and D_{3h} surroundings, respectively. Therefore, dinuclear Ln SMM with large diamagnetic linker between two lanthanides can be considered as having two molecular SMM effects (Fig. 23).

In the triple-decker-type di-rare-earth (RE) SMMs, the two sites occupied by RE ions are coupled by an f–f interaction, which is proved to disturb the slow relaxation of magnetization as mentioned previously. If connecting of two mononuclear double-decker complexes by a diamagnetic ion through coordination bonds into a quadruple-decker compound, large separation between two RE ions raises the question whether it would affect the relaxation. The first tetrakis(phthalocyaninato) rare-earth–cadmium quadruple-decker SMM is reported in compound [(obPc)Dy

(obPc)Cd(obPc)Dy(obPc)] (**90**), with $U_{eff} = 16$ cm^{-1} at zero field [96]. Then similar Tb^{III}-based compound [(obPc)Tb(obPc)Cd(obPc)Tb(obPc)] (**91**) was synthesized and also exhibits slow relaxation of the magnetization under an external 2 kOe field with a large energy barrier of 229 cm^{-1} [97]. In order to clarify the effect of long-range f–f interactions between the two lanthanide ions separated by a diamagnetic ion on the magnetic properties, heteroleptic compounds [(obPc)Tb(obPc)Cd(Pc)Tb(Pc)] (**92**) and its monoyttrium-replaced species [(obPc)Tb(obPc)Cd(Pc)Y(Pc)] (**93**) are designed. After comparatively investigated from the magnetic properties, a ferromagnetic interaction between the two Tb^{III} ions is confirmed to be present, which has a significant effect on the suppression of QTM at zero dc field and on the energy barriers obtained at an applied dc field in dynamic magnetic properties. Consequently, this long-distance intramolecular f–f interaction from sandwich-type quadruple-decker complexes can extend to quintuple-decker complexes. By comparing the magnetic properties of quintuple-decker {[Tb(obPc)$_2$]Cd (obPc)Cd[Tb(obPc)$_2$]} (**94**), quadruple-decker (**91**), and triple-decker (**6**), different responses of SMM behaviors to the applied dc magnetic fields occur, which can be ascribed to the differences in the intramolecular f–f interaction. Their Zeeman diagrams reveal that the QTM area for **94** is narrower than that for **91**, while **6** shows no QTM around $H_{dc} = 0$, indicating the Tb^{III}–Tb^{III} interactions affect the magnetic-field regions, especially the QTM region, and thus results in the different dynamic magnetic behaviors. These findings prompt a new way to fine-tune the SMM properties of multiple-decker complexes by controlling the magnitude of the intramolecular interactions [98, 99] (Fig. 24).

The multiple-decker Ln–(M)$_n$–Ln (M represents diamagnetic ion here) can extend to mixed phthalocyaninato–Schiff-base species. A sandwich-type structure in the form of Dy–Ca–Dy contains a Ca^{2+} ion bridging two phthalocyaninato–Schiff-base dysprosium double-deckers via coordination-bonding interactions, forming a mixed phthalocyaninato–Schiff-base quadruple-decker, namely, [CaDy$_2$(Pc)$_2$(BMBDA)$_2$(CH$_3$OH)$_2$] (**95**) [100]. The magnetic properties of **95** and the double-decker [KDy(Pc)(BMBDA)CH$_3$OH] are comparatively studied.
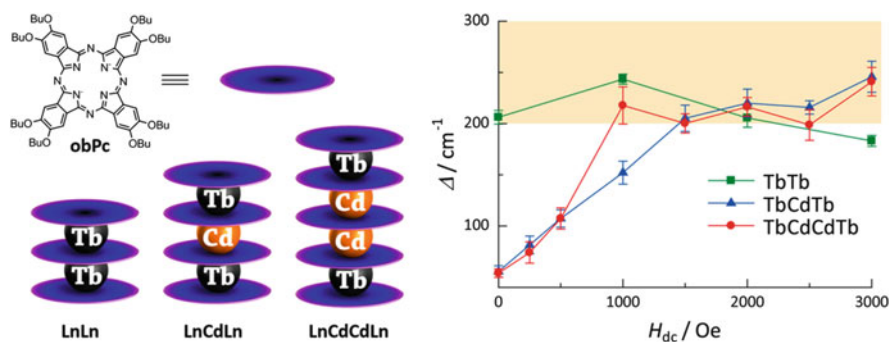
Fig. 24 Illustration (*left*) and U_{eff} vs H_{dc} plots (*right*) for multiple-decker complexes **91–93**. Reprinted with permission from [99]. Copyright 2015 American Chemical Society

Table 6 Dinuclear 4*f* SMMs with polyatomic bridges (II)

SMMs	CN of 4*f* ions	U_{eff}/cm^{-1} (H_{dc}/Oe)	hys (K)	References
(NEt$_4$)$_2$[Dy$_2$(bsp)$_4$]((CH$_3$)$_2$CO)$_{0.25}$ (**81**)	8(N$_2$O$_6$)	9,70(1600)	1.1	[92]
(NEt$_4$)$_2$[Dy$_2$(bsbp)$_4$](H$_2$O)(DMF)$_{0.5}$ (**82**)	8(N$_2$O$_6$)	49(1200)	5	[92]
(NEt$_4$)$_2$[Dy$_2$(bsbpm)$_4$] (Et$_2$O)$_2$((CH$_3$)$_2$CO)$_{1.5}$ (**83**)	8(N$_2$O$_6$)	14(1600)	5	[92]
[Dy$_2$(hfac)$_6$(H$_2$O)$_2$(ttdt)] (**84**)	9(O$_9$)	11	–	[93]
[Dy(hfac)$_3$(bpom)]$_2$ (**87**)	8(O$_8$)	9	–	[94]
[Dy$_2$(hfac)$_6$(bpdp)]·(CH$_2$Cl$_2$)$_2$·C$_6$H$_{14}$ (**88**)	8(N$_2$O$_6$), 9 (N$_3$O$_6$)	13,3	–	[95]
[Dy$_2$(hfac)$_3$(tta)$_3$(bpdp)] (**89**)	8(N$_2$O$_6$), 9 (N$_3$O$_6$)	30,15	–	[95]
[(obPc)Dy(obPc)Cd(obPc)Dy(obPc)] (**90**)	8(N$_8$)	16	–	[96]
[(obPc)Tb(obPc)Cd(obPc)Tb(obPc)] (**91**)	8(N$_8$)	229(2000)	–	[97]
[(obPc)Tb(obPc)Cd(Pc)Tb(Pc)] (**92**)	8(N$_8$)	213(2000)	–	[97]
[(obPc)Tb(obPc)Cd(Pc)Y(Pc)] (**93**)	8(N$_8$)	167(2000)	–	[97]
{[Tb(obPc)$_2$]Cd(obPc)Cd[Tb (obPc)$_2$]} (**94**)	8(N$_8$)	38	–	[98, 99]
[CaDy$_2$(Pc)$_2$(BMBDA)$_2$(CH$_3$OH)$_2$] (**95**)	8(N$_6$O$_2$)	20	–	[100]

Although both compounds show SMM behaviors, the QTM effect at zero field for the double-decker is much stronger than that for **95**, indicating the effective suppression of QTM by long-distance intramolecular f–f interaction again (Table 6).

2.1.3 Dinuclear 4*f* Clusters with Radical Bridges

Weak magnetic coupling is usually evidenced between lanthanides in multinuclear clusters owing to the limited radical extension of the inner 4*f* orbitals. In fact, strong coupling can not only provide an efficient exchange bias to improve SMM performance but also mitigate QTM process which may lead to the loss of magnetization. In this respect, the bridging ligands are not limited to diamagnetic species. Radical ligands that can survey strong exchange interaction between lanthanides are therefore employed to construct SMMs with high blocking temperatures, as the diffuse spin orbitals of some radical species are able to penetrate the core electron density of the lanthanide ions. Encouragingly, despite the paucity of SMMs containing radical ligand, remarkable progress has been made in dinuclear lanthanide-radical ligand-containing SMMs.

Reduction of N_2^{2-}-bridged complexes $\{[(Me_3Si)_2N]_2(THF)Ln\}_2(\mu-\eta^2:\eta^2-N_2)$ (**96**) with potassium graphite in THF generated a series of $N_2^{3-\bullet}$ radical-bridged dilanthanide complexes $[K(18-C-6)]\{[(Me_3Si)_2N]_2(THF)Ln\}_2(\mu-\eta^2:\eta^2-N_2)$ (**97**; Ln = Gd, Tb, Dy, Ho, Er) [101, 102]. In the resulting compounds, each lanthanide features a pseudotetrahedral coordination environment, with one vertex being occupied by the $N_2^{3-\bullet}$ radical. Meanwhile, the two Ln^{III} centers in the dinuclear anion are bridged by a $N_2^{3-\bullet}$ radical ligand to give a planar Ln_2N_2 moiety. An investigation on a Y(III) analogue shows that a single electron from the $N_2^{3-\bullet}$ unit occupies π^*orbital which is perpendicular to the Ln–N_2–Ln plane. Thus, the diffuse character of the orbital is expected to enhance exchange coupling with the lanthanide centers. Remarkably, a fit to the data for **97-Gd** reveals the strongest coupling parameter of $J = -27$ cm^{-1} (antiferromagnetic lanthanide-radical exchange) and yet observed for Gd compounds. In terms of **97-Dy**, **97-Tb**, **97-Ho**, and **97-Er**, significant high-temperature rises in the $\chi_M T$ vs T plots, compared to normal decline with decreasing temperature for the nonradical N_2^{2-}-bridged **96**, also indicate exceptionally strong magnetic exchange coupling between the Ln^{III} ions and central radical ligands. Ac susceptibility data demonstrate that **97-Dy**, **97-Tb**, **97-Ho**, and **97-Er** are all SMMs, with relaxation barriers of $U_{eff} = 123, 227, 73,$ and 36 cm^{-1}, respectively. Notably, 227 cm^{-1} is one of the highest barrier in multinuclear SMMs. The striking hysteresis loops for **97-Dy** and **97-Tb** are observed at temperatures up to 8.3 and 14 K, respectively, with a conventional magnetometer under available field-sweeping rates. In order to test the effect of radical on the dynamic magnetism, a comparison between **96-Dy** and **97-Dy** was taken. For very weakly coupled **96-Dy**, the energy barrier is reduced to 18 cm^{-1}, indicating the strong coupling transmitted by $N_2^{3-\bullet}$ radical is responsible for the outstanding SMM behavior.

Continuously, incorporating an inner-sphere K^+ counterion to the $N_2^{3-\bullet}$ radical-bridged dilanthanide complexes leads to $[\{((Me_3Si)_2N)_2(THF)Ln\}_2(\mu-\eta^2:\eta^2:\eta^2-N_2)K]$ (**98**; Ln = Gd, Tb, Dy) [103]. Structural characterization of **98** reveals the $K-(\eta^2\text{-}N_2)$ distance of 2.9 Å and thus a bend of the planar Ln–N_2–Ln unit. Ac magnetic data of **98-Dy** and **98-Tb** demonstrate that these complexes act as SMMs under zero applied dc field, but exhibit much smaller relaxation barriers (15 cm^{-1} and 41 cm^{-1}, respectively) compared to **97-Dy** and **97-Tb**. Analysis of the analogue **98-Gd** indicates that a competing antiferromagnetic Gd^{III}–Gd^{III} exchange interaction with $J \sim -2$ cm^{-1} becomes prominent, though the strength of antiferromagnetic coupling between the Gd^{III} and the $N_2^{3-\bullet}$ radical bridge remains. These results show the importance of exchange interaction to the slow magnetic relaxation (Figs. 25 and 26).

An organic radical bridging ligand bpym$^{\bullet-}$ (bpym = 2′-bipyrimidine) was utilized to facilitate strong coupling with two lanthanide ions in the dinuclear complexes $[(Cp^*_2Ln)_2(\mu\text{-bpym}^\bullet)](BPh_4)$ (**99**; Ln = Gd, Tb, Dy) [104]. The two lanthanide centers are symmetry equivalent, with each coordinated by two Cp^* ligands and two N atoms of a bridging bpym$^{\bullet-}$ ligand. According to the precise determination on **99-Gd**, an antiferromagnetic coupling between the Gd^{III} centers and the bridging bpym$^{\bullet-}$ligand is evidenced, with $J = -10$ cm^{-1}. This value is the second largest in magnitude and
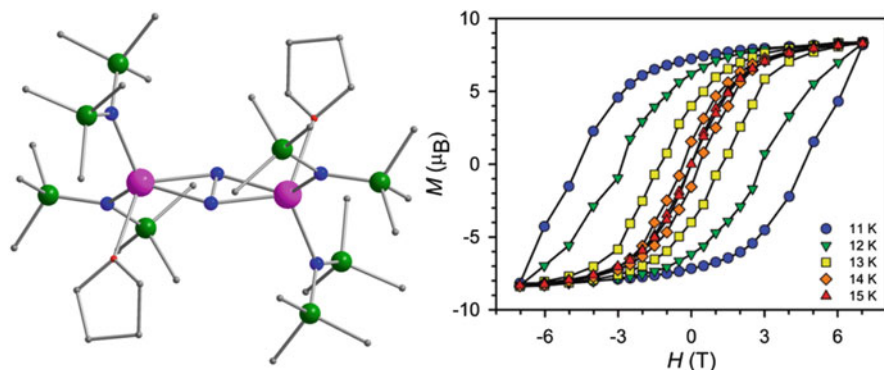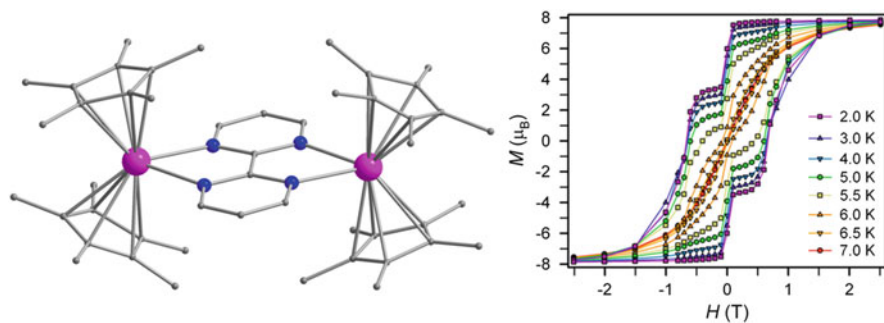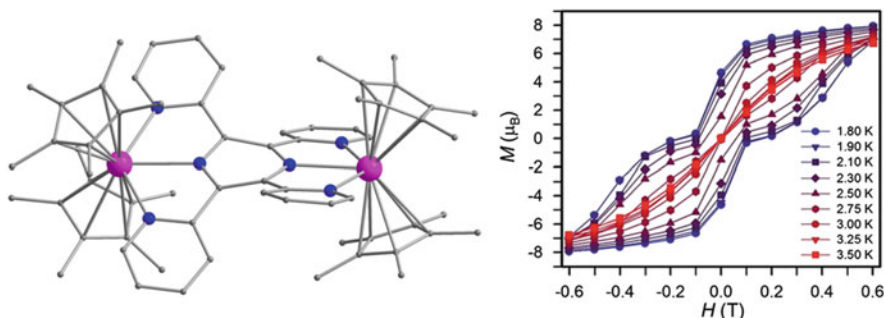
Fig. 25 Molecular structure for **97** (*left*) and plot of magnetization (*M*) vs dc magnetic field (*H*) for **97-Tb**. Reprinted with permission from [102]. 2011, American Chemical Society. Color codes: *pink*, Ln; *gray*, C; *blue*, N; *red*, O; and *green*, Si
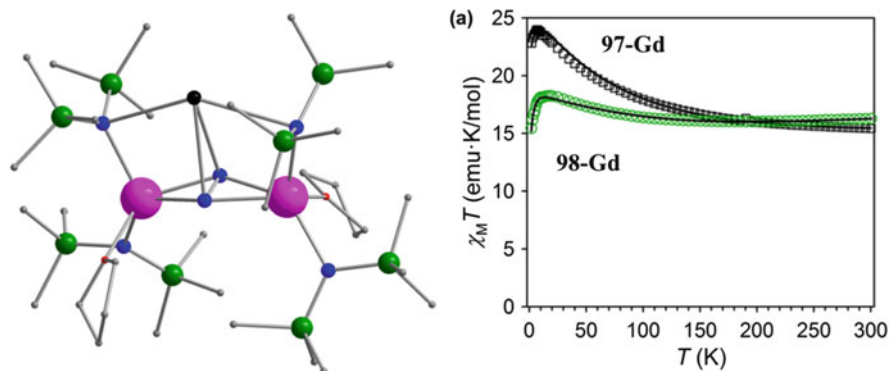
Fig. 26 Molecular structure for **98** (*left*) and $\chi_M T$ vs T plots for **97-Gd** and **98-Gd**. Reprinted with permission from [103]. Copyright 2014, American Chemical Society. Color codes: *pink*, Ln; *gray*, C; *blue*, N; *red*, O; *green*, Si; and *black*, K

yet reported for a Gd^{III} compound, only surpassed by the $J = -27$ cm^{-1} for the N$_2^{3-\bullet}$ radical-bridged complexes **97-Gd** and **98-Gd**. **99-Dy** and **99-Tb** are all SMMs with energy barriers of 88 and 44 cm^{-1}, respectively. Significantly, **99-Dy** shows open hysteresis loops for temperatures up to 6.5 K (Fig. 27).

Due to its bridging capability and ability to accept multiple electrons, tetra-2-pyridinylpyrazine (tppz) was employed in the synthesis of the complexes [(Cp*$_2$Ln)$_2$(μ-tppz$^\bullet$)](BPh$_4$)(**100**) and [K(crypt-222)][(Cp*$_2$Ln)$_2$(μ-tppz$^\bullet$)] (**101**; Ln = Gd, Tb, Dy), where **100** contains monoanionic radical tppz$^{\bullet-}$ and **101** contains trianionic radical tppz$^{\bullet 3-}$ [105]. Despite the rather similar coupling strength revealed by the exchange constant of $J = -6.91$ cm^{-1} for the monoanionic radical-bridged complex **100-Gd** and $J = -6.29$ cm^{-1} for the trianionic radical-bridged complex **101-Gd**, SMM behaviors are only observed in the monoanionic radical-bridged Tb^{III} and Dy^{III} complexes **100-Dy** and **100-Tb**. The absence of slow

Fig. 27 Molecular structure for **99** (*left*) and plot of magnetization (*M*) vs dc magnetic field (*H*) for **99-Dy**. Reprinted with permission from [104]. Copyright 2012 American Chemical Society. Color codes: *pink*, Ln; *gray*, C; and *blue*, N

Fig. 28 Molecular structure for **100** (*left*) and plot of magnetization (*M*) vs dc magnetic field (*H*) for **100-Dy**. Reprinted with permission from [105]. Copyright 2014, Royal Society of Chemistry. Color codes: *pink*, Ln; *gray*, C; and *blue*, N

magnetic relaxation for **101-Dy** and **101-Tb** is probably due to a different distribution for the spin density orientation toward the Ln^{III} centers. As a result of the appreciable exchange interaction, **100-Dy** displays open hysteresis loops at temperatures below 3.25 K with a coercive field of $H_c = 0.1$ T at 1.8 K (Fig. 28).

The stable nitronyl nitroxide radicals (NITRs) are widely used to construct 2*p*–4*f* complexes. For SMMs, the pyridine-functionalized NIT as a building block was firstly employed to bridge two lanthanides via the oxygen atom of the N–O group and the nitrogen atom of the pyridine ring. Meanwhile, each lanthanide coordinates to one oxygen atom of the nitronyl nitroxide unit from one radical, one nitrogen atom of the pyridine from another radical in *cis*-configuration, and six oxygen atoms from three hfac ligands, forming a cyclic four-spin dimer. The Dy^{III} compound, [Dy(hfac)$_3$\{NIT-4Py\}]$_2$ (**102-Dy**), exhibits slow magnetic relaxation following a gradual crossover from a thermally activated mechanism to a QTM regime upon cooling, with $U_{eff} = 9$ cm^{-1} [106]. There are three types of magnetic exchange interactions in this system: coupling between the metal center and the directly coordinated N–O group, and the generally weaker interaction between the metal center and the N–O group transmitted by the ancillary R group of the radical ligand,

as well as the metal–metal interaction via the radical ligand. When the Dy(III) centers are mostly substituted by diamagnetic Y(III) ions, very weak χ'' feature corresponding to only significantly reduced Dy–Dy pair content is observed in zero field. Its Tb(III) analogue, **102-Tb**, shows no clear χ'' signals above 2 K. However, if replacing the hfac coligand with phenyltrifluoroacetylacetonate (Phtfac), both Dy^{III} and Tb^{III} compounds, [Ln(Phtfac)$_3$(NIT-4Py)]$_2$ (**103**; Ln = Dy, Tb), reveal relaxation barrier of 14 cm^{-1} (at 3 kOe dc field) and 18 cm^{-1}, respectively [107].

Instead of NIT-4Py, non-chelating NIT-3Py also can give a similar cyclic four-spin dimer [Tb(hfac)$_3$(NIT-3Py)]$_2$ (**104**), but with different ligand field originating from different bond angles and possible stronger magnetic couplings [108]. As a result, **104** shows disparate dynamic magnetism from **102-Tb**, that is, frequency-dependent χ'' signals occur, and an energy barrier of 13 cm^{-1} is obtained under 3 kOe dc field. The introduction of Br atom to the pyridine ring of NIT-3Py can give rise to the ligand NIT-5-Py-3Br, and correspondingly, cyclic complex [Tb(hfac)$_3$(NIT-5-Br-3py)]$_2$ (**105**) was synthesized [109]. Ac magnetic data reveal the SMM behavior with $U_{eff} = 20$ cm^{-1} in zero dc field, directing a higher blocking temperature and energy barrier in comparison with Br-free complex **104**.

A related complex, [Tb(hfac)$_3$(NITPhPO(OEt)$_2$)]$_2$ (**106**), involving the substituted phosphine oxide radical NITPhPO(OEt)$_2$, resembles the aforementioned cyclic four-spin dimers in structure [110]. During the crystallization, two packing modes are obtained. One packing mode leads to well-isolated molecules (**106A**), whereas the other leads to short intermolecular contacts between N–O radical groups (**106B**). Though both compounds exhibit SMM behavior, the observation window centers at higher temperatures and lower frequencies for **106A** than for **106B**, as also suggested by the energy barrier of 17 cm^{-1} for **106A** in zero dc field and 15 cm^{-1} for **106B** under 2 kOe dc field. An intermolecular exchange interaction is thus presented to modulate dynamics of the magnetization in Ln–NIT system (Fig. 29).
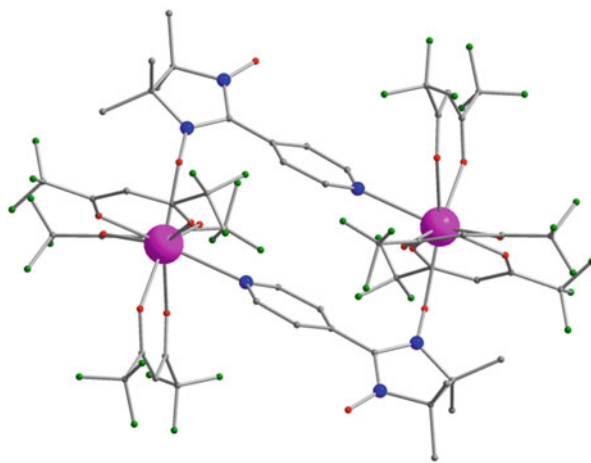
Fig. 29 Molecular structure for **106**. Color codes: *pink*, Ln; *gray*, C; *blue*, N; and *green*, F

Phenol-functionalized NIT radicals were employed in the syntheses of phenoxo-bridged binuclear complexes $[Dy_2(hfac)_4(NITPhO)_2]$ (**107**) and $[Dy_2(hfac)_4(NIT5BrPhO)_2]$ (**108**) [111]. Each Ln center is coordinated to seven oxygen atoms from two bidentate hfac ligands, one N–O group, and two bridging phenoxo-O atoms. Despite similar structures for these two compounds, distinct magnetic properties are displayed due to the electronic effect of the Br substituent: **107** shows slow relaxation of the magnetization, whereas **108** is without out-of-phase signal.

Dinuclear phthalocyanine-based sandwich-type dysprosium complex [(obPc)Dy(Bi-obPc)Dy(obPc)] (**109**) is an especially $2p$–$4f$ integrated system involving π-bridged polyradicals [112]. Specifically, it reveals a biradical character with each delocalized over one double-decker unit. From the magnetic investigation of Y(III) analogue, an antiferromagnetic interaction between the two radicals performs, leading to a singlet ground-state nature of the biradical. And so, though the SMM behavior is observed for both biradical species **109** and its nonradical form [N(C$_4$H$_9$)$_4$]$_2$$^{2+}$·[(obPc)Dy(Bi-obPc)Dy(obPc)]$^{2-}$ (**110**), QTM is significantly mitigated for **109**. Moreover, the energy barrier is increased from 28 cm^{-1} for **110** to 47 cm^{-1} for **109**, which confirms the effect of intramolecular π-bridged biradical-based antiferromagnetic interaction on the SMM properties. The magnetic hysteresis loop for the biradical compound **109** is observed at temperatures up to 5 K, the highest ever reported for the sandwich-type tetrapyrrole dysprosium SMMs (Fig. 30, Table 7).
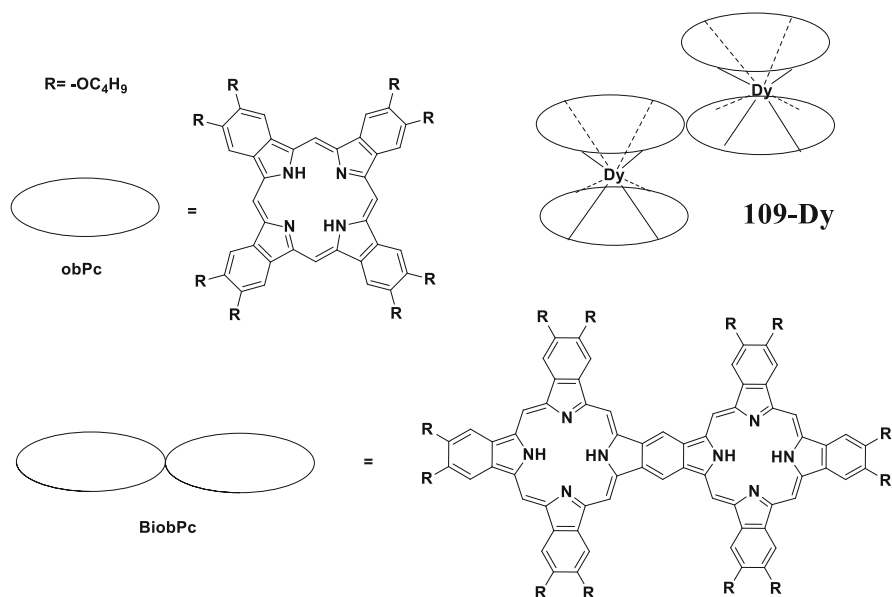
Fig. 30 Schematic illustration for complex **109**

Table 7 Dinuclear 4f SMMs with radical bridges

SMMs	CN of 4f ions	U_{eff}/cm^{-1} (H_{dc}/Oe)	hys (K)	References
$\{[(Me_3Si)_2N]_2(THF)Dy\}_2(\mu-\eta^2:\eta^2-N_2)$ (**96-Dy**)	5(N_4O)	18	–	[101]
$[K(18-C-6)]\{[(Me_3Si)_2N]_2(THF)Dy\}_2(\mu-\eta^2:\eta^2-N_2)$ (**97-Dy**)	5(N_4O)	123	8.3	[101]
$[K(18-C-6)]\{[(Me_3Si)_2N]_2(THF)Tb\}_2(\mu-\eta^2:\eta^2-N_2)$ (**97-Tb**)	5(N_4O)	227	14	[102]
$[K(18-C-6)]\{[(Me_3Si)_2N]_2(THF)Ho\}_2(\mu-\eta^2:\eta^2-N_2)$ (**97-Ho**)	5(N_4O)	73	–	[102]
$[K(18-C-6)]\{[(Me_3Si)_2N]_2(THF)Er\}_2(\mu-\eta^2:\eta^2-N_2)$ (**97-Er**)	5(N_4O)	36(1000)	–	[102]
$[\{((Me_3Si)_2N)_2(THF)Dy\}_2(\mu-\eta^2:\eta^2:\eta^2-N_2)K]$ (**98-Dy**)	5(N_4O)	15	–	[103]
$[\{((Me_3Si)_2N)_2(THF)Tb\}_2(\mu-\eta^2:\eta^2:\eta^2-N_2)K]$ (**98-Tb**)	5(N_4O)	41	3.8	[103]
$[(Cp^*_2Dy)_2(\mu-bpym^\bullet)](BPh_4)$ (**99-Dy**)	12 ($C_{10}N_2$)	88	6.5	[104]
$[(Cp^*_2Tb)_2(\mu-bpym^\bullet)](BPh_4)$ (**99-Tb**)	12 ($C_{10}N_2$)	44	–	[104]
$[(Cp^*_2Dy)_2(\mu-tppz^\bullet)](BPh_4)$ (**100-Dy**)	13 ($C_{10}N_3$)	36	3.25	[105]
$[(Cp^*_2Dy)_2(\mu-tppz^\bullet)](BPh_4)$ (**100-Tb**)	13 ($C_{10}N_3$)	5	–	[105]
$[Dy(hfac)_3\{NIT-4Py\}]_2$ (**102-Dy**)	8(NO_7)	9	–	[106]
$[Dy(Phtfac)_3(NIT-4Py)]_2$ (**103-Dy**)	8(NO_7)	14(3000)	–	[107]
$[Tb(Phtfac)_3(NIT-4Py)]_2$ (**103-Tb**)	8(NO_7)	18	–	[107]
$[Tb(hfac)_3(NIT-3Py)]_2$ (**104**)	8(NO_7)	13(3000)	–	[108]
$[Tb(hfac)_3(NIT-5-Br-3py)]_2$ (**105**)	8(NO_7)	20	–	[109]
$[Tb(hfac)_3(NITPhPO(OEt)_2)]_2$ (**106A**)	8(O_8)	17	–	[110]
$[Tb(hfac)_3(NITPhPO(OEt)_2)]_2$ (**106B**)	8(O_8)	15(2000)	–	[110]
$[Dy_2(hfac)_4(NITPhO)_2]$ (**107**)	8(O_7)	–	–	[111]
$[(obPc)Dy(Bi-obPc)Dy(obPc)]$ (**109-Dy**)	8(N_8)	47	5	[112]

2.2 Trinuclear 4f Clusters

Trinuclear 4f clusters in the context of SMMs can be subdivided into two types: triangular and linear Ln_3 SMMs. Although they represent a relatively small group, unprecedented magnetic properties, especially for the triangular Dy_3, make them famous.

2.2.1 Triangular Trinuclear 4*f* Clusters

The unprecedented magnetic properties are firstly reported in complex $[Dy_3(\mu_3\text{-}OH)_2(o\text{-}vanillin)_3Cl_2(H_2O)_4][Dy_3(\mu_3\text{-}OH)_2(o\text{-}vanillin)_3Cl(H_2O)_5]Cl_5\cdot19H_2O$ (**111**) or $[Dy_3(\mu_3\text{-}OH)_2(o\text{-}vanillin)_3Cl(H_2O)_5]Cl_3\cdot4H_2O\cdot2MeOH\cdot0.7MeCN$ (**112**), which show the unusual coexistence of the slow magnetic relaxation and an almost diamagnetic ground state [24]. The crystal structures of **111** and **112** contain the same triangular Dy_3 core capped by two μ_3-hydroxo centers. Along each side of the triangle, a deprotonated o-vanillin ligand bridges by its phenoxo group. Each of the dysprosium centers is eight-coordinate, and for Dy1/Dy2 the coordination sphere is completed by two water molecules. However, for Dy3 these sites are occupied by a chloride ion above the plane and below a chloride or a water molecule with a 50:50 disorder in complex **111**, while a chloride ion and a water molecule coordinate to Dy3 for **112**. This leads to different chloride-bridged hydrogen-bonding networks, but both compounds display identical dc and ac magnetic properties. The dc magnetic properties of the Dy_3 reveal the presence of antiferromagnetic interactions, but, rather surprisingly, magnetic susceptibility shows a maximum around 6.5 K and the vanishing susceptibility at low T, indicating an almost nonmagnetic ground state, which is unexpected for a system comprising odd number of spin centers with half-integer J value. This is confirmed by the magnetization versus field data with a well-defined step at around 8 kOe. In spite of the nonmagnetic ground state, SMM behavior is observed with an energy barrier of 43 cm^{-1} at zero dc field for the thermally populated excited state, suggesting that a resonant under-barrier relaxation process is also active. Single-crystal magnetic studies and ab initio calculations for the Dy_3 triangle consistently point to the nature of the nonmagnetic ground state [113]. The Dy^{III} ions are found to be very anisotropic, and the local anisotropy axes lie almost in the Dy_3 plane and almost perpendicular to the bisector lines of the Dy_3 triangle. The magnetic interaction (exchange and dipolar) between Dy sites is predominantly of none-collinear Ising type. Such spin structure can be described as almost perfectly toroidal or vortex-spin chirality. In general, the two states of the ground doublet have opposite vortex chirality, with clockwise or anticlockwise rotation of the spins. To convert one spin "enantiomer" into the other, consecutive reversal of spins is necessary and hence the energy barrier to blocking of the magnetization (Fig. 31).

When introducing bulky hydrazine into the vanillin group, ligands like H_2povh and H_3vovh were obtained, which were utilized to assemble the fascinating spin Dy_3 triangles. Interestingly, two triangular Dy_3 compounds, namely, $[Dy_3(\mu_3\text{-}OH)_2(Hpovh)_3(NO_3)_3(CH_3OH)_2H_2O]\cdot NO_3\cdot3CH_3OH\cdot2H_2O$ (**113**) and $[Dy_3(\mu_3\text{-}OH)_2(H_2vovh)_3Cl_2(CH_3OH)(H_2O)_3][Dy_3(\mu_3\text{-}OH)_2(H_2vovh)_3Cl_2(H_2O)_4]\cdot Cl_4\cdot2CH_3OH\cdot2CH_3CN\cdot7H_2O$ (**114**), maintain the peculiar vortex-spin structure of the ground nonmagnetic doublet [115]. They are both capped by two μ_3-OH ligands, and the vertices of the triangles are linked via bridging phenol oxygen atoms of three ligands. However, the coordination spheres of Dy^{III} ions in **113** are all completed by nine oxygen atoms, whereas those in **114** are all eight-coordinate
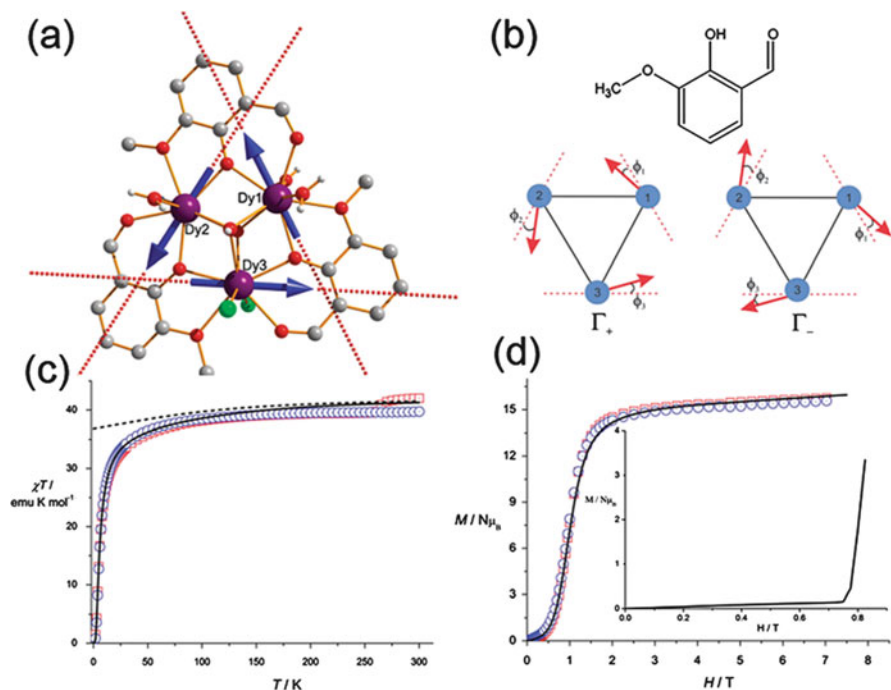
Fig. 31 (**a**) The structure of Dy$_3$ with main anisotropy axes (*dashed lines*) and local magnetizations (*arrows*) in the ground state. (**b**) The two components of the ground Kramers doublet. (**c**, **d**) The static magnetic properties of Dy$_3$ and their ab initio simulations (*lines*). Reprinted with permission from [114]. Copyright 2014, Royal Society of Chemistry

possessing O$_8$ or O$_7$ Cl coordination sites. As a result, despite the vortex-spin structures for both compounds, they perform a distinct behavior of magnetic dynamics. Indeed, for **113**, χ'' only accounts for a small component of the total susceptibility under zero field, and upon application of 1 kOe, energy barriers according to the presence of dual thermally activated relaxations can be determined as 4 and 37 cm^{-1}, while **114** maintains the slow relaxation of magnetization as the parent type, with $U_{eff} = 15$ cm^{-1} in zero dc field.

In contrast, two novel triangular Dy$_3$ compounds, [Dy$_3$(μ_3-OCH$_3$)$_2$(Hmdb)$_3$(SCN)]·4CH$_3$OH·2CH$_3$CN·2H$_2$O (**115**) and [Dy$_3$(μ_3-N$_3$)(μ_3-OH) (H$_2$mdb)$_3$(SCN)$_3$](SCN)·3CH$_3$OH·H$_2$O (**116**), show different dc magnetic properties that indicate both compounds are not nonmagnetic ground state [116]. Structural analyses reveal that the Dy$_3$ triangle in **115** is capped by two μ_3-OCH$_3$ and that in **116** is capped by one μ_3-N$_3$ and one μ_3-OH, instead of two μ_3-OH bridges. In both compounds, three edges of the triangle are bridged by three deprotonated phenoxide oxygen atoms of the ligands. Two distinct peaks in the out-of phase ac signals are observed for **115**, which demonstrates the possible occurrence of two relaxation processes, giving $U_{eff} = 3$ and 6 cm^{-1} for the fast and slow relaxation phase, respectively, while only a temperature-dependent out-of-phase signal without

peaks is observed in **116**. This disparity in the relaxation dynamics is probably due to the distinct coordination environments around the Dy^{III} ions.

A paramagnetic ground state is also found in two triangular Dy_3 complexes $[Dy_3(\mu_3\text{-OMe})_2(Habp)_3(NO_3)_3]BPh_4\cdot 4CH_3OH\cdot H_2O$ (**117**) and $[Dy_3(\mu_3\text{-OMe})_2(Habp)_3(NO_3)_3][Dy(NO_3)_6]_{0.33}\cdot CH_3OH\cdot 6H_2O$ (**118**) that possess the same $[Dy_3]$ cationic units [117]. This Dy_3 equilateral triangle is capped by two μ_3-OMe groups above and below the plane, while each pair of Dy^{III} ions is additionally bridged by one phenolate group, thereby giving rise to a common hexagonal bipyramidal Dy_3O_5 core. Magnetic susceptibility studies and ab initio calculations indicate that the Dy^{III} ions exhibit high axial anisotropy in the ground state and a large energy gap between the ground and first-excited doublets. To reduce the electron repulsion from the coordinating oxygen atom with the shortest Dy–O distance, the local magnetic moments are almost perpendicular to the Dy_3 plane. With the weak antiferromagnetic coupling between the Dy^{III} ions, the Dy_3 finally has a paramagnetic ground state. Both compounds exhibit SMM behavior, with available energy barrier under an applied dc field of 1 kOe. For **117** two thermally activated processes are observed with U_{eff} values of 20 and 35 cm^{-1}, whereas only one activated process occurs for **118** with $U_{eff} = 19$ cm^{-1}. Different dipole–dipole interactions should be responsible for various U_{eff}.

It is noteworthy that obvious ferromagnetic interactions occur in a triangular Dy_3 compound $[Dy_3(\mu_3\text{-OH})(hmmp)(Hhmmp)_4](ClO_4)_2\cdot 1.5C_2H_5OH\cdot 3.5H_2O$ (**119**), as is indicated by the sharp rise of the $\chi_M T$ at low temperatures [118]. The Dy_3 triangle is capped by one μ_3-OH group and one μ_3-alkoxyl group from the ligand where the alkoxyl oxygen atom is pulled far away from the Dy_3 plane by the ligand backbone, resulting in a large Dy–O distance and a small Dy–O–Dy angle. This structural difference is probably responsible for the ferromagnetic interactions observed in **119**. In zero dc field, **119** shows SMM behavior with the energy barrier of 9 cm^{-1}.

Introducing a second property into the SMM system is of great interest to assemble multifunctional materials. By employing enantiopure ligands, chiral Dy_3 compounds showing the combination of SMM and optical properties were obtained, that is, $[Dy_3L_{RRRRRR/SSSSSS}(\mu_3\text{-OH})_2(H_2O)_2(SCN)_4]\cdot xCH_3OH\cdot yH_2O$ (**120-R**, $x = 6$, $y = 0$; **120-S**, $x = 6$, $y = 1$) [119]. The structures consist of three Dy^{III} ions encapsulated by one tri-deprotonated macrocyclic ligand, featuring a triangular Dy_3 core capped by two μ_3-OH groups, as in the prototype Dy_3. The circular dichroism and vibrational circular dichroism spectra of **120-R** and **120-S** confirm the enantiomeric nature and optical activity, where the chirality is transferred from the ligands to the Dy_3 cores. Interestingly, for the enantiomers **120-R** and **120-S**, a dominant intramolecular ferromagnetic interaction is present as indicated by a sharp increase in the $\chi_M T$ below 40 K. Furthermore, both compounds reveal very similar field-induced SMM behavior, with $U_{eff} = 26$ cm^{-1} under 300 Oe dc field.

The coexistence of SMM and ferroelectric bistabilities is first realized in a triangular Dy_3 compound $[Dy_3(Hted)(H_2ted)(NO_3)_4]\cdot ethanol$ (**121**) which is assembled in an acentric space group $Pna2_1$ [120]. In this compound, the three Dy^{III} ions are doubly bridged by two μ_3-O from ligands, and two pairs of Dy ions are mono-bridged by a μ_2-O from the ligand, thus giving a Dy_3O_4 core which is different from

Table 8 Triangular trinuclear 4f SMMs

SMMs	CN of 4f ions	$U_{\text{eff}}/\text{cm}^{-1}$ (H_{dc}/Oe)	hys (K)	References
[Dy$_3$(μ_3-OH)$_2$(o-vanillin)$_3$Cl(H$_2$O)$_5$] Cl$_3$·4H$_2$O·2MeOH·0.7MeCN (**112**)	8(O$_8$), 8 (O$_7$Cl)	43	0.1	[24]
[Dy$_3$(μ_3-OH)$_2$(Hpovh)$_3$(NO$_3$)$_3$(CH$_3$OH)$_2$H$_2$O]· NO$_3$·3CH$_3$OH·2H$_2$O (**113**)	9(O$_9$)	4,37	–	[115]
[Dy$_3$(μ_3-OH)$_2$(H$_2$vovh)$_3$Cl$_2$(CH$_3$OH) (H$_2$O)$_3$][Dy$_3$(μ_3-OH)$_2$(H$_2$vovh)$_3$Cl$_2$(H$_2$O)$_4$]· Cl$_4$·2CH$_3$OH·2CH$_3$CN·7H$_2$O (**114**)	8(O$_8$), 8 (O$_7$Cl)	15	–	[115]
[Dy$_3$(μ_3-OCH$_3$)$_2$(Hmdb)$_3$(SCN)]· 4CH$_3$OH·2CH$_3$CN·2H$_2$O (**115**)	8(N$_2$O$_6$), 9 (N$_3$O$_6$)	3,6	–	[116]
[Dy$_3$(μ_3-N$_3$)(μ_3-OH)(H$_2$mdb)$_3$(SCN)$_3$] (SCN)·3CH$_3$OH·H$_2$O (**116**)	9(N$_4$O$_5$)	–	–	[116]
[Dy$_3$(μ_3-OMe)$_2$(Habp)$_3$(NO$_3$)$_3$] BPh$_4$·4CH$_3$OH·H$_2$O (**117**)	8(O$_8$)	20,35 (1000)	0.4	[117]
[Dy$_3$(μ_3-OMe)$_2$(Habp)$_3$(NO$_3$)$_3$][Dy (NO$_3$)$_6$]$_{0.33}$·CH$_3$OH·6H$_2$O (**118**)	8(O$_8$)	19(1000)	0.4	[117]
[Dy$_3$(μ_3-OH)(hmmp)(Hhmmp)$_4$] (ClO$_4$)$_2$·1.5C$_2$H$_5$OH·3.5H$_2$O (**119**)	8(NO$_7$), 8 (N$_2$O$_6$), 9 (N$_2$O$_7$)	9	–	[118]
[Dy$_3$L$_{RRRRRR}$(μ_3-OH)$_2$(H$_2$O)$_2$(SCN)$_4$]· 6CH$_3$OH·H$_2$O (**120-R**)	8(N$_2$O$_6$), 8 (N$_4$O$_4$)	26(300)	–	[119]
[Dy$_3$(Hted)(H$_2$ted)(NO$_3$)$_4$]·ethanol (**121**)	8(O$_8$), 9 (N$_2$O$_7$)	30,63	3.5	[120]

the previous triangular cores. Its static magnetic studies and ab initio calculations reveal the toroidal arrangement of local magnetic moments of Dy$^{\text{III}}$ ions but a nonvanishing magnetic moment in the Kramers doublet since the magnetic moments do not compensate each other. Strikingly, magnetic hysteresis loops and a two-step slow relaxation of the magnetization are observed below 30 K; moreover, dielectric hysteresis loops and a dielectric transition between a paraelectric and a ferroelectric phase at 470 K are also observed. Though the SMM behavior and the dielectric transition occur at a different temperature range, this work opens up new opportunity to develop molecular multiferroic materials (Table 8, Fig. 32).

2.2.2 Linear Trinuclear 4f Clusters

The reaction between the Schiff-base o-vanillin oxime (H$_2$msa) and Dy (ClO$_4$)$_3$·6H$_2$O results in a trinuclear compound [Dy$_3$(msa)$_2$(Hmsa)$_4$(EtOH)$_2$] (ClO$_4$)·1.5EtOH·H$_2$O (**122**), which contains a nearly linear Dy$_3$ core with a Dy···Dy···Dy angle of 166.29(1)° [121]. The central Dy$^{\text{III}}$ ion is linked to the outer metal ions through two single-atom O$_{\text{phenolate}}$ and one two-atom N–O$_{\text{oxime}}$ from ligands with the same bridging mode. Below 20 K, the $\chi_{\text{M}}T$ product for **122**
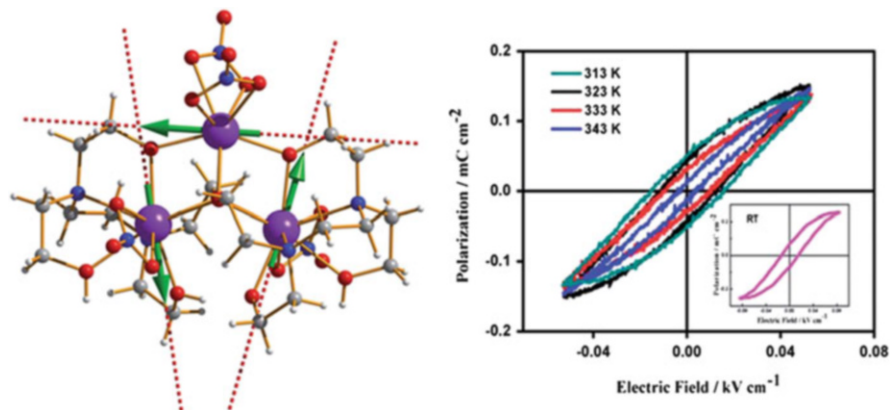
Fig. 32 (*Left*) Calculated local anisotropy axes on Dy(III) sites (*dashed lines*) and the local magnetic moments in the ground state (*arrows*). Color codes: *purple*, Dy; *red*, O; *gray*, C; and *blue*, N. (*Right*) Dielectric hysteresis loops of **121**. Reprinted with permission from [120]. Copyright 2012, Royal Society of Chemistry

rises sharply, indicative of ferromagnetic interactions. The ac susceptibility measurements reveal more than one magnetic relaxation process operating in this compound. The Arrhenius analysis allows two anisotropy barriers to be extracted, with $U_{eff} = 20$ cm^{-1} and 48 cm^{-1}, respectively. In contrast to the prototype Dy$_3$, the orientations of the easy axes determined by ab initio calculations are essentially collinear and parallel as a result of a favorable ferromagnetic dipolar interaction (Fig. 33).

By altering the reaction conditions, three compounds containing a similar linear Dy$_3$ core were obtained, namely, [Dy$_3$(msa)$_2$(Hmsa)$_4$(X)(Y)]·S (X/Y/S = OH/H$_2$O/ MeOH·7H$_2$O for **123**, NO$_3$/MeOH/MeOH·0.5H$_2$O for **124**, Cl$_3$CCO$_2$/MeOH/ MeOH for **125**) [122]. As the Dy$_3$ core in **122**, the three Dy^{III} ions in **123–125** are all bridged by two couples of single-atom O$_{phenolate}$ and a couple of two-atom N–O$_{oxime}$ bridges. Each Dy^{III} ion is eight-coordinate with a N$_2$O$_6$ environment, except an outer Dy^{III} ion in **124** featuring N$_2$O$_7$ environment because of a chelated NO$_3^-$ anion. The dc magnetic susceptibility studies reveal the presence of significant intra-Dy$_3$ Dy···Dy ferromagnetic interaction, and the ac magnetic susceptibility data show the onset of a slow relaxation of the magnetization. Similar energy barriers are determined, with $U_{eff} = 26$, 27 and 28 cm^{-1} for **123–125**, respectively. The ab initio calculations performed on **123** demonstrate that the local anisotropy axes lie in one plane, but are far from being parallel to each other in contrast to what is observed in **122**.

Tritopic hydrazone-based ligands are also suitable candidates for synthesis of linear trimetallic lanthanide clusters, such as [Dy$_3$(pomp)$_2$(NO$_3$)$_5$(DMF)]·DMF (**126**) and [Dy$_3$(pmp)$_2$(H$_2$O)$_9$](Cl)$_5$·6H$_2$O (**127**) [123, 124]. Both compounds consist of a linear Dy$_3$ core which is bound by two ligands, whereas the coordination environments of Dy^{III} ions are further completed by NO$_3^-$/DMF for **126** and H$_2$O
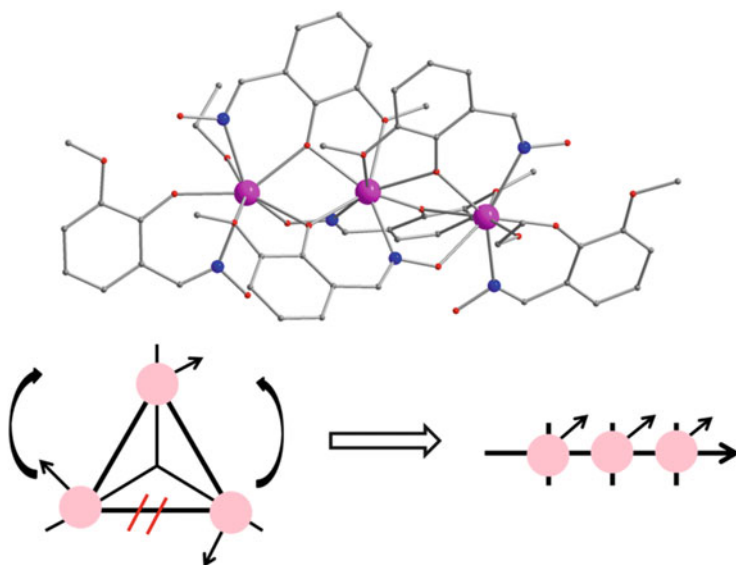
Fig. 33 Molecular structure for **122** (*top*) and schematic view of the effect of the opening of the triangle (*bottom*). Color codes: *pink*, Ln; *gray*, C; *blue*, N; and *red*, O

for **127**, resulting in a totally different local ligand field. They both show slow relaxation of magnetization characteristic of SMM behavior under zero dc field, but no full peaks can be observed. Only a substantial energy barrier of 10 cm^{-1} for **126** is obtained after an application of $H_{dc} = 1.8$ kOe.

Two novel complexes ([Dy$_3$(BSPDA)$_3$(CH$_3$OH)$_2$(NO$_3$)$_3$]· CH$_2$Cl$_2$·CH$_3$OH·2H$_2$O (**128**) and [Dy$_3$(BMBDA)$_3$(OAc)$_3$]·3CH$_3$OH·H$_2$O (**129**)) constructed from salen-type ligands feature the same but unique triple-decker trinuclear sandwich structure [125]. The neighboring Dy^{III} ions are bridged by two oxygen atoms, except an additional bridging acetate group between Dy2 and Dy3 in **129**, leading to a larger Dy1···Dy2···Dy3 angle in **129** (154.56°) compared to that in **128** (109.23°). As a result, dissimilar static magnetic behaviors are observed, especially the obvious ferromagnetic interaction in **129**. Both compounds display slow magnetic relaxation, but without available energy barriers.

Other examples of linear trimetallic SMMs include a luminescent complex [Dy$_3$(Hsal)$_5$(sal)$_2$(phen)$_3$] (**130**), which adopts a linear Dy$_3$ arrangement with Dy···Dy···Dy angle of 165.34° and shows slow magnetic relaxation with $U_{eff} = 45$ cm^{-1}, and a series of complexes [Ln$_3$(oq)$_9$] (Ln = Dy, **131-Dy**; Ln = Tb, **131-Tb**) with Ln···Ln···Ln angle of 134° [126, 127]. The latter compound **131-Dy** displays weak ferromagnetic exchange and two distinct relaxation processes under zero dc field, with energy barriers of 33 and 64 cm^{-1} for the fast and slow process, respectively, while **131-Tb** exhibits field-induced slow relaxation behavior (Table 9).

Table 9 Linear trinuclear 4*f* SMMs

SMMs	CN of 4*f* ions	U_{eff}/cm^{-1} (H_{dc}/Oe)	hys (K)	References
[Dy$_3$(msa)$_2$(Hmsa)$_4$(EtOH)$_2$](ClO$_4$)· 1.5EtOH·H$_2$O (**122**)	8(N$_2$O$_6$)	20,48	–	[121]
[Dy$_3$(msa)$_2$(Hmsa)$_4$(OH)(H$_2$O)]· MeOH·7H$_2$O (**123**)	8(N$_2$O$_6$)	26	–	[122]
[Dy$_3$(msa)$_2$(Hmsa)$_4$(NO$_3$)(MeOH)]· MeOH·0.5H$_2$O (**124**)	8(N$_2$O$_6$), 9(N$_2$O$_7$)	27	–	[122]
[Dy$_3$(msa)$_2$(Hmsa)$_4$(Cl$_3$CCO$_2$) (MeOH)]·MeOH (**125**)	8(N$_2$O$_6$)	28	–	[122]
[Dy$_3$(pomp)$_2$(NO$_3$)$_5$(DMF)]·DMF (**126**)	9(N$_4$O$_5$), 10 (N$_2$O$_8$), 10(N$_4$O$_6$)	10(1800)	–	[123]
[Dy$_3$(pmp)$_2$(H$_2$O)$_9$](Cl)$_5$·6H$_2$O (**127**)	9(N$_2$O$_7$), 9(N$_4$O$_5$)	–	–	[124]
[Dy$_3$(BSPDA)$_3$(CH$_3$OH)$_2$(NO$_3$)$_3$]· CH$_2$Cl$_2$·CH$_3$OH·2H$_2$O (**128**)	7(N$_2$O$_5$), 8(N$_4$O$_4$), 9(O$_9$)	–	–	[125]
[Dy$_3$(BMBDA)$_3$(OAc)$_3$]· 3CH$_3$OH·H$_2$O (**129**)	8(N$_4$O$_4$), 8(N$_2$O$_6$), 8(O$_8$)	–	–	[125]
[Dy$_3$(Hsal)$_5$(sal)$_2$(phen)$_3$] (**130**)	8(O$_8$), 8(N$_2$O$_6$), 8 (N$_4$O$_4$)	45	–	[126]
[Dy$_3$(oq)$_9$] (**131-Dy**)	8(N$_4$O$_4$), 8(NO$_7$)	33,64	–	[127]
[Tb$_3$(oq)$_9$] (**131-Tb**)	8(N$_4$O$_4$), 8(NO$_7$)	–(5000)	–	[127]

2.3 Tetranuclear 4f Clusters

After dinuclear 4*f* SMMs, the second largest number of 4*f* clusters with the SMM behavior is that of tetranuclear 4*f* SMMs. With respect to the arrangement of metal ions, tetranuclear 4*f* SMMs can form many types including rhombus, square, linear chain, zigzag chain, cubane, tetrahedron, trigonal pyramid, edge-sharing bi-triangle, Y shape, and [2 + 2] geometries. Meanwhile, the metal ions found here mostly are dysprosium, which are usually oxygen bridging.

2.3.1 Rhombus Topology

In the rhombus Dy$_4$, the four Dy^{III} ions are coplanar and usually are bridged by two μ$_3$-OH ligands. Compound [Dy$_4$(μ$_3$-OH)$_2$(bmh)$_2$(msh)$_4$Cl$_2$] (**132**), prepared via in situ solvothermal synthesis including o-vanillin and hydrazine hydrate, features a rhombus Dy$_4$ bridged by two μ$_3$-OH ligands and also by a combination of four phenoxides and two diaza-bridging groups [128]. Ac susceptibility measurement reveals that two modes of relaxation perform at 30 and 9 K for 1500 Hz, with $U_{eff} = 7$ cm^{-1} and 118 cm^{-1} for low- and high-temperature dynamics, respectively. Moreover, a hysteresis loop can be opened at temperatures up to 7 K on a micro-SQUID magnetometer, giving an excellent polynuclear SMM. Ab initio calculation demonstrates that the g factors for the lowest Kramers doublets on each dysprosium

Fig. 34 Temperature
dependence of out-of-phase
ac susceptibility of **132**
under zero dc field at
indicated frequencies. *Inset*:
anisotropy axis direction on
each Dy(III) site. Reprinted
with permission from
[128]. Copyright 2009
WILEY-VCH Verlag
GmbH & Co. KGaA,
Weinheim
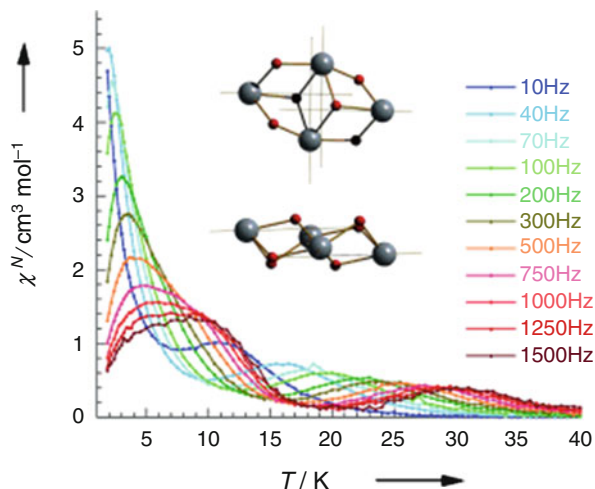
sites are very anisotropic, and the directions of the anisotropy axes are parallel to each other for the opposite ions and orthogonal for the adjacent ions. Since the calculated energy for the first-excited Kramers doublet over the ground one for each ion is much larger than the exchange interaction, the magnetic blocking is mainly attributable to the individual dysprosium ions (Fig. 34).

When o-vanillin and pivalic acid were utilized, a rhombus Dy_4 core is formed in $[Dy_4(\mu_3\text{-}OH)_2(\text{o-vanillin})_4(O_2CC(CH_3)_3)_4(NO_3)_2]\cdot CH_2Cl_2\cdot 1.5H_2O$ (**133**), with two $\mu_3\text{-}OH$ ligands lying above and below the plane of the metal sites [129]. Strong frequency-dependent signal at zero dc fields, indicative of SMM behavior, is observed above 1.8 K, but with only a small energy barrier of 3 cm^{-1}. By comparing with **132**, the different local coordination environment might be responsible for the disparate SMM performance.

In situ condensation of o-vanillin and 2-aminoethanol leads to the formation of a Schiff-base H_2hmmp and hence compounds $[Dy_4(\mu_3\text{-}OH)_2(hmmpH)_2(hmmp)_2(Cl)_4]\cdot 3MeCN\cdot MeOH$ (**134**) and $[Dy_4(\mu_3\text{-}OH)_2(hmmpH)_2(hmmp)_2(N_3)_4]\cdot 4MeOH$ (**135**) [130]. Both two compounds display a rhombus Dy_4 core, bridged by two $\mu_3\text{-}OH$ ligands and phenoxy/alcohol oxygen atoms, whereas the terminal chlorides in **134** are replaced by azides in **135**. As a result, though both compounds show slow relaxation behavior, the energy barrier, obtained by fitting relaxation times at different temperatures, can only be given for **135**. This anion perturbation on relaxation is probably via local environment and/or orientation of the anisotropy axes. In situ condensation of 3-formylsalicylic acid and 2-aminoethanol leads to the formation of another Schiff-base H_2hba and hence compound $\{[Dy_4(Hhba)_2(hba)_4(\mu_3\text{-}OH)_2]\cdot 5MeOH\cdot 7H_2O$ (**136**) [131]. The Dy^{III} ions are also arranged with a planar rhomboidal scaffold. However, it exhibits SMM behavior with two relaxation processes, one with $U_{eff} = 58$ cm^{-1} for high-temperature dynamics and the other one with $U_{eff} = 2$ cm^{-1} and $\tau_0 = 2.5 \times 10^{-3}$ for

low-temperature dynamics. The large τ_0 for the fast relaxation may originate from the dominated QTM or weak dipolar/intermolecular interactions.

After the preparation of Schiff-base H_2hmbp from *o-vanillin* and 2-aminophenol, introducing Dy^{III} ion in the system affords a tetranuclear compound $[Dy_4(\mu_3\text{-OH})_2(\text{hmbp})_4(\text{Hhmbp})_2]\cdot 2THF$ (**137**), possessing a rhombus Dy_4 core [132]. An overall ferromagnetic interaction can be deduced from an increase of the χT value upon cooling. Moreover, slow relaxation of the magnetization is observed for **137**, with an energy barrier of ~3 cm^{-1} at 0 or 500 Oe dc field.

Apart from the Schiff-base ligands mentioned above, Salen-type ligands were also utilized to construct rhombus Dy_4 cores in compounds $[Dy_4(\mu_3\text{-OH})_2(\text{BSCDA})_2(\text{acac})_6]\cdot 2H_2\text{BSCDA}\cdot 2CH_3CN$ (**138**) and $[Dy_4(\mu_3\text{-OH})_2(\text{abc})_2(\text{acac})_6]\cdot 2CH_3CN$ (**139**) [133, 134]. The centrosymmetric Dy_4 cores in both compounds are coplanar and linked by a combination of two μ_3-hydroxide, four phenoxide, and two ketonate oxygen atoms. Moreover, the two asymmetric Dy^{III} ions in these Dy_4 clusters are encapsulated by O_8 and N_2O_6 coordination pockets. Nevertheless, **138** is a field-induced SMM ($U_{eff} = 15$ cm^{-1}), while **139** possesses an SMM nature at zero dc field ($U_{eff} = 10$ cm^{-1}). Incorporating H_2BSCDO into the $4f$ system gives a tetranuclear compound $[Dy_4(\text{BSCDO})_2(\text{HBSCDO})_2Cl_2(\mu_3\text{-OH})_2]_2Cl_2(\text{OH})_2\cdot 3CH_3CH_2OH\cdot H_2O$ (**140**), where four Dy^{III} ions form a rhombus $\{Dy_4O_8\}$ core [135]. Strikingly, magnetic studies indicate that **140** exhibits SMM behavior at zero dc field with $U_{eff} = 39$ cm^{-1}. This relatively high energy barrier is presumably ascribed to the coordination of the Cl ion in terms of the electron and steric effects that strengthens the magnetic anisotropy of the Dy^{III} ions.

Polyalcohols have been successfully employed to build Dy_4 SMMs. Using chelating ligand mdeaH$_2$ or H_4ampd with the coligand pivalic acid leads to two rhombus Dy_4 compounds, formulated as $[Dy_4(\mu_3\text{-OH})_2(\text{mdeaH})_2(\text{piv})_8]$ (**141**) and $[Dy_4(\mu_3\text{-OH})_2(H_4\text{ampd})_2(\text{piv})_{10}]\cdot 4CH_3CN$ (**142**), respectively [136, 137]. Both two compounds have a similar tetranuclear Dy_4 core, which is bridged by two μ_3-OH ligands. Though the coordination environments are DyO_8 and $DyNO_7$ for **141**, while only DyO_8 for **142**, they both show an SMM behavior at low temperatures in zero dc field with the same energy barrier of 4 cm^{-1}. In fact, a slight decrease in U_{eff} for **142** (3.8 cm^{-1}) compared to that for **141** (4.3 cm^{-1}) should ascribe to the presence of intermolecular interactions. In contrast, compound $[Dy_4(H_3\text{bmap})_2(\text{OAc})_6]\cdot 2EtOH$ (**143**), derived from the bis–tris propane ligand, H_6bmap, displays an excellent SMM behavior [138]. In this complex, a crystallographically centrosymmetric and planar Dy_4 core is bridged by four μ_3-CH$_2$O$^-$ arm oxygen atoms from two bis–tris propane ligands placed above and below the Dy_4 plane, which is different from the common rhombus Dy_4 linked by two μ_3-hydroxide. Two types of distinct coordination environment of the Dy^{III} ions in **143** result in two separate relaxation processes that can be described by the sum of two Debye functions, with $U_{eff} = 31$ cm^{-1} and $U_{eff} = 74$ cm^{-1}. It is worth noting that the latter barrier is pretty high for tetranuclear Dy_4 SMMs.

The ligand 2,2-bptH is also famous for its constructive role in the tetranuclear Dy_4 SMMs, as in compounds $[Dy_4(\mu_3\text{-OH})_2(\mu\text{-OH})_2(2,2\text{-bpt})_4(\text{NO}_3)_4(\text{EtOH})_2]$ (**144**), $[Dy_4(\mu_3\text{-OH})_2(\mu\text{-OMe})_2(2,2\text{-bpt})_4(\text{NO}_3)_4]\cdot 3MeOH$ (**145**), $[Dy_4Cl_2(\mu_3\text{-}$

OH)$_2$(μ-OH)$_2$(2,2-bpt)$_4$(H$_2$O)$_4$]Cl$_2$·2H$_2$O·4EtOH (**146**), and [Dy$_4$Br$_2$(μ$_3$-OH)$_2$(-μ-OH)$_2$(2,2-bpt)$_4$(H$_2$O)$_4$]Br$_2$·2H$_2$O·4EtOH (**147**), which were obtained under different reaction conditions [139–141]. Single-crystal studies reveal that four Dy^{III} ions in these complexes are nearly coplanar and bridged by two internal μ$_3$-OH groups, two external μ-OH or μ-OMe groups, and four μ-2,2-bpt ligands. Moreover, each eight-coordinate Dy^{III} ion is coordinated by terminal NO$_3^-$ group or terminal NO$_3^-$ group and ethanol molecule for **144**, terminal or chelating NO$_3^-$ group for **145**, and H$_2$O molecule or H$_2$O molecule and Cl (Br) atom for **146** (**147**) to complete its coordination sphere. Interestingly, all the four complexes reveal slow relaxation of the magnetization at zero dc field and give effective energy barriers $U_{eff} = 56$ cm^{-1} (**144**), 81 cm^{-1} (**145**), 132 cm^{-1} (**146**), and 137 cm^{-1} (**147**), which are among the highest in the tetranuclear lanthanide-based SMMs. An ab initio calculation performed on **144** helps us to gain insight into their magnetic behaviors. The result shows that the main values of the g tensors of the lowest doublets on Dy^{III} sites are very axial and the main four anisotropy axes form an almost perfect parallelogram. Furthermore, the calculated exchange interactions are much smaller than the fitted dipole–dipole interactions between Dy^{III} ions, as shown in Fig. 35. Thus, the ground exchange state is nonmagnetic and corresponds to a toroidal arrangement of local magnetic moments on Dy^{III} sites. Moreover, the magnetic blocking comes from the local Dy sites rather than the exchange interaction. Thereupon, in this stable Dy$_4$ skeleton, the SMM properties can be improved by optimizing the ligand field around the Dy^{III} ions, especially through the alteration on donor atoms in the transverse plane to weaken electrostatic repulsions, as supported apparently by variations of energy barriers for **146** and **147**.

An exception to the rhombus-shaped tetranuclear lanthanide SMMs is [{(Hhhp)$_2$Dy$_4$}(μ$_2$-O)$_4$](H$_2$O)$_8$·2CH$_3$OH·8H$_2$O (**148**), which are without two μ$_3$-OH-bridging ligands. In complex **148**, four Dy^{III} ions are in a perfect plane, with two asymmetric Dy^{III} ions encapsulated by the distinct coordination pockets of

	J_1	J_2	J_3	J_4
$J_i^{dipolar}$	5.06	1.71	2.64	0.42
J_i^{exch}	-0.62	-0.49	0.45	0.00
J_i	4.44	1.22	3.09	0.42
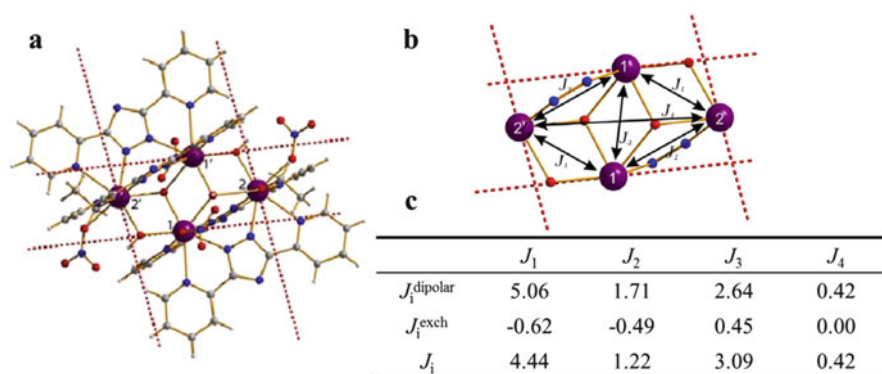
Fig. 35 (**a**) Calculated magnetic axes corresponding to the lowest Kramers doublet on dysprosium sites of **144**. (**b**) The model for the exchange coupling employed for **144**. (**c**) Parameters of the magnetic interactions between Dy ions in **144**. Color codes: *purple*, Dy; *red*, O; *blue*, N; and *gray*, C. Reprinted with permission from [139]. Copyright 2012, American Chemical Society

ligand H_3hhp and bridged by an enolate oxygen that arises from keto–enol tautomerism [142]. Such two dinuclear subunits are further linked by four μ_2-O ligands to form a rhombus-shaped Dy_4 core. Dynamic magnetic analysis reveals this compound shows two relaxation processes below 20 K, leading to two energy barriers: 12 cm^{-1} and 38 cm^{-1} for the low- and high-temperature relaxation, respectively. This behavior is probably related to the presence of two Dy^{III} sites with different coordination environments (Table 10, Fig. 36).

2.3.2 Square Topology

Square cores in Ln_4 SMMs often have a μ_4-OH center. Tetranuclear complex $[Dy_4(\mu_4\text{-OH})(PTC4A)_2Cl_3(CH_3OH)_2(H_2O)_3]\cdot4.7CH_3OH\cdot2H_2O$ (**149**) supported by calixarene H_4PTC4A features the first square Dy_4 SMM [143]. Two crystallographic Dy sites and two metal sites generated by the symmetry operation are bridged by a μ_4-OH in the cross and eight μ_2-$O_{phenoxo}$ in the four edges of the square. The sulfur atoms and other components (i.e., H_2O, MeOH, Cl^-) are to complete the nine-coordinate environments of Dy^{III} ions. Ac susceptibilities under 0 or 1 kOe dc field show frequency-dependent behavior for **149**, indicating a slow relaxation of magnetization.

Some $[2 \times 2]$ square Dy_4 can be produced by using construction principles developed for transition metal grids. By using mono-acylhydrazone, a μ_4-OH-centered square Dy_4 molecule $[Dy_4(\mu_4\text{-OH})(Hhpch)_8)]\cdot(ClO_4)_3\cdot2CH_3CN\cdot MeOH\cdot4H_2O$ (**150**) was obtained [144]. In addition, all the μ_2-O_{phenol} bridges the edges of the square plane, creating a twelve-membered Dy_4O_8 core. All Dy sites are nine-coordinate with the geometry of a quasi-monocapped square antiprism. Ac susceptibilities in zero dc field reveal two relaxation processes, which is probably due to the different Dy^{III} centers in terms of the local coordination spheres. Strikingly, applying a dc field of 1 kOe leads to relatively symmetrical Cole–Cole plots, as well as a strongly enhanced barrier (64 cm^{-1}), which is more than triple that of the zero dc field (Fig. 37).

By using ditopic carbohydrazone ligands, two square Dy_4 SMMs with a central μ_4-O atom were obtained, formulated as $[Dy_4(\mu_4\text{-O})(dchm)_2(Hdchm)_2(N_3)_4]\cdot14H_2O$ (**151**) and $[Dy_4(\mu_4\text{-O})(Hdch)_3(H_2dch)(N_3)_4]Cl_3\cdot3H_2O\cdot1.5CH_3CN$ (**152**) [145, 146]. The ligands, H_2dchm and H_2dch, differ in only methyl groups being substituted by hydrogen, so the overall structures of the two complexes are essentially the same. The four Dy^{III} ions are arranged in a $[2 \times 2]$ square grid, in which four deprotonated hydrazone oxygen atoms and four μ_2-1,1-N_3 bridges link the metal ions along the square edges, and a μ_4-O atom occupies the central position of the square. Each Dy^{III} ion is nine-coordinate with a N_6O_3 coordination sphere. Both complexes exhibit SMM behavior with two relaxation processes under zero dc field with $U_{eff} = 35$ cm^{-1} and 63 cm^{-1} for **151**. With the application of an optimal dc field, the low-temperature response in zero dc field disappears for **152**, while the related low-temperature response for **151** persists. The energy barriers in the high-

Table 10 Tetranuclear 4f SMMs (I)

Geometry	SMMs	CN of 4f ions	$U_{\text{eff}}/$ cm^{-1} ($H_{\text{dc}}/$ Oe)	hys (K)	References
Rhombus	[Dy$_4$(μ_3-OH)$_2$(bmh)$_2$(msh)$_4$Cl$_2$] (**132**)	8(N$_2$O$_6$), 8 (N$_2$O$_5$Cl)	7,118	7	[128]
	[Dy$_4$(μ_3-OH)$_2$(o-vanillin)$_4$(O$_2$CC (CH$_3$)$_3$)$_4$(NO$_3$)$_2$]·CH$_2$Cl$_2$·1.5H$_2$O (**133**)	8(O$_8$), 9 (O$_9$)	3	–	[129]
	[Dy$_4$(μ_3-OH)$_2$(hmmpH)$_2$(hmmp)$_2$(Cl)$_4$]· 3MeCN·MeOH (**134**)	8(N$_2$O$_6$), 8(O$_6$Cl$_2$)	–	–	[130]
	[Dy$_4$(μ_3-OH)$_2$(hmmpH)$_2$(hmmp)$_2$(N$_3$)$_4$]·4MeOH (**135**)	8(N$_2$O$_6$)	5	–	[130]
	{[Dy$_4$(Hhba)$_2$(hba)$_4$(μ_3-OH)$_2$]· 5MeOH·7H$_2$O (**136**)	8(NO$_7$)	2,58	–	[131]
	[Dy$_4$(μ_3-OH)$_2$(hmbp)$_4$(Hhmbp)$_2$]·2THF (**137**)	8(NO$_7$)	3	–	[132]
	[Dy$_4$(μ_3-OH)$_2$(BSCDA)$_2$(acac)$_6$]· 2H$_2$BSCDA·2CH$_3$CN (**138**)	8(O$_8$), 8 (N$_2$O$_6$)	15 (1400)	–	[133]
	[Dy$_4$(μ_3-OH)$_2$(abc)$_2$(acac)$_6$]·2CH$_3$CN (**139**)	8(O$_8$), 8 (N$_2$O$_6$)	10	–	[134]
	[Dy$_4$(BSCDO)$_2$(HBSCDO)$_2$Cl$_2$(μ_3-OH)$_2$]$_2$Cl$_2$(OH)$_2$·3CH$_3$CH$_2$OH·H$_2$O (**140**)	8(N$_2$O$_6$), 9(O$_8$Cl)	39	–	[135]
	[Dy$_4$(μ_3-OH)$_2$(mdeaH)$_2$(piv)$_8$] (**141**)	8(O$_8$), 8 (NO$_7$)	4	1.1	[136]
	[Dy$_4$(μ_3-OH)$_2$(H$_4$ampd)$_2$(piv)$_{10}$]· 4CH$_3$CN (**142**)	8(O$_8$)	4		[137]
	[Dy$_4$(H$_3$bmap)$_2$(OAc)$_6$]·2EtOH (**143**)	8(O$_8$), 9 (N$_2$O$_7$)	31,74		[138]
	[Dy$_4$(μ_3-OH)$_2$(-μ-OH)$_2$(2,2-bpt)$_4$(NO$_3$)$_4$(EtOH)$_2$] (**144**)	8(N$_4$O$_4$)	56	–	[139]
	[Dy$_4$(μ_3-OH)$_2$(-μ-OMe)$_2$(2,2-bpt)$_4$(NO$_3$)$_4$]·3MeOH (**145**)	8(N$_4$O$_4$)	81	–	[140]
	[Dy$_4$Cl$_2$(μ_3-OH)$_2$(-μ-OH)$_2$(2,2-bpt)$_4$(H$_2$O)$_4$] Cl$_2$·2H$_2$O·4EtOH (**146**)	8(N$_4$O$_4$), 8 (N$_4$O$_3$Cl)	132	–	[141]
	[Dy$_4$Br$_2$(μ_3-OH)$_2$(-μ-OH)$_2$(2,2-bpt)$_4$(H$_2$O)$_4$] Br$_2$·2H$_2$O·4EtOH (**147**)	8(N$_4$O$_4$), 8 (N$_4$O$_3$Br)	137	–	[141]
	[{(Hhhp)$_2$Dy$_4$}(μ_2-O)$_4$] (H$_2$O)$_8$·2CH$_3$OH·8H$_2$O (**148**)	8(N$_2$O$_6$), 7(NO$_6$)	12,38	–	[142]
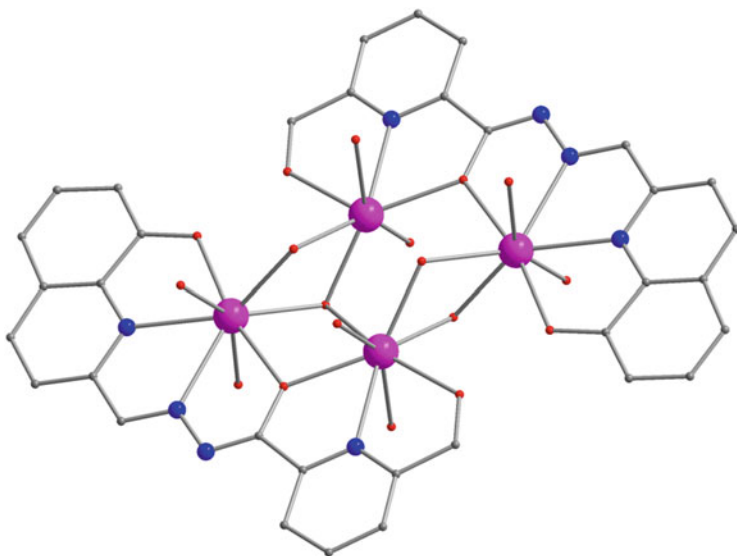
Fig. 36 Molecular structure for **148**. Color codes: *pink*, Ln; *gray*, C; *blue*, N; and *red*, O
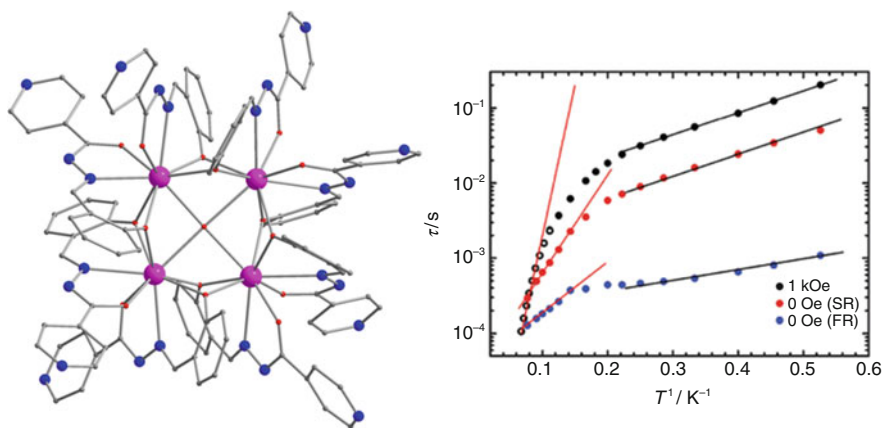
Fig. 37 Molecular structure for **150** (*left*) and magnetization relaxation time, τ vs T^{-1} plot for **150** under 0 and 1 kOe (*right*). Color codes: *pink*, Ln; *gray*, C; *blue*, N; and *red*, O. Reprinted with permission from [144]. Copyright 2012, Royal Society of Chemistry

temperature range are calculated to be 188 cm^{-1} (1600 Oe) for **151** and 76 cm^{-1} (1800 Oe) for **152**.

By using bis-acylhydrazone, a rare [2 × 2] square Dy$_4$ SMM (**153**) without central μ_4-OH group was obtained [147]. In this complex ([Dy$_4$(Hbhmh)$_4$(MeOH)$_4$]$_2$·7CH$_2$Cl$_2$·MeOH), each ligand bridges three Dy^{III} ions through its carbonyl oxygen and phenol oxygen atoms in a μ_3-η^1:η^1:η^1:η^2:η^2 fashion. Such four ligands link four Dy^{III} ions to construct the Dy$_4$ unit and create

a twelve-membered Dy_4O_8 central core. Each Dy^{III} ion is eight-coordinate with a distorted dodecahedral geometry. This compound does not exhibit significant slow magnetic relaxation at zero dc field, but peaks in the χ'' as a function of the frequency occur under a 900 Oe dc field, highlighting the presence of fast QTM. The SMM behavior above 4 K follows a thermally activated relaxation with $U_{eff} = 11\ cm^{-1}$.

Thiolate-bridged SMMs are extremely rare, including the first example of dinuclear Dy_2 SMM (**68**) and the second and third examples of tetranuclear Tb_4 and Dy_4 SMMs ([Li(thf)$_4$][Ln$_4$\{N(SiMe$_3$)$_2$\}$_4$(μ-SEt)$_8$(μ_4-SEt)], **154-Tb**, Ln = Tb; **154-Dy**, Ln = Dy) [148]. The latter compounds produced via organometallic chemistry features four chemically similar, coplanar Ln^{III} ions, each of which coordinates to four μ-SEt ligands at two edges of the square plane, one μ_4-SEt ligand that residues approximately 0.95 Å out of the square plane and one terminal N(SiMe$_3$)$_2$ ligand, with a very distorted octahedral coordination geometry. Dynamic magnetic studies reveal SMM behaviors for both compounds at zero dc field. For **154-Tb**, a small anisotropy barrier of $U_{eff} = 5\ cm^{-1}$ is determined, while a larger U_{eff} value of $46\ cm^{-1}$ is obtained for **154-Dy**. This is probably related to a well-defined axial symmetry required for a non-Kramers ion of Tb^{III}. But **154-Tb** is still the first \{Tb$_4$\} SMM. Moreover, the SMMs **154-Tb** and **154-Dy** expand the family of polymetallic SMMs based on soft-donor ligands (Table 11, Fig. 38).

2.3.3 Linear and Zigzag Chain Topology

The rigid N,O-donor hydrazone ligand H$_3$hmmh was used to generate a tetranuclear complex [Dy$_4$(hmmh)$_4$(MeOH)$_6$]·2MeOH (**155**) characterized by a nearly Dy$_4$ core with Dy–Dy–Dy angles of 150° [149]. In this complex, two independent Dy centers are in a distorted bicapped trigonal-prismatic geometry and a monocapped square-antiprismatic environment separately. Its dynamic magnetic measurement reveals two distinct peaks for the out-of-phase ac signals, indicating the operation of two relaxation processes with effective energy barriers of $14\ cm^{-1}$ and $120\ cm^{-1}$. Interestingly, the Cole–Cole plots can be well described by the sum of two modified Debye functions, which is firstly used to explain such a dual relaxation processes (Fig. 39).

The tetranuclear [Dy$_4$(ncps)$_4$(Hncps)$_2$(C$_6$H$_4$NH$_2$COO)$_2$(CH$_3$OH)$_4$]·5CH$_3$OH (**156**), derived from a tetradentate N,O-donor ligand H$_2$ncps, features a nearly linear, centrosymmetric Dy$_4$ core characterized by Dy–Dy–Dy angles of 110° [150]. The coordination sphere of one Dy^{III} ion is a nearly perfect square-antiprismatic geometry, while another Dy^{III} ion is in between a bicapped trigonal-prismatic and a square-antiprismatic geometry. This Dy$_4$ compound behaves as an SMM with an energy barrier of $14\ cm^{-1}$ and a quantum regime of relaxation below 3 K. Similarly, compound [Dy$_4$(bfmp)$_2$(C$_6$H$_5$COO)$_{12}$(MeOH)$_4$] (**157**) acts as an SMM with an energy barrier of $12\ cm^{-1}$, by using Schiff-base ligand Hbfmp [151]. This centrosymmetric complex also has a nearly linear Dy$_4$ core with Dy–

Table 11 Tetranuclear 4*f* SMMs (II)

Geometry	SMMs	CN of 4*f* ions	U_{eff}/cm^{-1} (H_{dc}/Oe)	hys (K)	References
Square	[Dy$_4$(μ_4-OH)(PTC4A)$_2$Cl$_3$(CH$_3$OH)$_2$(H$_2$O)$_3$]·4.7CH$_3$OH·2H$_2$O (**149**)	9(O$_7$S$_2$), 9(O$_6$S$_2$Cl)	–	–	[143]
	[Dy$_4$(μ_4-OH)(Hhpch)$_8$)]·(ClO$_4$)$_3$·2CH$_3$CN·MeOH·4H$_2$O (**150**)	9(N$_2$O$_7$)	11,21(0) 64(1000)	–	[144]
	[Dy$_4$(μ_4-O)(dchm)$_2$(Hdchm)$_2$(N$_3$)$_4$]·14H$_2$O (**151**)	9(N$_6$O$_3$)	35,63(0) 188(1600)	–	[145]
	[Dy$_4$(μ_4-O)(Hdch)$_3$(H$_2$dch)(N$_3$)$_4$]Cl$_3$·3H$_2$O·1.5CH$_3$CN (**152**)	9(N$_6$O$_3$)	76(1800)	–	[146]
	[Dy$_4$(Hbhmh)$_4$(MeOH)$_4$]$_2$·7CH$_2$Cl$_2$·MeOH (**153**)	8(N$_2$O$_6$)	11(900)	–	[147]
	[Li(thf)$_4$][Tb$_4${N(SiMe$_3$)$_2$}$_4$(μ-SEt)$_8$(μ_4-SEt)] (**154-Tb**)	6(NS$_5$)	5	–	[148]
	[Li(thf)$_4$][Dy$_4${N(SiMe$_3$)$_2$}$_4$(μ-SEt)$_8$(μ_4-SEt)] (**154-Dy**)	6(NS$_5$)	46	–	[148]
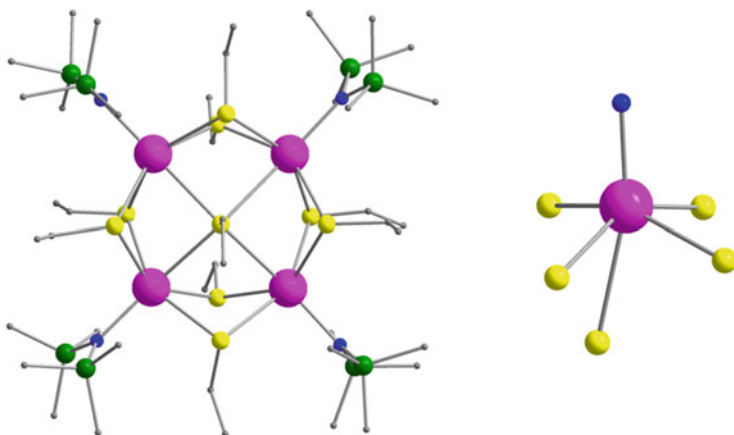
Fig. 38 Molecular structure for **154** (*left*) and coordination environment for the lanthanide ion (*right*). Color codes: *pink*, Ln; *gray*, C; *blue*, N; *green*, Si; and *yellow*, S
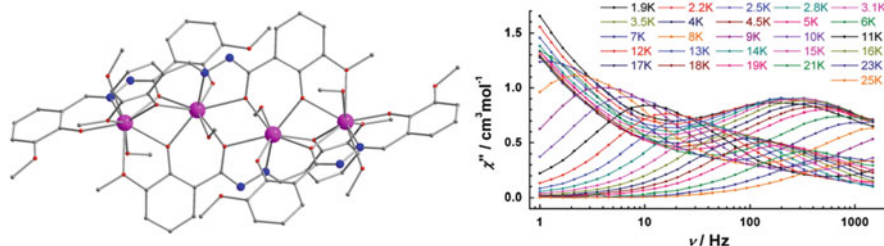
Fig. 39 Molecular structure for **155** (*left*) and temperature dependence of out-of-phase ac susceptibility under zero dc field at indicated temperatures (*right*). Color codes: *pink*, Ln; *gray*, C; *blue*, N; and *red*, O. Reprinted with permission from [149]. Copyright 2010, American Chemical Society

Dy–Dy angles of 176° and two dependent Dy^{III} ions, both being in a similar distorted bicapped trigonal-prismatic geometry.

Most zigzag Ln_4 SMMs contain a $[Ln_4(\mu\text{-}OR)_6]^{6+}$ core, as in **158–161** [152–156]. Two of them were prepared from pyridine-2,6-dimethanol, formulated as $[Dy_4(pdmH)_2(pdm)_4(PhCO_2)_2(PhCO_2H)_4] \cdot CH_3OH \cdot H_2O$ (**158**) and $[Dy_4(NO_3)_2(pdmH)_6(pdmH_2)_2](NO_3)_4$ (**159**) [152, 153]. In both compounds, two independent Dy^{III} ions are bridged by two $\mu\text{-}O_{alkoxide}$ atoms, forming a binuclear unit, which are further connected by $\mu\text{-}O_{alkoxide}$ atoms, leading to a tetranuclear zigzag arrangement core. All eight-coordinate Dy^{III} ions are in a distorted square-antiprismatic geometry for **158**, whereas the Dy^{III} ions are in triangular dodecahedron and biaugmented trigonal-prismatic geometry for **159**. Nevertheless, ac magnetic susceptibility at zero dc field for both compounds shows frequency-dependent out-of-phase signals without maxima, indicating slow relaxation of the magnetization (Fig. 40).
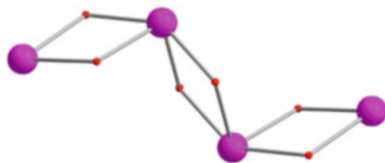
Fig. 40 Core in **158**. Color codes: *pink*, Dy, and *red*, O
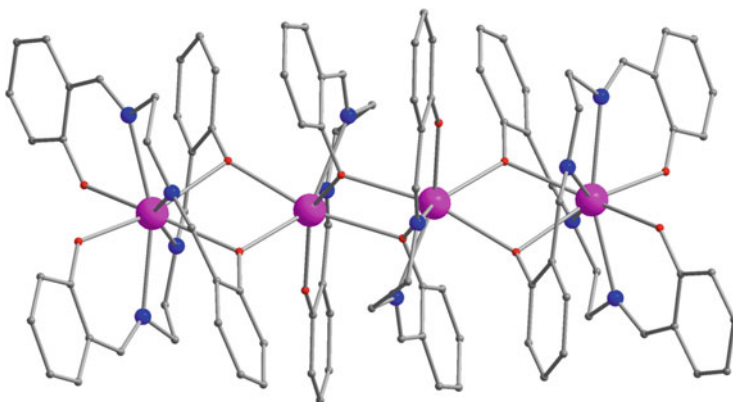
Fig. 41 Molecular structure for **160**. Color codes: *pink*, Ln; *gray*, C; *blue*, N; and *red*, O

Compounds $[Er_4(abc)_6] \cdot 13H_2O$ (**160-Er**) and $[Dy_4(abc)_6] \cdot 5.5H_2O$ (**160-Dy**) have similar tetranuclear zigzag entity based on the simple salen-type ligand H_2abc, that is, the four Ln centers are doubly bridged by phenoxide O atoms. Both compounds contain two asymmetric Ln^{III} ions, one being eight-coordinate in a distorted dodecahedron and the other being seven-coordinate in a distorted capped trigonal prism [154, 155]. In the dynamic magnetic measurement, **160-Er** exhibits weak frequency-dependent ac signals at zero dc field, showing a relaxation that can be slowed down at appropriate dc fields, and hence gives an energy barrier of 9 cm^{-1} at $H_{dc} = 1$ kOe. Meanwhile, **160-Dy** acts as an SMM at zero dc field with $U_{eff} = 12$ cm^{-1}. When $H_{dc} = 1.4$ kOe is applied, two relaxation processes are observed, which is attributable to the disparate coordination geometries around Dy. The observed discrepancy in the relaxation modes between **160-Er** and **160-Dy** should be ascribed to the different shape of the electron distribution for Ln^{III} ion. It is noteworthy that **160-Er** is the first example of a tetranuclear Er^{III} system that exhibits field-induced SMM behavior (Fig. 41).

The ligand 2,2-bptH can construct not only rhombus-shaped tetranuclear lanthanide SMMs but also a zigzag Dy_4 SMM $[Dy_4(OH)_2(2,2\text{-bpt})_4(NO_3)_6(EtOH)_2] \cdot$ EtOH (**161**) [156]. In this complex, two $\{Dy_2(2,2\text{-bpt})_2\}$ subunits, each of which is composed of two Dy^{III} ions bridged by two 2,2-bpt ligands, are linked by a pair of $\mu\text{-OH}^-$ groups, forming a zigzag Dy_4 structure. Two Dy^{III} ions sit in a distorted monocapped square-antiprismatic geometries, while the other Dy^{III} ions possess

distorted square-antiprismatic geometries. Ac magnetic susceptibility measurements reveal dual slow magnetic relaxation of magnetization with energy barriers of 29 and 31 cm^{-1}, which is possibly related to the nonequivalent Dy^{III} ions in different coordination environments. In addition, white-light emission is obtained for this Dy$_4$ via mixing dichromatic mixture of blue (bpt$^-$)- and yellow (Dy^{3+})-emissive colors. Moreover, ferroelectricity is added into the Dy$_4$ cluster. Thus, **161** displays properties of SMMs, white-light emission, and ferroelectricity (Table 12, Fig. 42).

2.3.4 Other Tetranuclear 4f Clusters

Dy$_4$O$_4$ cubane-like cores can behave as effective SMMs. The first discrete dysprosium cubane showing slow magnetic relaxation is found in compound [Dy$_4$(μ_3-OH)$_4$(isonicotinate)$_6$(py)(CH$_3$OH)$_7$](ClO$_4$)$_2$·py·4CH$_3$OH (**162**) [157]. Four Dy^{III} ions and four bridging μ_3-OH groups form a distorted cubane-like [Dy$_4$(μ_3-OH)$_4$]$^{8+}$ core. Each Dy^{III} ion is eight-coordinate either in an O$_8$ or NO$_7$ sphere. The frequency-dependent out-of-phase signals are observed below 6 K, indicating the onset of slow relaxation, but without available peak.

A calix[4]arene-supported SMM [Dy$_4$(OH)$_4$(TBSOC)$_2$(H$_2$O)$_4$(CH$_3$OH)$_4$]·4H$_2$O (**163**) contains a totally distorted [Dy$_4$(μ_3-OH)$_4$]$^{8+}$ core, which is sandwiched between two antiparallel calixarene macrocycles [158]. The Dy^{III} ions are all coordinated to eight oxygen atoms, and the Dy–O–Dy angles are in the range of 105.7(4)–107.9(3)°. Its ac susceptibility measurement reveals obvious slow relaxation of the magnetization below 7 K at zero dc field, with the $U_{eff} = 16$ cm^{-1}. This is the largest energy barrier for the calixarene-supported pure 4f SMMs so far.

A hydroxide-free cubane-shaped tetranuclear [Dy$_4$] SMM [Dy$_4$(hpm)$_4$(μ_2-$\eta^1\eta^1$Piv)$_4$]·6CH$_3$OH·4H$_2$O (**164**) involves a distorted [Dy$_4$(μ_3-OR)$_4$]$^{8+}$ core, which is formed by the concerted coordination action of four hpm^{2-} ligands in a μ_3-η^3:η^1:η^1 fashion [159]. Each Dy^{III} ion is eight-coordinate (N$_2$O$_6$), and the Dy–O–Dy angles lie in the range of 99.20(2)–115.10(2)°. This Dy$_4$ shows typical SMM behavior below 13 K under zero dc field with two out-of-phase peaks. When 1 kOe dc field is applied to fully or partly suppress the QTM effect, the anisotropic barriers for the slow and fast relaxations can be clearly obtained as 51 and 33 cm^{-1}, respectively (Fig. 43).

A unique complex [Dy$_4$(μ_4-O)(μ-OMe)$_2$(beh)$_2$(esh)$_4$]·3MeOH (**165**) consists of four Dy^{III} ions arranged in a distorted tetrahedral fashion around the central μ_4-O atom [160]. Each octacoordinate Dy^{III} ion is filled by two nitrogen atoms and six oxygen atoms. Interestingly, conformational chirality is induced via a twisted diazine bridge from a Schiff-base ligand upon coordination. This tetrahedral Dy$_4$ complex shows frequency-dependent ac signals below 15 K, as expected for an SMM. The analysis of this thermally activated behavior provides an energy barrier of 16 cm^{-1}. Moreover, a large coercive field of 0.6 T at 0.04 K is detected on a micro-SQUID magnetometer, confirming the SMM behavior. It is known that the slow relaxation of the magnetization originates mainly from the local anisotropy of

Table 12 Tetranuclear $4f$ SMMs (III)

Geometry	SMMs	CN of $4f$ ions	U_{eff}/cm^{-1} (H_{dc}/Oe)	hys (K)	References
Linear chain	$[Dy_4(hmmh)_4(MeOH)_6]\cdot2MeOH$ (**155**)	$8(NO_7)$, $9(NO_8)$	14,120	–	[149]
	$[Dy_4(ncps)_4(Hncps)_2(C_6H_4NH_2COO)_2(CH_3OH)_4]\cdot5CH_3OH$ (**156**)	$8(NO_7)$	14	–	[150]
	$[Dy_4(bfmp)_2(C_6H_5COO)_{12}(MeOH)_4]$ (**157**)	$8(NO_7)$, $8(O_8)$	12	–	[151]
Zigzag chain	$[Dy_4(pdmH)_2(pdm)_4(PhCO_2)_2(PhCO_2H)_4]\cdot CH_3OH\cdot H_2O$ (**158**)	$8(N_2O_6)$, $8(NO_7)$	–	–	[152]
	$[Dy_4(NO_3)_2(pdmH)_6(pdmH_2)_2](NO_3)_4$ (**159**)	$8(N_2O_6)$	–	–	[153]
	$[Er_4(abc)_6]\cdot13H_2O$ (**160-Er**)	$8(N_4O_4)$, $7(N_2O_5)$	9(1000)	–	[154]
	$[Dy_4(abc)_6]\cdot5.5H_2O$ (**160-Dy**)	$8(N_4O_4)$, $7(N_2O_5)$	12	–	[155]
	$[Dy_4(OH)_2(2,2\text{-bpt})_4(NO_3)_6(EtOH)_2]\cdot EtOH$ (**161**)	$8(N_4O_4)$, $9(N_4O_5)$	29,31	–	[156]
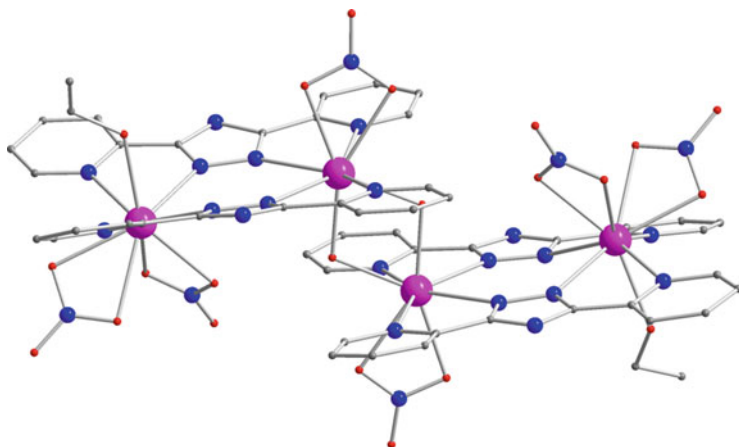
Fig. 42 Molecular structure for **161**. Color codes: *pink*, Ln; *gray*, C; *blue*, N; and *red*, O
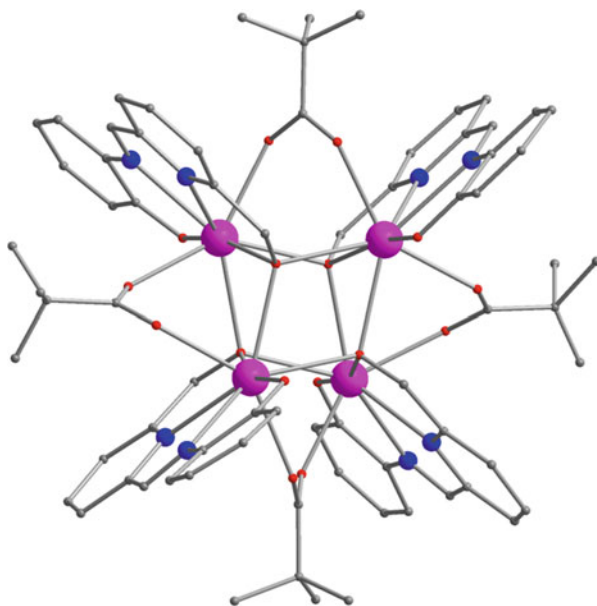
Fig. 43 Molecular structure for **164**. Color codes: *pink*, Ln; *gray*, C; *blue*, N; and *red*, O

the 4*f* ions in pure lanthanide systems. Therefore, the ab initio calculation calculates main magnetic axes for individual Dy sites, which point in all different directions corresponding to four nonequivalent Dy^{III} ions. Furthermore, the exchange interaction between Dy^{III} ions is found to be -0.30 cm^{-1}, indicating the overall antiferromagnetic exchange coupling. The spread of the calculated exchange spectrum between the lowest Kramers doublets on the Dy sites is of the order of the obtained energy barrier (Fig. 44).

Fig. 44 Calculated magnetic axes corresponding to the lowest Kramers doublet (*dotted lines*) and the orientation of the local magnetic moment in the ground state (*arrow*) in **165**. Reprinted with permission from [160]. Copyright 2011 WILEY-VCH Verlag GmbH & Co. KGaA, Weinheim
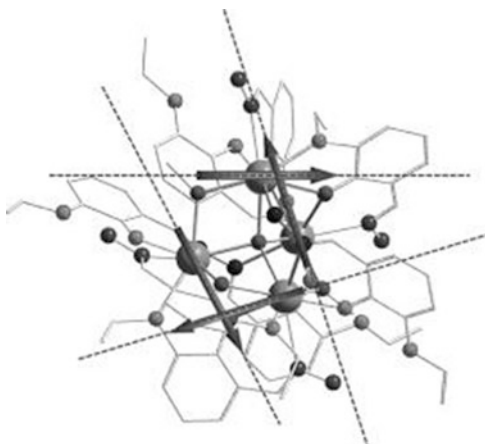
Very similar to **165**, $[Dy_4(\mu_4\text{-}O)(BSCDO)_2(C_6H_5COO)_6]\cdot3CH_3OH$ (**166**) is a μ_4-O-bridged Dy_4 tetrahedron molecule [161]. Each eight-coordinate Dy^{III} ion exhibits a distorted bicapped trigonal-prismatic geometry with an N_2O_6 coordination environment for Dy2 (Dy4) and an O_8 coordination environment for Dy1 (Dy3). The frequency-dependent signals of the out-of-phase susceptibility can be observed under zero dc field, indicative of the slow magnetic relaxation. However, the energy barrier could not be obtained by extracting the relaxation time characteristics even at an optimal dc field of 1 kOe.

$[Dy_4(3\text{-}bpp)_3(CO_3)_6(H_2O)_3]\cdot DMSO\cdot18H_2O$ (**167**) is a trigonal pyramidal $[Dy_4]$ carbonato-bridged complex, where the CO_3^{2-} was obtained by fixation of atmosphere CO_2 [162]. The basal Dy^{III} ions in the triangular plane are bridged by three CO_3^{2-} ions in a $\eta^1:\eta^1:\eta^2:\mu_3$ fashion, resulting them eight-coordinate with a distorted square-antiprismatic geometry. These are then bridged to the apical Dy^{III} ion via six CO_3^{2-} ions, where three of them are in a $\eta^1:\eta^1:\mu_2$ fashion and the other of them are in a $\eta^1:\eta^1:\eta^2:\mu_3$ fashion, making this Dy^{III} ion nine-coordinate with a distorted tricapped trigonal-prismatic geometry. AC susceptibility data reveal slow magnetic relaxation at zero dc field, indicating possible SMM behavior for this $[Dy_4]$ trigonal pyramid (Fig. 45).

Oxo-centered $[Dy_4K_2O(O^tBu)_{12}]\cdot C_6H_{14}$ (**168-Dy**), containing four Dy^{III} ions and two K^+ ions arranged in an octahedron geometry, is actually a tetranuclear Dy complex from a magnetic perspective with the record energy barrier [163]. Each face of the $\{Dy_4K_2\}$ octahedron is bridged by a μ_3-O^tBu ligand. With a terminal O^tBu ligand on each Dy center and the central μ_6 oxide, Dy sites are six-coordinate with distorted octahedral geometries. Ac measurements show two distinct thermal relaxation processes at relatively high temperatures, for example, two peaks of χ'' at about 30 and 47 K for a frequency of 1.2 kHz. The energy barriers are estimated to be 220 and 481 cm^{-1}. After magnetic dilution, only a single dominant relaxation process is observed with $U_{eff} = 585\ cm^{-1}$, which is among the highest reported for SMMs. Hysteresis loop can be opened up to ~5 K for single crystal of **168-Dy** on

Fig. 45 Molecular
structure for **167**. Color
codes: *pink*, Ln; *gray*, C;
blue, N; and *red*, O
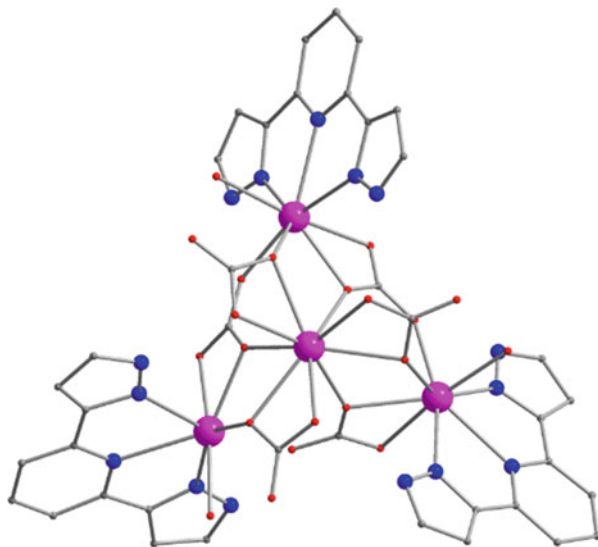
micro-SQUID. The ab initio calculations show that the ground and first-excited
Kramers doublet (referred to as 1± and 2±) are pure Ising states with $m_J = \pm 15/2$
and $m_J = \pm 13/2$, respectively, while the second-excited Kramers doublet (state 3±)
is the lowest energy state with a substantial transverse magnetic moment. The
average calculated energy gaps to the 2± and 3± states are 373 and 617 cm^{-1},
respectively. Hence, in the dilute compound, relaxation via the first Kramers
doublet is quenched or at least uncompetitive, and the preferential relaxation is
via state 3±. This indicates a possible relaxation via the second-excited state,
leading to higher energy barriers (Fig. 46).

The ab initio calculation on the analogue [Ho$_4$K$_2$O(O$'$Bu)$_{12}$]·C$_6$H$_{14}$ (**168-Ho**)
reveals a highly axial magnetic structure at each site, but the tunnel splitting for the
ground doublet is large for this non-Kramers ion. Therefore, experimentally, **168-
Ho** acts as an SMM with $U_{eff} = 63$ cm^{-1} but which is lower than that for **168-
Dy** [163].

Four Dy^{III} ions arranged in an edge-sharing bi-triangular geometry are realized
in a tetranuclear complex [Dy$_4$(bcd)$_2$(μ_3-OH)$_2$(μ_4-NO$_3$)(NO$_3$)$_4$(OCH$_3$)(H$_2$O)]·
MeCN·1.5MeOH (**169**) [164]. Each triangular Dy$_3$ motif is capped by one μ_3-OH
ligand, while a NO$_3^-$ ligand coordinates to four Dy^{III} ions in a rare μ_4-η^4:η^1:η^1
coordination mode, resulting in a dihedral angle between two triangles smaller than
90°. All the Dy^{III} ions are nine-coordinate, but Dy1 and Dy4 ions are in a distorted
tricapped trigonal-prismatic geometry and Dy2 and Dy3 in a hula-hoop-like geom-
etry. Ac susceptibility measurements under zero dc field reveal a slow relaxation of
the magnetization that is typical of SMM behavior, affording an energy barrier of
19 cm^{-1}.
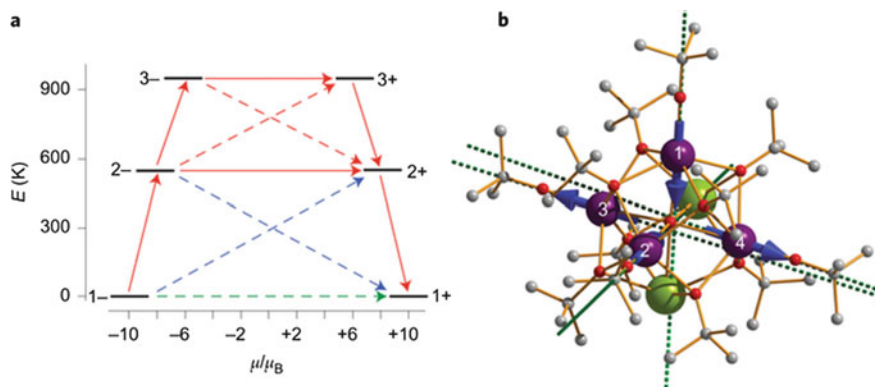
Fig. 46 Low-lying electronic structure for **168-Dy**. (**a**) The lowest three Kramers doublets for individual Dy sites and possible relaxation paths (indicative energies). The *thick black lines* represent the Kramers doublets as a function of their magnetic moment along the main anisotropy axis. The *green dashed line* corresponds to ground-state QTM, and the *solid red lines* to TA-QTM via the first- and second-excited Kramers doublets. *Dashed red* and *blue lines* show possible Orbach processes. (**b**) Calculated orientations of the principal magnetic axes in **168-Dy**. *Arrows* show the local magnetic moments in the ground Kramers doublets. Reprinted with permission from [163]. Copyright 2013, Rights Managed by Nature Publishing Group
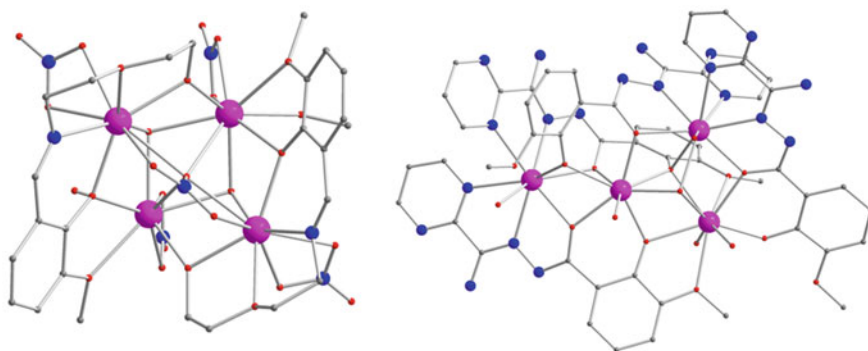
Fig. 47 Molecular structures for **169** (*left*) and **170** (*right*). Color codes: *pink*, Ln; *gray*, C; *blue*, N; and *red*, O

A novel Y-shaped Dy_4 SMM $[Dy_4(\mu_3\text{-OH})(pmv)_4(H_2O)_6]\cdot(ClO_4)_3\cdot6H_2O$ (**170**) contains a two μ_3-OH-capped triangle Dy_3 and a terminal Dy linked by two $O_{alkoxide}$ and one $O_{phenoxide}$ atoms acting as a "tail," which can be described as trinodal (1,2,3) with total v.s. $(1)_1(3)_3$ [165]. Three nine-coordinate Dy^{III} ions are arranged in a monocapped square-antiprismatic coordination sphere, while one eight-coordinate Dy^{III} ion is in a triangular dodecahedron geometry. Strong temperature and frequency-dependent ac signals can be observed below 22 K for **170**, indicating a slow relaxation of the magnetization. In addition, both a shoulder peak and a crossover in the Arrhenius plot suggest the presence of dual relaxation pathways with energy barriers of 5 and 58 cm^{-1} (Fig. 47).

Some tetranuclear complexes, such as $[Dy_4(Hhmp)_2(H_2hmp)_2(\mu_2\text{-}\eta^1\eta^1Piv)_2(\eta^1$ $Piv)_4]\cdot 2CHCl_3$ (**171**) and $[Tb(obPc)_2]Tb(Fused\text{-}Pc)Tb[Tb(obPc)_2]$ (**172**), can be considered as two related dinuclear subunits [166, 167]. In **171**, two symmetrically dinuclear Dy_2 units which are interconnected through the ligand contain two different types of Dy^{III} ions. One Dy^{III} ion is eight-coordinate in a distorted triangular dodecahedral geometry, while the other is nine-coordinate in a distorted spherical capped square-antiprismatic geometry. Ac susceptibility measurements reveal two relaxation processes under 1 kOe dc field, affording the anisotropic barriers of 18 and 44 cm^{-1}, which can be correlated to the difference in the geometric sphere of the Dy^{III} ions. For **172**, the obtained structure is simulated as two triple-decker moieties linked by the fused-Pc ligand in an *anti*mode. Thus, there are two kinds of magnetic dipole–dipole interactions. As revealed by the dc magnetic susceptibility measurements, this [Tb$_4$] can be described as a weakly ferromagnetically coupled dimer of triple-decker complexes with stronger dipole–dipole interactions in the triple-decker moieties. In ac magnetic susceptibility measurements, one magnetic relaxation process under zero dc field splits into dual processes under a dc field, which is similar to other reported dinuclear (obPc)Tb(obPc)Tb(obPc) (**6**). Hence, the triple-decker unit dominates the magnetic properties of [Tb$_4$], and the unit feels a much smaller internal magnetic field from the neighboring one because of the long distance (estimated to be 1.16 nm). This provides a way to control the magnetic dipole–dipole interactions with different spatial arrangements of the Tb^{III} ions in a multinuclear complex (Table 13).

2.4   Pentanuclear and Hexanuclear 4f Clusters

The pentanuclear 4f clusters that exhibit SMM behavior are rather limited. Despite this, one of the {Dy$_5$} square-based pyramid has the largest energy barrier observed for any d- or f-block cluster at that time. This excellent performance is realized in the compound $[Dy_5O(OiPr)_{13}]$ (**173-Dy**), in which all Dy sites are six-coordinate [168]. Each Dy locates at the vertices of a regular tetragonal pyramid, with a C_{4v} local symmetry. The slow magnetic relaxation process for **173-Dy** covers a large temperature range (3–56 K) under zero dc field, with the χ'' signal being observed at temperatures as high as 41 K for $v = 1400$ Hz. Hence, a high energy barrier is obtained as 367 cm^{-1}. For a further study on this {Ln$_5$} (Ln = Tb, Ho, Er) family, only {Ho$_5$} (**173-Ho**) shows clear SMM behavior [169]. The observable temperature for the slow relaxation of **173-Ho** in zero dc field is up to 33 K, though without a clear peak. When 3.5 kOe dc field is applied, an energy barrier of 278 cm^{-1} is determined and remains unchanged to 5.5 kOe dc field, indicating an effective suppression of QTM. Thus, this compound is one of the few reports on Ho^{III} SMMs. Unfortunately, only narrow hysteresis is found for both **173-Dy** and **173-Ho**, possibly ascribed to dominant QTM at low temperatures (Fig. 48).

In fact, the first pentanuclear dysprosium SMM is reported earlier in compound $[Dy_5(\mu_4\text{-}OH)(\mu_3\text{-}OH)_4(\mu\text{-}\eta^2\text{-}Ph_2acac)_4(\eta^2\text{-}Ph_2acac)_6]$ (**174**) [170]. This {Dy$_5$}

Table 13 Tetranuclear 4f SMMs (IV)

Geometry	SMMs	CN of 4f ions	U_{eff}/cm^{-1} (H_{dc}/Oe)	hys (K)	References
Cubane	[Dy$_4$(μ_3-OH)$_4$(isonicotinate)$_6$(py)(CH$_3$OH)$_7$](ClO$_4$)$_2$·py·4CH$_3$OH (**162**)	8(O$_8$), 8(NO$_7$)	–	–	[157]
	[Dy$_4$(OH)$_4$(TBSOC)$_2$(H$_2$O)$_4$(CH$_3$OH)$_4$]·4H$_2$O (**163**)	8(O$_8$)	16	–	[158]
	[Dy$_4$(hpm)$_4$(μ_2-η^{1}η^{1}Piv)$_4$]·6CH$_3$OH·4H$_2$O (**164**)	8(N$_2$O$_6$)	30, 33,51(1000)	–	[159]
Tetrahedron	[Dy$_4$(μ_4-O)(μ-OMe)$_2$(beh)$_2$(esh)$_4$]·3MeOH (**165**)	8(N$_2$O$_6$)	16	0.04	[160]
	[Dy$_4$(μ_4-O)(BSCDO)$_2$(C$_6$H$_5$COO)$_6$]·3CH$_3$OH (**166**)	8(N$_2$O$_6$), 8(O$_8$)	–	–	[161]
Trigonal pyramid	[Dy$_4$(3-bpp)$_3$(CO$_3$)$_6$(H$_2$O)$_3$]·DMSO·18H$_2$O (**167**)	8(N$_3$O$_5$), 9(O$_9$)	–	–	[162]
	[Dy$_4$K$_2$O(O^{t}Bu)$_{12}$]·C$_6$H$_{14}$ (**168-Dy**)	6(O$_6$)	220,481	5	[163]
	[Ho$_4$K$_2$O(O^{t}Bu)$_{12}$]·C$_6$H$_{14}$ (**168-Ho**)	6(O$_6$)	63	–	[163]
Edge-sharing bi-triangle	[Dy$_4$(bcd)$_2$(μ_3-OH)$_2$(μ_4-NO$_3$)(NO$_3$)$_4$(OCH$_3$)(H$_2$O)]·MeCN·1.5MeOH (**169**)	9(O$_9$), 9(NO$_8$)	19	–	[164]
Y-shape	[Dy$_4$(μ_3-OH)(pmv)$_4$(H$_2$O)$_6$]·(ClO$_4$)$_3$·6H$_2$O (**170**)	8(O$_8$), 9(N$_4$O$_5$), 9(O$_9$)	5,58	–	[165]
Ln$_2$ + Ln$_2$	[Dy$_4$(Hhmp)$_2$(H$_2$hmp)$_2$(μ_2-η^{1}η^{1}Piv)$_2$(η^{1}Piv)$_4$]·2CHCl$_3$ (**171**)	8(NO$_7$), 9(N$_3$O$_6$)	18,44(1000)	–	[166]
	[Tb(obPc)$_2$]Tb(Fused-Pc)Tb[Tb(obPc)$_2$] (**172**)	8(N$_8$)	149	–	[167]
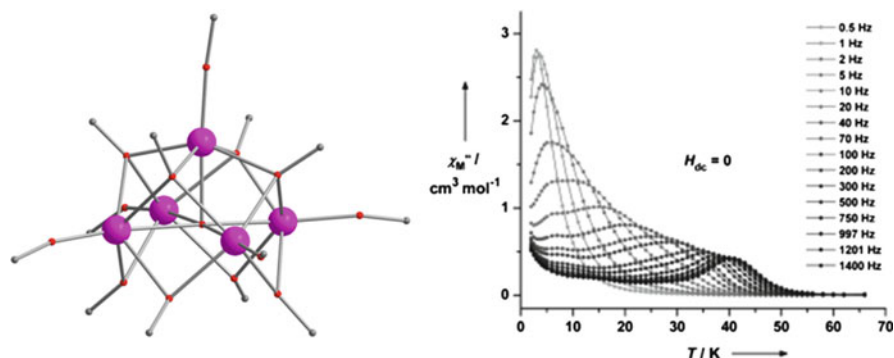
Fig. 48 Molecular structure for **173** (*left*) and temperature dependence of out-of-phase ac susceptibility under zero dc field at indicated temperatures (*right*). Color codes: *pink*, Ln; *gray*, C; and *red*, O. Reprinted with permission from [168]. Copyright 2011 WILEY-VCH Verlag GmbH & Co. KGaA, Weinheim

features a similar square-pyramidal shape, but each Dy^{III} ion is eight-coordinate with distorted square-antiprismatic geometry (CSM measurement). Its SMM behavior becomes apparent at very low temperatures between 3.6 and 1.8 K, following a thermally activated process with $U_{eff} = 23$ cm^{-1}. The less-pronounced performance should be mainly attributable to the different coordination environment and bridging mode (the absence of μ_5-oxide).

Amino acids can be utilized to encapsulate the square-based pyramidal-shaped $\{Ln_5(OH)_5\}^{10+}$-core, as in compounds $[Dy_5(OH)_5(\alpha\text{-AA})_4(Ph_2acac)_6]$($\alpha$-AA = D-PhGly (**175**), L-Trp (**176**), L-Pro (**177**), Ph$_2$Gly (**178**)) which also exhibit SMM behavior [171]. Although the four compounds and **173-Dy** and **174** are all square-pyramidal arrangement, the coordination environment in **175–178** that the Dy^{III} ions have an NO$_7$ and an O$_8$ coordination sphere differs significantly from **173-Dy** and **174**. In addition, no μ_5-oxide is present in **174** and **175–178**. Thus, the magnetic properties for **175–178**, determined by the molecular anisotropy, are obviously different from the compounds mentioned above. Here **175–178** exhibit similar dynamic magnetic behavior, frequency-dependent ac susceptibility signals, but without available relaxation times.

A pentanuclear dysprosium cluster, $[Dy_5(\mu_3\text{-OH})_6(Acc)_6(H_2O)_{10}]\cdot Cl_9\cdot 24H_2O$ (**179**), obtained via incorporating 1-aminocyclohexanecarboxylic acid (Acc), features an unprecedented trigonal bipyramidal geometry in lanthanide cluster [172]. Three Dy^{III} centers in the equatorial plane are eight-coordinate with square-antiprismatic geometry, whereas two Dy^{III} centers occupying the apical positions are in a dicapped trigonal prism coordination environment. Ac magnetic susceptibility data for **179** display slow relaxation of the magnetization, indicative of SMM behavior.

Two pentanuclear Dy^{III} complexes, $[Dy_5(\mu_3\text{-OH})_3(opch)_6(H_2O)_3]\cdot$ 3MeOH$\cdot$9H$_2$O (**180**) and $[Dy_5(\mu_3\text{-OH})_3(Hopch)_2(opch)_4(MeOH)(H_2O)_2]\cdot$ (ClO$_4$)$_2\cdot$6MeOH$\cdot$4H$_2$O (**181**), both contain $[Dy_5(\mu_3\text{-OH})_3]^{12+}$ core in a butterfly

Table 14 Pentanuclear $4f$ SMMs

Geometry	SMMs	CN of $4f$ ions	$U_{eff}/$ cm^{-1} $(H_{dc}/$ Oe)	hys (K)	References
Tetragonal pyramid	$[Dy_5O(OiPr)_{13}]$ (**173-Dy**)	$6(O_6)$	367	–	[168]
	$[Ho_5O(OiPr)_{13}]$ (**173-Ho**)	$6(O_6)$	278 (3500)	–	[169]
	$[Dy_5(\mu_4\text{-}OH)(\mu_3\text{-}OH)_4(\mu\text{-}\eta^2\text{-}Ph_2acac)_4(\eta^2\text{-}Ph_2acac)_6]$ (**174**)	$8(O_8)$	23	–	[170]
	$[Dy_5(OH)_5(D\text{-}PhGly)_4(Ph_2acac)_6]$ (**175**)	$8(NO_7)$, 8 (O_8)	–	–	[171]
	$[Dy_5(OH)_5(L\text{-}Trp)_4(Ph_2acac)_6]$ (**176**)	$8(NO_7)$, 8 (O_8)	–	–	[171]
	$[Dy_5(OH)_5(L\text{-}Pro)_4(Ph_2acac)_6]$ (**177**)	$8(NO_7)$, 8 (O_8)	–	–	[171]
	$[Dy_5(OH)_5(Ph_2Gly)_4(Ph_2acac)_6]$ (**178**)	$8(NO_7)$, 8 (O_8)	–	–	[171]
Trigonal bipyramidal	$[Dy_5(\mu_3\text{-}OH)_6(Acc)_6(H_2O)_{10}]\cdot$ $Cl_9\cdot24H_2O$ (**179**)	$8(O_8)$	–	–	[172]
Butterfly	$[Dy_5(\mu_3\text{-}OH)_3(opch)_6(H_2O)_3]\cdot$ $3MeOH\cdot9H_2O$ (**180**)	$8(NO_7)$, 8 (N_2O_6), 9 (N_3O_6), 9 (N_2O_7)	6,26	1.9	[173]
	$[Dy_5(\mu_3\text{-}OH)_3(Hopch)_2(opch)_4(MeOH)(H_2O)_2]\cdot(ClO_4)_2\cdot6MeOH\cdot4H_2O$ (**181**)	$8(NO_7)$, 8 (N_2O_6), 9 (N_3O_6), 9 (N_2O_7)	137	1.9	[173]

topology. Their magnetic investigations reveal that compound **180** acts as an SMM with two relaxation regimes ($U_{eff} = 6$ and 26 cm^{-1} for the low- and high-temperature domains) and a very narrow hysteresis loop at 1.9 K [173]. In contrast, compound **181** exhibits only one relaxation regime, but with a larger energy barrier of 137 cm^{-1} and spindle-shaped hysteresis loop at 1.9 K. The structural differences, which arose from the various coordination modes of the H_2opch ligand with particular keto–enol tautomerism, are likely responsible for the dynamic magnetic disparity (Table 14, Fig. 49).

An intriguing hexanuclear Dy_6 group is available via linking two highly anisotropic, triangular Dy_3 building blocks that can relax their magnetization slowly originating from the noncollinearity of the single-ion easy axes of magnetization of the Dy^{III} ions. In complex $[Dy_6(\mu_3\text{-}OH)_4(o\text{-}vanillin)_4(avn)_2(NO_3)_4(H_2O)_4]$ $(NO_3)_2\cdot(H_2O)\cdot3(CH_3)_2CO$ (**182**), there is a $[Dy_6(\mu_3\text{-}OH)_4(OR)_2]$ core [174]. It consists of two triangular $[Dy_3(\mu_3\text{-}OH)_2]^{7+}$, in which the vertices of the triangles are linked via two bridging alkoxide oxygen atoms. The increase of χT upon cooling to ~42 K indicates the presence of the dominant intramolecular ferromagnetic interaction between Dy^{III} ions. At low temperatures, this Dy_6 reveals slow magnetic relaxation with $U_{eff} = 7$ cm^{-1}. Moreover, hysteresis loop can be observed
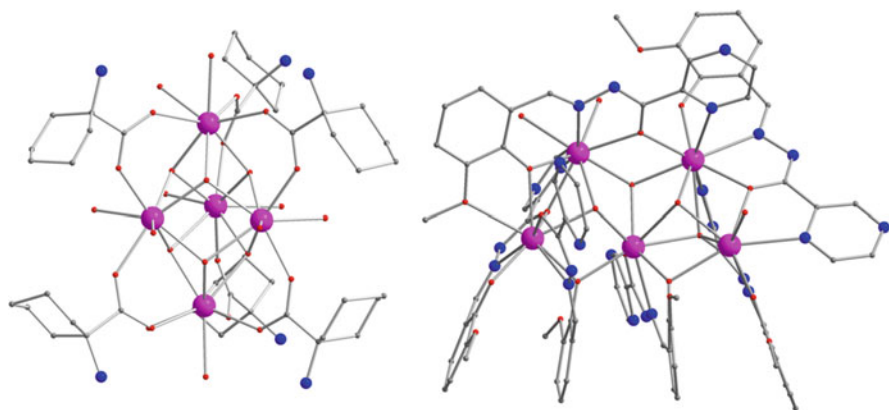
Fig. 49 Molecular structures for **179** (*left*) and **180** (*right*). Color codes: *pink*, Ln; *gray*, C; *red*, O; and *blue*, N

below 1 K, confirming an SMM for **182**. On the contrary, the antiferromagnetic linkage of two Dy_3 building blocks enhances slow magnetic relaxation compared with the precursor Dy_3. This is observed in SMM [$Dy_6(\mu_3$-OH)$_4$(o-vanillin)$_4$(o-vanillin')$_2$(H$_2$O)$_9$Cl]Cl$_5$·15H$_2$O (**183**), where two Dy_3 triangles in the Dy_6 unit are strictly co-parallel, but not coplanar [175]. As in the case of Dy_3 [24], the ground state of this Dy_6 is also calculated to be nonmagnetic, arising from the weak antiferromagnetic interaction between the triangles. In fact, a weakly magnetic state is found due to the symmetry breaking by linking the triangles, but at only 0.6 K above. A feature for this Dy_6 is the presence of two different relaxation processes, apparently associated to an unprecedented change in magnetic anisotropy from an easy plane to easy axis type on increasing the temperature. Thus, a slower relaxation process with a large barrier of 139 cm^{-1} for higher temperature occurs. However, the interaction between the two triangles is weak and hence of a reduced toroidal magnetization, in contrast to a strong coupling between the two triangles and hence of a very large toroidal moments in the SMM **184** [176]. The complex **184**, formulated as [$Dy_6(dme)_4(\mu_4$-O)(NO$_3$)$_4$(CH$_3$OH)]·CH$_3$OH, can be regarded as the linkage of two triangles via one μ_4-O^{2-} and four bridging deprotonated phenol oxygen atoms in an edge-to-edge arrangement, in which the dihedral angle between the two Dy_3 planes is 30°. As a result, the spin chirality of the Dy_3 triangle and the nonmagnetic ground state is retained, and strong coupling between the triangles through the μ_4-O^{2-} ion prompts similar anticlockwise arrangement of toroidal moments, leading to a stronger magnetic chirality. This Dy_6 shows two observable relaxation processes, perhaps induced by the distinct anisotropic centers and the exchange interactions, indicating the preserved SMM behavior (Figs. 50 and 51).

Complex [$Dy_6(\mu_3$-OH)$_3(\mu_3$-CO$_3$)(μ-OMe)(Hpch)$_6$(MeOH)$_4$(H$_2$O)$_2$]·3MeOH·2H$_2$O (**185**) presents a new topology based on vertex- and edge-sharing Dy_3 triangle units, where singly μ_3-OH-capped triangle A is connected to a doubly
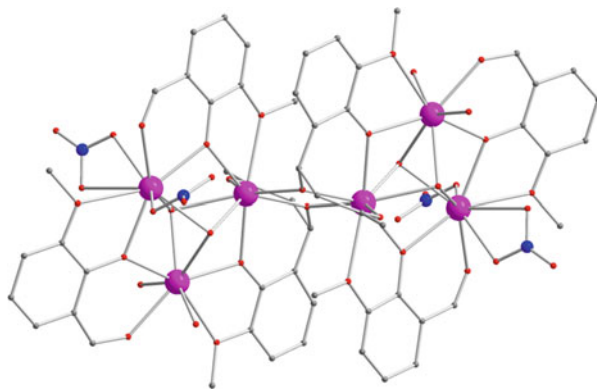
Fig. 50 Molecular structure for **182**. Color codes: *pink*, Ln; *gray*, C; *red*, O; and *blue*, N
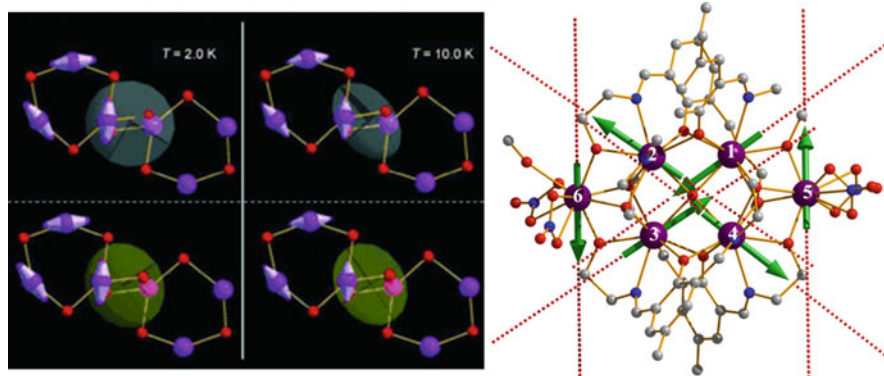
Fig. 51 (*Left*) Ellipsoidal representation of the experimental (*top*) and calculated (*bottom*) susceptibility tensors of **183** at two different temperatures. The tensors are superimposed onto the molecular structure of the magnetic core (Dy *violet*, O *red*); the orientation of the Dy easy axes estimated from ab initio calculations is also shown. Reprinted with permission from [175]. Copyright 2010 WILEY-VCH Verlag GmbH & Co. KGaA, Weinheim. (*Right*) Main anisotropy axes (*dashed lines*) on Dy ions and local magnetizations (*arrows*) in the ground state in **184**. Reprinted with permission from [176]. Copyright 2012 WILEY-VCH Verlag GmbH & Co. KGaA, Weinheim

capped triangle B via an edge-sharing arrangement, while the vertex of the triangle B is linked to two Dy^{III} ions forming singly μ_3-OH-capped triangle C [177]. An SMM behavior and two relaxation regimes can be observed in this compound, with $U_{eff} = 4$ cm^{-1} for low-temperature domain and 26 cm^{-1} for high-temperature domain, probably associated with single-ion relaxation of Dy^{III} ion and weak coupling between them.

Trigonal-prismatic geometry in hexanuclear Dy_6 SMMs is first found in $[Dy_6(OAc)_3(\mu_3\text{-}CO_3)_2(opch)_5(Hopch)(MeOH)_2]\cdot4H_2O\cdot5MeOH\cdot EtOH$ **(186)** [178]. In the core of the molecule, each of two CO_3^{2-} ligands derived from the capture of atmospheric CO_2 adopts a rare μ_3-η^2:η^2:η^2-tridentate mode to bridge
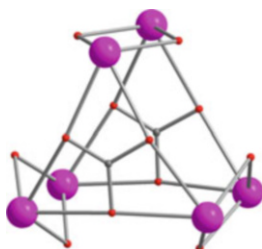
Fig. 52 The core for **186**. Color codes: *pink*, Ln; *gray*, C; and *red*, O
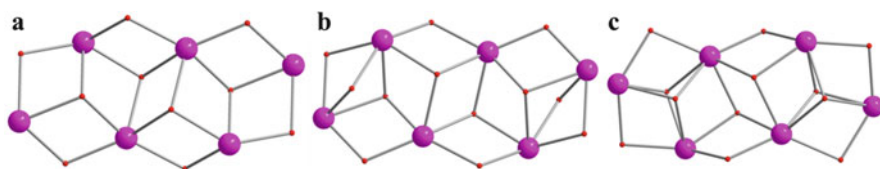
Fig. 53 The cores for **188** (**a**), **189** (**b**), and **190** (**c**). Color codes: *pink*, Ln, and *red*, O

three Dy^{III} ions, while these two triangular Dy^{III} planes linked through the hydrazone ligands are parallel to each other, yielding the hexanuclear trigonal prism. Similar arrangement is present in $[Dy_6(ovph)_4(Hovph)_2Cl_4(H_2O)_2(CO_3)_2]\cdot$ $CH_3OH\cdot H_2O\cdot CH_3CN$ (**187**), which can be further regarded as three petals of the Dy_2 units in **15** linked by two CO_3^{2-} ligands [179]. Both **186** and **187** behave as SMMs and show a crossover from a thermally activated mechanism at high temperature ($U_{eff} = 39$ cm^{-1} in the range of 8–26 K for **186** and $U_{eff} = 53$ cm^{-1} in 11–20 K for **187**) to a quantum tunneling relaxation pathway (0.07 s for **186** and 0.2 s for **187**). In addition, hysteresis loops can be observed below 5 K for **186** with a sweep rate of 70 mT s^{-1} (Fig. 52).

When four Dy_3 triangle units are fused to each other via edge sharing, a new type of hexanuclear Dy_6 is formed, as found in the compounds $[Dy_6(bpch)_2(HCO_2)_4(\mu_3\text{-}OH)_4(DMF)_6(H_2O)_2]Cl_2\cdot 4H_2O$ (**188**), $[\{Dy_6(hmp)_2(Hhmp)_2\}(\mu_3\text{-}OH)_4]$ $(MeOH)_2(H_2O)_6Cl_4\cdot 8H_2O\cdot 4CH_3OH$ (**189**), and $[Dy_6(bspo)_4(\mu_3\text{-}OH)_4(CH_3OH)_2(NO_3)_2]\cdot 6CH_3CN$ (**190**) [124, 180, 181]. Both **188** and **189** contain a hexanuclear $[Dy_6(OH)_4]^{14+}$ core consisting of triangular $[Dy_3(OH)]^{8+}$ that are fused to each other at the edge, while **190** has a$[Dy_6(OH)_6]^{12+}$ core comprising central $[Dy_3(OH)]^{8+}$ and terminal $[Dy_3(OH)_2]^{7+}$ triangles that are linked via edge sharing. Ac susceptibility measurements show that the three compounds display SMM behavior at low temperatures, with the determined energy barrier of 32 cm^{-1} under 5 kOe dc field for **189** and 2 cm^{-1} for **190** (Fig. 53).

$[Dy_6(\mu_4\text{-}O)_2(C4A)_2(NO_3)_2(HCOO)_2(CH_3O)_2(DMF)_4(CH_3OH)_4]$ (**191**) is an example of hexanuclear lanthanide cluster with an octahedral arrangement of the metals, featuring a sandwich-like unit constructed from two tail-to-tail calixarene molecules [182]. This octahedral Dy_6 exhibits SMM behavior in zero dc field, with an energy barrier of 5 cm^{-1} in the thermally activated regime. In compounds

[Ln$_6$(teaH)$_2$(teaH$_2$)$_2$(CO$_3$)(NO$_3$)$_2$(chp)$_7$(H$_2$O)](NO$_3$)·4.5MeOH·1.5H$_2$O (Ln = Tb, **192-Tb**; Dy, **192-Dy**), four of the Ln^{III} ions are coplanar, forming a trapezoid, but a significant difference from **191** is that the final two ions lying below and above the plane are out the longest rectangular edge [183]. This unusual arrangement of metal ions, for Tb$_6$ or Dy$_6$, shows slow relaxation of the magnetization in zero dc field, typical of SMM behavior, but without any available energy barrier. In contrast, compound [Na$_2$Dy$_6$(hmab)$_8$(C$_6$H$_4$NH$_2$COO)$_2$(C$_2$H$_5$OH)$_2$(H$_2$O)$_4$(NO$_3$)]· NO$_3$·C$_2$H$_5$OH·nH$_2$O (**193**) contains a magnetic Dy$_6$ core which can be viewed as a Dy$_4$ cubane and a Dy$_2$ unit [184]. Specially, the nitrate ligand displays an unusual μ_6-η^2:η^2:η^2-bonding mode, the same as CO$_3$$^{2-}$ ligand acts in **192**. Frequency-dependent χ'' signal without peak maxima in the ac measurement for **193** is observed, suggesting the presence of slow magnetic relaxation (Table 15, Fig. 54).

2.5 Heptanuclear and Octanuclear 4f Clusters

Heptanuclear 4f clusters that can relax magnetization slowly are relatively scarce. To date, the only heptametallic Ln SMM with a substantial energy barrier is the disk complex [Dy$_7$(OH)$_6$(H$_2$thme)$_5$(Hthme)(tpa)$_6$(MeCN)$_2$](NO$_3$)$_2$ (**194**) [185]. The cluster has a centered-hexagonal Dy$_7$ core bounded by six μ_3-OH groups, where the central Dy^{III} ion lies out of the hexagonal Dy$_6$. All the Dy^{III} ions are eight-coordinate, but with peripheral Dy^{III} ions in an O$_8$ coordination environment and central Dy^{III} ion in a N$_2$O$_6$ environment. Frequency-dependent ac signals with peaks can be observed below 28 K in zero dc field, characteristic of SMM behavior. Moreover, the energy barrier for **194** is estimated to be 97 cm^{-1} by fitting to an Arrhenius law, which is among the highest observed for a high-nuclearity SMM (Fig. 55).

The other Dy$_7$ clusters such as [Dy$_7$(μ_3-OH)$_5$(msa)$_2$(Hmsa)$_4$(PhCO$_2$)$_7$(OH) (H$_2$O)$_{1.5}$(MeOH)$_{0.5}$]·2.5MeOH·5.25H$_2$O (**195**), [Dy$_7$(OH)$_2$(def)$_9$(aib)]·4MeOH (**196**), and [Dy$_7$(OH)$_6$(CO$_3$)$_3$(sach)$_3$(Hsach)$_3$(MeOH)$_6$] (**197**) display possible SMM behaviors without available energy barriers based on ac magnetic susceptibility measurements, although they feature different Dy arrangements: five edge-sharing Dy$_3$ triangles; centered-octahedral and centered-trigonal-prismatic geometry for **195**, **196**, and **197**, respectively; and even various coordination environments [186–189] (Table 16).

Octanuclear 4f clusters are often observed as double cubane cores, which adopt two Ln$_4$ cubanes being bridged to form Ln$_8$ clusters. In [Dy$_4$(μ_3-OH)$_2$(μ_3-O)$_2$(cpt)$_6$(MeOH)$_6$(H$_2$O)]$_2$ (**198**), each cubane core consists of four Dy^{III} centers bridged by two μ_3-OH and two μ_3-O groups, and then two cubanes are linked to each other by two externally coordinated ligands (cpt), leading to the dumbbell {Dy$_4$}$_2$ moiety [190]. The static and dynamic data corroborate the fact that **198** exhibits slow relaxation of the magnetization below 5 K associated with an SMM behavior.

Table 15 Hexanuclear 4f SMMs

Geometry	SMMs	CN of 4f ions	U_{eff}/cm^{-1} (H_{dc}/Oe)	hys (K)	References
Dy3 + Dy3 vertex to vertex	[Dy$_6$(μ$_3$-OH)$_4$(o-vanillin)$_4$(avn)$_2$(NO$_3$)$_4$(H$_2$O)$_4$](NO$_3$)$_2$·(H$_2$O)·3(CH$_3$)$_2$CO (**182**)	8(O$_8$), 9(O$_9$)	7	1	[174]
Dy3 + Dy3 vertex to vertex	[Dy$_6$(μ$_3$-OH)$_4$(o-vanillin)$_4$(o-vanillin')$_2$(H$_2$O)$_9$Cl]Cl$_5$·15H$_2$O (**183**)	8(O$_8$), 8(O$_7$Cl)	139	–	[175]
Dy3 + Dy3 edge to edge	[Dy$_6$(dme)$_4$(μ$_4$-O)(NO$_3$)$_4$(CH$_3$OH)]·CH$_3$OH (**184**)	8(N$_2$O$_6$), 8(O$_8$), 9(O$_9$)	24,28	–	[176]
Dy3 + Dy3 + Dy3 vertex and edge sharing	[Dy$_6$(μ$_3$-OH)$_3$(μ$_3$-CO$_3$)(μ-OMe)(Hpch)$_6$(MeOH)$_4$(H$_2$O)$_2$]·3MeOH·2H$_2$O (**185**)	8(NO$_7$), 8(N$_2$O$_6$), 8(N$_3$O$_5$), 9(NO$_8$)	26,4	–	[177]
Trigonal prism	[Dy$_6$(OAc)$_3$(μ$_3$-CO$_3$)$_2$(opch)$_5$(Hopch)(MeOH)$_2$]·4H$_2$O·5MeOH·EtOH (**186**)	8(N$_2$O$_6$)	39	5	[178]
	[Dy$_6$(ovph)$_4$(Hovph)$_2$Cl$_4$(H$_2$O)$_2$(CO$_3$)$_2$]·CH$_3$OH·H$_2$O·CH$_3$CN (**187**)	8(N$_2$O$_5$Cl), 8(N$_2$O$_6$)	53	–	[179]
Four Dy3 edge sharings	[Dy$_6$(bpch)$_2$(HCO$_2$)$_4$(μ$_3$-OH)$_4$(DMF)$_6$(H$_2$O)$_2$]Cl$_2$·4H$_2$O (**188**)	8(NO$_7$)	–	–	[124]
	[{Dy$_6$(hmp)$_2$(Hhmp)$_2$}(μ$_3$-OH)$_4$](MeOH)$_2$(H$_2$O)$_6$Cl$_4$·8H$_2$O·4CH$_3$OH (**189**)	8(NO$_7$), 9(N$_2$O$_7$)	32(5000)	–	[180]
	[Dy$_6$(bspo)$_4$(μ$_3$-OH)$_4$(CH$_3$OH)$_2$(NO$_3$)$_2$]·6CH$_3$CN (**190**)	8(NO$_7$), 8(N$_2$O$_6$)	2	–	[181]
Octahedron	[Dy$_6$(μ$_4$-O)$_2$(C4A)$_2$(NO$_3$)$_2$(HCOO)$_2$(CH$_3$O)$_2$(DMF)$_4$(CH$_3$OH)$_4$] (**191**)	7(O$_7$), 8(O$_8$)	5	–	[182]
Planar Dy4 + Dy2	[Tb$_6$(teaH)$_2$(teaH$_2$)$_2$(CO$_3$)(NO$_3$)$_2$(chp)$_7$(H$_2$O)](NO$_3$)·4.5MeOH·1.5H$_2$O (**192-Tb**)	8(NO$_7$), 8(N$_2$O$_6$), 9(NO$_8$)	–	–	[183]
	[Dy$_6$(teaH)$_2$(teaH$_2$)$_2$(CO$_3$)(NO$_3$)$_2$(chp)$_7$(H$_2$O)](NO$_3$)·4.5MeOH·1.5H$_2$O (**192-Dy**)	8(NO$_7$), 8(N$_2$O$_6$), 9(NO$_8$)	–	–	[183]
Cubane Dy4 + Dy2	[Na$_2$Dy$_6$(hmab)$_8$(C$_6$H$_4$NH$_2$COO)$_2$(C$_2$H$_5$OH)$_2$(H$_2$O)$_4$(NO$_3$)]·NO$_3$·C$_2$H$_5$OH·nH$_2$O (**193**)	8(O$_8$), 9(NO$_8$)	–	–	[184]
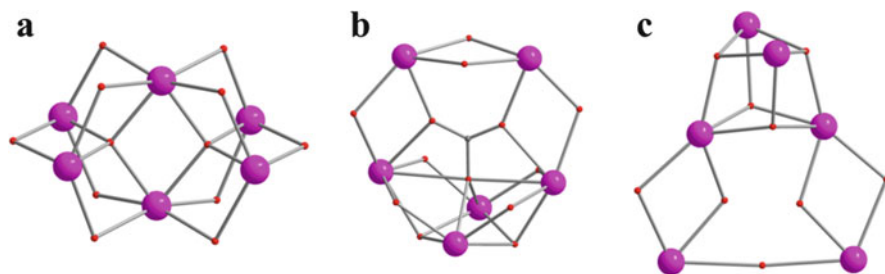
Fig. 54 The cores for **191** (**a**), **192** (**b**), and **193** (**c**). Color codes: *pink*, Ln; *red*, O; and *gray*, C
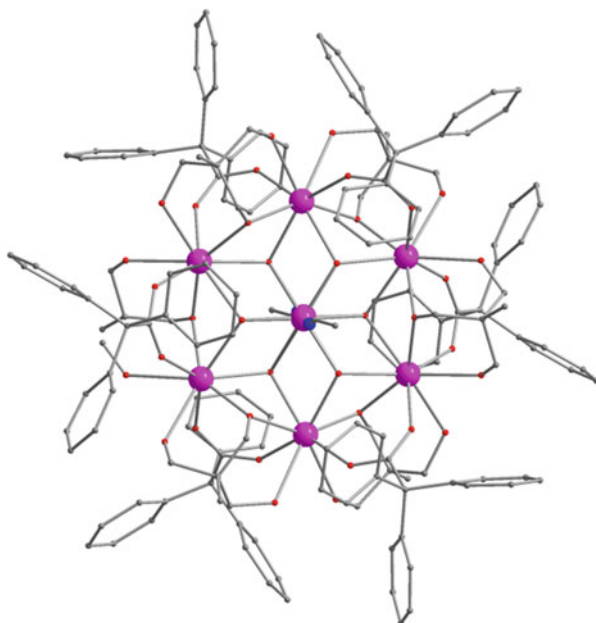
Fig. 55 Molecular structure for **194**. Color codes: *pink*, Ln; *gray*, C; *red*, O; and *blue*, N

Similar bis-cubane complexes were obtained, such as $Dy_8(Hhmab)_{10}(C_6H_4NH_2COO)_2(\mu_3\text{-}OH)_8(OH)_2(NO_3)_2(H_2O)_4]$ (**199**) where cubane $[Dy_4(\mu_3\text{-}OH)_4]$ is connected to an adjacent symmetry-related cubane by two $\mu\text{-}O,O'$-carboxylato units, $[Dy_8(OH)_8(phendox)_6(H_2O)_8]$ $Cl_2(OH)_2 \cdot 18H_2O \cdot 18MeOH$ (**200**) being regarded as a fused dicubane $[Dy_4(\mu_3\text{-}OH)_4]$ core bridged by two $\mu_3\text{-}\eta^2\text{-}ON^-$ groups, and $[Dy_8(OH)_6(OMe)_6(cmnm)_{10}(ccnm)_2(H_2O)_2(MeOH)_2]$ (**201**)in which two equivalent $[Dy_4(\mu_3\text{-}OH)_3(\mu_3\text{-}OMe)]$ moieties are bridged by four μ_2-methoxide ligands [191–193]. Their dynamic magnetic data reveal slow relaxation of the magnetization at low temperatures under zero dc field, but without available energy barriers, indicating possible SMM behaviors for the three complexes (Fig. 56).

Table 16 Heptanuclear $4f$ SMMs

Geometry	SMMs	CN of $4f$ ions	U_{eff}/cm^{-1} (H_{dc}/Oe)	hys (K)	References
Centered hexagon	[Dy$_7$(OH)$_6$(H$_2$thme)$_5$(Hthme)$_5$(tpa)$_6$(MeCN)$_2$](NO$_3$)$_2$ (**194**)	8(O$_8$), 8(N$_2$O$_6$)	97	–	[185]
Five edge-sharing Dy$_3$ triangles	[Dy$_7$(μ_3-OH)$_5$(msa)$_2$(Hmsa)$_4$(PhCO$_2$)$_7$(OH)(H$_2$O)$_{1.5}$(MeOH)$_{0.5}$]·2.5MeOH·5.25H$_2$O (**195**)	9(O$_9$), 8(O$_8$), 8(NO$_7$), 8(N$_2$O$_6$), 8(N$_3$O$_5$)	–	–	[186]
Centered octahedron	[Dy$_7$(OH)$_2$(def)$_9$(aib)]·4MeOH (**196**)	7(NO$_6$), 7(N$_2$O$_5$), 8(N$_2$O$_6$), 8(O$_8$)	–	–	[187, 188]
Centered-trigonal prism	[Dy$_7$(OH)$_6$(CO$_3$)$_3$(sach)$_3$(Hsach)$_3$(MeOH)$_6$] (**197**)	8(NO$_7$), 9(O$_9$)	–	–	[189]

Fig. 56 Molecular
structure for **199**. Color
codes: *pink*, Ln; *gray*, C;
red, O; and *blue*, N
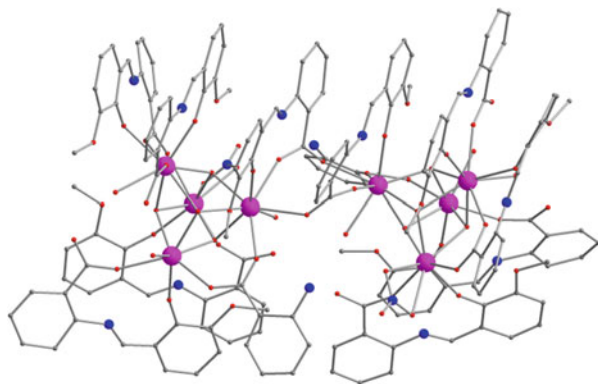
Additionally, octanuclear complex $[Dy_8(2,2\text{-bpt})_8(\mu_4\text{-O})_2(\mu\text{-OMe})_8(\mu_{1,1,3,3}\text{-N}_3)$
$(\mu_{1,3}\text{-N}_3)(N_3)_2]\cdot 11H_2O\cdot 9MeOH$ (**202**) consists of a pair of $[Dy_4(\mu_4\text{-O})]$ tetrahedral
units bridged by two azido groups in $\mu_{1,1,3,3}$ and $\mu_{1,3}$ modes as well as two 2,2-bpt
ligands. Strikingly, **202** displays obvious SMM behavior with a substantial energy
barrier of 7 cm^{-1} [194].

When incorporating multidentate Schiff-base ligands into octanuclear lantha-
nide clusters, two unique Dy_8 cores with tub conformation were realized in com-
plexes $[Dy_8(\mu_4\text{-CO}_3)_4(\text{opch})_8(H_2O)_8]\cdot 10MeOH\cdot 2H_2O$ (**203**) and $[Dy_8(\mu_4\text{-}$
$CO_3)_4(\text{ovph})_8(H_2O)_8]\cdot 12CH_3CN\cdot 6H_2O$ (**204**) [179, 195]. Both complexes possess
a similar $[Dy_8(\mu_4\text{-CO}_3)_4(\mu_2\text{-O})_8]$ core which can be considered as two nearly
parallel Dy_4 planes sandwiched by four CO_3^{2-} anions. Along the sides of the tub,
each O_{alkoxido} atom from eight deprotonated ligands bridges two Dy^{III} ions. The
coordination geometries of the Dy^{III} ions are either eight-coordinate in an N_2O_6
environment or nine-coordinate in an N_2O_7 environment. Despite high similarity in
structures of **203** and **204**, disparate SMM behaviors are observed. **203** exhibits an
energy barrier of 52 cm^{-1} and a quantum regime of relaxation below 8 K as well as
an open hysteresis loop at 1.9 K on a traditional SQUID magnetometer, whereas
204 shows possible SMM behavior without observable maxima in χ'' component
(Fig. 57).

Besides, $[Dy_8(\text{sao})_4(\mu_3\text{-OH})_4(NO_3)_{12}(DMF)_{12}]$ (**205**) contains a central $[Dy_4(\mu_3\text{-}$
$OH)_4]$ cubane, which is encapsulated by a peripheral Dy_4 square [196]. The metal-
lic skeleton can thus be described as a tetrahedron inside a square. Two asymmetric
Dy^{III} ions are eight-coordinate with a $[O_7N]$ coordination sphere and nine coordi-
nate with a $[O_9]$ coordination sphere. Dynamic magnetic study shows typical SMM
behavior for **205**, with $U_{\text{eff}} \approx 4$ cm^{-1} at zero dc field as indicated by ac suscepti-
bility data and dc magnetization decay measurements. The observed open hyster-
esis loops below 1 K by means of micro-SQUID magnetometry confirm that **205** is
indeed an SMM. $(Et_4N)_4[Dy_8O(\text{nd})_8(NO_3)_{10}(H_2O)_2]$ (**206**) features a central
$[Dy_4(\mu_4\text{-O})]$ tetrahedron whose four edges are each fused with the edge of a
$[Dy_3(\mu_3\text{-OR})_2(\mu\text{-OR})_2]$ triangle [197]. Thus, the resulting core has a "Christmas-

Fig. 57 Molecular structure for **203**. Color codes: *pink*, Ln; *gray*, C; *red*, O; and *blue*, N
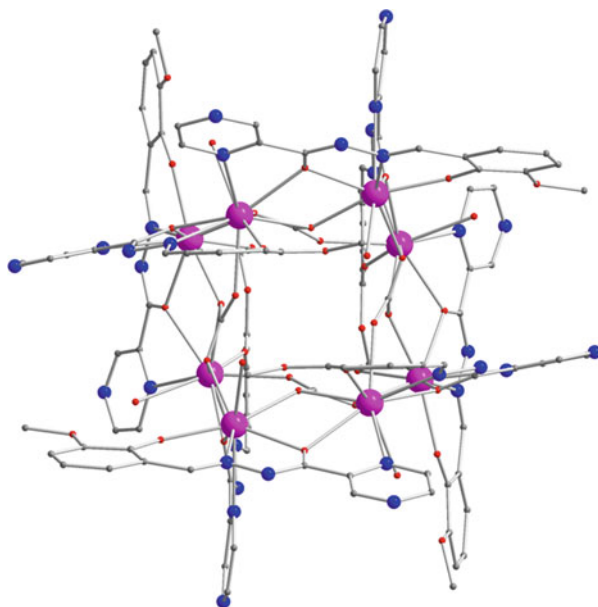
star" topology. **206** shows a weak temperature dependence of χ'' below 9 K, and an anisotropy barrier could not be determined.

In the structure of complex $[Dy_8(\mu_3\text{-}OH)_4(o\text{-vanillin})_2(mvn)_2(p\text{-}NO_2bz)_{14}(CH_3OH)_2]\cdot 3.09CH_3CN\cdot 6CH_3OH\cdot H_2O$ (**207**), eight Dy^{III} ions are held together by six $\mu_3\text{-}OH/OR$ groups to form a $[Dy_8(\mu_3\text{-}OH)_4(\mu_3\text{-}OR)_2]$ core, which is composed of six triangular Dy_3 units sharing vertices [152]. An interesting feature is the methyl hemiacetal derivative of o-vanillin linking four Dy^{III} ions in a $\mu_4\text{-}\eta^1:\eta^2:\eta^3:\eta^1$ fashion. **207** shows a weak temperature dependence below 8 K; hence an anisotropy barrier could not be determined.

The octanuclear $[Dy_8(OH)_6(teaH)_6(teaH_2)_2(teaH_3)_2]$ $(O_3SCF_3)_4\cdot 0.5MeOH\cdot 2H_2O$ (**208**) consists of eight Dy^{III} ions bridged by eight μ_3-O atoms, forming multiple triangular units associated with three fused butterfly motifs. Its ac magnetic susceptibility measurements reveal peak "tails" in the χ'' below 8 K, indicating possible SMM behavior [198] (Table 17).

2.6 Higher-Nuclearity 4f Clusters

Two nonanuclear Dy^{III} clusters, $[Dy_9(OH)_{10}(homp)_8(NO_3)_8(DMF)_8](OH)\cdot 1.6H_2O\cdot 0.6CH_2Cl_2$ (**209**) and $[Dy_9(hmhp)_4(\mu_4\text{-}OH)_2(\mu_3\text{-}OH)_8(NO_3)_8(CH_3OH)_2(H_2O)_2](NO_3)\cdot 4CH_3OH\cdot 9H_2O$ (**210**), feature similar sandglass-like topology [199, 200]. Their skeletons consist of nine Dy^{III} atoms with eight Dy^{III} at the apexes and one Dy^{III} at the center of a Dy_8 square antiprism; meanwhile, two μ_4-OH-centered Dy_4 square bases connect to the apical Dy^{III} ion

Table 17 Octanuclear $4f$ SMMs

Geometry	SMMs	CN of $4f$ ions	U_{eff}/cm^{-1} (H_{dc}/Oe)	hys (K)	References
Double cubane	[Dy$_4$(μ_3-OH)$_2$(μ_3-O)$_2$(cpt)$_6$(MeOH)$_6$(H$_2$O)$_2$]$_2$ (**198**)	8(NO$_7$), 8(O$_8$)	–	0.04	[190]
	Dy$_8$(Hhmab)$_{10}$(C$_6$H$_4$NH$_2$COO)$_2$(μ_3-OH)$_8$(OH)$_2$(NO$_3$)$_2$(H$_2$O)$_4$] (**199**)	8(O$_8$), 7(O$_7$)	–	–	[191]
	[Dy$_8$(OH)$_8$(phendox)$_6$(H$_2$O)$_8$]Cl$_2$(OH)$_2$·18H$_2$O·18MeOH (**200**)	9(N$_4$O$_5$), 8(O$_8$)	–	–	[192]
	[Dy$_8$(OH)$_6$(OMe)$_6$(cmmm)$_{10}$(ccmm)$_2$(H$_2$O)$_2$(MeOH)$_2$] (**201**)	8(N$_4$O$_4$), 8(O$_8$), 8 (N$_2$O$_6$), 9(N$_4$O$_5$)	–	–	[193]
Double tetrahedron	[Dy$_8$(2,2-bpt)$_8$(μ_4-O)$_2$(μ-OMe)$_8$($\mu_{1,1,3,3}$-N$_3$)($\mu_{1,3}$-N$_3$)(N$_3$)$_2$]·11H$_2$O·9MeOH (**202**)	8(N$_5$O$_3$)	7	–	[194]
Tub conformation	[Dy$_8$(μ_4-CO$_3$)$_4$(opch)$_8$(H$_2$O)$_8$]·10MeOH·2H$_2$O (**203**)	9(N$_2$O$_7$), 8(N$_2$O$_6$)	52	1.9	[195]
	[Dy$_8$(μ_4-CO$_3$)$_4$(ovph)$_8$(H$_2$O)$_8$]·12CH$_3$CN·6H$_2$O (**204**)	9(N$_2$O$_7$), 8(N$_2$O$_6$)	–	–	[179]
Cubane in the square	[Dy$_8$(sao)$_4$(μ_3-OH)$_4$(NO$_3$)$_{12}$(DMF)$_{12}$] (**205**)	8(NO$_7$), 9(O$_9$)	4	1	[196]
Christmas star	(Et$_4$N)$_4$[Dy$_8$O(nd)$_8$(NO$_3$)$_{10}$(H$_2$O)$_2$] (**206**)	8(O$_8$), 9(O$_9$)	–	–	[197]
Six triangular Dy$_3$ units sharing vertices	[Dy$_8$(μ_3-OH)$_4$(o-vanillin)$_2$(mvn)$_2$(p-NO$_2$bz)$_{14}$(CH$_3$OH)$_2$]·3.09CH$_3$CN·6CH$_3$OH·H$_2$O (**207**)	8(O$_8$)	–	–	[152]
Three fused butterfly motifs	[Dy$_8$(OH)$_6$(teaH)$_6$(teaH$_2$)$_2$(teaH$_3$)$_2$](O$_3$SCF$_3$)$_4$·0.5MeOH·2H$_2$O (**208**)	8(NO$_7$), 9(N$_2$O$_7$)	–	–	[198]

via eight μ_3-OH ligands. In both complexes, the basal Dy^{III} ions are nine-coordinate with NO_8 donor set, while the apical Dy^{III} ion is eight-coordinate completed by eight oxygen atoms. So a similar magnetic behavior is observed for **209** and **210**: a weak temperature dependence of χ'' below 6 K occurs, indicating possible SMM behavior.

Most of the decametallic cages like $[Dy_{10}(\mu_3\text{-OH})_4(OAc)_{20}(H_2hmhp)_2(H_3hmhp)_2\{NH_2C(CH_2OH)_3\}_2]$ (**211**), $[Dy_{10}O_2(OH)_6(o\text{-vanillin})_6(isonicotinate)_{13}(H_2O)_2](NO_3)$ (**212**), and $[Dy_{10}(bmch)_5(\mu_2\text{-OH})_6(H_2O)_{22}](Cl)_4\cdot7H_2O$ (**213**) can be described as two connected Dy_5 units [198, 201, 202]. Specifically, in **211**, two Dy triangles are fused in a vertex-sharing fashion forming a $\{Dy_5(\mu_3\text{-OH})_2\}$ subcore, and such two Dy_5 subunits are further doubly bridged by acetates in a *syn-anti* mode into the Dy_{10} core; **212** contains two trigonal prismatic metallic cores that are bridged by one μ_4-O and three μ_3-OH for each $\{Dy_5\}$ unit, which are then held together via the isonicotinate ligand displaying $\mu_2\text{-}\eta^1\text{:}\eta^1$ bonding mode; for **213**, ten Dy^{III} ions are linked to five ligands in a $2 \times [1 \times 5]$ rectangular array, leading to a ladder-shaped cage that is built up with three "rungs" and two "rails." Ac magnetic susceptibility measurements of the three compounds show weak temperature dependences below 10 K at zero dc field; hence energy barriers could not be determined.

Strikingly, only the decametallic cluster $[Dy_{10}(2,2\text{-bpt})_6(\mu_4\text{-O})_4(\mu_3\text{-OMe})_4(\text{-}\mu\text{-OMe})_8(\mu\text{-OAc})_2(OAc)_2]\cdot40H_2O$ (**214**) possessing four edge-sharing $[Dy_4(\mu_4\text{-O})]$ tetrahedral units has a substantial anisotropic barrier [194]. It behaves as an SMM under zero dc field, and the energy barrier is estimated to be 8 cm^{-1} after linear fitting by the Arrhenius law.

A hendecanuclear cluster $[Dy_{11}(OH)_{11}(phendox)_6(phenda)_3(OAc)_3](OH)\cdot40H_2O\cdot7MeOH$ (**215**) can be described as two cubane-like $[Dy_4(\mu_3\text{-OH})_4]$ motifs positioned above and below the center of a Dy_3 equilateral triangle [192]. The frequency-dependent behavior is observed in the ac susceptibility measurement under zero dc field, but without maxima of χ'' and hence a substantial energy barrier.

Two dodecanuclear clusters $[2Cl\subset\{Dy_{12}(OH)_{16}(phenda)_8(H_2O)_8\}](X)_2\cdot S$, where $(X)_2\cdot S = [Dy(phenda)_2]_2\cdot16DMSO\cdot10MeOH\cdot45H_2O$ for **216** and $(X)_2\cdot S = (OH)_2\cdot15MeOH\cdot40H_2O$ for **217**, contain similar $[Dy_{12}(OH)_{16}(phenda)_8(H_2O)_8]$ core yet the counterion is $[Dy(phenda)_2]^-$ in **216** and OH$^-$ in **217** [203]. This large Dy_{12} cluster can be regarded as the fusion of four vertex-sharing cubane-like $[Dy_4(\mu_3\text{-OH})_4]$ units with each unit capped by the η^2-O atom. Below 6 K, both **216** and **217** show weak temperature dependences in χ'' but with no maxima.

A novel dodecanuclear wheel $[Dy_{12}(valdien)_6(OH)_4O_2(CO_3)_6][Dy_{12}(valdien)_6(OH)_4O_4(CO_3)_6]\cdot(ClO_4)_4\cdot xH_2O$ (**218**) is composed of two similar Dy_{12} units featuring six vertex-sharing Dy_3 triangle motifs [204]. The adjacent capped Dy^{III} ions of the Dy_3 triangles are alternately positioned above and below the approximately equilateral hexagonal six-membered ring. Ac magnetic susceptibility measurement reveals the onset of slow magnetic relaxation for **218**, but without an available energy barrier.

The pentadecanuclear cluster compound $[\{Dy_{15}(OH)_{20}(PepCO_2)_{10}(Ph_2acac)_{10}Cl\}Cl_4]$ (**219**) consists of five doubly vertex-sharing $[Dy_4(\mu_3\text{-OH})_4]$ subunits that are cyclically aligned to enclose a pentagonal plane [205]. In the
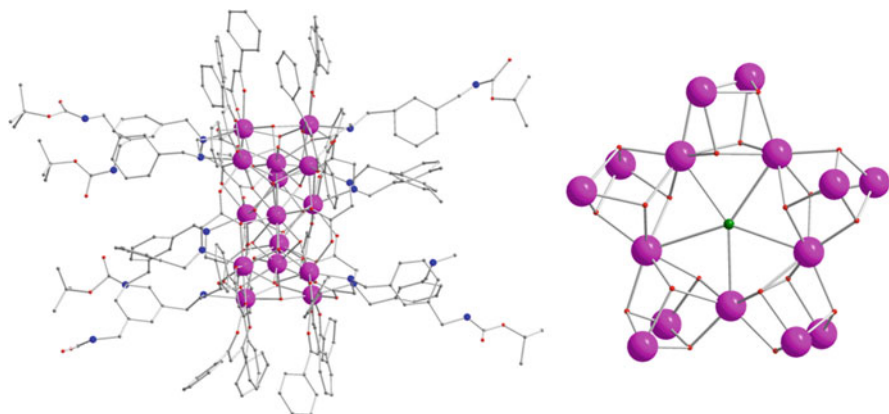
Fig. 58 Molecular structure (*left*) and the core (*right*) for **219**. Color codes: *pink*, Ln; *gray*, C; *red*, O; *blue*, N; and *green*, Cl

middle of the pentagon, a Cl atom bridges all five vertex-sharing Dy^{III} ions in a μ_5-mode, resulting in a $[Dy_{15}(\mu_3\text{-OH})_{20}Cl]$ core. Ac susceptibility measurement in the absence of dc field exhibits frequency-dependent behavior with no maxima in χ''. However, when applying a dc field of 2 kOe, the relaxation times can be deduced and follow an activated Arrhenius law, giving an energy barrier of 6 cm^{-1} (Fig. 58).

The highest-nuclearity lanthanide cluster in the context of single-molecule magnetism is $[Dy_{30}I(\mu_3\text{-OH})_{24}(\mu_3\text{-O})_6(NO_3)_9(\text{isonicotinate})_{41}(OH)_3(H_2O)_{38}]_2$ (**220**) [206]. It consists of two {Dy_{26}} clusters and two {Dy_4} clusters that are linked by isonicotinate ligands, forming a tetramer in a rhombic shape with the size of 28.40×25.11 Å. Magnetic studies of **220** reveal a frequency-dependent out-of-phase signal below 6 K, indicative of the slow relaxation of magnetization, but with no maximum (Table 18).

3 Conclusion and Perspective

The field of polynuclear lanthanide SMMs has grown rapidly in the last decade. In hundreds of examples reported, the remarkable progress includes the following: (1) a radical-bridged Tb$_2$ complex [102] and a nonradical-bridged $[Er_2(COT'')_3]$ complex [31] equally hold the highest blocking temperature 14 K; (2) a triangular Dy$_3$ showing toroidal arrangement of the magnetic moments and SMM behavior [24]; (3) an oxo-centered Dy$_4$K$_2$ complex with $U_{eff} = 585$ cm^{-1} after magnetic dilution [163]; (4) a square-based pyramid Dy$_5$ with $U_{eff} = 367$ cm^{-1} [168]; and so on. Strikingly, the energy barriers achieved for $4f$ SMMs far exceed that for $3d$ SMMs.

The relaxation process in the cluster-based lanthanide SMMs can be influenced by many factors, in which one of the most important aspects is single-ion anisotropy, determined by the metal ion and crystal field. Until now, the most common

Table 18 Higher-nuclearity 4f SMMs

Geometry	SMMs	CN of 4f ions	U_{eff}/cm^{-1} (H_{dc}/Oe)	hys (K)	References
Dy_9	$[Dy_9(OH)_{10}(homp)_8(NO_3)_8(DMF)_8](OH)\cdot1.6H_2O\cdot0.6CH_2Cl_2$ (**209**)	$8(O_8), 9(NO_8)$	–	–	[199]
	$[Dy_9(hmhp)_4(\mu_4-OH)_2(\mu_3-OH)_8(NO_3)_8(CH_3OH)_2(H_2O)_2](NO_3)\cdot 4CH_3OH\cdot9H_2O$ (**210**)	$8(O_8), 9(NO_8)$	–	–	[200]
Dy_{10}	$[Dy_{10}(\mu_3-OH)_4(OAc)_{20}(H_2hmhp)_2(H_3hmhp)_2[NH_2C(CH_2OH)_3]_2]$ (**211**)	$8(O_8), 8(NO_7), 9(O_9), 9(NO_8)$	–	–	[201]
	$[Dy_{10}O_2(OH)_6(o\text{-}vanillin)_6(isonicotinate)_{13}(H_2O_2)_2](NO_3)$ (**212**)	$7(O_7), 8(O_8)$	–	–	[198]
	$[Dy_{10}(bmch)_5(\mu_2-OH)_6(H_2O_{22})](Cl)_4\cdot7H_2O$ (**213**)	$8(N_2O_6), 9(O_9), 9(N_2O_7)$	–	–	[202]
	$[Dy_{10}(2,2\text{-}bpt)_6(\mu_4-O)_4(\mu_3-OMe)_8(\mu-OMe)_4(\mu-OAc)_2(OAc)_2]\cdot4OH_2O$ (**214**)	$7(N_2O_5), 7(O_7), 8(N_4O_4)$	8	–	[194]
Dy_{11}	$[Dy_{11}(OH)_{11}(phendox)_6(phenda)_3(OAc)_3](OH)\cdot40H_2O\cdot7MeOH$ (**215**)	$9(N_4O_5), 9(O_9), 9(N_2O_7)$	–	–	[192]
Dy_{12}	$[2Cl\subset[Dy_{12}(OH)_{16}(phenda)_8(H_2O)_8]]Dy(phenda)_2]_2\cdot16DMSO\cdot10MeOH\cdot45H_2O$ (**216**)	$8(O_8), 9(N_2O_7), 8(N_4O_4)$	–	–	[203]
	$[2Cl\subset[Dy_{12}(OH)_{16}(phenda)_8(H_2O)_8]](OH)_2\cdot15MeOH\cdot40H_2O$ (**217**)	$8(O_8), 9(N_2O_7)$	–	–	[203]
	$[Dy_{12}(valdien)_6(OH)_4O_2(CO_3)_6][Dy_{12}(valdien)_6(OH)_4O_4(CO_3)_6]\cdot(ClO_4)_4\cdot xH_2O$ (**218**)	$8(O_8), (N_3O_5), 9(N_3O_6), 10(N_3O_7)$	–	–	[204]
Dy_{15}	$[\{Dy_{15}(OH)_{20}(PepCO_2)_{10}(Ph_2acac)_{10}Cl\}Cl_4]$ (**219**)	$8(O_8), 8(NO_7)$	6(2000)	–	[205]
Dy_{60}	$[Dy_{30}](\mu_3-OH)_{24}(NO_3)_6(isonicotinate)_{41}(OH)_3(H_2O)_{38}]_2$ (**220**)	$8(O_8), 8(NO_7), 9(O_9)$	–	–	[206]

lanthanide ion used to obtain SMMs is Dy^{III}, probably due to its strong spin–orbit coupling and Kramers ion nature which ensures a doubly degenerate ground-state $\pm M_J$ sublevels irrespective of the ligand field, while other ions like Tb^{III}, Ho^{III}, and Er^{III} are also used. Interestingly, although the crystal-field effect is generally smaller than the spin–orbit coupling energy for lanthanide, it still strongly affects the magnetic anisotropy in creating $4f$ SMMs. To maximize the magnetic anisotropy for individual f-elements, Long's group launched a qualitative and visual method for predicting the ligand architectures [207]. According to the basic overall shape of free-ion electron density, there are two general optimum ligand architectures: for oblate ions such as Ce(III), Pr(III), Nd(III), Tb(III), Dy(III), and Ho(III), the crystal field should be such that the ligand electron density is concentrated above and below the xy plane; for prolate ions such as Pm(III), Sm(III), Er(III), Tm (III), and Yb(III), an equatorial coordination geometry is preferable. This is very helpful in the first step toward the design of high-performance $4f$ SMMs. However, this theory was challenged by a recent work which indicates that strictly prolate f-electron density is not required to stabilize a crystal field that favors SMM behavior [208]. Hence, with the ongoing development of this area, the control of single-ion anisotropy is being improved step by step.

Besides the intrinsic magnetic anisotropy, weak magnetic interactions such as dipolar and exchange coupling are the second factor to affect the relaxation process, which may mitigate quantum tunneling relaxation processes. Extensive bridging ligands have been used in constructing polynuclear lanthanide SMMs, from monatomic bridges such as oxygen, nitrogen, hydrogen, carbon, sulfur, and chlorine to polyatomic bridges like carboxylate, oxalate, pyrazine, azide, and carbonate. Weak exchange-coupling interactions between lanthanide ions usually occur, presenting a means for fine-tuning the SMM behavior, but it is worth noting that a record blocking temperature is achieved in a strong coupling system through the use of a radical bridge [102], and an efficient suppression of quantum tunneling with $\tau_{QTM} = 35$ is realized via the high axiality and Ising exchange interaction [47]. These provide promising strategies for enhancing the SMM properties.

The arrangement of metal ions could generate different lowest exchange multiplets, therefore affecting the dynamic magnetic behavior. Typically, amazing toroidal arrangement of magnetic moments was found in a triangular Dy_3 [24]. In spite of the almost nonmagnetic ground state, the Dy_3 triangle is an SMM for the thermally populated excited state. When opening out the triangle to a near linear Dy_3, parallel alignment of the magnetic moments and ferromagnetic interaction are observed, featuring SMM behavior but without strong resonant tunneling observed in the Dy_3 triangle [121]. Hence, various geometries of lanthanide clusters are attempted to help further enhance the SMM properties. However, when the structure of lanthanide cluster becomes more elaborate as the number of lanthanide ions increases, its SMM property is found to be worse from our survey of the literatures.

On the whole, the ultimate goal of this research is to develop future devices for application. On one side, we expect a more clear view of magneto-structural correlations in the cluster-based lanthanide SMMs, with the development of the chemical species, physical measurements, and computational methods, guiding the

construction of better SMMs with practical blocking temperatures. On the other side, attempts should be made to organize these molecules into addressable arrays, thereby affording operable devices.

4 Addenda

Polynuclear 4f SMMs have constantly grown during the writing, and some recent works are highlighted as follows.

4.1 Phosphorus-, Arsenic-, and Selenium-Ligated Ln SMMs

A phosphide-bridged complex, $[(Cp'_2Dy)\{\mu\text{-}P(H)Mes\}]_3$·toluene (**221**, Mes = mesityl), is a cyclic trimer in which three $\{Cp'_2Dy\}$ units are bridged by μ-P(H)Mes ligands with a $\{Dy_3P_3\}$ core. Deprotonation of the P–H bonds in **221** produces a phosphinidene-bridged complex $[Li(THF)_4]_2[(Cp'_2Dy)_3(\mu\text{-}PMes)_3Li]$·THF (**222**) which contains a similar $\{Dy_3P_3\}$ core but with a central lithium cation. The ac susceptibility measurement on **221** reveals a large energy barrier of 210 cm^{-1}, and, when doping 5% dysprosium into a diamagnetic matrix, the U_{eff} increases to 256 cm^{-1} and magnetic hysteresis up to 4.4 K [209]. In contrast, the U_{eff} for **222** and its diluted sample are more than an order of magnitude smaller than that in **221**. Theoretical studies demonstrate that the thermal magnetic relaxation in **221** proceeds via the second-excited doublet states due to the strong magnetic axiality in the ground and first-excited doublets as well as their near-collinearity of the anisotropy axes. However, the phosphinidene ligand in **222** provides a stronger equatorial ligand field, leading to a weaker magnetic axiality of the ground state. Meanwhile, the main magnetic axes in the ground and first-excited doublets have different orientations, which is responsible for the reduced SMM property in **222**.

At a later time, a dysprosium arsenide $[(Cp'_2Dy)\{\mu\text{-}As(H)Mes\}]_3$·toluene (**223**), dysprosium arsinidene $[Li(THF)_4]_2[(Cp'_2Dy)_3(\mu_3\text{-}AsMes)_3Li]$·THF (**224**), and dysprosium selenolate complex $[(Cp'_2Dy)\{\mu\text{-}SeMes\}]_3$·toluene (**225**) are identified to be SMMs [210]. The structures of **223** and **225** are similar to that of **221**, while **224** is similar to **222**, all featuring a Dy_3As_3 (Dy_3Se_3) ring in a chair conformation. Both **223** and **225** relax their magnetization via the second-excited Kramers doublet, giving large energy barriers in the region of 250 cm^{-1} in zero dc field. In comparison, a much smaller barrier for **224** is determined because of a stronger crystal field generated by the arsinidene ligands (Fig. 59).
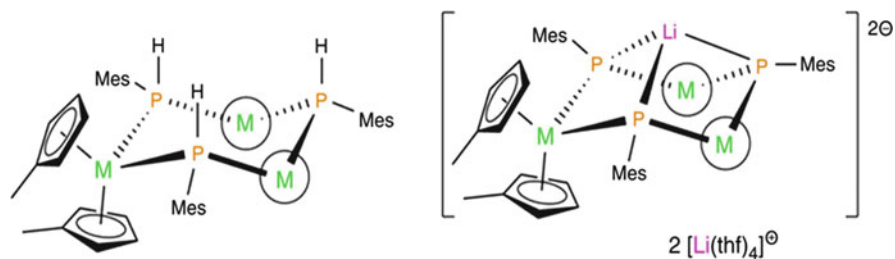
Fig. 59 Schematic illustration for complex **221** (*left*) and **222** (*right*). Reprinted with permission from [209]. Copyright 2015, Rights Managed by Nature Publishing Group

4.2 Single-Ion Anisotropy and Magnetic Interaction in Dy$_2$ SMMs

An asymmetric Dy$_2$ compound [Dy$_2$(Hhpph)$_2$Cl$_2$(H$_2$O)$_3$]·2H$_2$O·MeCN (**226**) is assembled and found to be structurally similar to compound **15** [211]. For two Dy centers in each compound, while three methanol molecules coordinated to Dy1 in **15** are replaced with three water molecules in **226**, resulting differences in Dy1 centers and Dy2 centers in both compounds are located in almost identical environments with pentagonal–bipyramidal geometries. As a result, by ab initio calculations, obvious changes including decreased energy gap between the ground and first-excited states and increased transversal components of the g tensor only occur at the Dy1 site. Intriguingly, a two-step relaxation process is operative in both compounds, with the similar high-temperature relaxations, which can be assigned to originate from the Dy2 center, and the low-temperature relaxations that shift to the lower temperatures for **226**, which is correlated with the local modulation of coordination environment at the Dy1 site. Such site resolution from experimental determination combined with theoretical result is evidenced for the first time in a complicated multinuclear system.

Utilizing the metallacrown synthetic approach, a hexanuclear Ga$_4$^{III}–Dy$_2$^{III} [Ga$_4$Dy$_2$(shi)$_4$(Hshi)$_2$(H$_2$shi)$_2$(C$_5$H$_5$N)$_4$(CH$_3$OH)(H$_2$O)]·3C$_5$H$_5$N·2CH$_3$OH·3H$_2$O (**227**) is assembled, where the Dy^{III} ions are bridged by oxygen atoms forming a Dy$_2$O$_2$ unit that is protected by the diamagnetic Ga$_4$ ring [212]. An inflection point around 0.5 T in the curve of magnetization vs applied field at 2 K has been confirmed to be due to the intramolecular antiferromagnetic interaction via experimental and theoretical studies, leading to a diamagnetic ground state. Nevertheless, the presence of an easy axis of magnetization for the Dy^{III} ion brings a slow relaxation of the magnetization. Two relaxation processes are observed for **227**, with the low-temperature process assigned to the ferromagnetic excited state and the high-temperature process assigned to the isolated Dy^{III} ions. This assignment is also proved by the slow relaxation with a close energy barrier for the magnetically diluted sample. Thus, this provides a rare example of an antiferromagnetically
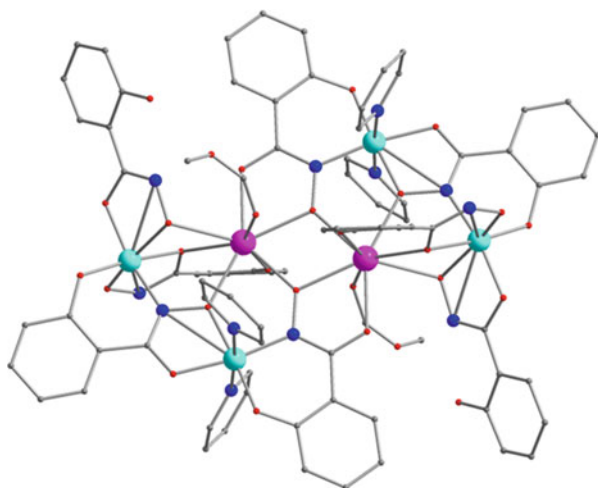
coupled Ising-like lanthanide dimer with a diamagnetic ground state, behaving similarly to the antiferromagnetically coupled Dy_3 complex [24] (Fig. 60).

A centrosymmetric dinuclear compound $[Dy_2(pmv)_2(OAc)_2(DMF)_2]$ (**228**) containing fourfold linkage derived from bis(μ_2-O)-bridging groups and two acetate ligands in a *syn–syn* μ_2-η^1:η^1 mode shows high-performance SMM behavior with a thermal energy barrier of 224 cm^{-1} [213]. The introduction of two Zn^{II} ions in the pockets on either side of the Dy_2O_2 core affords the compound $[Zn_2Dy_2(pmv)_2(OAc)_6]\cdot4H_2O$ (**229**) with only twofold connection derived from bis(μ_2-O)-bridging groups, in which only slow relaxation is observed. Ab initio calculations reveal more axial *g* tensors as well as larger energy separation between the ground and first-excited doublets, corresponding to the higher energy barrier in **228**. Interestingly, during the change from N_2O_6 (**228**) to O_8 (**229**) for coordination sphere of Dy^{III} ion, strong axiality in **228** is significantly produced by one pronounced covalent bond. Further insight into magnetic coupling indicates that considerable antiferromagnetic interaction via the four bridging paths in **228** is crucial in leading to a nonmagnetic ground state, by suppressing zero-field quantum tunneling of magnetization.

4.3 High-Nuclearity Ln SMMs: Dy₇, Dy₁₀, and Dy₁₄

A heptanuclear cluster $[Dy_7(eddc)(opch)_4(npa)_3(OAc)_5(MeOH)_2]\cdot4MeOH$ (**230**), which was obtained by incorporating the single and double pyrazinyl hydrazone as well as phosphonate ligands, features the largest non-centered odd-number rings of lanthanide thus far [214]. When doubling the amount of H$_2$npa in the reaction, a tetradecanuclear cluster $[Dy_{14}(eddc)_4(opch)_4(npa)_{10}(OAc)_6(H_2O)_4]\cdot xH_2O$ (**231**), consisting of two symmetry-related cyclic heptamers, is isolated. Both compounds

exhibit SMM behaviors at low temperatures, especially a clear two-step thermally activated relaxations for **230** with large energy barriers of 51 cm^{-1} (fast relaxation phase) and 123 cm^{-1} (slow relaxation phase).

A decanuclear Dy_{10} compound, $[Dy_{10}(Hhhmp)_{10}(k^2\text{-Piv})_{10}]\cdot9CHCl_3\cdot4CH_3CN$ (**232**), is a macrocycle that involves ten $[Hhhmp]^{2-}$ ligands and ten pivalate ions in participation of coordination without oxide or hydroxide group which is often found in polynuclear lanthanide complexes [215]. Alternate Dy atoms lie above and below the mean plane of the Dy_{10} wheel. Under 4 kOe dc field, this Dy_{10} compound shows a clear SMM behavior with $U_{eff} = 11$ cm^{-1}.

Ligands:

A

H₂abc

H₂abp

Acc

Haib

H₄ampd

H₃api

H₂avn

B

H₂bcd

bdeaH₂

H₂beh

Hbfmp

H₄bhmh

H₆bmap

H₂BMBDA

H₄bmch

H₃bmd

H₂bmh

H₄bpch

bpdp

bpoe

bpom
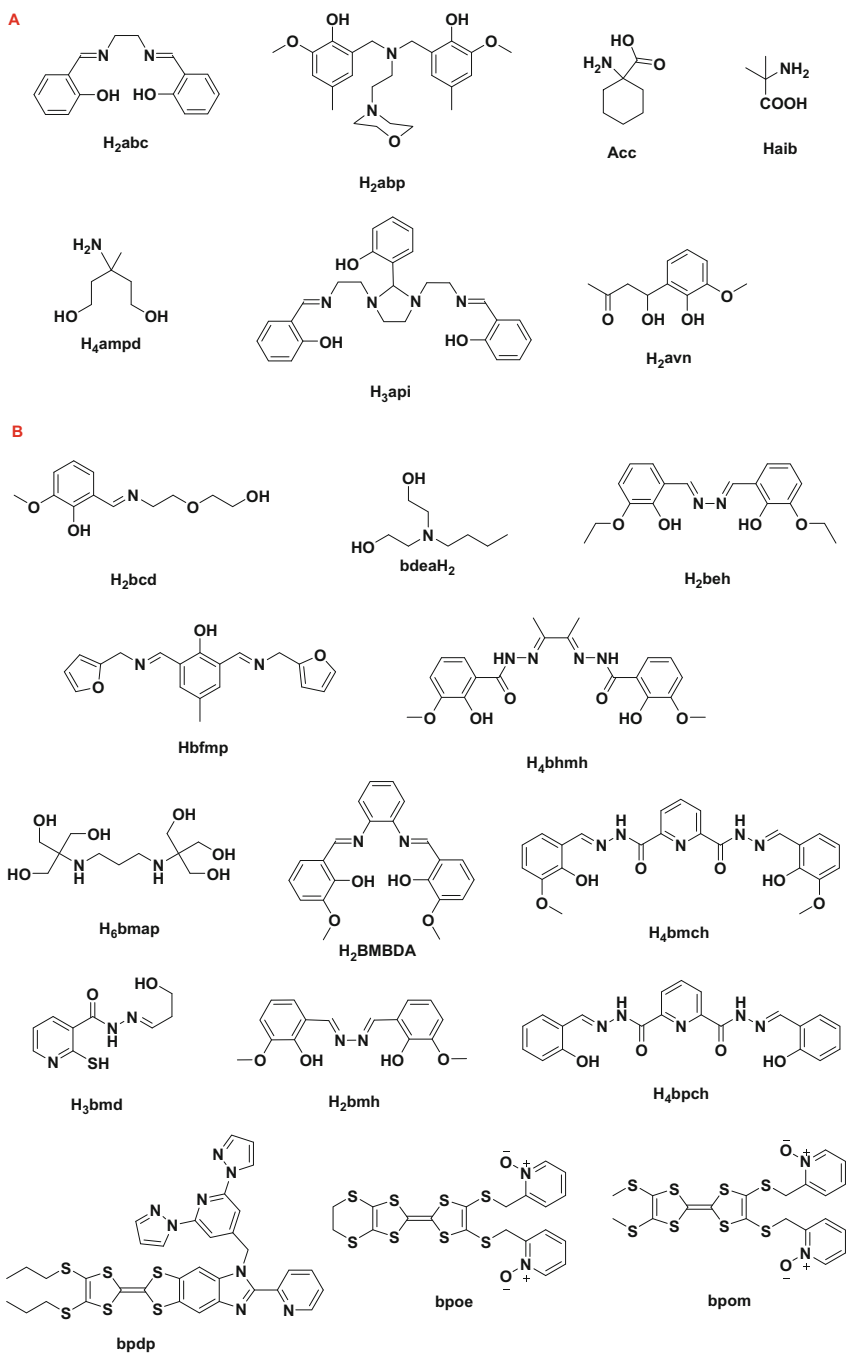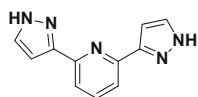
3-bpp
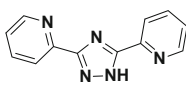
2,2-bptH

H₂BSCDA

H₂BSCDO

—R— = **H₂bsp**

H₂bsbp

H₂bsbpm
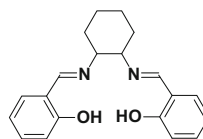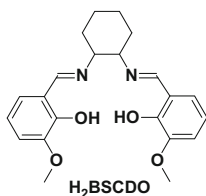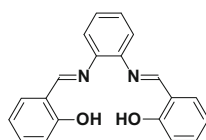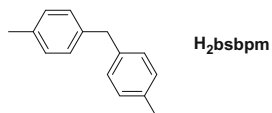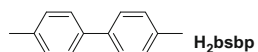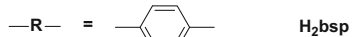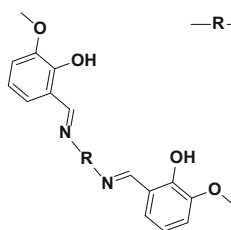
H₂BSPDA
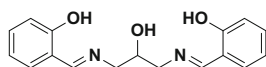
H₃bspo

C
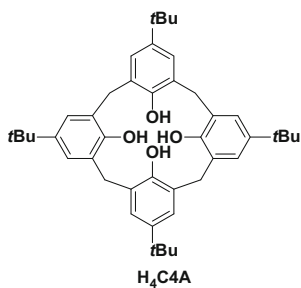
H₄C4A
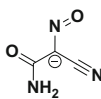
ccnm
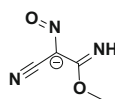
cmnm
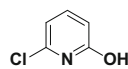
H₃chp

COT''

Hcpt

D
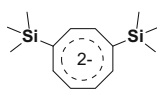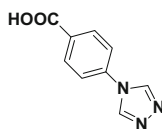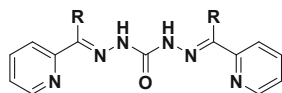
H$_2$dchm, R = CH$_3$
H$_2$dch, R = H
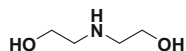
deaH$_2$
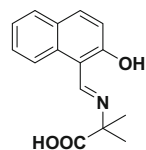
H$_2$def
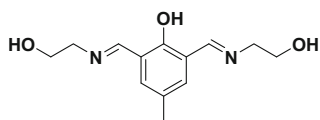
H$_3$dme
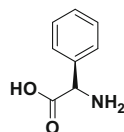
D-PhGlyH

E
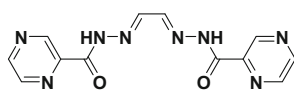
H$_2$eddc
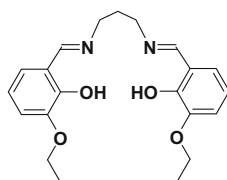
H$_2$Eobde
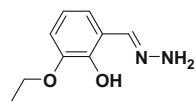
Hesh

F
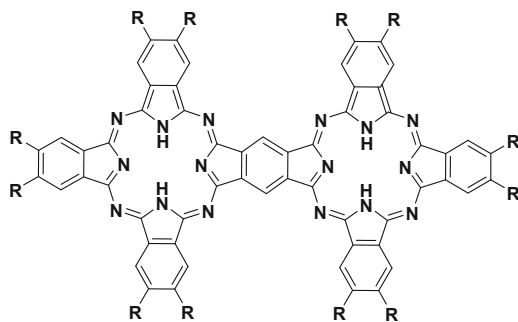
Fused-Pc, R = OBu

H
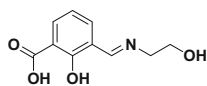
H₂hba
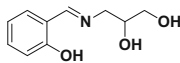
H₃hbp
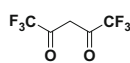
hfac
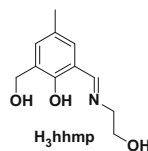
H₃hhmp
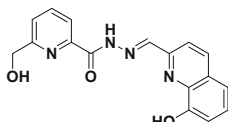
H₃hhp
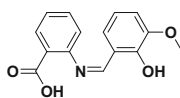
H₂hmab
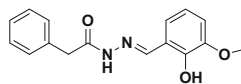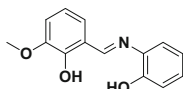
H₂hmb

H₂hmbp
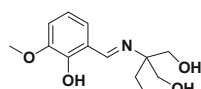
H₄hmhp
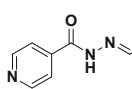
H₂hmi
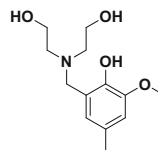
H₃hmmde
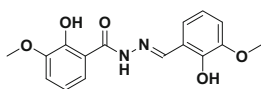
H₃hmmh
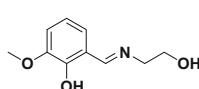
H₂hmmp
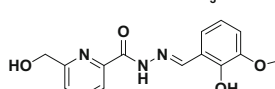
H₃hmp
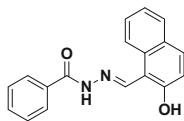
H₂hnb
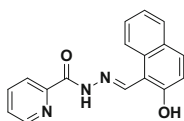
H₂hnp
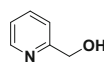
Hhomp
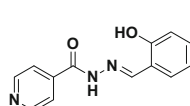
H₂hpch
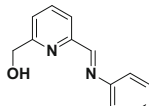
H₂hpm
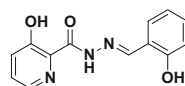
H₃hpph
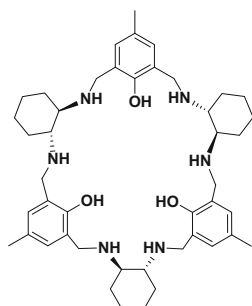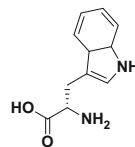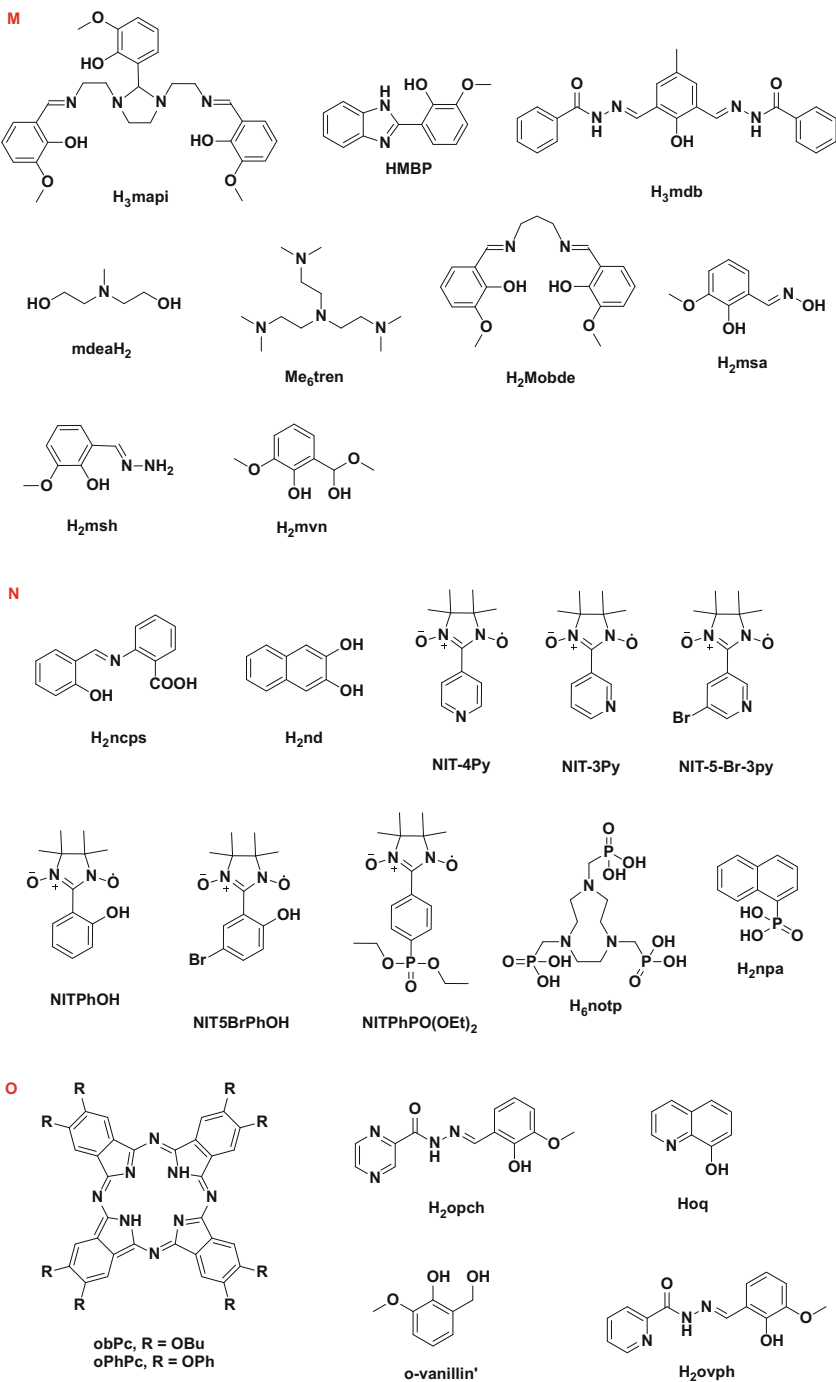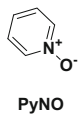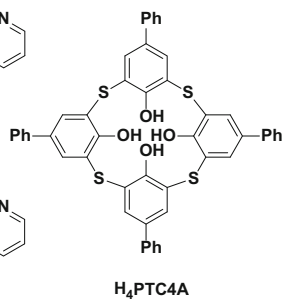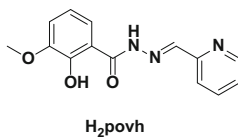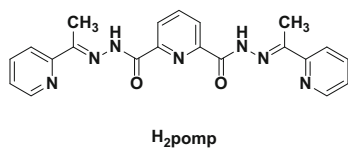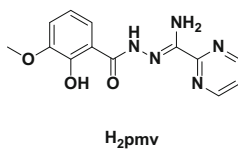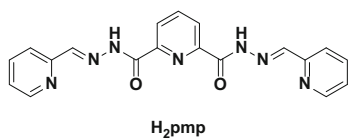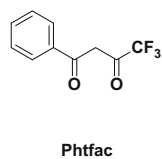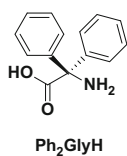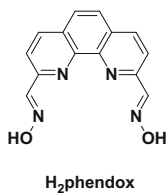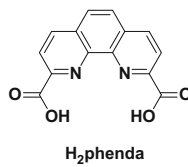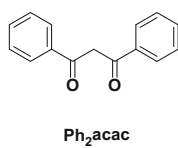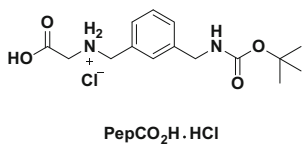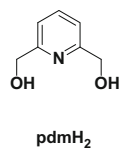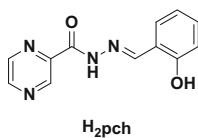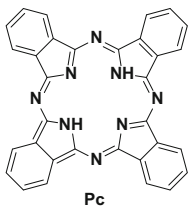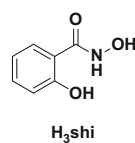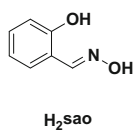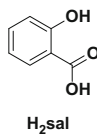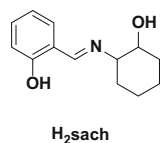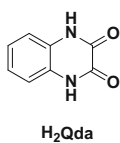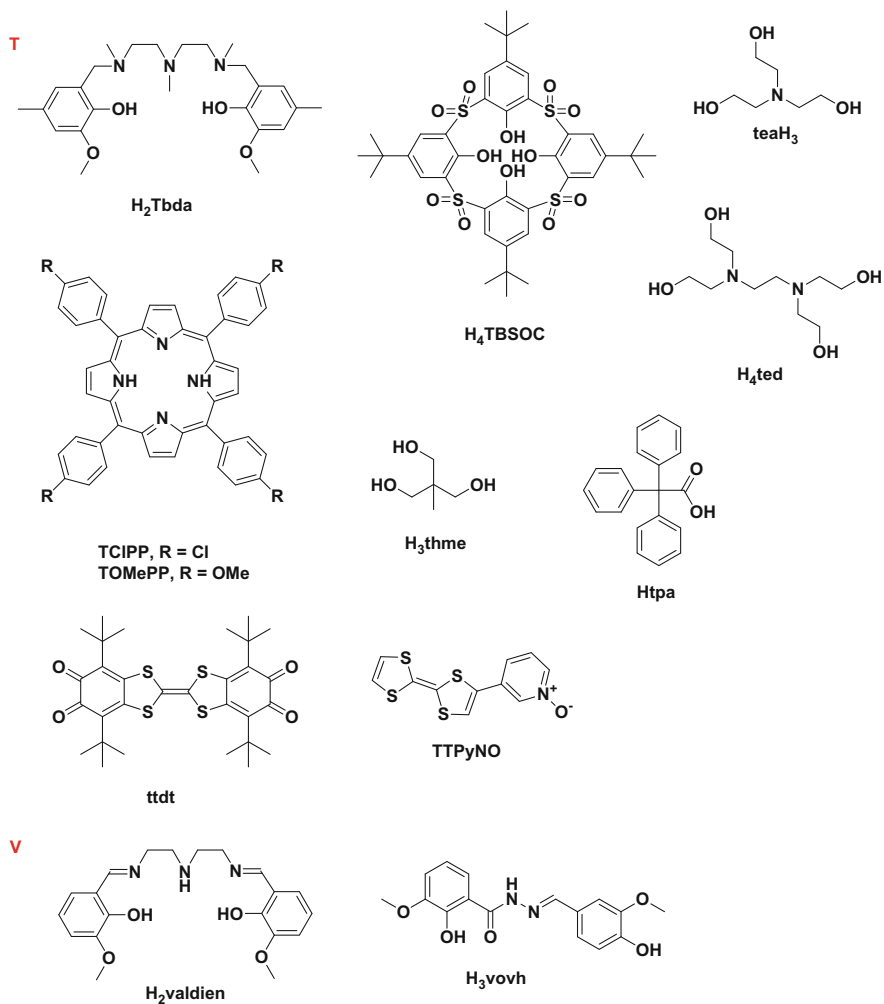
L

H₃L$_{RRRRRR}$

L-ProH

L-TrpH

M

H₃mapi

HMBP

H₃mdb

mdeaH₂

Me₆tren

H₂Mobde

H₂msa

H₂msh

H₂mvn

N

H₂ncps

H₂nd

NIT-4Py

NIT-3Py

NIT-5-Br-3py

NITPhOH

NIT5BrPhOH

NITPhPO(OEt)₂

H₆notp

H₂npa

O

obPc, R = OBu
oPhPc, R = OPh

H₂opch

Hoq

o-vanillin'

H₂ovph

P

Pc

H₂pch

pdmH₂

PepCO₂H·HCl

Ph₂acac

H₂phenda

H₂phendox

Ph₂GlyH

Phtfac

H₂pmp

H₂pmv

H₄PTC4A

H₂pomp

H₂povh

PyNO

Q, S

H₂Qda

H₂sach

H₂sal

H₂sao

H₃shi

T H₂Tbda

H₄TBSOC

teaH₃

H₄ted

TCIPP, R = Cl
TOMePP, R = OMe

H₃thme

Htpa

ttdt

TTPyNO

V H₂valdien

H₃vovh

References

1. Gatteschi D, Sessoli R, Villain J (2006) Molecular nanomagnets. Oxford University Press, Oxford

2. Sessoli R, Gatteschi D, Caneschi A, Novak M (1993) Magnetic bistability in a metal-ion cluster. Nature 365:141–143
3. Sessoli R, Tsai HL, Schake AR, Wang S, Vincent JB, Folting K, Gatteschi D, Christou G, Hendrickson DN (1993) High-spin molecules: $[Mn_{12}O_{12}(O_2CR)_{16}(H_2O)_4]$. J Am Chem Soc 115:1804–1816
4. Yamanouchi M, Chiba D, Matsukura F, Ohno H (2004) Current-induced domain-wall switching in a ferromagnetic semiconductor structure. Nature 428:539–542
5. Saitoh E, Miyajima H, Yamaoka T, Tatara G (2004) Current-induced resonance and mass determination of a single magnetic domain wall. Nature 432:203–206
6. Leuenberger MN, Loss D (2001) Quantum computing in molecular magnets. Nature 410:789–793
7. Aromí G, Brechin EK (2006) Synthesis of 3d metallic single-molecule magnets. Struct Bond 122:1–67
8. Winpenny REP (2012) Molecular cluster magnets. World Scientific Publishing Company, Singapore
9. Ako AM, Hewitt IJ, Mereacre V, Clérac R, Wernsdorfer W, Anson CE, Powell AK (2006) A ferromagnetically coupled Mn19 aggregate with a record S = 83/2 ground spin state. Angew Chem Int Ed 118:5048–5051
10. Ruiz E, Cirera J, Cano J, Alvarez S, Loose C, Kortus J (2008) Can large magnetic anisotropy and high spin really coexist? Chem Commun 2008:52–54
11. Waldmann O (2007) A criterion for the anisotropy barrier in single-molecule magnets. Inorg Chem 46:10035–10037
12. Neese F, Pantazis DA (2011) What is not required to make a single molecule magnet. Faraday Discuss 148:229–238
13. Wang B, Jiang S, Wang X, Gao S (2009) Magnetic molecular materials with paramagnetic lanthanide ions. Sci China Ser B Chem 52:1739–1758
14. Sorace L, Benelli C, Gatteschi D (2011) Lanthanides in molecular magnetism: old tools in a new field. Chem Soc Rev 40:3092–3104
15. Guo Y-N, Xu G-F, Guo Y, Tang J (2011) Relaxation dynamics of dysprosium (III) single molecule magnets. Dalton Trans 40:9953–9963
16. Luzon J, Sessoli R (2012) Lanthanides in molecular magnetism: so fascinating, so challenging. Dalton Trans 41:13556–13567
17. Zhang P, Guo Y-N, Tang J (2013) Recent advances in dysprosium-based single molecule magnets: structural overview and synthetic strategies. Coord Chem Rev 257:1728–1763
18. Habib F, Murugesu M (2013) Lessons learned from dinuclear lanthanide nano-magnets. Chem Soc Rev 42:3278–3288
19. Woodruff DN, Winpenny REP, Layfield RA (2013) Lanthanide single-molecule magnets. Chem Rev 113:5110–5148
20. Zhang P, Zhang L, Tang J (2015) Lanthanide single molecule magnets: progress and perspective. Dalton Trans 44:3923–3929
21. Ishikawa N, Sugita M, Ishikawa T, Koshihara S, Kaizu Y (2003) Lanthanide double-decker complexes functioning as magnets at the single-molecular level. J Am Chem Soc 125:8694–8695
22. Ishikawa N, Sugita M, Wernsdorfer W (2005) Quantum tunneling of magnetization in lanthanide single-molecule magnets: bis (phthalocyaninato) terbium and bis (phthalocyaninato) dysprosium anions. Angew Chem Int Ed 44:2931–2935
23. Ishikawa N, Sugita M, Ishikawa T, Koshihara S, Kaizu Y (2004) Mononuclear lanthanide complexes with a long magnetization relaxation time at high temperatures: a new category of magnets at the single-molecular level. J Phys Chem B 108:11265–11271
24. Tang J, Hewitt I, Madhu NT, Chastanet G, Wernsdorfer W, Anson CE, Benelli C, Sessoli R, Powell AK (2006) Dysprosium triangles showing single-molecule magnet behavior of thermally excited spin states. Angew Chem Int Ed 45:1729–1733

25. Wernsdorfer W, Aliaga-Alcalde N, Hendrickson DN, Christou G (2002) Exchange-biased quantum tunnelling in a supramolecular dimer of single-molecule magnets. Nature 416:406–409
26. Tang J, Zhang P (2015) Lanthanide single molecule magnets. Springer, Heidelberg
27. Tang J, Zhang P (2015) Polynuclear lanthanide single molecule magnets. In: Layfield RA, Murugesu M (eds) Lanthanides and actinides in molecular magnetism. Wiley, New York, pp 61–88
28. Benelli C, Gatteschi D (2015) SMM with lanthanides in introduction to molecular magnetism. Wiley, New York, pp 239–249
29. Venugopal A, Tuna F, Spaniol TP, Ungur L, Chibotaru LF, Okuda J, Layfield RA (2013) A hydride-ligated dysprosium single-molecule magnet. Chem Commun 49:901–903
30. Le Roy JJ, Jeletic M, Gorelsky SI, Korobkov I, Ungur L, Chibotaru LF, Murugesu M (2013) An organometallic building block approach to produce a multidecker 4f single-molecule magnet. J Am Chem Soc 135:3502–3510
31. Le Roy JJ, Ungur L, Korobkov I, Chibotaru LF, Murugesu M (2014) Coupling strategies to enhance single-molecule magnet properties of erbium-cyclooctatetraenyl complexes. J Am Chem Soc 136:8003–8010
32. Le Roy JJ, Korobkov I, Murugesu M (2014) A sandwich complex with axial symmetry for harnessing the anisotropy in a prolate erbium (III) ion. Chem Commun 2014:1602–1604
33. Huang W, Le Roy JJ, Khan SI, Ungur L, Murugesu M, Diaconescu PL (2015) Tetraanionic biphenyl lanthanide complexes as single-molecule magnets. Inorg Chem 54:2374–2382
34. Ishikawa N, Otsuka S, Kaizu Y (2005) The effect of the f–f interaction on the dynamic magnetism of a coupled $4f^8$ system in a dinuclear terbium complex with phthalocyanines. Angew Chem Int Ed 44:731–733
35. Ishikawa N, Iino T, Kaizu Y (2002) Interaction between f-electronic systems in dinuclear lanthanide complexes with phthalocyanines. J Am Chem Soc 124:11440–11447
36. Ishikawa N, Iino T, Kaizu Y (2002) Determination of ligand-field parameters and f-electronic structures of hetero-dinuclear phthalocyanine complexes with a diamagnetic yttrium (III) and a paramagnetic trivalent lanthanide ion. J Phys Chem A 106:9543–9550
37. Katoh K, Kajiwara T, Nakano M, Nakazawa Y, Wernsdorfer W, Ishikawa N, Breedlove BK, Yamashita M (2011) Magnetic relaxation of single-molecule magnets in an external magnetic field: an Ising dimer of a terbium(III)-phthalocyaninate triple-decker complex. Chemistry 17:117–122
38. Katoh K, Yamamoto K, Kajiwara T, Takeya J, Breedlove BK, Yamashita M (2011) Magnetic properties of lanthanoid(III) phthalocyaninato triple-decker complexes in an external magnetic field and electronic transport properties for molecular spintronics. J Phys Conf Ser 303:012035/012031-012035/012010
39. Katoh K, Asano R, Miura A, Horii Y, Morita T, Breedlove BK, Yamashita M (2014) Effect of f-f interactions on quantum tunnelling of the magnetization: mono- and dinuclear Dy(III) phthalocyaninato triple-decker single-molecule magnets with the same octacoordination environment. Dalton Trans 43:7716–7725
40. Sakaue S, Fuyuhiro A, Fukuda T, Ishikawa N (2012) Dinuclear single-molecule magnets with porphyrin-phthalocyanine mixed triple-decker ligand systems giving SAP and SP coordination polyhedra. Chem Commun 48:5337–5339
41. Kan J, Wang H, Sun W, Cao W, Tao J, Jiang J (2013) Sandwich-type mixed tetrapyrrole rare-earth triple-decker compounds. Effect of the coordination geometry on the single-molecule-magnet nature. Inorg Chem 52:8505–8510
42. Wang H, Liu C, Liu T, Zeng S, Cao W, Ma Q, Duan C, Dou J, Jiang J (2013) Mixed (phthalocyaninato)(Schiff-base) di-dysprosium sandwich complexes. Effect of magnetic coupling on the SMM behavior. Dalton Trans 42(43):15355–15360
43. Zhu J, Song H-F, Yan P-F, Hou G-F, Li G-M (2013) Slow relaxation processes of salen type Dy2 complex and 1D ionic spiral Dyn coordination polymer. CrystEngComm 15(9):1747–1752

44. Yi X, Bernot K, Cador O, Luzon J, Calvez G, Daiguebonne C, Guillou O (2013) Influence of ferromagnetic connection of Ising-type Dy^{III}-based single ion magnets on their magnetic slow relaxation. Dalton Trans 42:6728–6731

45. Sato R, Suzuki K, Sugawa M, Mizuno N (2013) Heterodinuclear lanthanoid-containing polyoxometalates: stepwise synthesis and single-molecule magnet behavior. Chemistry 19:12982–12990

46. Suzuki K, Sato R, Mizuno N (2013) Reversible switching of single-molecule magnet behaviors by transformation of dinuclear dysprosium cores in polyoxometalates. Chem Sci 4:596–600

47. Guo Y-N, Xu G-F, Wernsdorfer W, Ungur L, Guo Y, Tang J, Zhang H-J, Chibotaru LF, Powell AK (2011) Strong axiality and Ising exchange interaction suppress zero-field tunneling of magnetization of an asymmetric Dy2 single-molecule magnet. J Am Chem Soc 133:11948–11951

48. Guo Y-N, Chen X-H, Xue S, Tang J (2011) Modulating magnetic dynamics of three Dy$_2$ complexes through Keto-Enol tautomerism of the o-vanillin picolinoylhydrazone ligand. Inorg Chem 50:9705–9713

49. Zou L, Zhao L, Chen P, Guo Y-N, Guo Y, Li Y-H, Tang J (2012) Phenoxido and alkoxido-bridged dinuclear dysprosium complexes showing single-molecule magnet behaviour. Dalton Trans 41:2966–2971

50. Hutchings A-J, Habib F, Holmberg RJ, Korobkov I, Murugesu M (2014) Structural rearrangement through lanthanide contraction in dinuclear complexes. Inorg Chem 53:2102–2112

51. Lin P-H, Burchell TJ, Clerac R, Murugesu M (2008) Dinuclear dysprosium(III) single-molecule magnets with a large anisotropic barrier. Angew Chem Int Ed 47:8848–8851

52. Kahn ML, Ballou R, Porcher P, Kahn O, Sutter JP (2002) Analytical determination of the {Ln-aminoxyl radical} exchange interaction taking into account both the ligand-field effect and the spin-orbit coupling of the lanthanide ion (Ln = Dy^{III} and Ho^{III}). Chemistry 8:525–531

53. Zhang P, Zhang L, Lin S-Y, Xue S, Tang J (2013) Modulating magnetic dynamics of Dy$_2$ system through the coordination geometry and magnetic interaction. Inorg Chem 52:4587–4592

54. Long J, Habib F, Lin P-H, Korobkov I, Enright G, Ungur L, Wernsdorfer W, Chibotaru LF, Murugesu M (2011) Single-molecule magnet behavior for an antiferromagnetically superexchange-coupled dinuclear dysprosium(III) complex. J Am Chem Soc 133:5319–5328

55. Habib F, Lin P-H, Long J, Korobkov I, Wernsdorfer W, Murugesu M (2011) The use of magnetic dilution to elucidate the slow magnetic relaxation effects of a Dy$_2$ single-molecule magnet. J Am Chem Soc 133:8830–8833

56. Habib F, Brunet G, Vieru V, Korobkov I, Chibotaru LF, Murugesu M (2013) Significant enhancement of energy barriers in dinuclear dysprosium single-molecule magnets through electron-withdrawing effects. J Am Chem Soc 135:13242–13245

57. Lin P-H, Sun W-B, Yu M-F, Li G-M, Yan P-F, Murugesu M (2011) An unsymmetrical coordination environment leading to two slow relaxation modes in a Dy$_2$ single-molecule magnet. Chem Commun 47:10993–10995

58. Lin P-H, Sun W-B, Tian Y-M, Yan P-F, Ungur L, Chibotaru LF, Murugesu M (2012) Ytterbium can relax slowly too. A field-induced Yb$_2$ single-molecule magnet. Dalton Trans 41:12349–12352

59. Liu T-Q, Yan P-F, Luan F, Li Y-X, Sun J-W, Chen C, Yang F, Chen H, Zou X-Y, Li G-M (2015) Near-IR luminescence and field-induced single molecule magnet of four salen-type ytterbium complexes. Inorg Chem 54:221–228

60. Nematirad M, Gee WJ, Langley SK, Chilton NF, Moubaraki B, Murray KS, Batten SR (2012) Single molecule magnetism in a μ-phenolato dinuclear lanthanide motif ligated by heptadentate Schiff base ligands. Dalton Trans 41:13711–13715

61. Zhao L, Wu J, Ke H, Tang J (2013) Three dinuclear lanthanide(III) compounds of a polydentate Schiff base ligand: slow magnetic relaxation behavior of the Dy[III] derivative. CrystEngComm 15:5301–5306

62. Pointillart F, Le Gal Y, Golhen S, Cador O, Ouahab L (2011) Single-molecule magnet behaviour in a tetrathiafulvalene-based electroactive antiferromagnetically coupled dinuclear dysprosium(III) complex. Chemistry 17:10397–10404

63. Yi X, Bernot K, Pointillart F, Poneti G, Calvez G, Daiguebonne C, Guillou O, Sessoli R (2012) A luminescent and sublimable Dy[III]-based single-molecule magnet. Chemistry 18:11379–11387

64. Langley SK, Chilton NF, Ungur L, Moubaraki B, Chibotaru LF, Murray KS (2012) Heterometallic tetranuclear [Ln[III]₂Co[III]₂] complexes including suppression of quantum tunneling of magnetization in the [Dy[III]₂Co[III]₂] single molecule magnet. Inorg Chem 51:11873–11881

65. Langley SK, Ungur L, Chilton NF, Moubaraki B, Chibotaru LF, Murray KS (2014) Single-molecule magnetism in a family of {Co[III]₂Dy[III]₂} butterfly complexes: effects of ligand replacement on the dynamics of magnetic relaxation. Inorg Chem 53:4303–4315

66. Langley SK, Le C, Ungur L, Moubaraki B, Abrahams BF, Chibotaru LF, Murray KS (2015) Heterometallic 3d-4f single-molecule magnets: ligand and metal ion influences on the magnetic relaxation. Inorg Chem 54(7):3631–3642

67. Funes AV, Carrella L, Rentschler E, Alborés P (2014) {Co[III]₂Dy[III]₂} single molecule magnet with two resolved thermal activated magnetization relaxation pathways at zero field. Dalton Trans 43:2361–2364

68. Langley SK, Chilton NF, Moubaraki B, Murray KS (2013) Single-molecule magnetism in three related {Co[III]₂Dy[III]₂}-acetylacetonate complexes with multiple relaxation mechanisms. Inorg Chem 52:7183–7192

69. Langley SK, Chilton NF, Moubaraki B, Murray KS (2013) Anisotropy barrier enhancement via ligand substitution in tetranuclear {Co[III]₂Ln[III]₂} single molecule magnets. Chem Commun 49:6965–6967

70. Leng J-D, Liu J-L, Zheng Y-Z, Ungur L, Chibotaru LF, Guo F-S, Tong M-L (2013) Relaxations in heterolanthanide dinuclear single-molecule magnets. Chem Commun 49:158–160

71. Yang F, Zhou Q, Zeng G, Li G, Gao L, Shi Z, Feng S (2014) Anion effects on the structures and magnetic properties of binuclear lanthanide single-molecule magnets. Dalton Trans 43:1238–1245

72. Moreno Pineda E, Chilton NF, Marx R, Dörfel M, Sells DO, Neugebauer P, Jiang S-D, Collison D, van Slageren J, McInnes EJL, Winpenny REP (2014) Direct measurement of dysprosium(III) dysprosium(III) interactions in a single-molecule magnet. Nat Commun 5:5243

73. Wang C, Lin S-Y, Wu J, Yuan S-W, Tang J (2015) Employment of triketones to construct a dysprosium(III) single-molecule magnet. Dalton Trans 44:4648–4654

74. Ehama K, Ohmichi Y, Sakamoto S, Fujinami T, Matsumoto N, Mochida N, Ishida T, Sunatsuki Y, Tsuchimoto M, Re N (2013) Synthesis, structure, luminescent, and magnetic properties of carbonato-bridged Zn[II]₂Ln[III]₂ complexes [(μ4-CO₃)₂{Zn[II]LnLn[III](NO₃)}₂] (Ln[III] = Gd[III], Tb[III], Dy[III]; L1 = N,N′-Bis(3-methoxy-2-oxybenzylidene)-1,3-propanediaminato, L2 = N,N′-Bis(3-ethoxy-2-oxybenzylidene)-1,3-propanediaminato). Inorg Chem 52:12828–12841

75. Titos-Padilla S, Ruiz J, Herrera JM, Brechin EK, Wersndorfer W, Lloret F, Colacio E (2013) Dilution-triggered SMM behavior under zero field in a luminescent Zn₂Dy₂ tetranuclear complex incorporating carbonato-bridging ligands derived from atmospheric CO₂ fixation. Inorg Chem 52:9620–9626

76. Zhang P, Zhang L, Lin S-Y, Tang J (2013) Tetranuclear [MDy]₂ compounds and their dinuclear [MDy] (M = Zn/Cu) building units: their assembly, structures, and magnetic properties. Inorg Chem 52:6595–6602

77. Ruiz J, Lorusso G, Evangelisti M, Brechin EK, Pope SJA, Colacio E (2014) Closely-related $Zn^{II}_2Ln^{III}_2$ complexes (Ln^{III} = Gd, Yb) with either magnetic refrigerant or luminescent single-molecule magnet properties. Inorg Chem 53:3586–3594

78. Vallejo J, Cano J, Castro I, Julve M, Lloret F, Fabelo O, Canadillas-Delgado L, Pardo E (2012) Slow magnetic relaxation in carbonato-bridged dinuclear lanthanide(III) complexes with 2,3-quinoxalinediolate ligands. Chem Commun 48:7726–7728

79. Ren M, Bao S-S, Hoshino N, Akutagawa T, Wang B, Ding Y-C, Wei S, Zheng L-M (2013) Solvent responsive magnetic dynamics of a dinuclear dysprosium single molecule magnet. Chemistry 19:9619–9628

80. Bag P, Rastogi CK, Biswas S, Sivakumar S, Mereacre V, Chandrasekhar V (2015) Homodinuclear lanthanide {Ln_2} (Ln = Gd, Tb, Dy, Eu) complexes prepared from an o-vanillin based ligand: luminescence and single-molecule magnetism behavior. Dalton Trans 44:4328–4340

81. Zhang H, Lin S-Y, Xue S, Wang C, Tang J (2014) Acetato-bridged dinuclear lanthanide complexes with single molecule magnet behaviour for the Dy_2 species. Dalton Trans 43:6262–6268

82. Tuna F, Smith CA, Bodensteiner M, Ungur L, Chibotaru LF, McInnes EJL, Winpenny REP, Collison D, Layfield RA (2012) A high anisotropy barrier in a sulfur-bridged organodysprosium single-molecule magnet. Angew Chem Int Ed 51:6976–6980

83. Sulway SA, Layfield RA, Tuna F, Wernsdorfer W, Winpenny REP (2012) Single-molecule magnetism in cyclopentadienyl-dysprosium chlorides. Chem Commun 48:1508–1510

84. Layfield RA, McDouall JJW, Sulway SA, Tuna F, Collison D, Winpenny REP (2010) Influence of the N-bridging ligand on magnetic relaxation in an organometallic dysprosium single-molecule magnet. Chemistry 16:4442–4446

85. Ma Y, Xu G-F, Yang X, Li L-C, Tang J, Yan S-P, Cheng P, Liao D-Z (2010) Pyrazine-bridged Dy_2 single-molecule magnet with a large anisotropic barrier. Chem Commun 46:8264–8266

86. Li X-L, Chen C-L, Gao Y-L, Liu C-M, Feng X-L, Gui Y-H, Fang S-M (2012) Modulation of homochiral Dy^{III} complexes: single-molecule magnets with ferroelectric properties. Chemistry 18:14632–14637

87. Liang L, Peng G, Li G, Lan Y, Powell AK, Deng H (2012) In situ hydrothermal synthesis of dysprosium(III) single-molecule magnet with lanthanide salt as catalyst. Dalton Trans 41:5816–5823

88. Song Y-M, Luo F, Luo M-B, Liao Z-W, Sun G-M, Tian X-Z, Zhu Y, Yuan Z-J, Liu S-J, Xu W-Y, Feng X-F (2012) The application of single-crystal-to-single-crystal transformation towards adjustable SMM properties. Chem Commun 48:1006–1008

89. Liu S-J, Zhao J-P, Song W-C, Han S-D, Liu Z-Y, Bu X-H (2013) Slow magnetic relaxation in two new 1D/0D Dy^{III} complexes with a sterically hindered carboxylate ligand. Inorg Chem 52:2103–2109

90. Song Y-M, Luo F, Zhu Y, Tian X-Z, Sun G-M (2013) Carboxylate-bridged dinuclear Dy_2 single-molecule magnets: synthesis, structure, and magnetic studies. Aust J Chem 66:98–104

91. Xu G-F, Wang Q-L, Gamez P, Ma Y, Clerac R, Tang J, Yan S-P, Cheng P, Liao D-Z (2010) A promising new route towards single-molecule magnets based on the oxalate ligand. Chem Commun 46:1506–1508

92. Habib F, Long J, Lin P-H, Korobkov I, Ungur L, Wernsdorfer W, Chibotaru LF, Murugesu M (2012) Supramolecular architectures for controlling slow magnetic relaxation in field-induced single-molecule magnets. Chem Sci 3:2158–2164

93. Pointillart F, Klementieva S, Kuropatov V, Le Gal Y, Golhen S, Cador O, Cherkasov V, Ouahab L (2012) A single molecule magnet behaviour in a D3h symmetry Dy(III) complex involving a quinone-tetrathiafulvalene-quinone bridge. Chem Commun 48:714–716

94. Pointillart F, Le Guennic B, Cauchy T, Golhen S, Cador O, Maury O, Ouahab L (2013) A series of tetrathiafulvalene-based lanthanide complexes displaying either single molecule

magnet or luminescence-direct magnetic and photo-physical correlations in the ytterbium analogue. Inorg Chem 52:5978–5990

95. Feng M, Pointillart F, Lefeuvre B, Dorcet V, Golhen S, Cador O, Ouahab L (2015) Multiple single-molecule magnet behaviors in dysprosium dinuclear complexes involving a multiple functionalized tetrathiafulvalene-based ligand. Inorg Chem 54:4021–4028

96. Wang H, Qian K, Wang K, Bian Y, Jiang J, Gao S (2011) Sandwich-type tetrakis (phthalocyaninato) dysprosium-cadmium quadruple-decker SMM. Chem Commun 47:9624–9626

97. Wang H, Liu T, Wang K, Duan C, Jiang J (2012) Tetrakis(phthalocyaninato) rare-earth-cadmium-rare-earth quadruple-decker sandwich SMMs: suppression of QTM by long-distance f-f interactions. Chemistry 18:7691–7694

98. Katoh K, Horii Y, Yasuda N, Wernsdorfer W, Toriumi K, Breedlove BK, Yamashita M (2012) Multiple-decker phthalocyaninato dinuclear lanthanoid(III) single-molecule magnets with dual-magnetic relaxation processes. Dalton Trans 41:13582–13600

99. Horii Y, Katoh K, Yasuda N, Breedlove BK, Yamashita M (2015) Effects of f-f interactions on the single-molecule magnet properties of terbium(III)-phthalocyaninato quintuple-decker complexes. Inorg Chem 54:3297–3305

100. Wang H, Cao W, Liu T, Duan C, Jiang J (2013) Synthesis, structure, and single-molecule magnetic properties of rare-earth sandwich complexes with mixed phthalocyanine and Schiff base ligands. Chemistry 19:2266–2270

101. Rinehart JD, Fang M, Evans WJ, Long JR (2011) Strong exchange and magnetic blocking in $N_2^{3-\bullet}$-radical-bridged lanthanide complexes. Nat Chem 3:538–542

102. Rinehart JD, Fang M, Evans WJ, Long JR (2011) A $N_2^{3-\bullet}$ radical-bridged terbium complex exhibiting magnetic hysteresis at 14 K. J Am Chem Soc 133:14236–14239

103. Meihaus KR, Corbey JF, Fang M, Ziller JW, Long JR, Evans WJ (2014) Influence of an inner-sphere K^+ ion on the magnetic behavior of $N_2^{3-\bullet}$ radical-bridged dilanthanide complexes isolated using an external magnetic field. Inorg Chem 53:3099–3107

104. Demir S, Zadrozny JM, Nippe M, Long JR (2012) Exchange coupling and magnetic blocking in bipyrimidyl radical-bridged dilanthanide complexes. J Am Chem Soc 134:18546–18549

105. Demir S, Nippe M, Gonzalez MI, Long JR (2014) Exchange coupling and magnetic blocking in dilanthanide complexes bridged by the multi-electron redox-active ligand 2,3,5,6-tetra (2-pyridyl)pyrazine. Chem Sci 5:4701–4711

106. Poneti G, Bernot K, Bogani L, Caneschi A, Sessoli R, Wernsdorfer W, Gatteschi D (2007) A rational approach to the modulation of the dynamics of the magnetisation in a dysprosium-nitronyl-nitroxide radical complex. Chem Commun 2007:1807–1809

107. Mei X-L, Liu R-N, Wang C, Yang P-P, Li L-C, Liao D-Z (2012) Modulating spin dynamics of cyclic Ln^{III}-radical complexes (Ln^{III} = Tb, Dy) by using phenyltrifluoroacetylacetonate coligand. Dalton Trans 41:2904–2909

108. Tian H, Liu R, Wang X, Yang P, Li Z, Li L, Liao D (2009) Magnetic slow relaxation in cyclic Tb^{III}-nitronyl nitroxide radical complexes. Eur J Inorg Chem 2009:4498–4502

109. Xu J-X, Ma Y, Xu G-F, Liao D-Z, Tang J, Wang C, Zhou N, Yan S-P, Cheng P, Li L-C (2009) Four new lanthanide-nitronyl nitroxide (Ln^{III} = Pr^{III}, Sm^{III}, Eu^{III}, Tm^{III}) complexes and a Tb^{III} complex exhibiting single-molecule magnet behavior. Inorg Chem 48:8890–8896

110. Pointillart F, Bernot K, Poneti G, Sessoli R (2012) Crystal packing effects on the magnetic slow relaxation of Tb(III)-nitronyl nitroxide radical cyclic dinuclear clusters. Inorg Chem 51:12218–12229

111. Liu R, Zhang C, Li L, Liao D, Sutter J-P (2012) Ligand substitution effect on single-molecule magnet behavior in dinuclear dysprosium complexes with radical functionalized phenol as bridging ligands. Dalton Trans 41:12139–12144

112. Wang K, Qi D, Wang H, Cao W, Li W, Liu T, Duan C, Jiang J (2013) Binuclear phthalocyanine-based sandwich-type rare earth complexes: unprecedented two π-bridged biradical-metal integrated SMMs. Chemistry 19:11162–11166

113. Ungur L, Van den Heuvel W, Chibotaru LF (2009) Ab initio investigation of the non-collinear magnetic structure and the lowest magnetic excitations in dysprosium triangles. New J Chem 33:1224–1230

114. Ungur L, Lin S-Y, Tang J, Chibotaru LF (2014) Single-molecule toroics in Ising-type lanthanide molecular clusters. Chem Soc Rev 43:6894–6905

115. Xue S, Chen X-H, Zhao L, Guo Y-N, Tang J (2012) Two bulky-decorated triangular dysprosium aggregates conserving vortex-spin structure. Inorg Chem 51:13264–13270

116. Lin S-Y, Zhao L, Guo Y-N, Zhang P, Guo Y, Tang J (2012) Two new Dy3 triangles with trinuclear circular helicates and their single-molecule magnet behavior. Inorg Chem 51:10522–10528

117. Hänninen MM, Mota AJ, Aravena D, Ruiz E, Sillanpää R, Camón A, Evangelisti M, Colacio E (2014) Two C3-symmetric Dy_3^{III} complexes with triple Di-μ-methoxo-μ-phenoxo bridges, magnetic ground state, and single-molecule magnetic behavior. Chemistry 20:8410–8420

118. Shen S, Xue S, Lin S-Y, Zhao L, Tang J (2013) A triangular dysprosium with asymmetric central caps featuring ferromagnetic coupling and single-molecule magnet behaviour. Dalton Trans 42:10413–10416

119. Lin S-Y, Wang C, Zhao L, Tang J (2014) Enantioselective self-assembly of triangular Dy_3 clusters with single-molecule magnet behavior. Chem Asian J 9:3558–3564

120. Wang Y-X, Shi W, Li H, Song Y, Fang L, Lan Y, Powell AK, Wernsdorfer W, Ungur L, Chibotaru LF, Shen M, Cheng P (2012) A single-molecule magnet assembly exhibiting a dielectric transition at 470 K. Chem Sci 3:3366–3370

121. Hewitt IJ, Lan Y, Anson CE, Luzon J, Sessoli R, Powell AK (2009) Opening up a dysprosium triangle by ligand oximation. Chem Commun 2009:6765–6767

122. Guo F-S, Liu J-L, Leng J-D, Meng Z-S, Lin Z-J, Tong M-L, Gao S, Ungur L, Chibotaru LF (2011) Pure trinuclear 4f single-molecule magnets: synthesis, structures, magnetism and ab initio investigation. Chemistry 17:2458–2466

123. Anwar MU, Tandon SS, Dawe LN, Habib F, Murugesu M, Thompson LK (2012) Lanthanide complexes of tritopic bis(hydrazone) ligands: single-molecule magnet behavior in a linear Dy_3^{III} complex. Inorg Chem 51:1028–1034

124. Adhikary A, Sheikh JA, Biswas S, Konar S (2014) Synthesis, crystal structure and study of magnetocaloric effect and single molecular magnetic behaviour in discrete lanthanide complexes. Dalton Trans 43:9334–9343

125. Yang F, Yan P, Li Q, Chen P, Li G (2012) Salen-type triple-decker trinuclear Dy3 complexes showing slow magnetic relaxation behavior. Eur J Inorg Chem 2012:4287–4293

126. Liu C-S, Du M, Sañudo EC, Echeverria J, Hu M, Zhang Q, Zhou L-M, Fang S-M (2011) A luminescent linear trinuclear Dy^{III} complex exhibiting slow magnetic relaxation of single ion origin. Dalton Trans 40:9366–9369

127. Chilton NF, Deacon GB, Gazukin O, Junk PC, Kersting B, Langley SK, Moubaraki B, Murray KS, Schleife F, Shome M, Turner DR, Walker JA (2014) Structure, magnetic behavior, and anisotropy of homoleptic trinuclear lanthanoid 8-quinolinolate complexes. Inorg Chem 53:2528–2534

128. Lin P-H, Burchell TJ, Ungur L, Chibotaru LF, Wernsdorfer W, Murugesu M (2009) A polynuclear lanthanide single-molecule magnet with a record anisotropic barrier. Angew Chem Int Ed 48:9489–9492

129. Langley SK, Chilton NF, Gass IA, Moubaraki B, Murray KS (2011) Planar tetranuclear lanthanide clusters with the Dy_4 analogue displaying slow magnetic relaxation. Dalton Trans 40:12656–12659

130. Zheng Y-Z, Lan Y, Anson CE, Powell AK (2008) Anion-perturbed magnetic slow relaxation in planar {Dy4} clusters. Inorg Chem 47:10813–10815

131. Yadav M, Mereacre V, Lebedkin S, Kappes MM, Powell AK, Roesky PW (2015) Mononuclear and tetranuclear compounds of yttrium and dysprosium ligated by a salicylic Schiff-base derivative: synthesis, photoluminescence, and magnetism. Inorg Chem 54:773–781

132. Mondal KC, Kostakis GE, Lan Y, Powell AK (2013) Magnetic properties of five planar defect dicubanes of $[Ln^{III}_4(\mu_3\text{-OH})_2(L)_4(HL)_2]\cdot2THF$ (Ln = Gd, Tb, Dy, Ho and Er). Polyhedron 66:268–273

133. Yan P-F, Lin P-H, Habib F, Aharen T, Murugesu M, Deng Z-P, Li G-M, Sun W-B (2011) Planar tetranuclear Dy(III) single-molecule magnet and its Sm(III), Gd(III), and Tb(III) analogues encapsulated by salen-type and β-diketonate ligands. Inorg Chem 50:7059–7065

134. Sun W-B, Han B-L, Lin P-H, Li H-F, Chen P, Tian Y-M, Murugesu M, Yan P-F (2013) Series of dinuclear and tetranuclear lanthanide clusters encapsulated by salen-type and β-diketonate ligands: single-molecule magnet and fluorescence properties. Dalton Trans 42:13397–13403

135. Luan F, Liu T, Yan P, Zou X, Li Y, Li G (2015) Single-molecule magnet of a tetranuclear dysprosium complex disturbed by a salen-type ligand and chloride counterions. Inorg Chem 54:3485–3490

136. Abbas G, Lan Y, Kostakis GE, Wernsdorfer W, Anson CE, Powell AK (2010) Series of isostructural planar lanthanide complexes $[Ln^{III}_4(\mu_3\text{-OH})_2(mdeaH)_2(piv)_8]$ with single molecule magnet behavior for the Dy4 analogue. Inorg Chem 49:8067–8072

137. Abbas G, Kostakis GE, Lan Y, Powell AK (2012) Synthesis and characterization of isostructural tetranuclear lanthanide complexes $[Ln_4(\mu_3\text{-OH})_2(ampdH_4)_2(piv)_{10}]\cdot4CH_3CN$ (Ln = Sm, Eu, Gd, Tb, Dy, Ho, Er). Polyhedron 41:1–6

138. Liu C-M, Zhang D-Q, Zhu D-B (2013) A single-molecule magnet featuring a parallelogram $[Dy_4(OCH_2^-)_4]$ core and two magnetic relaxation processes. Dalton Trans 42:14813–14818

139. Guo P-H, Liu J-L, Zhang Z-M, Ungur L, Chibotaru LF, Leng J-D, Guo F-S, Tong M-L (2012) The first {Dy₄} single-molecule magnet with a toroidal magnetic moment in the ground state. Inorg Chem 51:1233–1235

140. Guo P-H, Liu J-L, Jia J-H, Wang J, Guo F-S, Chen Y-C, Lin W-Q, Leng J-D, Bao D-H, Zhang X-D, Luo J-H, Tong M-L (2013) Multifunctional Dy^{III}_4 cluster exhibiting white-emitting, ferroelectric and single-molecule magnet behavior. Chemistry 19:8769–8773

141. Liu J, Chen Y-C, Jiang Z-X, Liu J-L, Jia J-H, Wang L-F, Li Q-W, Tong M-L (2015) Efficient enhancement of magnetic anisotropy by optimizing the ligand-field in a typically tetranuclear dysprosium cluster. Dalton Trans 44:8150–8155

142. Chandrasekhar V, Hossain S, Das S, Biswas S, Sutter J-P (2013) Rhombus-shaped tetranuclear [Ln₄] complexes [Ln = Dy(III) and Ho(III)]: synthesis, structure, and SMM behavior. Inorg Chem 52:6346–6353

143. Bi Y, Wang X-T, Liao W, Wang X, Deng R, Zhang H, Gao S (2009) Thiacalix[4]arene-supported planar Ln4 (Ln = Tb^{III}, Dy^{III}) clusters: toward luminescent and magnetic bifunctional materials. Inorg Chem 48:11743–11747

144. Xue S, Zhao L, Guo Y-N, Chen X-H, Tang J (2012) Field enhanced thermally activated mechanism in a square Dy4 aggregate. Chem Commun 48:7031–7033

145. Anwar MU, Thompson LK, Dawe LN, Habib F, Murugesu M (2012) Predictable self-assembled $[2\times2]$ Ln(III)₄ square grids (Ln = Dy,Tb)-SMM behaviour in a new lanthanide cluster motif. Chem Commun 48:4576–4578

146. Randell NM, Anwar MU, Drover MW, Dawe LN, Thompson LK (2013) Self-assembled Ln (III)₄ (Ln = Eu, Gd, Dy, Ho, Yb) $[2\times2]$ square grids: a new class of lanthanide cluster. Inorg Chem 52:6731–6742

147. Xue S, Zhao L, Guo Y-N, Tang J (2012) A novel windmill-type Dyiii $[2\times2]$ grid exhibiting slow magnetic relaxation. Dalton Trans 41:351–353

148. Woodruff DN, Tuna F, Bodensteiner M, Winpenny REP, Layfield RA (2013) Single-molecule magnetism in tetrametallic terbium and dysprosium thiolate cages. Organometallics 32:1224–1229

149. Guo Y-N, Xu G-F, Gamez P, Zhao L, Lin S-Y, Deng R, Tang J, Zhang H-J (2010) Two-step relaxation in a linear tetranuclear dysprosium(III) aggregate showing single-molecule magnet behavior. J Am Chem Soc 132:8538–8539

150. Ke H, Xu G-F, Guo Y-N, Gamez P, Beavers CM, Teat SJ, Tang J (2010) A linear tetranuclear dysprosium(III) compound showing single-molecule magnet behavior. Chem Commun 46:6057–6059

151. Lin S-Y, Zhao L, Ke H, Guo Y-N, Tang J, Guo Y, Dou J (2012) Steric hindrances create a discrete linear Dy_4 complex exhibiting SMM behaviour. Dalton Trans 41:3248–3252

152. Yang P-P, Gao X-F, Song H-B, Zhang S, Mei X-L, Li L-C, Liao D-Z (2011) Slow magnetic relaxation in novel Dy_4 and Dy_8 compounds. Inorg Chem 50:720–722

153. Alexandropoulos DI, Cunha-Silva L, Pham L, Bekiari V, Christou G, Stamatatos TC (2014) Tetranuclear lanthanide(III) complexes with a zigzag topology from the use of pyridine-2,6-dimethanol: synthetic, structural, spectroscopic, magnetic and photoluminescence studies. Inorg Chem 53:3220–3229

154. Koo BH, Lim KS, Ryu DW, Lee WR, Koh EK, Hong CS (2012) A unique tetranuclear Er^{III}_4 cluster exhibiting field-induced single-molecule magnetism. Chem Commun 48:2519–2521

155. Koo BH, Lim KS, Ryu DW, Lee WR, Koh EK, Hong CS (2013) Synthesis, structures and magnetic characterizations of isostructural tetranuclear Ln_4 clusters (Ln = Dy, Ho, and Eu). Dalton Trans 42:7204–7209

156. Guo P-H, Meng Y, Chen Y-C, Li Q-W, Wang B-Y, Leng J-D, Bao D-H, Jia J-H, Tong M-L (2014) A zigzag DyIII4 cluster exhibiting single-molecule magnet, ferroelectric and white-light emitting properties. J Mater Chem C 2:8858–8864

157. Gao Y, Xu G-F, Zhao L, Tang J, Liu Z (2009) Observation of slow magnetic relaxation in discrete dysprosium cubane. Inorg Chem 48:11495–11497

158. Liu C-M, Zhang D-Q, Hao X, Zhu D-B (2012) Syntheses, crystal structures, and magnetic properties of two p-tert-butylsulfonylcalix[4]arene supported cluster complexes with a totally disordered $Ln_4(OH)_4$ cubane core. Cryst Growth Des 12:2948–2954

159. Das S, Dey A, Biswas S, Colacio E, Chandrasekhar V (2014) Hydroxide-free cubane-shaped tetranuclear $[Ln_4]$ complexes. Inorg Chem 53:3417–3426

160. Lin P-H, Korobkov I, Wernsdorfer W, Ungur L, Chibotaru LF, Murugesu M (2011) A rare μ_4-O centered Dy_4 tetrahedron with coordination-induced local chirality and single-molecule magnet behaviour. Eur J Inorg Chem 2011:1535–1539

161. Zhang L, Zhang P, Zhao L, Lin S-Y, Xue S, Tang J, Liu Z (2013) Two locally chiral dysprosium compounds with salen-type ligands that show slow magnetic relaxation behavior. Eur J Inorg Chem 2013:1351–1357

162. Gass IA, Moubaraki B, Langley SK, Batten SR, Murray KS (2012) A π-π 3D network of tetranuclear μ_2/μ_3-carbonato Dy(III) bis-pyrazolylpyridine clusters showing single molecule magnetism features. Chem Commun 48:2089–2091

163. Blagg RJ, Ungur L, Tuna F, Speak J, Comar P, Collison D, Wernsdorfer W, McInnes EJL, Chibotaru LF, Winpenny REP (2013) Magnetic relaxation pathways in lanthanide single-molecule magnets. Nat Chem 5:673–678

164. Zou H-H, Wang R, Chen Z-L, Liu D-C, Liang F-P (2014) Series of edge-sharing bi-triangle Ln_4 clusters with a μ_4-NO_3- bridge: syntheses, structures, luminescence, and the SMM behavior of the Dy_4 analogue. Dalton Trans 43:2581–2587

165. Xue S, Guo Y-N, Zhao L, Zhang P, Tang J (2014) Unique Y-shaped lanthanide aggregates and single-molecule magnet behaviour for the Dy_4 analogue. Dalton Trans 43:1564–1570

166. Chandrasekhar V, Das S, Dey A, Hossain S, Sutter J-P (2013) Tetranuclear lanthanide (III) complexes containing dimeric subunits: single-molecule magnet behavior for the Dy_4 analogue. Inorg Chem 52:11956–11965

167. Morita T, Katoh K, Breedlove BK, Yamashita M (2013) Controlling the dipole-dipole interactions between terbium(III) phthalocyaninato triple-decker moieties through spatial control using a fused phthalocyaninato ligand. Inorg Chem 52:13555–13561

168. Blagg RJ, Muryn CA, McInnes EJL, Tuna F, Winpenny REP (2011) Single pyramid magnets: Dy_5 pyramids with slow magnetic relaxation to 40 K. Angew Chem Int Ed 50:6530–6533

169. Blagg RJ, Tuna F, McInnes EJL, Winpenny REP (2011) Pentametallic lanthanide-alkoxide square-based pyramids: high energy barrier for thermal relaxation in a holmium single molecule magnet. Chem Commun 47:10587–10589

170. Gamer MT, Lan Y, Roesky PW, Powell AK, Clérac R (2008) Pentanuclear dysprosium hydroxy cluster showing single-molecule-magnet behavior. Inorg Chem 47:6581–6583

171. Thielemann DT, Wagner AT, Lan Y, Anson CE, Gamer MT, Powell AK, Roesky PW (2013) Slow magnetic relaxation in four square-based pyramidal dysprosium hydroxo clusters ligated by chiral amino acid anions - a comparative study. Dalton Trans 42:14794–14800

172. Peng J-B, Kong X-J, Ren Y-P, Long L-S, Huang R-B, Zheng L-S (2012) Trigonal bipyramidal Dy_5 cluster exhibiting slow magnetic relaxation. Inorg Chem 51:2186–2190

173. Tian H, Zhao L, Lin H, Tang J, Li G (2013) Butterfly-shaped pentanuclear dysprosium single-molecule magnets. Chemistry 19:13235–13241

174. Hussain B, Savard D, Burchell TJ, Wernsdorfer W, Murugesu M (2009) Linking high anisotropy Dy_3 triangles to create a Dy_6 single-molecule magnet. Chem Commun 2009:1100–1102

175. Hewitt IJ, Tang J, Madhu NT, Anson CE, Lan Y, Luzon J, Etienne M, Sessoli R, Powell AK (2010) Coupling Dy_3 triangles enhances their slow magnetic relaxation. Angew Chem Int Ed 49:6352–6356

176. Lin S-Y, Wernsdorfer W, Ungur L, Powell AK, Guo Y-N, Tang J, Zhao L, Chibotaru LF, Zhang H-J (2012) Coupling Dy_3 triangles to maximize the toroidal moment. Angew Chem Int Ed 51:12767–12771

177. Tian H, Guo Y-N, Zhao L, Tang J, Liu Z (2011) Hexanuclear dysprosium(III) compound incorporating vertex- and edge-sharing Dy_3 triangles exhibiting single-molecule-magnet behavior. Inorg Chem 50:8688–8690

178. Tian H, Wang M, Zhao L, Guo Y-N, Guo Y, Tang J, Liu Z (2012) A discrete dysprosium trigonal prism showing single-molecule magnet behaviour. Chemistry 18:442–445

179. Guo Y-N, Chen X-H, Xue S, Tang J (2012) Molecular assembly and magnetic dynamics of two novel Dy_6 and Dy_8 aggregates. Inorg Chem 51:4035–4042

180. Das S, Hossain S, Dey A, Biswas S, Sutter J-P, Chandrasekhar V (2014) Molecular magnets based on homometallic hexanuclear lanthanide(III) complexes. Inorg Chem 53:5020–5028

181. Ke H, Zhao L, Guo Y, Tang J (2011) A Dy6 cluster displays slow magnetic relaxation with an edge-to-edge arrangement of two Dy3 triangles. Eur J Inorg Chem 2011:4153–4156

182. Bi YF, Xu GC, Liao WP, Du SC, Deng RP, Wang BW (2012) Calixarene-supported hexadysprosium cluster showing single molecule magnet behavior. Sci China Chem 55:967–972

183. Langley SK, Moubaraki B, Murray KS (2012) Magnetic properties of hexanuclear lanthanide (III) clusters incorporating a central μ_6-carbonate ligand derived from atmospheric CO_2 fixation. Inorg Chem 51:3947–3949

184. She S, Chen Y, Zaworotko MJ, Liu W, Cao Y, Wu J, Li Y (2013) Synthesis, structures and magnetic properties of a family of nitrate-bridged octanuclear $[Na_2Ln_6]$ (Ln = Dy, Tb, Gd, Sm) complexes. Dalton Trans 42:10433–10438

185. Sharples JW, Zheng Y-Z, Tuna F, McInnes EJL, Collison D (2011) Lanthanide discs chill well and relax slowly. Chem Commun 47:7650–7652

186. Guo F-S, Guo P-H, Meng Z-S, Tong M-L (2011) Slow magnetic relaxation in a novel heptanuclear Dy_7 cluster with five edge-sharing Dy_3 triangles. Polyhedron 30:3079–3082

187. Canaj AB, Tzimopoulos DI, Philippidis A, Kostakis GE, Milios CJ (2012) A strongly blue-emitting heptametallic $[Dy^{III}_7]$ centered-octahedral single-molecule magnet. Inorg Chem 51:7451–7453

188. Canaj AB, Tsikalas GK, Philippidis A, Spyros A, Milios CJ (2014) Heptanuclear lanthanide $[Ln_7]$ clusters: from blue-emitting solution-stable complexes to hybrid clusters. Dalton Trans 43:12486–12494

189. Mazarakioti EC, Poole KM, Cunha-Silva L, Christou G, Stamatatos TC (2014) A new family of Ln_7 clusters with an ideal D_{3h} metal-centered trigonal prismatic geometry, and SMM and photoluminescence behaviors. Dalton Trans 43:11456–11460

190. Savard D, Lin P-H, Burchell TJ, Korobkov I, Wernsdorfer W, Clerac R, Murugesu M (2009) Two-dimensional networks of lanthanide cubane-shaped dumbbells. Inorg Chem 48:11748–11754

191. Ke H, Gamez P, Zhao L, Xu G-F, Xue S, Tang J (2010) Magnetic properties of dysprosium cubanes dictated by the M–O–M angles of the $[Dy_4(\mu_3\text{-}OH)_4]$ core. Inorg Chem 49:7549–7557

192. Miao Y-L, Liu J-L, Li J-Y, Leng J-D, Ou Y-C, Tong M-L (2011) Two novel Dy_8 and Dy_{11} clusters with cubane $[Dy_4(\mu_3\text{-}OH)_4]^{8+}$ units exhibiting slow magnetic relaxation behaviour. Dalton Trans 40:10229–10236

193. Chesman ASR, Turner DR, Moubaraki B, Murray KS, Deacon GB, Batten SR (2012) In situ ligand formation in the synthesis of an octanuclear dysprosium 'double cubane' cluster displaying single molecule magnet features. Dalton Trans 41:3751–3757

194. Guo P, Liao X, Leng J, Tong M (2013) Synthesis, structures and single-molecule magnet behavior of octanuclear and decanuclear dysprosium clusters based on $[Dy_4(\mu_4\text{-}O)]$ tetrahedral subunits. Huaxue Xuebao 71:173–178

195. Tian H, Zhao L, Guo Y-N, Guo Y, Tang J, Liu Z (2012) Quadruple-CO32- bridged octanuclear dysprosium(III) compound showing single-molecule magnet behaviour. Chem Commun 48:708–710

196. Fang M, Zhao H, Prosvirin AV, Pinkowicz D, Zhao B, Cheng P, Wernsdorfer W, Brechin EK, Dunbar KR (2013) Squaring the cube: a family of octametallic lanthanide complexes including a Dy_8 single-molecule magnet. Dalton Trans 42:14693–14701

197. Alexandropoulos DI, Fournet A, Cunha-Silva L, Mowson AM, Bekiari V, Christou G, Stamatatos TC (2014) Fluorescent naphthalene diols as bridging ligands in Ln^{III} cluster chemistry: synthetic, structural, magnetic, and photophysical characterization of Ln^{III}_8 "Christmas stars". Inorg Chem 53:5420–5422

198. Langley SK, Moubaraki B, Murray KS (2013) Trinuclear, octanuclear and decanuclear dysprosium(III) complexes: synthesis, structural and magnetic studies. Polyhedron 64:255–261

199. Alexandropoulos DI, Mukherjee S, Papatriantafyllopoulou C, Raptopoulou CP, Psycharis V, Bekiari V, Christou G, Stamatatos TC (2011) A new family of nonanuclear lanthanide clusters displaying magnetic and optical properties. Inorg Chem 50:11276–11278

200. Zou H-H, Sheng L-B, Chen Z-L, Liang F-P (2015) Lanthanide nonanuclear clusters with sandglass-like topology and the SMM behavior of dysprosium analogue. Polyhedron 88:110–115

201. Ke H, Xu G-F, Zhao L, Tang J, Zhang X-Y, Zhang H-J (2009) A Dy_{10} cluster incorporates two sets of vertex-sharing Dy_3 triangles. Chemistry 15:10335–10338

202. Adhikary A, Jena HS, Khatua S, Konar S (2014) Synthesis and characterization of two discrete Ln_{10} nanoscopic cage-type cages: magnetic studies reveal a significant cryogenic magnetocaloric effect and slow magnetic relaxation. Chem Asian J 9:1083–1090

203. Miao Y-L, Liu J-L, Leng J-D, Lin Z-J, Tong M-L (2011) Chloride templated formation of $\{Dy_{12}(OH)_{16}\}^{20+}$ cluster core incorporating 1,10-phenanthroline-2,9-dicarboxylate. CrystEngComm 13:3345–3348

204. Zhao L, Xue S, Tang J (2012) A dodecanuclear dysprosium wheel assembled by six vertex-sharing Dy_3 triangles exhibiting slow magnetic relaxation. Inorg Chem 51:5994–5996

205. Thielemann DT, Wagner AT, Lan Y, Oña-Burgos P, Fernández I, Rösch ES, Kölmel DK, Powell AK, Bräse S, Roesky PW (2015) Peptoid-ligated pentadecanuclear yttrium and dysprosium hydroxy clusters. Chemistry 21:2813–2820

206. Gu X, Clérac R, Houri A, Xue D (2008) Slow relaxation of the magnetization in high-nuclearity Ln-complexes. Inorg Chim Acta 361(14):3873–3876

207. Rinehart JD, Long JR (2011) Exploiting single-ion anisotropy in the design of f-element single-molecule magnets. Chem Sci 2:2078–2085
208. Brown AJ, Pinkowicz D, Saber MR, Dunbar KR (2015) A trigonal-pyramidal erbium (III) single-molecule magnet. Angew Chem Int Ed 127:5962–5966
209. Pugh T, Tuna F, Ungur L, Collison D, McInnes EJ, Chibotaru LF, Layfield RA (2015) Influencing the properties of dysprosium single-molecule magnets with phosphorus donor ligands. Nat Commun 6:7492
210. Pugh T, Vieru V, Chibotaru LF, Layfield RA (2016) Magneto-structural correlations in arsenic-and selenium-ligated dysprosium single-molecule magnets. Chem Sci 7:2128–2137
211. Zhang L, Jung J, Zhang P, Guo M, Zhao L, Tang J, Le Guennic B (2016) Site-resolved two-step relaxation process in an asymmetric Dy_2 single-molecule magnet. Chemistry 22 (4):1392–1398
212. Chow CY, Bolvin H, Campbell VE, Guillot R, Kampf JW, Wernsdorfer W, Gendron F, Autschbach J, Pecoraro VL, Mallah T (2015) Assessing the exchange coupling in binuclear lanthanide (iii) complexes and the slow relaxation of the magnetization in the antiferromagnetically coupled Dy_2 derivative. Chem Sci 6(7):4148–4159
213. Xue S, Guo YN, Ungur L, Tang J, Chibotaru LF (2015) Tuning the magnetic interactions and relaxation dynamics of Dy_2 single-molecule magnets. Chemistry 21(40):14099–14106
214. Tian H, Bao S-S, Zheng L-M (2016) Cyclic single-molecule magnets: from the odd-numbered heptanuclear to a dimer of heptanuclear dysprosium clusters. Chem Commun 52:2314–2317
215. Das S, Dey A, Kundu S, Biswas S, Narayanan RS, Titos-Padilla S, Lorusso G, Evangelisti M, Colacio E, Chandrasekhar V (2015) Decanuclear Ln_{10} wheels and vertex-shared spirocyclic Ln_5 cores: synthesis, structure, SMM behavior, and MCE properties. Chemistry 21 (47):16955–16967

Molecular Rare Earth Hydride Clusters

Takanori Shima and Zhaomin Hou

Abstract This chapter describes the synthesis, structure, and reactivity of molecular rare earth hydride clusters consisting of the dihydride species "(L)LnH$_2$" bearing one anionic supporting ligand per metal. Generally, hydrogenolysis of the dialkyl precursors [(L)LnR$_2$] with H$_2$ easily leads to formation of polynuclear rare earth hydride clusters through self-assembly of the resulting dihydride species. The molecular structure and reactivity of the hydride clusters are significantly influenced by both the bulkiness of the ancillary ligands and the size of the metal ions. Unique reactivities are observed with various substrates, including CO, CO$_2$, H$_2$, and unsaturated C–C and C–N bonds, because of the synergistic effects of the multiple metal-hydride sites.

Keywords Cluster • Heteromultimetallic • Hydride • Multimetallic • Synergistic effect

Contents

T. Shima and Z. Hou (✉)
Organometallic Chemistry Laboratory, RIKEN Center for Sustainable Resource Science, RIKEN, 2-1 Hirosawa, Wako, Saitama 351-0198, Japan
e-mail: houz@riken.jp

1   Introduction

Rare-earth metal hydrides play an important role in a wide range of catalytic and stoichiometric reactions. They are highly reactive and effective for a number of chemical transformations not only due to the nucleophilicity and basicity of the hydride species, but also due to the strong Lewis acidity and oxophilicity of the metal centers. Moreover, as rare-earth metals are constituents in materials which have high hydrogen storage capacities (e.g., $LaNi_5H_x$), molecular hydride clusters are expected to shed light on the chemistry of hydrogen in these systems.

Since the 1980s, well-defined rare-earth metal hydrides bearing two monoanionic cyclopentadienyl ligands per metal (such as **A**, Scheme 1) have been well investigated [1–3]. Such metallocene hydride complexes are highly reactive for a number of transformations including addition of the metal hydride to C=C, C=O, and C≡N bonds of organic compounds and reduction of carbon monoxide (CO) to an enediolate unit (OCH=CHO). Whilst such complexes have been shown to adopt bi- or polymeric structures in solid state, their reactions in solution tend to occur at a mononuclear metal center containing a single hydride ligand [4].

Recently, rare earth dihydrides of the type "(L)LnH$_2$" (**B**) (Ln = rare-earth metals) bearing one anionic supporting ligand per metal have received much attention. These species can undergo "self-assembly" to give the corresponding multimetallic rare earth hydride clusters, which show unique structures and reactivities that are different from those bearing two anionic supporting ligands per metal. This is a consequence of both synergistic effects among those metal atoms and the number of reactive hydrides present. This chapter focuses on the synthesis, structures, and reactivities of this new class of molecular rare earth hydride clusters [5, 6].

Scheme 1 Rare earth hydride complexes bearing two (**A**) and one (**B**) cyclopentadienyl ligands
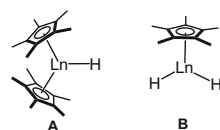
2 Synthesis and Structure of Neutral Rare Earth Hydride Clusters

2.1 *Cyclopentadienyl-Ligated Hydride Clusters*

Recently, a series of highly reactive half-sandwich type rare earth dialkyl complexes, $[(C_5Me_4R)LnR'_2(THF)_n]$ (**1-Ln**: R = $SiMe_3$; R' = CH_2SiMe_3, $o\text{-}CH_2C_6H_4NMe_2$; **1-Ln^R**: R = Me, H; R' = CH_2SiMe_3, $o\text{-}CH_2C_6H_4NMe_2$), have been isolated and structurally characterized, which possess the monoanionic cyclopentadienyl ligands such as $C_5Me_4SiMe_3$ with the nucleophilic primary alkyl groups such as CH_2SiMe_3 or $o\text{-}CH_2C_6H_4NMe_2$. Treatment of those dialkyl complexes with one equivalent of a borate compound such as $[Ph_3C][B(C_6F_5)_4]$ can generate the cationic monoalkyl species, which serve as excellent catalysts for the polymerization and copolymerization of various olefins as well as for other chemical transformations such as methylalumination of alkenes and alkynes and C–H alkylation of anisoles and pyridines with alkenes [7, 8]. Remarkably, hydrogenolysis of the half-sandwich dialkyl complexes with H_2 has led to the formation of a new family of rare earth hydride clusters consisting of the "$(C_5Me_4R)LnH_2$" units.

The structures of the rare earth hydride clusters are dependent, to some extent, on the size of the metal radius [9, 10]. For example, the reaction of the $C_5Me_4SiMe_3$-ligated scandium dialkyl complex $[Cp'Sc(CH_2SiMe_3)_2(THF)]$ (**1-Sc**) (Cp' = $C_5Me_4SiMe_3$) with H_2 at room temperature provides the THF-free tetranuclear octahydride cluster $[\{Cp'Sc(\mu\text{-}H)_2\}_4]$ (**2-Sc**) (Scheme 2) [9, 10]. This complex can be considered a self-assembled architecture comprising four "$Cp'ScH_2$" units held together via "intermolecular" Sc–H interactions. Eight hydride ligands are present in the whole molecule; six of which are edge-bridged adopting a μ_2-H–Sc_2 coordination mode, one of which is face-capped in a μ_3-H–Sc_3 mode, and one of which is body-centered in a μ_4-H–Sc_4 fashion. The THF ligand is no longer present in the hydride cluster **2-Sc**.

Hydrogenolysis of the dialkyl complexes of medium sized rare-earth metals such as Y, Er, Tm, and Lu in toluene gives the corresponding tetranuclear octahydride clusters $[\{Cp'Ln(\mu\text{-}H)_2\}_4(THF)]$ (Ln = Y, Er, Tm, Lu) (**2-Ln**), in which one THF molecule is ligated to one of the four metal centers (Scheme 2) [9–13]. Despite the presence of a coordinated solvent, the structures of **2-Ln** are remarkably similar to that of the THF-free Sc cluster **2-Sc**.

As the size of the metal center increases to include Gd, Dy, and Ho, an agostic interaction between a methyl group of a $C_5Me_4SiMe_3$ ligand and an adjacent metal center is also observed, likely due to greater steric unsaturation caused by larger radius of the metal centers (Scheme 2) [9, 10]. It is worth noting that in the case of Dy and Y, the bis(THF)-coordinated clusters **2-Ln**(THF)$_2$ can also be isolated by recrystallization in THF solvent. In these cases, an interstitial μ_4-H ligand is not observed, and the tetranuclear metal frame is thus connected by four μ_2-H and four μ_3-H ligands. One THF molecule in **2-Ln**(THF)$_2$ is labile and can easily be
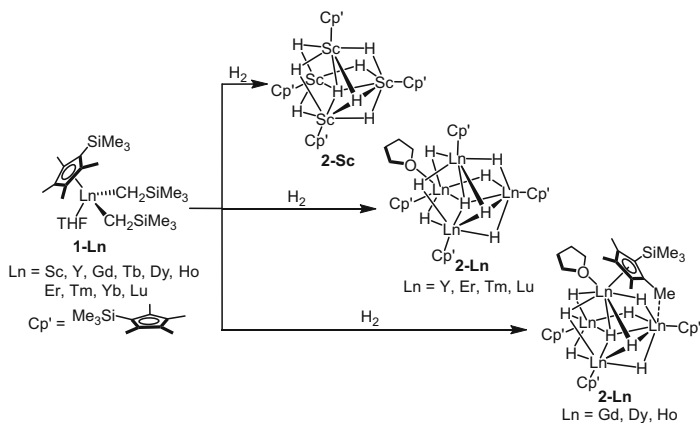
Scheme 2 Hydrogenolysis of dialkyl complexes **1-Ln**
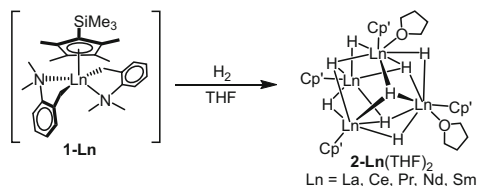
Scheme 3 Hydrogenolysis of bis(*o*-dimethylaminobenzyl)complexes of early lanthanide metals

removed to give the mono(THF)-coordinated analogues through recrystallization in appropriate solvents, such as toluene.

Due to difficulties in the synthesis of the half-sandwich CH_2SiMe_3 complexes of early (larger) lanthanide metals (La, Ce, Pr, Nd, and Sm), the analogous *o*-dimethylaminobenzyl complexes $[Cp'Ln(o\text{-}CH_2C_6H_4NMe_2)_2]$ were used for the synthesis of the corresponding hydride clusters, which upon hydrogenolysis in THF gave tetranuclear octahydride clusters $[\{Cp'Ln(\mu\text{-}H)_2\}_4(THF)_2]$ (**2-Ln**$(THF)_2$) bearing two THF ligands (Scheme 3) [10]. A mono(THF)-coordinated analogue was not obtained by recrystallization of bis(THF)-coordinated complexes **2-Ln** $(THF)_2$ of these larger metals in toluene, in contrast to **2-Y**$(THF)_2$ and **2-Dy** $(THF)_2$ described above.

The sterically less demanding pentamethylcyclopentadienyl-ligated samarium hydride cluster $[\{Cp*Sm(\mu\text{-}H)_2\}_6\{KH(THF)_2\}_3]$ ($Cp* = \eta^5\text{-}C_5Me_5$) was obtained by the reaction of the Sm^{II} alkyl complex $[\{Cp*SmCH(SiMe_3)_2\}\{Cp*K(THF)_2\}]$ with $PhSiH_3$ [14]. Previous attempts to hydrogenate the C_5Me_5-ligated dialkyl complexes $[Cp*Lu(CH_2CMe_3)_2(THF)]$ or $[Cp*Lu(CH_2CMe_3)\{CH(SiMe_3)_2\}$ (THF)] did not give a structurally characterizable hydride species [15]. However, hydrogenolysis of THF-free *o*-dimethylaminobenzyl *o*-$CH_2C_6H_4NMe_2$-ligated complexes $[(C_5Me_4R)Y(o\text{-}CH_2C_6H_4NMe_2)_2]$(**1-Y** and **1-Y**^{R}) (R = $SiMe_3$, Me, H) with H_2 or $PhSiH_3$ in THF or toluene afforded the corresponding tetra-, penta-, and
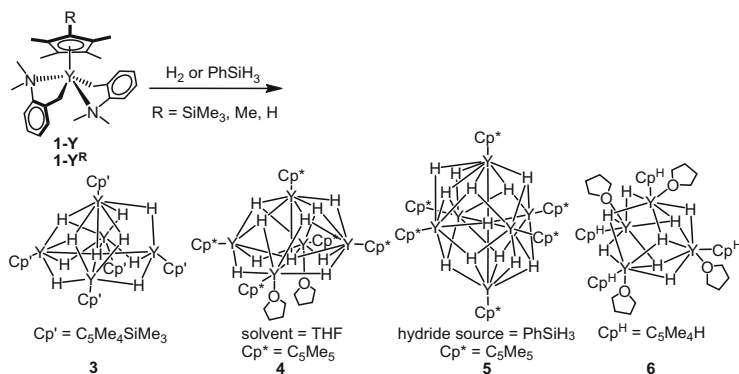
Scheme 4 Synthesis of tetra- (**6**), penta- (**3**, **4**), and hexanuclear (**5**) yttrium hydride clusters with different Cp ligands
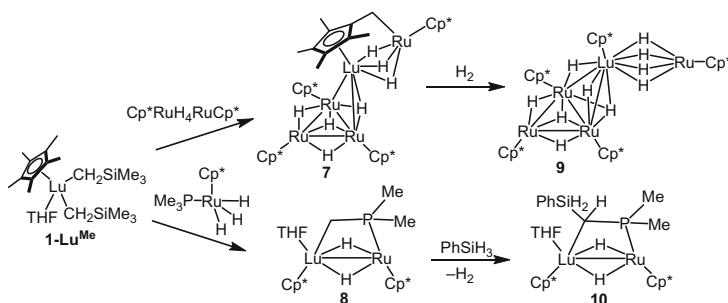
Scheme 5 Synthesis of d-f heterometallic hydrides

hexanuclear yttrium hydride clusters $[\{Cp'Y(\mu\text{-}H)_2\}_5]$ (**3**), $[\{Cp*Y(\mu\text{-}H)_2\}_5(THF)_2]$ (**4**), or $[\{Cp*Y(\mu\text{-}H)_2\}_6]$ (**5**), and $[\{(C_5Me_4H)Y(\mu\text{-}H)_2\}_4(THF)_4]$ (**6**) (Scheme 4) [16]. The nuclearities of these clusters are dependent on the ligand size, the reaction solvent, and the source of hydride used in the synthesis.

By use of a half-sandwich rare earth dialkyl complex such as $[Cp*Lu(CH_2SiMe_3)_2(THF)]$ (**1-Lu^{Me}**) as a building block to react with d-transition metal hydrides such as $[Cp*Ru(\mu\text{-}H)_4RuCp*]$ and $[Cp*Ru(PMe_3)H_3]$, the corresponding heterometallic hydride compounds (**7** and **8**) were synthesized as shown in Scheme 5 [17, 18]. Hydrogenolysis of **7** with H_2 afforded a decahydride cluster **9** as a result of addition of two molecules of H_2, while the reaction of **8** with PhSiH$_3$ provided a dehydrogenative silylation product **10**.

2.2 Pyrazolyl Borate-Ligated Hydride Clusters

Hydrogenolysis of the rare earth dialkyl complexes bearing tris (3,5-dimethylpyrazolyl)borate (Tp^{Me2}) ligands $[(Tp^{Me2})Ln(CH_2SiMe_3)_2(THF)]$
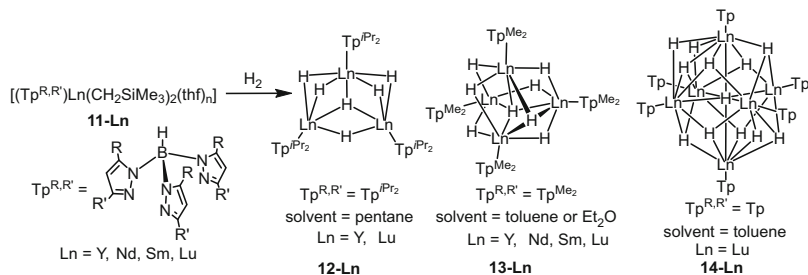
Scheme 6 Hydrogenolysis of pyrazolyl borate-ligated dialkyl complexes **11-Ln** to tri- (**12-Ln**), tetra- (**13-Ln**), and hexanuclear (**14-Ln**) hydride clusters

(**11-Ln**) with H_2 afforded the corresponding tetranuclear octahydride clusters $[\{(Tp^{Me2})Ln(\mu\text{-}H)_2\}_4]$ (**13-Ln**) (Ln = Y, Nd, Sm, Lu), in which the coordination modes of the hydride ligands are similar to those of the $C_5Me_4SiMe_3$-ligated analogues (see **2-Ln**). In contrast, hydrogenolysis of the more sterically demanding ^iPr substituted Tp^{iPr2}-ligated dialkyl complex $[(Tp^{iPr2})Ln(CH_2SiMe_3)_2(THF)]$ (Tp^{iPr2} = tris(3,5-diisopropylpyrazolyl)borate) afforded the trinuclear hexahydride clusters $[\{(Tp^{iPr2})Ln(\mu\text{-}H)_2\}_3]$ (**12-Ln**) (Ln = Y, Lu) [19], while hydrogenolysis of the less sterically demanding non-substituted Tp-ligated dialkyl complexes $[(Tp)Ln(CH_2SiMe_3)_2(THF)]$ (Tp = tris(pyrazolyl)borate) gave the hexanuclear dodecahydride clusters $[\{(Tp)Lu(\mu\text{-}H)_2\}_6]$ (**14-Ln**) (Scheme 6) [20].

2.3 Bis(Pyrazolyl)Carbazole-Ligated Hydride Clusters

The pyrazole-based lutetium trinuclear pentahydride cluster $[\{(CzPz^{iPr})Lu\}_3(\mu\text{-}H)_5]$ (**16**) was obtained by hydrogenolysis of the bis(alkyl) complex $[(CzPz^{iPr})Lu(CH_2SiMe_3)_2]$ (**15**) ($CzPz^{iPr}$ = 1,8-bis(3-isopropylpyrazolyl)carbazol) with H_2 (Scheme 7) [21]. Notably, one C–H bond on the pyrazolyl substituent of the ligand was activated via dehydrogenative metalation. Attempts to prepare the sterically less hindered $CzPz^{Me}$-ligated analogue of hydride cluster were unsuccessful.

2.4 NNNN Macrocycle-Ligated Hydride Clusters

Hydrogenolysis of rare earth dialkyl or diallyl complexes **17-Ln** bearing a monoanionic macrocyclic [NNNN] ligand such as Me_3TACD (Me_3TACD = 1,4,7-trimethyl-1,4,7,10-tetraazacyclododecane) with H_2 or $PhSiH_3$ afforded the corresponding multinuclear hydride clusters $[\{(Me_3TACD)Ln(\mu\text{-}H)_2\}_n]$ (n = 3: Ln = Y, Ho, Lu (**18-Ln**); n = 4: Ln = La, Ce, Pr (**19-Ln**)) (Scheme 8) [22–24]. The trinuclear hydride clusters **18-Ln** contained only μ_2-
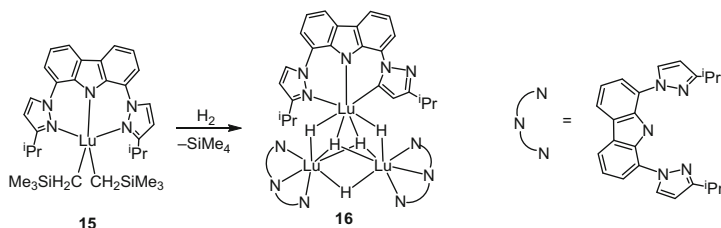
Scheme 7 Hydrogenolysis of a bis(pyrazolyl)carbazole-ligated dialkyl complex **15**
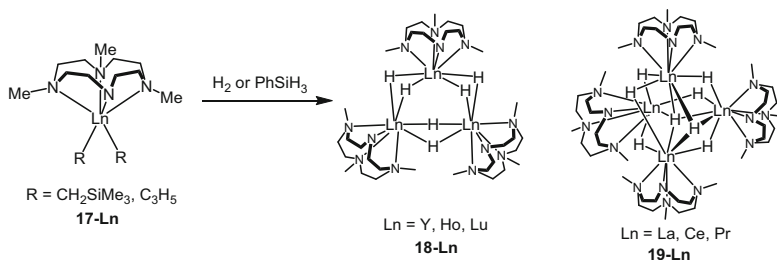
Scheme 8 Hydrogenolysis of macrocyclic [NNNN]-ligated dialkyl complexes **17-Ln** to tri-(**18-Ln**) and tetranuclear (**19-Ln**) hydride clusters

bridging hydrides, in contrast with those found in the trinuclear yttrium hydrides [{(Tp^{iPr2})Y(μ-H)$_2$}$_3$] (**12-Y**) [19] and [{(Me-PNP^{iPr})Y(μ-H)$_2$}$_3$] (**21-Y**) (Me-PNP^{iPr} = {4-Me-2-(^{i}Pr$_2$P)-C$_6$H$_3$}$_2$N) [25]. The core structures of the tetranuclear hydride clusters **19-Ln** are similar to those found in [{(Tp^{Me2})Ln(μ-H)$_2$}$_4$] (**13-Ln**) [20].

2.5 PNP-Ligated Hydride Clusters

Trinuclear rare earth hydride clusters [{(Me-PNP^{iPr})Ln(μ-H)$_2$}$_3$] (**21-Ln**) (Me-PNP^{iPr} = {2-(^{i}Pr$_2$P)-4-Me-C$_6$H$_3$}$_2$N) bearing the monoanionic bis(phosphinophenyl) amido ligands (PNP) were synthesized by hydrogenolysis of the dialkyl precursors **20-Ln** with H$_2$ (Scheme 9) [25]. The isolability of the hydride clusters is highly dependent on the substituents of the phosphine ligands. Hydrogenolysis of the dialkyl complex bearing the phenyl substituted phosphine (PNP^{Ph}) ligand gave a mixture of uncharacterized products, while hydrogenolysis of the dialkyl complex bearing an analogous diisopropyl-substituted ligand afforded the hydride cluster cleanly. The core structure of [{(Me-PNP^{iPr})Y(μ-H)$_2$}$_3$] (**21-Y**) contains two μ$_3$-H capping ligands and four μ$_2$-H bridging ligands, which is contrast to those of other trinuclear hexahydrides such as [{(Me$_3$TACD)Y(μ-H)$_2$}$_3$] (**18-Y**) (all six μ$_2$-H) [22] or [{(Tp^{iPr2})Y(μ-H)$_2$}$_3$] (**12-Y**) (one μ$_3$-H, five μ$_2$-H) [19].

The reaction of the PNP-ligated yttrium dialkyl complex **20-Y** with the ruthenium hydride complex [Cp*Ru(PPh$_2$Me)H$_3$] afforded heterobimetallic hydride
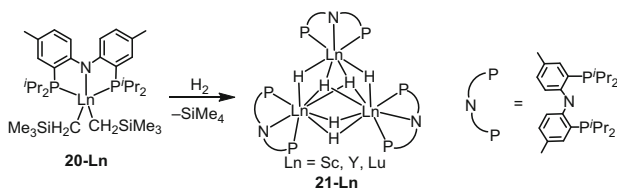
Scheme 9 Hydrogenolysis of PNP-ligated dialkyl complexes **20-Ln**
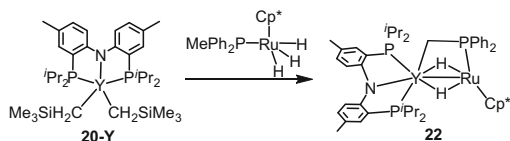
Scheme 10 Synthesis of a Y/Ru heterobimetallic hydride compound consisting of a PNP-ligated rare earth unit
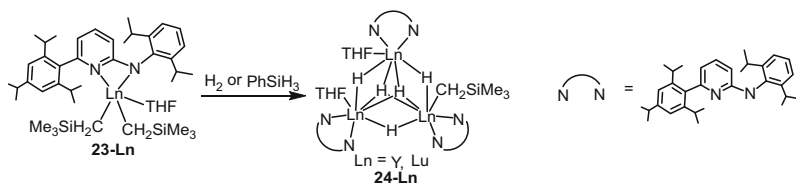
Scheme 11 Hydrogenolysis of amidinate-ligated dialkyl complexes **23-Ln**

compound [(Me-PNP^{iPr})Y(μ-H)$_2$(μ-CH$_2$PPh$_2$)RuCp*] (**22**) (Scheme 10) [26], similar to the Cp*-ligated lutetium analogue **8** [17].

2.6 Amidinate-Ligated Hydride Clusters

Hydrogenolysis of the amidopyridinate-ligated dialkyl complex [Ap*Ln(CH$_2$SiMe$_3$)$_2$(THF)] (**23-Ln**) (Ap* = ((2,6-diisopropylphenyl){6-(2,4,6)-triisopropylphenyl}pyridin-2-yl)amido) with H$_2$ or PhSiH$_3$ provided a partially hydrogenated trinuclear mixed alkyl/hydride cluster [(Ap*Ln)$_3$(μ-H)$_5$(CH$_2$SiMe$_3$)(THF)$_2$] (**24-Ln**) (Ln = Y, Lu) (Scheme 11) [27]. All attempts to remove the remaining alkyl group with hydride ligands to form polyhydride clusters consisting of Ap*LnH$_2$ units failed. Similar trinuclear alkyl/hydride clusters supported by the sterically less bulky analogous ligand, ((2,4,6-trimethylphenyl){6-(2,4,6)-triisopropylphenyl}pyridin-2-yl)amido ligand, were also recently reported [28].

Hydrogenolysis of the amidinate-ligated dialkyl complex **25** with H$_2$ gave the dinuclear hydride [{(NCN)YH$_2$}$_2$(THF)$_3$] (**26**) (NCN = PhC(NC$_6$H$_3$^{i}Pr$_2$-2,6)$_2$), which contains three μ_2-H ligands and one terminal hydride ligand (Scheme 12)
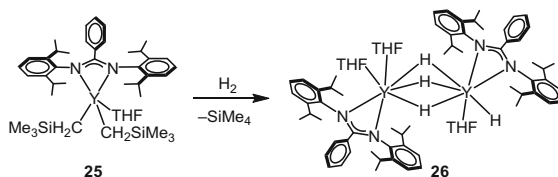
Scheme 12 Hydrogenolysis of amidinate-ligated dialkyl complex **25**
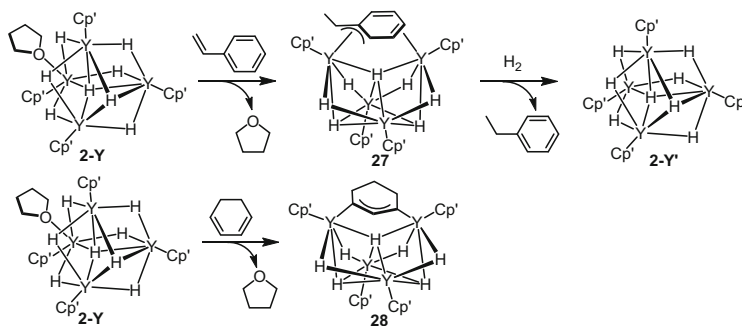
Scheme 13 Reactions of **2-Y** with styrene and 1,3-cyclohexadiene

[29]. This represents the first example of a structurally characterized bi- or multimetallic rare earth complex bearing a terminal hydride ligand.

3 Reactivity of Neutral Rare Earth Hydride Clusters

3.1 Reactions with Unsaturated C–C Bonds

The reaction of the mono(THF)-coordinated tetranuclear yttrium octahydride cluster $[\{Cp'Y(\mu\text{-H})_2\}_4(THF)]$ (**2-Y**) ($Cp' = C_5Me_4SiMe_3$) with styrene afforded the benzylic allyl heptahydride cluster **27**, in which the allyl moiety is bonded to one Y atom in an η^3-fashion and the phenyl moiety is bonded to another Y atom in an η^2-form (Scheme 13) [11]. No further reaction was observed even in the presence of excess styrene. Hydrogenolysis of **27** with H_2 afforded the THF-free yttrium octahydride cluster $[\{Cp'Y(\mu\text{-H})_2\}_4]$ (**2-Y′**) and ethylbenzene. Under atmospheric pressure of H_2, styrene can be catalytically hydrogenated into ethylbenzene by **2-Y** or **2-Y′**. Treatment of **2-Y** with 1,3-cyclohexadiene (CHD) provided the CHD insertion product **28**, in which the resulting allyl unit is bonded to two Y atoms in an η^1:η^1-fashion (Scheme 13). The addition of an excess of CHD to **28** did not lead to further reaction, as in the case of styrene [30].

The reaction of **2-Y** with 1,4-bis(trimethylsilyl)-1,3-butadiyne gave the tetranuclear yttrium tetrahydride cluster **29**, which consists formally of a
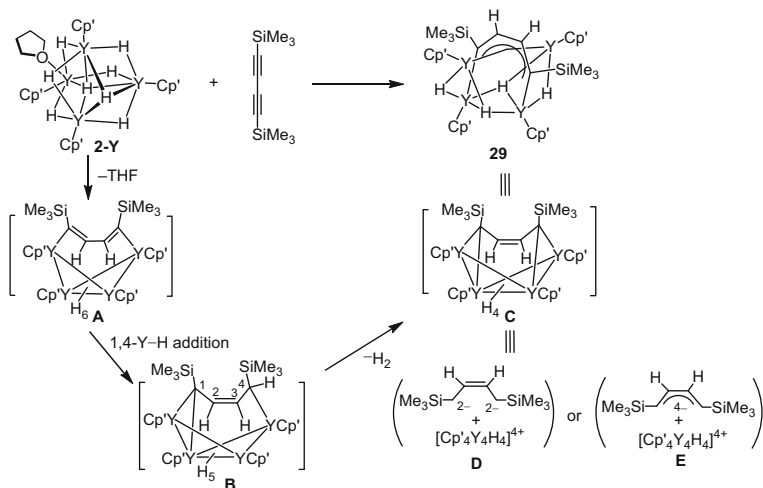
Scheme 14 Reactions of **2-Y** with 1,4-bis(trimethylsilyl)-1,3-butadiyne

$[\{Cp'YH\}_4]^{4+}$ unit bonded to a butene-tetraanion species (Scheme 14) [11]. The butene-tetraanion moiety in **29** is bonded in an "inverse sandwich" fashion, in which the butene-tetraanion adopts a planar structure with μ_4-coordination to two Y atoms and $\sigma{:}\eta^1$-coordination to the other two Y atoms. The formation of **29** can be explained by the following reaction paths. First, the two C≡C units of 1,4-bis (trimethylsilyl)-1,3-butadiyne react with two Y–H units of **2-Y** to afford the 1,3-butadiene-1,4-diyl hexahydride cluster **A**. Subsequently 1,4-Y–H addition to the 1,3-butadiene unit in **A** gives the 2-butene-1,1′,4-triyl/pentahydride species **B**. Deprotonation at the C4 position of the butene species by a Y–H unit affords the 2-butene-1,1′,4,4′-tetrayl/tetrahydride species **C** which can be described by the resonance structures **29**, **D**, and **E**.

The formation of a 2-butene-1,1′,4,4′-tetrayl species in the present reaction is in sharp contrast with the reaction of the binuclear ytterbium dihydride complex $[\{(Tp^{tBu,Me})Yb(\mu\text{-}H)\}_2]$ or the binuclear yttrium tetrahydride complex $[\{(NCN)Y(\mu\text{-}H)_2\}_2(THF)_3]$ (**26**) with 1,4-bis(trimethylsilyl)-1,3-butadiyne or 1,4-diphenyl-1,3-butadiyne, which yielded the enyne species $[(Tp^{tBu,Me})Yb(Me_3SiC\equiv C{-}C{=}CHSiMe_3)]$ [31] or 1,4-diphenyl-2-butyne-1,4-diyl species $[\{(NCN)YH(THF)\}_2(PhCH{-}C\equiv C{-}CHPh)]$ [29], respectively.

3.2 Reactions with Carbon Monoxide and Carbon Dioxide

Previous studies have shown that the reaction of rare earth metallocene monohydride complexes with CO mostly gave enediolate species $[CpLnOCH{=}CHOLnCp]$. In contrast, the reaction of the rare-earth metal-hydride
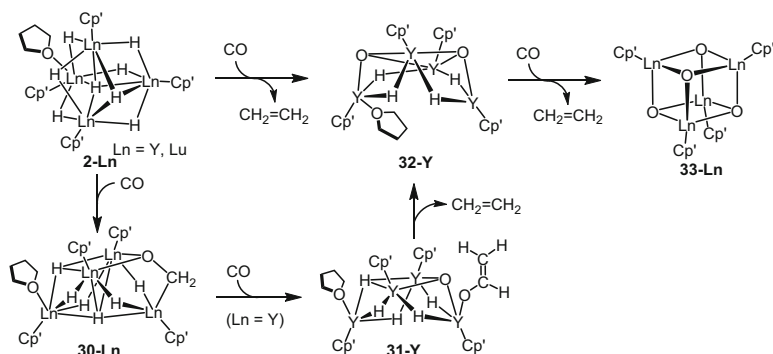
Scheme 15 Reactions of **2-Ln** with CO

clusters [{Cp′Ln(μ-H)$_2$}$_4$(THF)] (Ln = Y, Lu) (**2-Ln**) with CO resulted in unprecedented selective formation of ethylene and the corresponding tetraoxo cluster [{Cp′Ln(μ$_3$-O)}$_4$] (**33-Ln**) under mild conditions (Scheme 15). Stepwise formation of some key reaction intermediates, such as the oxymethylene [(Cp′Y)$_4$(μ-OCH$_2$)(μ-H)$_6$(THF)] (**30-Ln**), the enolate [(Cp′Y)$_4$(OCH=CH$_2$)(μ-O)(μ-H)$_5$(THF)] (**31-Y**), and the dioxo species [(Cp′Y)$_4$(μ$_3$-O)$_2$(μ-H)$_4$(THF)] (**32-Y**), has been confirmed, some of which have been isolated and structurally characterized by X-ray diffraction studies. These results may shed light on the mechanistic aspects of the Fischer–Tropsch processes, which produce hydrocarbons and oxygenates by hydrogenation of CO on heterogeneous transition metal catalysts [32].

With regard to non-Cp-ligated rare earth polyhydrides, the reaction of the tris (3,5-diisopropylpyrazolyl)borate-ligated trinuclear yttrium hydride cluster [{(Tp^{iPr2})Y(μ-H)$_2$}$_3$] (**12-Y**) with CO at room temperature was reported to afford the trinuclear hydride/oxo/propanolate cluster [(Tp^{iPr2}Y)$_3$(μ-H)(μ-O)$_2$ (μ-OCH$_2$CHCH$_2$)] (**34**) through hydrogenation and coupling of three CO molecules (Scheme 16) [19]. Heating a toluene solution of this complex released only propene with no observed formation of ethylene.

Reactions of the rare earth hydride clusters [{Cp′Ln(μ-H)$_2$}$_4$(THF)] (Ln = Y, Lu) (**2-Ln**) with CO$_2$ took place immediately, but no characterizable products could be obtained. In contrast, their action of the butene-tetraanion/tetrahydride cluster **29** with CO$_2$ afforded the structurally characterizable bis(methylene diolate) complex **35** in high yield (Scheme 17) [33]. In this reaction, both C=O double bonds in CO$_2$ are reduced to C–O single bonds, in contrast with the reactions of most transition metal hydrides, which usually give formate MOCHO species. The reaction of an aryl isocyanate compound ArNCO with **29** afforded the μ$_3$-oxo cluster **36**. The methylene diolate **35** and the oxo cluster **36** can undergo CO$_2$ insertion to give the structurally characterizable carbonate cluster **37**.
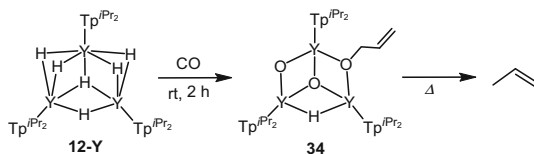
Scheme 16 Reaction of **12-Y** with CO
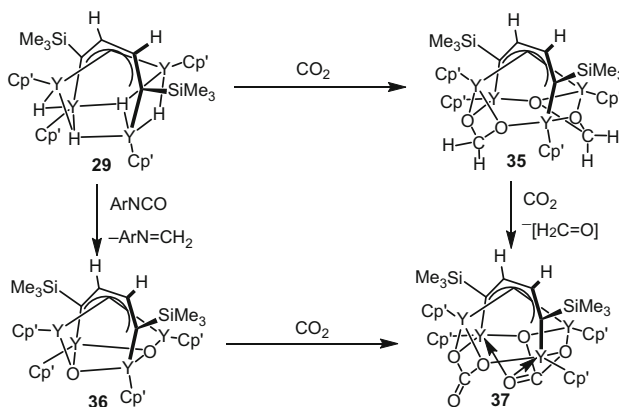
Scheme 17 Reactions of **29** with CO_2

3.3 Reactions with Nitriles

The reaction of the rare earth hydride clusters $[\{Cp'Ln(\mu\text{-}H)_2\}_4(THF)]$ (**2-Ln**) (Ln = Y, Lu) with 4 equiv. of benzonitrile gave the corresponding tetranuclear cubane-like imido clusters $[\{Cp'Ln(\mu_3\text{-}NCH_2Ph)\}_4]$ (Ln = Y, Lu) (**38-Ln**) (Scheme 18) [11]. In these reactions, the C≡N triple bond of the nitrile compound is completely reduced to a C–N single bond following double Ln–H addition. This is in contrast to the previously reported reduction of nitriles by rare earth metallocene hydride complexes or group 4 metallocene dihydride complexes, which afforded only single-insertion products.

The reaction of an excess amount of benzonitrile with the benzylimido clusters **38-Ln** gave the benzonitrile tetramerization products **40-Ln**, via the benzamidinate-dianion compound **39-Ln** (Scheme 18). The direct reaction of compound **39-Ln** with three equivalents of benzonitrile also gave **40-Ln** in high yield. These results indicate that **39-Ln** should be an intermediate in the formation of **40-Ln** from **38-Ln**. The one step reaction of **2-Y** with 14 equivalents of benzonitrile also yielded **40-Y**.

When an excess of benzonitrile was added to a toluene solution of **40-Ln**, the cyclotrimerization product of benzonitrile, namely triphenyl triazine $C_3N_3Ph_3$, was obtained selectively (Scheme 18). The recovery of **40-Ln** from the reactions confirms that the benzonitrile-tetramerized complex **40-Ln** is the active catalyst. The
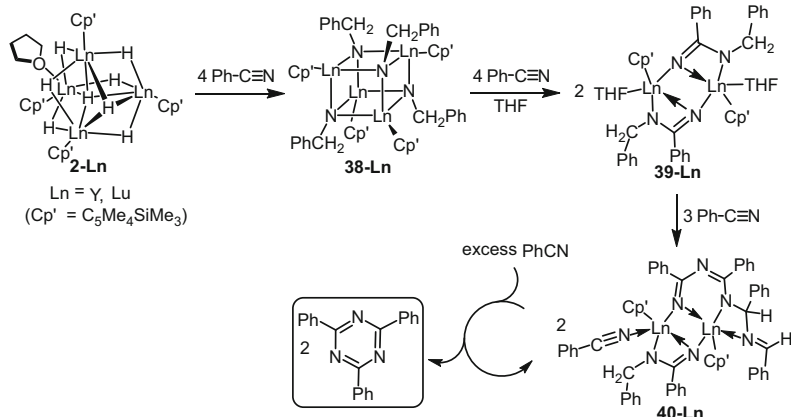
Scheme 18 Reactions of **2-Ln** with nitriles

polyhydride clusters [{Cp′Ln(μ-H)₂}₄(THF)] (**2-Ln**), the imido clusters **38-Ln**, and the benzamidinate-dianion compounds **39-Ln** are also active for the catalytic cyclotrimerization of benzonitrile [34].

3.4 Reactions with d-Transition Metal Carbonyl Complexes

The reduction of metal carbonyl complexes M(CO) by rare earth hydrides has hardly been studied. Until recently, the only precedent was the reaction of scandocene hydride complex [Cp*₂ScH(THF)] with [CpCo(CO)₂], which yielded the scandoxycarbene species [CpCo(CO)=CH–O–ScCp*₂] [35]. On the other hand, the reactions of the yttrium hydride cluster [{Cp′Y(μ-H)₂}₄(THF)] (**2-Y**) with various transition metal carbonyl complexes such as [Cp*W(CO)₂(NO)], [Cp*Ir(CO)₂], or [Cp*Rh(CO)₂] were examined, which afforded selectively oxycarbene/oxymethyl (**41**), oxo/carbene/methyl (**42**), or oxo/methyl (**43**) clusters, with the reaction patterns being dependent on the nature of the transition metal carbonyls (Scheme 19) [36]. In the reaction of **2-Y** with [Cp*Rh(CO)₂], two C≡O triple bonds of the carbonyl ligands were completely reduced and cleaved by addition of six Y–H bonds from **2-Y**. These reactions not only provide a novel series of heteromultimetallic clusters bearing a robust tetranuclear yttrium frame, but they can also afford the mechanistic aspects of the Fischer–Tropsch synthesis, which involves the hydrogenation of CO in the presence of transition metal catalysts.

3.5 Reactions with d-Transition Metal Hydrides

Heteromultimetallic hydride clusters containing both d-transition metals and rare-earth metals (including f-block metals) are of substantial interest, since they may
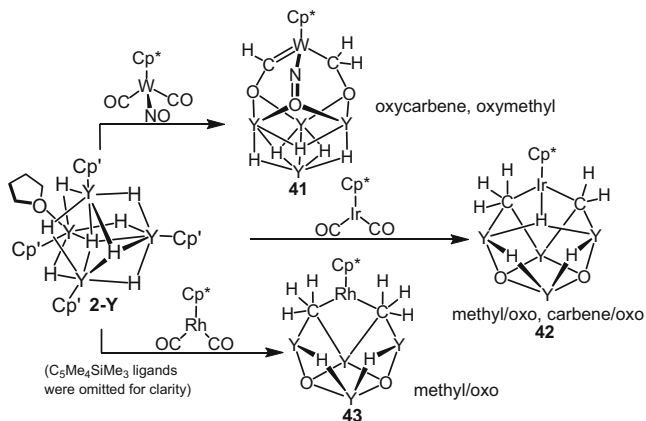
Scheme 19 Reactions of **2-Y** with transition metal carbonyl complexes

demonstrate unique reactivity as a result of the multimetallic synergistic effect between the two substantially different metal types. Well-defined hydride clusters of this type are also of great interest as molecular models for hydrogen storage alloys such as LaNi$_5$. However, such heteromultimetallic clusters have not yet been deeply explored due to difficulty in their synthesis and structural characterization. The reaction of the yttrium hydride cluster [{Cp$'$Y(μ-H)$_2$}$_4$(THF)] (**2-Y**) with the molybdenum hydride [Cp*Mo(PMe$_3$)H$_5$] easily afforded the corresponding heteromultimetallic polyhydride cluster [(Cp$'$Y)$_4$(μ-H)$_{11}$MoCp*] (**44**) (Scheme 20a) [37]. Cluster **44** released one H$_2$ molecule under vacuum condition to give a new cluster [(Cp$'$Y)$_4$(μ-H)$_9$MoCp*] (**45**). Unprecedented structural features including a trigonal bipyramidal μ_5-H atom in **44** and unique reactivities such as hydrogen addition/release reactions between **44** and **45** have been clarified. Monitoring of H$_2$ addition to the cluster **45** in a single-crystal-to-single-crystal process by X-ray diffraction has been achieved (Scheme 20b) [37]. Density functional theory (DFT) studies have demonstrated that the hydrogen addition process is cooperatively promoted by the Y/Mo heteromultimetallic sites, thus offering unprecedented insight into the hydrogen addition and release process of metal-hydride clusters.

Changing the steric bulk of the ancillary ligands on the Y atom could also allow the construction of the corresponding heteromultimetallic hydride clusters in the reaction with [Cp*Mo(PMe$_3$)H$_5$]. The structural features and hydrogen uptake and release properties of the resulting heteromultimetallic hydride clusters are significantly influenced by the supporting ligands. The reaction of the C$_5$Me$_4$H-ligated tetranuclear yttrium hydride cluster **6** (see Sect. 2.1) with [Cp*Mo(PMe$_3$)H$_5$] afforded a hexanuclear heterometallic hydride cluster **46** consisting of 4 yttrium, 2 molybdenum, and 14 hydride ligands (Scheme 21) [38]. Cluster **46** released two

a)

b)
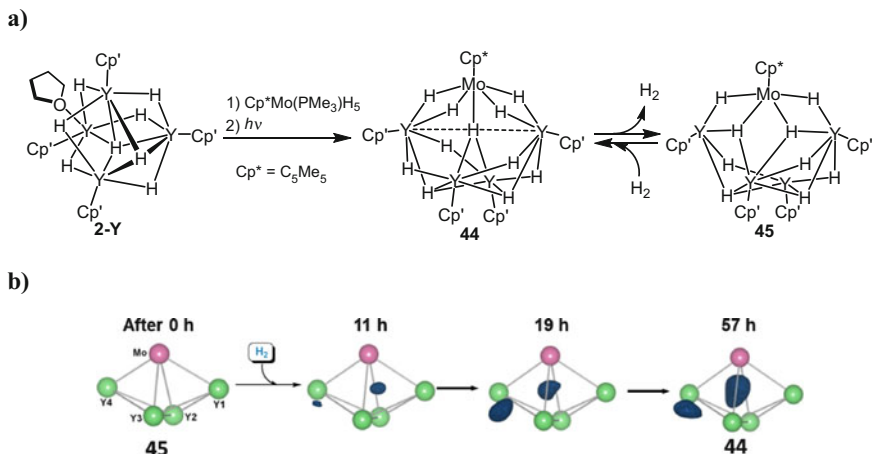
Scheme 20 (**a**) Synthesis of the d-f heteromultimetallic hydride cluster **44** by the reaction of **2-Y** with the molybdenum hydride complex Cp*Mo(PMe$_3$)H$_5$, and its reversible H$_2$ release and uptake. (**b**) X-ray monitoring of the solid **45** with H$_2$ in a single-crystal to single-crystal process. Gradual increase of the electron density in the metal frame is observed, which represents the formation of the hydride ligands through H$_2$ addition to **45**
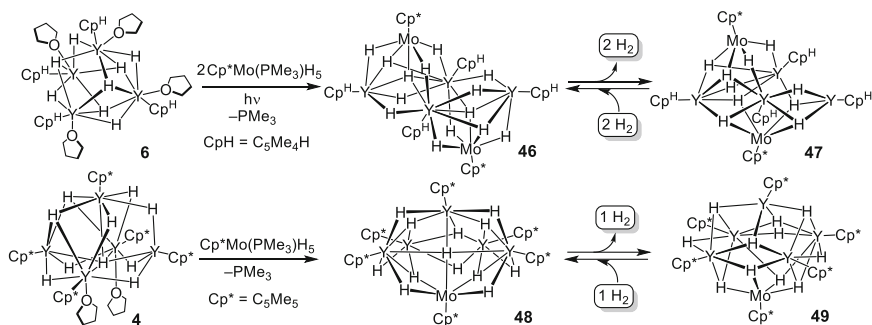
Scheme 21 Synthesis and reversible H$_2$ release/uptake of d-f heteromultimetallic hydride clusters

molecules of H$_2$ to give a new hydride cluster **47**, which could take up two molecules of H$_2$ to regenerate **46**. On the other hand, the reaction of the Cp*-ligated pentanuclear yttrium hydride cluster **4** with [Cp*Mo(PMe$_3$)H$_5$] afforded a d-f heterometallic hydride cluster **48** containing 5 yttrium, 1 molybdenum, and 11 hydride ligands (Scheme 21). Cluster **48** could lose only one molecule of H$_2$ and gave **49**. Addition of one molecule of H$_2$ to **49** could easily regenerate **48**.

4   Synthesis and Reactivity of Cationic Rare Earth Hydride Clusters

Cationic rare earth hydride clusters differ in their structure and reactivity from their neutral analogues. However, cationic clusters of this type have not been extensively studied. The reaction of the cyclopentadienyl-ligated yttrium octahydride cluster $[\{Cp'Y(\mu\text{-}H)_2\}_4]$ (**2-Y'**) with one equivalent of $[Ph_3C][B(C_6F_5)_4]$ afforded the structurally characterized cationic heptahydride cluster, $[(Cp'Y)_4(\mu\text{-}H)_7]$ $[B(C_6F_5)_4]$ (**50**), in which a bonding interaction between one of the yttrium atoms in the $[Cp'_4Y_4H_7]^+$ cation and one fluorine atom in the $[B(C_6F_5)_4]^-$ anion is observed (Scheme 22). This is the first example of a well-defined cationic rare earth hydride cluster [30]. The cationic cluster **50** or the in-situ combination of **2-Y'** and $[Ph_3C][B(C_6F_5)_4]$ showed moderate activity for the regiospecific polymerization of either 1,3-cyclohexadiene or styrene (Scheme 22). This is in contrast with the reactions of the neutral hydride **2-Y** or **2-Y'** with 1,3-cyclohexadiene and styrene, which gave only the 1:1 addition products **28** and **27**, respectively.

The reaction of the PNP-ligated trinuclear rare earth hydride cluster $[\{(Me\text{-}PNP^{iPr})$ $Ln(\mu\text{-}H)_2\}_3]$ (**21-Ln**) (see Sect. 2.5) with one equiv. of $[NEt_3H][BPh_4]$ afforded the cationic pentahydride cluster $[(Me\text{-}PNP^{iPr})_3Ln_3(\mu\text{-}H)_5][BPh_4]$ (**51-Ln**). Hydrogenolysis of the dialkyl complex $[(Me\text{-}PNP^{iPr})Ln(CH_2SiMe_3)_2]$ (**20-Ln**) with H_2 in the presence of 0.5 equiv. of $[NEt_3H][BPh_4]$ provided the cationic rare earth binuclear trihydride clusters $[(Me\text{-}PNP^{iPr})_2Ln_2(\mu\text{-}H)_3(THF)_2][BPh_4]$ (**52-Ln**) (Scheme 23). This is in sharp contrast with the hydrogenolysis of **20-Ln** in the absence of $[NEt_3H][BPh_4]$, which yielded the neutral hydride cluster **21-Ln** (see Scheme 9). The binuclear trihydride clusters **52-Ln** could be viewed as a combination of a monomeric dihydride "$(Me\text{-}PNP^{iPr})LnH_2$" and a cationic monohydride "$[(Me\text{-}PNP^{iPr})LnH]^+$" species.

Protonation of the amidopyridinate-ligated trinuclear alkyl/hydride cluster $[(Ap^*Y)_3(\mu\text{-}H)_5(CH_2SiMe_3)(THF)_2]$ (**24-Y**) with $[NHMe_2Ph][B(C_6F_5)_4]$ afforded an alkyl-free cationic pentahydride cluster **53**, in which the core structure Y_3H_5
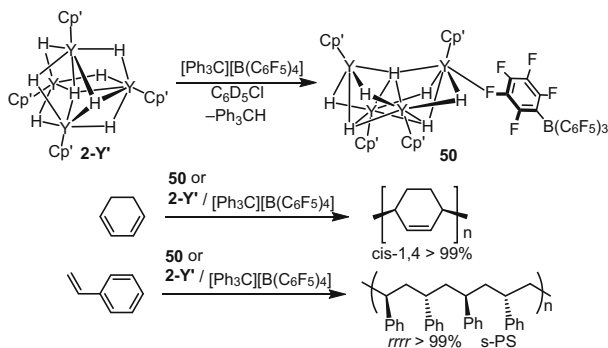
Scheme 22   Synthesis of a cationic yttrium hydride cluster **50** and its catalysis for the polymerization of 1,3-cyclohexadiene and styrene
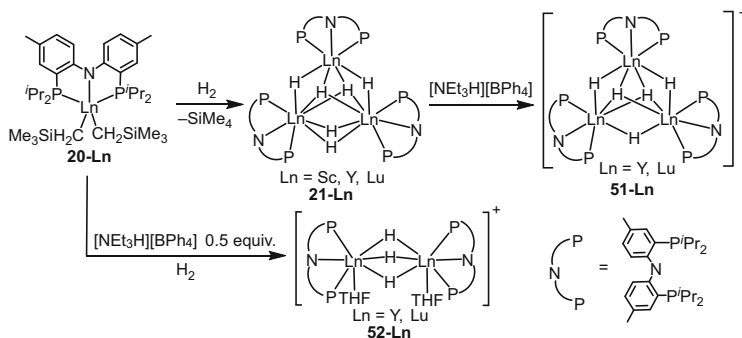
Scheme 23 Synthesis of cationic di- and trinuclear rare-earth metal-hydride clusters **51-Ln** and **52-Ln** bearing PNP ligands
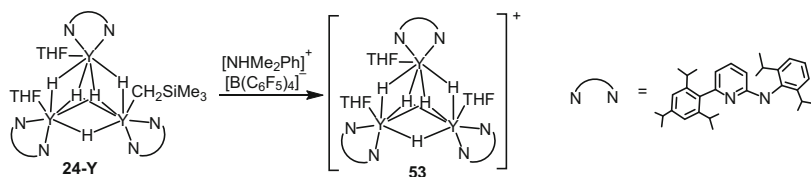
Scheme 24 Synthesis of a monocationic yttrium hydride cluster **53** bearing an amidopyridinate ligands

resembles that found in $[(\text{Me-PNP}^{i\text{Pr}}\text{Y})_3(\mu\text{-H})_5]^+$(**51-Y**) (Scheme 24) [39]. DFT calculations on the neutral cluster **24-Y** demonstrate that the Y–alkyl bond should possess enhanced reactivity compared to the Y–H bonds, thus accounting for the observation that the reaction occurred selectively through protonolysis of the Y–C bond rather than the Y–H bond.

Although hydrogenolysis of the cationic alkyl precursors such as $[\text{Cp}'\text{Ln}(\text{CH}_2\text{SiMe}_3)]^+$ and $[(\text{Me-PNP}^{i\text{Pr}})\text{Ln}(\text{CH}_2\text{SiMe}_3)]^+$ did not give a characterizable cationic hydride species, the hydrogenolysis of the amidinate-ligated cationic alkyl species $[(\text{NCN})\text{Y}(\text{CH}_2\text{SiMe}_3)(\text{THF})_3]^+$ (**54**) ($\text{NCN} = \text{PhC}(\text{NC}_6\text{H}_3{}^i\text{Pr}_2\text{-2,6})_2$), generated in situ from the reaction of the dialkyl precursor **25** with 1 equiv. of $[\text{NEt}_3\text{H}][\text{BPh}_4]$, afforded a cationic terminal hydride compound $[(\text{NCN})\text{YH}(\text{THF})_3]^+$ (**55**) in good yield. Crystallization from a chlorobenzene solution provided the dicationic dihydride species $[\{(\text{NCN})\text{YH}(\text{THF})_2\}_2]^{2+}$ (**56**), while dissolution of this dimer in THF quantitatively regenerated the monomeric hydride **55** (Scheme 25) [40].

In a manner similar to the synthesis of the cationic hydride compound **55**, hydrogenolysis of the macrocyclic [NNNN]-ligated cationic dialkyl precursor $[(\text{Me}_4\text{TACD})\text{Lu}(\text{CH}_2\text{SiMe}_3)_2]^+$(**57**) ($\text{Me}_4\text{TACD} = 1,4,7,10\text{-tetramethyl-}1,4,7,10\text{-tetraazacyclododecane}$) with H_2 afforded the cationic bimetallic lutetium tetrahydride cluster $[(\text{Me}_4\text{TACD})\text{Lu}(\mu\text{-H})_4\text{Lu}(\text{Me}_4\text{TACD})]^{2+}$ (**58**). One of the methyl substituents on the Me_4TACD ligand in **58** was found to undergo
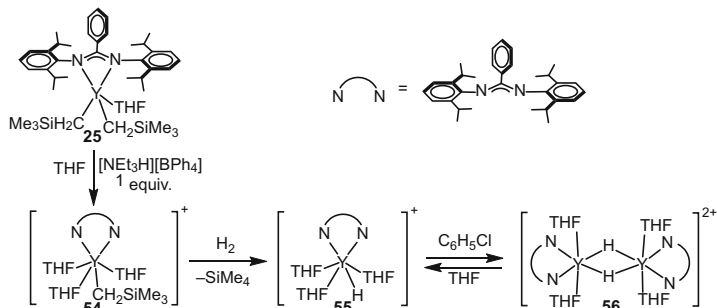
Scheme 25 Synthesis of a cationic terminal hydride compound **55** bearing an amidinate ligand and the interconversion between monomeric (**55**) and dimeric (**56**) yttrium hydrides
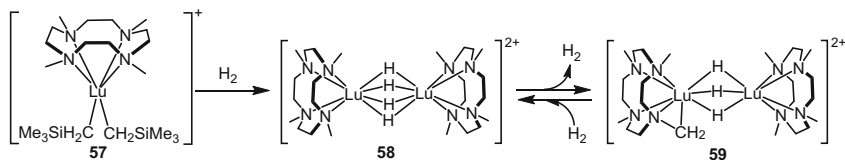
Scheme 26 Synthesis of dicationic lutetium hydride clusters and its reversible hydrogen uptake and release

dehydrogenative C–H bond activation with Lu–H bond to give the cyclometalated trihydride **59** and one H_2 molecule. This species undergoes reversible H_2 uptake to regenerate the tetrahydride **58** under H_2 atmosphere (Scheme 26) [41].

5 Concluding Remarks and Outlook

Polynuclear rare earth hydride clusters with well-defined molecular structures can be obtained by hydrogenolysis of the dialkyl precursors bearing one anionic ancillary ligand such as $C_5Me_4SiMe_3$ per metal, through self-assembly of the resulting dihydride species. By using these hydride clusters as a building block, novel heteromultimetallic hydride clusters can also be prepared. It is now clear that the rare earth hydride clusters bearing one anionic ancillary ligand per metal can show more diverse and richer chemistry than those of monohydride relatives with two anionic ancillary ligands such as conventional metallocene compounds, because of the cooperation of multiple metals and hydrides. Recently, remarkable progress was found in the synthesis and chemistry of the analogous group 4 transition metal-hydride clusters bearing the $C_5Me_4SiMe_3$ ligands, which showed unique reactivity for the activation of inert molecules such as N_2 [42] and benzene [43]. As more hydride clusters are prepared and further investigations proceed, the diverse chemistry and applications available from rare earth and other transition metal

elements will definitely be further extended. An exciting and rich future in this area can be expected.

References

1. Evans WJ, Atwood JL et al (1982) Organolanthanide hydride chemistry. 1. Synthesis and X-ray crystallographic characterization of dimeric organolanthanide and organoyttrium hydride complexes. J Am Chem Soc 104:2008–2014
2. Marks TJ et al (1985) Highly reactive organolanthanides. Systematic routes to and olefin chemistry of early and late bis(pentamethylcyclopentadienyl) 4f hydrocarbyl and hydride complexes. J Am Chem Soc 107:8091–8103
3. Bercaw JE et al (1987) σ-Bond metathesis for C-H bonds of hydrocarbons and Sc-R (R = H, alkyl, aryl) bonds of permethylscandocene derivatives. Evidence for noninvolvement of the π system in electrophilic activation of aromatic and vinylic C-H bonds. J Am Chem Soc 109:203–219
4. Den Haan KH, Wielstra Y, Teuben JH (1987) Reaction of yttrium-carbon bonds with active hydrogen-containing molecules. A useful synthetic method for permethylyttrocene derivatives. Organometallics 6:2053–2060
5. Nishiura M, Hou Z (2011) Novel polymerization catalysts and hydride clusters from rare-earth metal dialkyls. Nat Chem 2:257–268
6. Fegler W, Okuda J et al (2015) Molecular rare-earth-metal hydrides in non-cyclopentadienyl environments. Angew Chem Int Ed 54:1724–1736
7. Nishiura M, Hou Z (2010) Half-sandwich rare earth metal complexes as novel catalysts for olefin polymerization and other chemical transformations. Bull Chem Soc Jpn 83:595–608
8. Nishiura M, Guo F, Hou Z (2015) Half-sandwich rare-earth-catalyzed olefin polymerization, carbometalation, and hydroarylation. Acc Chem Res 48:2209–2220
9. Hou Z, Nishiura M, Shima T (2007) Synthesis and reactions of polynuclear polyhydrido rare earth metal complexes containing "(C$_5$Me$_4$SiMe$_3$)LnH$_2$" units: a new frontier in rare earth metal hydride chemistry. Eur J Inorg Chem 2007:2535–2545
10. Nishiura M, Hou Z et al (2011) Synthesis and structures of the C$_5$Me$_4$SiMe$_3$-supported polyhydride complexes over the full size range of the rare earth series. Chem Eur J 17:5033–5044
11. Cui D, Tardif O, Hou Z (2004) Tetranuclear rare earth metal polyhydrido complexes composed of "(C$_5$Me$_4$SiMe$_3$)LnH$_2$" units. Unique reactivities toward unsaturated C-C, C-N, and C-O bonds. J Am Chem Soc 126:1312–1313
12. Tardif O, Nishiura M, Hou Z (2003) Isolation and structural characterization of a polyhydrido lanthanide cluster complex consisting of "(C$_5$Me$_4$SiMe$_3$)LuH$_2$" units. Organometallics 22:1171–1173
13. Hultzsch K, Spaniol TP, Okuda J (1999) Half-sandwich alkyl and hydrido complexes of yttrium: convenient synthesis and polymerization catalysis of polar monomers. Angew Chem Int Ed 38:227–230
14. Hou Z, Wakatsuki Y et al (2001) (Pentamethylcyclopentadienyl)samarium(II) alkyl complex with the neutral "C$_5$Me$_5$K" ligand: a precursor to the first dihydrido lanthanide(III) complex and a precursor for hydrosilylation of olefins. J Am Chem Soc 123:9216–9217
15. van der Heijden H, Schaverien CJ, Orpen AG et al (1989) Neutral monocyclopentadienyllutetium alkyls: in search of steric unsaturation. Organometallics 8:1459–1467
16. Shima T, Nishiura M, Hou Z (2011) Tetra-, penta-, and hexanuclear yttrium hydride clusters from half-sandwich bis(aminobenzyl) complexes containing various cyclopentadienyl ligands. Organometallics 30:2513–2524

17. Shima T, Hou Z (2008) Activation and dehydrogenative silylation of the C–H bonds of phosphine-coordinated ruthenium in Lu/Ru heteromultimetallic hydride complexes. Chem Lett 37:298–299
18. Shima T, Hou Z (2009) Rare earth/d-transition metal heteromultimetallic polyhydride complexes based on half-sandwich rare earth moieties. Organometallics 28:2244–2252
19. Cheng J, Ferguson MJ, Takats J (2010) Synthesis and reaction of [(Tp^{iPr2})LnH$_2$]$_3$ (Ln = Y, Lu) with CO: trinuclear cluster-bound propenolate en route to selective formation of propene. J Am Chem Soc 132:2–3
20. Cheng J, Takats J et al (2008) Scorpionate-supported dialkyl and dihydride lanthanide complexes: ligand- and solvent-dependent cluster hydride formation. Angew Chem Int Ed 47:4910–4913
21. Johnson KRD, Kamenz BL, Hayes PG (2014) Bis(pyrazolyl)carbazole as a versatile ligand for supporting lutetium alkyl and hydride complexes. Organometallics 33:3005–3011
22. Ohashi M, Okuda J et al (2008) Rare-earth metal alkyl and hydride complexes stabilized by a cyclen-derived [NNNN] macrocyclic ancillary ligand. J Am Chem Soc 130:6920–6921
23. Abinet E, Okuda J et al (2011) Rare-earth metal allyl and hydrido complexes supported by an (NNNN)-type macrocyclic ligand: synthesis, structure, and reactivity toward biomass-derived furanics. Chem Eur J 17:15014–15026
24. Martin D, Okuda J et al (2013) Hydrido and allyl/hydrido complexes of early lanthanides supported by an NNNN-type macrocyclic ligand. Eur J Inorg Chem 2013:3987–3992
25. Cheng J, Shima T, Hou Z (2011) Rare-earth polyhydride complexes bearing bis (phosphinophenyl)amido pincer ligands. Angew Chem Int Ed 50:1857–1860
26. Wylie WNO, Hou Z et al (2014) PNP-ligated heterometallic rare-earth/ruthenium hydride complexes bearing phosphinophenyl and phosphinomethyl bridging ligands. Organometallics 33:1030–1043
27. Lyubov DM, Kempe R, Trifonov AA et al (2008) Selective assembly of trinuclear rare-earth alkyl hydrido clusters supported by amidopyridinate ligands. Organometallics 27:2905–2907
28. Lyubov DM, Trifonov AA et al (2014) Trinuclear alkyl hydrido rare-earth complexes supported by amidopyridinato ligands: synthesis, structures, C–Si bond activation and catalytic activity in ethylene polymerization. Dalton Trans 43:14450–14460
29. Cheng J, Hou Z et al (2012) Binuclear rare-earth polyhydride complexes bearing both terminal and bridging hydride ligands. Chem Sci 3:2230–2233
30. Li X, Baldamus J, Hou Z et al (2006) Cationic rare-earth polyhydrido complexes: synthesis, structure, and catalytic activity for the cis 1,4-selective polymerization of 1,3-cyclohexadiene. Angew Chem Int Ed 45:8184–8188
31. Ferrence GM, McDonald R, Takats J (1999) Stabilization of a discrete lanthanide(II) hydrido complex by a bulky hydrotris(pyrazolyl)borate ligand. Angew Chem Int Ed 38:2233–2237
32. Shima T, Hou Z (2006) Hydrogenation of carbon monoxide by tetranuclear rare earth metal polyhydrido complexes. Selective formation of ethylene and isolation of well-defined polyoxo rare earth metal clusters. J Am Chem Soc 128:8124–8125
33. Tardif O, Hashizume D, Hou Z (2004) Hydrogenation of carbon dioxide and aryl isocyanates by a tetranuclear tetrahydrido yttrium complex. Isolation, structures, and CO$_2$-insertion reactions of methylene diolate and 3-oxo yttrium complexes. J Am Chem Soc 126:8080–8081
34. Cui D, Nishiura M, Hou Z (2005) Lanthanide–imido complexes and their reactions with benzonitrile. Angew Chem Int Ed 44:959–961
35. St. Clair MA, Santarsiero BD, Bercaw JE (1989) Addition of scandium-hydrogen, scandium-carbon, and scandium-nitrogen bonds to coordinated carbon monoxide. Structure of a methylscandoxycarbene derivative of cobalt. Organometallics 8:17–22
36. Takenaka Y, Shima T, Hou Z et al (2009) Reduction of transition-metal-coordinated carbon monoxide by a rare-earth hydride cluster: isolation of well-defined heteromultimetallic oxycarbene, oxymethyl, carbene, and methyl complexes. Angew Chem Int Ed 48:7888–7891
37. Shima T, Luo Y, Hou Z et al (2011) Molecular heterometallic hydride clusters composed of rare-earth and d-transition metals. Nat Chem 3:814–820

38. Shima T, Hou Z (2013) Heterometallic polyhydride complexes containing yttrium hydrides with different Cp ligands: synthesis, structure, and hydrogen-uptake/release properties. Chem Eur J 19:3458–3466
39. Lyubov DM, Kempe R, Trifonov AA et al (2011) Selective protonation of the Y–C bond in trinuclear yttrium alkyl-hydrido clusters and formation of the cationic polyhydrido core. Chem Eur J 17:3824–3826
40. Cheng J, Hou Z (2012) Cationic terminal hydrido rare earth complexes bearing an amidinate ancillary ligand. Chem Commun 48:814–816
41. Fegler W, Venugopal A, Okuda J et al (2013) Reversible dihydrogen activation in cationic rare-earth-metal polyhydride complexes. Angew Chem Int Ed 52:7976–7980
42. Shima T, Hu S, Hou Z et al (2013) Dinitrogen cleavage and hydrogenation by a trinuclear titanium polyhydride complex. Science 340:1549–1552
43. Hu S, Shima T, Hou Z (2014) Carbon-carbon bond cleavage and rearrangement of benzene by a trinuclear titanium hydride. Nature 512:413–415

Index